Collisionless magnetic reconnection in relativistic plasmas with particle-in-cell simulations

Mickaël Melzani

THÈSE

en vue de l'obtention du grade de
Docteur de l'Université de Lyon, délivré par l'École Normale Supérieure de Lyon

Discipline : physique

Laboratoire : Centre de Recherche Astrophysique de Lyon

École doctorale : Physique et Astrophysique de Lyon

Présentée et soutenue publiquement le 5 novembre 2014
par
Monsieur Mickaël Melzani

Reconnexion magnétique non-collisionelle dans les plasmas relativistes et simulations particle-in-cell

---

Collisionless magnetic reconnection in relativistic plasmas with particle-in-cell simulations

---

Directeur de thèse :

M. Rolf Walder

Devant la commission d'examen formée de :

M. Gérard Belmont, Laboratoire de Physique des Plasmas (Palaiseau), Rapporteur
M. Mark Eric Dieckmann, Université de Linköping, Examinateur
M. Giovanni Lapenta, Université de Leuven, Rapporteur
M. Alexandre Marcowith, Laboratoire Univers et Particules (Montpellier), Examinateur
M. Guy Pelletier, Institut de Planétologie et d'Astrophysique (Grenoble), Examinateur
M. Rolf Walder, Centre de Recherche Astrophysique de Lyon, Directeur

Contents

Abstract

English

The purpose of this thesis is to study magnetic reconnection in collisionless and relativistic plasmas. Such plasmas can be encountered in various astrophysical objects (microquasars, AGNs, GRBs...), where reconnection could explain high-energy particle and photon production, plasma heating, or transient large-scale outflows. However, a first principle understanding of reconnection is still lacking, especially in relativistic ion-electron plasmas. We first present the basis of reconnection physics. We derive results relevant to relativistic plasma physics, including properties of the Maxwell-Jüttner distribution. Then, we provide a detailed study of our numerical tool, particle-in-cell simulations (PIC). The fact that the real plasma contains far less particles than the PIC plasma has important consequences concerning relaxation times or noise, that we describe. Finally, we study relativistic reconnection in ion-electron plasmas with PIC simulations. We stress outstanding properties: Ohm's law (dominated by bulk inertia), structure of the diffusion zone, energy content of the outflows (thermally dominated), reconnection rate (and its relativistic normalization). Ions and electrons produce power law distributions, with indexes that depend on the inflow Alfvén speed and on the magnetization of the corresponding species. They can be harder than those produced by collisionless shocks. Also, ions can get more or less energy than the electrons, depending on the guide field strength. These results provide a solid ground for astrophysical models that, up to now, assumed with no prior justification the existence of such distributions or of such ion/electron energy repartition.

Français

L'objectif de cette thèse est l'étude de la reconnexion magnétique dans les plasmas non-collisionels et relativistes. De tels plasmas sont présents dans divers objets astrophysiques (MQs, AGNs, GRBs...), où la reconnexion pourrait expliquer la production de particules et de radiation de haute énergie, un chauffage, ou des jets. Une compréhension fondamentale de la reconnexion n'est cependant toujours pas acquise, en particulier dans les plasmas relativistes ion-électron. Nous présentons d'abord les bases de la reconnexion magnétique. Nous démontrons des résultats particuliers à la physique des plasmas relativistes, concernant par exemple la distribution de Maxwell-Jüttner. Ensuite, nous réalisons une étude détaillée de l'outil numérique utilisé : les simulations particle-in-cell (PIC). Le fait que le plasma réel contienne beaucoup plus de particules que le plasma PIC a des conséquences importantes (collisionalité, relaxation, bruit) que nous décrivons. Enfin, nous étudions la reconnexion magnétique dans les plasmas ion-électron et relativistes à l'aide de simulations PIC. Nous soulignons des points spécifiques : loi d'Ohm (l'inertie de bulk dominante), zone de diffusion, taux de reconnexion (et sa normalisation relativiste). Les ions et les électrons produisent des lois de puissance, avec un index qui dépend de la vitesse d'Alfvén et de la magnétisation, et qui peut être plus dur que dans le cas des chocs non-collisionels. De plus, les ions peuvent avoir plus ou moins d'énergie que les électrons selon la valeur du champ guide. Ces résultats fournissent une base solide à des modèles d'objets astrophysiques qui, jusque là, supposaient a priori ces résultats.

Remerciements

Je remercie tout d'abord Rolf, pour m'avoir proposé cette thèse, pour m'avoir fait confiance, et pour avoir été toujours présent, prêt à donner avis et conseils. C'est lui qui a fait le pari d'aborder la thématique des phénomènes hors-équilibres dans les plasmas non-collisionels. C'est à partir de là que j'ai exploré la physique des chocs, puis de la reconnexion, pour aboutir aujourd'hui à ce manuscrit. Vu l'importance prise par ce sujet dans la communauté, et vu les avancées que notre petite équipe a effectuées depuis trois ans, c'est un pari largement réussi. Doris m'a également énormément aidé, par ses questions, ses critiques, et par ses relectures attentives. Merci à la SNCF d'assurer une liaison lente entre Genève et Lyon, afin d'offrir l'occasion à Doris de relire mes longs articles. Christophe a aussi contribué à mon travail par ses relectures, ses remarques et avis, et par ses questions sur le code qui, souvent, ont permis de trouver des bugs bien cachés ! L'équipe, c'est aussi Jean qui, depuis la Suisse, nous a aidé avec la visualisation des données. Sans lui, de grands pans de cette thèse n'auraient pas pu être réalisés (ou alors, beaucoup moins facilement !).

Je remercie tous mes professeurs – ceux dont j'ai suivi les cours, mais aussi ceux des livres – qui, depuis des années, m'ont fait découvrir et aimer la physique. Je pense en particulier à Odd Erik, Norvégien du bout du monde, avec qui j'ai réellement commencé la physique des plasmas. Être un scientifique signifie aussi connaître le monde de la recherche. J'ai pu apprendre ceci auprès de Rolf bien sûr, de Odd Erik, et en échangeant avec des chercheurs du monde entier lors de conférences ici ou là-bas. Je pense par exemple à Nicolas et à Benoît, qui ont su me communiquer leur enthousiasme pour la reconnexion.

Je remercie les deux rapporteurs, Gérard Belmont et Giovanni Lapenta, pour avoir accepté de lire mon manuscrit, ainsi que les membres du jury, Gérard Belmont, Giovanni Lapenta, Mark Eric Dieckmann, Alexandre Marcowith, et Guy Pelletier, pour venir m'écouter à Lyon. J'ai également profité des discussions avec des chercheurs venus nous rendre visite, Antoine Bret, Maria Elena Innocenti, Andrei Bykov, avec la plupart des membres du jury, et bien d'autres.

Je remercie les divers organismes de financement, PNPS, PNHE, CBP, et l'école doctorale PHAST et son directeur, qui m'ont permis de partager mes travaux dans diverses conférences ou d'en organiser à Lyon, ainsi que GENCI et la procédure DARI qui m'ont permis de calculer au CINES, à l'IDRIS et au CCRT. Pour compléter la liste des sigles, je dois également dire que l'ENS et le CRAL m'ont offert d'excellentes conditions de travail.

Les travaux présentés ici ont nécessité plus d'un million d'heures de calcul. Cela signifie plus d'un siècle sur un seul processeur mais, heureusement, le calcul parallèle existe. Je remercie les équipes responsables des machines sur lesquelles j'ai fait tourner mes simulations, au CINES, à l'IDRIS, au

CCRT, et ici à Lyon au PSMN, pour leurs réponses et leur aide technique. Que ceux qui veulent faire une thèse numérique soient prévenus : il faut être prêt à anticiper les coupures de courant, à toujours surveiller ses jobs, à trouver des moyens de transférer des fichiers de 3 TB chacun, ou à passer son code au crible pendant trois semaines pour découvrir qu'un `<` aurait du être un `<=`.

Mais tout ceci est possible grâce à la bonne humeur de l'équipe ENS, et je dois remercier tous les astronautes du CRAL que j'ai côtoyé pendant ces trois années. Jacques, montagnard fou, ou Christophe, ping-pongiste fou, en sont deux beaux exemples. Et il y a bien sûr les amis physiciens de l'autre coté du parking, toujours prêt à donner un coup de main, à partager un repas au fabuleux RU, ou, plus récemment, à venir me chercher pour faire des photos d'interférences !

Cette thèse a été l'occasion d'essayer l'enseignement. Je remercie les professeurs avec qui j'ai enseigné pour m'avoir accordé leur confiance, en particulier les géophysiciens Fabien, Vincent, Stéphane et Frédéric, ainsi que tous mes élèves pour avoir écouté avec autant d'attention. Et je pense à Nicolás, qui avec moi a évité de justesse les TP de cartographie ! J'ai également apprécié de travailler avec les stagiaires, Stefan, Paul, Laura, Pacôme, sur des histoires très instructives de photons dans des boîtes.

Je remercie enfin Charlotte, qui commence une thèse quand je finis la mienne (hélas, sur un sujet assez peu proche), en particulier pour ses attentives relectures.

Outline of the manuscript

The purpose of this thesis is to contribute to the understanding of magnetic field reconnection in relativistic and collisionless plasmas, with applications to relativistic outflow production, non-thermal particle acceleration, and high-energy radiation in the context of various high-energy astrophysical objects. The outline can be summarized as follows:

Chapter	Content and aim
1	Introduction.
2	Fundamentals of reconnection and state of the art. *Introductory chapter to the field.*
3	Elements of relativistic plasma physics. *Mostly technical, list of formula and tools.*
4 and 5	Presentation, tests of the PIC code. PIC against real plasma, effects of coarse-graining. *Include important results concerning PIC algorithms.* Mostly contain the article Melzani et al. (2013) (and its shorter version Melzani et al. 2014a).
6 and 7	Ion-electron relativistic reconnection with PIC simulations. *Main results of the manuscript.* Mostly contain, for respectively Chapter 6 and 7, the articles Melzani et al. (2014b,c).
8	Summary and perspectives.

In addition to the introduction (Chapter 1) and conclusion (Chapter 8), the manuscript is divided in four main parts, that we detail below.

The second chapter exposes the principles of magnetic reconnection and reviews the state of the art regarding this complex subject. Its first sections (from 2.2 to 2.7) are a pedagogic introduction to reconnection physics. They are mostly addressed to students or researchers new to the field. The remaining sections (from 2.8 to 2.14) are more advanced, and address the latest (and often still ongoing) developments on the subject. The chapter reviews many topics: large scale MHD motions, magnetic field geometries and their perturbations in 3D allowing reconnection, magnetic separatrices, dissipation zone and non-ideal microphysics, turbulence, and others.

It also invokes several examples in the Earth's and Sun's magnetospheres or in astrophysical objects. One of the aim of this variety is to underline that magnetic reconnection cannot be understood on the basis of one aspect only (such as 2D kinetic studies, 3D MHD simulations, observations, ...), but requires a knowledge of all of its facets. Indeed, large scale dynamics sets the geometry where the reconnection will start, and these geometries can be 2D-like or fully 3D and have to be known and understood. Only then kinetic studies can explore the properties of the reconnection itself, with kinetic effects possibly occurring on rather large scales (e.g., along magnetic separatrices). Energy conversion is then a key issue, and the heated plasma, the launched outflows, or the non-thermal particle populations, feedback on the large scale motions, sometimes in an essential way by providing the very source of heating or of outflow production at large scales.

The third chapter introduces notions and derives results concerning relativistic plasma dynamics. The aim is to gather relations or methods useful for relativistic plasma physics, that are often scattered in the literature. It may be of interest for researchers to pick up some results here. Part of the material presented is already known, part of it is new, including a relativistic Harris equilibrium for arbitrary mass and temperature ratios, expressions for the moments of Maxwell-Jüttner distribution, and a method to correctly load this distribution in a particle-in-cell code.

The fourth and fifth chapters are devoted to numerics: we study the tools – particle-in-cell (or PIC) algorithms – that we use to investigate magnetic reconnection. In Chapter 4, we detail the algorithm. There are several PIC methods available, and we believe that the interpretation of numerical results justifies a precise knowledge of the method employed and of its limits. We also conduct several validation tests, that will assert the validity of our results. In Chapter 5 we discuss the limits of the PIC method to describe a plasma, with an emphasis on the fact that the PIC plasma contains only a few particles per Debye sphere, while for the real plasma this number amounts to millions. This approximation has consequences on the thermalization times, the slowing-down time of fast particles, or on the level of fluctuations, that we explore quantitatively for the first time with a 3D electromagnetic PIC code. We underline that the artificially enhanced collisional physics must be kept negligible toward the collisionless processes. The conclusions help us to correctly conduct our numerical experiments.

The sixth and seventh chapters are the heart of this work, and represent our contribution to the understanding of magnetic reconnection. Armed with the previous parts, we explore reconnection in relativistic collisionless plasmas with PIC simulations, for the first time in the literature in an ion-electron plasma. Such plasmas are present in active galactic nuclei and microquasar disk coronae, in extragalactic jets, or possibly in microquasar jets and gamma-ray burst jets, where several key features remain unexplained and possibly linked to reconnection. As previously underlined, reconnection is a multi-scale subject for which each building block has to be understood. Here we concentrate on a two-dimensional setup, simulated around the central dissipation region (and not, e.g., along extended separatrices). This is motivated by the large values reached by the reconnection electric field in relativistic reconnection, so that the central area is expected to produce high-energy particle populations. Chapter 6 explores the specific aspects of relativistic reconnection. In particular, we show that at

relativistic inflow magnetization, bulk inertia dominates in Ohm's law, and the outflows are thermally dominated. We also study the reconnection rate and the diffusion region structure, with the evidence for sharp transitions at low beta. Chapter 7 focuses on the energetics of the reconnection event. We show that particles from the background plasma form power law distributions as soon as the inflow plasma magnetization is larger than unity and that the inflow Alfvén speed is mildly relativistic. These two parameters also control the hardness of the distribution, that can be harder as compared to collisionless shocks. This holds for ions and for electrons. We also study the energy repartition between ions and electrons, and show that it is mainly influenced by the guide field strength, with ions getting more energy than electrons at low values, and vice versa at higher values. Finally, we draw some conclusions regarding astrophysical applications, where power law indexes and ion-electron energy repartition are key parameters.

Chapter 1

Introduction

> *This reminds him of the way blood plasma carries around red and white corpuscles and germs. So he proposed to call our "uniform discharge" a "plasma". Of course we all agreed.*
>
> Mott-Smith (1971), referring to Irving Langmuir coining the word plasma in 1927

Contents

In this introductory chapter, we first expose the reasons that led us to study magnetic reconnection in relativistic ion-electron plasmas and to focus on the central non-ideal dissipation region (Sect. 1.1). We then briefly explain the basic idea of reconnection, showing that particle-in-cell algorithms are well suited in this case (Sect. 1.2). We next turn to an overview of environments where reconnection is a key player (Sect. 1.3), and we detail in Appendix 1.A the orders of magnitude of the plasma parameters encountered in these objects.

1.1 Motivation of the present study

Magnetic reconnection occurs in man-made plasmas like those of tokamaks or inertial fusion devices, in natural plasmas as close as our magnetosphere, 200 km above the surface of the Earth, and as far as in gamma-ray bursts looming at the edge of the observable universe. It is a fundamental plasma process, a key element to many plasma dynamical evolutions.

Intuitively, magnetic reconnection happens when two magnetic field lines are pushed together, cut at their intersection point, and reconnected with one another. Reconnection has been an active area of research since its introduction by Giovanelli (1947, 1948) to explain the sudden release of energy in solar flares. The change of field line connectivity involves magnetic flux variations and induced electric fields, that convert magnetic energy into particle kinetic energy, either heat, bulk motion, or high-energy non-thermal particles. The amount of energy channeled in each of these three components, the rate at which the transfer occurs, the spectrum of the

possible non-thermal component, the velocity of the ejected bulk flows, the conditions allowing reconnection to happen, especially in 3D geometries, or the back-coupling of reconnection events to large scales, are all questions that are still being actively investigated and to which, for a few of them and for some regimes, we want to provide answers.

Magnetic field reconnection was first applied to space physics, i.e., to a variety of phenomena taking place in the Earth's magnetosphere and in the Sun's heliosphere: magnetic storms and substorms, coronal heating, solar flares, coronal mass ejections, solar jets, and so on. It is also a key element in man-made machines such as tokamaks, and is studied in dedicated experiments. Inspired by its success in space and solar physics, reconnection was later used in high-energy astrophysics because whenever magnetic energy is present in large amounts, it is a way to quickly produce high-energy particles and radiation in flare-like events, as observed in pulsar wind nebulae, extragalactic jets, microquasars or gamma-ray bursts, or to heat the corona formed above dense objects such as the accretion disks of X-ray binaries and of active galactic nuclei, or to launch transient large scale outflows like possibly in microquasars and gamma-ray bursts.

The plasmas of these high-energy objects often feature a magnetization larger than unity, which means that there is more energy in the magnetic field than in the particles' restmass. The transfer of magnetic energy can consequently produce relativistic particles, and reconnection in such regimes is termed *relativistic reconnection*. There is a lack of first principle studies in these regimes. Questions such as whether reconnection exhibits specific aspects when relativistic, or regarding the hardness of the particle distributions at high-energies, remain open. In addition, all the presently existing studies of relativistic reconnection concern pair plasmas (see the references of Sects. 6.2 and 7.2), but ion-electron relativistic plasmas are expected for instance in microquasar coronae, or to some extent in microquasar jets, extragalactic jets, gamma-ray bursts, or radio galaxy lobes. In particular, the questions of the energy distribution between ions and electrons, as well as the possibility to produce high-energy ions, are very relevant. This is why we mostly focus on such plasmas.

One of the most challenging issue regarding reconnection is its multiscale nature, both in time and space. In a given environment, large scale dynamics set the stage for reconnection events to take place. How often and with which magnetic geometry is a first question. Reconnection events then take place locally. What is the outcome of these individual events, in terms of energy distribution and timescale, is another question, which now involves microphysical scales. In return, the small scale reconnection events have a dramatic influence on the large scales, by changing the field line connectivity, thus allowing the magnetic field to be rearranged to a different, lower energy state. The result is global plasma heating, large scale motions and outflows, or out-of-equilibrium particle populations significantly contributing to the plasma dynamics. Even the small scale reconnection events are expected to imply a large range of spatial and temporal scales, with energy conversion occurring both around the central non-ideal region and further downstream along the magnetic separatrices. All these questions cannot be addressed at once, and should first be understood separately. In the present work we choose to restrict ourselves to collisionless ion-electron plasmas, to 2D setups, and to the physics at and around the central non-

ideal region. The choice of this location is justified by the fact that the reconnection electric field induced in the central non-ideal region, compared to the magnetic field, is all the more strong than the inflow Alfvén speed is large (Eq. 6.14). When the latter is relativistic, large electric to magnetic field ratios are reached, which leads to extended non-ideal regions, and to significant non-thermal high-energy particle production. Of course, energy conversion at other locations, especially along the separatrices, should also be investigated.

1.2 Basic principles

In order to better understand the whys and hows of the present work, it is necessary to briefly expose the basic principles of magnetic reconnection and of particle-in-cell algorithms.

The fundamental principle for the triggering of magnetic reconnection is that magnetic field flux variations induce, via Faraday's equation, electric fields. These induced electric fields imply a response from the plasma, that tries to screen it. An ideal plasma (where the electrons are massless, never collide, ...) does so perfectly, and the currents arising from charges set in motion by these electric fields produce magnetic fields that cancel the former magnetic flux variations: reconnection cannot occur, magnetic field lines cannot break apart. Non-ideal effects are thus needed for reconnection to initiate. Once initiated, these same non-ideal processes sustain the finite reconnection electric field and allow reconnection to go on. It is remarkable that slow and large scale motions of the ideal plasma can move the magnetic field to produce metastable configurations, where non-idealness becomes important. The system then relaxes its energy during explosive reconnection events where, due to field line breaking, the magnetic field can be rearranged on large scales and can reach lower-energy states with a transfer of the previously stored magnetic energy to the plasma (see Fig. 2.1).

The first non-ideal effect advocated in the pioneering works of Sweet (1958) and Parker (1957, 1963) was ion-electron collisions, i.e., a finite resistivity. It was however realized at the same time that collisional resistivity results in very slow reconnection events, much too slow to explain the fast energy release seen in solar flares. Fast reconnection was thus sought. Petschek (1964) model, and its extensions by Priest and Forbes (1986) (see Priest 2011), provided faster rates, but were theories of the outer ideal zone surrounding a very localized non-ideal zone with a non-ideal mechanism unspecified. Whether they hold in real plasmas and under which conditions was not clear.

Since the environments quoted above are nearly or completely collisionless, the question of fast reconnection in collisionless plasmas was opened[a]. Important advances were allowed by the rising computer power available to conduct numerical simulations. Among the different numerical methods, particle-in-cell simulations were maybe the ones that produced the most interesting results. They are still actively in use today, and it is by means of such simulations that we will investigate magnetic reconnection in Chapters 6 and 7.

[a]The question of fast reconnection in collisional environments, such as observed in the solar chromosphere, is also not settled.

Particle-in-cell (PIC) codes are in use since 1965, and consist in simulating the trajectories of particles subjected to the Lorentz force, with electric and magnetic fields stored on a grid and computed from the particles themselves. As every model, it comes with approximations that have to be well understood and controlled. The two main ones for PIC models are field storage on a grid, which implies that particles have a finite size equal to that of the grid, and coarse-graining. The latter stems from the limited capabilities of computers that can handle only up to 10^{10} particles, while real plasmas comprise up to 10^{20} real particles per Debye sphere: each computer particle actually represents a large number of real particles. The effects of coarse-graining and the differences between real, PIC and Vlasov plasmas are explored in Chapter 5. We first present and test our own code in Chapter 4.

The plasmas we are interested in are collisionless plasmas. What does collisionless exactly means? In these plasmas, the mean distance traveled by a particle between two collisions vastly exceeds the relevant lengths of the system or of the physical process studied (system size, gradient scales, wavelengths, instability scales, microphysical scales, ...). Particle interactions then occur through the electric and magnetic fields in a collective way: one particle interacts with the fields generated by many others. Correlations between smaller numbers of particles can also happen, and complicate things. Collisionless plasmas are complex systems, highly non-linear, where a whole zoo of waves and instabilities have been discovered. It has been found that shocks can form and live without collisions, that waves can be damped by collisionless dissipation, and that reconnection can happen without collisional resistivity.

The mean time between two collisions is given by the plasma period times the plasma parameter Λ[b], where Λ is the number of particles per Debye sphere, so that plasmas with large Λ are likely to be collisionless[c]. A large Λ also implies a small level of correlation between particles. Figure 1.1 summarizes the value of Λ for several objects, and gives an idea of which objects hold collisionless plasmas. Magnetic reconnection is important in almost all of them.

1.3 An (incomplete) account of magnetic reconnection applications

We now give an overview of the variety of environments filled by collisionless plasmas and of the importance of magnetic reconnection. The discussion is more general and historical than technical – orders of magnitude are drawn in Fig. 1.1, and many details can be found in the references (including those of the figure in Appendix 1.A).

[b] Actually, it takes less time to deviate a particle by 90° by many grazing collisions, than by a single large angle collision. The 90° collision time so defined is $\Lambda/\log\Lambda$ times the plasma period. However, we neglect the contribution of the Coulomb logarithm $\log\Lambda$ for the present discussion.

[c] But a large Λ does not guarantee the plasma to be collisionless. A large Λ is an intrinsic property of the plasma, while collisionless behavior is defined via comparison with other time- and length-scales. For example, the collisionless nature of magnetic reconnection does not depend only on Λ, but on the thickness of the current sheet compared to kinetic lengths (this is the subject of Sect. 2.11.3).

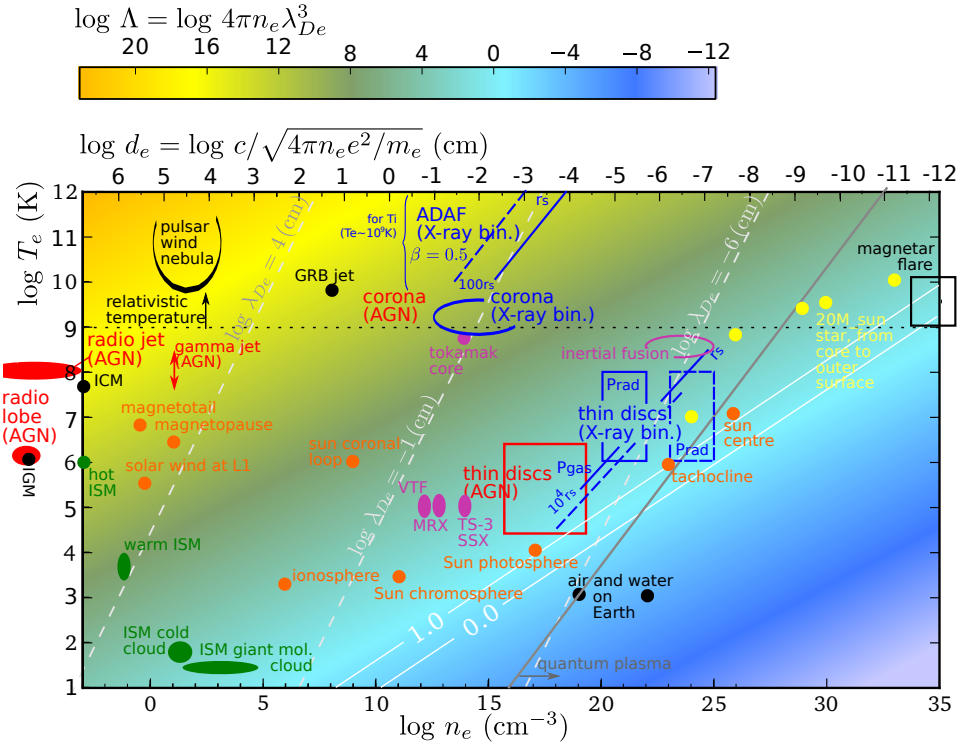

Figure 1.1: Orders of magnitude in number density n_e and temperature T_e for different environments. The colorbar represents the plasma parameter Λ, i.e., the number of particles per Debye sphere. Also shown is the electron Debye length λ_{De}. References for these numbers are listed in Appendix 1.A. In Sect. 2.11.3, and especially in Fig. 2.42, we discuss which of these environments are collisionless with respect to magnetic reconnection. Table 7.5 also gives estimates specific to high-energy objects.

Earth and solar physics

Ptolemy, who was maybe the most influential physicist of the western world between 100 and 1500 A.D., described the Earth and its surroundings as composed of four concentric spheres, made of four fundamental substances: solid rock at the center of the Earth, liquid water on top of it, gaseous air for the atmosphere, and fire surrounding it.

He was not far from some truth. Above 50 km, the atoms of the atmosphere are partly ionized by ultraviolet and X-ray radiation from the Sun, so that the Earth is indeed surrounded by matter in a fourth state, the plasma state, consisting of neutral atoms, of charged ions and of their electrons. The ionosphere is of great help to reflect radio waves and to allow their transmission around the globe, and it was from the first successful transatlantic radio transmission that its existence was inferred in 1902. It was later confirmed in 1924 by the radio experiments of Edward Appleton (see Appleton 1947).

Above the ionosphere space is filled by plasma expelled – both continuously and in large bursts – from the Sun's corona. The first documented connection between solar activity and phenomena on Earth was made by Carrington (1859) and Hodgson (1859), who reported an observation of a solar flare – a bright flash at the Sun's surface – associated, 18 hours later, with large magnetic disturbances in the Earth magnetic field and large auroral activity: something must have flown from the Sun to the Earth. Starting

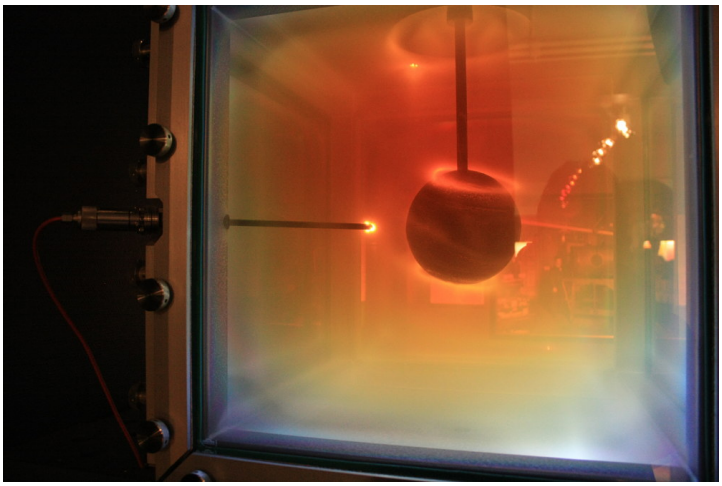

Figure 1.2: Reproduction of Birkeland's terella at Tromsø museum. A potential difference is applied between the cathode (the stick on the left) and the terella (the sphere), so that a stream of electrons flows from the cathode to the terella. The terella is an electromagnet representing the Earth and its dipolar magnetic field, and vacuum is made in the chamber. The electrons follow the field lines and emit radiation when encountering the surface of the terella.

from 1897, Birkeland made decisive steps by conducting extensive observations of aurorae and by reproducing them in the laboratory with his terella experiments (Fig. 1.2), and explained them by charged particles, ions and electrons, coming from the Sun and entering the Earth's atmosphere.

These sporadic and violent eruptions of plasma coming from the Sun are named coronal mass ejections (CMEs), and they are now explained by large scale reconnection events (see Sect. 2.10.6). CMEs are one of the manifestations of the complex dynamics of the coronal magnetized plasma. Magnetic fields are generated by dynamo processes under the surface of the Sun, up to a local equipartition with the thermal and convective energies. They rise up to the surface, and form an entangled web of emerging magnetic flux tubes that populate the solar corona and dominate the energy budget. These flux tubes are anchored in the Sun's surface at their footpoints, and are thus entrained by motions of the Sun's surface (as in Fig. 1.3). When two flux tubes are brought together their magnetic fields reconnect, thus transferring energy to the plasma, and providing a possible explanation for the heating of the corona to millions of Kelvins. These reconnection events also lead, depending on the geometry, to a large variety of phenomena at all heights in the solar atmosphere: the bright solar flares, ejections of plasma in space during solar jets or coronal mass ejections, etc (see Sect. 2.10.7 and 2.10.8).

It took some time to reach this picture of a Sun whose dynamics is, starting from the chromosphere, dictated by magnetic field and magnetic field reconnection. Hale (1908) described vortices around sunspots and, with measurements using Zeeman's effect, showed that sunspots are magnetized (for a review see Harvey 2006). Giovanelli (1947, 1948) then explained solar flares by a transfer of energy from magnetic to kinetic form, via electric fields created at neutral points by induction when the magnetic field of sunspots varies because of their growing. This was an electromagnetic description, and magnetohydrodynamics (MHD) was just appearing from the works of Alfvén (1942). The frozen-in flux concepts then appeared along with notions

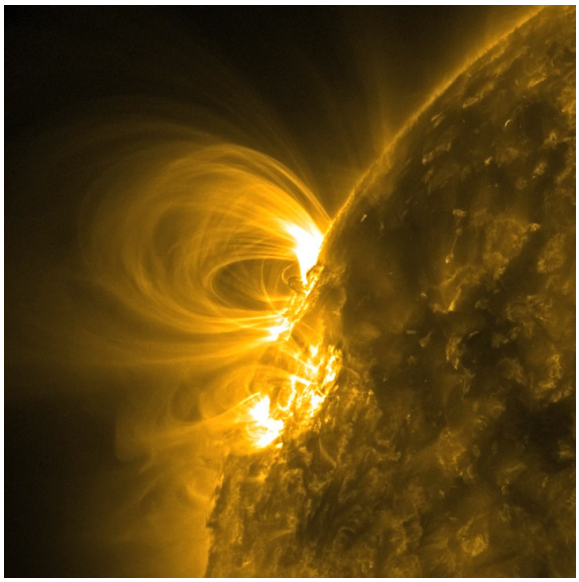

Figure 1.3: Active regions in the solar atmosphere (or sunspots). This is an ultraviolet view by SDO[d]. Particles gyrating around the field lines as they travel along them emit in this wavelength, so that what we see are indeed magnetic field lines.

of topology, and a MHD description of flares was built by Dungey (e.g., Dungey 1958), who also coined the term "magnetic reconnection".

In addition to these transient outbursts, the Sun also emits a continuous stream of particles named the solar wind. It originates from the Sun's hot corona, as predicted by Parker in 1958. Reconnection events occur also in the solar wind.

The Earth also has its own magnetosphere, generated by dynamo processes in its conducting iron liquid outer core. The solar wind meets this magnetosphere with a supersonic and superalfvénic velocity, so that a bow shock forms around the Earth (Fig. 2.15). Several satellites have crossed and studied this shock. It has a width of roughly 1000 km, while the mean free path of particles between two collisions is of the order of 0.1 AU[e], and the shock is thus completely collisionless. Outbursts from the Sun, such as CMEs, carry plasma and magnetic field. When they reach the Earth, the magnetosphere is contracted and electric currents are induced, leading to particles being accelerated and pushed inside the magnetosphere. It results in a magnetic storm, with for visible consequences large auroral display, and large perturbations in the magnetic field. Moreover, on the dayside the magnetic field of the Earth is directed northward: if the magnetic field from the solar disturbance is directed southward, then large reconnection events can occur, allowing even more plasma from the Sun to enter the Earth's magnetosphere and particles to gain energy. The currents induced in man-made electrical arrays can provoke important damages to electric power infrastructures (Schrijver et al. 2014), and it is believed that a Carrington-like event would have a severe impact. Another kind of event are geomagnetic substorms, which are smaller in terms of timescale and amplitude, and which occur more frequently (several can occur during a geomagnetic storm). They are triggered when a reconnection event takes place in the

[d]For more pictures and movies from SDO, see http://sdo.gsfc.nasa.gov/gallery/.
[e]One Astronomical Unit is $\sim 150 \times 10^6$ km.

tail of the Earth magnetic field, then producing particle outflows directed toward the Earth and penetrating deeply into Van Allen belts. First steps into the understanding of these phenomena were undertaken by Chapman and Ferraro (1930) and Dungey (1961).

The solar wind ends its direct course at 120 AU from the Sun, where it stalls through a termination shock with, on the other side, the interstellar medium (ISM). The Voyager 1 spacecraft, launched in 1977, is currently crossing this shock. The cause of the large scale solar magnetic field can be approximated by a magnetic dipole, the axis of which is not aligned with the rotation axis of the Sun. There is thus an area above and below the ecliptic plane where the magnetic field reverses its polarity at every turn[f]. When these reversals reach the termination shock, they are compressed, and the opposite magnetic fields can be forced to reconnect. This scenario may explain part of the high-energy particles that we receive on Earth (Drake et al. 2010).

Of course, satellites are privileged tools to observe closely space plasmas. They can be divided into two categories: those that observe the Sun's or the Earth's atmosphere by collecting photons in various wavelengths, and those that measure in-situ electromagnetic fields and particle velocities and distributions. The solar atmosphere is observed by the first category, which includes Soho, Trace, Hinode, SDO, or Stereo. The Earth's magnetosphere and the solar wind are mostly analyzed by satellites from the second category, which includes Geotail, Wind, Cluster, or Themis (see Yamada et al. 2010, for a short description and references). The structure of a reconnection event is best studied by several probes, and the Cluster and Themis missions actually consist in, respectively, four and five identical satellites that flight in close formation. The upcoming MMS mission will also be composed of four satellites.

Laboratory experiments

Magnetic reconnection also occurs on Earth, inside man-made machines such as magnetic or inertial fusion devices. In particular in tokamaks, reconnection events can disturb the overall equilibrium via the sawtooth instability, and lead to disruptions (Yamada et al. 2010). Reconnection in ITER will be collisionless (Fig. 2.42), and it strongly motivates an understanding of this process in tokamak geometries.

In addition, several experiments dedicated to the study of reconnection have been built. They include TS-3, SSX, MRX, or VTF (see Yamada et al. 2010, for a short description and references). They often use geometries with two parallel current coils that each produce a circular magnetic field, that can be pushed against each other by moving the coils (as in Fig. 2.10). Typical parameters are shown in Fig. 1.1 (see also Appendix 1.A for magnetic fields). Laser experiments are also emerging, in which two laser beams producing circular magnetic fields are focused close together on a target (e.g., Ping et al. 2014). Interestingly, such devices may reach relativistic regimes.

[f]Note that the large scale magnetic field of the Sun is not simply a dipole, because it is dragged by the Solar wind, resulting in the Parker spiral.

Galactic and extragalactic objects

The realm of plasmas is not restricted to circumstellar environments, and the interstellar medium that fills the space between the wind bubbles blown up by stars[g] is also in a plasma state. Plasmas are produced by many high-energy objects lying in our Galaxy and outside, objects that produce highly magnetized outflows and/or magnetized coronae, where magnetic reconnection can play an important role. Unlike for the Sun or the Earth's magnetosphere, these objects are not observed closely. The role of magnetic reconnection to create flares, outflows, or heat, is thus harder to assert. Studies must rely on knowledge acquired in space physics or in experiments, and extrapolated to the conditions of high-energy objects (for example, to a relativistic magnetization). Numerical simulations, kinetic for small scales or fluid for large scales, are then a privileged tool.

High-energy objects are distant, and observed via telescopes. The discovery of most of them was allowed by the opening of the observation spectrum to wavelengths other than optical, starting with radio waves in 1931-32 with the work of Karl Jansky. Pulsars were discovered in 1967 by radio astronomy, and X-ray binaries, active galactic nuclei, and hence black holes, by X-ray observations. Nowadays, satellites and Earth-based observatories cover a large frequency range with, for example, the VLA at radio wavelengths, Spitzer in infrared, Hubble in optical, Chandra in X-rays, or Fermi in γ-rays.

Microquasars are a particular class of X-ray binaries, where a black hole orbits around a star. The black hole captures material from the star, either by Roche lobe overflow for a low mass donor, or by wind accretion for a high mass donor, or by both. The accreted material has a finite angular momentum, that must be removed to allow a radial transport of matter toward the black hole. This can be done via viscous transport, or by shocks, and the accretion flow can be disk-like or more spherical. If it is a disk, then a magnetized corona should form above it, very much like above the solar chromosphere. Models often explain emission from microquasars by a thermal component from the disk, that is inverse Comptonized by the corona to higher energies. It requires electron coronal temperatures of 10^9 K, and magnetic reconnection is a candidate to explain this heating. It could also fuel the corona with a non-thermal particle population, as required by other models (see Sect. 7.5.3). Our study of Chapters 6 and 7 applies to the conditions encountered in these coronae, and we focus on the amount of magnetic energy transferred to the plasma, on its repartition between ions and electrons, and on the possible generation of non-thermal particles. Magnetic reconnection can also have other dynamical consequences: if plasma accreted inward carries a magnetic field with a polarity opposed to that of the inner parts, then large reconnection events can be triggered and could produce transient relativistic outflows from the pole of the black hole, as observed during state transitions (see Sects. 6.6.2 and 7.5.3).

Another class of high-energy objects regroups active galactic nuclei (or AGNs). These are galaxies whose centers emit large amounts of radiation and particles (they are the most luminous objects known). The current paradigm explaining active galactic nuclei and their various manifestations

[g]Stars others than the Sun also blow their own stellar winds, with mechanisms that depend on their mass: winds can be pressure driven, MHD driven, radiation driven, ..., and by doing so they fill large expanding bubbles of plasma.

(radio loud or quiet quasars, blazars, Seyfert, ...) is that these galaxies host at their center a supermassive black hole that accretes large amounts of matter, and in some cases ejects part of it via two relativistic jets at its poles. The accretion proceeds through an accretion disk, and here again, this disk is likely to be surrounded above and below by a magnetized corona where reconnection events could explain the emission of short and energetic flares, or the heating of the plasma. The relativistic jets expelled from the black hole poles remain collimated well outside the galaxy, and this collimation is a sign that they are magnetized. Hence, magnetic reconnection events could occur inside these extragalactic jets. They are invoked in some models to explain flare-like events observed in gamma-rays. Reconnection in jets can also accelerate particles that then radiate synchrotron radiation in radio wavelengths. Again, our study aims at covering the relativistic magnetizations encountered in these coronae and jets, where the same issues as for microquasar coronae are explored.

The surroundings of pulsars also host magnetized plasmas. A pulsar (a fast rotating neutron star) produces a wind of positrons and electrons with relativistic energies, that propagates inside the remnant of the supernova explosion. The outflowing plasma from the pulsar is magnetized, the rotation axis of the pulsar is not necessarily aligned with the axis of its magnetic field: the situation is similar to that for the Sun, i.e., near the equatorial plane there is an alternating succession of positive and negative magnetic field. Again as for the Sun, the pulsar wind ends its course in a termination shock where the stripes of alternating magnetic field are compressed, and are likely to undergo reconnection. The magnetic energy of the wind can thus be efficiently dissipated, and a non-thermal, power law-like particle population can be injected into the rest of the nebula. Such a population is required by observations (see Sect. 2.59 and Table 7.5 for references). In addition, gamma-ray observations of the Crab nebula – a well studied pulsar – show that very high energy photons are produced (with energies reaching hundreds of GeV). They may be produced by electrons with Lorentz factors above 10^9. A way to produce these electrons and the conditions in which they can radiate is during relativistic magnetic reconnection events. We remark that conditions in pulsars are very relativistic, and particle Lorentz factors are so high that radiative braking should be taken into account (Sect. 7.5.4). This is not done in our work.

Of course, there are other objects where magnetic reconnection can be important, with similar effects as mentioned above: γ-ray binaries, wind-wind interaction zones, magnetars, gamma-ray bursts, and so on.

Another, very interesting subject, is related to dark matter. Dark matter models predict interactions that can produce various, model-dependent, high-energy particles. Neutrino detectors such as IceCube, or cosmic ray detectors such as Auger, now routinely detect such high-energy products. To know whether they come from dark matter interactions, or from usual acceleration processes in high-energy objects, thus requires the understanding of particle acceleration in the previously listed environments. For example, IceCube recently detected extraterrestrial PeV neutrinos, which could originate from photopion interactions of energetic protons with photons[h]. Can

[h] High-energy protons can interact with photons. The most important chain of reaction is $p+\gamma \rightarrow \Delta^+ \rightarrow (n+\pi^+)$ or $(p+\pi^0)$, and the π^+ pion then decays to produce a neutrino. There are other channels that produce neutrinos (see Winter 2012, for a review).

magnetic reconnection produce these high-energy protons or ions? In what quantity? It is to such questions that a first-principle study of relativistic ion-electron reconnection aims at answering, and we do show in Chapter 7 that ions can form high-energy power law distributions.

Appendix 1.A References for orders of magnitude

We present here the references relevant to Fig. 1.1. They are more or less sorted by category. Other references and orders of magnitude can be found in Fig. 2.42, and also in Table 7.5.

Outside of galaxies

- IGM stands for inter-galactic medium. It is the space in the large stretched filaments of matter (the largest large-scale structure of the Universe), at the intersection of which one finds the galaxy clusters. Outside of filaments the particle density is even lower (not shown in Fig. 1.1). Source: `http://en.wikipedia.org/wiki/Intergalactic_medium#Intergalactic`. We take $n_\mathrm{e} \sim 10^{-5}\,\mathrm{cm}^{-3}$, $T_\mathrm{e} \sim 10^6\,\mathrm{K}$.
- ICM stands for intra-cluster medium. It is the space inside a cluster of galaxies, between the galaxies. Source: `http://en.wikipedia.org/wiki/Intracluster_medium` and Ji and Daughton (2011). We take $n_\mathrm{e} \sim 10^{-3}\,\mathrm{cm}^{-3}$, $T_\mathrm{e} \sim 5 \times 10^7\,\mathrm{K}$.

Inside galaxies, outside of star winds

- ISM stands for inter-stellar medium. It is the space inside a galaxy, but outside the volume of influence of stars (i.e., outside the envelope created by stellar winds). The ISM is far from homogeneous, and can be very roughly thought as a volume composed of the hot (ionized) and warm (ionized and neutral) ISM, locally patched by cold clouds (giant molecular clouds, HI clouds, HII, ...). See Padmanabhan (Chap. 9, 2000). We take, for the hot ISM $n_\mathrm{e} \sim 10^{-3}\,\mathrm{cm}^{-3}$, $T_\mathrm{e} \sim 10^6\,\mathrm{K}$; for the warm ISM $n_\mathrm{e} \sim 10^{-1}\,\mathrm{cm}^{-3}$, $T_\mathrm{e} \sim 10^3$–$10^4\,\mathrm{K}$; for cold clouds $n_\mathrm{e} \sim 10\,\mathrm{cm}^{-3}$, $T_\mathrm{e} \sim 10^2\,\mathrm{K}$; and for giant molecular clouds $n_\mathrm{e} \sim 10^2$–$10^5\,\mathrm{cm}^{-3}$, $T_\mathrm{e} \sim 50\,\mathrm{K}$.

Earth magnetosphere

A representation of the Earth magnetosphere is shown in Fig. 2.15.

- Earth ionosphere: Bellan (p. 24, Tab. 1.2, 2006) or Fitzpatrick (Tab. 1, 2011). We take $n_\mathrm{e} = 10^6\,\mathrm{cm}^{-3}$, $T_\mathrm{e} = 10^3\,\mathrm{K}$.
- Magnetotail and magnetopause, from the table of Ji and Daughton (2011). For the magnetotail we take $n_\mathrm{e} = 0.1$-$1\,\mathrm{cm}^{-3}$, $T_\mathrm{e} = 6 \times 10^6\,\mathrm{K}$; for the magnetopause we take $n_\mathrm{e} = 10\,\mathrm{cm}^{-3}$, $T_\mathrm{e} = 2 \times 10^6\,\mathrm{K}$.

Heliosphere

A detail of the structure of the solar atmosphere can be found page 59. See also Fig. 2.39 for a picture of the lower parts.

- Chromosphere and solar tachocline are taken from the table of Ji and Daughton (2011). Other solar values are taken elsewhere, but agree with Ji and Daughton (2011).

- Solar wind at L1 means at the Lagrange point between the Earth and the Sun. We use Bellan (p. 24, Tab. 1.2, 2006), Fitzpatrick (Tab. 1, 2011), or real time measurements at L1 at `http://www.swpc.noaa.gov/ace/ace_rtsw_data.html`. See also Ji and Daughton (2011). We take $n_e \sim 1\,cm^{-3}$, $T_e \sim 5 \times 10^5\,K$.
- Solar coronal loop: Bellan (p. 24, Tab. 1.2; p. 74, Tab. 2.1, 2006), or for example in many articles of Drake and coworkers (e.g. Drake et al. 2006, 2009a, 2010). See also Ji and Daughton (2011). We take $n_e \sim 10^9\,cm^{-3}$, $T_e \sim 10^6\,K$.

X-ray binaries

- X-ray binary disk coronae: large uncertainties exist. Analytical disk and corona models include de Gouveia dal Pino and Lazarian (2005), Di Matteo (1998), Merloni and Fabian (2001), and Reis and Miller (2013). Close values are also given by matching observed spectra with radiative models, e.g., Del Santo et al. (2013) or Romero et al. (2014). See also Table 7.5 for values of the magnetic field. We take $n_e \simeq 10^{13}$-$10^{16}\,cm^{-3}$, $T_e \simeq 10^9\,K$, $B \simeq 10^5$-$10^7\,G$.
- X-ray binary disk models. The disk models are simple analytical models computed here for a black hole of mass $M = 10 M_\odot$, which gives a Schwarzschild radius $r_{Sch} = 3 \times 10^6\,cm = 30\,km$, and an Eddington accretion rate $\dot{M}_{Edd} = 1.4 \times 10^{19} g/s = 2.2 \times 10^{-7} M_\odot/yr$. The viscosity parameter is $\alpha = 0.1$. We try two accretion rates: $\dot{M} = 10^{-1} \dot{M}_{Edd}$ (plain lines or plain squares in Fig. 1.1), and $\dot{M} = 10^{-3} \dot{M}_{Edd}$ (dashed lines or dashed squares). In a disk model, heat generated by viscosity is taken away either by advection toward the black hole or by efficient radiation.

  When advection dominates, we obtain the ADAF model (advection dominated accretion flow). We take here the simple self-similar solution of Narayan et al (Narayan and Yi 1994; Narayan et al. 1998; Narayan and McClintock 2008), which among other things assumes a plasma $\beta = P_{gas}/P_B$ of 0.5. The ions are assumed to be hotter than the electrons, and it is the ion temperature that is shown in Fig. 1.1. Electron temperatures are of the order of $10^9\,K$.

  The other case is when radiative cooling dominates, in which case we arrive at the Shakura and Sunyaev solution of optically thick and geometrically thin disk. For this model, since we are near the hole, electron scattering is assumed to dominate the opacity (compared mainly to free-free absorption), and we consider the case where pressure is dominated either by the radiation (represented in Fig. 1.1 by the red square for AGNs and the blues squares for X-ray binaries) or by the gas (represented by the blue lines labeled P_{gas}). The formula can be found in Padmanabhan (p. 367, §7.5.3, 2001) (in this reference, see also the graph p. 369, Fig. 7.3 and Fig. 1.7). Note that magnetic fields are ignored in the thin disk models.

Active galactic nuclei

- AGN jets: two distinct parts are considered. The outer part, at kiloparsec scales, where the radio emission originates, is constrained by observations (Schwartz et al. 2006). See also Romanova and Lovelace

(1992), and Ji and Daughton (2011). At smaller scales ($< 0.05\,\mathrm{pc}$) there is a gamma-ray emitting region, where direct measurements are still lacking. We take values from an analytical model (Giannios et al. 2009) assuming an ion magnetization $\sigma_{\mathrm{i}}^{\mathrm{cold}} = 100$ (defined in Eq. 6.5). The temperature is not specified. See also Table 7.5 for values of the magnetic field. For the radio region we take $n_{\mathrm{e}} \simeq$ 1-$5 \times 10^{-8}\,\mathrm{cm}^{-3}$, $T_{\mathrm{e}} \simeq 10^{8}\,\mathrm{K}$, $B \simeq 10^{-5}\,\mathrm{G}$; for the gamma-ray region we take $n_{\mathrm{e}} \simeq 80\,\mathrm{cm}^{-3}$, $B \simeq 10\,\mathrm{G}$, and the temperature is not specified.

- AGN disks: see the discussion for X-ray binary disks. We take a black hole mass of $10^{8}\,M_{\odot}$, and the same accretion rates as for X-ray binaries.
- AGN coronae: analytical disk and corona models include those of Di Matteo (1998), Merloni and Fabian (2001), and Reis and Miller (2013). See also Table 7.5.
- Lobes of giant radio galaxies: observations from Kronberg et al. (2004). See also Table 7.5 for values of the magnetic field. We take $n_{\mathrm{e}} \simeq 3 \times 10^{-6}\,\mathrm{cm}^{-3}$, $T_{\mathrm{e}} \simeq 10^{6}\,\mathrm{K}$, $B \simeq 10^{-6}$-$10^{-5}\,\mathrm{G}$.

Experimental devices

- Tokamak core: for ITER, from Freidberg (2007). See also Bellan (p. 24, Tab. 1.2; p. 74, Tab. 2.1, 2006) or Fitzpatrick (Tab. 1, 2011).
- Inertial fusion: Bellan (p. 24, Tab. 1.2, 2006) or Fitzpatrick (Tab. 1, 2011).
- TS-3: Todai Spheromak 3 facility. Standard parameters are $n_{\mathrm{e}} \simeq$ 2-$5 \times 10^{14}\,\mathrm{cm}^{-3}$, $T_{\mathrm{e}} \simeq 10^{5}\,\mathrm{K}$, $B \simeq 0.5$-$1 \times 10^{3}\,\mathrm{G}$ (Yamada et al. 2010).
- MRX: Magnetic Reconnection Experiment device. Standard parameters are $n_{\mathrm{e}} \simeq 0.1$-$1 \times 10^{14}\,\mathrm{cm}^{-3}$, $T_{\mathrm{e}} \simeq 5$-$15 \times 10^{4}\,\mathrm{K}$, $B \simeq 0.2$-$1 \times 10^{3}\,\mathrm{G}$ (Yamada et al. 2010).
- SSX: Swarthmore Spheromak Experiment facility. Standard parameters are $n_{\mathrm{e}} \simeq$ 1-$10 \times 10^{14}\,\mathrm{cm}^{-3}$, $T_{\mathrm{e}} \simeq 4$-$8 \times 10^{5}\,\mathrm{K}$, $B \simeq 10^{3}\,\mathrm{G}$ (Yamada et al. 2010).
- VTF: Versatile Toroidal Facility. Standard parameters are $n_{\mathrm{e}} \simeq 1 \times 10^{12}\,\mathrm{cm}^{-3}$, $T_{\mathrm{e}} \simeq 10^{5}\,\mathrm{K}$, $B \simeq 10^{3}\,\mathrm{G}$. From VTF website[i].

Others

- Twenty solar mass star: from a radial structure in Begelman and Rees (p. 32, 2009)
- Gamma-ray burst (GRB) jet: analytical model of McKinney and Uzdensky (2012). Values taken at the radius where fast reconnection sets up. See also Table 7.5 for values of the magnetic field.
- Magnetar flare: from Ji and Daughton (2011).
- Pulsar wind nebula: the case of the Crab. Analytical models and observations: Atoyan and Aharonian (1996), Meyer et al. (2010), Uzdensky et al. (2011), and Cerutti et al. (2013). This is a pair plasma. The plasma distribution function is actually a broken power law with Lorentz factors γ in the range 10 to 10^{8}, so that there is no defined

[i] http://www.psfc.mit.edu/research/physics_research/vtf/machine.html

temperature. Here we indicate T_e such that the mean Lorentz factor is in the range 10 to 10^8, i.e., $10 < T_\mathrm{e}/m_\mathrm{e}c^2 < 10^8$ (we recall that $m_\mathrm{e}c^2 = 6 \times 10^9\,\mathrm{K}$). See also Table 7.5 for values of the magnetic field.

Air and water (non-plasma)

- Air and water: for standard conditions on Earth. These values are here for comparison purpose only. They are not in a plasma state.

Quantum limit

The quantum limit drawn on Fig. 1.1 represents the fact that quantum effects for the electrons are not important when the two following inequalities are satisfied:

$$n_\mathrm{e}^{-1/3} \gg \lambda_\mathrm{De\,Broglie} \equiv \frac{h}{\sqrt{2\pi m_\mathrm{e} T_\mathrm{e}}}, \tag{1.1a}$$

$$T \gg T_\mathrm{Fermi} \equiv \frac{\hbar^2}{2m_\mathrm{e}} \left(3\pi^2 n_\mathrm{e}\right)^{2/3}. \tag{1.1b}$$

The first inequality states that particles are separated from each others by a distance larger than their quantum extension (which is the typical size of their wavefunction, of the order of the thermal De Broglie wavelength).

The second condition states that particles have a thermal kinetic energy larger than the Fermi energy, so that the exclusion principle imposes no constraint.

The two conditions can be rearranged to give

$$n_\mathrm{e}^{1/3} T_\mathrm{e}^{1/2} > a \times \hbar \sqrt{\frac{2\pi}{m_\mathrm{e}}}, \tag{1.2}$$

with $a = 1$ for Eq. 1.1a and $a = 3^{1/3}\pi^{1/6}/2 = 0.87$ for Eq. 1.1b.

The quantum limit for protons or ions is less constraining (replace m_e by m_i in Eqs. 1.1 or 1.2).

Relativistic limit

The relativistic limit drawn on Fig. 1.1 corresponds to $T_\mathrm{e} = m_\mathrm{e}c^2 = 6 \times 10^9\,\mathrm{K}$, a temperature above which a significant fraction of the electrons in a thermal distribution have relativistic velocities. Note that for protons, this limit is $T_\mathrm{i} = m_\mathrm{i}c^2 = 1.1 \times 10^{13}\,\mathrm{K}$. Relativistic plasma physics is discussed in Chapter 3.

Chapter 2

Fundamentals of magnetic reconnection and state of the art

The effect of the discharge is to "reconnect" the lines of force at a neutral point, and this happens quickly. The "reconnection" upsets the mechanical equilibrium in the neighborhood in a way that can be visualized, if the lines of force are seen as strings. Then the mechanical disturbance will spread from the neutral point and may have energy comparable to the energy of the spot field in the solar atmosphere.

Dungey (1958), coining reconnection

Contents

2.1 Outline

The aim of this chapter is to provide an introduction to magnetic reconnection in non-relativistic plasmas. We introduce the process itself from a basic level, with an emphasis on flux variations and induced electric fields in Sects. 2.2 to 2.7. These first sections are mostly designed for students new to the field, and the reader familiar with plasma physics and reconnection can skip them. Then in Sects. 2.8 to 2.14, we explore the landscape of reconnection, starting from the large scale ideal magnetohydrodynamic view, cascading down to the formation and localization of reconnection sites in 2D

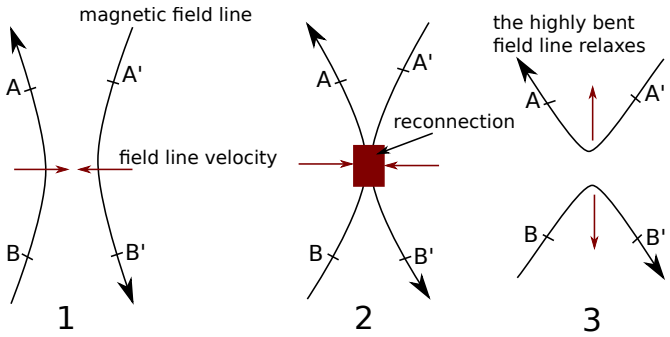

Figure 2.1: Two field lines pushed together reconnect. Before the reconnection event, point A is connected to point B. After the event, it is connected to point A', which is far away from the original point B: the "connectivity" has changed very quickly.
More precisely, if we build a function f that maps point A to a point at a fixed distance from A along the field line where A is anchored, then on the first image we have $f(A) = B$, with smooth variations as the field line moves, while during the second image $f(A)$ suddenly jumps to point A'. (Note that points A, A', B and B' should be taken away from the reconnection region, in the ideal zone where both the plasma and the magnetic field move together, so that the notion of field line motion makes sense, see Sect. 2.4.2.)

and 3D with the involved geometry, to the local configuration of the sites, to the microphysics of non-idealness, and to particle trajectories and acceleration. Nothing new is presented here, but this overview may be helpful to new researchers and students. We illustrate the subject by examples from solar or space physics and from high-energy astrophysics. With this large overview, we want to underline that reconnection physics involves many scales, each being important to predict the final outcome of reconnection events.

Of course, magnetic reconnection is a wide and complex subject, that cannot be covered in a few pages (nor can it be fully grasped in a three years PhD!). Very instructive reviews have been written: the book of Birn and Priest (2007) reviews large and small scale aspects, 3D, and space applications, Treumann and Baumjohann (2013) review collisionless small scale physics, Yamada (2011) or Yamada et al. (2010) cover mainly experimental and observational facts, Pontin (2011) is concerned with 3D reconnection, Karimabadi et al. (2013) briefly review 3D microphysics and turbulence, and several others exist. The field being quickly evolving, some are now slightly out-of-date (e.g., Biskamp 2000). Indeed, we underline that the subject of magnetic reconnection is still a research area, with several aspects that remain misunderstood, or others for which no consensus is yet reached.

2.2 A first definition, and some motivations

The most intuitive definition of magnetic reconnection is that it occurs *when the connections of the magnetic field lines change*[a]. This is what happens

[a]It is actually difficult to give a precise definition, that in particular excludes field line diffusion. But the intuitive definition remains satisfactory. And the explanations of Sect. 2.4.2 (field lines have a defined identity and velocity and can be followed through time only in an ideal plasma where $\boldsymbol{E} \cdot \boldsymbol{B}/B = E_{\parallel} = 0$), Sect. 2.5 (field lines stick to the plasma motions in an ideal plasma), Sect. 2.6.3 (magnetic reconnection is not magnetic diffusion), and Sect. 2.10.4 (magnetic reconnection in 3D domains), should give a precise

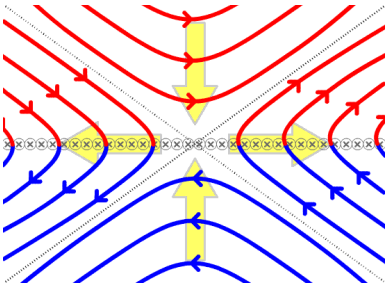

Figure 2.2: Yellow arrows: plasma motion, and also motion of the field lines, which are drawn in red and blue. Reconnection occurs at the center. Figure taken from the Wikipedia article on magnetic reconnection.

on Fig. 2.1.

On Fig. 2.2, a convergent flow from above and below forces the field lines to reconnect, and the flow is then ejected to the right and left sides by magnetic tension (because the newly created red-and-blue field lines are highly bent and, due to the MHD force $\boldsymbol{j} \wedge \boldsymbol{B} \propto [\boldsymbol{\nabla} \wedge \boldsymbol{B}] \wedge \boldsymbol{B}$ acting on the plasma, they tend to straighten).

Even though magnetic reconnection is a local process, it has dramatic consequences on the large scale dynamics. We can quote some important effects.

- It changes the magnetic topology. Macroscopic regions initially not connected by any field line can become connected[b]. It consequently affects the path of accelerated particles and of heat, that flow more easily along the field lines than perpendicularly to them.

  Another example of macroscopic topological change is the possible growth of magnetic islands up to the system size, that concentrates currents and drastically changes the overall dynamics. For instance, a coronal mass ejection can be seen as a giant island of magnetic flux and plasma detaching from the solar corona and expelled into space.

  The change of topology also allows the magnetic field to relax to a lower energy state, a change previously forbidden by the fact that an ideal plasma is constrained to preserve the field lines identity (so that they cannot break, Sect. 2.4.2). Newly reconnected field lines can undergo a large tension force and drive plasma motions.

- It converts magnetic energy into kinetic energy. This kinetic energy can be

  - an increase of the bulk flow velocity: the flow is accelerated;
  - thermal: the plasma is heated;
  - non-thermal: high-energy particles are produced.

  The kinetic energy of the particles can be partly converted into radiation.

- It creates areas where the plasma is not ideal, either in the central dissipation region where the field lines reconnect, or further away along

picture of what reconnection is.

[b] We remark that this property is not general. There can be reconnection between field lines originating from the same spatial domain, for example in Fig. 2.39 with braided fields.

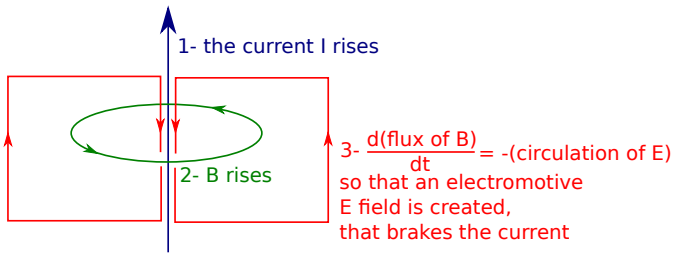

Figure 2.3: Illustration of the fact that a rising current is braked by the inductive fields that it creates.

the separatrices or in the exhausts. These are places where strong electric fields, currents, waves and instabilities are present. They can produce non-thermal high-energy particle populations.

- It can create turbulence (see Sects. 2.11.2 and 2.12.3 for details concerning the interplay between reconnection and turbulence).

2.3 What is magnetic energy

Magnetic energy can be transfered to kinetic energy, and it is thus worth reminding what magnetic energy actually means. To do so, we have to look at the transient phase where the magnetic field is growing, i.e., the phase where the particles transfer their energy to the magnetic field.

In order to create a magnetic field, charges have to be accelerated to create currents. Charge acceleration creates an increasing magnetic field. Since the flux of this field across a surface enclosing the current increases, inductive electric fields are created (via $\boldsymbol{\nabla} \wedge \boldsymbol{E} = -\partial_t \boldsymbol{B}$, which integrates into $\frac{\mathrm{d}}{\mathrm{d}t} \iint_S \boldsymbol{B} \cdot \mathrm{d}^2\boldsymbol{S} = -\oint_C \boldsymbol{E} \cdot \mathrm{d}\boldsymbol{l}$), and these inductive electric fields tend to slow down the accelerated charges (see Fig. 2.3). Consequently, the charges have to do a work $W = q\boldsymbol{E} \cdot \boldsymbol{v}$ ($\boldsymbol{v}$ is the velocity of the charges). Once the acceleration phase ends, a steady situation is reached, $\partial_t \boldsymbol{B} = 0$ and the inductive electric fields vanish. The currents flow, and maintain a steady magnetic field following Faraday's law: $\boldsymbol{\nabla} \wedge \boldsymbol{B} = \mu_0 \boldsymbol{j}$.

But where has the work done by the charge gone? Since there is no dissipation in our problem, this work cannot have contributed to a temperature increase. It is actually stored in the magnetic field energy. Indeed, one can show that the energy of the magnetic field,

$$W_B = \iiint_V \mathrm{d}^3 r \, \frac{B^2(\boldsymbol{r})}{2\mu_0}, \tag{2.1}$$

is equal to the work done by inductive electric fields when the charges at the origin of the magnetic field were accelerated (see for example Jackson 1998, §6.2)[c].

How can the magnetic field restore this energy? If the magnetic configuration varies in a way where the flux is not preserved across some fixed contour, then inductive fields will appear, that can accelerate particles. The plasma thus gains energy from the magnetic field. This is exactly what happens during magnetic reconnection[d]: the transfer of energy occurs through

[c] And concerning the electric field energy density, $\epsilon_0 E^2/2$, §1.11 of the same reference.

[d] Magnetic reconnection is a non-ideal instability. On the other hand, in ideal plasmas

the creation of an inductive electric field[e].

2.4 Why magnetic reconnection?

One may wonder why it is so special that magnetic field lines reconnect, and why, despite 60 years of intense research, it is still not fully understood. One may also wonder why nobody considers electric field reconnection. To better grasp the problem, we first need to introduce the concepts of field line and flux tube, and to describe some of their basic properties. Most importantly, we precise the notion of magnetic field line motion: a given field line preserves its identity through time as it moves in space only under special circumstances, which can be imposed by the ideal response of the plasma. When this is the case, the field line identity is preserved along all its length, it cannot break, and reconnection cannot occur.

2.4.1 Field line

Definition

We recall that the magnetic field is described by a *vector field* in the whole domain under consideration. That is, for a given time t, at each location $\boldsymbol{x}$ is associated a vector $\boldsymbol{B}(\boldsymbol{x}, t)$.

A field line is defined by starting from a point $\boldsymbol{x}$, and by drawing a line, the tangent of which is given by $\boldsymbol{B}(\boldsymbol{x}, t_0)$. The time t_0 is held fixed. In more mathematical terms, the field line is parametrized by a scalar s (for example it can be the length of the field line from a starting point) and is a curve $\boldsymbol{x}(s) = (x(s), y(s), z(s))$, with

$$\frac{\mathrm{d}\boldsymbol{x}}{\mathrm{d}s}(s) = \boldsymbol{B}(\boldsymbol{x}(s), t_0). \tag{2.2}$$

Properties deduced from the rotational and divergence of the field

Some properties of the field lines can be deduced from the divergence and rotational of the vector field (see Fig. 2.4):

- If the divergence of the vector field is positive (negative) at point $\boldsymbol{x}$, then there are field lines starting from (ending at) this point.
- If the rotational of the vector field is zero everywhere, then there are no closed field lines[f]. This is the case of the gravitational field ($\boldsymbol{\nabla} \wedge \boldsymbol{g} = 0$ in Newtonian dynamic), of an electrostatic field ($\boldsymbol{\nabla} \wedge \boldsymbol{E} = -\partial_t \boldsymbol{B} = 0$), or of a steady magnetic field in the absence of currents ($\boldsymbol{\nabla} \wedge \boldsymbol{B} = 0$).

---

there can be no flux variations across plasma elements, so that it may seem that in this case magnetic energy cannot be transferred to the plasma. This is not true: inductive electric fields still arise in ideal plasmas, specifically to maintain the absence of flux variation. From a microscopic point of view, it is these electric fields that transfer energy from magnetic to kinetic (magnetic fields alone cannot work). From a fluid point of view, e.g., ideal MHD, this transfer occurs via the Lorentz force, $\boldsymbol{J} \wedge \boldsymbol{B}$, that can work ($[\boldsymbol{J} \wedge \boldsymbol{B}] \cdot \boldsymbol{v}_{\text{center of mass}} \neq 0$, with $\boldsymbol{v}_{\text{center of mass}} \sim \boldsymbol{v}_{\text{ions}}$ in an ion-electron plasma).

[e] The reality is slightly more complex: if a steady state is reached, there is no flux variations, but the electric field remains and still allows the energy transfer (as explained in Sect. 2.6.2).

[f] Note however that the opposite is not true: if the rotational is not zero, nothing can be said (e.g., for helical fields $\boldsymbol{\nabla} \wedge \boldsymbol{B} \neq 0$ and there are no closed lines; but for the field created by a current, $\boldsymbol{\nabla} \wedge \boldsymbol{B} \neq 0$ and all field lines are closed).

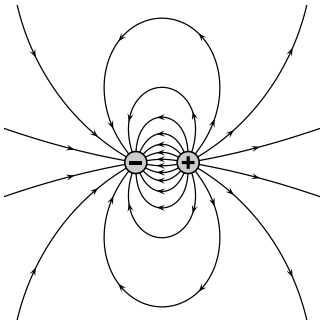

Figure 2.4: Example of the divergence of a field. The lines are the electric field lines created by two charges. At the location of the positive charge, the divergence is positive ($\boldsymbol{\nabla}\cdot\boldsymbol{E} = \rho/\epsilon_0 > 0$) and the field lines diverge, while at the location of the negative charge the divergence is negative and the field lines converge. Elsewhere, the divergence is zero and the field lines are neither ending nor starting.

Since there are no magnetic monopoles, $\boldsymbol{\nabla}\cdot\boldsymbol{B} = 0$, an important consequence is that there are no magnetic field charges, and thus no points where magnetic field lines end or start. Consequently, *magnetic field lines either form closed loops, extend to infinity, or intersect the domain boundary* (which can be the wall of a device, the surface of a star or of an accretion disk, ...). This is what gives an interest to the concept of magnetic field lines.

We remark that electric field lines can be considered, but in a plasma every charged particle acts as a source (positive charge, $\boldsymbol{\nabla}\cdot\boldsymbol{E} = \rho/\epsilon_0$) or as a sink (negative charge), so that they do not form extended field lines or flux tubes and are not really interesting to study.

2.4.2 Field line velocity, field line identity

Magnetic field lines are defined (via Eq. 2.2) at a fixed time t. If the magnetic field varies, they will be different at a later time $t + \delta t$. An interesting question is to know whether we can say that a given field line has moved between these two times, i.e., whether we can define a velocity field $\boldsymbol{v}_\mathrm{m}$ such that a field line $\mathcal{C}_1$ at time t is transformed, by moving all its points at $\boldsymbol{v}_\mathrm{m}$, into another *single* field line at time $t + \delta t$. The answer is yes only under special circumstances: if $\boldsymbol{B}\wedge(\boldsymbol{\nabla}\wedge\boldsymbol{E}_\parallel) = 0$ all along the field line, and in particular if the parallel-to-$\boldsymbol{B}$ electric field $\boldsymbol{E}_\parallel$ vanishes everywhere along the field line (i.e., if $\boldsymbol{E}\cdot\boldsymbol{B} = 0$). Then, the field line velocity is given by

$$\boldsymbol{v}_\mathrm{m} = \frac{\boldsymbol{E}\wedge\boldsymbol{B}}{B^2}. \tag{2.3}$$

We provide a demonstration below, but we first discuss this result. It relies only on Maxwell's equations, and is thus true independently of the plasma behavior. It is however the plasma response that controls $\boldsymbol{E}_\parallel$, and as we will see the plasma does tend to always impose $\boldsymbol{E}_\parallel = 0$ as much as it can.

When $\boldsymbol{E}_\parallel = 0$, the field lines "move" at $\boldsymbol{v}_\mathrm{m}$ and preserve their identity. An obvious consequence is that magnetic reconnection (in the topological sense of the breaking of field lines, Sect. 2.2) is not allowed. Conversely, magnetic reconnection requires the existence of an electric field parallel to

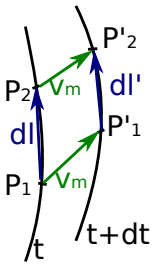

Figure 2.5: Illustration of a field line motion at velocity $\boldsymbol{v}_\mathrm{m}$: the two points P_1 and P_2 located on the same field line at time t are still on the same field line at time $t+\delta t$ if they are moved from a vector $\boldsymbol{v}_\mathrm{m}\delta t$.

$\boldsymbol{B}$, $E_\parallel = \boldsymbol{E}\cdot\boldsymbol{B}/B \neq 0$, with $\boldsymbol{\nabla}\wedge\boldsymbol{E}_\parallel \neq 0$[g]. When this is the case, field lines between two different times cannot be related to each others, and in particular they can break and reconnect. This is the case of Fig. 2.1, where there is no smooth vector field $\boldsymbol{v}$ that can transform the field lines of panel 1 into those of panel 3[h].

We will use again the notion of field line motion at velocity $\boldsymbol{v}_\mathrm{m}$ to discuss the frozen-in theorems at the end of Sect. 2.5.1, and when discussing 3D reconnection in Sect. 2.10.3. We make two final remarks.

First, the field line motion at $\boldsymbol{v}_\mathrm{m}$ when $\boldsymbol{E}_\parallel = 0$ also holds in steady state when $\partial\boldsymbol{B}/\partial t = 0$. It may seem counter-intuitive, but it is not a paradox. Recall for example that in steady state there is also an energy flux associated with the electromagnetic fields ($\boldsymbol{E}\wedge\boldsymbol{B}/\mu_0$).

Second, we stress that the field line motion at $\boldsymbol{v}_\mathrm{m}$ is not a real motion. Field lines do not move, they actually do not exist as physical objects. They are concepts, sometimes very useful, sometimes misleading when considered as real objects (the concept of flux tube is much more robust). For example, the notion of field line motion at $\boldsymbol{v}_\mathrm{m}$ also holds when $E > cB$, even if in this case the "motion" is supraluminal ($|\boldsymbol{v}_\mathrm{m}| = E/B$).

Demonstration

We mostly follow the demonstration of Belmont et al. (2014, §1.3.1.3) (see also Boozer 2013). We consider two points P_1 and P_2 located on the same field line denoted by $\mathcal{C}_1$, and separated by an infinitesimal distance $\delta\boldsymbol{l} = \overrightarrow{P_1P_2}$ (Fig. 2.5). We have, by definition, $\delta\boldsymbol{l}\wedge\boldsymbol{B} = 0$. We move these points, during a time interval δt, with the velocity $\boldsymbol{v}_\mathrm{m}$ of Eq. 2.3. We then obtain two new points P_1' and P_2'. If P_1' and P_2' are still located on the same field line, then it means that all points initially located on $\mathcal{C}_1$ are again on the same field line, and consequently that the field line $\mathcal{C}_1$ has "moved" with a velocity $\boldsymbol{v}_\mathrm{m}$. P_1' and P_2' are on the same field line if and only if $\delta\boldsymbol{l'} \parallel \boldsymbol{B'}$, i.e., if $\delta\boldsymbol{l'}\wedge\boldsymbol{B'} = 0$. If we note $\boldsymbol{C} = \delta\boldsymbol{l}\wedge\boldsymbol{B}$ and $\mathrm{D}_t = \partial_t + \boldsymbol{v}_\mathrm{m}\cdot\boldsymbol{\nabla}$, this is equivalent to $\mathrm{D}_t\boldsymbol{C} = 0$.

The operator D_t is linear, so that $\mathrm{D}_t\boldsymbol{C} = (\mathrm{D}_t\delta\boldsymbol{l})\wedge\boldsymbol{B} + \delta\boldsymbol{l}\wedge\mathrm{D}_t\boldsymbol{B}$. We

[g] Actually magnetic reconnection requires the existence of $\boldsymbol{\nabla}\wedge\boldsymbol{E}_\parallel \neq 0$ only if $\boldsymbol{B}$ never vanishes. If $\boldsymbol{B} = 0$ at some point, then $\boldsymbol{v}_m = +\infty$ is singular, and field lines can break and reconnect without the need of $\boldsymbol{E}_\parallel$. This is the case for example in 2D magnetic reconnection of antiparallel fields (see, e.g., Sect. 2.10.2). All in all, reconnection requires either $E_\parallel \neq 0$, or $B = 0$. But in the latter case, the magnetic null point is often surrounded by a non-ideal zone where $\boldsymbol{B}$ is finite and $E_\parallel \neq 0$.

[h] Provided that points A and B are in a zone where the field lines can be identified, so that one cannot say that panel 1 has been rotated by 90° to obtain panel 3!

first compute $\mathrm{D}_t\delta\boldsymbol{l}$. It is equal to

$$\mathrm{D}_t\delta\boldsymbol{l} = \frac{\overrightarrow{OP_2'} - \overrightarrow{OP_1'} - \overrightarrow{OP_2} + \overrightarrow{OP_1}}{\delta t} = \frac{\overrightarrow{P_1'P_2'} - \overrightarrow{P_1P_2}}{\delta t} = \frac{\overrightarrow{P_2P_2'} - \overrightarrow{P_1P_1'}}{\delta t}, \quad (2.4)$$

where O is any fixed point. The last expression is the derivative of the vector $\boldsymbol{v}_\mathrm{m}$ along the direction $\delta\boldsymbol{l}$, and is thus expressed as $(\delta\boldsymbol{l}\cdot\boldsymbol{\nabla})\boldsymbol{v}_\mathrm{m}$. We thus have $\mathrm{D}_t\delta\boldsymbol{l} = (\delta\boldsymbol{l}\cdot\boldsymbol{\nabla})\boldsymbol{v}_\mathrm{m}$, and

$$(\mathrm{D}_t\delta\boldsymbol{l})\wedge\boldsymbol{B} = [(\delta\boldsymbol{l}\cdot\boldsymbol{\nabla})\boldsymbol{v}_\mathrm{m}]\wedge\boldsymbol{B}. \quad (2.5)$$

Concerning $\mathrm{D}_t\boldsymbol{B}$, we first use $\partial_t\boldsymbol{B} = -\boldsymbol{\nabla}\wedge\boldsymbol{E}$. We then decompose $\boldsymbol{E}$ as the sum of its parallel component $\boldsymbol{E}_\parallel = (\boldsymbol{b}\cdot\boldsymbol{E})\boldsymbol{b}$, with $\boldsymbol{b} = \boldsymbol{B}/B$, and of its perpendicular component $\boldsymbol{E}_\perp = \boldsymbol{E} - \boldsymbol{E}_\parallel = \boldsymbol{b}\wedge(\boldsymbol{E}\wedge\boldsymbol{b}) = \boldsymbol{B}\wedge\boldsymbol{v}_\mathrm{m}$. We thus have $\partial_t\boldsymbol{B} = -\boldsymbol{\nabla}\wedge\boldsymbol{E}_\parallel - \boldsymbol{\nabla}\wedge[\boldsymbol{B}\wedge\boldsymbol{v}_\mathrm{m}]$. The next step is to use a vector identity to develop the rotational of the cross-product[i], and to write the whole expression for $\delta\boldsymbol{l}\wedge\mathrm{D}_t\boldsymbol{B}$, where cancellations lead to

$$\delta\boldsymbol{l}\wedge\mathrm{D}_t\boldsymbol{B} = -\delta\boldsymbol{l}\wedge(\boldsymbol{\nabla}\wedge\boldsymbol{E}_\parallel) + \boldsymbol{B}\wedge[(\delta\boldsymbol{l}\cdot\boldsymbol{\nabla})\boldsymbol{v}_\mathrm{m}]. \quad (2.6)$$

All in all, we arrive at

$$\mathrm{D}_t\boldsymbol{C} = -\delta\boldsymbol{l}\wedge(\boldsymbol{\nabla}\wedge\boldsymbol{E}_\parallel), \quad (2.7)$$

which proves that whenever $\boldsymbol{B}\wedge(\boldsymbol{\nabla}\wedge\boldsymbol{E}_\parallel) = 0$, the field line "moves" with velocity $\boldsymbol{v}_\mathrm{m}$.

2.4.3 Flux tube

A flux tube is defined by drawing a closed contour in space, and by considering all the field lines that start from the points of this contour (Fig. 2.6). The resulting surface can be quite intricate, but resembles a tube. The divergence free character of $\boldsymbol{B}$ insures that the flux of the magnetic field through each section of the tube is constant.

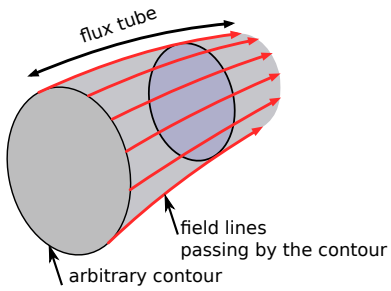

Figure 2.6: Example of the construction of a flux tube. Here, the geometry is quite simple.

2.5 Lenz's law, frozen-in laws, and reconnection

We have seen that the divergence free nature of $\boldsymbol{B}$ makes relevant the use of field lines and flux tubes. There is, however, a second reason that makes magnetic fields outstandingly interesting: Lenz's law, or $\boldsymbol{\nabla}\wedge\boldsymbol{E} = -\partial_t\boldsymbol{B}$.

[i] For any vector fields $\boldsymbol{u}$ and $\boldsymbol{v}$: $\boldsymbol{\nabla}\wedge(\boldsymbol{u}\wedge\boldsymbol{v}) = (\boldsymbol{v}\cdot\boldsymbol{\nabla})\boldsymbol{u} - (\boldsymbol{u}\cdot\boldsymbol{\nabla})\boldsymbol{v} + (\boldsymbol{\nabla}\cdot\boldsymbol{v})\boldsymbol{u} - (\boldsymbol{\nabla}\cdot\boldsymbol{u})\boldsymbol{v}$.

Lenz's law is a moderation law. Such laws are general and state that the causes tend to suppress the effects that caused them[j]. Lenz's law is specific to electrodynamics, and states that "*An induced electromotive force always gives rise to a current whose magnetic field opposes the original change in magnetic flux.*"[k]

This law is of fundamental importance not only for magnetic reconnection, but also for plasma physics in general. It is at the heart of the $\boldsymbol{E} + \boldsymbol{U} \wedge \boldsymbol{B} = 0$ relation of ideal MHD, of the $E \times B$ velocity, of particle magnetization and adiabaticity, and of course of magnetic reconnection. All these processes are different facets of the same fundamental law: magnetic flux conservation via Lenz's law. We will now explain why.

2.5.1 Frozen-in laws

Plasma at rest

Consider the situation of Fig. 2.7, where a bundle of field lines is localized in space. Suppose that these field lines move upward. Then, the flux across the surface delimited by the *fixed* (in time and in space) contour C of Fig. 2.7 decreases:

$$\frac{\mathrm{d}}{\mathrm{d}t} \iint_S \mathrm{d}\boldsymbol{S} \cdot \boldsymbol{B} < 0. \tag{2.8}$$

But integrating $\boldsymbol{\nabla} \wedge \boldsymbol{E} = -\partial_t \boldsymbol{B}$ along the closed contour C leads to the well known result:

$$\oint_C \mathrm{d}\boldsymbol{l} \cdot \boldsymbol{E} = \iint_S \mathrm{d}\boldsymbol{S} \cdot \boldsymbol{\nabla} \wedge \boldsymbol{E} = -\frac{\mathrm{d}}{\mathrm{d}t} \iint_S \mathrm{d}\boldsymbol{S} \cdot \boldsymbol{B}. \tag{2.9}$$

Consequently in our case, there is a positive circulation of $\boldsymbol{E}$ along the contour. It means that somewhere along the contour, there is an electric field.

If we are in vacuum, nothing more happens. The magnetic field can vary freely, and the flux variations create an electric field as the consequence of Maxwell's equations.

If charged particles are present and able to move freely, such as in a plasma, then they will be accelerated by the electric field and a current will be created. This current, in turn, will produce a magnetic field. As shown on the last panel of Fig. 2.7, this induced magnetic field is oriented in the same direction as the original field. Consequently, just where the old field was, a new field is created to compensate for this variation.

If we were to consider a closed line above the first one, at the place where there was no magnetic field and where the old field was displaced, we would see that here the flux across the closed line *increases*, and creates an electric field and a current leading to a magnetic field *opposed* to the newly brought magnetic field. Consequently, the new field is decreased here.

If the plasma is ideal, i.e., if it can respond perfectly to the electric field to create the needed current, the consequence of what we just presented is that *the magnetic configuration does not change at all*. We change the

[j] Otherwise, our world would be highly unstable!

[k] Lenz's law can also be seen as a kind of analog to Newton's third law: to every action there is an opposite reaction. We also note that Lenz's law is the key of the reasoning on magnetic energy of Sect. 2.3. This law specifies how energy is transferred between mechanical and magnetic forms, via the creation of an electric field opposed to charge motion.

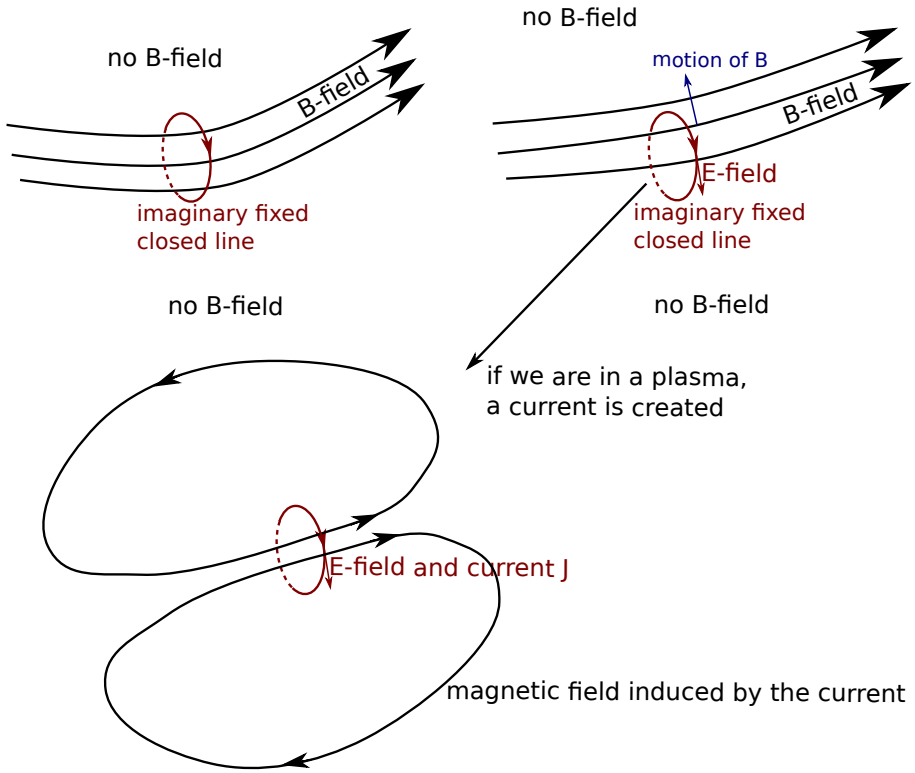

Figure 2.7: Illustration of Lenz's law. **Upper left:** the initial situation, which is a flux tube surrounded by a $\boldsymbol{B} = 0$ environment.
Upper right: we move the field lines and consequently induce a current along the red contour.
Lower part: the magnetic field generated by the induced current is in the same direction as the original field, tending to restore the original configuration.

magnetic field in a way that do not conserve the magnetic flux: the plasma responds and destroy our new arrangement of magnetic field.

Moving plasma

We have learned that in a perfect or ideal plasma[l] at rest, the magnetic field cannot change in a non flux-conserving way, because of the response of the charged particles to the induced electric fields. Since we assume that the plasma is ideal, we can use the notion of field lines. We can thus say that because of the response of the plasma, the field lines cannot move in a way that do not preserve the magnetic flux (across any contour fixed in the plasma rest frame). Of course, the field lines can actually move if the whole plasma moves. Consider, for example, the case of a plasma at rest embedded in a magnetic field, and suppose that we now see this plasma from a frame moving with velocity $-\boldsymbol{U}$ with respect to the plasma: we see the magnetic field lines and the plasma moving altogether at the same speed (which is $\boldsymbol{U}$).

In the non-relativistic limit, the magnetic field remains the same, but the formula for the change of frames[m] also imply that in our moving frame,

[l] Ideal means no collisions between particles, no inertia so that the plasma response is instantaneous, no interaction with collectively generated fields and other fluctuations, ... We will detail this point in Sects. 2.7 and 2.11.

[m] The expressions for a change of frame at velocity $\boldsymbol{v}$, with $\parallel$ ($\perp$) denoting the compo-

there is an electric field given by $\boldsymbol{E}' = -\boldsymbol{U} \wedge \boldsymbol{B}$[n]. So: when a plasma moves and drags with it a magnetic field, there is an electric field given by $\boldsymbol{E} = -\boldsymbol{U} \wedge \boldsymbol{B}$. (We will detail just afterward what "drags" means, and when it occurs.)

This situation can be generalized. Consider a plasma, part of which is moving with velocity $\boldsymbol{U}$. If the plasma motion drags the magnetic field (which is due, as we have seen, to the plasma creating induced currents), then it creates an electric field $\boldsymbol{E} = -\boldsymbol{U} \wedge \boldsymbol{B}$. We have just demonstrated that in an ideal plasma, plasma motion, electric and magnetic fields are linked by the relation

$$\boldsymbol{E} + \boldsymbol{U} \wedge \boldsymbol{B} = 0. \tag{2.12}$$

We remark that this relation can be inverted to give the perpendicular to $\boldsymbol{B}$ velocity: $\boldsymbol{U}_\perp = \boldsymbol{E} \wedge \boldsymbol{B}/B^2$, which indeed holds in ideal MHD[o].

An easier (but less instructive) derivation of $\boldsymbol{E} + \boldsymbol{U} \wedge \boldsymbol{B} = 0$

This important relation is seldom introduced as we just did. Instead, we often read that the plasma is a perfect conductor, so that the electric field $\boldsymbol{E}'$ in the plasma rest frame is zero ($\boldsymbol{E}' = \eta \boldsymbol{J}'$ with a vanishing resistivity η) and, by a change of frame, $0 = \boldsymbol{E}' = \boldsymbol{E} + \boldsymbol{U} \wedge \boldsymbol{B}$. Then, the variation of the flux of $\boldsymbol{B}$ through a contour $C(t)$ delimiting a surface $S(t)$ and moving with the plasma is derived[p]:

$$\frac{\mathrm{d}}{\mathrm{d}t} \iint_{S(t)} \mathrm{d}\boldsymbol{S} \cdot \boldsymbol{B} = \iint_{S(t)} \mathrm{d}\boldsymbol{S} \cdot \left(\frac{\partial \boldsymbol{B}}{\partial t} - \boldsymbol{\nabla} \wedge (\boldsymbol{U} \wedge \boldsymbol{B}) \right), \tag{2.14}$$

and since $\boldsymbol{E} + \boldsymbol{U} \wedge \boldsymbol{B} = \boldsymbol{R}$ (we introduce $\boldsymbol{R}$ for later purposes, it is zero here) and $\partial_t \boldsymbol{B} + \boldsymbol{\nabla} \wedge \boldsymbol{E} = 0$ (Lenz's law again), we have $\partial_t \boldsymbol{B} + \boldsymbol{\nabla} \wedge [\boldsymbol{R} - \boldsymbol{U} \wedge \boldsymbol{B}] = 0$

---

nent parallel (perpendicular) to $\boldsymbol{v}$, are

$$\boldsymbol{E}'_{//} = \boldsymbol{E}_{//}, \qquad \boldsymbol{B}'_{//} = \boldsymbol{B}_{//}, \tag{2.10}$$

$$\boldsymbol{E}'_{\perp} = \gamma(\boldsymbol{E}_\perp + \boldsymbol{v} \wedge \boldsymbol{B}_\perp), \qquad \boldsymbol{B}'_{\perp} = \gamma \left(\boldsymbol{B}_\perp - \frac{\boldsymbol{v} \wedge \boldsymbol{E}_\perp}{c^2} \right). \tag{2.11}$$

[n] Where does this field comes from? In the plasma rest frame, ions and electrons are flowing with different velocities to create a current, that in turn creates the magnetic field. In the moving frame, the ion and the electron number density are Lorentz-contracted differently, and it results in a net charge density. This charge density is at the origin of the electric field.

One can check that this is indeed the case by considering a thin current flowing in straight line, produced by counterstreaming ions and electrons of the same charge density and opposed velocities. There is then no electric field. Boosting to another frame moving parallel to the current, the number densities are contracted differently, and to lowest order in the boost speed we do find a charge density producing the desired electric field.

[o] As a side remark, we note that particle drifts other than $E \times B$, derived from the fluid picture (the diamagnetic and polarization drifts), or derived from the particle picture (the gradient and curvature drifts), requires a finite particle mass to be non-zero. They are consequently non-ideal effects, absent from our previous derivation.

[p] We copy here a note from Jackson (§6.1, 1998): for a general vector field $\boldsymbol{B}(\boldsymbol{x}, t)$ and a contour following the velocity field $\boldsymbol{v}(\boldsymbol{x}, t)$ (which can be anything, not necessarily a fluid velocity), we have

$$\begin{aligned} \frac{\mathrm{d}}{\mathrm{d}t} \iint_{S(t)} \mathrm{d}\boldsymbol{S} \cdot \boldsymbol{B} &= \iint_{S(t)} \mathrm{d}\boldsymbol{S} \cdot \frac{\partial \boldsymbol{B}}{\partial t} + \iint_{S(t)} \mathrm{d}\boldsymbol{S} \cdot \boldsymbol{\nabla} \wedge (\boldsymbol{B} \wedge \boldsymbol{v}) + \iint_{S(t)} \mathrm{d}\boldsymbol{S} \cdot \boldsymbol{v}(\boldsymbol{\nabla} \cdot \boldsymbol{B}) \\ &= \iint_{S(t)} \mathrm{d}\boldsymbol{S} \cdot \frac{\partial \boldsymbol{B}}{\partial t} + \oint_{C(t)} \mathrm{d}\boldsymbol{l} \cdot (\boldsymbol{B} \wedge \boldsymbol{v}) + \iint_{S(t)} \mathrm{d}\boldsymbol{S} \cdot \boldsymbol{v}(\boldsymbol{\nabla} \cdot \boldsymbol{B}). \end{aligned} \tag{2.13}$$

and:

$$\frac{\mathrm{d}}{\mathrm{d}t}\iint_{S(t)} \mathrm{d}\boldsymbol{S}\cdot\boldsymbol{B} = -\iint_{S(t)} \mathrm{d}\boldsymbol{S}\cdot(\boldsymbol{\nabla}\wedge\boldsymbol{R}) = 0. \tag{2.15}$$

It is thus deduced that the magnetic field flux through contours moving with the plasma cannot vary. We also say that the magnetic field flux is frozen into the plasma (or vice-versa, that the plasma is frozen into the field).

A consequence of $\boldsymbol{E}+\boldsymbol{U}\wedge\boldsymbol{B}=0$: field line motion at $\boldsymbol{U}=\boldsymbol{v}_\mathrm{m}$

In Sect. 2.4.2, we showed that when $\boldsymbol{\nabla}\wedge\boldsymbol{E}_\parallel = 0$ along any field line (with $\boldsymbol{E}_\parallel$ the electric field parallel to $\boldsymbol{B}$), then the field lines can be thought of as moving with a velocity $\boldsymbol{v}_\mathrm{m} = \boldsymbol{E}\wedge\boldsymbol{B}/B^2$. But if $\boldsymbol{E}+\boldsymbol{U}\wedge\boldsymbol{B}=0$, then $\boldsymbol{E}_\parallel = 0$ and this field line motion holds. Moreover, it also implies that the plasma velocity perpendicular to $\boldsymbol{B}$, $\boldsymbol{U}_\perp$, is given by $\boldsymbol{U}_\perp = \boldsymbol{E}\wedge\boldsymbol{B}/B^2$, which is precisely the field line velocity $\boldsymbol{v}_\mathrm{m}$.

A consequence of the relation $\boldsymbol{E}+\boldsymbol{U}\wedge\boldsymbol{B}=0$ is thus that the plasma moves with the field lines (and vice versa).

More elaborated thoughts

We think that it is worth keeping in mind that the relation $\boldsymbol{E}+\boldsymbol{U}\wedge\boldsymbol{B}=0$ holds because charged particles move in response to induced electric fields and create currents that act to cancel any magnetic field flux variation. Several lessons can be drawn from this.

First, since it is the lightest particles that will respond faster, it is the electrons that insure that the field is frozen-in. Consequently, $\boldsymbol{U}$ in Eq. 2.12 is the electron velocity. However, in MHD the $\boldsymbol{U}$ appearing in the equations is the center-of-mass velocity, which is very close to the ion velocity (because the ion and electron fluids have velocities of the order of the thermal speed or higher, and the difference between them, proportional to the current, is small in the MHD approximation, see, e.g., Fitzpatrick 2011, §3.9). Forcing $\boldsymbol{U}$ to be the ion velocity leads to the apparition of the Hall term: $\boldsymbol{E}+\boldsymbol{V}_\mathrm{i}\wedge\boldsymbol{B} = \boldsymbol{E}+\boldsymbol{V}_\mathrm{e}\wedge\boldsymbol{B}+(\boldsymbol{V}_\mathrm{i}-\boldsymbol{V}_\mathrm{e})\wedge\boldsymbol{B} = 0+(ne)^{-1}\boldsymbol{J}\wedge\boldsymbol{B}$. Similarly, in a partially ionized gas, forcing $\boldsymbol{U}$ to be the neutral component velocity will lead to a term $(\boldsymbol{V}_n-\boldsymbol{V}_\mathrm{i})\wedge\boldsymbol{B}$, which is responsible for ambipolar diffusion.

Second, it is only magnetic field *flux* variations that induce electric fields and a response of the plasma, and not motion across field lines. It helps understanding the meaning of "the plasma drags a magnetic field": when does that happens?

It happens of course if the plasma itself is at the origin of the magnetic field. Moving the plasma then moves $\boldsymbol{B}$. It also happens if the magnetic field is created by external sources: a plasma embedded in this external magnetic field, or a plasma arriving into this field from outside, will modify the field and possibly drag it if the motion of the plasma across the field cannot be done in a manner that preserves the flux of $\boldsymbol{B}$. The general way to preserve the flux of $\boldsymbol{B}$ through plasma elements is that the flux of $\boldsymbol{B}$ entering a plasma element equals the flux of $\boldsymbol{B}$ escaping from it. It is thus not required that $\boldsymbol{B}$ and the plasma move together.

More precisely, the relevant equation is Eq. 2.14: preserving the flux of the magnetic field through moving plasma contours requires that $\partial_t\boldsymbol{B} = \boldsymbol{\nabla}\wedge(\boldsymbol{U}\wedge\boldsymbol{B})$. This equation links the temporal variations of the magnetic field implied by a transverse motion of the plasma in the magnetic field, if

flux is to be preserved (if the plasma response is ideal). If the plasma motion is such that $\boldsymbol{\nabla} \wedge (\boldsymbol{U} \wedge \boldsymbol{B}) = 0$, then we also have $\partial_t \boldsymbol{B} = 0$, and no matter the magnetic field spatial variations, $\boldsymbol{B}(\boldsymbol{r}, t)$ will remain as it is[q]. On the other hand, if the plasma motion is such that $\boldsymbol{\nabla} \wedge (\boldsymbol{U} \wedge \boldsymbol{B}) \neq 0$, then circulating electric fields will be present ($\boldsymbol{\nabla} \wedge \boldsymbol{E} = \boldsymbol{\nabla} \wedge (\boldsymbol{U} \wedge \boldsymbol{B}) \neq 0$), and the magnetic field will be modified and dragged by the plasma. In conclusion, there is a whole class of motions that can occur in an ideal plasma without the need to change the magnetic field. This is for example the case of the $E \times B$ drift in a constant electric and magnetic field, or of motions parallel to $\boldsymbol{B}$. See Bellan (2006, §3.5.5) and Liang et al. (2011) for more examples.

2.5.2 Adiabatic invariant

The conservation of the first adiabatic invariant of a particle is also linked to magnetic flux conservation. This invariant,

$$\mu = \frac{m v_\perp^2 / 2}{B}, \tag{2.16}$$

where $v_\perp$ is the particle velocity perpendicular to $\boldsymbol{B}$, is conserved under the assumption of an ideal plasma response (see below). This can be linked to the fact that the flux of $\boldsymbol{B}$ through the circles described by the particle is conserved, simply by writing this flux as

$$\Phi_B = B \times \pi r_\mathrm{L}^2 = \frac{2m\pi}{q^2}\,\mu. \tag{2.17}$$

(Here $r_\mathrm{L} = v_\perp/(qB/m)$ is the Larmor radius.) Conservation of μ then implies conservation of Φ_B.

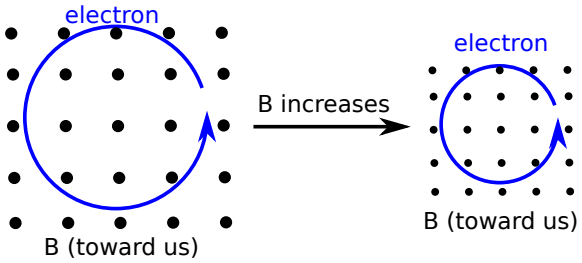

Figure 2.8: Conservation of the first adiabatic invariant, and of the flux linked by particles gyromotion, during an increase in magnetic field strength. On the left and on the right, there is the same number of field lines inside the particle orbit, and hence the same magnetic flux.

Physically, this also holds because of Lenz's law: a variation of the flux of $\boldsymbol{B}$ through the gyromotion generates an inductive electric field that accelerates or decelerates the particle so as to conserve Φ_B. This can be seen in Fig. 2.8, where an electron circles in a constant magnetic field. When the strength of B rises, the flux through the contour defined by the particle orbit also increases, and it produces a circulating electric field along the

[q] We thus have a moving plasma in a fixed magnetic field. Is there a motional electric field $-\boldsymbol{U} \wedge \boldsymbol{B}$ in this case? We have said (footnote n) that the origin of the motional electric field is the motion of the sources of the magnetic field. Since here it is not the moving plasma that creates $\boldsymbol{B}$, there is no motional electric field. Of course, this holds for the motional electric fields, i.e., for the ideal part of Ohm's law only. If there are non-ideal terms, there can be an electric field.

trajectory, oriented so as to accelerate the charge. The net result is that the gain in kinetic energy is proportional to the increase in B: $(mv_\perp^2/2)/B$ remains constant[r].

This holds as long as the particle trajectory in the plane normal to B is quasi-periodic, i.e., as long as the particle indeed describes circles in the magnetic field, or at least trajectories not far from circles. It is true under two conditions:

- The scales of variation of $\boldsymbol{B}$ must be small toward the gyroradius: $B/\boldsymbol{\nabla} B \ll r_\mathrm{L}$.
- During one gyration, the particle should not be perturbed by, for example, collisions or electromagnetic fluctuating fields. In terms of frequencies it means $\nu \ll \omega_\mathrm{c}$, where ω_c is the cyclotron period and ν either the collision frequency or the frequency of the fluctuations, whatever they are.

If these conditions hold, then the particle is said to be *magnetized* or *adiabatic*. This will be important in what follows, especially when discussing non-ideal processes in Sect. 2.11.

2.5.3 Reconnection

We now come to magnetic reconnection. Let us consider the simple configuration of Fig. 2.9. In the initial state (a), the magnetic field is created by a current sheet flowing normal to the paper plane.

The current layer can become unstable for various reasons (for example through the collisionless or collisional tearing instability) and these instabilities lead to the creation of a magnetic field pattern as shown in panel (b), thus leading to magnetic flux variations. Another possibility is that the magnetic field and plasma from above and below the current sheet are pushed toward the central current sheet by external large scale motions: then, the magnetic flux also varies.

In either cases, this variation of magnetic flux induces an electric field in panel (c), oriented so as to increase the initial current. This current produces a new magnetic field that cancels the former variations.

If the plasma response is ideal, we come back to the initial state. If it is not, then the non-ideal effects allow the magnetic field and the plasma to decouple from each others. This happens in panel (d) in what we call a non-ideal region, where non-ideal terms prevail over idealness (this region is variously called the dissipation, or diffusion region).

This allows, in panel (e), the magnetic field to change its topology and reconnect at the center. Note that since the magnetic field lines newly reconnected are highly bent, the tension force expels the plasma out.

Finally in panel (f), the electric field spreads in the ideal region, and/or plasma is brought toward the current sheet by the pressure gradient caused by the expelled plasma, so that an inflow at the $E \times B$ velocity appears. It is then possible to reach a steady state where new plasma arrives in the dissipation region, to be expelled in the outflows. Alternatively, the final

[r]The derivation is as follows: Integrating Lenz's law across the contour leads to $2\pi r_\mathrm{L}(t)E(t) = B'(t)\pi r_\mathrm{L}^2(t)$, i.e., $E(t) = 0.5B'(t)r_\mathrm{L}(t) = 0.5B'(t)/B(t) \times (m/q)v(t)$. The energy gain for the particle is $m(v^2(t))'/2 = qE(t)v(t)$, that can be written, after simple manipulations, $2v'(t)/v(t) = B'(t)/B(t)$. This last equality integrates into $v^2/B = \mathrm{const}$.

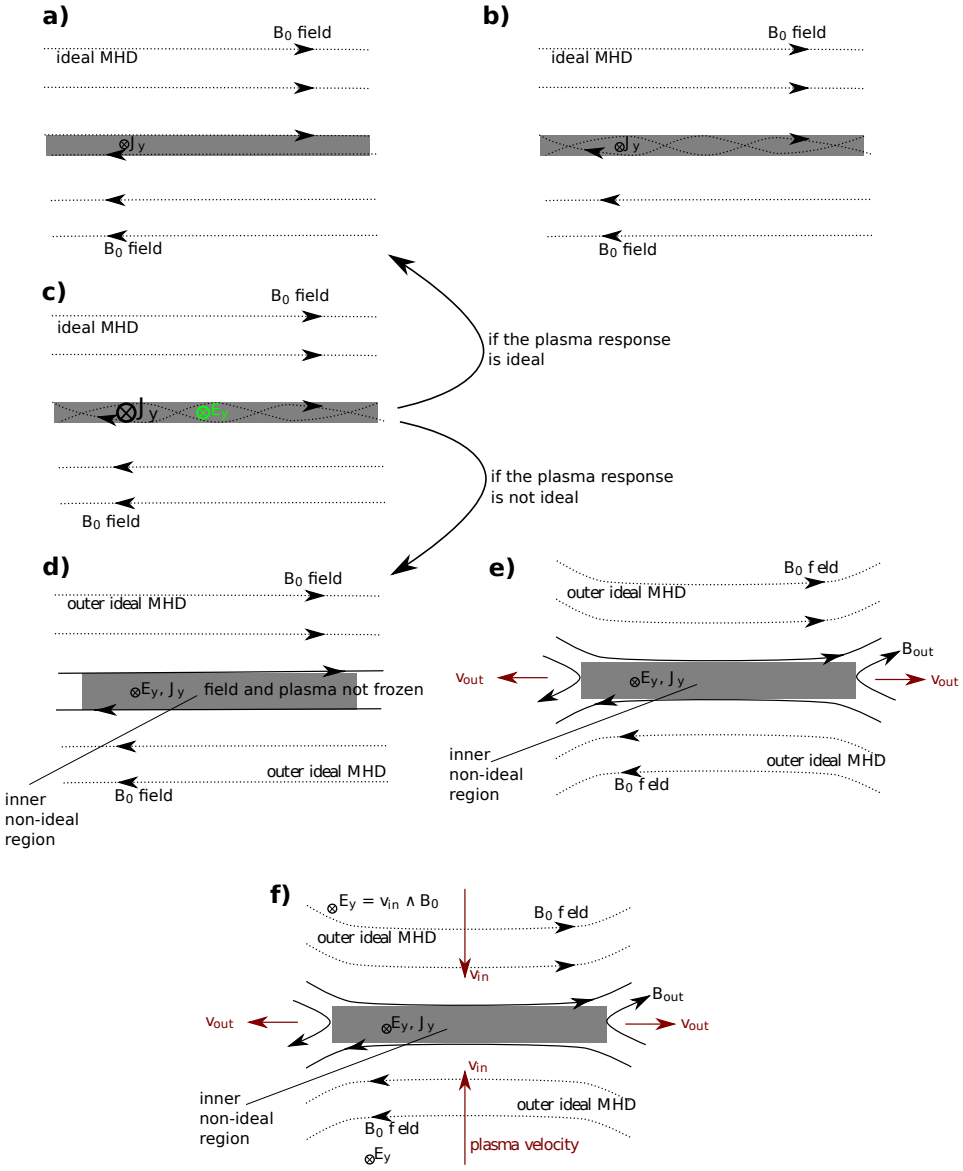

Figure 2.9: Illustration of the beginning of reconnection, in a simplified 2D geometry, from the initial state a to the possible final steady state f. See text for comments.

state can be quasi-steady with the periodic formation of magnetic islands, can be turbulent, or can end shortly if the current sheet undergoes another kind of instability.

Once again, if the plasma is ideal, then it will perfectly respond and forbid any magnetic field reconnection. This is what makes reconnection hard to study: it is a non-ideal effect. Non-ideal effects are numerous, and allow reconnection to occur in nature. They can be due to (see Sect. 2.11.2 for details):

- Collisions. Electrons can be hindered in their motions by collisions with ions, with neutrals, or with themselves.
- Electron inertia. The electrons have a finite mass which prevents them from responding instantaneously to the induced electric fields, thus delaying the response. This is particularly important in collisionless plasmas. Finite inertia allows collective effects: electromagnetic fields

created by groups of particles can hinder the motion of electrons.

- Non-adiabaticity. When the magnetic field scale varies on a scale smaller than the particles gyroradii, the plasma response cannot be ideal.
- The Hall term (which reflects the different dynamics of electrons and ions) is a non-ideal term, but it does not lead to reconnection. Its presence implies that the magnetic field moves with the electrons, not with the ions. It can however accelerate the reconnection rate (see Sect. 2.12.1).

2.6 Instructive examples

We now develop several examples: a basic and illustrative case of reconnection between two current coils (Sect. 2.6.1), the well known Sweet-Parker case that also shows that reconnection can be steady (Sect. 2.6.2), and we stress that reconnection is neither field diffusion nor field annihilation (Sect. 2.6.3).

2.6.1 The example of the coils

It is easy to follow misleading reasoning about reconnection and flux considerations when working with a model that is not self-consistent. It is often important to think on a situation which encompasses the plasma, the magnetic field, *and its sources*. A simple and instructive example is that of two circular coils, mechanically fixed to an axis, in which flows an equal current I_0 (see Fig. 2.10). Besides its pedagogical interest, this setup is also the one used in the TS-3 experimental device, which is devoted to the study of magnetic reconnection (e.g., Ono et al. 2011, and Sect. 1.3).

The problem has an axis of symmetry $\boldsymbol{z}$. The symmetries of the distribution of currents involve a magnetic field $(B_r(r,z), 0, B_z(r,z))$. This, and the fact that the magnetic field is divergence free, allow the use of a stream-function Ψ such that[s]

$$\boldsymbol{B}(r,z) = \frac{1}{2\pi r}\begin{vmatrix} -\partial_z\Psi \\ 0 \\ \partial_r\Psi \end{vmatrix} = \frac{1}{2\pi}\boldsymbol{\nabla}\Psi\wedge\boldsymbol{\nabla}\Phi. \tag{2.18}$$

(Φ is the angle of cylindrical coordinates.) If we compute the evolution of Ψ along a field line parametrized by s:

$$\frac{\mathrm{d}\Psi}{\mathrm{d}s} = \partial_x\Psi\frac{\mathrm{d}x}{\mathrm{d}s} + \partial_y\Psi\frac{\mathrm{d}y}{\mathrm{d}s} = (\partial_x\Psi)B_x + (\partial_y\Psi)B_y, \tag{2.19}$$

and with Eq. 2.18, we have that $\mathrm{d}\Psi/\mathrm{d}s = 0$. It means that the curves $\Psi = \text{const}$ are field lines of $\boldsymbol{B}$.

The stream-function is also a tracer of the magnetic flux. Consider the flux of the magnetic field through a circle centered on the z axis (center $(0, z_0)$), of radius R_0. It is:

$$F(R_0, z_0, t) = \int_{r=0}^{R_0} 2\pi r\mathrm{d}r B_z(r, z_0, t) = \Psi(R_0, z_0, t) - \Psi(0, z_0, t). \tag{2.20}$$

[s] In 2D, since $\partial_x B_x + \partial_y B_y = 0$, there exists a stream function such that $B_x = -\partial_y\Psi$ and $B_y = \partial_x\Psi$. This result also applies to an axisymmetric case, adapted with a factor $2\pi r$ in the divergence as done here.

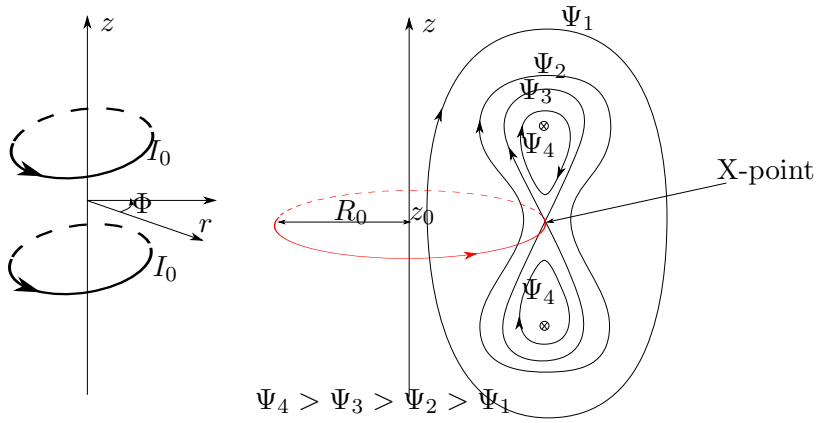

Figure 2.10: **Left:** the setup is that of two current coils mechanically fixed to an axis ($\boldsymbol{z}$).
Right: magnetic field lines created by the two currents in a r-z plane.

From this, we can deduce that on Fig. 2.10, $\Psi_1 < \Psi_2 < \Psi_3 < \Psi_4$. This is because a circle extending up to the $\Psi_1 = \text{const}$ contour obviously encompasses less flux than a circle extending to the $\Psi_2 = \text{const}$ contour, and so on.

In vacuum

Now, we start from the situation in Fig. 2.10. We assume that we are in vacuum. The two coils are maintained in place mechanically, and we decide to bring them closer. (Actually, since their currents are in the same direction, they attract each other like two magnets. Anyway, that their motion is mechanical or natural is unimportant as long as they come closer.) By doing so, the $\Psi_4 = \text{const}$ contour will move toward the X-point, the $\Psi_3 = \text{const}$ contour will leave the X-point and resemble the $\Psi_2 = \text{const}$ contour.

At the X-point, reconnection of field lines occurs, with field lines turning around one coil only (the Ψ_4-likes field lines) reconnecting two by two to become field lines turning around the two coils: there is a topological change.

If we look at the flux through the circle passing by the X-point considered just before, we see with Eq. 2.20 that it increases (it was Ψ_3, and then Ψ_4, and so on). Visually, this is clear because there are more and more field lines captured by the circle.

But now, Faraday's law integrated along the circle gives

$$\oint_C \mathrm{d}\boldsymbol{l} \cdot \boldsymbol{E} = -\frac{\mathrm{d}}{\mathrm{d}t} \iint_S \mathrm{d}\boldsymbol{S} \cdot \boldsymbol{B} = -\frac{\mathrm{d}F(R_0, z_0, t)}{\mathrm{d}t} < 0. \tag{2.21}$$

There is an electric field directed along the circle, directed in the opposite direction relative to the circle orientation of Fig. 2.10 (along $-\Phi$).

Since we are in vacuum, nothing else happens.

In a plasma

Suppose now that the space between the coils is filled with a plasma. As we bring the coils closer to one another, the electric field $\boldsymbol{E}(R_0, \Phi, z_0) = (2\pi R_0)^{-1} \mathrm{d}F(R_0, z_0, t)/\mathrm{d}t \propto -\Phi$ will act on the free charges, and drive a

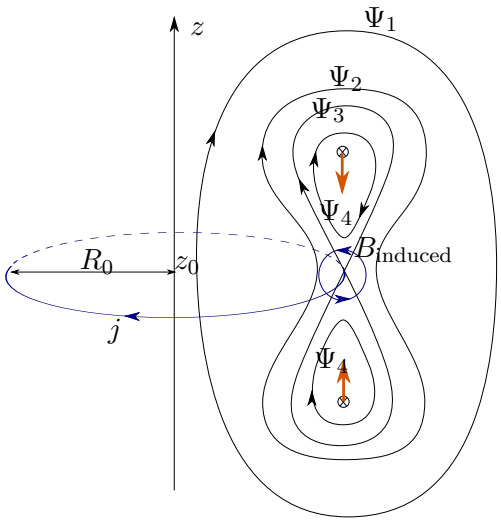

Figure 2.11: Current and magnetic field generated by the motion of the coils (orange arrows) and the magnetic field induced at the X-point.

current along the circle, in the $-\Phi$ direction. In turn, this current will induce a magnetic field as drawn in Fig. 2.11.

This magnetic field is in the same direction as the Ψ_4-like field lines: it will reinforce the field at the X-point where it was decreasing. But more than that: the force exerted by this induced field on the coils, $\boldsymbol{J}_{\text{coil}} \wedge \boldsymbol{B}_{\text{induced}}$, is directed so that the coils are repelled from the X-point. The response of the plasma is a force counter-acting our action to drive the coils closer, simply because this action changes the magnetic flux through some closed curve.

If the plasma is resistive, then $\boldsymbol{J}_{\text{induced}} = \sigma \boldsymbol{E}$ with σ the conductivity, and the force on the coil can be computed.

If the plasma is ideal, $\sigma = +\infty$, the current is infinite and instantaneous. It rebuilds the magnetic field as it reconnects, so that all in all, the magnetic field does not reconnect. The Ψ_4-like field lines are just compressed, and the force on the coils is all the more strong.

In the non-ideal case, field lines reconnect at a rate that depends on the forcing on the coils and on the plasma conditions, that will decide the nature of the dominant non-ideal effects. The induced current and the force on the coils will be less strong. This is then a situation of forced or driven reconnection.

2.6.2 The example of the Sweet-Parker case: steady magnetic reconnection

We now turn to a well known textbook case: the Sweet-Parker configuration. It is a situation where plasma from an outer ideal region flows toward a dissipation region where the resistivity is finite, then decouples from the magnetic field, and is expelled from this inner region by the tension force to form outflows. It is illustrated in Fig. 2.12.

We underline that seen in this frame, it is a steady situation. It thus happens at the end of an initial unstable phase, or because of an external forcing. In a steady state there is no variation of anything, and in particular no magnetic flux variation across a fixed contour. However, the rate at which the inflow is conveyed into the non-ideal diffusion zone, and the ratio of the

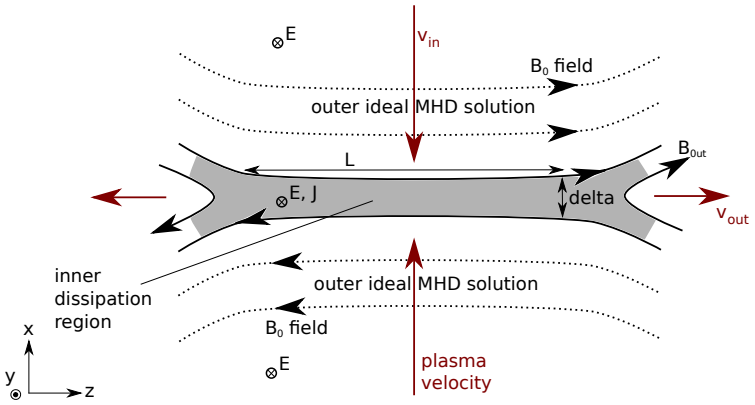

Figure 2.12: Sweet-Parker configuration.

inflowing kinetic energy to that in the outflow, are relevant quantities that can be computed with the use of conservation laws and some hypotheses. In particular, these quantities critically depend on the response of the plasma, i.e, on the nature and effects of the dominant non-ideal terms as well as other characteristic parameters.

We now derive these quantities by using a simple model, stressing that one of the main assumption is that non-idealness comes from a resistive term, $E_y = \eta j_y$. In Sect. 6.4.8 we will provide a similar analysis for the relativistic and collisionless case.

Linking the current in the layer to the magnetic field via $\boldsymbol{\nabla} \wedge \boldsymbol{B} = \mu_0 \boldsymbol{j}$ leads to

$$j_y = \frac{B_0}{\mu_0 \delta}, \tag{2.22}$$

with δ the width of the layer. The electric field at the center of the sheet is given by

$$E_y = \eta j_y = \frac{\eta B_0}{\mu_0 \delta}. \tag{2.23}$$

The inflow velocity in the ideal part is an $E \times B$ drift, so that

$$v_{\rm in} = E_y / B_0 = \frac{\eta}{\mu_0 \delta}, \tag{2.24}$$

where we have used Eq. 2.23 for E_y because it can be shown from $\boldsymbol{\nabla} \wedge \boldsymbol{E} = -\partial_t \boldsymbol{B} = 0$ that, if $\partial_y = 0$ (the 2D assumption), then $\partial_z E_y = \partial_x E_y = 0$ and E_y is constant.

Conservation of the number of particles leads to

$$n_{\rm in} v_{\rm in} L = n_{\rm out} v_{\rm out} \delta. \tag{2.25}$$

Conservation of energy, assuming that energy is dominated by the magnetic and electric fields in the inflow, and by bulk kinetic energy in the outflow, leads to

$$\left(\frac{\boldsymbol{E} \wedge \boldsymbol{B}}{\mu_0} \right)_{\rm in} L = n_{\rm out} \frac{m}{2} v_{\rm out}^2 \times \delta v_{\rm out}. \tag{2.26}$$

Using $E_y = v_{\rm in} B_0$, and combining the two previous equations, we obtain the important result

$$\boxed{v_{\rm out} = \sqrt{2} \frac{B_0}{\sqrt{\mu_0 m n_{\rm in}}} = \sqrt{2} V_{\rm A,in},} \tag{2.27}$$

i.e., the outflow velocity is given by the Alfvén speed in the inflow.

Assuming the flow incompressible ($n = \text{const}$) leads to $Lv_{\text{in}} = \delta v_{\text{out}}$, or

$$\frac{\delta}{L} = \frac{v_{\text{in}}}{V_{\text{A,in}}} = M_0. \tag{2.28}$$

Replacing v_{in} by $\eta/(\mu_0\delta)$ (Eq. 2.24) then leads to another expression for this ratio:

$$\boxed{\frac{\delta}{L} = \frac{v_{\text{in}}}{V_{\text{A,in}}} = \sqrt{\frac{\eta}{\mu_0 L V_{\text{A,in}}}} = {S_{\text{L}}}^{-1/2}.} \tag{2.29}$$

These two last equations are important. The Lundquist number

$$S_{\text{L}} \equiv \frac{\mu_0 L V_{\text{A,in}}}{\eta} \tag{2.30}$$

is generally very large: 10^4-10^8 in laboratory plasmas, 10^{10}-10^{14} in solar flares, 10^{15}-10^{20} in the interstellar medium (Ji and Daughton 2011, and Fig. 2.42). We thus see that $\delta \ll L$, and $v_{\text{in}} \ll v_{\text{out}}$. The flow is thus accelerated. But does this lead to an increase in kinetic energy of the flow? In order to see this, we manipulate the equations to arrive at

$$\begin{aligned} \frac{\text{incoming kinetic energy flux}}{\text{outcoming kinetic energy flux}} &= \frac{n_{\text{in}} L v_{\text{in}} \times v_{\text{in}}^2}{n_{\text{in}} \delta v_{\text{out}} \times v_{\text{out}}^2} \\ &= \frac{v_{\text{in}}^2}{v_{\text{out}}^2} = {S_{\text{L}}}^{-1} \ll 1. \end{aligned} \tag{2.31}$$

The kinetic energy of the flow thus increases. This new energy comes from the magnetic field energy.

Concretely, how are the particles accelerated? When they are in the incoming ideal zone, the electric field does not accelerate them because they are in a magnetic field $cB > E$ and simply $E \times B$ drift. However, when they arrive in the dissipative zone, the magnetic field becomes too weak, or electric fields parallel to $\boldsymbol{B}$ exist because of the non-idealness, and the electric field can transfer energy to the particles. The particles then escape in the exhausts because the magnetic field lines are oriented so as to deviate them there via the Lorentz force.

Note that the magnetic field configuration is stationary. Note also that the electric field is present in the non-ideal zone because $\boldsymbol{E} = \eta \boldsymbol{j}$, i.e., because collisions prevent the particles to screen it. (However, the initial transient phase where $\boldsymbol{E}$ rises is left unspecified here.)

This situation is somehow analogous to a MHD shock, where magnetic energy can be converted into plasma kinetic energy when the flow crosses the shock. The Rankine-Hugoniot relations, that use particle number density, momentum, and energy conservation across the discontinuity, are similar to the analysis that we performed. It is not surprising, as we will see, that Petschek introduced slow shocks around the diffusion region to increase the rate of magnetic energy conversion.

A final remark concerns the argument of magnetic flux variation. It is harder to invoke this argument in a steady state, because the magnetic flux across any fixed contour does not evolve in time. The reasoning that we applied for the two approaching current coils does not hold. Some researchers are reluctant to talk about magnetic field-line reconnection in steady state situations (Alfvén 1976), because the concept of moving field lines can lead

to erroneous interpretations – especially when the magnetic field is steady. Actually, there are no flux variation (flux variations matter only to trigger reconnection, or for unsteady cases). Here, there is a balance between inflow at the $E \times B$ speed and outflow, and a constant electric field that transfer energy from the magnetic field to the particles, electric field that is sustained (i.e., not screened) by the non-ideal effects.

2.6.3 Magnetic reconnection versus magnetic diffusion and magnetic annihilation

The presence of non-ideal effects does not necessarily lead to reconnection. Instead, the magnetic field can simply move at a velocity different from that of the plasma: it diffuses, or slips across the plasma. It can also annihilate when encountering a field of opposed sign, without any reconnection. In this section, we precise these two mechanisms.

Generally, current sheet diffusion and magnetic annihilation is what happens to current sheets too large to trigger instabilities and too large to undergo fast reconnection.

Magnetic diffusion

We have seen that the ideal Ohm's law $\partial_t \boldsymbol{B} = \boldsymbol{\nabla} \wedge [\boldsymbol{V} \wedge \boldsymbol{B}]$ means that the magnetic field is advected at velocity $\boldsymbol{V}$.

The non-ideal Ohm's law,

$$\boldsymbol{E} + \boldsymbol{V} \wedge \boldsymbol{B} = \boldsymbol{R}, \tag{2.32}$$

$$\text{or} \quad \partial_t \boldsymbol{B} = \boldsymbol{\nabla} \wedge [\boldsymbol{V} \wedge \boldsymbol{B} - \boldsymbol{R}], \tag{2.33}$$

can then allow either magnetic reconnection where the connections of the field lines change, or magnetic diffusion where the field lines drift at a velocity different from that of the fluid. In the case of reconnection, the connections of the field lines change very abruptly (as shown and explained in Fig. 2.1), while in the case of diffusion the connectivity changes, but in a slow and continuous way.

We can deduce hints as to which case is allowed depending on the nature of the non-ideal terms contained in $\boldsymbol{R}$ (for more details, see Birn and Priest 2007, Chap. 2):

- If there is a vector field $\boldsymbol{w}(\boldsymbol{x}, t)$ and a scalar field $\Phi(\boldsymbol{x}, t)$ such that $\boldsymbol{R} = \boldsymbol{\nabla}\Phi + \boldsymbol{w} \wedge \boldsymbol{B}$, then Eq. 2.33 can be written $\partial_t \boldsymbol{B} = \boldsymbol{\nabla} \wedge [(\boldsymbol{V} - \boldsymbol{w}) \wedge \boldsymbol{B}]$. It means that the magnetic field is advected at velocity $\boldsymbol{V} - \boldsymbol{w}$.
  - If $\boldsymbol{w}$ is continuous, then there is no reconnection, just diffusion. This is for example the case of the Hall term, $\boldsymbol{R} \propto \boldsymbol{j} \wedge \boldsymbol{B} \propto (\boldsymbol{v}_\mathrm{e} - \boldsymbol{v}_\mathrm{i}) \wedge \boldsymbol{B}$: the magnetic field is carried by the velocity $\boldsymbol{V} - \boldsymbol{v}_\mathrm{i} + \boldsymbol{v}_\mathrm{e} = \boldsymbol{v}_\mathrm{e}$, that is, by the electrons.
    This is also the case of ambipolar diffusion, when only the term $\boldsymbol{R} \propto (\boldsymbol{v}_n - \boldsymbol{v}_\mathrm{i}) \wedge \boldsymbol{B}$ is kept (with $\boldsymbol{v}_n$ the velocity of the neutral fluid): the magnetic field is carried by the ions, not by the neutrals.
  - If $\boldsymbol{w}$ is not continuous, vanishes, or infinite, then reconnection can occur. It is, for example, the case of the magnetic field velocity Eq. 2.3 at a magnetic null point.

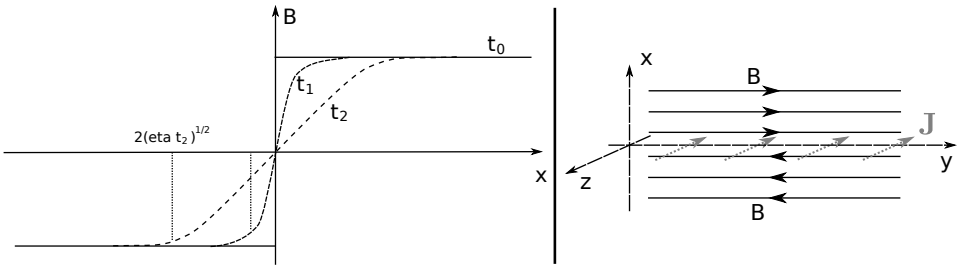

Figure 2.13: Diffusion of a 1D current sheet. **Right:** sketch of the configuration. **Left:** Profiles of the y magnetic field at different times.

- If there is no vector field $\boldsymbol{w}$ or scalar Φ such that $\boldsymbol{R} = \boldsymbol{\nabla}\Phi + \boldsymbol{w} \wedge \boldsymbol{B}$, then reconnection can occur.

In the cases where reconnection can occur, whether it does occur or not depends on the possible forcing, on the parameters of the current sheet (thickness, density, ...), and of the asymptotic magnetic field (strength, direction, ...), which have to be so that the initial situation is unstable.

Magnetic field annihilation

Field line diffusion can lead to field line annihilation or, without thinking in terms of field lines, to a decay of the magnetic field. We illustrate this case by an example.

We consider a one dimensional current sheet initially infinitely thin: $\boldsymbol{B} = B_0\hat{\boldsymbol{y}}$ for $x > 0$, and $\boldsymbol{B} = -B_0\hat{\boldsymbol{y}}$ for $x < 0$. In the absence of plasma motion ($\boldsymbol{V} = 0$), and under the assumption that $\boldsymbol{R} = \eta_0\boldsymbol{j} = \eta_0\mu_0^{-1}\boldsymbol{\nabla} \wedge \boldsymbol{B}$, the induction equation reads:

$$\partial_t \boldsymbol{B} = \eta \partial^2_{xx} \boldsymbol{B}, \tag{2.34}$$

with $\eta = \eta_0/\mu_0$. This equation is a diffusion equation. Consequently, the current sheet will diffuse away, as shown in Fig. 2.13. At time t, the width of the sheet is given by $4\sqrt{\eta t}$.

The total magnetic flux through the x-z plane, $\int \mathrm{d}x\, B_y$, remains constant (and null). The total current is given by $I = \int \mathrm{d}x\, j_y = \int \mathrm{d}x\, \partial_x B_y/\mu_0 = 2B_0/\mu_0$. It remains constant and is just spread away from the center. The total magnetic energy, $\int \mathrm{d}x\, B_y^2/(2\mu_0)$, decreases by Joule heating. This can be seen by writing $B_y\partial_t B_y = B_y\partial_x E_z = B_y\eta_0\partial_x j_z$, integrating by part to arrive at $-(\partial_x B_y)\eta_0 j_z$, using $(\partial_x B_y) = \mu_0 j_z = \mu_0\eta_0^{-1}E_z$, to arrive at

$$\frac{\mathrm{d}}{\mathrm{d}t}\int \mathrm{d}x\, \frac{B_y^2}{2\mu_0} = -\int \mathrm{d}x\, \eta_0 j_z^2. \tag{2.35}$$

At a fixed location x, the magnetic field decreases. This can be seen as if field lines were dragged toward the center at $x = 0$ by diffusion, where they disappear or annihilate with their opposed counterpart. It is however not necessary to think in terms of field lines.

There is no magnetic reconnection, but still a conversion of magnetic to kinetic energy via Joule heating, i.e., by collisions between particles accelerated by the inductive electric field E_z. Again, this electric field is induced by magnetic flux variations: $\partial_t B_y = \partial_x E_z$.

2.7 Non-ideal Ohm's laws

We are now ready to explore the subject of magnetic reconnection more frankly. We first start by describing the generalization of Ohm's law $\boldsymbol{E} + \boldsymbol{U} \wedge \boldsymbol{B} = 0$, and introduce the magnetic Reynolds number.

As we have seen with Eq. 2.15, a consequence of the relation $\boldsymbol{E}+\boldsymbol{U}\wedge\boldsymbol{B} = 0$, which holds in ideal MHD, is that ideal MHD does not allow for magnetic flux variations across plasma elements: the flux tubes are frozen to the plasma motion, topological changes of the magnetic field (such as those of Fig. 2.1) are forbidden, and more generally, induced electric fields cannot remain finite during a finite amount of time. A consequence is that the configuration reached after an ideal MHD instability, when the plasma has relaxed to an equilibrium state, is not necessarily the lowest magnetic energy state, but only the lowest energy state allowed by the preserved topology of the field.

Magnetic reconnection is a non-ideal process or instability that allows for flux variations in small area, that in turn allow global topological changes, and thus enables the possibility to relax to energy states lower than those accessible without topological changes[t]. Energy is taken from magnetic energy, because the field reaches a lower energy state. As we explained, the transfer of energy to the particles is realized via the electromotive electric fields induced by magnetic flux variations and, in steady state, sustained by the non-ideal plasma response.

2.7.1 Resistive Ohm's law and magnetic Reynolds number

The simplest model to allow for magnetic reconnection is to consider a finite resistivity η. In the rest frame of the plasma, Ohm's law is simply $\boldsymbol{E}' = \eta \boldsymbol{J}'$. In the lab frame, in which the plasma moves with a velocity $\boldsymbol{U}$ in a magnetic field $\boldsymbol{B}$, the electric field becomes $\boldsymbol{E} = \boldsymbol{E}' - \boldsymbol{U} \wedge \boldsymbol{B}$ and the current remains unchanged (in the non-relativistic limit), so that we have:

$$\boldsymbol{E} + \boldsymbol{U} \wedge \boldsymbol{B} = \eta \boldsymbol{J}. \tag{2.36}$$

It is then important to know when the resistive term dominates.

A particular case is at stagnation points of the flow (for example at the X-point in the center of Fig. 2.2) where the velocity vanishes, so that we simply have $\boldsymbol{E} = \eta \boldsymbol{J}$.

But more generally, we can take the curl of Eq. 2.36, use $\boldsymbol{\nabla} \wedge \boldsymbol{E} = -\partial_t \boldsymbol{B}$, assume the electric resistivity η independent of space, and use $\boldsymbol{\nabla} \wedge \mu_0 \boldsymbol{J} = \boldsymbol{\nabla} \wedge (\boldsymbol{\nabla} \wedge \boldsymbol{B}) = -\boldsymbol{\nabla}^2 \boldsymbol{B}$ (we neglect the displacement current, not important in non-relativistic situations) to obtain an advection-diffusion equation for the magnetic field:

$$\frac{\partial \boldsymbol{B}}{\partial t} = \boldsymbol{\nabla} \wedge (\boldsymbol{U} \wedge \boldsymbol{B}) + \frac{\eta}{\mu_0} \boldsymbol{\nabla}^2 \boldsymbol{B}. \tag{2.37}$$

In the absence of resistivity, we know that the magnetic field is carried by the plasma, so that the equation $\partial_t \boldsymbol{B} = \boldsymbol{\nabla} \wedge (\boldsymbol{U} \wedge \boldsymbol{B})$ means that the magnetic field is advected with a velocity $\boldsymbol{U}$. In the absence of plasma motion, the

[t] Note however that the magnetic field topology cannot completely freely change. It is constrained to preserve some quantities, such as the total helicity of the field lines (under some boundary conditions, see Bellan (2006), and not completely for 3D reconnection, see Priest (1987)).

equation reduces to a diffusion equation $\partial_t \boldsymbol{B} = \alpha \boldsymbol{\nabla}^2 \boldsymbol{B}$. Consequently, on the right-hand side of Eq. 2.37, the first term describes advection of the magnetic field by the fluid, while the second represents diffusion of the magnetic field without the need of any fluid motion: the fluid and the magnetic field decouple (here because collisions prevent particles to respond correctly). If we introduce a characteristic length of variation L_0 for B, a typical field strength B_0 and a typical velocity U_0, these terms can be evaluated as $\boldsymbol{\nabla} \wedge (\boldsymbol{U} \wedge \boldsymbol{B}) \sim L_0^{-1} U_0 B_0$ and $\eta \mu_0^{-1} \boldsymbol{\nabla}^2 \boldsymbol{B} \sim \eta \mu_0^{-1} L_0^{-2} B_0$, so that their ratio is what defines the magnetic Reynolds number:

$$R_m = \frac{\text{advection of B}}{\text{diffusion of B}} = \frac{U_0 L_0}{\eta/\mu_0}. \tag{2.38}$$

We recall that η is the electric resistivity, and we define η/μ_0 as the magnetic diffusivity[u].

If R_m is very high, then magnetic diffusion is negligible compared to magnetic field advection by the flow: ideal MHD applies and reconnection is not likely to occur. On the other hand, if R_m is small, non-ideal effects allow the field to diffuse significantly, it decouples from the plasma, and it can reconnect.

2.7.2 More general Ohm's law

Finite resistivity as described by Eq. 2.36 is due to electron-ion collisions, and is actually not always responsible for the reconnection observed in plasmas. Instead, in sufficiently collisionless plasmas, effects such as electron finite inertia, or the Hall term, are expected to play the key role and to provide faster reconnection rates than predicted by the Sweet-Parker resistive analysis. In more collisional plasmas, reconnection is believed to produce small scales by a turbulent cascade via the tearing of the current sheet, or to occur on small scales due to a pre-existing turbulence, or both (see Sect. 2.11.4), and the large scale Sweet-Parker analysis also fails. Since it is very complicated to consider the non-ideal effects or the turbulent cascade, one often considers resistive MHD with an anomalous resistivity η not linked to collisional resistivity. To illustrate this complexity, we derive a generalized Ohm's law including other terms.

Ohm's law is derived from the fluid equation of motion for the particles responsible for the frozen-in condition, i.e., the electrons. This equation of motion can differ according to the hypotheses made, and in particular to the fluid closure employed. We derive Ohm's law in a collisionless relativistic plasma in Sect. 6.4.3. Here we consider collisions and a non-relativistic plasma, with the following form for the conservation of momentum:

$$\begin{aligned} n_\mathrm{e} m_\mathrm{e} \frac{\partial \boldsymbol{v}_\mathrm{e}}{\partial t} + n_\mathrm{e} m_\mathrm{e} \boldsymbol{v}_\mathrm{e} \cdot \boldsymbol{\nabla} \boldsymbol{v}_\mathrm{e} = n_\mathrm{e}(-e)(\boldsymbol{E} + \boldsymbol{v}_\mathrm{e} \wedge \boldsymbol{B}) - \boldsymbol{\nabla} \cdot \boldsymbol{P}_\mathrm{e} \\ + \chi(\boldsymbol{v}_\mathrm{i} - \boldsymbol{v}_\mathrm{e}) + \chi_2 \boldsymbol{\nabla}^2 \boldsymbol{v}_\mathrm{e}, \end{aligned} \tag{2.39}$$

where n_e is the electron number density, m_e the electron mass, $\boldsymbol{v}_\mathrm{e}$ and $\boldsymbol{v}_\mathrm{i}$ the electron and ion fluid velocities, $\boldsymbol{P}_\mathrm{e}$ the electron pressure tensor (that can be anisotropic and with off-diagonal terms), $\chi(\boldsymbol{v}_\mathrm{e} - \boldsymbol{v}_\mathrm{i})$ accounts for

[u] We also remind that in fluid dynamic, the Reynolds number is the ratio of momentum advection by the bulk flow ($\rho[\partial_t \boldsymbol{v} + \boldsymbol{v} \cdot \boldsymbol{\nabla} \boldsymbol{v}]$) over momentum diffusion by collisions ($\rho \nu \boldsymbol{\nabla}^2 \boldsymbol{v}$), and is given by $R_e = U_0 L_0 / \nu$, with ν the kinematic viscosity.

collisions between electrons and ions (note that the collisionality could be anisotropic and depend on the magnetic field orientation), and $\chi_2 \boldsymbol{\nabla}^2 \boldsymbol{v}_\mathrm{e}$ electron viscosity (due to electron-electron collisions). From this we obtain Ohm's law as

$$\begin{aligned} \boldsymbol{E} + \boldsymbol{v}_\mathrm{e} \wedge \boldsymbol{B} = &-\frac{m_\mathrm{e}}{e}\left(\frac{\partial \boldsymbol{v}_\mathrm{e}}{\partial t} + \boldsymbol{v}_\mathrm{e} \cdot \boldsymbol{\nabla} \boldsymbol{v}_\mathrm{e}\right) - \frac{1}{n_\mathrm{e} e}\boldsymbol{\nabla} \cdot \boldsymbol{P}_\mathrm{e} \\ &+ \frac{1}{n_\mathrm{e} e}\chi(\boldsymbol{v}_\mathrm{i} - \boldsymbol{v}_\mathrm{e}) + \frac{1}{n_\mathrm{e} e}\chi_2 \boldsymbol{\nabla}^2 \boldsymbol{v}_\mathrm{e}. \end{aligned} \tag{2.40}$$

Moreover, in MHD the velocity of the fluid is the velocity of the center-of-mass between electrons and ions, and is to a very good approximation given by the ion fluid velocity (because $m_\mathrm{i} \gg m_\mathrm{e}$). We can thus force the velocity on the left-hand side to be that of the ions, by writing $\boldsymbol{v}_\mathrm{e} = \boldsymbol{v}_\mathrm{i} + (\boldsymbol{v}_\mathrm{e} - \boldsymbol{v}_\mathrm{i}) = \boldsymbol{v}_\mathrm{i} - \boldsymbol{J}/(e n_\mathrm{e})$, where we assume singly charged ions and quasi-neutrality ($n_\mathrm{e} = n_\mathrm{i}$). Also, the ion-electron collision term can be rewritten by using the current. We then obtain:

$$\begin{aligned} \underbrace{\boldsymbol{E} + \boldsymbol{v}_\mathrm{i} \wedge \boldsymbol{B}}_{\text{E}-\text{field in the ion plasma frame}} = &\underbrace{\frac{1}{n_\mathrm{e} e}\boldsymbol{J} \wedge \boldsymbol{B}}_{\text{Hall term}} - \underbrace{\frac{m_\mathrm{e}}{e}\left(\frac{\partial \boldsymbol{v}_\mathrm{e}}{\partial t} + \boldsymbol{v}_\mathrm{e} \cdot \boldsymbol{\nabla} \boldsymbol{v}_\mathrm{e}\right)}_{\text{electron bulk inertia}} \\ &- \underbrace{\frac{1}{n_\mathrm{e} e}\boldsymbol{\nabla} \cdot \boldsymbol{P}_\mathrm{e}}_{\text{e}^- \text{ thermal inertia}} \\ &+ \underbrace{\frac{\chi}{(n_\mathrm{e} e)^2}\boldsymbol{J}}_{\text{e}-\text{i collisions}} + \underbrace{\frac{\chi_2}{n_\mathrm{e} e}\boldsymbol{\nabla}^2 \boldsymbol{v}_\mathrm{e}}_{\text{e}-\text{e collisions}}. \end{aligned} \tag{2.41}$$

In a collisionless plasma, $\chi = \chi_2 = 0$ and the only source of non-idealness is electron inertia: either bulk inertial or thermal inertia[v]. The latter is due to bouncing electron motions into the non-ideal layer, which give a high pressure, and is the main contributor in non-relativistic collisionless magnetic reconnection.

We describe each of the non-ideal terms in Sect. 2.11.2, and discuss their relative importance in Sect. 2.11.3. Also, we detail the contribution of each term in Ohm's law for relativistic reconnection in Sect. 6.4.3.

2.8 From large to small scales: Global dynamics

Magnetic reconnection is really a multi-scale process, with large scale motions setting the local parameters and geometry allowing for reconnection to occur, and with reconnection acting back on the large scales by producing outflows, high-energy particles, and by heating the plasma. This multi-scale nature makes it very challenging to study, especially for numerical simulations. In Sects. 2.8 to 2.13, we go for a journey through plasma scales, from large ideal sizes to small non-ideal regions.

2.8.1 Large scale dynamics

On large scales, plasma flows usually exhibit large magnetic Reynolds numbers $R_m = U_0 L_0/(\eta/\mu_0)$ (Eq. 2.38), because their resistivity η is small, and

[v] The Hall term remains present, but as we explain, it allows a slippage of the field lines with respect to the ion fluid, and not reconnection.

their characteristic size L_0 very large. On these scales the magnetic field thus remains to a very good approximation frozen to the plasma, and ideal MHD provides a correct description. This is the case of many large-scale astrophysical environments, such as the solar magnetosphere, accretion flows around compact objects, or various magnetized jets and winds.

2.8.2 Examples: shocked winds, large scale motions in the solar corona

For example, the supersonic collision of two magnetized flows leads to a pair of shocks separated by a contact discontinuity[w], that the plasma cannot cross: there is no mixing between the two flows. This is the case of the boundary between the solar wind and the interstellar medium (Fig. 2.14), and of the solar wind meeting the Earth magnetosphere (Fig. 2.15). The ideal MHD large-scale world of stars and planets can be seen as isolated bubbles of plasma separated by thin impermeable boundaries.

In the solar atmosphere, large scale magnetic flux tubes emerge from under the surface of the Sun via Parker instability[x] and stay suspended in the solar corona. These tubes remain anchored under the Sun's surface at the so called footpoints (Fig. 2.16 and Fig. 1.3). The large scale dynamics of these tubes is governed by ideal MHD. A similar arrangement is believed to exist above accretion disks in X-ray binaries or active galactic nuclei.

2.9 From large to small scales: Formation of reconnection sites

In this ideal global dynamics, the magnetic flux is advected by the fluid and compressed at some locations, which can be, for example, at the previously mentioned thin boundaries, or between two flux tubes in the solar corona that are pushed together, or between an emerging flux tube and a pre-existing magnetic field. These compressions create zones of strong magnetic shear (strong $\boldsymbol{\nabla} \wedge \boldsymbol{B}$), and because of $\mu_0 \boldsymbol{j} = \boldsymbol{\nabla} \wedge \boldsymbol{B}$, the plasma responds by creating thin current sheets. Another way of seeing these current sheets is to integrate $\mu_0 \boldsymbol{j} = \boldsymbol{\nabla} \wedge \boldsymbol{B}$ across the sheet to have the passage relation:

$$\boldsymbol{n}_{12} \wedge (\boldsymbol{B}_2 - \boldsymbol{B}_1) = \mu_0 \boldsymbol{j}_s, \tag{2.42}$$

where 1 and 2 refer to the two sides of the sheet and $\boldsymbol{j}_s$ to the surface current flowing into the sheet. In particular, we see that it is the tangential discontinuity, $\boldsymbol{n}_{12} \wedge (\boldsymbol{B}_2 - \boldsymbol{B}_1)$, that matters. The thinning and subsequent current sheet creation are illustrated by numerical simulations in Fig. 2.17 in 2D, and in Fig. 2.18 in 3D.

If the situation is not stationary because of a varying forcing or because of growing instabilities, these sheets can become thinner, until the length scales involved make the ideal hypothesis break down. Idealness may be lost

[w] In MHD there are three wave modes: the slow and fast magnetosonic waves, and the Alfvén wave. If the flows are super-fast, then there can actually be two shocks and an Alfvén wave on each side of the contact discontinuity. But this does not change the discussion.

[x] Parker instability occurs to flux tubes immersed in a plasma in a gravity field. If the central part of the tube rises (so that the tube is bent upward and forms a bump), then by gravitation plasma will fall down. The bump is then less dense, and the buoyancy force makes it rise even more. So that plasma falls down, and so on.

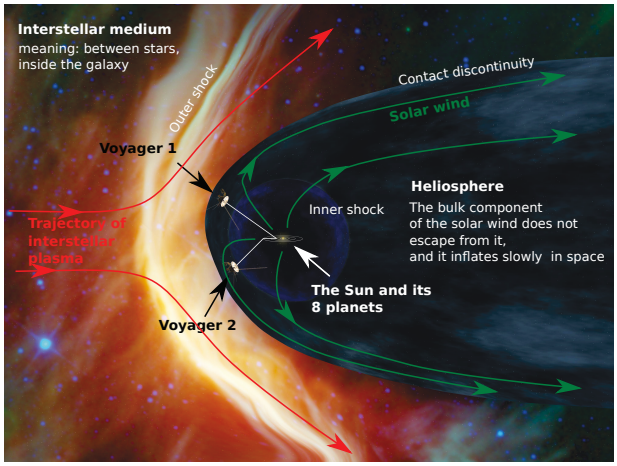

Figure 2.14: Artist view of the heliosphere. The solar wind meets the interstellar space and forms a shock. In ideal MHD, the two flows do not cross the contact discontinuity. In the real world, magnetic reconnection or other instabilities (e.g., Kelvin-Helmholtz) allow some passage. High-energy particles can pass through as well. Adapted from NASA Voyager website.

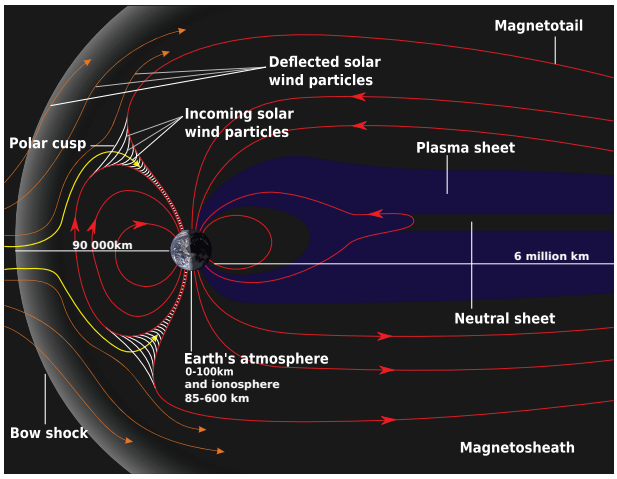

Figure 2.15: The magnetosphere of the Earth. Adapted from Wikipedia. Red arrows are magnetic field lines from the Earth.

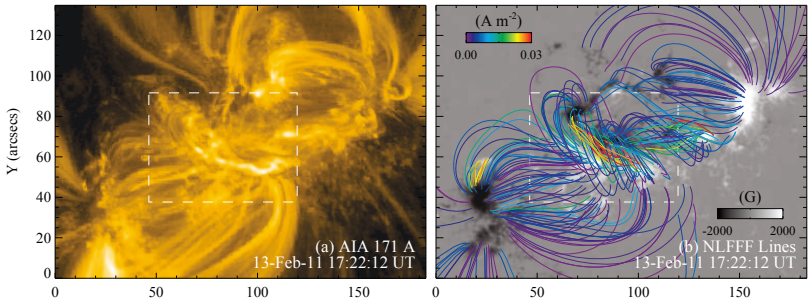

Figure 2.16: Left: picture of the solar surface, showing magnetic field lines. **Right:** reconstruction of the field lines seen on the left picture assuming a force-free MHD equilibrium. The white and black patches on the surface are the footpoints of the field lines, where they are anchored. Footpoint motions move the field lines. From Liu et al. (2013a).

either because the magnetic Reynolds number $R_m = U_0 L_0/(\eta/\mu_0)$ becomes lower and lower because L_0 shrinks, so that collisions become important, or alternatively because the other non-ideal terms (mainly, the ion and electron inertia contributions) start being important at these length scales. Consequently, *current sheets, or equivalently zones of strong magnetic gradients, are the loci of reconnection and of the subsequent field-to-plasma energy transfer.*

The locations where current sheets form and the mechanisms at stake are relatively simple in 2D, less so and still not fully understood in 3D. Three-dimensional setups indeed involve various geometries, where the topology plays a key role and sets the reconnection rate or the amount of energy conversion. We will discuss in more details in the next section (Sect. 2.10) where and how reconnection takes place in 2D and in 3D.

2.10 From large to small scales: A closer look at reconnection sites

We can now look closer at the current sheets. This section does not deal with the smaller scales where magnetic reconnection does take place due to non-ideal processes (this is the subject of the next sections, Sects. 2.11 and 2.12), but is concerned with the magnetic field configuration around the area where reconnection takes place.

The large scale structure of the magnetic field is indeed important to set up the conditions under which reconnection will happen at the kinetic scale, by fixing the magnetic energy that is brought into the non-ideal region, and that can be released, as well as the conditions at the boundary of the non-ideal region. In this section, the plasma is thus mostly considered as ideal, and we explore which magnetic field configuration can be unstable and give easily rise to reconnection. Of course, once reconnection happens, it can alter the structure of the plasma on large scales and make the ideal hypothesis break down, even hundreds of kinetic lengths aways from the reconnection site (along the magnetic separatrices for example). The physics of such effects will be discussed in Sect. 2.12, and we presently regard the plasma as ideal.

We first introduce some general vocabulary in Sect. 2.10.1. Then, in Sect. 2.10.2 we review the possibilities in two-dimensions, that include X- and O-points, and initial configurations such as Harris sheet, X-point collapse, or force-free equilibrium. Next, we turn to cases that have no invariant direction and that are thus fully 3D. In Sect. 2.10.3 we introduce the required definitions, and in Sect. 2.10.4 we present the various possibilities in 3D, with reconnection at a null point (and the kind of nulls or of perturbations), or away from null points (at separators and at quasi-separatrix layers).

2.10.1 Geometry and vocabulary

A **magnetic null** is a location where the magnetic field vanishes. There are several kinds of field line topology allowed around a null. In 2D, there are two possibilities only: a **X-point** or a **O-point** (see Fig. 2.19). In 3D, several cases are possible, that we will detail in Sect. 2.10.3.

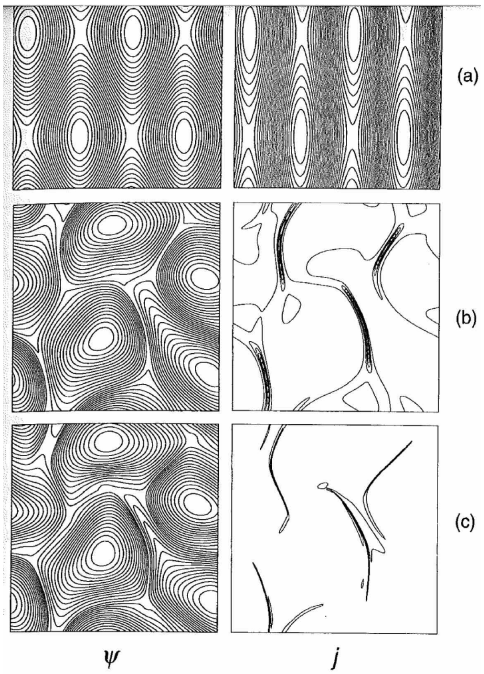

Figure 2.17: Two-dimensional resistive MHD simulation, from Biskamp (§3.2.1, 2000). The left panels represent magnetic field lines, and the right panels are the out-of-plane currents. The initial configuration, which is out-of-equilibrium, is that of line (*a*). Time increases in lines (*b*) and (*c*). We clearly see that the system evolves by increasing magnetic shear, thus reinforcing and localizing the current locations.

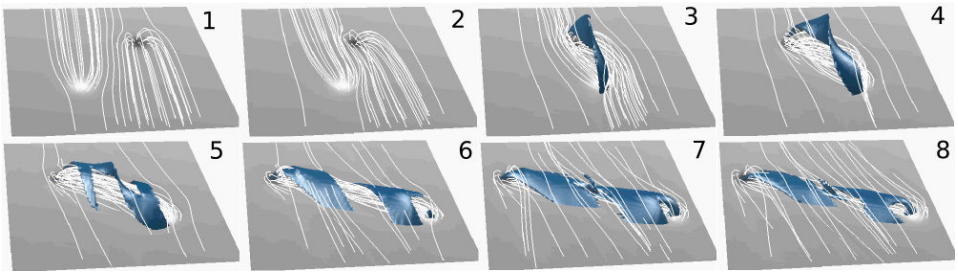

Figure 2.18: Three-dimensional resistive MHD simulation, from Parnell and Galsgaard (2004). The **white lines** are magnetic field lines. The initial configuration (panel 1) consists in two flux tubes anchored in the bottom plane at the black and white spots. The white spot is then brought to the right, and the black one to the left. The flux tubes meet, and, since they have field lines of opposed direction, strong gradients of $\boldsymbol{B}$ are created, which drive strong currents. These strong currents are represented by **shadowed blue area**, and are the places where reconnection occurs. Such a configuration may happen at the solar surface, when two flux tubes are brought into contact by the motion of their feet anchored in the photosphere.

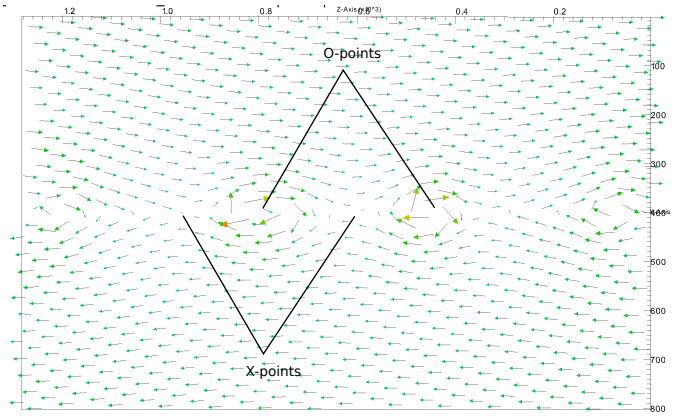

Figure 2.19: X and O points. Arrows are the magnetic field. From a PIC simulation.

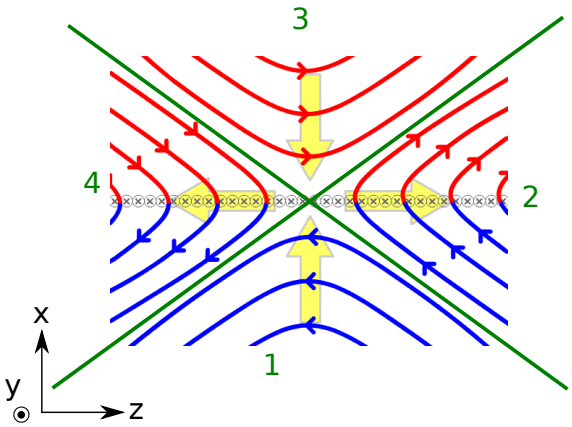

Figure 2.20: Separation of space into four domains by the separatrices (green lines), where field lines (in red and blue) have different origins. (Figure from Wikipedia.)

A **separatrix** (plural **separatrices**), is a surface (in 3D) or a curve (in 2D) that separates two regions where the field lines have distinct origins. It means that a field line from one domain cannot be continually moved to match a field line from another domain. Around the X-point of Fig. 2.20, the separatrix curves are drawn as green lines. In an ideal plasma, the plasma and the field lines never cross the separatrix surfaces. Flux exchange (or field line motions) across separatrices is only allowed by non-ideal effects. It involves a change of topology. For example in the case of Fig. 2.20, when field lines from domains 3 and 1 reconnect, they create new field lines in regions 4 and 2, increasing the flux there.

In 3D, the web formed by all separatrices surfaces can be very complex and intricate.

2.10.2 Geometry in two-dimensions

2D magnetic null

By two-dimensions, we mean a configuration invariant along one axis. We first consider the case where the magnetic field has only two components, in the plane normal to the axis of invariance. In two dimensions, the magnetic nulls allowed are the followings:

- The X-point, where the field around the null is hyperbolic. If reconnection is allowed, field lines pass one by one across the X-point.
- The O-point, where the field around the null is elliptic. If reconnection is allowed, there is destruction or creation of field lines as the O-point contracts or expands.
- Lines where $B = 0$, such as for example in the section on magnetic field annihilation (Sect. 2.6.3) and the corresponding Fig. 2.13. At the end of such lines we can find Y-points.

In the case of the O-point, field lines appear or disappear one by one at a point location. At a X-point, they reconnect two by two at a point location. Of course, multiple X-points can be involved during a reconnection event. In 3D the situation is more complex, and an infinite number of reconnecting field lines is involved at each time in the reconnection process, which occurs in a finite volume.

Structure of a linear 2D null

The structure of a *linear* 2D magnetic null can be made more explicit. The expansion of the field around the null to first-order can be written $B_x = \alpha x + \beta y$, $B_y = \gamma x + \delta y$ (and by assumption $B_z = 0$). By linear we mean that the Jacobian $\alpha\delta - \beta\gamma$ is not zero. If this is not the case, then other terms must be included in the expansion.

The zero divergence constraint reduces the four unknowns to three. Among these three unknowns, one degree of freedom describes a rigid rotation of space. The problem thus really has only two degrees of freedom, which can be seen as the strength of the magnetic field and the angle between the asymptotic field lines. All in all, a linear null can always be written in some coordinate system as (Priest 1987):

$$B_x = B_0 \frac{y}{r_0}, \qquad B_y = B_0 \, \alpha^2 \frac{x}{r_0}. \tag{2.43}$$

When $\alpha^2 < 0$, the field lines are elliptical and we have an O-point. The case $\alpha^2 = -1$ produces circles.

When $\alpha^2 > 0$, the field lines are hyperbolic and we have a X-point. The separatrices are given by $y = \pm\alpha x$ and form an angle θ such that $\tan\theta = \alpha$.

In both cases, the current is spatially constant and is given by

$$j_z = \mu_0^{-1} (\boldsymbol{\nabla} \wedge \boldsymbol{B})_z = \frac{B_0}{\mu_0 r_0} (\alpha^2 - 1). \tag{2.44}$$

For $\alpha^2 = 1$, there is no current.

Instability of a 2D X-point: X-point collapse

We consider the above linear null, and now show that it is an unstable equilibrium, that naturally leads to the formation of strong magnetic field gradients and, consequently, to localized current sheet formation.

We take the case where the separatrices form right angles ($\alpha = 1$), drawn on Fig. 2.21. At equilibrium, the magnetic pressure (given by the density of field lines in the figure) balances the magnetic tension due to field line curvature. Suppose now that we increase the angle between the separatrices as on Fig. 2.21, right. On the left and right sides, the magnetic

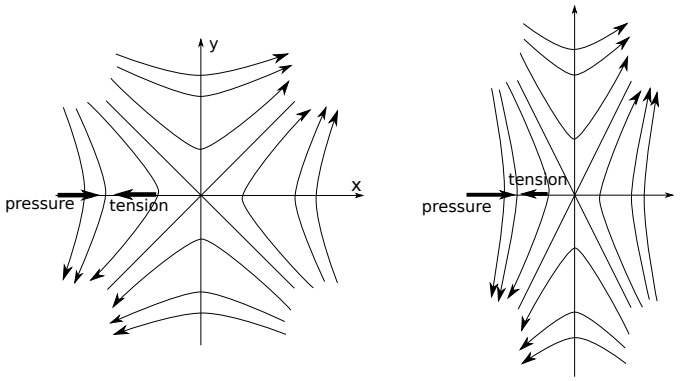

Figure 2.21: 2D linear X-point with $\alpha = 1$ (Eq. 2.43), collapsing (from left to right panels). On the left panel, the pressure and tension forces balance. If a perturbation contracts the X-point as on the right panel, then the pressure force exceeds the tension force and the collapse continues, which shows that it is unstable.

pressure increases and the magnetic tension decreases, so that they do not balance any more, their sum being directed inward. On the top and bottom sides, magnetic pressure decreases while magnetic tension increases, so that their resultant is directed outward. As a result, the collapse of the X point continues, and a X-point is indeed an unstable equilibrium.

A current is created as a function of the angle between the separatrices because the magnetic flux varies. If the plasma is ideal, this current is given by Eq. 2.44.

We remark that our reasoning is local and ignores the situation outside of what is drawn in Fig. 2.21. Boundary conditions or the plasma outside can either drive (by moving) or prevent (by staying still) the collapse.

Ultimately, a strong current sheet will be formed at the center, and if its width is small enough, magnetic reconnection will start and greatly affect the overall equilibrium by creating plasma inflows and outflows.

Particle-in-cell simulations of X-point collapse have been performed by Graf von der Pahlen and Tsiklauri (2014), and are very similar to simulations starting from a Harris configuration (described in Sect. 2.10.2).

Harris equilibrium as a starting point

The case of the X-point collapse is an example of initial conditions that are unstable and lead to reconnection. Another example is that of a current sheet such as in Fig. 2.22. The equilibrium configuration is called Harris equilibrium, and it is one of the rare fully consistent solutions of the Vlasov-Maxwell system in a non-homogeneous case.

It consists in a reversing magnetic field given by

$$\boldsymbol{B} = \hat{\boldsymbol{z}}\, B_0 \tanh\left(\frac{x}{L}\right), \tag{2.45}$$

sustained by a current. The current is built by a population of electrons and ions (or positrons) of equal number density

$$n_s(x) = \frac{n_0}{\cosh^2(x/L)} \tag{2.46}$$

flowing with opposite bulk velocities $U_\mathrm{e} = -U_\mathrm{i}$ in the $\pm y$ directions. The exact equilibrium relations for the relativistic case are derived in Sect. 3.7. See also Biskamp (2000) for subtleties about particle orbits.

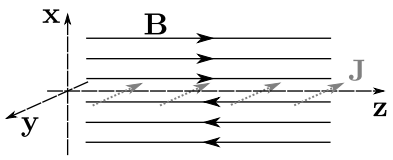

Figure 2.22: Setup for the Harris equilibrium.

A guide magnetic field $\boldsymbol{B}_G = \alpha B_0 \hat{\boldsymbol{y}}$ can be added, as well as a uniform population of background ions and electrons. The presence of the guide field implies that the magnetic field makes an angle θ with the z direction given by $\tan\theta = \alpha$. It then reverses, between $x = +\infty$ and $x = -\infty$, from an angle $\phi = \pi - 2\theta$ which is not π as in the no-guide-field case. In particular, the magnetic field never vanishes, there are no null points.

Harris equilibrium is used in simulations and analytical works to study instabilities that can arise in a current sheet without taking into account the complexity added by driving inflows. The majority of PIC simulations start from this setup. However, it should be stressed that this equilibrium is very peculiar. For example, the velocities of the electrons and ions carrying the current is uniform in space, so that the current is localized by localizing the particle density. In contrast, the background particle population is at rest and of uniform particle density: the difference between these two populations may seem artificial. Also, Harris equilibrium imposes a symetry between the two sides of the current sheet, which is a strong constraint. Consequently, conclusions drawn from a Harris startup should not been taken as general, and other configurations should be explored in more depths, for exemple asymetric layers (Belmont et al. 2012; Aunai et al. 2013), force-free layers (Liu et al. 2014), X-point collapse (Graf von der Pahlen and Tsiklauri 2014), geometries adapted to laser experiments (Smets et al. 2014), and 3D initializations (Baumann and Nordlund 2012; Olshevsky et al. 2013).

The tearing instability

When the current sheet width L is larger than the plasma kinetic scales (inertial length and Larmor radii), resistivity is likely to prevail over kinetic effects and resistive MHD or resistive two-fluid calculations can be used. Harris equilibrium can then be shown to be unstable to the (resistive) tearing mode. Its growth rate is a combination of the Alfvén timescale and resistive timescale (see Biskamp (§3.2.2, 2000) or Fitzpatrick (2011)).

If the current sheet width is of the order of kinetic plasma scales, then collisionless physics is likely to prevail, and the instabilities must be studied with Vlasov-Maxwell equations. The current sheet is again unstable to the (collisionless) tearing instability. The growth rate is now proportional to the ion or electron cyclotron periods, which can be much faster than in the collisional case.

As its name suggests, the tearing instability tears apart the current sheet in the $\hat{\boldsymbol{z}}$ direction, forming magnetic islands. In the non-linear phase, the islands contract because of the magnetic tension force. Each pair of island is separated by a X-point where reconnection occurs, with outflowing particles toward the islands. This is illustrated in Fig. 2.23. In Sect. 4.4.4, we study the tearing instability in a relativistic pair plasma, and show that analytical calculations and PIC simulations agree.

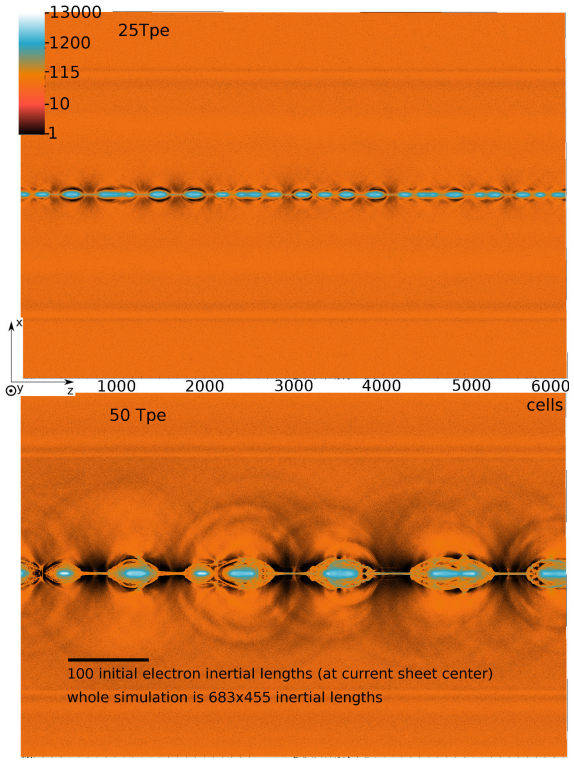

Figure 2.23: Electron number density at two different times, illustrating the tearing instability. The initial state is given by Harris equilibrium. From a PIC simulation detailed in Chapter 6.

Cross-field instabilities in three dimensions

The tearing mode is an instability only in the x-z plane of Fig. 2.22. In three dimensions, the current sheet can also be unstable in the y direction. An unstable mode, the kink instability, indeed bends the sheet in the y direction (Fig. 2.24). There are situations where it is faster than the tearing mode, and disrupts the sheet, dissipating the magnetic energy in small scale reconnection events and leading to a turbulent state. Oblique modes, which are a combination of the tearing and kink modes, also exist and can be the fastest growing ones (Daughton et al. 2011).

Force-free current sheet as a starting point

The Harris initial state with a guide magnetic field, $\boldsymbol{B} = \hat{\boldsymbol{z}}\, B_0 \tanh(x/L) + \hat{\boldsymbol{y}}\alpha B_0$, is a solution of the Vlasov-Maxwell system, but is not a force-free solution, i.e., it does not satisfy $\boldsymbol{j} \wedge \boldsymbol{B} = \mu_0^{-1}(\boldsymbol{\nabla} \wedge \boldsymbol{B}) \wedge \boldsymbol{B} = 0$. There are, however, cases where a force-free equilibrium may be privileged. For example at low plasma $\beta = P_{\rm gas}/P_{\rm mag}$, the plasma dynamics is governed by the magnetic forces and the plasma is likely to stay in a force-free equilibrium, where the magnetic force $\boldsymbol{j} \wedge \boldsymbol{B}$ vanishes.

It is possible to build an equilibrium that satisfies the force-free requirement. For a field $\boldsymbol{B} = \hat{\boldsymbol{z}}\, B_z(x) + \hat{\boldsymbol{y}}\, B_y(x)$, one has

$$(\boldsymbol{\nabla} \wedge \boldsymbol{B}) \wedge \boldsymbol{B} = -\frac{1}{2}\partial_x \left(B_z^2 + B_y^2\right) \hat{\boldsymbol{x}}. \tag{2.47}$$

Keeping the same dependence $B_z(x) = B_0 \tanh(x/L)$, the choice $B_y(x) = B_0[\alpha^2 + 1/\cosh^2(x/L)]^{1/2}$ implies that $B_z^2 + B_y^2 = B_0^2(1+\alpha^2)$ so that, with

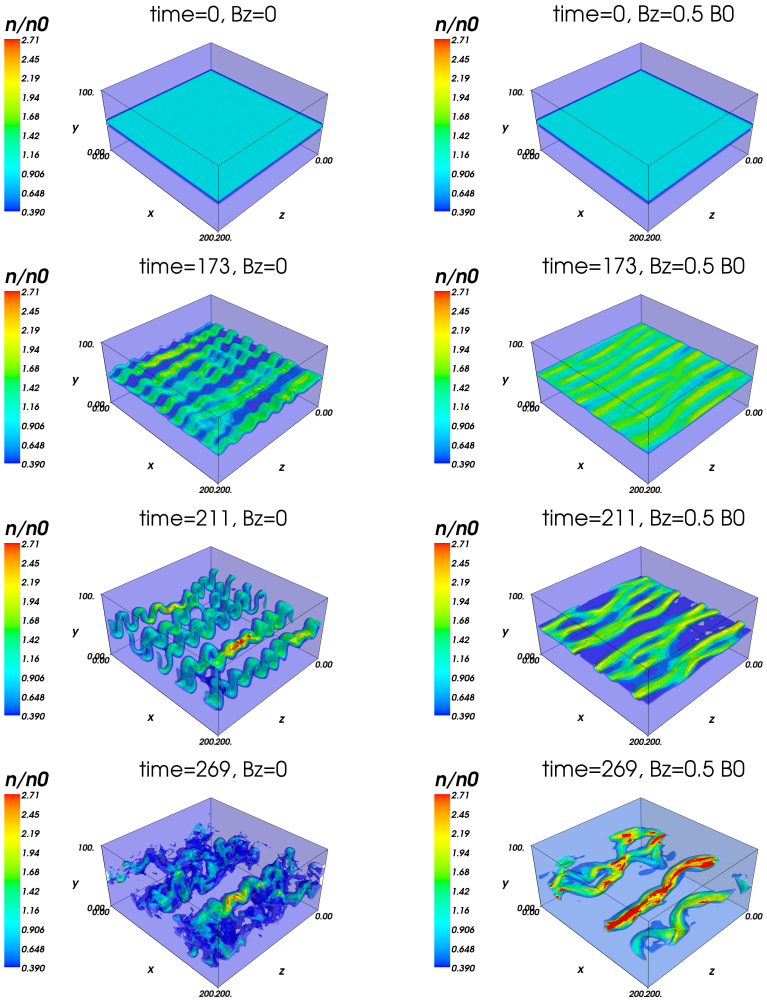

Figure 2.24: From Cerutti et al. (2014b). PIC simulation starting from a Harris equilibrium. The reconnecting magnetic field is along $\pm x$.
For the simulation on the left, the kink mode dominates and disrupts the current sheet.
For the simulation on the right, the presence of a guide field along z stabilizes the kink mode, and it is the tearing mode that dominates, producing a similar physics than in 2D (as in Fig. 2.23).

Eq. 2.47, the magnetic field is force-free. With this expression, the guide field is $B_0\alpha$ at large distances from the current sheet (just as for the Harris configuration), and increases up to $B_0\sqrt{\alpha^2+1}$ at the current sheet center. In particular, even for $\alpha = 0$, the guide field does not vanish at the center of the sheet

PIC simulations starting from a force-free current sheet are performed, among others, by Liu et al. (2014). These studies suggest that there are no significant differences between a force-free initial state and the Harris sheet initial state, even if a full comparison has not been performed.

Analytical models with inflows and outflows

The previous analysis of the X-point collapse, or the stability analysis of Harris current sheet, do not include magnetic reconnection, and neither inflowing or outflowing plasma from the reconnection zone. To do so requires to make assumptions about the dissipative processes that fix the rate at

which the reconnection proceeds (e.g., the resistivity). Some analytical solutions are then possible. The simplest ones are *steady and two-dimensional*:

- The Sweet-Parker configuration (Sect. 2.6.2 and Fig. 2.12). Outer region: ideal MHD. Inner region: collisional resistivity. This is the regime in which reconnection occurs when the current sheet width is larger than kinetic scales, and stable against instabilities (see the discussion of Sect. 2.11.3).
- The Petschek configuration (Fig. 2.26). Outer region: ideal MHD with irrotational flow and no current, plus the ad-hoc assumption of the existence of four slow shocks. The conditions $\boldsymbol{\nabla} \wedge \boldsymbol{v} = \boldsymbol{\nabla} \wedge \boldsymbol{B} = 0$ and the slow-shock jump conditions allow a determination of the flow.

  In this configuration, most of the conversion of magnetic energy to kinetic energy occurs when the plasma crosses the shocks. It thus allows for larger reconnection rates than the Sweet-Parker configuration, and it can be shown that the reconnection rate is almost independent of the resistivity (logarithmic dependence in S_{L}).

  The stability and existence of this configuration is still debated. Recent works (simulations and analytical developments in ideal and resistive MHD) show that it is stable if the resistivity is localized, or more generally if it presents strong enough gradients. The Petschek solution then survives. It is however still not clear whether this happens in real environments. We discuss further this issue in Sect. 2.12.4.
- The Petschek configuration can be generalized by allowing a finite vorticity in the outer region (the non-uniform configurations of Priest 2011).
- More general configurations can be imagined, for example asymmetric setups where the parameters above and below the dissipation zone are different.

These approaches are often only approximate. A full self-consistent description must employ numerical simulations. Figure 2.25 illustrates the structure of a current sheet with reconnection and outflows in a PIC simulation.

Of course, unsteady reconnection can also occur. In particular, PIC simulations have shown that in some cases, reconnection occurs in a non-steady state by the irregular formation of magnetic islands at the X-point, that are then advected out (the plasmoid instability of Sect. 2.11.3).

2.10.3 Geometry in three dimensions: definitions

We now discuss the geometries and the configurations encountered in three dimensions. We start by 3D nulls, which show a larger variety than in two-dimensions. We then introduce the definition of important topological objects. We will discuss reconnection in 3D in the next section (Sect. 2.10.4)[y].

[y] Given that visualizing 3D configurations is not easy, a well done cartoon can be of great help. We warmly recommend to browse the website `http://solarmuri.ssl.berkeley.edu/~hhudson/cartoons/`, where the best reconnection cartoons ever drawn are archived.

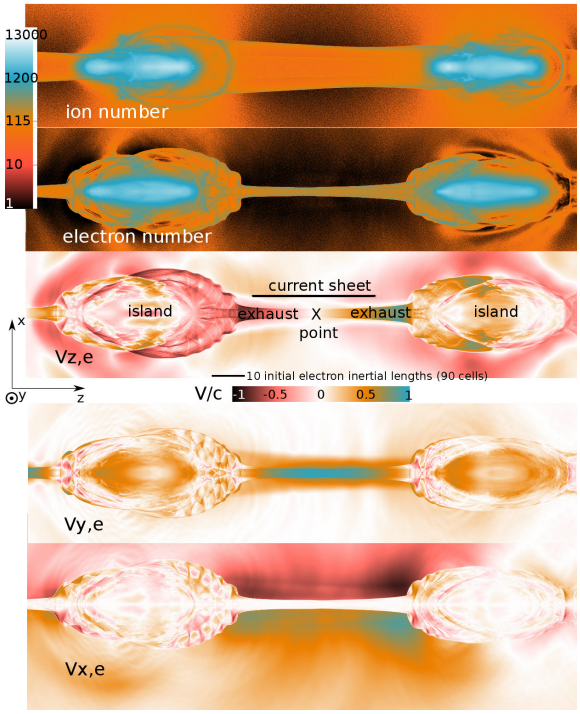

Figure 2.25: Zoom around a X-point showing various fluid quantities. The magnetic field is directed along $+\hat{\boldsymbol{z}}$ above the current sheet, and along $-\hat{\boldsymbol{z}}$ below. It reconnects at the X-point, and is expelled toward the islands. The islands are magnetic O-points, i.e., close to their center the magnetic field forms closed loops. From a PIC simulation (see Fig. 6.1 for the exact parameters).

3D nulls

An example of 3D null is drawn on Fig. 2.27. The **fan surface** is actually a separatrix between the orange and blue domains. The null is said to be **positive** if the field lines in the fan surface go away from the null, and **negative** if they converge into the null. The **spine** is the only field line, apart from those of the fan, that reaches the null.

The null of Fig. 2.27 satisfies $\boldsymbol{\nabla} \wedge \boldsymbol{B} = 0$ and is current free. It is called a **potential null**. But currents can be present (with effects illustrated in Fig. 2.28):

- If there is a current $\boldsymbol{J}_{//}$ parallel to the spine, the field lines in the fan plane spiral as they extend from the null. The null is said to be **improper** (and **proper** if field lines in the fan are straight lines).
- If there is a current $\boldsymbol{J}_{\perp}$ perpendicular to the spine, then the fan and spine are not any more perpendicular.
- The two preceding effects can be combined.

For 3D linear nulls, a similar analysis than in 2D (Sect. 2.10.2) can be done. Once again, the geometry around a null point is restricted by the divergence free nature of the field, and Faraday's law must also be fulfilled. The linear expansion of the field around the null can be written in matrix notation as $\boldsymbol{B} = J\boldsymbol{x}$, where J is the Jacobian matrix and has 9 components. $\boldsymbol{\nabla} \cdot \boldsymbol{B} = 0$ reduces the number of degrees of freedom by one. Two degrees of freedom are associated to a rigid rotation in space. There remains 6 degrees.

If the Jacobian is null, then the null point is non-linear and the expansion must go to second-order.

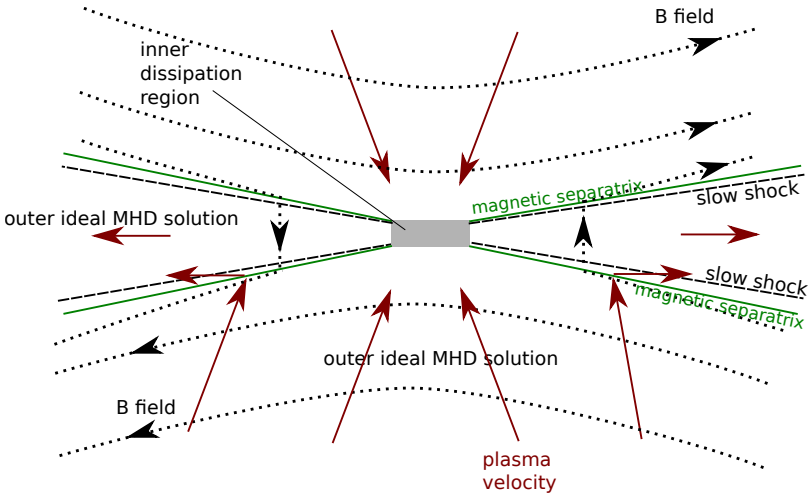

Figure 2.26: Petschek configuration. The magnetic field is shown as dotted lines. The plasma flows (red arrows) across the magnetic separatrices (green), inside which there are the standing slow-mode shocks. The shocks are switch-off shocks, which means that the tangential component of the magnetic field vanishes after the shock. The effect of the two shocks is thus a 180° rotation.

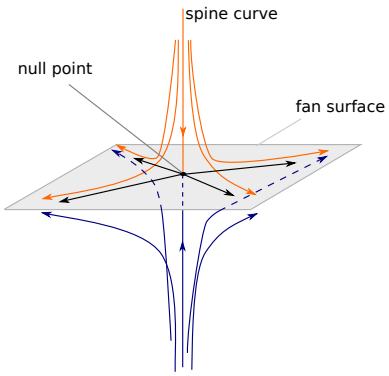

Figure 2.27: Example of a positive 3D null without current. Blue and orange lines are magnetic field lines.

Other topological structures

The intersection of two separatrix surfaces defines a curve called a **separator**. This is the case of Fig. 2.29.

In a global magnetic configuration, the web of separators is called the **skeleton**.

In the case of the Sun, the field lines of the corona are anchored in the solar photosphere. They form closed loops, where a field line starts from the photosphere and ends in the photosphere, or can also be open. In a 2D view, the separatrices separate regions of different connectivity, that is, regions where the field lines do not come from the same spot. An example is given in Fig. 2.30. If the field lines intersect in a X-point, the separatrices are then extensions of the fan surface of this null, or of the spine of this null. In the particular case of no null point, the separatrix is said to be a touching curve, and to form a bald patch.

Reconnection then consists in field lines from one region passing to another region, either at the X-point in 2D, or at any location in 3D.

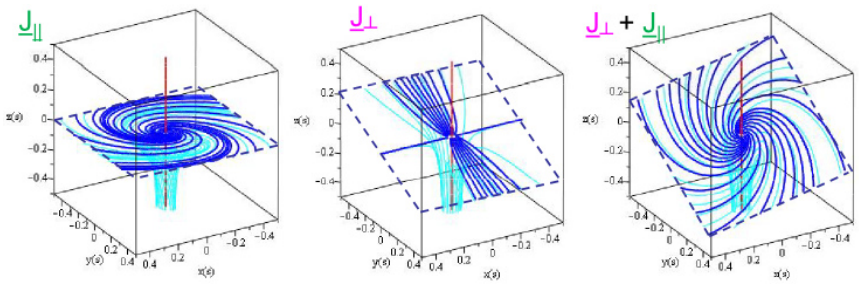

Figure 2.28: Examples of the incidence of a current on the local geometry around a null. Blue lines are magnetic field lines. From Parnell (2012).

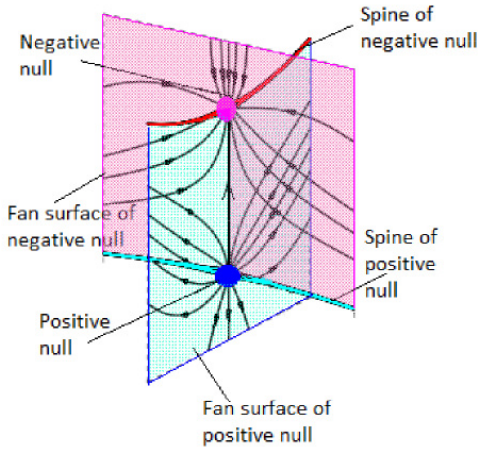

Figure 2.29: Two magnetic nulls. The separator line is the black line joining the two null points. From Parnell (2012).

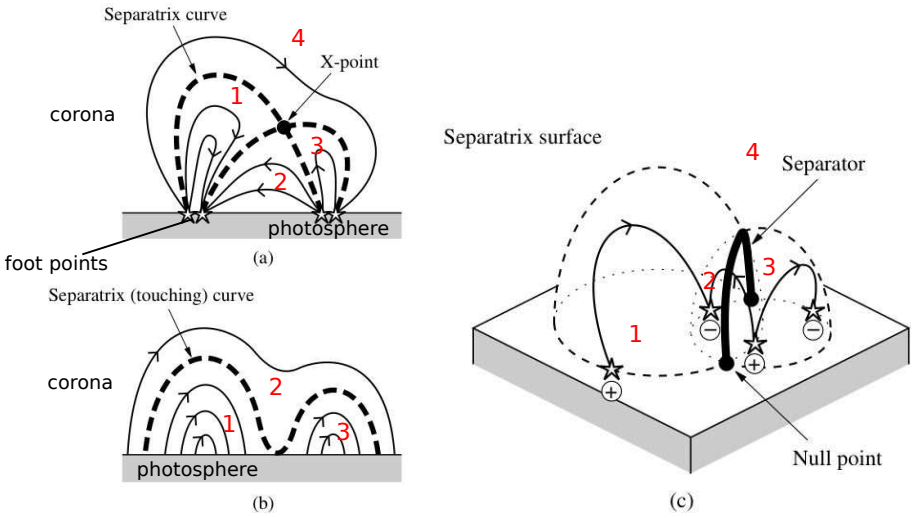

Figure 2.30: From Priest (1987). Magnetic field lines anchored in the Sun photosphere. In each domains (1 to 4), field lines start or end in the same magnetic domain. **(a)** With a X-point. There are four distinct topological regions. **(b)** Without X-point. There are three regions. **(c)** In 3D, the situation is more complex: the domains are now volumes (only a one field line is shown for each). Reconnection can occur at the separatrices, and particularly at the separator because there field lines from several domains (with different orientations) are close from each others.

2.10.4 Reconnection in three dimensions

We now turn to how reconnection proceeds in 3D configurations. In 2D, the only cases are at X-point-like configurations. In 3D, reconnection can occur at the magnetic nulls described above, differently depending on how the plasma around the null is perturbed. Reconnection can also occur away from null points, for example at a separator line, or at any place with strong magnetic field gradients.

There are still several open questions regarding 3D reconnection and the implied geometry. First, for a given geometry and perturbation (a separator or a null perturbed in a particular way), how does reconnection proceed? This question must be studied with analytical works, with fluid or with kinetic simulations when appropriate. Second, which of these geometries and perturbations are actually taking place in a real given environment? In other words, which configuration is dynamically accessible? This question requires either direct space observations, laboratory experiments, or global numerical simulations. These issues are obviously very relevant to know how reconnection proceeds in an environment. In what follows we briefly review answers to the first question.

The second question is partly answered in some particular cases. For example, the large scale field geometry is known for coronal mass ejections (or at least, we know some particular geometries that give rise to a CME, see Sect. 2.10.6), for solar jets (Sect. 2.10.7), for other small scale events in the Sun (Sect. 2.10.8), or at chromospheric levels where field line reconstruction revealed an intricate magnetic field (see p. 2.10.4). But even so, the perturbations imposed by plasma motions are often not well constrained. A short review and more references can be found in Pontin (2011) or in Birn and Priest (2007, Chap. 2).

Conditions allowing for reconnection

We have shown in Sect. 2.4.2 that the magnetic field lines move with a velocity

$$\boldsymbol{v}_{\mathrm{m}} = \frac{\boldsymbol{E} \wedge \boldsymbol{B}}{B^2}, \tag{2.48}$$

but only if $\boldsymbol{E} \cdot \boldsymbol{B} = 0$ everywhere along the field line. When it is so, field lines preserve their identity and reconnection does not occur. In 3D, there are consequently two possibilities to allow for reconnection: $\boldsymbol{E} \cdot \boldsymbol{B} \neq 0$ in a finite volume (which is possible if the plasma response is not ideal); or there is a null point where $\boldsymbol{B} = 0$, where the transport velocity $\boldsymbol{v}_m = +\infty$ becomes singular and allows for reconnection. But even in the latter case, whenever $\boldsymbol{B} = 0$ in a real plasma, it is very likely that a non-ideal zone surrounds the null-point[z]. Consequently, the condition $\boldsymbol{E} \cdot \boldsymbol{B} \neq 0$ in a finite volume is generic of 3D reconnection.

Specificities of 3D reconnection

A specificity of 3D reconnection, when compared to 2D reconnection, is that the magnetic field lines do not reconnect one by one. For instance, if points A and B lie on the same field line, and points X and Y on another field

[z] At least because particles' Larmor radii reach infinity, and are thus larger than the magnetic field gradient scale, so that particles behave non-ideally.

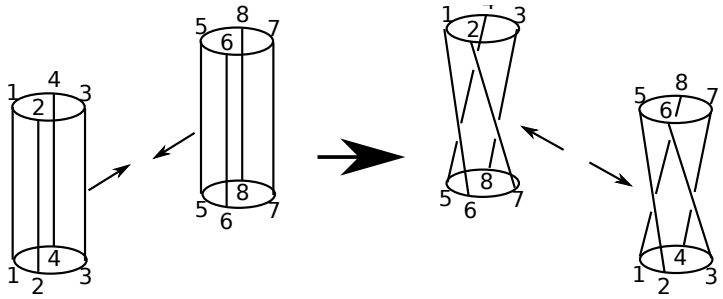

Figure 2.31: 3D reconnection of two flux tubes. Shown are four field lines on each tube. The reconnection does not occur pairwise, i.e., we do not have 1-6 and 6-1 connections on the two new flux tubes, but 1-6 and 1-8 connections, and so on. There is a twist on each new flux tube, that does not vanish when summed over the two tubes (it would be zero for pairwise reconnection, as the new tubes would be twisted in opposite directions). Adapted from Birn and Priest (2007).

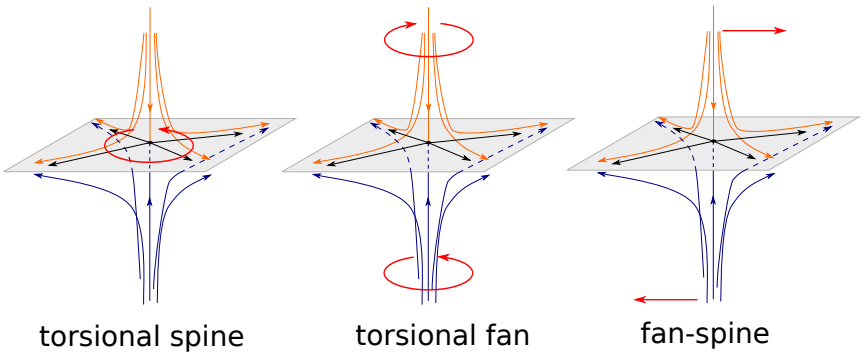

Figure 2.32: Plasma motion (red arrows) inducing a perturbation of a 3D null. Each case gives rise to different current patterns, and to different properties for the subsequent possible reconnection.

line, then after reconnection points A and X can be on the same line while B and Y are on two separate field lines. This is illustrated in Fig. 2.31, where the field lines of the two flux tubes do not reconnect two by two. The result is that the two tubes are twisted in the same direction. Their is a magnetic helicity associated with this twist, that has been produced during the reconnection. This weak magnetic helicity non-conservation is characteristic of 3D reconnection, and is linked to the non-pairwise field line reconnection (Birn and Priest 2007, §2.2).

When two flux tubes reconnect, there is actually no reason why the outcome should be again two distinct flux tubes. However, since the helicity production remains weak, this is more or less the case (Birn and Priest 2007, §2.2).

Reconnection at a 3D null

Reconnection at a 3D null can proceed in different ways. They essentially depends on where the current concentrates, and this concentration is dictated by flow motions around the null. We consider a simple symmetric null point.

- If the span surface is rotated, this creates a current in the spine and we have what is called **torsional spine reconnection** (Fig. 2.32, left). Torsional spine reconnection

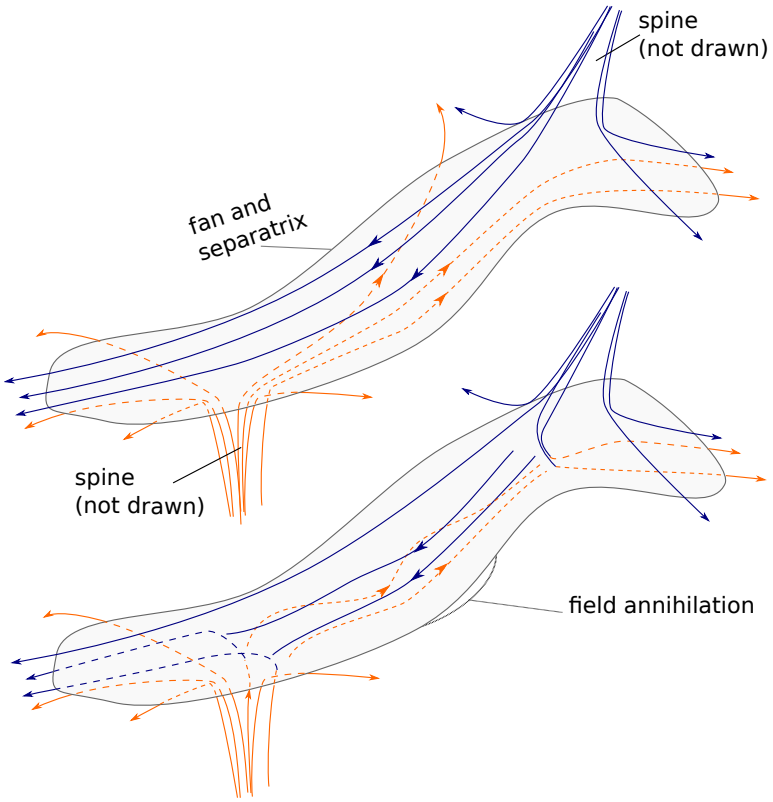

Figure 2.33: Spine-fan reconnection. The field lines are colored according to their origin.
Top: The configuration. The fan surface separates the field lines from the two topological domains.
Bottom: A reconnection event. Several field lines are involved at the same time. The "floating" field lines at the center actually do not exist ($\boldsymbol{\nabla} \cdot \boldsymbol{B} = 0$!): they annihilate (the magnetic flux is not conserved, unlike in 2D at X-points). As a result, the outflow production is affected. This is a 3D example where reconnection and field annihilation occur not a point locations, but in a whole volume, and not at a null point. We note that here we have drawn at most ten field lines, while in the real world, field lines fill space in a continuum.

- If the field lines near the spine line are rotated, in opposite directions above and below the fan surface, then a strong current is created in the spine and we have what is called **torsional fan reconnection** (Fig. 2.32, center).
- If we now consider shearing motions, another kind of reconnection configuration is possible. When the spine of a null is sheared (Fig. 2.32, right), we obtain **spine-fan** reconnection (Fig. 2.33).
- Other configurations are possible (Priest 2011; Pontin 2011). There should be as many possibilities as there are ways of deforming a magnetic null.

As explained above, it is then essential to know which case does occur in real situations. The cases of torsional reconnection require an ordered plasma motion, and are thus less probable than the case of fan-spine reconnection.

The case of spine-fan reconnection is particularly interesting, because it shows that in 3D reconnection does not involve field lines by pairs, but an

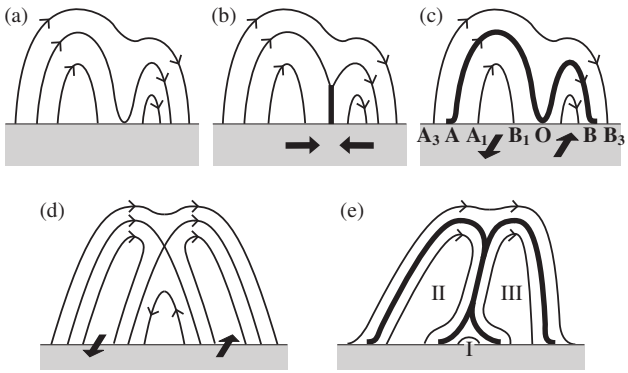

Figure 2.34: From Priest (1987). A quadrupolar field with initially no X-point in (a), or with a X-point in (d). Bringing the footpoints together in (b) forms a X-point and a current sheet. In (c) and (e), the footpoints are sheared, and this motion creates extended current sheets.

infinite number of volume filling field lines reconnecting and annihilating at each time (Fig. 2.33).

Where can we find magnetic null points? They are observed in magnetic structures involved in large scale events (e.g., in solar jets, Fig. 2.10.7), possibly in the Earth magnetosphere (Pontin 2011, §2 and references therein), and in the solar atmosphere at low levels. For the solar case, magnetic field measurements at the photospheric level allow to reconstruct the field lines above, and a very intricate structure has been revealed in quiet Sun regions. There, a high density of null points is found at chromospheric levels, with a density decaying exponentially (Régnier et al. 2008).

Reconnection away from null points

Reconnection can also occur away from magnetic nulls. A privileged location is along a separator line (Sect. 2.10.3), between two nulls. But more generally, magnetic reconnection is likely to take place at any location where strong magnetic field gradients are present. Such regions of high magnetic shear can have no particular topological role. An example is given in Fig. 2.34, where a *shearing* motion causes the creation of extended current sheets, where magnetic reconnection can take place.

Regions of strong shear with no particular topological role are called **quasi-separatrix layers** (**QSL**). As was said before, a separatrix is a surface that separates two regions of distinct topology, where the field lines originate from different area. The **connectivity** of the field lines is discontinuous across a separatrix. In contrast, across a quasi-separatrix layer, the connectivity strongly varies, but remains continuous. QSL are area of very strong shear, with intense currents, where most of the magnetic reconnection takes place in some numerical simulations (for a more formal definition and references, see Pontin 2011).

As an example of QSL, we can consider an initially vertical magnetic field anchored in the photosphere of the sun. If we imagine that the fluid where it is anchored rotates, the field lines will be twisted and strong current sheets will be formed. This process is called **braiding**.

Shearing and braiding are only special motions of the footpoints. Any motion can form current sheets and lead to reconnection at places with no topological role.

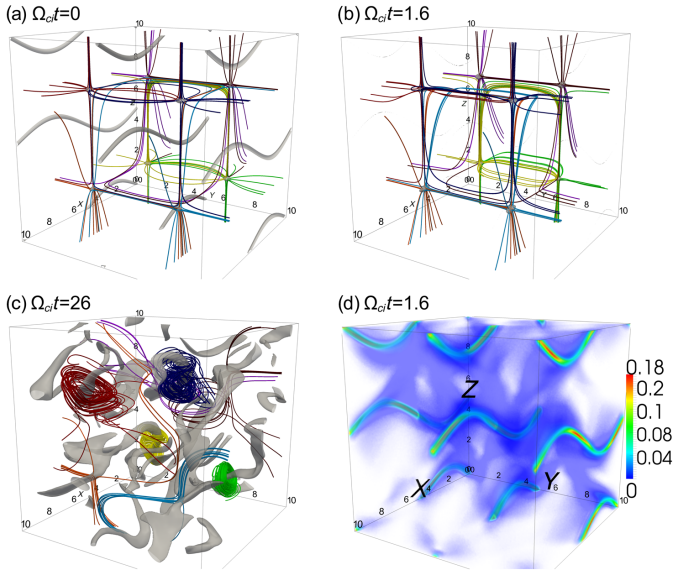

Figure 2.35: From Olshevsky et al. (2013). PIC simulation of a cluster of eight null points. Panels (a), (b) and (c) show magnetic field lines at different times, with gray contours as zones of low B. Panel (d) is the current density.

2.10.5 Example: PIC simulations of a 3D null

There are very few simulations of reconnection in geometries different from a Harris-like or force-free current sheet. The only examples known to us are Baumann and Nordlund (2012) and Olshevsky et al. (2013). The latter work simulates a cluster of eight null points (eight because this is the smallest number that allows to have periodic boundaries in the simulation), shown in Fig. 2.35. Initially, the magnetic pressure is larger than the plasma pressure, so that the configuration is unstable. There is a first phase where ions are pushed into zones of low B, where they form current channels (panels b and d). Later, the current channels are unstable and disappear. Reconnection then occurs everywhere chaotically, heating the plasma. Within $26\,\omega_{\rm ci}^{-1}$ (ion cyclotron frequency), 86% of the initial magnetic energy is transfered to the plasma. It is interesting to underline that no 2D local configurations are found in this simulation.

2.10.6 Example: coronal mass ejections

The Sun builds large amounts of magnetic field in its interior by a dynamo, and possesses a large scale dipolar magnetic field extending in all the solar system. In addition, the small scale magnetic field present inside the Sun rises toward the surface by buoyancy effects (see Parker instability p. 41), and when it reaches the surface it forms arcades of magnetic fields anchored in the solar surface by two footpoints. The solar corona[aa] is thus populated

[aa] Structure of the Sun's atmosphere and the layers above:
Photosphere (where the Sun becomes optically thin, 5 580 K),
temperature minimum area (500 km above, $\sim$ 4100 K),
chromosphere (2000 km thick, 20 000 K at the top, partially ionized at the top),
transition region (200 km thick, 10^6 K at the top),
corona (several $\times 10^6$ K).
The corona then expands into the solar wind (100 to 750 km/s),
which ends at the heliopause (50 AU) in a shock with the ISM.
The whole region filled with solar wind is the heliosphere.

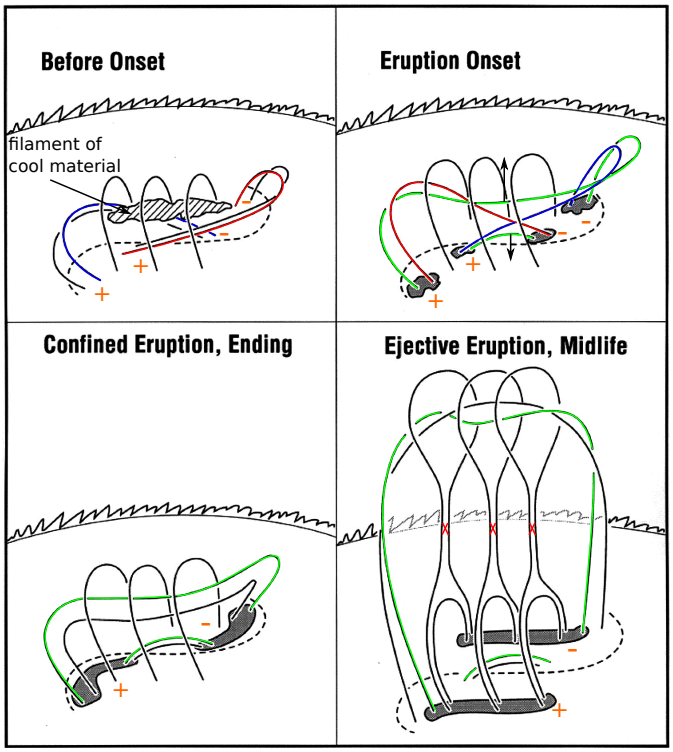

Figure 2.36: Mechanism of a coronal mass ejection. From Moore and Sterling (2006). The two top panels are the first phases. At the eruption onset, the blue and red field lines reconnect, and expel plasma downward and upward. Then, two outcomes are possibles: the ejection is retained by the covering magnetic field in the lower left panel, but not in the lower right panel. In this latter case, reconnection will occur at the red crosses, and the upper part will then be ejected in space.

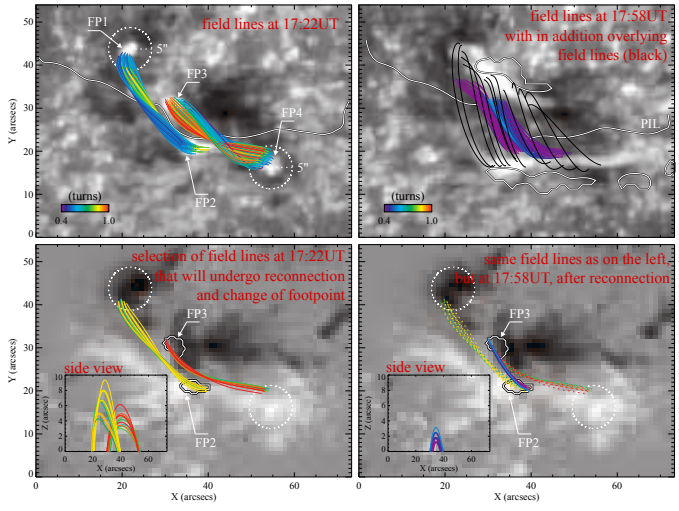

Figure 2.37: Reconstruction of the magnetic field from observations, using a force-free equilibrium, during a pre-CME event. From Liu et al. (2013a).

with a canopy of rising magnetic flux tubes. Obviously, when these tubes are forced to meet by the footpoint motions, reconnection can occur. Given the large number of possible geometries (involving two or more flux tubes), this can lead to many outcomes.

One of them are solar flares, i.e., very intense (energy release up to $\sim 10\%$ of the Sun quiet energy release) and brief (minute to several minutes) flashes of light. The very idea of magnetic reconnection came in order to explain these phenomena (Giovanelli 1947, 1948).

Solar flares are often accompanied by ejections of matter into space: coronal mass ejections (CME). A possible mechanism at the origin of these ejections is tether-cutting, described on Fig. 2.36. An observation illustrating this model is shown on Fig. 2.37. Note that other geometries can lead to flares.

2.10.7 Example: coronal solar jets

Coronal solar jets are ejections of matter from the solar corona. They occur on a smaller scale than coronal mass ejections, and involve a different topology for the magnetic field.

This is illustrated in Fig. 2.38. Initially the magnetic field is that of the quiet solar corona: uniform and directed upward as in domains 2 and 4 of Fig. 2.38 (domains 2 and 4 are actually the same domain, and we make this distinction only to clarify the discussion). Then, a flux tube emerges from under the solar surface, and forms the loops of the domain 1. This flux tube rises upward. It will thus reconnect with field lines of domain 2. This reconnection produces a current sheet (in red in the two top-left panels). Newly reconnected field lines are expelled on both sides of this sheet: below, forming the field lines of domain 3, and above, adding new field lines to domain 4. As shown in the temperature panel, the plasma carried by the newly reconnected field lines is very hot, because it gained energy from the magnetic field. In addition, the new field lines of domain 4 unbend rapidly and eject plasma upward along the magnetic field, thus creating the jet. In the end, all the field lines of domain 1 (the emerging flux tube) are transferred to domains 4 and 3.

It is worth noting that Baumann and Nordlund (2012) performed a PIC simulation of such a configuration.

2.10.8 Example: small scale events in the Sun

In addition to large scale events such as bright solar flares or coronal mass ejections, the Sun hosts a number of smaller scale events, that produce jets or flares. They are classified in Fig. 2.40 according to the height at which they occur above the Sun's surface. This location can range from the lower chromosphere to the corona (see p. 59 and Fig. 2.39 for the Sun's structure).

Most of these events are explained by two different classes of geometrical setup. The first is when a bundle of magnetic field rises or moves in an ambient magnetic field, just as for coronal solar jets (Sect. 2.10.7). The second is when two almost parallel flux tubes, possibly with internal kink, are pushed one against the other by the surrounding dynamics or by a twist in their footpoint motion (Fig. 2.39, right). These two geometrical setups give rise to more than two kinds of events, because they can occur at different

See Fig. 2.39 for an illustration of the lower parts.

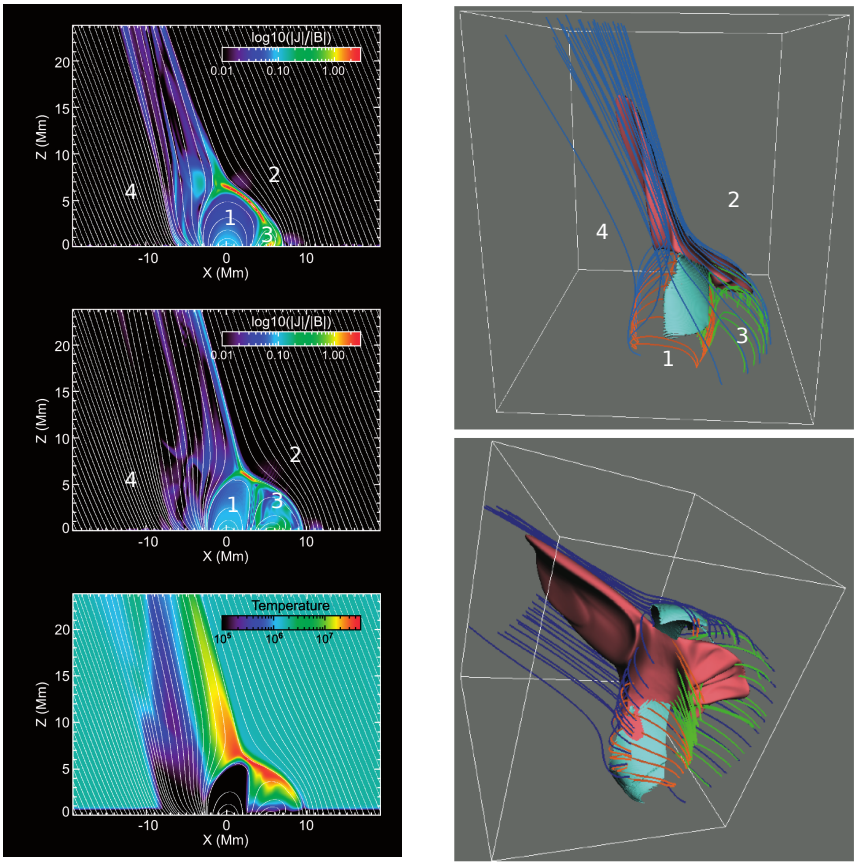

Figure 2.38: From Moreno-Insertis et al. (2008). MHD simulation of a solar jet. **Left:** Magnetic field lines in white. For the two upper panels, the colors are the current density at two different times. In the lower panel colors trace the temperature. In the upper panel, the current sheet is the most reddish part, and field lines from domains 1 and 2 reconnect and are expelled in domains 3 and 4. See Sect. 2.10.7 for details.
Right: 3D views from two angles, with magnetic field lines colored according to the domains 1, 2, 3 or 4. The blue surface traces the current sheet, and the red surface delimits a region of hot plasma (which is in the current sheet and in the jet).

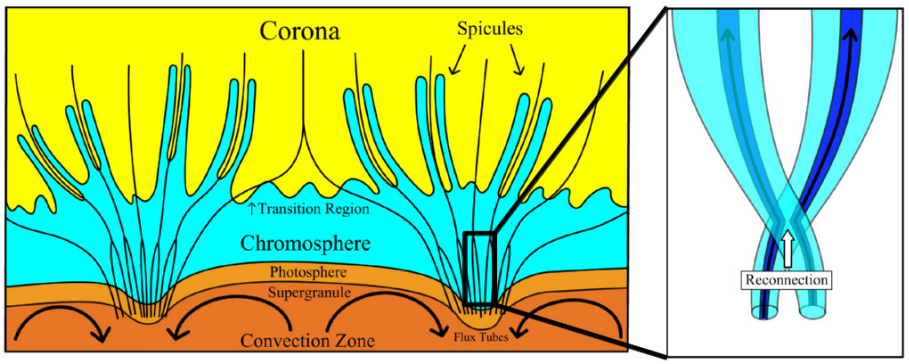

Figure 2.39: Structure of the lower solar atmosphere. The right panel illustrates reconnection between two vertical flux tubes. From a 2014 presentation of K. Shibata, credited to T. Suda.

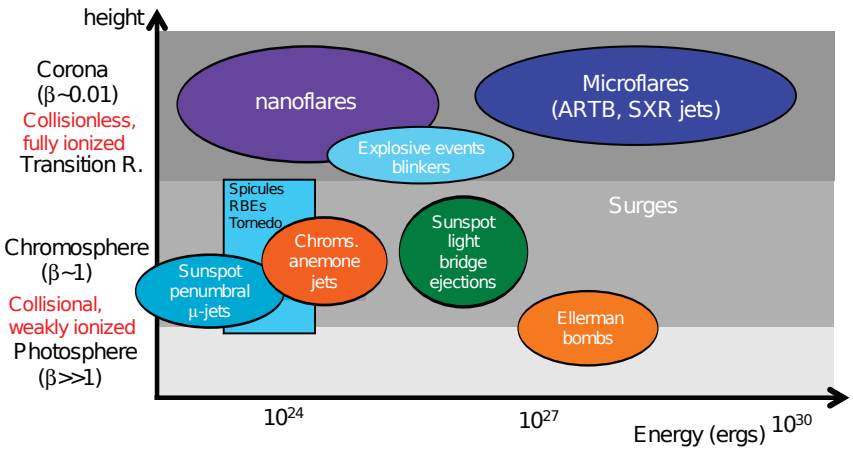

Figure 2.40: Classification of various small scale events in the solar atmosphere, as a function of released energy and height above the surface. See p. 59 and Fig. 2.39 for the Sun's structure. From a 2014 presentation of T. Shimizu.

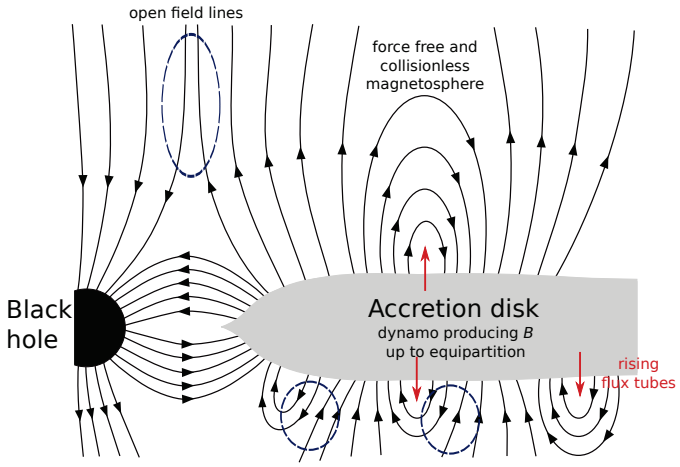

Figure 2.41: Adapted from de Gouveia dal Pino and Lazarian (2005). Sketch of the magnetic field arrangement around an accreting black hole. Magnetic reconnection can occur in the dotted-blue ovals, either heating the magnetosphere, or ejecting matter in the form of jets along open field lines.

scales and at different locations in the solar atmosphere, i.e., under different plasma regimes (for example the chromosphere is only partly ionized and is collisional, while the corona is ionized and collisionless).

2.10.9 Example: transient jet production in microquasars

Microquasars are binary systems in which a star and a black hole orbit closely. The black hole captures matter from the star, either because the star is massive and emits a strong wind, or because it is so close to the black hole that its surface is partly beyond the inner Lagrange point, resulting in matter flowing to the hole (Roche lobe overflow), or because of both. In either case, matter is accreted by the black hole. Because of the rotation of the star around the black hole, this matter has a net angular momentum, and is likely to form an accretion disk around the black hole where angular momentum is lost, either by viscosity, by oblique shocks, or by ejection in jets and disk-winds.

We observe that most microquasars oscillate between two states, the

hard state and the soft state (McClintock and Remillard 2006; Zhang 2013), characterized by different spectral properties. Steady jets are observed in the hard state, and more powerful, transient jets, are seen during the transition between the two states. The origin of these jets is still an open question. It could be that the transient jets are produced by magnetic reconnection events in the accretion disk magnetosphere (de Gouveia dal Pino and Lazarian 2005; Dexter et al. 2014), as illustrated in Fig. 2.41.

We underline that this picture is uncertain and, unlike for the Sun or the Earth magnetospheres, there is no resolved observations of accretion disks and of black hole magnetospheres. The magnetic field geometry is thus largely unknown.

2.11 From large to small scales: The non-ideal processes

The previous section 2.10 deals with the large scale magnetic field arrangements that lead to the formation of privileged sites with strong magnetic field gradients and associated current sheets, where reconnection can take place. The process of magnetic reconnection itself has microscopic origins, that we explore in this section. It is inside the dissipation zone and at other locations (such as along the separatrices or in the exhausts) that non-ideal processes, such as those of the generalized Ohm's law (Eq. 2.41), are important and allow the plasma and the magnetic field to partly decouple. The non-ideal processes and their physical origin are the focus of this section.

We first give, in Sect. 2.11.1, the definition of the reconnection rate, that is needed to quantify the speed of the reconnection. Then, in Sect. 2.11.2 we list the non-ideal processes, and in Sect. 2.11.3 we discuss when such or such non-ideal process dominates.

The next section 2.12 will more concretely explain how reconnection proceeds at a kinetic level.

2.11.1 The reconnection rate

The nature of the non-ideal terms can dictate whether reconnection is fast or slow, but these notions of fast and slow have to be characterized by measurable quantities that we now discuss. In two dimensions, this is done through the reconnection rate. In 3D configurations, the rate of reconnection is set by the parallel electric field $\boldsymbol{E} \cdot \boldsymbol{B}/B$, in a way that depends on the exact geometry (see, e.g., Pontin 2011).

We only focus on the 2D case. For a planar situation such as in Fig. 2.20, the relevant quantity is the rate of variation of magnetic field flux across the X-point,

$$\frac{\mathrm{d}\Phi_{B_z}}{\mathrm{d}t} = \frac{\mathrm{d}}{\mathrm{d}t}\int_{x=0}^{\text{X-point}} B_z \mathrm{d}x. \tag{2.49}$$

We can use the relation $\partial_t \boldsymbol{B} = -\boldsymbol{\nabla} \wedge \boldsymbol{E}$ and the simplified 2D geometry to show that this flux variation is equal to the y component E_y of the electric field at the X-point location, so that the reconnection electric field E_y allows to measure the rate of the reconnection process.

One often considers a normalization of E_y to obtain an adimensional reconnection rate. Since $\mathrm{d}\Phi_{B_z}/\mathrm{d}t$ is in part determined by the outflow velocity, because it sets the rate at which magnetic field is extracted from around

the X-point (see e.g., in a resistive MHD context, Borovsky and Hesse 2007; Cassak and Shay 2007), and since one expects $v_{\rm out} \propto V_{\rm A}$ (Eq. 2.27), the relevant normalization (variously denoted by R or E^*) is

$$R = E^* = \frac{E_y}{B_0 V_{\rm A,in}}, \tag{2.50}$$

with B_0 the strength of the asymptotic magnetic field that can reconnect (B_z here, if there is a guide field it is ignored) and $V_{\rm A,in}$ the associated Alfvén speed with the asymptotic inflow density.

Because the inflowing plasma is ideal, we also have the relation $v_{\rm in} = E_y/B_0$, so that

$$R = E^* = \frac{v_{\rm in}}{V_{\rm A}} \tag{2.51}$$

can also be used. Another expression can be obtained by using mass conservation between the plasma inflowing into the dissipation region (across a length L), and the plasma outflowing from it (through a width δ): $L n_{\rm in} v_{\rm in} = \delta n_{\rm out} v_{\rm out}$. This can be written as:

$$R \equiv \frac{v_{\rm in}}{V_{\rm A,in}} = \frac{\delta}{L} \times \frac{n_{\rm out}}{n_{\rm in}} \times \frac{v_{\rm out}}{V_{\rm A,in}}. \tag{2.52}$$

We showed in Sect. 2.6.2, with energy conservation arguments (Eq. 2.29), that the outflow speed is roughly given by the inflow Alfvén speed. Also, for an incompressible plasma $n_{\rm out} = n_{\rm in}$, and in general the inflow and outflow densities are not too different. The rate R is thus mostly controlled by the geometrical ratio δ/L.

A particular and important case is that of the Sweet-Parker model, where Eq. 2.29 shows that $R = S_{\rm L}^{-1/2}$.

We investigate in detail the dependence of the reconnection rate in relativistic 2D reconnection in Sect. 6.4.6.

2.11.2 The non-ideal processes

The reasons to behave non-ideally can be (1) collisions, (2) inertia and collective interactions, and (3) finite Larmor effects. Each one becomes important whenever it occurs on a length scale $d < r_{cs}$, where r_{cs} is the Larmor radius of the particles of species s, and d the scale of the process (1), (2), or (3), which is specified below.

This is because in order to maintain the magnetic field lines frozen with their motion, the particles of species s have to move over distances of the order of their gyroradius $r_{cs} = v_\perp/(qB/m_s)$. When the scale of occurrence of the impeding process is larger than r_{cs}, $d > r_{cs}$, the motion of the particles in response to B variations is not perturbed, and the magnetic field remains frozen. But when this scale shrinks below the particles' gyroradius, then a particle is perturbed several times during a single gyration around $\boldsymbol{B}$, so that particles cannot maintain the magnetic field lines frozen with their motion / cannot respond properly to magnetic field flux variations.

Then, the particles are said to be unmagnetized or non-adiabatic, and reconnection can occur. The link with adiabaticity is that the adiabatic invariant of a particle is conserved only if the particle trajectory is periodic or quasi-periodic (Sect. 2.5.2). Here, when a perturbation occurs with a frequency larger than the cyclotron pulsation, $\omega > \omega_{cs}$, disturbances occur

too often and the quasi-periodicity is lost: the adiabatic invariant is not conserved any more. Physically, we see from Fig. 2.8 that a particle remains frozen to the field variations only if it performs Larmor gyrations with a radius r_{cs} given by the local magnetic field.

The scale d of the non-ideal processes is:

1. For collisions, the mean free path l_{mfp} between collisions (either electron-electron, electron-ion, or electron-neutral collisions);
2. for finite inertia and collective interactions, the oscillation length of the particles due to fluctuating fields and finite inertia (which is the Debye length $\lambda_{\mathrm{D}s} = v_{\mathrm{th},s}/\omega_{\mathrm{p}s} = v_{\mathrm{th}}/c \times d_s$ for electrostatic Langmuir oscillations, but the inertial length d_s is often used instead);
3. for finite Larmor effects, the gradient scale of the magnetic field $l_{\boldsymbol{\nabla} B}$.

Since the Larmor radius and the inertial length vary with the particle mass, we immediately see that there are two non-ideal regions, one for the ions and one for the electrons. Since electrons are lighter than ions, they have smaller Larmor radii and will remain frozen-in longer than ions. The structure of the resulting two-scale dissipation region is detailed in Sect. 2.12.1. In the remaining of this section, we review each non-ideal process, and discuss which of them dominates depending on the plasma conditions in Sect. 2.11.3.

Collisions

Reconnection can be allowed by electron-ion collisions (the term $\chi \boldsymbol{J}$ in Ohm's law 2.41), and also possibly by electron-electron collisions (the term $\chi_2 \boldsymbol{\nabla}^2 \boldsymbol{J}$ in Ohm's law 2.41) or electron-neutral collisions. This is easy to understand: electrons are hindered in their motions by collisions, and do not respond perfectly to the induced electric fields. The magnetic field can then diffuse across the plasma.

Electron inertia

When an electron undergoes a force (electric for example), it is accelerated. If its mass were null, it would instantly respond and stop when the force ceases. However, its finite mass or inertia implies a delay for initiating the motion, and implies that it continues moving when the force stops. Electron inertia is thus the fundamental origin of several collisionless non-ideal processes, by degrading the plasma response to induced electric fields.

As an introductory example, we can consider the Langmuir oscillation of the electrons, which are primarily due to sub-Debye-length charge imbalance and to finite inertia. These oscillations occur at pulsation $\omega_{\mathrm{pe}} = \sqrt{ne^2/\epsilon_0 m_{\mathrm{e}}}$, and during one oscillation an electron of speed v moves across a length v/ω_{pe}, which is the Debye length if v is estimated by the thermal speed. Qualitatively, electrons cannot respond correctly to magnetic flux variations if their motion during a Langmuir oscillation is smaller than their gyroradius $r_{\mathrm{ce}} = v/(eB/m_{\mathrm{e}})$, i.e., if $v/\omega_{\mathrm{pe}} < r_{\mathrm{ce}}$, as then an electron undergoes several Langmuir oscillations during a single gyration. A more quantitative analysis can be performed by writing Ohm's law as

$$\boldsymbol{E} + \boldsymbol{v}_{\mathrm{e}} \wedge \boldsymbol{B} = -\frac{m_{\mathrm{e}}}{e} \frac{\mathrm{d}\boldsymbol{v}_{\mathrm{e}}}{\mathrm{d}t}, \tag{2.53}$$

with the right-hand side being electron motion due to electrostatic perturbations. These perturbations are Langmuir oscillations, so that it can be evaluated as $\mathrm{d}\boldsymbol{v}_\mathrm{e}/\mathrm{d}t \sim \omega_\mathrm{pe}\boldsymbol{v}_\mathrm{e}$. Ohm's law can then be written

$$\frac{e\boldsymbol{E}}{m_\mathrm{e}} + \boldsymbol{v}_\mathrm{e} \wedge \boldsymbol{\omega}_\mathrm{ce} = -\omega_\mathrm{pe}\boldsymbol{v}_\mathrm{e}, \tag{2.54}$$

with $\boldsymbol{\omega}_\mathrm{ce} = e\boldsymbol{B}/m_\mathrm{e}$. The ideal nature of the plasma is lost when the right-hand side is larger than the $\boldsymbol{v}_\mathrm{e} \wedge \boldsymbol{\omega}_\mathrm{ce}$ advective term, i.e., when $\omega_\mathrm{pe} > \omega_\mathrm{ce}$. This is equivalent to $r_\mathrm{ce} > v_\mathrm{e}/\omega_\mathrm{pe}$.

Consequently, electrostatic oscillations allowed by electron inertia plays a significant non-ideal effect when $r_\mathrm{ce} > v_\mathrm{th,e}/\omega_\mathrm{pe}$, or equivalently, when $\omega_\mathrm{pe} > \omega_\mathrm{ce}$. More generally for a species s, it is significant when $\omega_{ps} > \omega_{cs}$. But we have the relation

$$\left(\frac{\omega_{cs}}{\omega_{ps}}\right)^2 = \frac{B^2/\mu_0}{nm_sc^2} \equiv \sigma_s. \tag{2.55}$$

The quantity σ_s is the ratio of the electromagnetic energy flux[ab] to the restmass energy flux of the plasma[ac], and is called the magnetization (see Sect. 6.3.2 for more details). Two cases emerge:

- There is an area of weak magnetic field ($\sigma_s \ll 1$) (for example around a magnetic null in 2D or 3D): the condition $\omega_{ps} > \omega_{cs}$ is satisfied, and reconnection can occur due to the inertial effects described above. Moreover, if we take the example of a magnetic null, and in addition assume a linear variation for B close to the null, $B = B_0 x/l_{\boldsymbol{\nabla}B}$, we see that the species s will be demagnetized at scales $x < l_{\boldsymbol{\nabla}B}\sqrt{m_s n_s}/(B_0\sqrt{\epsilon_0})$. Assuming a particle density $n_s \sim$ const among the species s, we see that the width δ_s of the non-ideal region for species s is (under these hypotheses) $x \propto \sqrt{m_s}$ from the center: the non-ideal zone for ions is thus $\sqrt{m_\mathrm{i}/m_\mathrm{e}}$ larger than that for electrons. This is indeed seen in PIC simulations (e.g., in Fig. 2.25 when comparing the large density area for ions and for electrons), and discussed with more detailed in Sect. 2.12.1 for the 2D case.
- The magnetic field is strong everywhere. This is the case in 2D situations if there is a large guide field (a component of $\boldsymbol{B}$ normal to the 2D plane), or in more general 3D configurations. In this case, the induced non-ideal electric fields are parallel to the magnetic field, and the induced currents also: particles are accelerated along the field lines. Non-ideal processes then perturb particle motions along the field lines. This can be seen with the non-ideal Ohm's law: $\boldsymbol{E} + \boldsymbol{v}_\mathrm{e} \wedge \boldsymbol{B} = \boldsymbol{R} \neq 0$ implies that $\boldsymbol{E} \cdot \boldsymbol{B} \neq 0$. The existence of finite parallel electric fields is then the trace of ongoing reconnection.

  Here too, electrostatic (or more generally electromagnetic) fluctuations can provide the needed perturbation to maintain $\boldsymbol{E} \cdot \boldsymbol{B} \neq 0$.

We stress that the preceding approach focuses on electrostatic Langmuir oscillations only, and is at best approximate. Other waves, instabilities, or wave-particle resonant interactions, can disturb the electrons and allow

[ab] Which is $\boldsymbol{E} \wedge \boldsymbol{B}/\mu_0 = (B^2/\mu_0)\boldsymbol{v}_{E\times B}$ with $\boldsymbol{v}_{E\times B} = \boldsymbol{E} \wedge \boldsymbol{B}/B^2$.

[ac] Which is, if the plasma is ideal and thus $E \times B$ drift, $nm_sc^2 \times \boldsymbol{v}_{E\times B}$.

reconnection. Several such instabilities can arise in the context of reconnection. For example, there can be two-stream instabilities between the electrons and ions of the current sheet, or between electrons of neighboring magnetic islands. Weibel instability can develop due to the intrinsic anisotropies found in reconnection setups, and so on.

From the point of view of Ohm's law (Eq. 2.41), inertial effects manifest themselves in several terms:

- $(1/n_e e)\boldsymbol{\nabla}\cdot\boldsymbol{P}_e$ is called **thermal inertia**. In a 2D setup invariant along y the induced electric field $\boldsymbol{E}$ is along $\hat{\boldsymbol{y}}$. The contribution of the pressure in Ohm's law then reads $\partial_x P_{xy} + \partial_z P_{zy}$ (the y derivative vanishes), so that it is the divergence of the off-diagonal terms that contribute. In collisionless and non-relativistic plasmas, 2D PIC simulations have shown that this term dominates and sustains $\boldsymbol{E}$ at the center of the dissipation region (see Sect. 6.4.3 for detailed references). It corresponds to particles bouncing between the magnetic field reversal.

  Gradients in the diagonal components can also play an indirect role, by creating diamagnetic drift currents that can enhance or dwindle the reconnection rate (Biskamp 2000).

- $(m_e/e)(\partial_t \boldsymbol{v}_e + \boldsymbol{v}_e\cdot\boldsymbol{\nabla}\boldsymbol{v}_e)$ is called **bulk inertia**, because it is associated with global motions of the plasma ($\boldsymbol{v}_e$ is the bulk velocity). For non-relativistic reconnection, it is smaller than thermal inertia and almost negligible at the very center of the non-ideal region. However, our new findings (Sects. 6.4.3 and 6.4.8) indicate that it may contribute or even dominate under relativistic setups where the bulk momentum is large.

Finite Larmor effects and lost of electron adiabaticity

When

$$\frac{r_{ce}}{B}\times\frac{\mathrm{d}B}{\mathrm{d}z} > 1, \tag{2.56}$$

the hypothesis at the base of the drift motion theory breaks, the first adiabatic invariant is not conserved, magnetic flux through the electron cyclotron orbits is not either, electrons are not frozen any more, and reconnection is allowed.

This will necessarily be the case if there is a magnetic null. For a magnetized plasma without nulls, it happens if the field varies on length smaller than r_{ce}.

The Hall term

The presence of the Hall term $\boldsymbol{J}\wedge\boldsymbol{B}$ in Ohm's law (Eq. 2.41) simply means that the field lines are convected with the electron fluid velocity, not by the ions. Consequently, it does not give rise to reconnection, but to a slippage of the field lines with respect to the ion fluid.

However, the Hall term may, or may not (it is still presently debated), drastically enhance the reconnection mechanism. We discuss this point in Sect. 2.12.1.

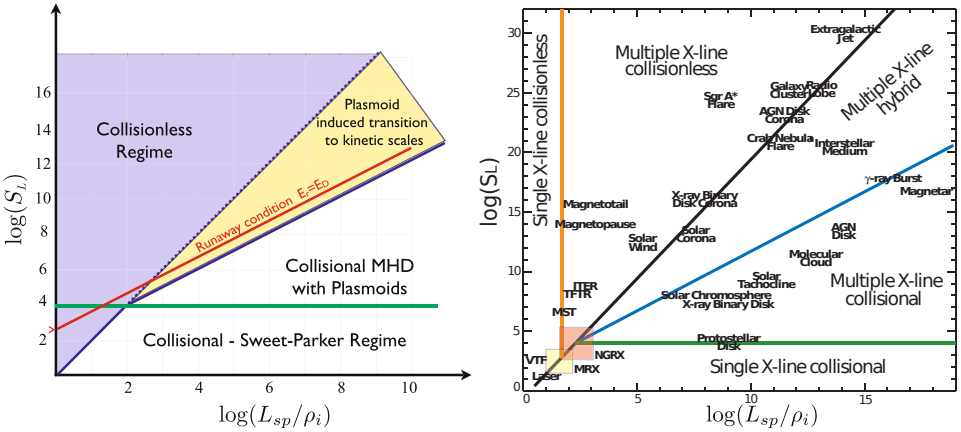

Figure 2.42: Parameter space for reconnection regimes, from Daughton and Roytershteyn (2012) and Ji and Daughton (2011), distinguishing between collisionless and collisional regimes, with or without plasmoid instabilities.
Left: Here the red curve is computed for $\beta = 0.2$ and a reconnection rate $R = 0.05$. S is the Lundquist number, $L_{\rm sp}$ the macroscopic system size, $\rho_{\rm i} = r_{\rm ci}$ the ion Larmor radius in the asymptotic magnetic field (including the guide field).
Right: Same picture, but with astrophysical objects placed according to order of magnitude estimates.

Turbulence and effective turbulent (or anomalous) resistivity

Instabilities or pre-existing turbulence can provide fluctuations in the electromagnetic fields that can, in turn, allow the magnetic field and the plasma to decouple, and reconnection to proceed at a fast rate.

Fluctuations then provide new effective non-ideal terms in Ohm's law. This can be seen by decomposing all quantities into a mean part plus a fluctuating part, for example $\boldsymbol{E} = \langle \boldsymbol{E} \rangle + \delta \boldsymbol{E}$, where the average can be taken over a timescale larger than that of the fluctuations but smaller than the reconnection timescale, or over a spatial direction that would be invariant in a 2D setup, but dynamically released in a 3D setup (e.g., along y in Fig. 2.49). We then take Ohm's law (Eq. 2.39), which reads $n_{\rm e}\boldsymbol{E} + n_{\rm e}\boldsymbol{v}_{\rm e} \wedge \boldsymbol{B} =$ (non-ideal terms), and take its average. The product of two or more quantities will give rise to additional terms, for example $\langle n_{\rm e}\boldsymbol{E} \rangle = \langle n_{\rm e} \rangle \langle \boldsymbol{E} \rangle + \langle \delta n_{\rm e} \delta \boldsymbol{E} \rangle$. Considering this term only, Ohm's law for the mean electric field then reads

$$\langle n_{\rm e} \rangle \langle \boldsymbol{E} \rangle + \langle n_{\rm e} \boldsymbol{v}_{\rm e} \wedge \boldsymbol{B} \rangle = \langle \text{non-ideal terms} \rangle + \langle \delta n_{\rm e} \delta \boldsymbol{E} \rangle. \tag{2.57}$$

The last term is seen as an "anomalous" resistivity, even if from a fundamental point of view, the fluctuations allow reconnection by enhancing inertial or finite Larmor effects, so that there is nothing anomalous. The importance of anomalous resistivity in collisionless 3D reconnection is still debated (see Sect. 2.12.3 for a discussion).

2.11.3 When does each non-ideal process dominate?

Magnetic reconnection can proceed in the collisional regime ($\eta \boldsymbol{J}$ in Ohm's law, description by MHD), or in the collisionless regime (electron inertia, finite Larmor effects, kinetic description). These two regimes feature very different reconnection rates and properties, so that it is important to know which occurs when.

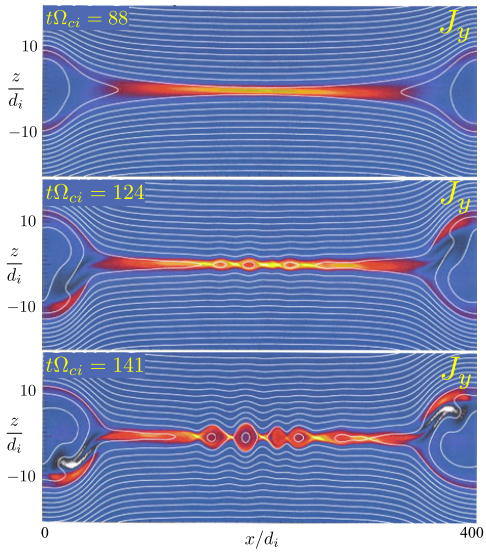

Figure 2.43: Evolution of a current sheet and formation of magnetic islands, from Daughton and Roytershteyn (2012), PIC simulation with a Fokker-Planck collision operator.

A simple criteria to decide between collisionless or collisional is the following. When a current sheet forms, it does so with a given width δ. If δ is far larger than kinetic scales, then kinetic effects are unimportant, and reconnection occurs due to resistivity. In particular, the Sweet-Parker analysis holds (Sect. 2.6.2), and gives the reconnection rate and the sheet width, that we denote by δ_{SP}. This is possible only if $\delta_{\rm SP}$ is larger than kinetic scales, because otherwise kinetic effects are important and take over resistivity before the sheet reaches the Sweet-Parker width. Consequently, in a given plasma, reconnection is collisionless if

$$\delta_{\rm SP} < d_{\rm i} \text{ or } r_{\rm ci} \text{ or } \rho_{\rm sound} \quad \text{(collisionless reconnection)}. \tag{2.58}$$

Here, $d_{\rm i}$ is the ion inertial length, $r_{\rm ci}$ the ion thermal Larmor radius, and $\rho_{\rm sound}$ the ion Larmor radius based on the ion acoustic speed (with the electron temperature and ion mass). Which term is to be used depends on the configuration and is not clearly established yet (see Daughton and Roytershteyn 2012), but it appears that with no guide field the relevant length is $d_{\rm i}$, while with a guide field it is $\rho_{\rm sound}$.

We recall the definition of the Lundquist number:

$$S_{\rm L} = \frac{\mu_0 L V_{\rm A,in}}{\eta} \tag{2.59}$$

with $\eta = E/J$ the resistivity, $V_{\rm A,in}$ the inflow Alfvén speed, and L the current sheet length. Starting from a stable Sweet-Parker current sheet, the limit between the collisional and collisionless behavior is $\delta_{\rm SP} = r_{\rm ci}$ (if we take for example the ion Larmor radius as the relevant kinetic scale). We showed that the Sweet-Parker width is given by $\delta_{\rm SP} = L/\sqrt{S_{\rm L}}$ (Eq. 2.29), so that the limit is equivalent to $S_{\rm L} = (L/\delta_{\rm SP})^2 = (L/r_{\rm ci})^2$. This is the blue line in Fig. 2.42 (left), partly dashed and partly solid, that starts from the origin. Reconnection is collisionless on the left side of this line, with rates $R \sim 0.1$, and is collisional on the right side, with rates $R = S_{\rm L}^{-1/2}$.

The previous reasoning assumes that the Sweet-Parker current sheet exists and remains stable. This is not always justified. When the length L

of the current sheet is too large, it is seen in simulations to be unstable to the generation of magnetic islands (also called plasmoids, see Fig. 2.43). These islands separate the current sheet in several shorter and thinner current sheets which can, in turn, again generate islands and smaller scale current sheets, and so on. This has two major consequences:

- Even if the dominant non-ideal process remains MHD for the smaller sheets, the rate of magnetic reconnection increases. This is because the resistive Sweet-Parker rate is limited by the small width to length ratio (the rate is in part fixed by the inflow velocity $v_{\rm in}$, see Eq. 2.51, and from Eq. 2.29, $v_{\rm in}/V_{\rm A,in} = \delta/L$, hence the importance of the aspect ratio), but this ratio becomes larger for a sheet broken in smaller sheets.

  Simulations show that the current sheet generates islands above a critical Lundquist number $S_c \sim 10^4$ (or lower if the initial conditions are turbulent, but apparently higher for relativistic reconnection: Zanotti and Dumbser (2011) find $S_c \sim 10^8$). This is the green line of Fig. 2.42 (left). The rate of reconnection defined as $R = v_{\rm in}/V_{\rm A,in} = \delta/L$ is then given by $S_c^{-1/2} \sim 0.01$, whatever $S_{\rm L}$, which is fast (Shibata and Tanuma 2001; Loureiro et al. 2007; Uzdensky et al. 2010; Loureiro et al. 2012).

- The generation of small scale current sheets can lead to the creation of sub-sheets with a width $\delta < d_{\rm i}$ or $r_{\rm ci}$ or $\rho_{\rm sound}$, so that kinetic processes ultimately control the reconnection rate and the energy conversion. The transition to the collisionless regime can thus occur sooner that when assuming a stable Sweet-Parker current sheet. This is the lower blue line of Fig. 2.42 (left). The reconnection rate is then given by the collisionless rate, $R \sim 0.1$.

Finally, reconnection cannot be collisional if the induced reconnection electric field exceeds the Dreicer runaway electric field[ad]. This is the red line of Fig. 2.42 (left).

Daughton et al. (2009a,b) performed simulations of a Harris current sheet with a PIC code that treats collisions with a Monte-Carlo treatment of the Fokker-Planck collision term. They probed the collisional Sweet-Parker regime, and the transition to collisionless reconnection for sheet thickness of the order of kinetic scales, as well as the trigger of the plasmoid instability.

Finally, the right part of Fig. 2.42 places various environments in the parameter space diagram. We see that magnetic reconnection is likely to be collisional in environments such as the solar chromosphere, inside accretion disks, or in molecular clouds, and collisionless in the solar corona, in the corona of accretion disks, in extragalactic jets, in the magnetotail and magnetosphere, or in the tokamak ITER.

[ad]Dreicer electric field: The concept of resistivity, and the relation $\boldsymbol{E} = \eta \boldsymbol{J}$, is based on an equilibrium for the electron fluid between acceleration by $\boldsymbol{E}$ and drag force against the ions: $0 = -e\boldsymbol{E} + \nu_{ei} m_{\rm e}(\boldsymbol{v}_{\rm i} - \boldsymbol{v}_{\rm e})$, which gives $\boldsymbol{E} = \eta \boldsymbol{J}$ with $\eta = m_{\rm e}\nu_{ei}/(n_{\rm e}e^2)$. But the frequency of Coulomb collisions of an electron of speed v with ions at rest is proportional to v^{-3}. It decreases with increasing velocity. If the electric field is too large, then the acceleration of an electron between two collisions allows the electron to gain too much energy, so that its collision frequency decreases dramatically, so that ultimately the force balance between collision drag and electric field acceleration cannot be maintained. The limiting electric field is called Dreicer electric field (see, e.g., Bellan 2006, §13.4). When it is so, particles can be freely accelerated to large velocities, and collisional theory fails.

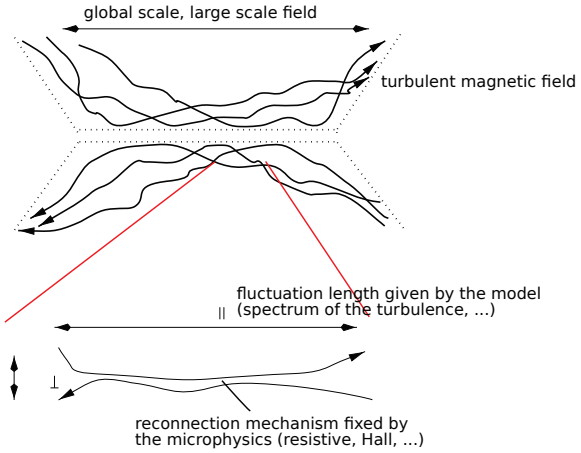

Figure 2.44: Reconnection in the model of Lazarian and Vishniac (1999).

2.11.4 Fast reconnection in collisional plasmas

From kinetic simulations and observations, magnetic reconnection is known to be fast in collisionless environments, with rates of the order of $R = E_y/(B_0 V_A) = 0.1$ (for reasons not completely clear, see Sect. 2.12.1). It also appears that the localization of the resistivity allowed by the collisionless Ohm's law allows to form Petsheck-like structures along the separatrices at large distances (Sect. 2.12.4).

The collisional case may be less clear. Fast reconnection is observed in collisional environments, in the solar chromosphere for example, but which mechanism allows fast rates remains debated. In addition, the lack of localization of the resistivity in a current sheet of width $\delta_{SP} \gg$ (kinetic scales) does not enable Petschek solution to set in. There are currently two main paradigms to explain fast collisional reconnection.

The first is via turbulence and small scale fluctuations. In the model of Lazarian and Vishniac (1999) (Fig. 2.44), the large scale field actually reconnects on small scale Sweet-Parker patterns of length fixed by the size between two significant deviations of the fluctuating field component (which depends on the spectrum of the turbulence). Even if the local rate is taken to be the Sweet-Parker collisional rate, the macroscopic rate for the mean field is independent on the resistivity η, and is fast. It is because of the multiplication of reconnecting sites and because of the increase of the Sweet-Parker reconnection rate when the length of the sheet decreases. This model has been tested numerically by Kowal et al. (2009, 2012), where the simulations essentially confirm the analytical model.

The second is the plasmoid-induced reconnection invoked in Sect. 2.11.3. The basic argument is similar to the turbulent model of Lazarian et al.: a fast rate can be achieved because the current sheet breaks into several shorter sheets, that in turn break again, and thus reconnection occurs at smaller scales with small aspect ratios.

We remark that if scales where collisionless physics dominates are eventually reached, then the reconnection setup may very well switch to the Petschek regime.

Finally, both paradigms can be linked (Lapenta and Lazarian 2012), and it seems that reconnection is indeed fast in collisional plasmas.

2.12 From large to small scales: The central non-ideal zone and the magnetic separatrices

We now turn to the structure and properties of a reconnection event at scales where kinetic non-ideal effects are important to decouple plasma and magnetic field. It is at these scales that the transfer of energy between the fields and the particles occur, and it is there that one can find the processes that allow reconnection to be fast, or that fix the amount of energy transfered to ions or to electrons, as well as the degree of thermalization of the plasma. Two locations are of paramount importance. The first is the central non-ideal region (also called the dissipation or the diffusion region), for example located around the X-point, where non-ideal processes allow the field lines to loose their connectivity and to reconnect. This region is investigated in Sect. 2.12.1 at ion and electron scales, and then in Sect. 2.12.2 at electron scales. The same region is briefly studied for 3D reconnection in configurations that are initially two-dimensional in Sect. 2.12.3, where we also briefly review the role of turbulence. The second key location is where the inflowing plasma, carrying unreconnected field lines, flows into the area embedded by reconnected field lines. This transition happens across the magnetic separatrices, where also non-ideal processes are important and allow the plasma to be energized. We describe this area in Sect. 2.12.4.

2.12.1 Ion-electron two-scale structure of the collisionless non-ideal region (in 2D)

We first detail the structure of the non-ideal region in the case of a collisionless plasma, two-dimensional, with no guide field. The presence of a guide field changes substantially the structure of the dissipation region, in a way that also depends on the plasma $\beta = P_{\rm gas}/P_{\rm mag}$, and we do not detail this here (see Sects. 6.4.2 and 6.5.1 and references therein). The passage to three dimensions is still being investigated, and may in some cases challenge what we now present.

The ion-electron two-scale structure

We explained in Sect. 2.11.2 that if the decoupling mechanism is particle inertia, then it is expected that the species s decouples from the magnetic field at a distance $x < l_{\boldsymbol{\nabla} B}\sqrt{m_s n_s}/(B_0\sqrt{\epsilon_0}) \propto \sqrt{m_s}$ from the current sheet center. A consequence is that ions decouple over a wider area than electrons.

Results from a PIC simulations starting from a Harris current sheet confirm this prediction. Examples are shown in Fig. 2.25 and, more quantitatively, in Fig. 2.45. In the latter, the electron and ion velocities are seen to be roughly equal to the $E \times B$ velocity in the outer region. Ions then decouple from the magnetic field, with a mean velocity dropping to zero[ae]. Electrons do the same, but closer to the center. The scaling of the non-ideal region for species s does scale as its inertial length d_s. This is further analyzed and discussed in Sect. 6.4.2.

[ae]The fact that this transition is so abrupt is a particular case (due to the cold nature of the inflow, as explained in Sect. 6.4.2), and should not be taken as general.

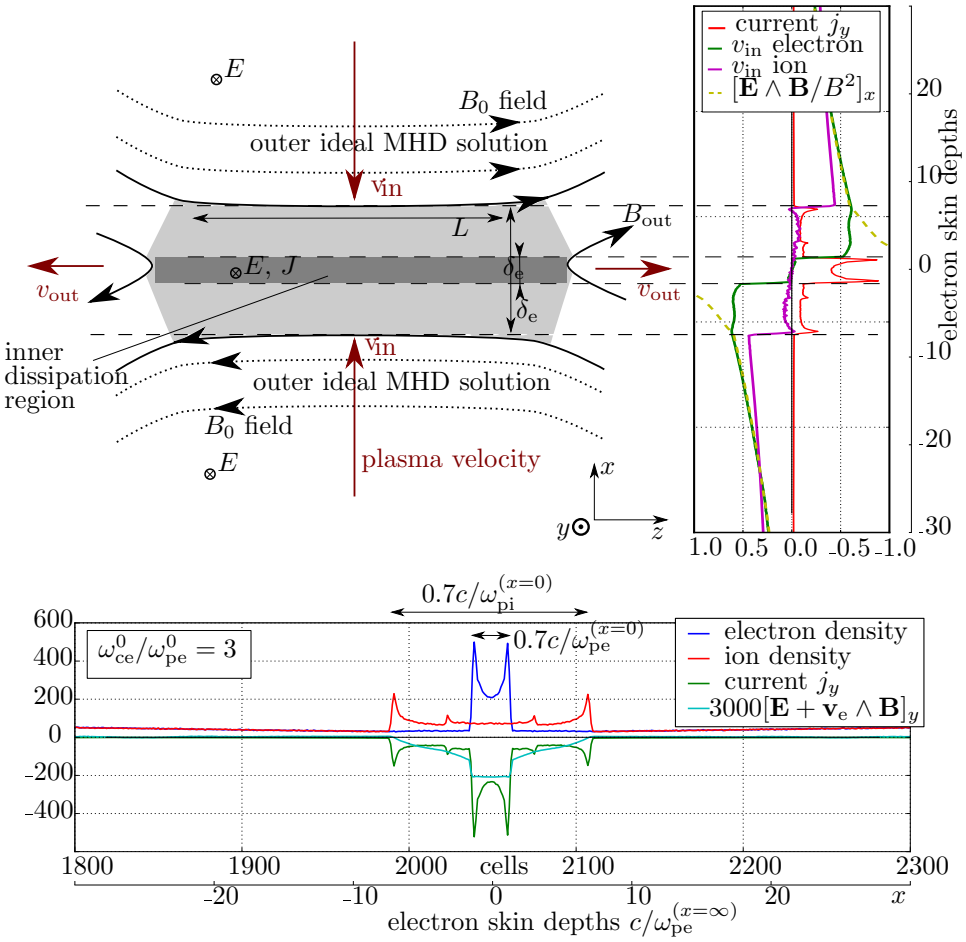

Figure 2.45: **Top:** Schematic representation of the non-ideal region for an ion-electron plasma, without guide field, in 2D. The curves on the right are a cut through the X-point of a PIC simulation (shown in Fig. 2.25, see also Fig. 6.1 for the exact parameters), where $m_i/m_e = 25$.
Bottom: Again a cut along x through the X-point, showing different quantities. Note in particular the difference between ion and electron number densities, that will give rise to an electrostatic field.

Consequence: the Hall current and quadripolar magnetic field

A consequence of the different behavior of ions and electrons is the formation of the Hall currents, Hall electric and Hall magnetic fields. Consider Fig. 2.46. Consider first the inflow of particles. In the ion non-ideal region, electrons are magnetized and follow the $E \times B$ drift with a velocity $\boldsymbol{v}_e = \boldsymbol{E} \wedge \boldsymbol{B}/B^2$, while the ions are unmagnetized and freely bounce back and forth within the ion non-ideal region, resulting in a zero average (or fluid-) velocity (this is indeed seen in the PIC simulation of Fig. 2.45). Consequently, there is a current flowing away from the inflow velocity, given by the electron contribution: $\boldsymbol{j}_{\text{Hall}} = -ne\boldsymbol{v}_e = -ne\boldsymbol{E} \wedge \boldsymbol{B}/B^2$, which is precisely the usual expression of the Hall current.

This current must be closed somewhere. Consider now the outflow of particles. The outflow of electrons is confined to a channel of width $\sim d_e$, while that of the ions to a larger channel of width d_i, and the electrons are expected to reach a higher velocity. These differences lead to the establishment of a current, usually located along the magnetic separatrices for

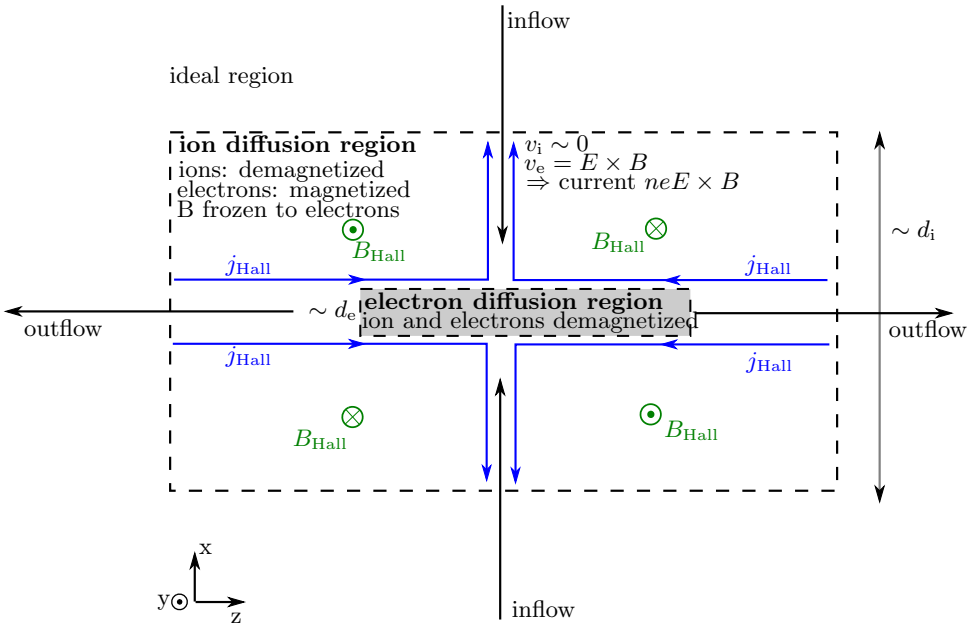

Figure 2.46: Hall quadrupolar magnetic field and currents, resulting from the electron/ion separation of scales around the diffusion region.

reasons explained below, that continues the circuit of the preceding $\boldsymbol{j}_{\text{Hall}}$.

These currents naturally result in a magnetic field with a quadripolar structure (via $\boldsymbol{\nabla} \wedge \boldsymbol{B} = \mu_0 \boldsymbol{j}$), as drawn in Fig. 2.46. See also Fig. 2.51. More details and properties can be found for example in Treumann et al. (2006).

Consequence: the Hall electric field

Another effect of the ion and electron different dynamics is the presence of a charge separation in the non-ideal region. Figure 2.45 shows that the electron and ion particle number densities are different. It results in a dipolar electric field, which in the case of Fig. 2.45 is along x (directed along $+\hat{\boldsymbol{x}}$ in the $x < 0$ part and along $-\hat{\boldsymbol{x}}$ in the $x > 0$ part). We will later see that this electrostatic field is also present far away from the dissipation zone, along the magnetic separatrices.

Consequence: the existence of dispersive waves

Early simulations (the GEM challenge, Birn et al. 2001) have shown that all models including the Hall term (PIC, EMHD, Hall-MHD, two-fluid with and without electron inertia, hybrid simulations) lead to the same fast reconnection rate[af], while models based on magnetic diffusivity only (neglecting the Hall term) lead to slow reconnection. These first studies were later confirmed by the large scale PIC simulations of Shay et al. (2007) or others, where in particular it is checked that the size of the domain has no influence.

An explanation could thus be that the Hall term, even if it is not responsible for magnetic reconnection, enhances the reconnection rates. The theoretical argument behind this idea is as follows. The different response of

[af] The differences between these models being in the shape of the reconnection zone, the fraction of accelerated particles, or of heating.

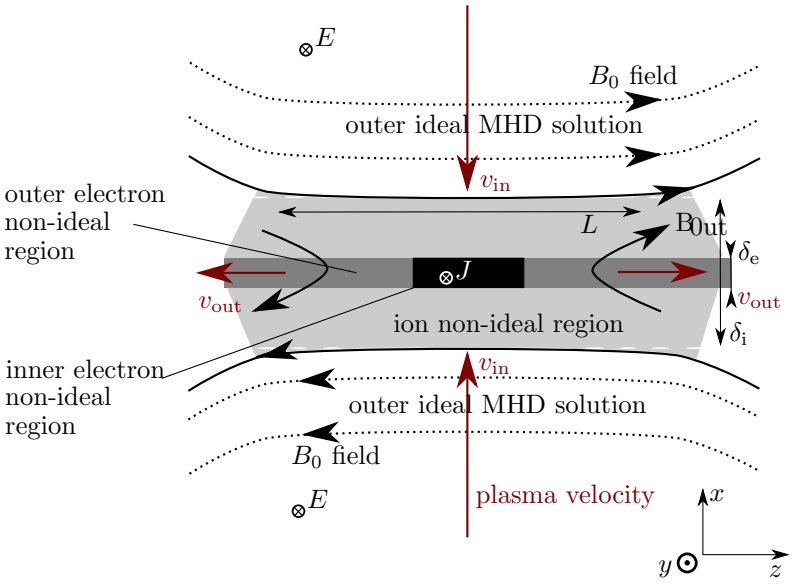

Figure 2.47: Schematic view of the ion non-ideal region, inner and outer electron non-ideal regions.

ions and electrons, because of their different masses, allows for the propagation of some waves with interesting dispersion relations. The cold two-fluid model for a magnetized plasma (or Vlasov-Maxwell system) shows that, for propagation parallel to the magnetic field, the mode corresponding to the MHD Alfvén wave at $\omega \ll \omega_{ci}$ is prolonged at higher frequencies into a branch called the whistler mode. In a portion of this branch, the dispersion relation is $\omega \propto k^2$. Another kind of wave with the same dispersion dependence, that prevails in some parameter regimes (Rogers et al. 2001), is the kinetic Alfvén wave. The idea is that the existence of these waves with a quadratic dispersion relation below ion scales makes the electron outflow velocity scale as the phase speed of the waves[ag]: $v_{out,e} \propto \omega/k \propto k$. The wavenumber k is then assumed to scale as the width of the outflow region: $k \sim 1/\delta_e$. Then, the mass flux $\delta_e v_{out,e} \propto \delta_e k$ does not depend on the layer width δ_e. It allows the reconnection rate to remain constant, and fast, even if the width δ_e shrinks to small scales. The reconnection rate should consequently be independent of the electron physics, and fixed only by the ion physics or the large scale conditions.

However, later studies have challenged this view. Simulations of pair plasmas (where the Hall term and quadratic dispersive waves are absent), or simulations with ions and with a strong guide field where the quadratic waves disappear, have produced reconnection rates as high as the previous ones (Karimabadi et al. 2004; Bessho and Bhattacharjee 2005; Daughton et al. 2006; Daughton and Karimabadi 2007; Liu et al. 2014), and controlled only by the electron physics.

It could be that the Hall magnetic field and currents, and the quadratic dispersive waves, are not of crucial importance for controlling the reconnection dynamics. But it then remains to explain why the reconnection rates in these various situations (ion-electron, positron-electron, strong-no guide field) are all fast and in a close range of values. Liu et al. (2014)

[ag]Note that we are not invoking any kind of wave turbulence: the flow remains laminar.

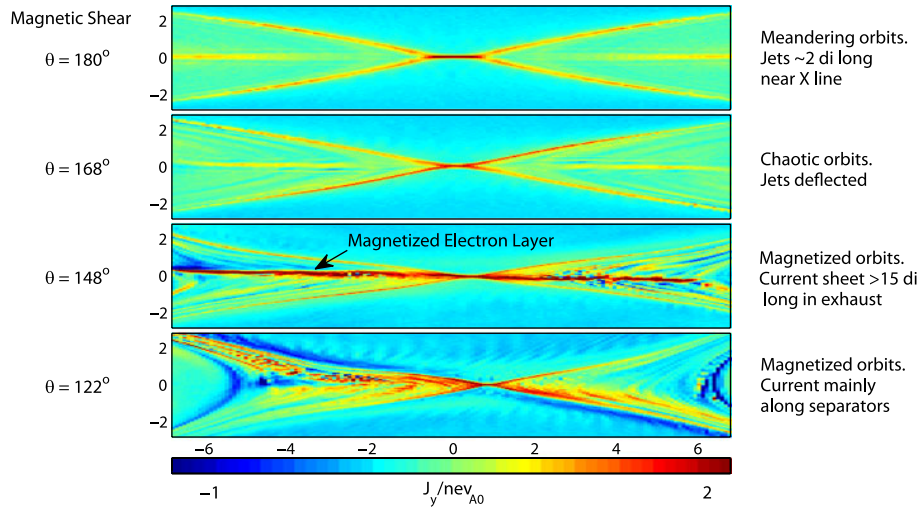

Figure 2.48: From Le et al. (2013). PIC simulations with $m_\mathrm{i}/m_\mathrm{e} = 1836$, showing the antiparallel case (magnetic field reversing from 180 degrees), a weak guide field case, the intermediate case where unprecedented long electron jets are seen, and the strong guide field case. Spatial units are in ion inertial lengths. The angle by which the asymptotic field reverses is θ.

suggest that this is because the scale set by the tearing instability, given by the most unstable mode, is $k\delta \sim 0.5$ independently of the guide field or mass ratio (with δ the width of the magnetic field reversal). If this most unstable k does constrain the dissipation zone length, then the aspect ratio is $\delta/(2\pi/k) = 0.08$ and is constant, thus allowing a constant reconnection rate.

In any case, the debate on the reasons for fast collisionless magnetic reconnection is still open.

2.12.2 The structure of the collisionless electron dissipation region (in 2D)

Section 2.12.1 deals with the difference between ions and electrons, and indicates important consequences. We now focus on the electron non-ideal region, and especially on its structure along the the outflow direction (the z direction in Fig. 2.45).

We showed in Sect. 2.11.1 that the reconnection rate is mostly controlled by the aspect ratio δ/L of the central diffusion region. The same reasoning actually applies to both species s, and the reconnection rate is controlled by the smaller aspect ratio δ_s/L_s.

What sets the length of the non-ideal layer, L_s, is presently not fully understood, and its extent is not clearly determined. According to Hall physics (with the waves with quadratic dispersion relation, Sect. 2.12.1) the length L_e of the electron layer is limited to microscopic scales (some tens of electron inertial lengths d_e). Since the width is typically of some d_e, it implies a ratio $\delta_\mathrm{e}/L_\mathrm{e}$ not so small, so that the electrons are not limiting the reconnection process: instead, it is the ions, via a smaller $\delta_\mathrm{i}/L_\mathrm{i}$, that controls the inflow speed.

However, kinetic simulations showed that the electron dissipation region can extend to large lengths, of the order of ion scales (i.e., $L_\mathrm{e} \sim$ some ion inertial lengths d_i). The ratio $\delta_\mathrm{e}/L_\mathrm{e}$ is then small, and the electrons

are limiting the inflow speed. They are said to form the bottleneck. For example, the simulations of Daughton et al. (2006) show that the electrons control the reconnection rate.

With these new simulations rejecting the Hall paradigm and its small electron non-ideal zone length, a new picture of the electron region emerged. First, in the antiparallel case (i.e., no guide field, Shay et al. 2007; Karimabadi et al. 2007), the electron non-ideal region is composed of two areas (Fig. 2.47). The inner non-ideal region is where reconnection occurs, i.e., where the magnetic field topology changes and where the out-of-plane (y here) currents are present. It has a length of some ion inertial lengths, and it controls the reconnection rate. The outer electron region consists in the electron jets, or outflows, with a width of the order of an electron inertial length, and a length that can extend with time to tens of ion inertial lengths. The inner and outer parts can be distinguished by the sign of $E_y + (\boldsymbol{v} \wedge \boldsymbol{B})_y$, which is opposite in the two areas. It means that the electrons in the outer jet are faster than the magnetic field. The length of the inner non-ideal region may be shortened, and therefore reconnection be speed up, by the formation of plasmoids (or magnetic islands) that break this layer into several shorter layers. The exact condition of occurrence of these plasmoids is not yet fully clear.

The addition of a guide magnetic field, normal to the simulation plane ($B_G \hat{\boldsymbol{y}}$), modifies the inner and outer structures in a way that depends on the relative strength B_G/B_0 (with B_0 the strength of the in-plane magnetic field) and on the mass ratio $m_\mathrm{i}/m_\mathrm{e}$. This is illustrated in Fig. 2.48, and detailed now.

(i) At low guide field strength, the situation is similar to the antiparallel case: electrons are unmagnetized in the inner and outer zones, and perform meandering orbits, i.e., they oscillate between the magnetic field reversal.

(ii) For larger guide fields, the meandering motion of the electrons is not allowed: the guide field deflects them, so that they quickly exit the magnetic field reversal. The inner jet is thus deflected, shortened to $\sim 1 d_\mathrm{i}$, and the outer jet does not form. Note that the electrons remain unmagnetized. The limiting guide field between regimes i and ii depends on the mass ratio $m_\mathrm{i}/m_\mathrm{e}$, and is lower for higher ratios. Goldman et al. (2011) have shown that for the real proton to electron mass ratio, it is of the order of $0.02 B_0$.

(iii) For higher guide fields, the electrons become magnetized everywhere. With a guide field, electron acceleration in the non-ideal zone occurs via parallel electric fields, $E_\parallel = \boldsymbol{E} \cdot \boldsymbol{B}/B$, so that a pressure anisotropy with $P_\parallel > P_\perp$ develops. The pressure tensor should then be written as $P_\perp \boldsymbol{I} + (P_\parallel - P_\perp)\boldsymbol{bb}$, with $\boldsymbol{I}$ the identity matrix and $\boldsymbol{b} = \boldsymbol{B}/B$ a unit vector along $\boldsymbol{B}$. As we explained in Sect. 2.11.2, pressure anisotropy is essential to break the electron frozen-in condition. Since the electrons are magnetized, drift theory can be applied, and the pressure anisotropy force $\boldsymbol{F} = -\boldsymbol{\nabla} \cdot [(P_\parallel - P_\perp)\boldsymbol{bb}]$ also leads to an electron perpendicular drift $\boldsymbol{b} \wedge \boldsymbol{F}/(-en_\mathrm{e}B)$. This drift gives rise to a corresponding current

$$\begin{aligned} \boldsymbol{J}_\perp &= \frac{\boldsymbol{b}}{B} \wedge \boldsymbol{\nabla} \cdot \left[(P_\parallel - P_\perp)\boldsymbol{bb}\right] \\ &\simeq \frac{P_\parallel - P_\perp}{B}\, \boldsymbol{b} \wedge \boldsymbol{\nabla} \cdot (\boldsymbol{bb}) \\ &= \frac{P_\parallel - P_\perp}{B}\, \boldsymbol{b} \wedge \boldsymbol{\kappa}, \end{aligned} \tag{2.60}$$

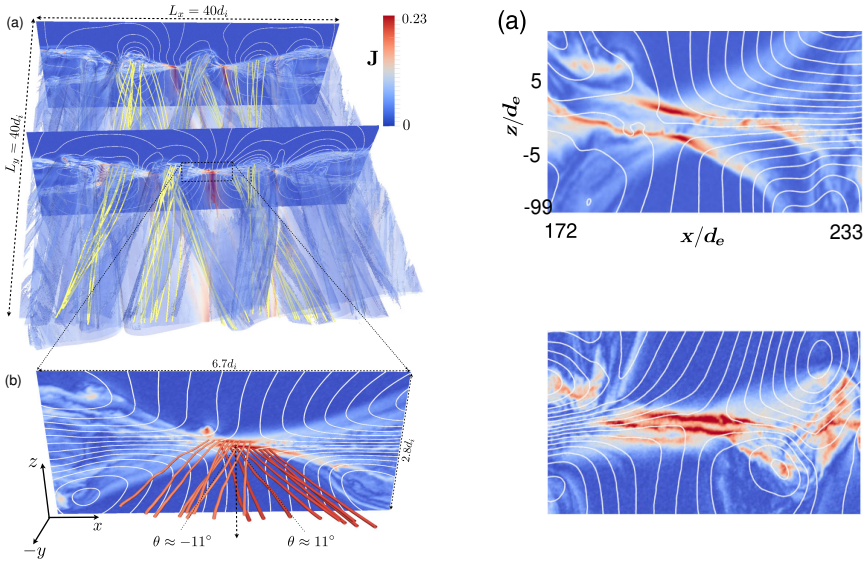

Figure 2.49: From Liu et al. (2013b). 3D PIC simulation with a guide field and $m_i/m_e = 100$. The two right panels are snapshots of the current density at two different times. They show that the electron non-ideal region is composed of two (top panel) or three (bottom panel) current sheets. The left panel is a 3D view.

where $\boldsymbol{\kappa} = (\boldsymbol{b} \cdot \boldsymbol{\nabla})\boldsymbol{b}$ is a curvature vector, pointing toward the center of curvature of the field lines, with a norm given by the inverse of the local curvature radius[ah].

Consequently, the pressure anisotropy, plus a strong enough guide field to magnetize the electrons, allow for the existence of a perpendicular current given by Eq. 2.60, that can flow across the magnetic field. This is the current layer shown in Fig. 2.48 (3rd panel). This layer is $\sim 10d_e$ wide and currently limited in length only by the simulation size ($15d_i$).

Also, this regime does not exist at mass ratios smaller than ~ 400 (Le et al. 2013).

(iv) When the guide field is too strong, the term $(P_\parallel - P_\perp)/B$ in Eq. 2.60 becomes small. The strong guide field then prevents the pressure anisotropy to drive a current and a jet. The electron orbits remain magnetized, similar to those of iii, but the current is localized along the separatrices.

Finally, we note that with large scale simulations, Le et al. (2014) also find extended current layers for ions, which are again allowed by ion anisotropic pressure.

2.12.3 The non-ideal region in three dimensions and the role of turbulence

The results described so far concerned two-dimensional analyses and simulations. The presence of the third dimension brings further complications to the physics of the non-ideal region. First, instabilities along the third direction can be faster than the reconnection instability, and can destroy the current sheet without leading to the reconnection scenario described so far (magnetic energy will still be dissipated, but rather in a turbulent way, with no reconnection outflows). In the following, we thus assume that the

[ah] For the second line of Eq. 2.60 we used the approximation $P_\parallel - P_\perp \sim$ const. For the third line we used the identity $\boldsymbol{\nabla} \cdot (\boldsymbol{bb}) = \boldsymbol{b}(\boldsymbol{b} \cdot \boldsymbol{\nabla B}) + (\boldsymbol{b} \cdot \boldsymbol{\nabla})\boldsymbol{b}$.

plasma parameters are so that the reconnection instability dominates the dynamics.

Second, 3D allows much more initial conditions for reconnection to start than the simple 2D cases considered above. As we have discussed in Sect. 2.10.4, reconnection can occur at various 3D magnetic nulls, or away from null points in the presence of strong magnetic field gradients such as along separators or at other locations. However, the vast majority of 3D kinetic studies start with a two-dimensional equilibrium, invariant in the third dimension, such as a Harris equilibrium or a force-free analogue (Sect. 2.10.2). In the following, we restrain ourselves to these cases.

Even with the above restrictions, the effect of the third dimension can be important. A first relevant question is the role of anomalous resistivity to sustain the reconnection electric field in Ohm's law. Instabilities allowed by the third dimension can indeed generate turbulence – large fluctuations in the electromagnetic fields, particle densities, velocities, ... – which can help decoupling particles from the magnetic field and provide an effective way to sustain a large reconnection electric field (anomalous resistivity, see Sect. 2.11.2). In collisional plasmas, turbulence is the only way to achieve fast reconnection (Sect. 2.11.4). In the collisionless domain, however, reconnection is already fast, mainly because of electron finite inertia, and anomalous resistivity is not needed. It thus appears, from recent large scale particle-in-cell simulations in 3D (Liu et al. 2013b; Karimabadi et al. 2013), that anomalous resistivity does not play a key role in 3D collisionless reconnection, but rather slightly alters the way it happens. An interesting and fully referenced review of these questions is provided by Karimabadi et al. (2013).

A second issue is the structure of the dissipation region. Liu et al. (2013b) show with 3D simulations in a force-free current sheet that, for large enough guide fields (i.e., for a magnetic field reversing by less than 80 degree between above and below), the electron dissipation region consists in several sublayers (between one and three, Fig. 2.49). They underline that, perhaps surprisingly, the physics of each layer is close to that of a two-dimensional layer: the dissipation is provided by electron bulk and thermal inertia, and the reconnection rate is similar to the 2D simulations.

2.12.4 The magnetic separatrices

The non-ideal dissipation zone, where the magnetic field reconnects, has a scale of the order of tens of kinetic scales (e.g., ion inertial lengths), and thus represents only the central part of a reconnection event. Most of the plasma does not flow across this region, but passes from upstream (the domain of unreconnected field lines) to downstream (the domain embedded by reconnected field lines) by flowing across the magnetic separatrices (e.g., as in Fig. 2.52). By doing so, it gets kinetic energy from the magnetic field, and is accelerated and/or heated. Since it concerns most of the plasma flow, the magnetic separatrices and what happens there are of crucial importance for the reconnection process. This section describes some basic aspects of the separatrices physics.

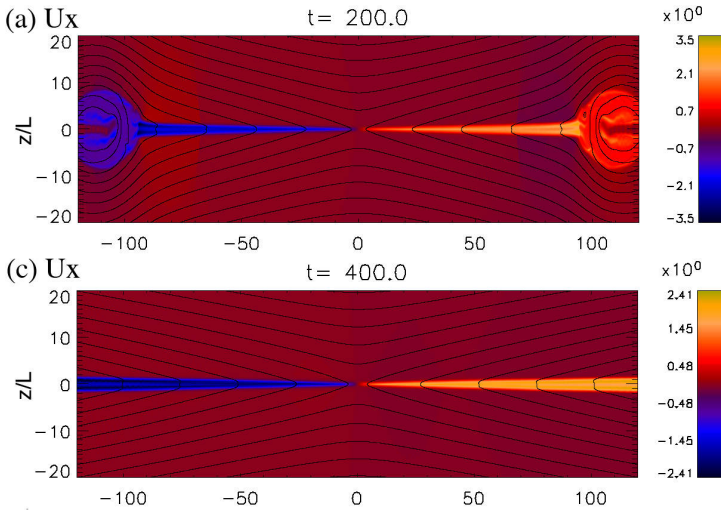

Figure 2.50: Two-dimensional two-fluid simulation of magnetic reconnection, from Zenitani et al. (2009b). The system is shown at two different times. Black lines are magnetic field lines. U_x is the total plasma velocity. At $t = 200$, the two lobes near the left and right boundaries are the dipolarization fronts (Sect. 2.12.5).

The slow shocks of the MHD view and their validity

In the MHD view, according to Petschek's proposition, the upstream to downstream transition is made by passing through slow-mode standing shocks, as pictured in Fig. 2.26 and described by a fluid simulation in Fig. 2.50, and the plasma gains kinetic energy from the magnetic field by passing through these shocks.

However, it is now clear (e.g., Le et al. 2014) that at distances smaller than $\sim 100 d_\mathrm{i}$ (ion inertial lengths) from the central diffusion region, the magnetic field gradients in the exhausts and across the separatrices are too small (compared to inertial lengths or to Larmor radii), and MHD does not apply. A kinetic picture is then required.

What happens at larger distances ($> 100 d_\mathrm{i}$)? The pressure anisotropy, naturally produced by the acceleration mechanisms, implies that the wave modes of the plasma are modified (Gedalin 1993), and so also the shock structure (Higashimori and Hoshino 2012; Liu et al. 2012). A too large anisotropy actually suppresses the slow-mode shock. Still, the kinetic simulations of Higashimori and Hoshino (2012) and Liu et al. (2012) have shown that at more than a hundred d_i from the dissipation region, the pressure anisotropy at the separatrices is small enough for shocks to form, and that the distance between the separatrices is far larger than the kinetic scales, so that anisotropic MHD-like shock analysis can be performed between inflow and outflow. This shock analysis should be performed in an anisotropic MHD framework, as done for example by Tenbarge et al. (2010). In collisionless plasmas, the shock structure remains collisionless and is sustained by kinetic processes, and the usual Rankine-Hugoniot jump conditions apply only if the plasma stays in thermal equilibrium (no significant non-thermal population). Slow-shocks have been crossed by satellites in the Earth's magnetotail (Eriksson et al. 2004).

At smaller distances ($< 100 d_\mathrm{i}$), the pressure anisotropy is too strong to allow shocks to develop (Higashimori and Hoshino 2012), and the distance between the separatrices and the field gradient scales are too short for the

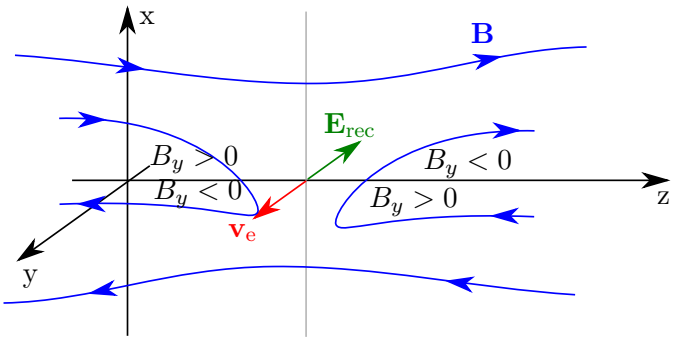

Figure 2.51: The electrons drag the magnetic field in the out of plane direction, thus creating the quadrupolar Hall pattern.

downstream plasma to be described by MHD. However, such distances are small enough (from a computational point of view) to allow numerical kinetic simulations, and a detailed investigation of the underlying processes (e.g., Drake et al. 2009b; Liu et al. 2012; Le et al. 2014; Lapenta et al. 2014). In particular, the vicinity of the separatrices are places with strong field gradients that prevent the particles to remain adiabatic, and are privileged locations for various instabilities. The plasma response is thus largely non-ideal at the separatrices (Lapenta et al. 2014).

We briefly review the small distance issue here ($< 100 d_{\rm i}$), noting that it is under recent active investigations. Most recent studies include Lapenta et al. (2014) (and references therein), or Le et al. (2014), and always concern an initial current sheet (Harris or force-free) invariant along the current direction, and ion-electron plasmas. We note that there is, to our knowledge, no such kinetic studies for pair plasmas (where the Hall-related physics is absent), or for relativistic plasmas (where the MHD waves have different phase velocities than in the non-relativistic case), or with an initial setup different from a Harris-like current sheet.

A final remark concerns collisional plasmas: there, the lack of localization or of gradients in the resistivity does not allow the shock structure to form. See Sect. 2.11.4.

Quadripolar magnetic field

As underlined in Sect. 2.12.1 (see Fig. 2.46), the ion-electron separation of scales implies the creation of a current (the Hall current), and in turn, of a quadripolar magnetic field. The total magnetic field is thus as in Fig. 2.51 and 2.53 (top), and it is as if the electrons were dragging the in-plane magnetic field with them in their outward motion.

This produces a quadripolar magnetic field around the central diffusion region, where reconnection takes place. However, as we explain next, the response of the electrons produce parallel currents along the separatrices that extend way downstream of the central diffusion region, and the quadripolar magnetic field structure is thus created over a large area (possibly hundreds of $d_{\rm i}$).

Electron trajectories

How do the electrons cross the separatrices? Let us first consider the anti-parallel case (no guide field). The electrons are accelerated by the reconnec-

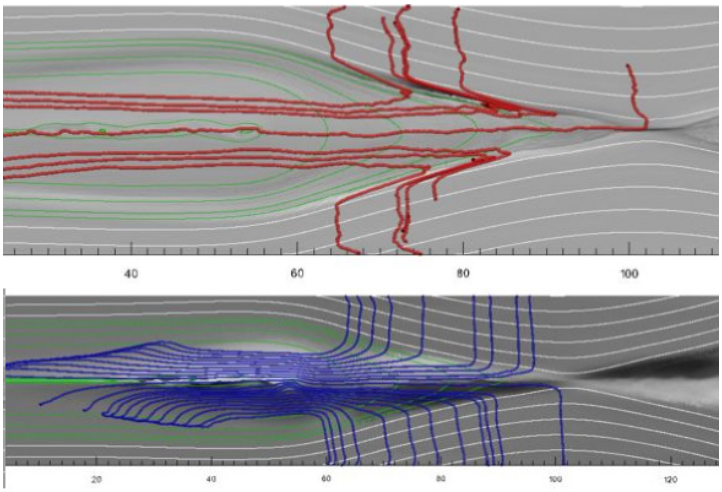

Figure 2.52: Flow lines crossing the separatrices. White lines are not-yet-reconnected field lines, and green lines are newly reconnected ones. **Top:** for electrons, **bottom:** for ions.
The central dissipation region is where the rightmost electron passes. From the implicit PIC simulations of Lapenta et al. (2014), guide field of 10% the reconnecting field, $m_\mathrm{i}/m_\mathrm{e} = 256$. Scales are ion inertial lengths. The flow lines are obtained by integrating the velocity field at a fixed time.

tion electric field $\boldsymbol{E}_y \propto -\hat{\boldsymbol{y}}$. The creation of the out-of-plane Hall magnetic field, B_y, means that there is now a parallel electric field $\boldsymbol{E}\cdot\boldsymbol{B}/B = E_y \neq 0$, and it consequently provides a way for the electrons to be accelerated along the field lines. This is easier than being accelerated across field lines, and the electrons coming from the inflow region do so as soon as they reach the $B_y \neq 0$ and $E_y \neq 0$ regions, i.e., at the separatrices. A consequence is that there are parallel electron flows along the separatrices. Because of the direction of B_y, these flows are always directed toward the X-point (Fig. 2.53, middle). Electrons running toward the X-point and reaching the central non-ideal region will then be expelled into the reconnection exhaust. But far away from the X-point, electrons pass across the separatrix into the exhaust before reaching the central region (as in Fig. 2.52, top). They do so because the motion along the separatrices toward the X-point is allowed by $E_\parallel \neq 0$, i.e., by a non-ideal plasma response, which holds only near the separatrices. Further downstream, the electrons become magnetized again, and the electric and magnetic fields are such that they $E \times B$ drift outward.

If there is a guide magnetic field along y, the particle trajectories are significantly affected. Neglecting the Hall magnetic field, we now see that the electrons accelerated by the reconnection electric field $\boldsymbol{E}_y \propto -\hat{\boldsymbol{y}}$ will flow along the field lines, which means that their motion projected onto the x-z plane is always to the right above the midplane, and to the left below the midplane (see Fig. 2.54). The Hall component B_y only adds up to the existent out of plane field, but if the guide field is strong enough, then the sign of the total B_y is not affected, and particles do follow the trajectories just described. This is also what we find with our own PIC simulations with a guide field, for the same reasons, near the dissipation region and around the magnetic islands (see Sect. 6.5.1, and in particular Fig. 6.12).

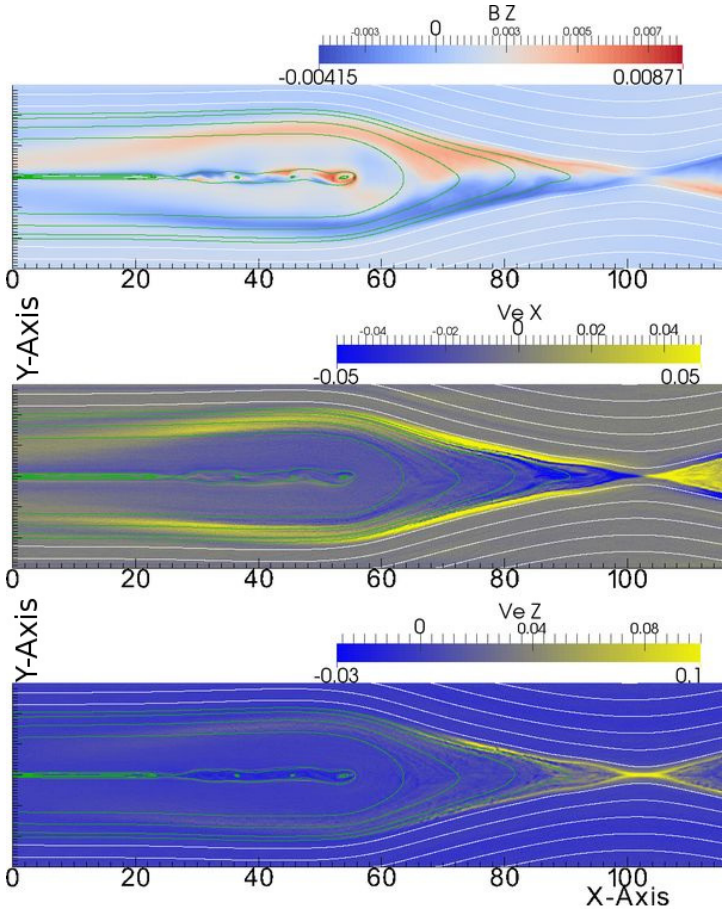

Figure 2.53: **Top:** Out of plane magnetic field, showing the Hall quadripolar structure.
Middle: Component x of the electron velocity. We see the strong and thin flows toward the central region localized all along the separatrices.
Bottom: Out of plane component of the electron velocity. Strong velocities are restricted to the central dissipation region and slightly outward along the separatrices.
From the implicit PIC simulations of Lapenta et al. (2014), guide field of 10% the reconnecting field, $m_i/m_e = 256$. Scales are ion inertial lengths.

Electrostatic in-plane field

The fast electron parallel motion along the separatrices naturally leads to a depletion in electron density, and to a charge separation that the ions cannot screen. The consequence is the existence of an electrostatic field, perpendicular to the separatrices, as shown in Fig. 2.55 (bottom). This electric field is the prolongation of the Hall electrostatic field already present inside the central diffusion region (and described in Sect. 2.12.1).

Ion trajectories

Ions are heavier than electrons, and are less affected by the parallel electric field present along the separatrices: they cross almost unperturbed into the downstream (see Fig. 2.52, bottom). However, they are greatly affected by the electrostatic in-plane field, that accelerates them. Most of the ions bounce between the two separatrices, as shown in Fig. 2.55.

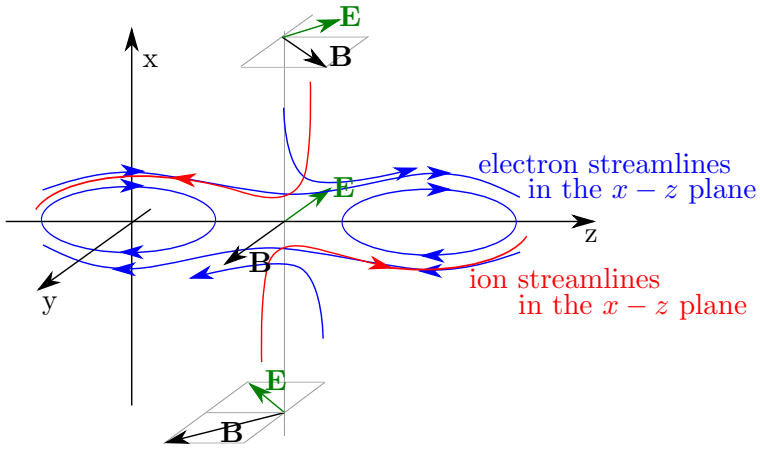

Figure 2.54: Schematic representation of magnetic reconnection with the presence of a guide field, here equal to the in plane field. Since electrons follow the field lines and are accelerated toward $-\hat{\boldsymbol{y}}$, they have a projected motion along $+\hat{\boldsymbol{z}}$ in the $x > 0$ area, and along $-\hat{\boldsymbol{z}}$ in the $x < 0$ area.

Instabilities at the separatrices, subsequent electron heating

The separatrices are prone to several instabilities for several reasons. The electron parallel motion is against the ion fluid, and also against other electrons at rest, so that Buneman or two-stream instabilities can develop. Moreover, the localization of these flows can trigger Kelvin-Helmoltz instabilities. All these instabilities are indeed seen to develop in 3D simulations (Lapenta et al. 2014). The Buneman or two-stream-like instabilities result in electron holes: localized charge imbalance and associated dipolar electrostatic field structure.

The effect of these instabilities is to significantly heat the electrons as they cross the separatrices, mainly in the parallel direction (Buneman or two-stream instabilities are electrostatic, parallel modes).

Electron and ion heating inside the exhausts

The ions are not much heated when crossing the separatrices, and most of their heating occurs in the exhausts via instabilities, or further downstream at the dipolarization fronts (see Sect. 2.12.5). Electrons are also heated by the same mechanisms.

2.12.5 The dipolarization fronts

There is, at the end of the reconnection exhausts, a region where the first reconnected field lines and the expelled plasma collide with the ambient plasma (as in Fig. 2.50). This region is called the dipolarization front. Various instabilities and particle-field energy exchange naturally occur in this area (see, e.g., Vapirev et al. 2013).

This is a region where the newly reconnected field lines pile-up, which leads to an increase in magnetic field strength. A systematic perpendicular heating mechanism is thus betatron acceleration acting on magnetized ions and electrons newly brought into this region[ai] (Lapenta et al. 2014). Also, the magnetic field configuration involves two magnetic mirrors, between

[ai] Said otherwise, the conservation of the first adiabatic invariant, $\mu = mv_\perp^2/(2B)$, implies an increase of $T_\perp$ if B increases.

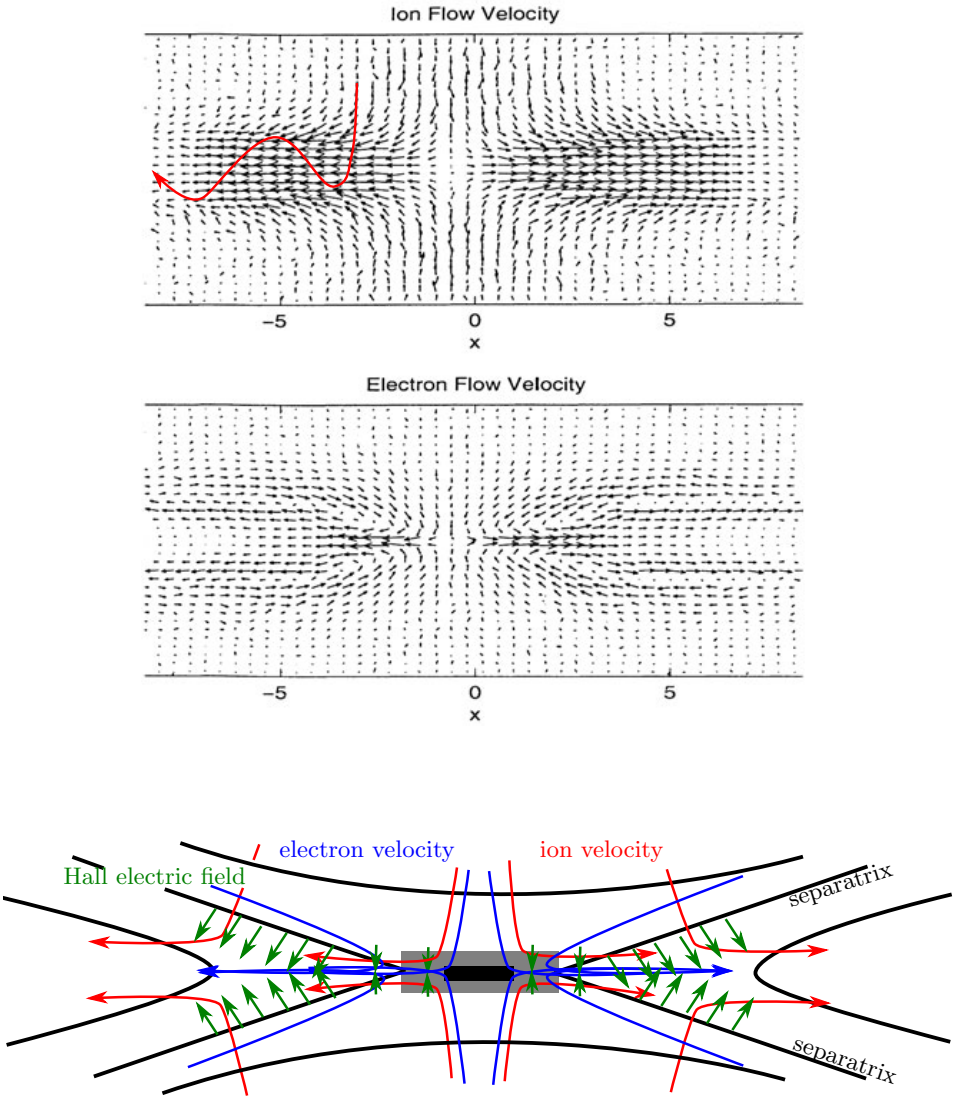

Figure 2.55: Flow structure of the ions and of the electrons.
Top and middle: Fluid velocities from a PIC simulation of Pritchett (2001). The red line shows a typical ion trajectory. Averaging over all such trajectories does lead to the fluid flow represented by the arrows.
Bottom: Schematic view of the fluid flow across the separatrices and of the electrostatic field. Ions are accelerated from inflow to outflow by the Hall electric field (in green) at all locations (from close to far away of the central non-ideal region). The black (gray) central part is the electron (ion) non-ideal region. The ion fluid velocity shown here result from individual trajectories represented in red. There is also an electric field normal to the paper plane, that drives the $E \times B$ drift of the particles in the outer ideal region, and that freely accelerates the particles in the out-of-plane direction in the central non-ideal regions.

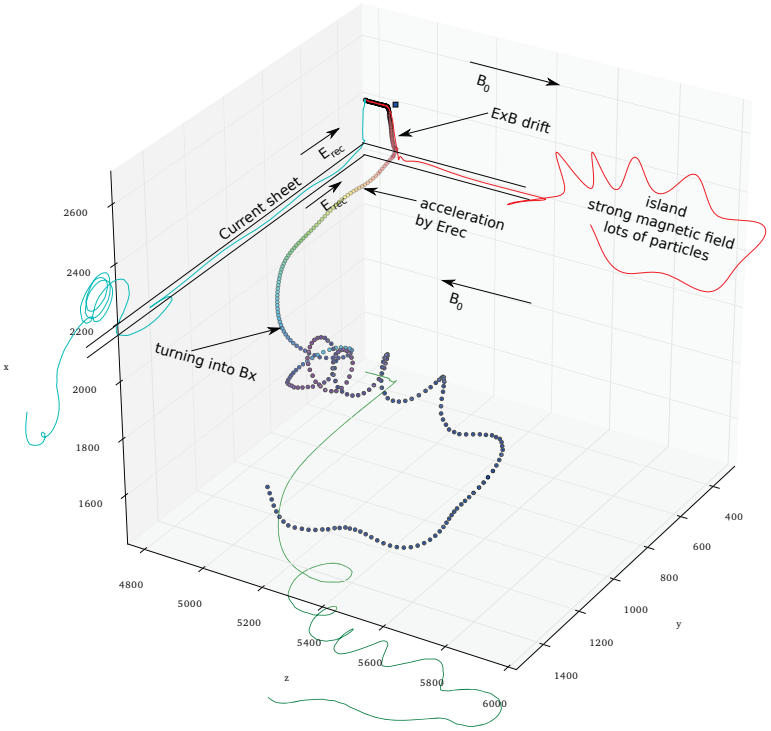

Figure 2.56: Dots are the trajectory of an electron in a PIC simulation. The color code is the particle energy, from red at low values to blue at high values. Solid lines are projection of the trajectory onto the x-y, y-z, and z-x planes. A similar picture in the presence of a guide field is shown in Fig. 6.13.

which the particles bounce, and as more magnetic field piles-up the mirrors get closer, and the bouncing particles are Fermi accelerated (Lapenta et al. 2014).

2.13 From large to small scales: Ultimately, reconnection of the field lines

When electrons decouple from the field lines because of inertia or of collisions with waves or particles, the field lines are released and behave as if they were in vacuum. The physics describing their relative attraction (for non-aligned lines) or repulsion (for aligned lines) and merging is then quantum mechanics. Treumann et al. (2012) describe these processes.

In this article, it is suggested that at the point where the gyroradius $r_{\rm ce}$ becomes larger than the skin-depth $d_{\rm e}$, the lattice of frozen magnetic field lines explodes, field lines are freed, and approach one another via gauge interactions. The presence of several field lines induces gradients in gauge potential, which produce a cloud of pairs, which produce micro-currents, which attract (or repel) anti-parallel (or parallel) field lines.

However, the scales involved are so small and fast that they are not of interest for us.

2.14 Particle trajectories

So far, we have not discussed what particles precisely do during a reconnection event. This can be best learned from PIC simulations, where the indi-

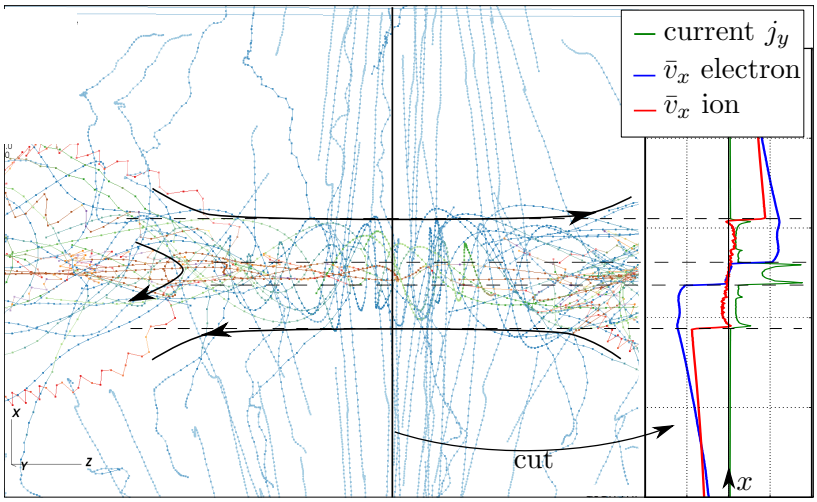

Figure 2.57: Projection, in the x-z plane, of the trajectories of a sample of particles from a PIC simulation starting from Harris equilibrium with no guide field. Ions are in blue-green, electrons in red-orange. The black arrows indicate the magnetic field geometry. The full 3D trajectories are more like in Fig. 2.56.
On the right are the fluid velocities and current for a cut through the X-point.

vidual trajectories can be tracked. This is relevant at scales where kinetic effects are important, and necessary for the fundamental understanding of magnetic reconnection. Studying particle trajectories allows to grasp the mechanisms at the origin of particle acceleration, that may form extended high-energy tails, and allows to understand the structure of the pressure tensor, and also the shape of measured particle distribution functions (Egedal et al. 2008).

There are many kinds of particle trajectories, that depend on the magnetic field geometry. The situation is complex even for a simple Harris initial state (e.g., Egedal et al. 2008; Zenitani et al. 2013)[aj]. Here, we only describe what happens for most particles entering into a 2D dissipation region, as can be seen in Fig. 2.57, in the absence of guide magnetic field. What happens with a guide field is discussed in Sect. 6.5.1.

The behavior of a typical particle from the background plasma is as follows (consult Fig. 2.56 and 2.57):

- Before the onset of reconnection, the particle moves along the background magnetic field lines (along z here), performing Larmor gyrations according to its velocity.
- When reconnection starts, the induced electric field E_y spreads away from the current sheet, and the outflows from reconnection imply a depletion of particles at the center, so that both of these effects set the background particles into motion. The combined action of the electric field $E_y\hat{\boldsymbol{y}}$ and of the magnetic field $\pm B_0\hat{\boldsymbol{z}}$ forces the particles to $E \times B$ drift toward the current sheet (along $\pm\hat{\boldsymbol{x}}$).
- As the particle gets closer to the current sheet, B dwindles, so that the velocity of the drift (which is E_y/B) increases, and the particle accelerates.

[aj] See http://th.nao.ac.jp/MEMBER/zenitani/research-e.html for movies of trajectories.

- When it reaches the area where $E_y > B$, the $E \times B$ drift ceases and the particle is freely accelerated by E_y. It gains energy. The particle is trapped between the magnetic field reversal, because on either side it turns around B toward the center of the sheet. Small oscillations can thus be seen. This part of the orbit is called a Speiser trajectory (Speiser 1965). These bouncing trajectories also explain the non-diagonal nature of the pressure tensor inside the dissipation region.
- If the particle enters in the dissipation region just at the X-point, then the magnetic field is null and it travels along y without turning. But this ideal case never happens, and fluctuations necessarily shift the particle away from the X-point. The newly reconnected magnetic field has a component along x, and the particle slowly turns around this field. Its y momentum is thus converted into a z component, and the particle then travel along z along the exhaust.

  This is how the reconnection outflows are built. This point of view from the particles complements the MHD point of view, which invokes outflows driven by the magnetic tension force of the newly reconnected field lines.
- At the end of the exhausts, the particles encounter the dipolarization front or a magnetic island. The islands are surrounded by a strong magnetic field, and the particle spirals around it and around the island.

2.15 Acceleration mechanisms

Magnetic reconnection is, with shock acceleration and turbulent media, one of the prime candidates to produce accelerated particles. These accelerated particles can then explain a heating of the plasma (as in microquasar and AGN disk coronae, or in the lobes of giant radio galaxies), or the presence of a non-thermal high-energy population (as in the Crab nebula or, again, in microquasar and AGN disk coronae), or they can emit continuous radiation (as for the radio emission from galactic nuclei, AGNs, and extragalactic jets). In particular, because of its fast nature, magnetic reconnection is appealing to explain flare-like events, i.e., high-energy radiation outbursts occurring on small timescales (compared to characteristic macroscopic timescales of the objects), as observed in the Crab nebula, in AGN and microquasar disk coronae, or in extragalactic jets. References associated to these physical environments can be found in Sect. 7.2.

There are several acceleration mechanisms that have been identified within a reconnection event. Which dominates depend on the magnetic field geometry, and on the plasma parameters, and is still an open question. Another key issue is the efficiency of each process, and the produced particle spectrum. Such questions are complicated by the fact that the acceleration physics is highly non-linear and best explored with simulations, which should be run over very long times and with large domains to really capture the relaxed particle distributions, and possibly in three dimensions when relevant. Also, as we show here, there are various acceleration locations (central X-point, separatrices, dipolarization front, ...). In the Chapter 7, we explore the acceleration mechanisms near the central dissipation zone for relativistic plasmas. But in the remaining of this section, we briefly review

the main known acceleration mechanisms. Other details and references, in particular the particle distribution indexes produced by the mechanisms, can be found in Sect. 7.2.

2.15.1 Acceleration by the reconnection electric field

The reconnection electric field, which is produced by magnetic flux variations and sustained in steady state by the non-ideal processes, is alone responsible for transfering energy between the magnetic field and the particles around the central dissipation region. It thus obviously accelerates particles. However, it does not necessarily lead to a population of non-thermal high-energy particles that can emit high-energy photons. We precise this below.

Production of Alfvénic electron jets

For two-dimensional setups, we explained in Sect. 2.14 that the reconnection outflows exiting from the central dissipation region origin from particle acceleration by the reconnection electric field and rotation around the reconnected magnetic field (in the MHD view, this is the tension force of the highly bent reconnected magnetic field).

The escape velocity of the fluid in this region is of the order of the Alfvén speed in the inflow (this was deduced from particle number and energy conservation, Eq. 2.27). Consequently, there are naturally Alfvénic jets in situations of 2D reconnection. PIC simulations confirm this, even if some show the intermittent production of magnetic islands at the X-point that may disturb this simple view.

Such Alfvénic jets are invoked by Giannios et al. (2009) to produce fast variability in the emission seen from extragalactic jets: small reconnection events inside the jet can eject Alfvénic blobs of plasma that emit radiation.

High-energy tails

The Alfvénic outflows are mostly bulk flow acceleration. It is however possible, in some conditions, that acceleration by the reconnection electric field produces high-energy tails in the particle distribution.

More specifically, this mechanism is inefficient for non-relativistic reconnection because the acceleration zone (where $E > cB$ in the no-guide field case, or where $\boldsymbol{E}\cdot\boldsymbol{B} \neq 0$ in the guide field case) has a too small length (along z) (Drake et al. 2010; Kowal et al. 2011; Drury 2012) and affects too few particles. But it is efficient under relativistic conditions, where the larger reconnection electric field creates a wider acceleration zone (Zenitani and Hoshino 2001, 2007). Various PIC simulation studies confirmed that power law tails of high-energy electrons can be created with this mechanism. The power law indexes found can be harder than for collisionless shocks, and the acceleration times shorter (Cerutti et al. 2014a; Sironi and Spitkovsky 2014, and Chapter 7 of the present manuscript). We also show, in Chapter 7, that this mechanism can produce power laws for ions.

2.15.2 Acceleration by contracting magnetic islands

Magnetic islands are closed field lines, such as around O-points in 2D. When two islands merge, there is contraction phase. Energetic particles inside

the islands are trapped by the magnetic structure and, when the island contracts, they bounce back and forth against the approaching sides of the island. The first-order Fermi mechanism can then operate and accelerate these particles. The particle energy gain is actually due to the electric field induced by the island sides motions in the magnetic field (it can be seen as a motional electric field, $\boldsymbol{E} = -\boldsymbol{v} \wedge \boldsymbol{B}$, and is always directed in the same direction).

This mechanism can be efficient in collisionless plasmas (Drake et al. (2006) for electrons in the solar corona; Drake et al. (2010) for ions at the heliospheric termination shock) or in collisional plasmas (Kowal et al. (2011) for pairs in microquasars). In non-relativistic plasmas, because of the small particle velocities, the Larmor radii can be smaller than the island gradient scales. If it is the case, then particle motions are adiabatic inside and around the islands, and particle-in-cell simulations and analytical estimations agree that this mechanism produces power law spectra. In plasmas with relativistic magnetizations, the Larmor radii of the accelerated particles likely exceed the island scales, at least at early times, so that another analytical approach has to be employed (Bessho and Bhattacharjee 2012), and there is no analytical expression for the resulting spectra. PIC simulations in relativistic pair plasmas show that it significantly contributes to the building of the high-energy populations (Bessho and Bhattacharjee 2012; Sironi and Spitkovsky 2014). It saturates if the firehose instability threshold is reached (see Sect. 2.A for the firehose instability).

We also find in Chapter 7 that this acceleration mechanism operates significantly. It is efficient for the particles trapped inside the islands, and also for the particles that swirl around the islands.

2.15.3 Acceleration by the motional electric field

As we have seen, in the ideal region around the dissipation region, there is the presence of a motional electric field $\boldsymbol{E} = \boldsymbol{B} \wedge \boldsymbol{V}$. A particle from the bulk flow cannot be accelerated by this electric field, because it is this field that allows the particle to have its velocity (the electric field in the frame of the bulk flow vanishes). Such particles are said to be adiabatic. However, a particle that is not from the bulk flow can be accelerated by the motional electric field. This leads to at least two possibilities, described below.

Particle pick-up

In reconnection configurations, the exhausts naturally provide places where particles can enter, be non-adiabatic, and be accelerated (see Fig. 2.58). This is true for heavy ions, for which the large m/q ratio, and consequently large Larmor radius, implies that they are easily non-adiabatic when entering the exhaust. This mechanism is called "pick-up"[ak]. It is invoked to explain heavy ion acceleration in solar flares, and also in the context of anomalous cosmic rays produced at the termination shock of the solar wind (Drake et al. 2009a; Knizhnik et al. 2011).

[ak] The name, introduced by J. Drake, refers to the standard pick-up mechanism of neutrals that get ionized and suddenly have to $E \times B$ drift.

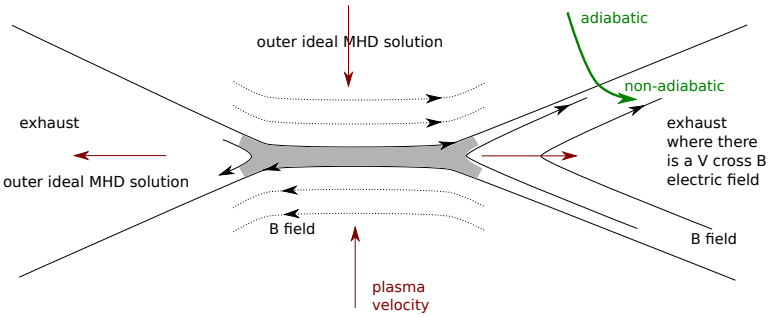

Figure 2.58: Ion pick-up. The particle in green is adiabatic in the upper part of the figure, but becomes non-adiabatic as it enters the exhaust. It can then be accelerated by the motional electric field during a transient phase, before becoming adiabatic again and $E \times B$ drifting at its terminal speed. Being non-adiabatic may require a large m/q ratio, and thus be valid only for heavier ions.

Acceleration between the two converging inflows

Another acceleration mechanism, also relying on the first-order Fermi process and on stochasticity, is the bouncing motion of particles between the two inflows converging from both sides of the current sheet. Energy is gained when the particle turns around, and is transferred by the motional electric field present in the inflow.

Drury (2012) derives the power law spectrum for non-relativistic particles: $\mathrm{d}n(v)/\mathrm{d}v \propto v^{-p}$ with v the velocity, $p = (r+2)/(r+1)$, where $r = n_{\mathrm{out}}/n_{\mathrm{in}}$ is the compression ratio that is not restricted to low values as in the case of shocks. Giannios (2010) derives the maximal Lorentz factor produced in the relativistic case, and Bosch-Ramon (2012) discusses conditions for entering in this acceleration regime. This mechanism does not rely on a direct acceleration by the reconnection electric field E_{rec} when particles are demagnetized at the center of the dissipation region, but lies on the motional electric field in the inflow. It is thus efficient in non-relativistic or/and collisional plasmas (Kowal et al. 2011) where direct acceleration by E_{rec} is known to be negligible. See also Bosch-Ramon (2012).

We remark that it requires particles crossing the current sheet and bouncing on the other side, i.e., having a Larmor radius in the asymptotic field that is larger than the sheet width (we discuss quantitatively this issue in Sect. 7.5.2), which is generally true only for pre-accelerated particles or hot inflows, that may or may not be present in the medium under consideration. Such pre-accelerated particles are generally absent from PIC simulations, so that the mechanism was never seen in a PIC run. Simulations with pre-accelerated populations remain to be done.

In addition, this Fermi mechanism implies that particles travel a length larger than the width of the current sheet before being deviated back along the opposite direction. Such trajectories may then be subject to significant collisions, even when the reconnection process itself is collisionless. Whether collisions restrain or cancel the energy gain remains an open question.

Acceleration in contracting current sheets

When current sheets contract (either because they are unstable or because of the large scale dynamics), the first-order Fermi mechanism can operate again. See for example Kowal et al. (2011) or Jaroschek et al. (2008).

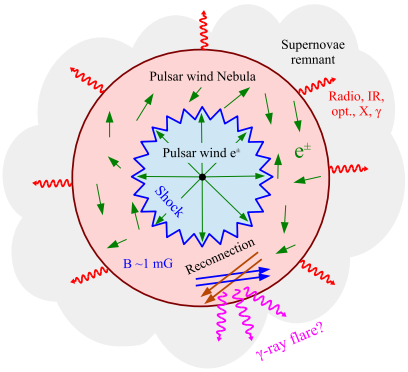

FIG. 1. This diagram sketches the classical (1D) model of pulsar wind nebulae in which the pulsar inf ates a relativistic and magnetized wind of $e^{\pm}$ pairs. The pulsar wind nebula forms between the termination shock of the wind and the contact discontinuity with the ambient medium, here the material from the supernova remnant. As argued in this paper, magnetic reconnection within the nebula could explain the gamma-ray f ares observed in the Crab Nebula.

Figure 2.59: From Cerutti et al. (2014a). Schematic representation of the Crab nebula. See also Table 7.5 for orders of magnitude.

2.15.4 Other mechanisms

Other acceleration mechanisms exist, especially far from the diffusion region. For example stochastic acceleration in the turbulence associated with reconnection (Kowal et al. 2011). Also, acceleration at the magnetic separatrices, or at the dipolarization front, remain largely unexplored. See also Sect. 7.5.4.

2.15.5 Example: The Crab nebula

Magnetic reconnection could be a key element of two fundamental problems concerning pulsars: one related to the termination shock of the pulsar wind, one related to high-energy flare emission in the nebula (see Fig. 2.59).

Particle acceleration at the wind termination shock

The best observed pulsar is hosted at the center of the Crab nebula. The pulsar emits a strong wind of electron-positron pairs, and it also has a strong magnetic field, that the wind plasma carries as it expands. The pulsar rotates quickly, and its rotation axis is not aligned with its magnetic axis. Consequently, in the equatorial plane there is a succession of positive and negative magnetic field regions, with current sheets in between (see Fig 2.60). A favored model is that when these magnetic field reversals are carried in the wind, the current sheets are too large and reconnection does not occur. But the wind ends in a termination shock, where the current sheets are compressed and unstable to magnetic reconnection.

There is, inside the nebula, a high-energy particle population (called the wind population) that is inferred from observations (according to Sironi and Spitkovsky (2011a), electron power law $\mathrm{d}n/\mathrm{d}\gamma \propto \gamma^{-1.5}$ over three decades at least are needed to explain the radio to optical emission of the nebula). Sironi and Spitkovsky (2011a) explore with PIC simulations the possibility that the reconnection events at the termination shock can produce this population.

High-energy flares from the pulsar nebula

The pulsar wind nebula is located between the first shock, where the free expansion of the pulsar wind ends (0.1pc for the pulsar), and the contact dis-

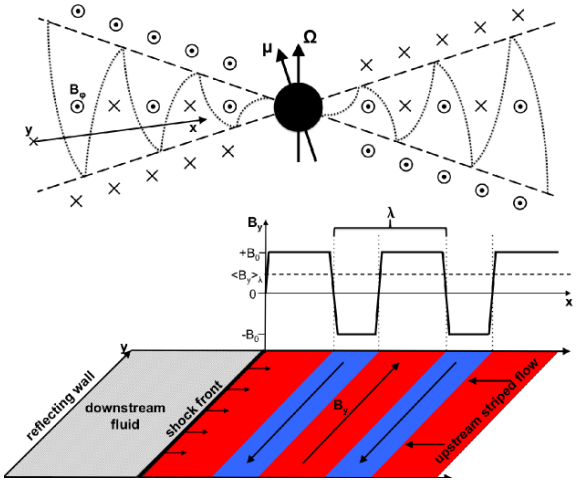

Figure 2.60: From Sironi and Spitkovsky (2011a). **Top:** The rotation axis of the pulsar is along Ω, while its magnetic field axis is along μ. Only the toroidal component of the field is shown (B_φ). The rotation creates alternating signs for B_φ near the equator. **Bottom:** At the termination shock of the wind, the stripes meet the shock and will be compressed, triggering reconnection events.

continuity with the external medium (which is here the supernova remnant material).

Pairs emit synchrotron radiation from radio to a hundred MeV, and upscatter photons to between 1 GeV to 100 TeV, thus producing a steady emission. In addition, there is the emission of flares, that occurs continuously for small flares up to once a year for very large ones, reaching energies of hundreds of GeV. These flares are believed to come from synchrotron-like emission, in fields of the order of $B \sim 1\,\mathrm{mG}$ (Uzdensky et al. 2011) by PeV electrons ($10^{15}\,\mathrm{eV}$, or Lorentz factor of 10^9). But the mechanism accelerating the particles to these energies is still unclear. A possibility is particle acceleration in reconnection events. Cerutti et al. (2012b) and Cerutti et al. (2012a) have produced PIC simulations of magnetic reconnection, that include radiative braking of the electrons. They have found that electrons can remain long enough at the X-point, where the magnetic field is almost null, where they are accelerated *directly by the reconnection electric field*. When they escape the X-point, they arrive in a region of significant magnetic field around the magnetic islands, and immediately radiate high-energy photons[al].

Appendix 2.A Pressure anisotropy and implications for wave speeds, the tension force, the firehose instability

The heating mechanisms implied in magnetic reconnection events often produce anisotropic particle distribution functions. A not so severe and natural form of anisotropy is a gyrotropic distribution function, where there remains

[al] We remark that these PIC simulations take into account only the wind population (Lorentz factors $10^5 < \gamma < 10^9$, Meyer et al. 2010), and not the so-called radio plasma population ($\gamma \in [20, 10^5]$), even if in terms of particle number density one has $n_{\mathrm{radio}} \sim 10^5 n_{\mathrm{wind}}$. The technical reason is that the low energy electrons have very small Larmor radius, and would require a high resolution. Their impact on the dynamics is yet unclear.

a cylindrical symmetry around the axis defined by the local magnetic field. The pressure tensor can then be written

$$\boldsymbol{P} = P_\perp \boldsymbol{I} + (P_\parallel - P_\perp)\boldsymbol{bb}, \tag{2.61}$$

with $\boldsymbol{I}$ the identity matrix and $\boldsymbol{b} = \boldsymbol{B}/B$ a unit vector along $\boldsymbol{B}$. This holds either for the pressure tensor of each species, or for the sum of both as used in the MHD models.

An important consequence of pressure anisotropy is that it modifies the magnetic tension force, and can ultimately lead to instabilities (the firehose and the mirror instabilities). The reason is that particles traveling along a curved field line exert a centrifugal force on the line, that tends to bend the line even more. In an isotropic plasma, this force is balanced by the perpendicular plasma pressure force and the net outcome vanishes. The only contribution is then the magnetic tension and pressure forces associated to the field lines. However, in an anisotropic plasma where $P_\parallel > P_\perp$, particles exert a net force that tends to bend even more the field lines (due to the particles traveling along the field line, producing $P_\parallel$), and that opposes the magnetic tension force. There are two consequences:

- In an anisotropic plasma where $P_\parallel > P_\perp$, the magnetic tension force – which intuitively tends to unbend field lines – is reduced.
- At the point where the total force (anisotropic plasma pressure plus magnetic tension) vanishes, the plasma becomes unstable to the firehose instability.

To precise these facts, we can first write the total force in the MHD model. The pressure force is minus the divergence of Eq. 2.61, while the $\boldsymbol{J} \wedge \boldsymbol{B} = \mu_0^{-1}(\boldsymbol{\nabla} \wedge \boldsymbol{B}) \wedge \boldsymbol{B}$ term can be rewritten in a similar form, so as to obtain:

$$-\boldsymbol{\nabla} \cdot \boldsymbol{P} + \boldsymbol{J} \wedge \boldsymbol{B} = -\boldsymbol{\nabla} \cdot \left[\left(P_\perp + \frac{B^2}{2\mu_0} \right) \boldsymbol{I} - \left(\frac{B^2}{\mu_0} + P_\perp - P_\parallel \right) \boldsymbol{bb} \right]. \tag{2.62}$$

With this form, we clearly see that the effective magnetic tension force (the term proportional to $\boldsymbol{bb}$) is reduced by a non-vanishing $P_\parallel - P_\perp$.

At the threshold where

$$\frac{P_\perp - P_\parallel}{B^2/2\mu_0} = \beta_\parallel - \beta_\perp = 2, \tag{2.63}$$

the force vanishes and the plasma then becomes unstable to the firehose instability (Hau and Wang 2007). The reason is that a slightly bent field line will tend to be even more bent, and so on, leading to an unstable behavior.

Another important, and related, consequence of pressure anisotropy is that it modifies the wave modes of the plasma. For example in a gyrotropic plasma, the Alfvén speed becomes (Gedalin 1993)

$$V_\mathrm{A}^2 = \left(\frac{\beta_\perp - \beta_\parallel}{2} + 1 \right) \frac{B^2}{\mu_0 \rho}, \tag{2.64}$$

with ρ the plasma mass density. It vanishes at the firehose threshold, and the square becomes negative for $\beta_\parallel - \beta_\perp > 2$, which means that the mode change from a propagating mode to an instability. This is precisely the origin of the firehose instability[am], which excites Alfvén waves.

[am] This is the origin of the MHD firehose instability. There are other firehose instabilities, for example the electron firehose instability (Hau and Wang 2007).

Chapter 3

Elements of relativistic plasma physics

> "Why," he said, "is there a sofa in that field?"
> "I told you!" shouted Ford, leaping to his feet. "Eddies in the space-time continuum!"
> "And this is his sofa, is it?"
>
> Douglas Adams, *Life, the Universe and Everything*

Contents

3.1 Outline

The purpose of this chapter is to review or establish useful results for plasma physics under relativistic conditions. Some of these results can be found scattered in the literature, others are new. These various points have been a necessary preliminary to our investigations on relativistic magnetic reconnection, and we hope that gathering them here will be useful to other relativistic plasma physicists.

By a relativistic plasma, we mean that the mean kinetic energy of the particles exceeds their restmass energy. For a thermal plasma, this happens when $T_\mathrm{e} > m_\mathrm{e}c^2 = 6\times10^9$ K for electrons, and when $T_\mathrm{i} > m_\mathrm{i}c^2 = 1.1\times10^{13}$ K for protons. Such temperatures are reached for electrons in microquasar or AGN disk coronae, in GRB jets, or in pulsar wind nebulae (see Fig. 1.1). The Maxwell-Boltzmann distribution then fails to describe the plasma thermal state, and it should be generalized to the Maxwell-Jüttner distribution. In Sect. 3.2 we describe properties of this distribution. We provide a method to compute various moments, such as the mean Lorentz factor, or mean momentum, enthalpy, or Larmor radius. The results are summarized in Table 3.1.

A plasma with a relativistic temperature has a non-trivial enthalpy, and we discuss how and why in Sect. 3.3. It is an important quantity for the adiabatic exponent and for wave velocities, that we also discuss.

Then, in Sect. 3.4 we rederive the relativistic fluid equations (conservation of particle number, momentum, and energy) from the relativistic Vlasov's equation, in order to express them with quantities defined in the laboratory frame. As opposed to the fluid equations usually found in the literature, the obtained equations do not involve the comoving enthalpy, which is hard to evaluate for an out-of-equilibrium PIC plasma. These equations will be used in Chapter 6 for interpreting PIC simulations and for building analytical theories.

In Sect. 3.5 we briefly review expressions for the MHD wave velocities in a relativistic plasma (i.e., magnetic energy density exceeding the restmass energy, and relativistic temperatures). This is a required preliminary to the investigation of relativistic reconnection, where in particular the Alfvén wave has a central role.

Section 3.6 is a reminder and summary concerning particle motions in constant electric and magnetic fields. The case of relativistic motions is less known than the non-relativistic counterpart, and leads to interesting results that are worth having in mind when interpreting particle trajectories.

In Sect. 3.7, we give the general equilibrium relations for the relativistic Harris configuration with arbitrary temperature and mass ratio between the two species. This will be used to initialize our PIC simulations.

Finally, in Sect. 3.8 we describe a method for loading a Maxwell-Jüttner momentum distribution with an arbitrary bulk velocity and temperature. The naive method, which initializes the comoving distribution and then boosts particles individually, is shown to be incorrect, mainly because space contraction is absent from the PIC code. A correct implementation has not been found elsewhere in the literature (except, after the publication of our method, by Swisdak 2013).

3.2 Properties of the Maxwell-Jüttner distribution

This section discusses properties of the Maxwell-Jüttner particle distribution. We briefly review the non-relativistic case in Sect. 3.2.1, and then turn to the relativistic generalization (Maxwell-Jüttner) in Sect. 3.2.2. We compute the average of various quantities for this distribution, either when the bulk velocity is zero (Sect. 3.2.3) or non-zero (Sect. 3.2.4).

3.2.1 The non-relativistic case

For a gas of non-relativistic classical particles at thermal equilibrium, the distribution function is given by the Maxwell-Boltzmann statistics. In three dimensions[a], it is defined by

$$\boxed{g(\boldsymbol{v}) = \left(\frac{m}{2\pi T}\right)^{3/2} \exp\left(-\frac{1}{2}\frac{m\boldsymbol{v}^2}{T}\right).} \tag{3.1}$$

Here, m is the particle mass, T the temperature (in energy units), and the distribution g is normalized to unity. Equation 3.1 holds for a gas with no bulk velocity, i.e., in the gas comoving frame. It can be shown to be the distribution that maximizes the entropy, so that this is the state that will eventually be reached in a gas or plasma where some dissipative processes exist. These processes can be collisions (hard sphere with neutrals, Coulombic with charges), or particle-particle correlations mediated by the fields. The Maxwell-Boltzmann distribution can be shown to be the only stationary distribution of various kinetic equations, for example Boltzmann equation for a neutral gas, or Landau equation for collisionless plasmas.

[a] For N dimensions, replace the 3/2 exponent by $N/2$.

We denote an average of a quantity $M(\boldsymbol{v})$ taken over the distribution 3.1 by $\langle M \rangle$, or occasionally by $\bar{M}$. We have the following identities:

$$\langle \boldsymbol{v} \rangle = 0 \tag{3.2a}$$

$$\langle v_i^2 \rangle^{1/2} = \sqrt{T/m}, \qquad i = x,\ y,\ z, \tag{3.2b}$$

$$\langle \boldsymbol{v}^2 \rangle^{1/2} = \left(\langle v_x^2 \rangle + \langle v_y^2 \rangle + \langle v_z^2 \rangle \right)^{1/2} = \sqrt{3T/m}, \tag{3.2c}$$

$$\frac{\mathrm{d}}{\mathrm{d}v} v^2 \exp\left(-\frac{1}{2} \frac{m\boldsymbol{v}^2}{T} \right) = 0 \Leftrightarrow v = \sqrt{\frac{2T}{m}}. \tag{3.2d}$$

Several relevant velocities can thus be defined (see, e.g., Callen 2006, App. A): the most probable speed (in 3D) $v_{\text{most prob}} = \sqrt{2T/m}$, the root mean square velocity $v_{\text{rms}} = \langle \boldsymbol{v}^2 \rangle^{1/2} = \sqrt{3} \langle v_x^2 \rangle^{1/2} = \sqrt{3T/m}$, or what we will denote the thermal velocity $v_{\text{th}} = \langle v_x^2 \rangle^{1/2} = \sqrt{T/m}$. The mean energy per particle is

$$\frac{m\langle \boldsymbol{v}^2 \rangle}{2} = \frac{m v_{\text{rms}}^2}{2} = 3 \times \frac{T}{2}, \tag{3.3}$$

i.e., $T/2$ by degree of freedom, while the pressure P is given by[b]

$$P = n \iiint \mathrm{d}^3 v\, g(\boldsymbol{v}) (m v_i^2) = n \frac{v_{\text{rms}}^2}{3} = nT, \tag{3.5}$$

with n the particle number density, and $i = x,\ y$ or z. We thus find the perfect gas law.

3.2.2 The relativistic generalization

The temperature becomes relativistic when a significant fraction of the particles reach a velocity close to the speed of light c. This happens when the mean energy per particle becomes close to or passes above the restmass energy of the particles, and occurs roughly when $\Theta \equiv \mu^{-1} \equiv T/(mc^2) > 1$.

A Maxwell-Boltzmann distribution is then not valid, because it would predict particles exceeding the speed of light. In the literature, there are some agreements around the fact that the particle distribution of a relativistic plasma in thermodynamic equilibrium is given by the Maxwell-Jüttner distribution (Jüttner 1911; Cubero et al. 2007; Chacón-Acosta et al. 2010; Dunkel and Hänggi 2009) and, even if some alternatives are also debated (e.g., Treumann et al. 2011, argue that another normalization factor should be used), this is the distribution used in PIC simulations (e.g., Pétri and Lyubarsky 2007; Zenitani and Hoshino 2008; Jaroschek and Hoshino 2009) or other analytical studies (e.g., Kirk and Skjæraasen 2003).

In the plasma rest frame

In the plasma rest frame (subscript 0), the Maxwell-Jüttner distribution is given by $f_{0|\tilde{\boldsymbol{p}}}(\boldsymbol{x}_0, \tilde{\boldsymbol{p}}_0) = n_0 g_{0|\tilde{\boldsymbol{p}}}(\tilde{\boldsymbol{p}}_0)$, with

$$\boxed{g_{0|\tilde{\boldsymbol{p}}}(\tilde{\boldsymbol{p}}_0) = \frac{\mu}{4\pi K_2(\mu)} \exp\left\{ -\mu \sqrt{1 + \tilde{\boldsymbol{p}}_0^2} \right\}, \quad \tilde{\boldsymbol{p}}_0 \in \mathbb{R}^3,} \tag{3.6}$$

[b] The definition of the pressure comes from a derivation of the fluid equations from a kinetic description (see Sect. 3.4), the pressure tensor P_{ij} being the flux along the direction i of j-directed momentum due to microscopic motions:

$$P_{ij} = \int \mathrm{d}^3 v\, \delta v_i (m \delta v_j) [n(\boldsymbol{x}) g(\boldsymbol{v})] = mn \int \mathrm{d}^3 v\, \delta v_i \delta v_j g(\boldsymbol{v}), \tag{3.4}$$

with $\delta v_i = v_i - \overline{v}_i$. Because $g(\boldsymbol{v})$ is isotropic, we have $P_{i \neq j} = 0$ and $P_{xx} = P_{yy} = P_{zz} \equiv P$.

with $n_0 = \iiint \mathrm{d}^3\tilde{\boldsymbol{p}}_0\, f_{0|\tilde{\boldsymbol{p}}}(\boldsymbol{x}_0, \tilde{\boldsymbol{p}}_0)$ the uniform particle number density and $g_{0|\tilde{\boldsymbol{p}}}$ the momentum distribution, both in the rest frame, $\tilde{\boldsymbol{p}}_0 = \gamma_0 \boldsymbol{v}_0/c$, $\tilde{\boldsymbol{p}} = \gamma \boldsymbol{v}/c$, K_2 the modified Bessel function of the second kind, and $\mu^{-1} \equiv \Theta \equiv T/(mc^2)$ the normalized temperature (which is always defined in the rest frame of the plasma, by Eq. 3.6).

The distribution for the norm of $\tilde{\boldsymbol{p}}_0$ is $g_{0|\tilde{p}}(\tilde{p}_0) = 4\pi \tilde{p}_0^2 g_{0|\tilde{\boldsymbol{p}}}(\tilde{\boldsymbol{p}}_0)$. Change of variables can also lead to the expression of the distribution in terms of velocities or of Lorentz factors. We provide these formula, along with their derivations, in Appendix 3.A.

Drifting distributions

We want the equilibrium distribution, now called f, for a plasma moving with a bulk velocity $\boldsymbol{U}_0$ (with associated Lorentz factor $\Gamma_0 = (1 - U_0)^{-1/2}$). An easy way to obtain this distribution is to set up a Maxwell-Jüttner plasma at rest in a frame $\mathcal{R}_0$, with distribution $f_0 = n_0 g_0$ given by Eq. 3.6, and then to see it from a frame $\mathcal{R}$ moving with velocity $-\boldsymbol{U}_0$. The drifting distribution f is then obtained by a Lorentz transformation of the distribution f_0.

To do this, we use the invariance of the total (in position and in velocity) distribution function $f(\boldsymbol{x}, \tilde{\boldsymbol{p}})$, i.e., $f_{\boldsymbol{x},\tilde{\boldsymbol{p}}}(\boldsymbol{x}, \tilde{\boldsymbol{p}}) = f_{0|\boldsymbol{x},\tilde{\boldsymbol{p}}}(\boldsymbol{x}_0, \tilde{\boldsymbol{p}}_0)$. We prove this relation in Sect. 3.8.1. Next, we assume that f and g are linked by

$$f_{\boldsymbol{x},\tilde{\boldsymbol{p}}}(\boldsymbol{x}, \tilde{\boldsymbol{p}}) = n(\boldsymbol{x}) g_{\tilde{\boldsymbol{p}}}(\tilde{\boldsymbol{p}}) \quad \text{and} \quad f_{0|\boldsymbol{x},\tilde{\boldsymbol{p}}}(\boldsymbol{x}_0, \tilde{\boldsymbol{p}}_0) = n_0(\boldsymbol{x}_0) g_{0|\tilde{\boldsymbol{p}}}(\tilde{\boldsymbol{p}}_0), \tag{3.7}$$

where n and n_0 are the particle number densities in each frame. We note that the usual contraction/dilatation of volumes directly yields $n(\boldsymbol{x}) = \Gamma_0 n_0(\boldsymbol{x}_0)$.

Using Eq. 3.6 for $g_{0|\tilde{\boldsymbol{p}}}(\tilde{\boldsymbol{p}}_0)$, and the relation $\gamma_0 = \Gamma_0(\gamma - \tilde{\boldsymbol{p}} \cdot \boldsymbol{U}_0/c)$ (which is simply the Lorentz boost linking γ_0 in $\mathcal{R}_0$ to γ and $\tilde{\boldsymbol{p}}$ in $\mathcal{R}$), we obtain:

$$\boxed{\begin{aligned} g_{\tilde{\boldsymbol{p}}}(\tilde{\boldsymbol{p}}) &= \frac{\mu}{4\pi K_2(\mu)\Gamma_0} \exp\left\{-\mu\Gamma_0\left(\sqrt{1+\tilde{p}^2} - \tilde{\boldsymbol{p}} \cdot \boldsymbol{U}_0/c\right)\right\}, \\ f_{\boldsymbol{x},\tilde{\boldsymbol{p}}}(\boldsymbol{x}, \tilde{\boldsymbol{p}}) &= n(\boldsymbol{x}) g_{\tilde{\boldsymbol{p}}}(\tilde{\boldsymbol{p}}). \end{aligned}} \tag{3.8}$$

This distribution is normalized to unity: $\iiint \mathrm{d}^3\tilde{\boldsymbol{p}}\, g_{\tilde{\boldsymbol{p}}}(\tilde{\boldsymbol{p}}) = 1$, so that also $\iiint \mathrm{d}^3\tilde{\boldsymbol{p}}\, f_{\boldsymbol{x},\tilde{\boldsymbol{p}}}(\boldsymbol{x}, \tilde{\boldsymbol{p}}) = n$. We note that the factor Γ_0 appears because $g_{\tilde{\boldsymbol{p}}}(\tilde{\boldsymbol{p}}) = g_{0|\tilde{\boldsymbol{p}}}(\tilde{\boldsymbol{p}}_0) \times n_0(\boldsymbol{x}_0)/n(\boldsymbol{x}) = g_{0|\tilde{\boldsymbol{p}}}(\tilde{\boldsymbol{p}}_0)/\Gamma_0$, and is not present in some articles where the distribution function f is normalized to n_0 (and not to n as here).

3.2.3 Averages over Maxwell-Jüttner distribution, comoving frame

We provide the analytical expressions of various quantities averaged over the Maxwell-Jüttner distribution, for example the mean velocity, mean Lorentz factor, mean momentum, or the enthalpy. They are summarized in Table 3.1, and a plot of the function κ_{32} is shown in Fig. 3.1. This section concerns plasmas at rest, and Sect. 3.2.4 deals with drifting Maxwell-Jüttner distributions. We present the method used to derive these expressions, and comment some important points. We note that besides being of general interest, these expressions served to further validate our method for loading Maxwell-Jüttner distributions in PIC simulations (Sect. 3.8), by comparing

Without drift velocity: $U_0 = 0$			
Parameter	Value	NR	UR
$\langle\gamma\rangle$	$\kappa_{32}(\mu) - \mu^{-1}$	$1 + 3\Theta/2$	3Θ
$\langle(\gamma\beta)^2\rangle$	$3\Theta\kappa_{32}(\mu)$	3Θ	$12\Theta^2$
$\langle\beta^2\rangle$	$3\Theta\kappa_{12}(\mu)$	3Θ	$3/2$
$\langle\gamma\beta^2\rangle$	3Θ		
Larmor radius	$(c/\omega_{\rm ce})\sqrt{2\Theta\kappa_{32}(\mu)}$	$(c/\omega_{\rm ce})\sqrt{2\Theta}$	$(c/\omega_{\rm ce})2\sqrt{2}\Theta$
Pressure P	nT		
Enthalpy h_0	$\kappa_{32}(\mu)$	$1 + 5\Theta/2$	4Θ
Adiabatic exponent $\hat{\gamma}$	$1 + (\mu\kappa_{32}(\mu) - \mu - 1)^{-1}$	$5/3$	$4/3$

With a drift velocity $\boldsymbol{U}_0 = U_0\hat{\boldsymbol{y}}$			
Parameter	Value	NR	UR
$\langle\boldsymbol{v}\rangle$	$\boldsymbol{U}_0$		
$\langle\gamma\boldsymbol{v}\rangle$	$\kappa_{32}(\mu)\Gamma_0\boldsymbol{U}_0$ [a]	$\Gamma_0\boldsymbol{U}_0$	$4\Theta\Gamma_0\boldsymbol{U}_0$
$\langle\gamma\rangle$	$\Gamma_0\kappa_{32}(\mu) - \frac{1}{\mu\Gamma_0}$	Γ_0	$\frac{4\Gamma_0}{\mu} - \frac{1}{\mu\Gamma_0}$
$\langle p_x v_x\rangle = \langle p_z v_z\rangle$	$\Theta c^2/\Gamma_0$		
$\langle p_y v_y\rangle$	$\frac{\Theta c^2}{\Gamma_0} + \Gamma_0 U_0^2\kappa_{32}(\mu)$		
$\big\langle(p_i - \langle p_i\rangle)(v_j - \langle v_j\rangle)\big\rangle$	$\delta_{ij}c^2\,\Theta/\Gamma_0$		

[a] Remains true for an isotropic comoving distribution function, not necessarily Maxwell-Jüttner, with κ_{32} replaced by the enthalpy h_0.

Table 3.1: Useful averages for the Maxwell-Jüttner distribution $f(\boldsymbol{x},\boldsymbol{p}) = ng(\boldsymbol{p})$ (for example defined by Eq. 3.8 in terms of $\tilde{\boldsymbol{p}}$), of temperature $\Theta = 1/\mu = T/(mc^2)$. We define $\kappa_{ij}(\mu) = K_i(\mu)/K_j(\mu)$, with K_n the modified Bessel function of the nth kind (see Fig. 3.1 for a plot of κ_{32}).
The Larmor radius is defined by $\langle r_{\rm ce}\rangle = \langle(\gamma v_\perp)^2\rangle^{1/2}/\omega_{\rm ce}$, $\omega_{\rm ce} = qB/m$,
the pressure by $P = (1/3)n\langle\boldsymbol{v}\cdot(\gamma m\boldsymbol{v})\rangle$,
the enthalpy by $h_0 = (n\langle\gamma mc^2\rangle + P)/(nmc^2)$ (Sect. 3.3),
the adiabatic exponent by $\hat{\gamma} - 1 = P/(n\langle\gamma - 1\rangle mc^2)$ (Sect. 3.3).
NR means non-relativistic limit ($\Theta \to 0$, $\kappa_{32}(\mu) \sim 1 + 5\Theta/2$), and UR ultrarelativistic limit ($\Theta \to +\infty$, $\kappa_{32}(\mu) \sim 4\Theta$), with in both cases no constraints on Γ_0.
Asymptotic relations for the Bessel functions are given in Appendix 3.A.
Other averages can be found in Table. 3.2. The UR and NR limits for the adiabatic exponent are generalized to N dimensions in Sect. 3.3.2.

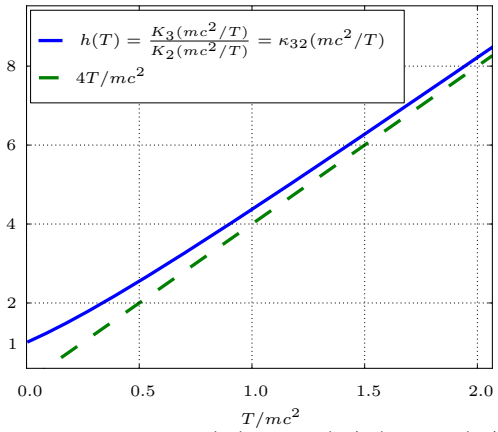

Figure 3.1: Plot of the function $h_0(\Theta) = \kappa_{32}(1/\Theta) = K_3(1/\Theta)/K_2(1/\Theta)$ against Θ. This is the normalized comoving enthalpy for a Maxwell-Jüttner distribution of temperature Θ. We see that the ultrarelativistic approximation $h_0 \simeq 4\Theta$ is reasonable even starting from $\Theta = 1$.

the analytical results of Table 3.1 with averages performed over particles generated with our method.

We start by the calculation of averages over the distribution with zero drift velocity (i.e., the distribution in the frame comoving with the plasma). The calculations are easier when the distribution function is expressed in terms of Lorentz factors γ_0 (see Appendix 3.A):

$$g_{0|\gamma}(\gamma_0) = \frac{\mu}{K_2(\mu)}\,\gamma_0\sqrt{\gamma_0^2-1}\,\exp\{-\mu\gamma_0\}\,, \quad \gamma_0 \in [1,+\infty[. \tag{3.9}$$

We introduce two relations[c]:

$$I(\mu) \equiv \int_1^{+\infty} \mathrm{d}\gamma_0\sqrt{\gamma_0^2-1}\,\exp\{-\mu\gamma_0\} = \mu^{-1}K_1(\mu), \tag{3.11}$$

and (*NIST Digital Library of Mathematical Functions* 2013, Eq. 10.29.4):

$$\frac{\mathrm{d}}{\mathrm{d}\mu}\left[\mu^{-\nu}K_\nu(\mu)\right] = -\mu^{-\nu}K_{\nu+1}(\mu), \tag{3.12}$$

where K_n is the modified Bessel function of the nth kind.

The method is then to derive Eq. 3.11 as many times as needed with respect to μ, with the help of Eq. 3.12. We give details for the integral of $g_{0|\gamma}$, and then give the results for other averages with some comments.

Normalization of g_0

We deduce the integral of $g_{0|\gamma}$ from $\mathrm{d}I/\mathrm{d}\mu$:

$$\frac{\mathrm{d}I}{\mathrm{d}\mu} = -\int_1^{+\infty}\mathrm{d}\gamma\sqrt{\gamma^2-1}\,\gamma\exp\{-\mu\gamma\}\,, \tag{3.13}$$

[c]To evaluate the right-hand side of Eq. 3.11, we use (*NIST Digital Library of Mathematical Functions* 2013, Eq. 10.32.8):

$$K_\nu(z) = \frac{\sqrt{\pi}}{\Gamma(\nu+1/2)}(z/2)^\nu\int_1^{+\infty}\mathrm{d}\gamma(\gamma^2-1)^{\nu-1/2}\exp\{-z\gamma\}\,, \tag{3.10}$$

with for Euler's gamma function: $\Gamma(1/2+1) = \sqrt{\pi}/2$.

and on the other hand:

$$\frac{\mathrm{d}I}{\mathrm{d}\mu} = \frac{\mathrm{d}}{\mathrm{d}\mu}[\mu^{-1}K_1(\mu)] = -\mu^{-1}K_2(\mu). \tag{3.14}$$

From this, we deduce that $g_{0|\gamma}$ is indeed normalized to unity:

$$\int_1^{+\infty} \mathrm{d}\gamma\, g_{0|\gamma}(\gamma) = \frac{\mu}{K_2(\mu)} \int_1^{+\infty} \mathrm{d}\gamma \sqrt{\gamma^2-1}\,\gamma \exp\{-\mu\gamma\} = 1. \tag{3.15}$$

This also proves the normalization to unity of $g_{0|\tilde{\boldsymbol{p}}}$, $g_{0|v/c}$, and $g_{0|\boldsymbol{p}}$.

Mean squared momentum

$$\langle \tilde{\boldsymbol{p}}^2 \rangle = \langle (\gamma\beta)^2 \rangle = \int_1^{+\infty} \mathrm{d}\gamma\, \gamma^2(\beta_x^2+\beta_y^2+\beta_z^2) g_{0|\gamma}(\gamma) = 3\mu^{-1}\kappa_{32}(\mu). \tag{3.16}$$

The non-relativistic limit, for $\mu \to +\infty$, is $\langle (\gamma\beta)^2 \rangle \to 3/\mu = 3T/(mc^2)$, and is coherent with the non-relativistic calculation with a Maxwell-Boltzmann distribution, that gives $\langle \boldsymbol{v}^2 \rangle = 3T/m$.

We note that the mean square momentum is not where the function $4\pi\tilde{p}^2 g_{0|\tilde{p}}(\tilde{p})$ reaches its maximum (it occurs for $\tilde{p} = (2+\sqrt{4+\mu^2})/\mu^2$).

Thermal Larmor radius

The thermal Larmor radius is, independently of the distribution function:

$$\langle r_{\mathrm{ce}} \rangle = \omega_{\mathrm{ce}}^{-1} \langle (\gamma v_\perp)^2 \rangle^{1/2}, \tag{3.17}$$

with $\omega_{\mathrm{ce}} = qB/m$ the non-relativistic cyclotron period, and $\perp$ denoting the component perpendicular to the local magnetic field. For the Maxwell-Jüttner distribution with no drift velocities, we have (from Eq. 3.16) $\langle \boldsymbol{p}_\perp^2 \rangle = \langle p_x^2 \rangle + \langle p_y^2 \rangle = 2c^2\mu^{-1}\kappa_{32}(\mu)$, so that the thermal Larmor radius is

$$\langle r_{\mathrm{ce}} \rangle = c\omega_{\mathrm{ce}}^{-1} \sqrt{2\Theta\kappa_{32}(\mu)}. \tag{3.18}$$

Mean squared velocity

$$\left\langle \frac{\boldsymbol{v}^2}{c^2} \right\rangle = \langle \beta^2 \rangle = \int_1^{+\infty} \mathrm{d}\gamma\, (\beta_x^2+\beta_y^2+\beta_z^2) g_{0|\gamma}(\gamma) = 3\mu^{-1}\kappa_{12}(\mu). \tag{3.19}$$

The non-relativistic limit, for $\mu \to +\infty$, is $\langle \beta^2 \rangle \to 3/\mu = 3T/(mc^2)$. This is coherent with the non-relativistic calculation with a Maxwell-Boltzmann distribution, that gives $\langle \boldsymbol{v}^2 \rangle = 3T/m$.

The ultrarelativistic limit, for $\mu \to 0$, is $\langle \beta^2 \rangle \to 3 \times 1/2$. Since the velocity is bounded by c, we expected the mean square velocity to saturate to some finite value as $T \to \infty$. The exact calculation shows that this is $c^2/2$ per component.

Mean momentum flux (and the relativistic equation of state)

$$\langle \gamma\beta^2 \rangle = \int_1^{+\infty} \mathrm{d}\gamma\, \gamma(\beta_x^2+\beta_y^2+\beta_z^2) g_{0|\gamma}(\gamma) = \frac{3}{\mu} = 3\frac{T}{mc^2}. \tag{3.20}$$

This is a very important quantity, as it enters in the definition of the pressure (appearing in the fluid equations derived from the kinetic level, see Sect. 3.4). It shows that just as in the non-relativistic case, we have:

$$\boxed{P \equiv n\frac{1}{3}\langle \boldsymbol{v} \cdot (\gamma m \boldsymbol{v}) \rangle = nmc^2\langle \gamma\beta^2 \rangle/3 = nT.} \tag{3.21}$$

3.2.4 Averages over Maxwell-Jüttner distribution, drifting distribution

We now consider the distribution with a drift velocity $U_0/c\,\hat{\boldsymbol{y}} = \beta_0\hat{\boldsymbol{y}}$. Suppose that we want the average of a quantity $M(\tilde{\boldsymbol{p}})$:

$$\langle M\rangle = \iiint_{\mathbb{R}^3} \mathrm{d}^3\tilde{\boldsymbol{p}}\, g_{\tilde{\boldsymbol{p}}}(\tilde{\boldsymbol{p}}) M(\tilde{\boldsymbol{p}}), \tag{3.22}$$

with $g_{\tilde{\boldsymbol{p}}}$ given by Eq. 3.8. We use the change of variables

$$\begin{aligned} \tilde{p}_{0x} &= \tilde{p}_x, \\ \tilde{p}_{0y} &= \Gamma_0(\tilde{p}_y - \beta_0\sqrt{1+\tilde{p}^2}), \\ \tilde{p}_{0z} &= \tilde{p}_z, \end{aligned} \tag{3.23}$$

which amounts to pass back into the comoving frame. It involves $\sqrt{1+\tilde{p}_0^2} = \gamma_0 = \Gamma_0(\sqrt{1+\tilde{p}^2} - \beta_0\tilde{p}_y)$. The elements of integration $\mathrm{d}^3\tilde{\boldsymbol{p}}$ and $\mathrm{d}^3\tilde{\boldsymbol{p}}_0$ are linked by the Jacobian of the transformation, and it can be shown (see e.g., Mihalas and Mihalas 1984; Pomraning 1973) that $\mathrm{d}^3\tilde{\boldsymbol{p}}/\gamma = \mathrm{d}^3\tilde{\boldsymbol{p}}_0/\gamma_0$. We show in Sect. 3.8.1 that the distribution function $f(\boldsymbol{x},\boldsymbol{p})$ is a Lorentz invariant, so that $f_{0|\tilde{\boldsymbol{p}}}(\boldsymbol{x}_0,\tilde{\boldsymbol{p}}_0) = f_{\tilde{\boldsymbol{p}}}(\boldsymbol{x},\tilde{\boldsymbol{p}})$, and, given the definitions of Eq. 3.7 ($f = ng$ and $f_0 = n_0 g_0$) and the relation $n = \Gamma_0 n_0$, it implies $g_{0|\tilde{\boldsymbol{p}}}(\tilde{\boldsymbol{p}}_0) = \Gamma_0 g_{\tilde{\boldsymbol{p}}}(\tilde{\boldsymbol{p}})$. Consequently, we arrive at

$$\langle M\rangle = \Gamma_0^{-1}\iiint_{\mathbb{R}^3}\frac{\mathrm{d}^3\tilde{\boldsymbol{p}}_0}{\gamma_0}\, g_{0|\tilde{\boldsymbol{p}}}(\tilde{\boldsymbol{p}}_0)\gamma M(\tilde{\boldsymbol{p}}) = \Gamma_0^{-1}\left\langle\frac{\gamma M(\tilde{\boldsymbol{p}})}{\gamma_0}\right\rangle_0, \tag{3.24}$$

where $\langle\cdot\rangle_0$ means that the average is taken with $g_{0|\tilde{\boldsymbol{p}}}$ (Eq. 3.6), and where γ and $\tilde{\boldsymbol{p}}$ are to be expressed with comoving quantities (subscript 0). With this last formula, one is left with averages in the comoving frame and can use the previous method.

Several averages are given in Table 3.1, and we comment some of them here.

Normalization of the relativistic drifting distribution

In Sect. 3.2.2, we derived the expression of $f_{\tilde{\boldsymbol{p}}}$ using a change of frames, starting from $f_{0|\tilde{\boldsymbol{p}}}$ in the comoving frame. In Eq. 3.7, we decided that n and n_0 are the spatial number densities in each frames, linked by $n/n_0 = \Gamma_0$. The normalization of $g_{0|\tilde{\boldsymbol{p}}}$ to unity, previously demonstrated, thus implies the normalization of $g_{\tilde{\boldsymbol{p}}}$:

$$\begin{aligned} &\iiint_{\mathbb{R}^3}\mathrm{d}^3\tilde{\boldsymbol{p}}\, g_{\tilde{\boldsymbol{p}}}(\tilde{\boldsymbol{p}}) \\ &= \iiint_{\mathbb{R}^3}\mathrm{d}^3\tilde{\boldsymbol{p}}\,\frac{\mu}{4\pi K_2(\mu)\Gamma_0}\exp\left\{-\mu\Gamma_0\left(\sqrt{1+\tilde{p}^2} - \beta_0\tilde{p}_y\right)\right\} = 1. \end{aligned} \tag{3.25}$$

Mean momentum

$$\langle\boldsymbol{p}\rangle = \kappa_{32}(\mu)\Gamma_0 U_0\,\hat{\boldsymbol{y}}, \tag{3.26}$$

or, written otherwise:

$$\langle\gamma\boldsymbol{v}\rangle = \kappa_{32}(\mu)(1-\langle\boldsymbol{v}\rangle^2)^{-1/2}\langle\boldsymbol{v}\rangle. \tag{3.27}$$

It is instructive to detail the demonstration for this case. We use Eq. 3.24 for $M = p_y = \gamma v_y$: $\langle p_y \rangle = \Gamma_0^{-1} \langle \gamma p_y / \gamma_0 \rangle_0$. From the Lorentz transformation 3.23, we have $\gamma p_y = \Gamma_0^2 (p_{0y} + U_0 \gamma_0)(\gamma_0 + U_0 p_{0y}/c^2)$, and after some manipulations we obtain:

$$\langle \gamma \boldsymbol{v} \rangle = \Gamma_0 U_0 \left(\langle \gamma_0 \rangle_0 + \langle \gamma_0 v_{0y} v_{0y} / c^2 \rangle_0 \right) \hat{\boldsymbol{y}}. \tag{3.28}$$

But the second term is the definition of the pressure (Eq. 3.21), $P = (1/3) nm \langle \gamma_0 \boldsymbol{v}_0 \cdot \boldsymbol{v}_0 \rangle_0 = nm \langle \gamma_0 v_{0y} v_{0y} \rangle_0$ (*if the distribution* g_0 *is isotropic*), so that

$$\langle \gamma_0 \rangle_0 + \langle \gamma_0 v_{0y} v_{0y} / c^2 \rangle_0 = (\langle \gamma_0 mc^2 \rangle_0 + P)/(nmc^2) = h_0, \tag{3.29}$$

which is defined in Sect. 3.3 as the normalized comoving enthalpy.

All in all, when the distribution function in the comoving frame g_0 is isotropic, and independently of its expression (Maxwell-Jüttner or not), we have the interesting result

$$\boxed{\langle \gamma \boldsymbol{v} \rangle = h_0 \Gamma_0 \langle \boldsymbol{v} \rangle.} \tag{3.30}$$

Mean Lorentz factor

The derivation reads:

$$\begin{aligned}
\langle \gamma \rangle &= \Gamma_0^{-1} \langle \gamma^2 / \gamma_0 \rangle_0 && \text{(3.31a)} \\
&= \Gamma_0 \big\langle (\gamma_0 + \beta_0 \tilde{p}_{y0})(1 + \beta_0 v_{y0}/c) \big\rangle_0 && \text{(3.31b)} \\
&= \Gamma_0 \langle \gamma_0 \rangle_0 + \Gamma_0 \beta_0^2 \langle \tilde{p}_{y0} v_{y0} / c \rangle_0 && \text{(3.31c)} \\
&= \Gamma_0 \langle \gamma_0 \rangle_0 + \Gamma_0 \beta_0^2 \Theta && \text{(3.31d)} \\
&= \Gamma_0 h_0 - \frac{1}{\mu \Gamma_0} && \text{(3.31e)} \\
&= \Gamma_0 \kappa_{32}(\mu) - \frac{1}{\mu \Gamma_0}. && \text{(3.31f)}
\end{aligned}$$

The derivation is general up to Eq. 3.31c. Passing to Eq. 3.31d requires an isotropic temperature: $\langle \tilde{p}_{y0} v_{y0} / c \rangle_0 \equiv \Theta_{yy} = \Theta$, and passing to Eq. 3.31e requires the definition of the enthalpy (Eq. 3.43), $h_0 = \langle \gamma_0 \rangle_0 + P/(n_0 mc^2)$, with the law $P = n_0 T$. Equation 3.31f then uses the Maxwell-Jüttner relation $h_0 = \kappa_{32}(\mu)$.

We stress that $\langle \gamma \rangle \neq \Gamma_0$. The Lorentz factor Γ_0 appearing in relativistic hydrodynamics is thus not the mean Lorentz factor of the particles. The non-relativistic limit (in terms of temperature, $\Theta \to 0$), is $\langle \gamma \rangle \to \Gamma_0$.

Quadratic velocity spread

The velocity spread $\langle v_i^2 \rangle$ does not seem exprimable with Bessel functions.

We can instead compute $\langle \gamma (\boldsymbol{v} - \langle \boldsymbol{v} \rangle)^2 \rangle = \Theta (3c^2 - U_0^2)/\Gamma_0$, where the Bessel functions disappear.

Pressure tensor (fluctuating velocity times momentum)

$$\boxed{\big\langle (p_i - \bar{p}_i \rangle)(v_j - \bar{v}_j) \big\rangle = \delta_{ij} c^2 \frac{\Theta}{\Gamma_0},} \tag{3.32}$$

with δ_{ij} Kronecker's delta. This is a very important quantity, as it directly enters into the fluid equation of motion. We note that $\langle (p_i - \bar{p}_i)(v_j - \bar{v}_j)\rangle = \langle (p_i - \bar{p}_i) v_j\rangle$, so that it represents the flux of i-directed microscopic momentum along j.

In order to derive expression 3.32, we first note that

$$\langle p_i v_j\rangle = \langle p_i\rangle\langle v_j\rangle + \langle (p_i - \bar{p}_i))(v_j - \bar{v}_j)\rangle. \tag{3.33}$$

We first compute $\langle p_i v_j\rangle$. We use Eq. 3.24:

$$\langle p_i v_j\rangle = \Gamma_0^{-1}\langle \gamma p_i v_j/\gamma_0\rangle_0 = \Gamma_0^{-1}\langle p_i p_j/\gamma_0\rangle_0. \tag{3.34}$$

We then express p_i and p_j as a function of the comoving quantities: $p_i = p_{0i}$ for $i = x$ or z, and $p_y = \Gamma_0(p_{0y} + U_0\gamma_0)$ (with U_0 the bulk velocity of the plasma, and Γ_0 the associated Lorentz factor). We trivially have $\langle p_i v_j\rangle = \langle p_{0i} v_{0j}\rangle_0/\Gamma_0$ when $(i,j) = (x,x)$, (x,z), or (z,z). For $i = x$ or z, we also have $\langle p_i v_y\rangle = \langle p_{0i} v_{0y}\rangle_0/\Gamma_0$, because the excess term implies $\langle p_{0y}\rangle_0 = 0$. We remark that all the cross-terms vanish. Given the definition of the comoving pressure, $P \equiv n_0 m\langle p_{0i} v_{0i}\rangle_0$ for either $i = x$, y, or z (Eq. 3.21), we have that $\langle p_i v_j\rangle = \delta_{ij} P/(\Gamma_0 n_0 m)$ whenever $(i,j) \neq (y,y)$. The case $(i,j) = (y,y)$ yields:

$$\begin{aligned}\langle p_y v_y\rangle &= \Gamma_0^{-1}\left\langle \frac{\Gamma_0^2(p_{0y} + U_0\gamma_0)^2}{\gamma_0}\right\rangle_0 \\ &= \Gamma_0\left\langle \frac{p_{0y}^2}{\gamma_0}\right\rangle_0 + \Gamma_0\langle 2U_0 p_{0y}\rangle_0 + \Gamma_0 U_0^2\langle\gamma_0\rangle_0 \\ &= \Gamma_0\frac{P}{n_0 m} + 0 + \Gamma_0 U_0^2\left(h_0 - \frac{P}{n_0 m c^2}\right).\end{aligned} \tag{3.35}$$

In the last line we used the definition of the plasma comoving enthalpy (Eq. 3.43), i.e., $h_0 \equiv \langle\gamma\rangle_0 + P/(n_0 m c^2)$. We then arrive at:

$$\langle p_y v_y\rangle = \Gamma_0^{-1}\frac{P}{n_0 m} + \Gamma_0 U_0^2 h_0. \tag{3.36}$$

All in all, we have for any (i,j):

$$\boxed{\langle p_i v_j\rangle = \Gamma_0^{-1}\frac{\delta_{ij} P}{n_0 m} + \delta_{iy}\delta_{jy}\Gamma_0 U_0^2 h_0.} \tag{3.37}$$

The only assumption used to derive this result is that the comoving distribution function is isotropic[d]. If, in addition, we assume that the distribution is given by the Maxwell-Jüttner formula, we have:

$$\langle p_i v_j\rangle = \delta_{ij} c^2\frac{\Theta}{\Gamma_0} + \delta_{iy}\delta_{jy}\Gamma_0 U_0^2\kappa_{32}(\mu). \tag{3.38}$$

The derivation of Eq. 3.32 ends by identifying the second term in the right-hand of Eq. 3.38 as $\langle p_i\rangle\langle v_j\rangle$.

[d] It is particularly crucial when we define the comoving enthalpy. Also, terms such as $\delta_{ij} P$ could be replaced by the comoving pressure tensor $P_{ij} \equiv n_0 m\langle p_{0i} v_{0j}\rangle$ to slightly generalize the result.

3.2.5 Debye length

A plasma tends to screen any charge imbalance, and it does so perfectly in the absence of thermal fluctuations. But for a finite temperature, thermal motions forbid this perfect screening, and potentials of the order of T/e can leak out of the screening cloud over a finite distance $\sim \lambda_D$, resulting in a finite Debye length λ_D below which the plasma is not neutral (see Belmont et al. 2014, §4.1.3, for a non-conventional presentation). In a non-relativistic plasma, the Debye length is given by

$$\lambda_D = \left(\sum_s \lambda_{\mathrm{D}s}^{-2} \right)^{-1/2}, \tag{3.39}$$

where $\lambda_{\mathrm{D}s}$ is defined for species s:

$$\lambda_{\mathrm{D}s} = \frac{\sqrt{T_s/m_s}}{\omega_{\mathrm{p}s}} = \sqrt{\frac{\epsilon_0 T_s}{n_s q_s^2}}. \tag{3.40}$$

Debye screening can be derived by finding the linear modes of the two-fluid model, plus Poisson's equation for the electric field, with a polytropic closure $P/n^\Gamma = \text{const}$ (Bellan 2006). It then appears as a spatial damping of all modes of phase-speed $\omega/k \ll v_{\mathrm{th,e}}, v_{\mathrm{th,i}}$, where $v_{\mathrm{th},s}$ is the thermal speed.

We naturally expect this length to change for a relativistic plasma (i.e., for a relativistic temperature, in which case the plasma enthalpy h_0 becomes non-trivial). The two-fluid equations now use both the momentum and the velocity (Eqs. 3.71 and 3.72), that can be linked by the plasma enthalpy via Eq. 3.30, and linearizing this model appears more complex than in the non-relativistic case[e].

Instead, Laing and Diver (2013) follow a simpler and qualitative approach. Classically, the Debye length can be estimated in a 1D electrostatic model, by equating the mean kinetic energy of a particle, $T_s/2$ in one direction, to the potential energy created by a charge imbalance over a length l, $n_s q_s^2 l^2/(2\epsilon_0)$. When the kinetic energy dominates, the screening cannot occur, while when the potential energy dominates, charge imbalance does act on the particles and the screening is effective. The Debye length is thus the length l at which the two terms are equal. For a plasma with a relativistic temperature, the potential energy remains unchanged, while the mean kinetic energy is to be taken as one third of $\langle \gamma - 1 \rangle_s m_s c^2$. In the ultra-relativistic limit, this is given by $(1/3)\langle \gamma - 1 \rangle_s m_s c^2 = T_s$ (see Table 3.1). Consequently, there is only a factor 2 of difference with the non-relativistic case, and with this argument the ultrarelativistic Debye length can be estimated as

$$\lambda_{\mathrm{D}s}^{\mathrm{UR}} \sim \sqrt{\frac{\epsilon_0 2T_s}{n_s q_s^2}}. \tag{3.41}$$

This is $\sqrt{2}$ larger than the non-relativistic expression. We can thus reasonably assume that the expression for the Debye length is not much affected by a relativistic plasma temperature.

[e] The Langmuir oscillation and Langmuir waves can also be derived from this model, so that we expect them to change also. In particular, it is not clear whether the oscillation at the plasma pulsation will be modified, as it is a cold mode (in the sense that it is valid for phase speeds $\omega/k \gg v_{\mathrm{th,e}}, v_{\mathrm{th,i}}$). The Langmuir wave, however, has a group velocity given by the thermal velocity, which is inconsistently larger than c in the non-relativistic treatment.

3.3 Enthalpy

The enthalpy of a non-relativistic gas is dominated by the restmass contribution, and is thus equivalent to the mass density of the gas. It consequently never appears in the equations of conservation of momentum or energy. However, for relativistic temperatures the kinetic energy of the particles starts contributing significantly, and makes the enthalpy a central quantity for momentum and energy conservation relations. This section poses definitions and derives expressions in the Maxwell-Jüttner case for the internal energy, the adiabatic exponent, and the enthalpy. Just as in Sect. 3.2, we adopt a kinetic point of view.

3.3.1 Definition

We consider an ensemble of particles, uniform in space, with a zero bulk velocity (or equivalently, all quantities are expressed in the comoving frame). The individual particle masses are denoted by m, their number density by n_0, and the distribution function in momentum space by $g_{0|\boldsymbol{p}}(\boldsymbol{p})$ (normalized to unity).

The enthalpy of these particles is the particle energy (kinetic and rest-mass), plus the pressure:

$$w_0 = n_0 mc^2 + n_0 me_0 + P = n_0 \langle \gamma mc^2 \rangle_0 + P, \tag{3.42}$$

where P is the scalar pressure and e_0 the internal energy. Just as in Sect. 3.2, $\langle\cdot\rangle_0$ denotes an average taken over the distribution function $g_{0|\boldsymbol{p}}$, so that $\langle \gamma mc^2 \rangle_0$ is the mean energy per particle (including kinetic and restmass energies). The normalized enthalpy is

$$\boxed{h_0 = \frac{w_0}{n_0 mc^2} = \langle \gamma \rangle_0 + \frac{P}{n_0 mc^2}.} \tag{3.43}$$

For a Maxwell-Jüttner distribution at temperature $\Theta = 1/\mu$, we can use the expression for $\langle\gamma\rangle_0$ (Eq. 3.31f or Table 3.1), to find:

$$\boxed{h_0 = \frac{w_0}{n_0 mc^2} = \kappa_{32}(\mu).} \tag{3.44}$$

The function κ_{32} is plotted in Fig. 3.1. The non-relativistic limit is $h_0 = 1 + 5\Theta/2 + O(\Theta^2)$, while the ultrarelativistic limit is $h_0 = 4\Theta$.

3.3.2 Internal energy and adiabatic exponent

For a plasma of point-like particles, and neglecting the interactions between charges, the internal energy $\hat{e}_0$ is the kinetic energy of the particles. We have:

$$\begin{aligned} \hat{e}_0 \equiv n_0 me_0 &= n_0 \iiint_{\mathbb{R}^3} \mathrm{d}^3\boldsymbol{p}\, g_{0|\boldsymbol{p}}(\boldsymbol{p})(\gamma - 1)mc^2 \\ &= n_0 \langle \gamma mc^2 \rangle_0 - n_0 mc^2. \end{aligned} \tag{3.45}$$

The adiabatic exponent $\hat{\gamma}$ is defined by writing the pressure $P = (\hat{\gamma} - 1)\hat{e}_0$.

Non-relativistic case

In the non-relativistic case, the particle Lorentz factor is $\gamma - 1 \sim v^2/(2c^2)$, so that the expression 3.45 for the internal energy simplifies. In addition, we use Eq. 3.2c to evaluate $\langle v^2 \rangle$. We then have the well known relation

$$\hat{e}_0 = n_0 m \frac{1}{2} \langle v^2 \rangle = \frac{3}{2} n_0 T. \tag{3.46}$$

It follows that

$$P = n_0 T = \frac{2}{3} \hat{e}_0 = (\hat{\gamma} - 1)\hat{e}_0, \qquad \hat{\gamma} = \frac{5}{3}. \tag{3.47}$$

At N dimensions, we have $\hat{e}_0 = (N/2) n_0 T$, so that $P = (2/N)\hat{e}_0$, and

$$\hat{\gamma} = \frac{2}{N} + 1. \tag{3.48}$$

General case

In the general case, we use the expression for $\langle \gamma \rangle_0$ for a Maxwell-Jüttner distribution (Eq. 3.31f or Table 3.1) to find from the expression 3.45:

$$\hat{e}_0 = \left(\kappa_{32}(\mu) - 1 - \frac{1}{\mu} \right) n_0 m c^2. \tag{3.49}$$

In the non-relativistic limit ($T \ll mc^2$), with the asymptotic development of κ_{32} (Eq. 3.111), we indeed have $\hat{e}_0 = (3/2) n_0 T$.

To find the adiabatic exponent, we adjust $\hat{\gamma}$ so that $P = n_0 T$ and $P = (\hat{\gamma} - 1)\hat{e}_0$:

$$\hat{\gamma} = 1 + \frac{1}{\mu \kappa_{32}(\mu) - \mu - 1}. \tag{3.50}$$

We remark that this is not easily to generalize to N dimensions, because the computation of $\langle \gamma \rangle_0$ is here specific to Maxwell-Jüttner distribution, where all dimensions are coupled through the Lorentz factor. In particular, $\langle \gamma \rangle_0$ depends on the normalization of the distribution function, which may or may not be computable with Bessel functions for $N \neq 3$.

Ultrarelativistic limit

In the ultrarelativistic limit ($T \gg mc^2$), Eq. 3.49 and the asymptotic formula 3.112 lead to $\hat{e}_0 = 3T\, n_0 mc^2$, which gives

$$P = n_0 T = \frac{1}{3} \hat{e}_0 = (\hat{\gamma} - 1)\hat{e}_0, \qquad \hat{\gamma} = \frac{4}{3}. \tag{3.51}$$

This is a well known result, derived here on a kinetic basis.

It can be extended to N dimensions in the following way. For ultrarelativistic particles, $\gamma \simeq p/mc = \tilde{p}$. Consequently, $\langle \gamma \rangle_0 = \langle \tilde{p} \rangle_0$. Since $\hat{e}_0 = n_0 \langle \gamma mc^2 \rangle_0 - n_0 mc^2 \simeq n_0 \langle \gamma mc^2 \rangle_0$, we also have $\hat{e}_0 = n_0 mc^2 \langle \tilde{p} \rangle_0$.

On the other hand, the pressure is given by $P = n_0 \langle v_i \tilde{p}_i mc \rangle_0$, where i is any direction, so that it can actually be written $P = n_0 mc \langle (\boldsymbol{v} \cdot \boldsymbol{l})(\tilde{\boldsymbol{p}} \cdot \boldsymbol{l}) \rangle_0$ for any unit vector $\boldsymbol{l}$. We approximate $\boldsymbol{v} \simeq c\boldsymbol{n}$, with $\boldsymbol{n}$ a unit vector giving the particle's direction. Also, $\tilde{\boldsymbol{p}} = \tilde{p}\boldsymbol{n}$. Then, $P = n_0 mc^2 \langle \tilde{p} (\boldsymbol{n} \cdot \boldsymbol{l})^2 \rangle_0$. Since

$\tilde{p}$ depends only on the norm of $\tilde{\boldsymbol{p}}$, and $(\boldsymbol{n}\cdot\boldsymbol{l})^2$ only on its direction, the last expression can be factorized into $P = n_0 mc^2 \langle\tilde{p}\rangle_0 \langle(\boldsymbol{n}\cdot\boldsymbol{l})^2\rangle_{\Omega^N} / \langle 1\rangle_{\Omega^N}$, where

$$\alpha_N = \frac{\langle(\boldsymbol{n}\cdot\boldsymbol{l})^2\rangle_{\Omega^N}}{\langle 1\rangle_{\Omega^N}} = \frac{\int_{\Omega^N} \mathrm{d}\Omega\, (\boldsymbol{n}\cdot\boldsymbol{l})^2}{\int_{\Omega^N} \mathrm{d}\Omega} \tag{3.52}$$

an average over all solid angles in N dimensions. For $N = 3$, we have $\alpha_N = 1/3$, and for $N = 2$ we have $\alpha_N = 1/2$. We thus have $P = \alpha_N \hat{e}_0$.

Finally, writing $P = (\hat{\gamma} - 1)\hat{e}_0$ leads to

$$P = \alpha_N \hat{e}_0, \qquad \hat{\gamma} = \alpha_N + 1. \tag{3.53}$$

At 3D we find again $\hat{\gamma} = 4/3$, while at 2D $\hat{\gamma} = 3/2$.

3.3.3 Laplace's law for a relativistic gas and the sound speed

In this section, we make comments about the relation between the polytropic index and the adiabatic index, and we show that there is no simple Laplace's law[f] for a relativistic gas or plasma, because its adiabatic exponent then depends on the temperature. We conclude by the impossibility to obtain a simple expression for the sound speed in a relativistic gas.

A gas is polytropic if for any evolution between states 1 and 2, its temperature T and number density n verify $T_2/T_1 = (n_2/n_1)^{\Gamma-1}$, where Γ is a free parameter called the polytropic index[g]. This is an assumption, that can hold or not depending on the nature of the gas and on the transformation that it undergoes. The value of Γ depends on where energy is deposited during the transformation (e.g., Lamers and Cassinelli 1999, p. 102). If no energy is deposited into the internal energy of the gas (an adiabatic transformation), then $\Gamma = \hat{\gamma} = c_p/c_v$ coincides with the ratio of specific heats (the adiabatic exponent $\hat{\gamma}$) that we computed in Sect. 3.3.2. In the limit of an isothermal transformation, $T = \text{const}$ and thus $\Gamma = 1$. In an isothermal expansion, energy must be supplied to the gas to maintain its temperature constant.

However, we point out that a perfect gas undergoing an adiabatic transformation follows Laplace's law $PV^{\hat{\gamma}} = \text{const}$ only if it is a non-relativistic gas ($\hat{\gamma} = 5/3$) or an ultrarelativistic gas ($\hat{\gamma} = 4/3$), but not in intermediary cases. This can be seen by writing the demonstration. The gas is assumed to be in a volume V, and to consist of N particles. Its internal energy is $U = V\hat{e}_0$. For an adiabatic transformation involving a change of internal energy $\mathrm{d}U$, and a work done on the gas $\delta W = -P\mathrm{d}V$, the heat transfer to the gas is $\delta Q = 0$, so that we have:

$$\mathrm{d}U - \delta W = \delta Q = 0. \tag{3.54}$$

Because $P = n_0 T = (\hat{\gamma} - 1)\hat{e}_0$, we have $\hat{e}_0 = n_0 T/(\hat{\gamma} - 1) = \alpha n_0 T$, with $\alpha \equiv 1/(\hat{\gamma} - 1)$. We also have $U = V\hat{e}_0 = \alpha n_0 VT = \alpha NT$. The ideal gas law reads $PV = NT$. With this we easily arrive at

$$\left[\alpha + \alpha'(T)T\right] V\mathrm{d}P = -\left[1 + \alpha + \alpha'(T)T\right] P\mathrm{d}V, \tag{3.55}$$

with $\alpha'(T) = \mathrm{d}\alpha/\mathrm{d}T$. If $\alpha = \text{const}$, then it integrates into the Laplace's law:

$$PV^{1+1/\alpha} = \text{const}, \tag{3.56}$$

[f] The $PV^{\hat{\gamma}} = \text{const}$ law.

[g] Or equivalently, $PV^{\Gamma} = \text{const}$ for a perfect gas, or $P/\rho^{\Gamma} = \text{const}$.

which also reads $PV^{\hat{\gamma}} = \text{const}$ because $\hat{\gamma} = 1 + 1/\alpha$.

But the constant nature of α holds only in the non-relativistic limit ($\alpha = 3/2$, Eq. 3.46), and in the ultrarelativistic limit ($\alpha = 3$, Eq. 3.51). Equation 3.49 shows that $\alpha = \alpha(T)$ in the general case. The derivation of the $PV^{\hat{\gamma}} = \text{const}$ law then stops at Eq. 3.55, and leads to nothing obvious.

A consequence is that there is no simple expression for the sound speed of a relativistic gas. Indeed, the sound speed derived from linearized fluid equations is (Gedalin 1993)

$$c_s^2 = \frac{P}{\rho h_0} \frac{\partial \log P}{\partial \log \rho}, \tag{3.57}$$

and it has a simple expression only if the Laplace relation $P/\rho^{\hat{\gamma}}$ holds. When this is the case, we obtain

$$c_s^2 = \frac{\hat{\gamma} P}{\rho h_0}, \tag{3.58}$$

which gives for the non-relativistic case ($\hat{\gamma} = 5/3$, $h_0 = 1$):

$$c_s^2 = \frac{5}{3} \frac{T}{m}, \tag{3.59}$$

and for a ultrarelativistic gas ($\hat{\gamma} = 4/3$, $h_0 = 4T/mc^2$, Eq. 3.51 and Table 3.1):

$$c_s^2 = \frac{c^2}{3}. \tag{3.60}$$

3.4 From the Vlasov to the fluid picture

Fluid equations employed in numerical codes are usually expressed in terms of comoving quantities (i.e., defined in the rest frame of the plasma), such as, for species s, the comoving particle number density n_{0s}, the comoving enthalpy h_{0s}, the comoving pressure P_{0s}, and in terms of the fluid velocity $\bar{\boldsymbol{v}}_s$ and its associated Lorentz factor $\Gamma_s = (1 - \bar{\boldsymbol{v}}_s^2/c^2)^{-1/2}$. The conservation of particle number and of momentum for each species, and of total energy, then read (see e.g., Mihalas and Mihalas 1984; Barkov et al. 2014)[h]:

$$\frac{\partial}{\partial t}(\Gamma_s n_{0s}) + \frac{\partial}{\partial \boldsymbol{x}} \cdot (\Gamma_s n_{0s} \bar{\boldsymbol{v}}_s) = 0, \tag{3.62a}$$

$$\begin{aligned} &\frac{\partial}{\partial t}(\Gamma_s^2 n_{0s} h_{0s} \bar{\boldsymbol{v}}_s) + \frac{\partial}{\partial \boldsymbol{x}} \cdot (n_{0s} h_{0s} \Gamma_s \bar{\boldsymbol{v}}_s \Gamma_s \bar{\boldsymbol{v}}_s) \\ &\qquad = -\frac{1}{m_s} \frac{\partial P_{0s}}{\partial \boldsymbol{x}} + \frac{q_s}{m_s} \Gamma_s n_{0s} (\boldsymbol{E} + \bar{\boldsymbol{v}}_s \wedge \boldsymbol{B}), \end{aligned} \tag{3.62b}$$

$$\begin{aligned} &\frac{\partial}{\partial t} \left\{ \sum_s (\Gamma_s^2 n_{0s} h_{0s} m_s c^2 - P_{0s}) + \frac{E^2}{2\mu_0 c^2} + \frac{B^2}{2\mu_0} \right\} \\ &\quad + \frac{\partial}{\partial \boldsymbol{x}} \cdot \left\{ \sum_s (\Gamma_s^2 n_{0s} h_{0s} m_s c^2 \bar{\boldsymbol{v}}_s) + \frac{\boldsymbol{E} \wedge \boldsymbol{B}}{\mu_0} \right\} = 0. \end{aligned} \tag{3.62c}$$

These equations are, however, not well suited for the analysis of particle simulations. First, because accessible quantities are those defined in the

[h] With the help of Eq. 3.62a, Eq. 3.62b can also be written:

$$\Gamma_s n_{0s} \left(\frac{\partial}{\partial t} + \bar{\boldsymbol{v}}_s \cdot \frac{\partial}{\partial \boldsymbol{x}} \right) (h_{0s} \Gamma_s \bar{\boldsymbol{v}}_s) = -\frac{1}{m_s} \frac{\partial P_{0s}}{\partial \boldsymbol{x}} + \frac{q_s}{m_s} \Gamma_s n_{0s} (\boldsymbol{E} + \bar{\boldsymbol{v}}_s \wedge \boldsymbol{B}). \tag{3.61}$$

simulation (or lab) frame, while those in the comoving frame of the plasma must be obtained by a boost at the local mean speed $\bar{\boldsymbol{v}}_s$. Second, because they assume a comoving particle distribution that is isotropic in momentum space in order to use a scalar pressure P_{0s} instead of the full pressure tensor and, as we show below, to write relations such as $\bar{\boldsymbol{p}}_s = \langle \gamma \boldsymbol{v} \rangle_s = h_{0s} \Gamma_s \bar{\boldsymbol{v}}_s$ for the mean momentum that are necessary to their derivation. Rest frame distributions are, however, not isotropic in the out-of-equilibrium plasmas that we study.

Instead, in the remaining of this section, we derive the fluid equations directly from the collisionless Vlasov's equation expressed in the lab frame. We also show that the obtained equations are equivalent to the set of Eqs. 3.62, and under which hypotheses. We will use them in Chapter 6 to derive analytical models.

3.4.1 Pressure, stress, and temperature tensors

We first define the pressure, temperature, and stress tensors.

Measure of the temperature tensor

The kinetic temperature is a second-order moment of the particle distribution function and is, as such, not always suited to characterizing the velocity distribution of a population strongly out-of-equilibrium. We will nevertheless use it as an indication of the thermal energy content of the population, and of the momentum flux transfers, the latter being especially relevant to Ohm's law. We consider a species s. We first recall that the pressure tensor, which appears in the equation of conservation of momentum, Eq. 3.72, is defined as

$$\boldsymbol{P}_s = n_{\mathrm{lab},s} m_s \langle \delta \boldsymbol{p}_s \delta \boldsymbol{v}_s \rangle_s, \tag{3.63}$$

with $n_{\mathrm{lab},s}$ the particle number density in the laboratory frame, $\langle \cdot \rangle_s$ an average over the distribution function in the laboratory frame, and $\delta \boldsymbol{p}_s = \boldsymbol{p}_s - \bar{\boldsymbol{p}}_s$ the momentum difference with the bulk momentum $\bar{\boldsymbol{p}} = \langle \gamma \boldsymbol{v} \rangle_s$, and similarly for $\delta \boldsymbol{v}_s$.

We define the temperature tensor as the ratio of the pressure tensor to the comoving particle number density n_{0s}. Since $n_{\mathrm{lab},s} = \Gamma_s n_{0,s}$, the temperature tensor is

$$\frac{T_{s,ij}}{m_s c^2} = \Gamma_s \frac{\langle \delta p_i \delta v_j \rangle_s}{c^2}, \tag{3.64}$$

with i, $j = x$, y or z.

For the special case of a Maxwell-Jüttner distribution function of temperature $\Theta_s = 1/\mu_s = T_s/(m_s c^2)$, of drift velocity $\boldsymbol{\beta}_{0,s}$ and associated Lorentz factor $\Gamma_{0,s}$, given in the simulation or lab frame by $f_s(\boldsymbol{x}, \tilde{\boldsymbol{p}}) = n_{\mathrm{lab},s}(\boldsymbol{x}) g_s(\tilde{\boldsymbol{p}})$, $\tilde{\boldsymbol{p}} = \gamma \boldsymbol{v}/c$, and

$$g_s(\tilde{\boldsymbol{p}}) = \frac{\mu_s}{4\pi K_2(\mu_s) \Gamma_{0,s}} \exp\left\{ -\mu \Gamma_{0,s} \left(\sqrt{1 + \tilde{p}^2} - \boldsymbol{\beta}_{0,s} \cdot \tilde{\boldsymbol{p}} \right) \right\}, \tag{3.65}$$

we do have (see Eq. 3.32 and its derivation):

$$\Gamma_s \frac{\langle \delta p_i \delta v_j \rangle_s}{c^2} = \Theta_s \delta_{ij}, \tag{3.66}$$

where δ_{ij} is Kronecker's delta. Based upon these considerations, we measure the temperatures in the particle-in-cell simulations with expression 3.64.

Stress tensor

The fluid stress tensor for species s is defined, in the lab frame, as

$$\Pi_{s,ij} = \int \mathrm{d}^3\boldsymbol{p}\, m_s p_i v_j f_s(\boldsymbol{x},\boldsymbol{p}) = n_{\mathrm{lab},s} m_s \langle p_i v_j \rangle_s. \tag{3.67}$$

Note that $n_{\mathrm{lab},s}$ is the laboratory density, not the comoving density, and that $\boldsymbol{p} = \gamma\boldsymbol{v}$. The stress tensor can be expressed with comoving quantities by using Eq. 3.37 (that holds for an isotropic comoving distribution function) and $n_{\mathrm{lab},s} = \Gamma_0 n_{0,s}$:

$$\Pi_{s,ij} = \delta_{ij} P_s + \delta_{iy}\delta_{jy}\Gamma_{0s}^2 U_{0s}^2 m_s n_{0s} h_{0s}. \tag{3.68}$$

Non symmetric tensors

We remark that the tensors $\bar{\boldsymbol{p}}\bar{\boldsymbol{v}}$ and $\langle(\boldsymbol{p}-\bar{\boldsymbol{p}})(\boldsymbol{v}-\bar{\boldsymbol{v}})\rangle$ are not symmetric for arbitrary distributions. There is then two conventions to compute their divergence, for example for the component i: $[\boldsymbol{\nabla}\cdot(\bar{\boldsymbol{p}}\bar{\boldsymbol{v}})]_i = \partial_j(\bar{p}_j\bar{v}_i)$, or $= \partial_j(\bar{p}_i\bar{v}_j)$ (we sum over repeated subscripts). One should thus be careful. The tensor that originally enters into the equation of conservation of momentum, when derived from Vlasov's equation, is $\langle\boldsymbol{p}\boldsymbol{v}\rangle$, which is also $\langle\gamma\boldsymbol{v}\boldsymbol{v}\rangle$, and is thus symmetric. The non-symmetric tensors arrive when splitting $\langle\boldsymbol{p}\boldsymbol{v}\rangle = \bar{\boldsymbol{p}}\bar{\boldsymbol{v}} + \langle(\boldsymbol{p}-\bar{\boldsymbol{p}})(\boldsymbol{v}-\bar{\boldsymbol{v}})\rangle$. Consequently, no matter the convention used, the result will be coherent if the same is applied to both non-symmetric tensors. We will see that the convention $[\boldsymbol{\nabla}\cdot(\bar{\boldsymbol{p}}\bar{\boldsymbol{v}})]_i = \partial_j(\bar{p}_i\bar{v}_j)$ is to be preferred (footnote i, p. 115).

3.4.2 Fluid equations

We now turn to the derivation of fluid equations from moments of Vlasov's equation. Vlasov's equation reads

$$\frac{\partial f_s(\boldsymbol{x},\boldsymbol{p},t)}{\partial t} + \boldsymbol{v}\cdot\frac{\partial f_s}{\partial \boldsymbol{x}} + \frac{q_s}{m_s}(\boldsymbol{E}+\boldsymbol{v}\wedge\boldsymbol{B})\cdot\frac{\partial f_s}{\partial \boldsymbol{p}} = 0, \tag{3.69}$$

where $\boldsymbol{p} = \gamma\boldsymbol{v}$, and f_s is the distribution function in the simulation or lab frame. We denote its counterpart in the comoving frame by f_{0s}. Since the $\boldsymbol{p}$-divergence of $\boldsymbol{F} = (q_s/m_s)(\boldsymbol{E}+\boldsymbol{v}\wedge\boldsymbol{B})$ is zero, Vlasov's equation can also be written in conservation form as:

$$\frac{\partial f_s(\boldsymbol{x},\boldsymbol{p},t)}{\partial t} + \frac{\partial}{\partial \boldsymbol{x}}\cdot\boldsymbol{v} f_s + \frac{\partial}{\partial \boldsymbol{p}}\cdot\boldsymbol{F} f_s = 0. \tag{3.70}$$

Conservation of particle number

The first moment (with 1) of Eq. 3.69 gives the equation of conservation of the number of particles:

$$\frac{\partial}{\partial t} n_{\mathrm{lab},s} + \frac{\partial}{\partial \boldsymbol{x}}\cdot(n_{\mathrm{lab},s}\bar{\boldsymbol{v}}_s) = 0. \tag{3.71}$$

Here $n_{\mathrm{lab},s} = \int \mathrm{d}^3\boldsymbol{p}\, f_s(\boldsymbol{p})$ is the lab-frame particle number density, and $\langle\cdot\rangle_s$ or an overbar again denote an average over the distribution function f_s, i.e., $\langle M\rangle_s = n_{\mathrm{lab},s}^{-1}\int \mathrm{d}^3\boldsymbol{p}\, f_s(\boldsymbol{p}) M(\boldsymbol{p})$. We have the relation $n_{\mathrm{lab},s} = \Gamma_s n_{0s}$, so that we indeed recover Eq. 3.62a.

Conservation of momentum

The second moment (with $\boldsymbol{p}$) gives the equation of conservation of momentum:

$$\begin{aligned}\frac{\partial}{\partial t}(n_{\mathrm{lab},s}\bar{\boldsymbol{p}}_s) + \frac{\partial}{\partial \boldsymbol{x}}\cdot(n_{\mathrm{lab},s}\bar{\boldsymbol{p}}_s\bar{\boldsymbol{v}}_s)\\ = -\frac{\partial}{\partial \boldsymbol{x}}\cdot(n_{\mathrm{lab},s}\langle\delta\boldsymbol{p}_s\delta\boldsymbol{v}_s\rangle_s) + \frac{q_s}{m_s}n_{\mathrm{lab},s}(\boldsymbol{E}+\bar{\boldsymbol{v}}_s\wedge\boldsymbol{B}).\end{aligned} \tag{3.72}$$

We used the definitions $\delta\boldsymbol{v} = \boldsymbol{v} - \bar{\boldsymbol{v}}_s$ and $\delta\boldsymbol{p} = \boldsymbol{p} - \bar{\boldsymbol{p}}_s$, where $\boldsymbol{p} = \gamma\boldsymbol{v}$ is the momentum[i]. We now show how to recover Eq. 3.62b. First, we use the relation $\bar{\boldsymbol{p}}_s = h_{0s}\Gamma_s\bar{\boldsymbol{v}}_s$ for the mean momentum $\bar{\boldsymbol{p}}_s \equiv \langle\gamma\boldsymbol{v}\rangle_s$. The demonstration preceding Eq. 3.30 shows that this relation is valid whenever the comoving distribution function $f_{0s}(\boldsymbol{p}_0)$ is isotropic with respect to $\boldsymbol{p}_0$. Second, we note that the stress tensor is defined as $\Pi_{ij} = n_{\mathrm{lab},s}m_s\langle p_iv_j\rangle_s = n_{\mathrm{lab},s}m_s(\bar{p}_i\bar{v}_j + \langle\delta p_i\delta v_j\rangle_s)$, and is also equal (again if f_{0s} is isotropic) to $\Pi_{ij} = P_{0s}\delta_{ij} + \Gamma^2_{\bar{\boldsymbol{v}}_s}h_{0s}n_{0s}m_s\bar{v}_{s,i}\bar{v}_{s,j}$ (see Eq. 3.38). Inserting these new expressions into Eq. 3.72 does lead to Eq. 3.62b.

We also note that Eq. 3.72 can be put into a conservative form by using the conservation of momentum for the electromagnetic field, which reads

$$\frac{\partial}{\partial t}\epsilon_0(\boldsymbol{E}\wedge\boldsymbol{B}) - \frac{\partial}{\partial \boldsymbol{x}}\cdot\boldsymbol{T} = -[\rho\boldsymbol{E} + \boldsymbol{j}\wedge\boldsymbol{B}], \tag{3.74}$$

where $T_{ij} = \epsilon_0(E_iE_j - E^2\delta_{ij}/2) + \mu_0^{-1}(B_iB_j - B^2\delta_{ij}/2)$ is Maxwell stress tensor, $\rho = \sum_s q_sn_{\mathrm{lab},s}$ is the charge density, and $\boldsymbol{j} = \sum_s q_sn_{\mathrm{lab},s}\bar{\boldsymbol{v}}_s$ is the current density. One thus has to sum Eq. 3.72 over all species and then use Eq. 3.74, to obtain[j]:

$$\begin{aligned}\frac{\partial}{\partial t}\left(\epsilon_0\boldsymbol{E}\wedge\boldsymbol{B} + \sum_s m_sn_{\mathrm{lab},s}\bar{\boldsymbol{p}}_s\right)\\ + \frac{\partial}{\partial \boldsymbol{x}}\cdot\left(-\boldsymbol{T} + \sum_s m_sn_{\mathrm{lab},s}\left[\bar{\boldsymbol{p}}_s\bar{\boldsymbol{v}}_s + \langle\delta\boldsymbol{p}_s\delta\boldsymbol{v}_s\rangle_s\right]\right) = 0.\end{aligned} \tag{3.76}$$

[i] We note that an alternative form of Eq. 3.72 is

$$n_{\mathrm{lab},s}\left(\frac{\partial}{\partial t} + \bar{\boldsymbol{v}}_s\cdot\frac{\partial}{\partial \boldsymbol{x}}\right)\bar{\boldsymbol{p}}_s = -\frac{\partial}{\partial \boldsymbol{x}}\cdot(n_{\mathrm{lab},s}\langle\delta\boldsymbol{p}_s\delta\boldsymbol{v}_s\rangle_s) + \frac{q_s}{m_s}n_{\mathrm{lab},s}(\boldsymbol{E}+\bar{\boldsymbol{v}}_s\wedge\boldsymbol{B}). \tag{3.73}$$

It is obtained by using the equation of conservation of particle number, Eq. 3.71. Note that it makes use of the relation $[\boldsymbol{\nabla}\cdot(n_{\mathrm{lab},s}\bar{\boldsymbol{p}}_s\bar{\boldsymbol{v}}_s)]_i = \partial_j[n_{\mathrm{lab},s}\bar{p}_{si}\bar{v}_{sj}] = \bar{p}_{si}\partial_j[n_{\mathrm{lab},s}\bar{v}_{sj}] + n_{\mathrm{lab},s}\bar{v}_{sj}\partial_j\bar{p}_{si}$, which fixes the convention to use to compute the divergence of the non-symmetric tensors (see Sect. 3.4.1).

[j] Expressed with comoving quantities, just as in Eq. 3.62b, Eq. 3.76 reads:

$$\begin{aligned}\frac{\partial}{\partial t}\left(\epsilon_0\boldsymbol{E}\wedge\boldsymbol{B} + \sum_s m_s\Gamma_s^2n_{0s}h_{0s}\bar{\boldsymbol{v}}_s\right)\\ + \frac{\partial}{\partial \boldsymbol{x}}\cdot\left(-\boldsymbol{T} + \sum_s m_sn_{0s}h_{0s}\Gamma_s\bar{\boldsymbol{v}}_s\Gamma_s\bar{\boldsymbol{v}}_s + \sum_s P_{0s}\boldsymbol{I}\right) = 0.\end{aligned} \tag{3.75}$$

Conservation of energy

Finally, multiplying Vlasov's equation Eq. 3.69 by $\gamma m_s c^2$ and integrating over $\boldsymbol{p}$ gives the equation of conservation of energy:

$$\frac{\partial}{\partial t}(n_{\mathrm{lab},s}\langle\gamma m_s c^2\rangle_s) + \frac{\partial}{\partial \boldsymbol{x}}\cdot(n_{\mathrm{lab},s}\langle\boldsymbol{v}\gamma m_s c^2\rangle_s) = q_s n_{\mathrm{lab},s}\langle\boldsymbol{E}\cdot\boldsymbol{v}\rangle_s. \tag{3.77}$$

The right-hand side accounts for the coupling between the species and the electromagnetic fields, and thus possibly with other species via collective interactions.

The non-relativistic limit of this equation is easily obtained by making the difference between Eqs. 3.77 and 3.71.

Also, Eq. 3.77 can be put into a useful conservative form by expressing its right-hand side through the energy conservation equation for the fields, which is:

$$\begin{aligned}\frac{\partial}{\partial t}\left(\frac{E^2}{2\mu_0 c^2}+\frac{B^2}{2\mu_0}\right)+\frac{\partial}{\partial \boldsymbol{x}}\cdot\frac{\boldsymbol{E}\wedge\boldsymbol{B}}{\mu_0} &= -\boldsymbol{E}\cdot\boldsymbol{j}\\ &= -\boldsymbol{E}\cdot\sum_s\int \mathrm{d}^3\boldsymbol{p} f_s(\boldsymbol{x},\boldsymbol{p})q_s\boldsymbol{v}\\ &= -\sum_s n_{\mathrm{lab},s}q_s\langle\boldsymbol{v}\cdot\boldsymbol{E}\rangle_s.\end{aligned} \tag{3.78}$$

We thus have to sum Eq. 3.77 for all species, to obtain:

$$\begin{aligned}&\frac{\partial}{\partial t}\left\{\sum_s(n_{\mathrm{lab,s}}\langle\gamma m_s c^2\rangle_s)+\frac{E^2}{2\mu_0 c^2}+\frac{B^2}{2\mu_0}\right\}\\ &+\frac{\partial}{\partial \boldsymbol{x}}\cdot\left\{\sum_s(n_{\mathrm{lab,s}}\langle\boldsymbol{v}\gamma m_s c^2\rangle_s)+\frac{\boldsymbol{E}\wedge\boldsymbol{B}}{\mu_0}\right\}=0.\end{aligned} \tag{3.79}$$

To recover Eq. 3.62c, we use the relation $n_{\mathrm{lab},s}\langle\gamma m_s c^2\rangle_s = \Gamma_s^2 n_{0s}h_{0s}m_s c^2 - P_{0s}$. According to the derivation of Eq. 3.31e, it holds only for an isotropic comoving distribution function. We also have to use the previous relations for $\bar{\boldsymbol{p}}_s$ and $n_{\mathrm{lab},s}$.

3.5 Relativistic MHD waves

Waves are the building blocks of many plasma processes. A magnetized plasma can host a large number of wave modes, that depend on the model used (e.g., cold or hot, magnetized or not, low-frequency range or not, out-of-equilibrium or not). A plasma with relativistic temperatures and magnetic fields complicates even more the matter.

In the hot, magnetized, and low-frequency limit of MHD, the relativistic case can be treated rather easily. Gedalin (1993) does so in the gyrotropic case (pressure parallel to the magnetic field different from the perpendicular pressure)[k]. The method is to linearize the relativistic MHD equations to find the modes of propagation. The phase velocities obtained are then valid in the frame where the plasma is at rest[l].

[k] See also McKinney et al. (2012) in the general relativistic MHD framework.

[l] The waves can then be studied in any frame by doing the proper Lorentz transformation for the four-vector $(\omega/c, \boldsymbol{k})$.

We do not repeat the expressions of Gedalin (1993) here. We just underline that in his notations, $\epsilon = n_0\langle\gamma mc^2\rangle_0$, where the right-hand side contains our quantities as in Eq. 3.42. Our manuscript contains some of its results. In particular:

- The sound speed (in the absence of magnetic field) is given by Eq. 3.57, and specified in Eq. 3.59 for a non-relativistic gas and in Eq. 3.60 for the ultrarelativistic limit (there is no simple expression is the intermediate cases).
- The Alfvén speed is given by Eq. 6.7b.

3.6 Relativistic particle motion in E and B fields

Understanding the motion of individual particles into prescribed magnetic and electric fields is of paramount importance to understand and interpret PIC simulations. For magnetic reconnection setups, the particles from the background plasma first $E \times B$ drift toward the current sheet in orthogonal $\boldsymbol{E}$ and $\boldsymbol{B}$ fields, and then accelerate in an area where $E > cB$, with either $\boldsymbol{E} \cdot \boldsymbol{B} = 0$ or $\neq 0$. Relativistic particle motion in such fields is not trivial, and deserves a detailed description. This section summarizes the essential results, while more details and analytical expressions can be found in Appendix 3.B.

We concentrate on motions in constant fields. We consider a particle of mass m, charge q, velocity $\boldsymbol{v}$, Lorentz factor γ, and momentum $\boldsymbol{p} = \gamma m\boldsymbol{v}$ (note that contrary to what is done in the rest of the manuscript, here $\boldsymbol{p}$ is not $\gamma\boldsymbol{v}$). We denote its initial velocity by $\boldsymbol{v}_0$.

3.6.1 Constant electric field

See Appendix 3.B.1. This case is encountered in magnetic reconnection configurations with no guide field, at the center of the dissipation zone, where the reconnection electric field freely accelerates particles.

The motion takes place in the plane containing $\boldsymbol{E}$ and $\boldsymbol{v}_0$. The particle is accelerated along $\boldsymbol{E}$, and the Lorentz factor asymptotically increases as $\gamma \propto t$. We stress that even if there is no force perpendicular to $\boldsymbol{E}$ (so that $p_\perp = \text{const}$), the velocity perpendicular to $\boldsymbol{E}$ ($v_\perp = p_\perp/\gamma m$) is affected through the coupling by the Lorentz factor, and shrinks toward zero as the parallel velocity reaches the speed of light.

3.6.2 Constant magnetic field

See Appendix 3.B.2. Let $\boldsymbol{B} = B\hat{\boldsymbol{z}}$. The energy is conserved: $\gamma = \text{const}$. Nothing happens along z: $v_z = \text{const}$, and so also $v_\perp = \text{const}$. The motion in the x-y plane is a circle, traveled with a pulsation

$$\omega_c^{\mathrm{R}} = \frac{qB}{\gamma m} \tag{3.80}$$

and radius $r_\mathrm{c} = v_\perp/\omega_c^{\mathrm{R}}$. It is interesting to notice that the Larmor radius of relativistic particles increases proportionally to their perpendicular velocity times their Lorentz factor, $r_\mathrm{c} \propto m\gamma v_\perp$, where the Lorentz factor also includes the velocity parallel to the magnetic field. This is, again, due to coupling via the Lorentz factor.

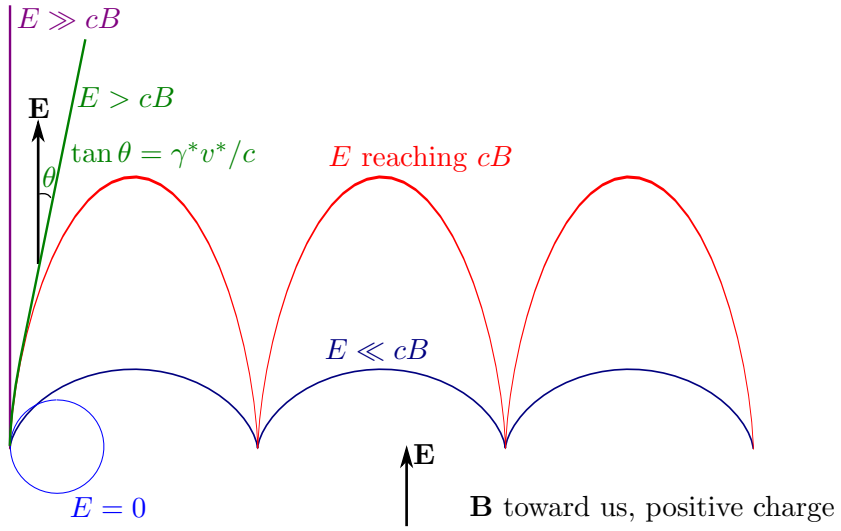

Figure 3.2: Trajectory of a charged particle in orthogonal magnetic and electric fields, depending on the ratio E/B. Except for the circle, the initial particle velocity is 0.

3.6.3 Constant electric and magnetic fields, non-relativistic case

See Appendix 3.B.3. We assume $\boldsymbol{B} = B\hat{\boldsymbol{z}}$ and $\boldsymbol{E} = E_z\hat{\boldsymbol{z}} + E_y\hat{\boldsymbol{y}}$, and we neglect relativistic effects. This situation is encountered in the upstream of magnetic reconnection dissipation zones, where particles evolve in the asymptotic magnetic field and in the motional reconnection electric field, with in addition $E_z = 0$.

The particle is freely accelerated in the direction parallel to $\boldsymbol{B}$: $v_z = qE_z t/m$. The motion in the plane perpendicular to $\boldsymbol{B}$ is the well known $E \times B$ drift, with a mean velocity given by $\boldsymbol{v}_{E\times B} = \boldsymbol{E} \wedge \boldsymbol{B}/B^2$ (illustrated for different initial conditions in Fig. 3.5).

In the non-relativistic case, there is no coupling between the parallel and perpendicular motions. This is valid as long as $v_0 \ll c$, $v_z(t) \ll c$, and $v_{E\times B} \ll c$. The last condition is equivalent to $E_\perp \ll cB$ (with $E_\perp$ the component perpendicular to $\boldsymbol{B}$). Note that when $E > cB$, then $v_{E\times B} > c$, and the motion is completely different (see below).

3.6.4 Constant and parallel electric and magnetic fields

See Appendix 3.B.4. The situation with a magnetic field parallel to the electric field occurs at the center of the dissipation region in magnetic reconnection with a guide field.

Let $\boldsymbol{B}$, $\boldsymbol{E} \propto \hat{\boldsymbol{z}}$. The motion is accelerated along z, while in the x-y plane it consists in circles with pulsation $\omega = |q|B/(\gamma m)$ and of radius $r_c = v_\perp/\omega$. Since $\gamma \to +\infty$, the pulsation decreases to 0. It follows that as in the case with an electric field alone, coupling through the Lorentz factor freezes the motion in the directions perpendicular to $\boldsymbol{E}$.

Another important remark is that since there is no force perpendicular to $\boldsymbol{B}$, the perpendicular momentum $p_\perp$ is constant. It follows that $r_c = p_\perp/(|q|B/m) = \text{const}$. Consequently, in the reconnection acceleration zone with a guide field, where $\boldsymbol{E} \parallel \boldsymbol{B}$, the particle Larmor radius remains constant.

3.6.5 Constant and orthogonal electric and magnetic fields of arbitrary magnitude

See Appendix 3.B.6. The non-relativistic description of the motion of a particle in orthogonal magnetic and electric fields leads to a mean velocity equal to $v_{E\times B} = E/B$, and is obviously valid only if $E/B \ll c$. We now describe the general case. This is of interest in magnetic reconnection with no guide field, where the asymptotic magnetic field decreases to 0 when particles approach the center of the dissipation zone, and thus evolves from $cB > E$ to $cB < E$. More generally, around any magnetic null there is an area where $cB < E$.

We assume that $\boldsymbol{E} \cdot \boldsymbol{B} = 0$. Because of the Lorentz invariants, when $E < cB$ there is no boost allowing to cancel the magnetic field, but a boost at $v^* = E/B$ allows to cancel the electric field; while when $E > cB$, there is no boost allowing to cancel the electric field, but a boost at $v^* = c^2 B/E$ allows to cancel the magnetic field. Two cases should thus be distinguished: $E < cB$ and $E > cB$ (the special case $E = cB$ is detailed in Appendix 3.B.5). The different outcomes are illustrated in Fig. 3.2.

When $E < cB$, the motion can be decomposed as the sum of a translation at the $\boldsymbol{E} \wedge \boldsymbol{B}/B^2$ velocity (identical to the non-relativistic case), plus an elliptical (and not circular) motion in the x-y plane, plus a translation along $\boldsymbol{B} \propto \hat{\boldsymbol{z}}$ due to the initial velocity along z. The ellipses are described with a non-uniform velocity, and the motion along z is not constant, despite the absence of force in this direction, because of the coupling with γ.

When E_y increases toward cB_z, the velocity $v^* = E_y/B_z$ reaches c. The ellipse deforms in the direction of the electric field. Physically, the magnetic field has more and more difficulties in containing the electric acceleration along y, so that the ellipse is wider and wider in the direction of $\boldsymbol{E}$. When E_y reaches cB_z, the ellipse extends to infinity along the direction of $\boldsymbol{E}$, and the motion is not confined any more in the y direction. When $E = cB$, the motion is indeed open, and the particle is freely accelerated by the electric field and endlessly gains energy.

We now turn to the $E > cB$ case. There is no gyration around $\boldsymbol{B}$ because the magnetic field is not strong enough to transform the trajectory into loops. The long term motion is a straight line (see Fig. 3.2), with $\gamma \to +\infty$, and with an angle θ with respect to the electric field direction given by

$$\tan\theta = \gamma^* v^*/c, \tag{3.81}$$

with $v^* = c^2|\boldsymbol{E} \wedge \boldsymbol{B}/E^2|$ and γ^* the associated Lorentz factor. The velocity actually reaches a steady state where the magnetic force $\boldsymbol{v} \wedge \boldsymbol{B}$ compensates the electric force.

3.7 Relativistic kinetic Harris equilibrium

Harris configuration is one of the rare fully consistent solutions of the Vlasov-Maxwell system in a non-homogeneous case. Particle trajectories in a Harris current sheet are discussed by Biskamp (2000). We note that all particles of a given species drift at the same velocity, so that it is a very particular case. Other equilibriums, such as the force-free case, also exist (see Sect. 2.10.2). Also, Harris equilibrium in an asymmetric current sheet is more complex, and has been given by Aunai et al. (2013).

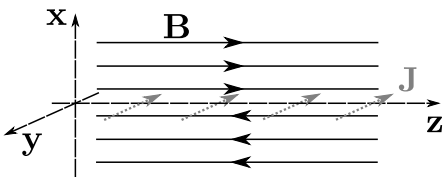

Figure 3.3: Setup for the Harris equilibrium.

Here, we are interested by the generalization of Harris equilibrium to the relativistic case. It is not difficult, and was partly done by Hoh (1966) for a Maxwell-Jüttner distribution and non-relativistic current speeds. The fully relativistic case appeared later for pair plasmas with the same temperature for both species, for example in Kirk and Skjæraasen (2003) or Pétri and Kirk (2007). We now propose a formulation for the relativistic case with an arbitrary temperature and mass ratios for ions (singly ionized) and electrons. We use these initial conditions to start our simulations in Chapters 6 and 7.

Derivation of the equilibrium equations

We define a frame $\mathcal{R}_0$, where the magnetic field is assumed to be

$$\mathbf{B} = \hat{\mathbf{z}}\, B_0 \tanh\left(\frac{x}{L}\right), \tag{3.82}$$

and the particles sustaining this field are assumed to have a Maxwell-Jüttner distribution function given in $\mathcal{R}_0$ by

$$f(\boldsymbol{x}, \widetilde{\boldsymbol{p}}) = \frac{\mu_s\, n'_s(x)}{4\pi K_2(\mu_s)} \exp\left\{-\mu_s \Gamma_s \left(\sqrt{1+\widetilde{p}^2} - \beta_s \widetilde{p}_y\right)\right\}, \tag{3.83}$$

with $s =$ i for ions or e for electrons, $\mu_s = 1/\Theta_s = m_s c^2/T_s$, $\widetilde{\boldsymbol{p}} = \gamma \boldsymbol{v}/c$, and K_2 the modified Bessel function of the second kind. U_s is the bulk velocity of species s, and Γ_s the associated Lorentz factor. We note that f_s is normalized with respect to $\widetilde{\boldsymbol{p}}$ to $\Gamma_s n'_s(x)$, so that n'_s is the density of species s in its comoving frame, and $\Gamma_s n'_s$ its density in $\mathcal{R}_0$. We will denote quantities defined in the comoving frame with a prime.

Inserting Eq. 3.83 into Vlasov's equation expressed in $\mathcal{R}_0$:

$$\boldsymbol{v} \cdot \frac{\partial f_s}{\partial \boldsymbol{x}} + \frac{q_s}{m_s c}\, \boldsymbol{v} \wedge \boldsymbol{B}(\boldsymbol{x}) \cdot \frac{\partial f_s}{\partial \widetilde{\boldsymbol{p}}} = 0, \tag{3.84}$$

leads to the relation for the comoving number density

$$n'_s(x) = \frac{n'_{0,s}}{\cosh^2(x/L)} \tag{3.85}$$

with

$$\boxed{\frac{\Gamma_s U_s}{c} = -\frac{2T_s}{q_s B_0 L c} = -2\Theta_s \frac{d'_\mathrm{e}}{L} \frac{\omega'_\mathrm{pe}}{\omega_{cs}} \mathrm{sgn}(q_s),} \tag{3.86}$$

with $\mathrm{sgn}(q_s)$ the sign of the charge, $\omega_{cs} = |q_s| B_0/m_s$, $\omega'_\mathrm{pe} = \sqrt{n'_0 e^2/(\epsilon_0 m_\mathrm{e})}$, and $d'_\mathrm{e} = c/\omega'_\mathrm{pe}$.

The absence of electric field in Eq. 3.84 implicitly assumes that the plasma is quasi neutral in $\mathcal{R}_0$, which is true only if the overall charge density in this frame vanishes:

$$\Gamma_i n'_{0,\mathrm{i}} = \Gamma_\mathrm{e} n'_{0,\mathrm{e}}. \tag{3.87}$$

We now use Maxwell-Ampère equation in $\mathcal{R}_0$: $\boldsymbol{\nabla} \wedge \boldsymbol{B} = \mu_0 e[\Gamma_\mathrm{i} n'_\mathrm{i}(x) U_\mathrm{i} - \Gamma_\mathrm{e} n'_\mathrm{e}(x) U_\mathrm{e}]$. Insertion of $n'(x)$ and $B(x)$ leads – not surprisingly – to a pressure balance between the unmagnetized center of the sheet and the magnetically dominated outer domain:

$$\frac{B_0^2}{2\mu_0} = n'_{0,\mathrm{e}} T_\mathrm{e} + n'_{0,\mathrm{i}} T_\mathrm{i}. \tag{3.88}$$

Manipulating Eq. 3.88 and defining $\chi = (1 + T_\mathrm{i}/T_\mathrm{e})/2$, we obtain

$$\boxed{\Theta_\mathrm{e} = \frac{1}{4\chi} \left(\frac{\omega_\mathrm{ce}}{\omega'_\mathrm{pe}} \right)^2.} \tag{3.89}$$

How to use them: from parameters in the comoving frames

Given a temperature ratio χ, the four variables L/d'_e, Θ_e, $\omega_\mathrm{ce}/\omega'_\mathrm{pe}$, and $\Gamma_\mathrm{e} U_\mathrm{e}/c$, are constrained by the two equations 3.86 (for $s = \mathrm{e}$) and 3.89. Consequently, one needs to specify two of these four variables. Then, the ion velocity and temperature are easily deduced with Eq. 3.86 for $s = \mathrm{i}$ and with the chosen value of χ. L and ω_ce expressed in units of d_e and ω_pe, that are useful for a setup in a simulation, are then deduced with Γ_e through $\omega'_\mathrm{pe} = \omega_\mathrm{pe}/\sqrt{\Gamma_\mathrm{e}}$ and $d'_\mathrm{e} = d_\mathrm{e} \times \sqrt{\Gamma_\mathrm{e}}$.

A special case is when the temperatures are equal: then $\Gamma_\mathrm{i} U_\mathrm{i} = -\Gamma_\mathrm{e} U_\mathrm{e}$, $n'_\mathrm{e} = n'_\mathrm{i}$, and $\Theta_\mathrm{e} = (1/4)(\omega_\mathrm{ce}/\omega'_\mathrm{pe})^2$.

How to use them: from parameters in the laboratory frame

We now assume that we know $\omega_\mathrm{ce}/\omega_\mathrm{pe}$, L/d_e and χ in the laboratory frame. We have to derive the counterparts of the two firsts in the primed frame. We recall that $n'_s = n_s/\Gamma_s$ and $\omega_{\mathrm{p}s} = \sqrt{\Gamma_s}\omega'_{\mathrm{p}s}$. From Eq. 3.89 we have

$$\boxed{\Theta_\mathrm{e} = \frac{\Gamma_\mathrm{e}}{4\chi} \left(\frac{\omega_\mathrm{ce}}{\omega_\mathrm{pe}} \right)^2.} \tag{3.90}$$

We insert this relation into Eq. 3.86 for electrons, and also note that $\omega'_\mathrm{pe} d'_\mathrm{e} = c = \omega_\mathrm{pe} d_\mathrm{e}$, so that we have

$$\boxed{\frac{U_\mathrm{e}}{c} = \frac{1}{2\chi} \frac{d_\mathrm{e}}{L} \frac{\omega_\mathrm{ce}}{\omega_\mathrm{pe}}.} \tag{3.91}$$

Equations 3.90 and 3.91 allow to specify the electron parameters. Those for ions then follow from the value of χ.

We remark from Eq. 3.91 that we have the condition $\omega_\mathrm{ce}/\omega_\mathrm{pe} < 2\chi L/d_\mathrm{e}$. If this is not the case, the equilibrium cannot be achieved. Why it is so can be seen by rewriting Eq. 3.86 as $\Theta_\mathrm{e} = (L/2d_\mathrm{e})(\omega_\mathrm{ce}/\omega_\mathrm{pe})\Gamma_e U_e/c$: satisfying Vlasov's equation is possible only if $\Theta_\mathrm{e} < (L/2d_\mathrm{e})(\omega_\mathrm{ce}/\omega_\mathrm{pe})\Gamma_e$, but this is not possible if the pressure balance condition (which is Eq. 3.90) requires a temperature exceeding this limit to balance the magnetic field pressure.

Particles Larmor radii

As a final note, we express the thermal Larmor radius of the particles, defined as $\langle(\gamma v_\perp)^2\rangle^{1/2}/\omega_\mathrm{ce}$, at the current sheet center:

$$\frac{\langle r_\mathrm{ce} \rangle}{d_\mathrm{e}} = \frac{\omega_\mathrm{pe}}{\omega_\mathrm{ce}} \sqrt{\Theta_\mathrm{e}} \sqrt{\kappa_{32}(\mu_\mathrm{e})} = \sqrt{\Gamma_\mathrm{e} \kappa_{32}(\mu_\mathrm{e})/2}, \tag{3.92}$$

where the first part of the equality is general (Table 3.1 and Sect. 3.2.3), and the second is obtained for the Harris equilibrium using Eq. 3.90 for the ratio ω_{ce}/ω_{pe}. The function κ_{32} is the plasma comoving enthalpy and is plotted in Fig. 3.1. The thermal Larmor radius is consequently temperature dependent via $\kappa_{32}(1/\Theta_e)$. This is negligible for non-relativistic temperatures, but significant when $\Theta_e \geq 1$.

3.8 Loading a relativistic particle distribution in a PIC simulation

This section is concerned with the general problem of loading particles with momenta that reproduce a given distribution function, and gives a method for the Maxwell-Jüttner distribution.

Very common cases are waterbag and Maxwell-Boltzmann distributions with a mean bulk velocity U_0. A simple method is then to load the particles in the frame comoving with the plasma, which is fairly easy because in this frame the distributions are isotropic, and then to add to every particle the velocity U_0 or, if U_0 is close to c, to boost every particle with the Lorentz boost corresponding to U_0. We will see, however, that this method is no longer correct when both U_0 and the rest frame distribution are relativistic, mainly because boosting particles in a PIC code does not boost space. We present here another method applicable to Maxwell-Jüttner distribution, correct for any temperature and bulk velocity[m]. We need such a method for the simulations of Chapters 6 and 7.

3.8.1 Transformation of the distribution function

We start by explaining how the particle distribution changes from one frame to another (see e.g. Mihalas and Mihalas 1984; Pomraning 1973).

In this section 3.8, we note $\boldsymbol{p} = \gamma\boldsymbol{v}/c$. We consider a frame $\mathcal{R}$ where the plasma has a mean velocity U_0 and follows the distribution $f(\mathbf{x}, \mathbf{p})$. In the comoving frame or plasma rest frame $\mathcal{R}_0$, the plasma mean velocity is zero and follows the distribution $f_0(\mathbf{x}, \mathbf{p})$. We follow a group of particles. Seen from $\mathcal{R}$, they are in a volume d^3x around $\mathbf{x}$ and have momentum $\mathbf{p}$ with a scatter d^3p; seen from $\mathcal{R}_0$ these quantities change respectively to d^3x_0, $\mathbf{x}_0$, $\mathbf{p}_0$, and d^3p_0. The number of particles in our group is

$$f_0(\mathbf{x}_0, \mathbf{p}_0)\mathrm{d}^3x_0\mathrm{d}^3p_0 = f(\mathbf{x}, \mathbf{p})\mathrm{d}^3x\mathrm{d}^3p, \tag{3.93}$$

so that to find the link between f and f_0 we have to find a relation between $\mathrm{d}^3x_0\mathrm{d}^3p_0$ and $\mathrm{d}^3x\mathrm{d}^3p$.

We start with the momentum. In the rest frame, our group of particles have momenta spanning a range d^3p_0. Seen in the boosted frame, their momenta transform according to the Lorentz transformation, and span a new range d^3p. These two volumes are thus linked by the Jacobian of the Lorentz transformation, and it can be shown that

$$\mathrm{d}^3p/\gamma = \mathrm{d}^3p_0/\gamma_0 \tag{3.94}$$

where γ and γ_0 are the Lorentz factors associated to $\mathbf{p}$ and $\mathbf{p}_0$.

[m] We note Swisdak (2013) independently proposed a similar method.

We now consider the space volumes. Because of space contraction or dilatation, the group of particles will occupy a different volume in different frames. We consider the frame $\mathcal{R}'$ comoving with the group of particles. This is possible because the particles all move at nearly the same velocity $\mathbf{v}_0 = \mathbf{p}_0/\gamma_0$. We denote by a prime all quantities seen from this frame. In $\mathcal{R}'$, the particles occupy a volume d^3x'. Since only one direction is contracted, and since $\mathcal{R}'$ moves relative to $\mathcal{R}_0$ with Lorentz factor $\gamma_0 = \sqrt{1+p_0^2}$, we have the relation $\mathrm{d}^3x_0 = \mathrm{d}^3x'/\gamma_0$. Similarly, $\mathcal{R}'$ moves relative to $\mathcal{R}$ with Lorentz factor $\gamma = \sqrt{1+p^2}$, and we have $\mathrm{d}^3x = \mathrm{d}^3x'/\gamma$. All in all:

$$\gamma\,\mathrm{d}^3x = \gamma_0\,\mathrm{d}^3x_0. \tag{3.95}$$

From this, we deduce that

$$f(\mathbf{x},\mathbf{p}) = f_0(\mathbf{x}_0,\mathbf{p}_0). \tag{3.96}$$

3.8.2 Why boosting particles from the rest frame is incorrect for relativistic distributions

We now come back to PIC simulations. We assume that we load particles uniformly in space, with momenta following $f_0(\mathbf{x}_0,\mathbf{p}_0)$, and that we boost each particle with a velocity U_0. The momentum volume elements are then transformed according to Eq. 3.94, but positions are not changed. Equation 3.95 does not hold, and we obtain a particle distribution

$$f_{\mathrm{PIC}}(\mathbf{x},\mathbf{p}) = f_0(\mathbf{x},\mathbf{p}_0)\mathrm{d}^3p_0/\mathrm{d}^3p = f_0(\mathbf{x},\mathbf{p}_0)\gamma_0/\gamma. \tag{3.97}$$

The volume contraction/dilatation is not performed, and the factor γ_0/γ does not cancel.

Consequently, boosting each particle from the rest frame leads to the expected distribution only if γ_0/γ is independent of the particle. We can write this ratio as

$$\frac{\gamma_0}{\gamma} = \frac{\gamma_0}{\Gamma_0(\gamma_0 + p_{0,y}\,U_0/c)}, \tag{3.98}$$

with $p_{0,y}$ the y component of $\mathbf{p}_0$ and $\Gamma_0 = (1-U_0^2/c^2)^{-1/2}$, so that this is the case only if $p_{0,y} \ll 1$ (or if the boost is non-relativistic, $U_0 \ll c$). If $p_{0,y} \ll 1$, then $\gamma_0/\gamma \sim 1/\Gamma_0$ and when it is inserted back into Eq. 3.97, we find the usual result of density contraction.

However, when the particle distribution is relativistic in the rest frame of the plasma, γ_0/γ is not a constant factor and Eq. 3.97 does not have the expected dependence on momentum $\mathbf{p}$.

3.8.3 A method to load a drifting Maxwell-Jüttner distribution with arbitrary temperature and drift speed

Introduction

We now present a method to load the superparticle momenta directly in the frame where the distribution has a bulk velocity. Since the particle distribution of a relativistic plasma in thermodynamic equilibrium is given by the Maxwell-Jüttner distribution (see Sect. 3.2.2 for a discussion and references), we choose to load this particular case in the simulations. We recall that it is given, in the plasma rest frame, by

$$f_0(\boldsymbol{x}_0,\boldsymbol{p}_0) = n_0 g_0(\boldsymbol{p}_0) = n_0 \frac{\mu}{4\pi K_2(\mu)} \exp\left\{-\mu\sqrt{1+p_0^2}\right\}, \tag{3.99}$$

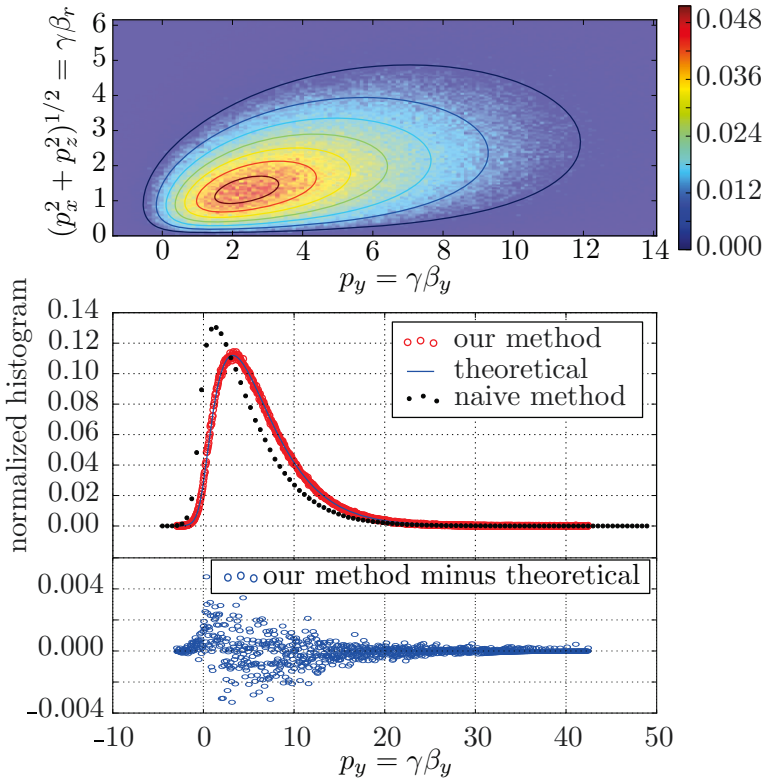

Figure 3.4: Maxwell-Jüttner distribution for $T = mc^2$ and $\Gamma_0\beta_0 = \sqrt{2}$.
Upper plot: Contours are drawn from the exact expression $2\pi r g(r, 0, p_y)$, with g from Eq. 3.100 and $(r, 0, p_y)$ defined in Appendix 3.8.3. The background color map is the 2D histogram of $((p_x^2 + p_z^2)^{1/2}, p_y)$ for 10^6 particles generated according to our method.
Middle plot: Normalized histogram of p_y for the particles (red dotted), to be compared to the exact expression in Eq. 3.102 (blue line), and for comparison (black dots) the histogram of p_y for particles generated the wrong way (initialization in the rest frame and boost of Γ_0).
Bottom plot: Difference between the red points and the blue curve.

with $n_0 = \iiint \mathrm{d}^3\boldsymbol{p}\, f_0(\boldsymbol{x}_0, \boldsymbol{p}_0)$ the uniform particle number density and g_0 the momentum distribution, both in the rest frame, $\mu = mc^2/T$, $\boldsymbol{p} = \gamma\boldsymbol{v}/c$, and K_2 the modified Bessel function of the second kind. We note again that Treumann et al. (2011) argue that another normalization factor should be used, but this is of no importance for this section because we use probability distributions normalized to 1. We also recall Eq. 3.8: in the frame where the plasma moves with a bulk velocity $c\beta_0$ (and associated Lorentz factor Γ_0), and where it has a particle density $n = \Gamma_0 n_0$ and a momentum distribution g, we have

$$g(\boldsymbol{p}) = \frac{\mu}{4\pi K_2(\mu)\Gamma_0} \exp\left\{-\mu\Gamma_0\left(\sqrt{1+p^2} - \beta_0 p_y\right)\right\}. \tag{3.100}$$

This distribution is normalized to unity: $\iiint \mathrm{d}^3\boldsymbol{p}\, g(\boldsymbol{p}) = 1$.

The main difficulty with Eq. 3.100 is that the variables p_x, p_y and p_z are coupled and cannot be chosen independently. The solution is to compute the marginal distribution for the variable p_y. With this, one can choose the y-component of $\boldsymbol{p}$ independently of the others, and then use the distribution $g(p_\perp, p_y)$ knowing p_y to choose the component normal to $\boldsymbol{y}$.

Details

Starting from the distribution 3.100, we make a first change of variables $(p_x, p_y, p_z) \to (x, y, z) = (p_x/\gamma_y, p_y, p_z/\gamma_y)$, where $\gamma_y = \sqrt{1+p_y^2}$, and we then change to cylindrical coordinates (r, θ, y) with the axis along y. We integrate along θ. Finally, a last change of variables $(r, y) \to (u, y) = (\sqrt{1+r^2}, y)$ leads to the distribution for the random variables $(U, Y) \in [1, +\infty[\times]-\infty, +\infty[$:

$$\begin{aligned} j_{U,Y}(u,y) = \frac{\mu}{2K_2(\mu)\Gamma_0}\gamma_y^2 \exp\{\mu\Gamma_0\beta_0\, y\} \\ \times\, u \exp\{-\mu\Gamma_0\gamma_y\, u\}\,. \end{aligned} \tag{3.101}$$

It is then easy to obtain the marginal distribution for Y:

$$\begin{aligned} j_Y(y) &= \int_1^\infty \mathrm{d}u\, j_{U,Y}(u,y) \\ &= \frac{1+\mu\Gamma_0\gamma_y}{2\mu\Gamma_0^3 K_2(\mu)} \exp\{-\mu\Gamma_0\,(\gamma_y - \beta_0 y)\}\,. \end{aligned} \tag{3.102}$$

From this, we deduce the conditional probability distribution of U given the value y of Y:

$$j_{U|y}(u) = \frac{j_{U,Y}(u,y)}{j_Y(y)} = \frac{a_y^2 e^{a_y}}{1+a_y}\, u \exp\{-a_y u\}\,, \tag{3.103}$$

with $a_y = \mu\Gamma_0\sqrt{1+y^2}$.

Then, for each particle, one has to generate $y = p_y$ according to distribution 3.102, compute a_y, and generate u according to distribution 3.103.

For the first step, we use the method of the inversion of the cumulative distribution. This method is based on the fact that if W is a uniform random variable on $[0,1]$, if $F(s) = \int_{-\infty}^s f(x)\,\mathrm{d}x$ is the cumulative distribution of the distribution f and F^{-1} its inverse, then $F^{-1}(W)$ follows the distribution f. In practice, one has to choose random numbers w_i in $[0,1]$, and the $y_i = F^{-1}(w_i)$ will be distributed according to f.

There is however no analytic expression for the cumulative distribution $J(y) = \int_{-\infty}^y j_Y(z)\,\mathrm{d}\,z$. We compute numerically $J^{-1}(t)$ on a grid of points $t_i = i/N$, $i = 1..(N-1)$. For each index i, we want to find y_i such that $\int_{-\infty}^{y_i} j_Y(z)\,\mathrm{d}\,z = t_i$. We thus compute numerically the integral $\int_{-\infty}^y j_Y(z)\,\mathrm{d}\,z$ up to the point where it reaches t_i, and then attribute the value of y to y_i. We use the following algorithm:

1. Choose a maximal integration step $\delta y_{\max}$, and set $\delta y = \delta y_{\max}$. Choose a tolerance tol.
2. Start from a low enough value y_0 such that $j_Y(y_0) \ll 1$, and set $y = y_0$. Also set $i = 1$.
3. Set $J = 0$, or if possible $J = \int_{-\infty}^{y_0} j_Y(z)\mathrm{d}z$.
4. Compute $J = J + \delta y\, j_Y(y)$.
5. J is now an estimation of $\int_{-\infty}^y j_Y(z)\,\mathrm{d}z$.

   If $|J - t_i| < \mathrm{tol}$, then the desired $y_i = J^{-1}(t_i)$ is y. Set $i = i+1$, and go back to 4.

   If $J < t_i$, set $y = y + \delta y$, and go back to 4.

   If $J > t_i$, set $\delta y = \delta y/2$ and go back to 4.

We run this algorithm once for the needed μ and $\Gamma_0\beta_0$ and store the y_i in a file. Then, during the particle initialization, we choose random integers i between 1 and $N-1$ and set $p_y = y_i$.

Once y is known, we have to pick a u according to Eq. 3.103. Since a_y can be anything between $\mu\Gamma_0$ and $+\infty$, we cannot generate a file before the program run, and we have to invert F on the flight. It turns out that we can integrate $j_{U|y}$. After some basic manipulations, we arrive at

$$v = \int_1^u \mathrm{d}t\, j_{U|y}(t) \quad \Leftrightarrow \quad l(x) = w\, l(a_y), \tag{3.104}$$

where $x = a_y u$, $l(x) = (1+x)\exp(-x)$, and v and w are two random numbers between 0 and 1. Inversion of the right side of Eq. 3.104 is easily done with a Newton method due to the smoothness of the function l. Starting from $x = a_y$ is a good idea, and one must enforce a minimum number of iterations.

Tests

Figure 3.4 shows an example of the distribution generated with this method for $T = mc^2$ and $\Gamma_0\beta_0 = 1.41$, and compares it to the theoretical expectation and to the the distribution obtained by boosting individually the superparticles from the rest frame. We clearly see the accuracy of our algorithm, and the mismatch between the simpler boosting method and the expected result. We note that this mismatch can have significant consequences. For example, when used for the tearing instability of Sect. 4.4.4 it leads to large adjustments in the initial conditions, and for the most extreme temperatures to a complete disruption of the current sheet.

Appendix 3.A More relations for Maxwell-Jüttner distribution

3.A.1 Change of variables for Maxwell-Jüttner distributions

We derive the expression of the Maxwell-Jüttner distribution with respect to the momentum $\hat{\boldsymbol{p}} = \gamma m \boldsymbol{v}$, the Lorentz factor γ_0, and the velocity $\boldsymbol{v}_0/c$.

For the momentum $\hat{\boldsymbol{p}} = \gamma m \boldsymbol{v}$, we have:

$$\boxed{g_{\hat{\boldsymbol{p}}}(\hat{\boldsymbol{p}}) = \left(4\pi m^3 c^3 \Gamma_0 \Theta K_2(\mu)\right)^{-1} \exp\left\{-\frac{\Gamma_0(\gamma mc^2 - \boldsymbol{U}_0\cdot\hat{\boldsymbol{p}})}{\Theta mc^2}\right\},} \tag{3.105}$$

which becomes for a plasma at rest:

$$g_{0|\hat{\boldsymbol{p}}}(\hat{\boldsymbol{p}}_0) = \left(4\pi m^3 c^3 \Theta K_2(\mu)\right)^{-1} \exp\left\{-\frac{\gamma_0 mc^2}{T}\right\}, \tag{3.106}$$

with again $\mu \equiv 1/\Theta \equiv mc^2/T$ the inverse of the temperature, always defined in the rest frame of the plasma through the definition of $g_{0|\boldsymbol{p}}$. For the momentum amplitude $\hat{p}_0 = |\hat{\boldsymbol{p}}_0|$, we simply have $g_{0|\hat{p}}(\hat{p}_0) = 4\pi\hat{p}_0^2 g_{0|\hat{\boldsymbol{p}}}(\hat{\boldsymbol{p}}_0)$.

The comoving distributions for the normalized momentum $\tilde{\boldsymbol{p}}_0$ and its norm $\tilde{p}_0$ were given with Eq. 3.6. From these, we can then express the comoving distribution in terms of Lorentz factors γ. Using $\gamma_0^2 = 1 + \tilde{p}_0^2$, we have $\gamma_0 \mathrm{d}\gamma_0 = \tilde{p}_0 \mathrm{d}\tilde{p}_0$. Since $g_{0|\gamma}(\gamma_0)\mathrm{d}\gamma_0 = g_{0|\tilde{p}}(\tilde{p}_0)\mathrm{d}\tilde{p}_0$, we obtain:

$$\boxed{g_{0|\gamma}(\gamma_0) = \frac{\mu}{K_2(\mu)}\,\gamma_0\sqrt{\gamma_0^2 - 1}\,\exp\{-\mu\gamma_0\}, \quad \gamma_0 \in [1, +\infty[.} \tag{3.107}$$

Parameter	Value
No drift velocity	
$\langle\gamma^2\rangle$	$1+3\kappa_{32}(\mu)/\mu$
$\langle\gamma^3\rangle$	$15\kappa_{32}(\mu)/\mu^2+2/\mu+\kappa_{32}(\mu)$
$\langle\gamma\lvert\boldsymbol{\beta}\rvert\rangle$	$2\left(\frac{2}{\pi}\right)^{1/2}\frac{K_{5/2}(\mu)}{\mu^{1/2}K_2(\mu)}$
$\langle\gamma(\gamma\beta)^2\rangle$	$3/\mu+15\kappa_{32}(\mu)/\mu^2$
With a drift velocity $\boldsymbol{U}_0=U_0\hat{\boldsymbol{y}}$	
$\left\langle(\boldsymbol{p}-\langle\boldsymbol{p}\rangle)^2\right\rangle$	$\Gamma_0^2U_0^2+3(2\Gamma_0^2-1)c^2\kappa_{32}(\mu)/\mu-\left(\Gamma_0U_0\kappa_{32}(\mu)\right)^2$
$\langle\tilde{p}_x^2\rangle=\langle\tilde{p}_z^2\rangle$	$\kappa_{32}(\mu)/\mu$
$\langle\tilde{p}_y^2\rangle$	$(\Gamma_0\beta_0)^2+(6\Gamma_0^2-5)\kappa_{32}(\mu)/\mu$

Table 3.2: Less useful averages for the Maxwell-Jüttner distribution. We use $\kappa_{32}(\mu)=K_3(\mu)/K_2(\mu)$.

Another way to express g_0 is with respect to the velocity $\boldsymbol{v}_0/c$. We start from Eq. 3.6 and use $\mathrm{d}\tilde{p}_0/\mathrm{d}v_0=\mathrm{d}(\gamma_0 v_0)/\mathrm{d}v_0=\gamma_0^3$, to obtain:

$$\boxed{g_{0|v/c}\left(\frac{v_0}{c}\right)=\frac{\mu}{K_2(\mu)}\gamma_0^5\left(\frac{v_0}{c}\right)^2\exp\left\{-\mu\gamma_0\right\},\quad \frac{v_0}{c}\in[0,1[.} \tag{3.108}$$

Coming back to the distribution for $\boldsymbol{v}_0$ is then straightforward:

$$g_{0|\boldsymbol{v}/c}\left(\frac{\boldsymbol{v}_0}{c}\right)=\frac{\mu}{4\pi K_2(\mu)}\gamma_0^5\exp\left\{-\mu\gamma_0\right\},\quad \frac{\boldsymbol{v}_0}{c}\in]-1,1[^3. \tag{3.109}$$

3.A.2 Asymptotic expressions for Bessel functions

We report the asymptotic relations that can be used to derive the non-relativistic and ultrarelativistic limits of the averages over Maxwell-Jüttner distributions:

$$K_\nu(x)\underset{x\to+\infty}{\sim}\sqrt{\frac{\pi}{2x}}e^{-x}\left(1+\frac{4\nu^2-1}{8x}+O(1/x^2)\right), \tag{3.110}$$

with for example

$$\begin{aligned}\frac{K_3(\mu)}{K_2(\mu)}&\underset{\mu\to+\infty}{=}\left[1+\frac{35}{8\mu}+O\left(\frac{1}{\mu^2}\right)\right]\left[1-\frac{15}{8\mu}+O\left(\frac{1}{\mu^2}\right)\right]\\&=1+\frac{5}{2\mu}+O\left(\frac{1}{\mu^2}\right);\end{aligned} \tag{3.111}$$

and:

$$K_\nu(x)\underset{x\to0}{\sim}\frac{1}{2}\Gamma(\nu)\left(\frac{2}{x}\right)^\nu. \tag{3.112}$$

They can be found in *NIST Digital Library of Mathematical Functions* (2013, §10.30).

Also useful is the recurrence relation (*NIST Digital Library of Mathematical Functions* 2013, §10.29), valid whatever u:

$$K_{\nu+1}(u)=\frac{2\nu}{u}K_\nu(u)+K_{\nu-1}(u). \tag{3.113}$$

Particular cases are $K_3/K_2=4/u+K_1/K_2$ and $K_4/K_2=1+6K_3/(uK_2)$.

Appendix 3.B Relativistic particle motion in E and B fields

This appendix provides derivations of the facts stated in Sect. 3.6, i.e., explores the motion of a charged particle in constant electric and magnetic fields. We consider a particle of mass m, charge q, velocity $\boldsymbol{v}$, Lorentz factor γ, and momentum $\boldsymbol{p} = \gamma m \boldsymbol{v}$.

3.B.1 Constant electric field

We assume that the particle moves in a constant electric field $\boldsymbol{E} = E\hat{\boldsymbol{y}}$. The equations of motion are:

$$\begin{aligned} \frac{\mathrm{d}p}{\mathrm{d}t} &= q\boldsymbol{E} = qE\hat{\boldsymbol{y}}, \\ \frac{\mathrm{d}\gamma mc^2}{\mathrm{d}t} &= \boldsymbol{v}\cdot(q\boldsymbol{E}). \end{aligned} \tag{3.114}$$

The motion takes place in the plane containing $\boldsymbol{E}$ and the initial velocity $\boldsymbol{v}_0$. We suppose that this plane is the x-y plane. Then, $v_z = 0$ at all times. It is easy to solve for the momentum:

$$\begin{aligned} p_x &= p_{0x}, \\ p_y &= p_{0y} + qEt. \end{aligned} \tag{3.115}$$

The Lorentz factor follows as

$$\gamma mc^2 = \sqrt{m^2c^4 + c^2p_{0x}^2 + c^2(p_{0y}+qEt)^2}, \tag{3.116}$$

and the velocity as

$$\begin{aligned} \frac{v_x}{c} &= \frac{p_{0x}c}{\sqrt{m^2c^4 + c^2p_{0x}^2 + c^2(p_{0y}+qEt)^2}}, \\ \frac{v_y}{c} &= \frac{(p_{0y}+qEt)c}{\sqrt{m^2c^4 + c^2p_{0x}^2 + c^2(p_{0y}+qEt)^2}}. \end{aligned} \tag{3.117}$$

We stress that even if there is no force along x, the x-component of the velocity is affected through the coupling by the Lorentz factor, and shrinks toward zero as v_y reaches the speed of light[n].

The position can be obtained as

$$\begin{aligned} x &= \frac{p_{0x}c}{qE}\operatorname{argsh}\left\{\frac{c(p_{0y}+qEt)}{\sqrt{m^2c^4+c^2p_{0x}^2}}\right\}, \\ y &= \frac{1}{qE}\sqrt{m^2c^4 + c^2p_{0x}^2 + c^2(p_{0y}+qEt)^2}, \end{aligned} \tag{3.119}$$

and the trajectory is given by

$$y = \frac{\sqrt{m^2c^4+c^2p_{0x}^2}}{qE}\cosh\left\{\frac{qE}{p_{0x}c}x\right\}. \tag{3.120}$$

[n] And indeed, the equations of motion can be rearranged to give (in the general case):

$$\frac{\mathrm{d}\boldsymbol{v}}{\mathrm{d}t} = \frac{q}{m}\sqrt{1-\frac{v^2}{c^2}}\left[\boldsymbol{E} + \boldsymbol{v}\wedge\boldsymbol{B} - \frac{1}{c^2}(\boldsymbol{v}\cdot\boldsymbol{E})\boldsymbol{v}\right]. \tag{3.118}$$

3.B.2 Constant magnetic field

We assume that the particle moves in a constant magnetic field $\boldsymbol{B} = B\hat{\boldsymbol{z}}$. The equations of motion are:

$$\begin{aligned} \frac{\mathrm{d}\boldsymbol{p}}{\mathrm{d}t} &= q\boldsymbol{v} \wedge \boldsymbol{B}, \\ \frac{\mathrm{d}\gamma mc^2}{\mathrm{d}t} &= \boldsymbol{v} \cdot [q\boldsymbol{v} \wedge \boldsymbol{B}] = 0. \end{aligned} \tag{3.121}$$

The discussion of Sect. 3.6 then easily follows.

3.B.3 Constant electric and magnetic fields, non-relativistic case

We assume that the particle moves in a constant magnetic field $\boldsymbol{B} = B\hat{\boldsymbol{z}}$ and a constant electric field $\boldsymbol{E} = E_z\hat{\boldsymbol{z}} + E_y\hat{\boldsymbol{y}}$, and we neglect relativistic effects.

In the non-relativistic case, the velocity components are not coupled via the Lorentz factor. It follows that the motion along $\boldsymbol{B}$ is not affected by the magnetic field, and consists in a constant acceleration:

$$v_z = (qE_z/m)t. \tag{3.122}$$

The motion in the plane normal to $\boldsymbol{B}$ is obtained with simple algebra. If we choose the x-axis to be directed along the initial velocity vector, we have (Landau and Lifshitz 1975):

$$\begin{cases} v_x = a\cos\omega t + \dfrac{E_y}{B}, \\ v_y = -a\sin\omega t, \end{cases} \tag{3.123}$$

$$\begin{cases} x = \dfrac{a}{\omega}\sin\omega t + \dfrac{E_y}{B}t, \\ y = \dfrac{a}{\omega}(\cos\omega t - 1). \end{cases} \tag{3.124}$$

Here $\omega = |q|B/m$, and a is linked to the initial x-velocity by $v_{x0} = a + E_y/B = a[1 + E_y/(aB)]$. These equations can be normalized to

$$\begin{cases} \tilde{x} = \dfrac{\omega}{|a|}x = \mathrm{sgn}(a)\sin\tilde{t} + \alpha\tilde{t}, \\ \tilde{y} = \dfrac{\omega}{|a|}y = \mathrm{sgn}(a)(\cos\tilde{t} - 1), \end{cases} \tag{3.125}$$

where we defined $\tilde{t} = \omega t$ and $\alpha = E_y/(|a|B)$. We further define $f = \mathrm{sgn}(a)\alpha$, with $\mathrm{sgn}(a)$ the sign of a. We have:

$$f = \frac{E_y}{aB} = \frac{v_{E\times B}}{v_{x0} - v_{E\times B}}, \tag{3.126}$$

with $v_{E\times B} = |E_y/B|$. f, or equivalently the ratio $v_{0x}/v_{E\times B}$, is the only parameter controlling the problem. There are two families of motion: with closed loops (i.e., v_x changes sign), or without closed loops. They are delimited by three limiting cases: the straight line where the Lorentz force always vanishes, the circle, and the trajectory with angular points. These cases, as well as the ranges in which they occur, are drawn in Fig. 3.5.

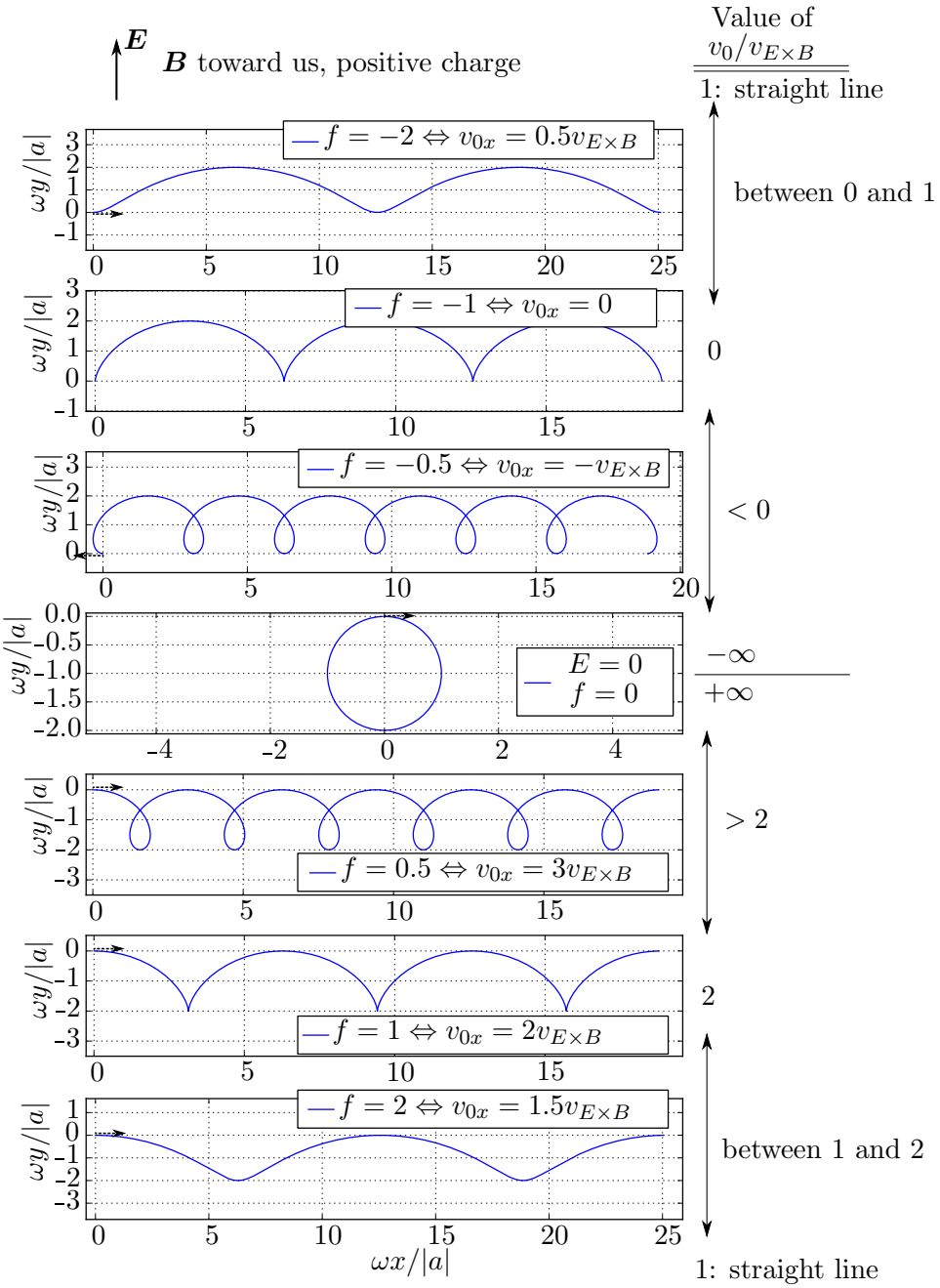

Figure 3.5: Different kind of motions for a non-relativistic particle in constants $\boldsymbol{E}$ and $\boldsymbol{B}$ fields. We have $\boldsymbol{B} \propto +\hat{\boldsymbol{z}}$, $\boldsymbol{E} \propto +\hat{\boldsymbol{y}}$, $\boldsymbol{v}_0 \propto \pm\boldsymbol{x}$, and the motion is drawn in the plane perpendicular to $\boldsymbol{B}$.

3.B.4 Constant and parallel electric and magnetic fields

Let $\boldsymbol{B}$, $\boldsymbol{E} \propto \hat{\boldsymbol{z}}$. The equations of motion are

$$\begin{aligned} \frac{\mathrm{d}\boldsymbol{p}}{\mathrm{d}t} &= q(E\hat{\boldsymbol{z}} + \boldsymbol{v} \wedge [B\hat{\boldsymbol{z}}]), \\ \frac{\mathrm{d}\gamma mc^2}{\mathrm{d}t} &= \boldsymbol{v} \cdot qE\hat{\boldsymbol{z}} = qEv_z. \end{aligned} \tag{3.127}$$

The momentum equation can be decomposed into parallel and perpendicular components: $\mathrm{d}p_z/\mathrm{d}t = qE$ and $\mathrm{d}\boldsymbol{p}_\perp/\mathrm{d}t = qB\boldsymbol{v}_\perp \wedge \hat{\boldsymbol{z}}$. We thus have $\boldsymbol{p}_\perp \cdot \mathrm{d}\boldsymbol{p}_\perp/\mathrm{d}t = 0$, and:

$$\begin{aligned} p_z(t) &= qEt + p_{z0}, \\ |\boldsymbol{p}_\perp| &= \text{const}. \end{aligned} \tag{3.128}$$

The Lorentz factor follows as

$$\gamma mc^2 = \sqrt{m^2c^4 + |\boldsymbol{p}_0 c|^2 + (qEct)^2}. \tag{3.129}$$

The motion is thus accelerated along z. In the plane perpendicular to $\boldsymbol{B}$, we can expect the particle to follow circles with a pulsation

$$\omega = \frac{qB}{\gamma m} = \frac{qBc}{\sqrt{m^2c^2 + |\boldsymbol{p}_0|^2 + (qEt)^2}}, \tag{3.130}$$

that decreases toward 0[o], and with a radius

$$r_\mathrm{c} = \frac{v_\perp}{\omega} = \frac{p_\perp}{qB/m} = \text{const} \tag{3.131}$$

that is constant. Landau and Lifshitz (problem 1, §22, 1975) show that this is indeed the case.

3.B.5 Constant and orthogonal electric and magnetic fields of equal magnitude

The motion of a charged particle in orthogonal magnetic and electric fields is treated in the general case (relativistic or not) in Sect. 3.B.6, but the special situation where $E = cB$ has to be considered separately.

Let us assume that $\boldsymbol{B} = B\hat{\boldsymbol{z}}$ and $\boldsymbol{E} = E\hat{\boldsymbol{y}}$, with $E = cB$. We obviously have $p_z = \text{const}$. The energy equation, $\mathrm{d}(\gamma mc^2)/\mathrm{d}t = qEv_y$, and the x-momentum equation, $\mathrm{d}p_x/\mathrm{d}t = qEv_y$, can be combined to yield $\gamma mc^2 - cp_x = \text{const} \equiv \alpha$. We also define $\epsilon^2 = m^2c^4 + c^2p_z^2 = \text{const}$. Skipping details (see Landau and Lifshitz 1975, problem 2, §22) we arrive at the following set of parametric equations (the parameter is p_y):

$$2qEt = \left(1 + \frac{\epsilon^2}{\alpha^2}\right) p_y + \frac{c^2}{3\alpha^2} p_y^3, \tag{3.132a}$$

$$\gamma mc^2 = \frac{\alpha}{2} + \frac{c^2p_y^2 + \epsilon^2}{2\alpha}, \tag{3.132b}$$

$$x = \frac{c}{2qE}\left(-1 + \frac{\epsilon^2}{\alpha^2}\right) p_y + \frac{c^3}{6\alpha^2 qE} p_y^3, \tag{3.132c}$$

$$y = \frac{c^2}{2\alpha qE} p_y^2, \tag{3.132d}$$

$$z = \frac{p_z c^2}{\alpha qE} p_y. \tag{3.132e}$$

[o] As in the case with an electric field alone, coupling through the Lorentz factor freezes the motion in the directions perpendicular to $\boldsymbol{E}$.

From the first equation, we see that the parameter p_y always increases with time. There is no $E \times B$ ($\propto x$) drift here: y increases indefinitely, and there is no constant mean velocity for x (there is not even a period to average over). We note however that the velocity increases more along x than along y.

3.B.6 Constant and orthogonal electric and magnetic fields of arbitrary magnitude

The non-relativistic description of the motion of a particle in orthogonal magnetic and electric fields leads to a mean velocity equal to $v_{E\times B} = E/B$, and is obviously valid only if $E/B \ll c$. We now describe the general case.

We start from a frame $\mathcal{R}$ where the fields are given by $\boldsymbol{B} = B\hat{\boldsymbol{z}}$ and $\boldsymbol{E} = E\hat{\boldsymbol{y}}$. We want to move to a frame $\mathcal{R}'$ where either $\boldsymbol{E}$ or $\boldsymbol{B}$ vanishes. But the Lorentz invariants of the electromagnetic field are:

$$\boldsymbol{E} \cdot \boldsymbol{B} = \text{inv}, \tag{3.133a}$$

$$c^2\boldsymbol{B}^2 - \boldsymbol{E}^2 = \text{inv}. \tag{3.133b}$$

From Eq. 3.133a, we see that this is possible only if $\boldsymbol{E}\cdot\boldsymbol{B} = 0$ in the original frame, while from Eq. 3.133b we see that this is possible only if $E \neq cB$ in the original frame. Consequently, we assume that $E \neq cB$ and $\boldsymbol{E} \cdot \boldsymbol{B} = 0$. The special case $E = cB$ and $\boldsymbol{E} \cdot \boldsymbol{B} = 0$ is dealt with in section 3.B.5.

We note all quantities in $\mathcal{R}'$ with a prime. For a boost along x, with a velocity $\boldsymbol{v}^*$ and associated Lorentz factor γ^*, the transformation formula read:

$$\begin{aligned} &E'_x = E_x, \quad E'_y = \gamma^*(E_y - v^*B_z), \qquad E'_z = \gamma^*(E_z + v^*B_y), \\ &B'_x = B_x, \quad B'_y = \gamma^*(B_y + v^*E_z/c^2), \quad B'_z = \gamma^*(B_z - v^*E_y/c^2), \end{aligned} \tag{3.134}$$

and in our case:

$$\begin{aligned} &E'_x = 0, \quad E'_y = \gamma^*(E_y - v^*B_z), \quad E'_z = 0, \\ &B'_x = 0, \quad B'_y = 0, \qquad\qquad\quad B'_z = \gamma^*(B_z - v^*E_y/c^2). \end{aligned} \tag{3.135}$$

There are clearly two situations: when $E < cB$, there is no boost allowing to cancel the magnetic field, but $v^* = E/B$ allows to cancel the electric field; while when $E > cB$, there is no boost allowing to cancel the electric field, but $v^* = c^2B/E$ allows to cancel the magnetic field. The different outcomes are illustrated in Fig. 3.2.

Electric field smaller than the magnetic field, $E < cB$

If $E < cB$, then we can choose $\boldsymbol{v}^* = E_y/B_z\hat{\boldsymbol{x}} = \boldsymbol{E} \wedge \boldsymbol{B}/B^2$. In this frame, the electric field vanishes:

$$\boldsymbol{E}' = 0, \quad \boldsymbol{B}' = \hat{\boldsymbol{z}}\,\frac{B_z}{\gamma^*}. \tag{3.136}$$

The motion in $\mathcal{R}'$ thus occurs in a constant magnetic field and was treated in Sect. 3.B.2. The particle energy is constant, $\gamma' mc^2 = \text{const}$, the impulsion along z' is constant, and so is the z'-velocity. In the x'-y' plane, the particle

gyrates in circles with a pulsation $\omega_c' = |q|B_z'/(\gamma' m)$:

$$\begin{cases} x' = \dfrac{v_\perp'}{\omega_c'} \sin \omega_c' t', \\ y' = \dfrac{v_\perp'}{\omega_c'} (\cos \omega_c' t' - 1), \\ z' = v_z'(0) t', \end{cases} \qquad \begin{cases} \dfrac{\mathrm{d}x'}{\mathrm{d}t'} = v_\perp' \cos \omega_c' t', \\ \dfrac{\mathrm{d}y'}{\mathrm{d}t'} = -v_\perp' \sin \omega_c' t', \\ \dfrac{\mathrm{d}z'}{\mathrm{d}t'} = v_z'(0). \end{cases} \tag{3.137}$$

In order to obtain the motion in the initial frame $\mathcal{R}$, we have to transform the trajectory back to $\mathcal{R}$. It is easier to perform the Lorentz transformation on the four velocity, which is (with $\tau = t'/\gamma'$ the proper time of the particle):

$$\begin{cases} c\dfrac{\mathrm{d}t'}{\mathrm{d}\tau} = \gamma' c \\ \dfrac{\mathrm{d}x'}{\mathrm{d}\tau} = \gamma' v_\perp' \cos \omega_c' \gamma' \tau, \\ \dfrac{\mathrm{d}y'}{\mathrm{d}\tau} = -\gamma' v_\perp' \sin \omega_c' \gamma' \tau, \\ \dfrac{\mathrm{d}z'}{\mathrm{d}\tau} = \gamma' v_z'(0), \end{cases} \tag{3.138}$$

and that transforms into (boost at $-v^*$ along x):

$$\begin{cases} \gamma c = \gamma^* \left(\gamma' c + \dfrac{v^*}{c} \dfrac{\mathrm{d}x'}{\mathrm{d}\tau} \right), \\ \dfrac{\mathrm{d}x}{\mathrm{d}\tau} = \gamma^* \left(\dfrac{\mathrm{d}x'}{\mathrm{d}\tau} + v^* \gamma' \right), \\ \dfrac{\mathrm{d}y}{\mathrm{d}\tau} = \dfrac{\mathrm{d}y'}{\mathrm{d}\tau}, \\ \dfrac{\mathrm{d}z}{\mathrm{d}\tau} = \dfrac{\mathrm{d}z'}{\mathrm{d}\tau}, \end{cases} \tag{3.139}$$

or equally:

$$\begin{cases} \gamma c = c\dfrac{\mathrm{d}t}{\mathrm{d}\tau} = \gamma^* \left(\gamma' c + \dfrac{v^*}{c} \gamma' v_\perp' \cos(\omega_c' \gamma' \tau) \right), \\ \dfrac{\mathrm{d}x}{\mathrm{d}\tau} = \gamma^* \left(\gamma' v_\perp' \cos(\omega_c' \gamma' \tau) + v^* \gamma' \right), \\ \dfrac{\mathrm{d}y}{\mathrm{d}\tau} = -\gamma' v_\perp' \sin(\omega_c' \gamma' \tau), \\ \dfrac{\mathrm{d}z}{\mathrm{d}\tau} = \gamma' v_z'(0). \end{cases} \tag{3.140}$$

The position of the particle as a function of proper time is easily deduced:

$$\begin{cases} x(\tau) = \dfrac{\gamma^* v_\perp'}{\omega_c'} \sin(\omega_c' \gamma' \tau) + (\gamma^* \gamma' v^*) \tau, \\ y(\tau) = \dfrac{v_\perp'}{\omega_c'} \left(\cos(\omega_c' \gamma' \tau) - 1 \right), \\ z(\tau) = \gamma' v_z'(0)\, \tau. \end{cases} \tag{3.141}$$

Written like this, we see that the motion can be decomposed as the sum of

- a translation with respect to proper time in the x direction, which corresponds to the $\boldsymbol{E} \wedge \boldsymbol{B}$ direction,

- an elliptical gyration in the x-y plane (and not circular as in the non-relativistic case),
- a constant motion with respect to proper time in the z direction if the particle has an initial velocity in this direction.

However, the proper time is linked to the time t in a non-trivial way by the upper line in Eq. 3.140, that integrates into

$$t = (\gamma^*\gamma')\tau + \frac{\gamma^* v^* v'_\perp}{\omega'_c c^2} \sin(\omega'_c \gamma' \tau). \tag{3.142}$$

The motion is thus more complex, and reads:

$$\begin{cases} x(t) = \dfrac{v'_\perp}{\gamma^* \omega'_c} \sin[\omega'_c \gamma' \tau(t)] + v^* t, \\ y(t) = \dfrac{v'_\perp}{\omega'_c} \left(\cos[\omega'_c \gamma' \tau(t)] - 1\right), \\ z(t) = \dfrac{v'_z(0)}{\gamma^*} t - \dfrac{v'_z(0) v^* v'_\perp}{\omega'_c c^2} \sin[\omega'_c \gamma' \tau(t)]. \end{cases} \tag{3.143}$$

It is interesting to see that the drift velocity in the $\boldsymbol{E} \wedge \boldsymbol{B}$ direction is given by $v^* = E_y/B_z$, just as in the non-relativistic case.

If we neglect for a moment the term proportional to sinus in the proper time expression 3.142, and use simply $t = (\gamma^*\gamma')\tau$ (and equivalently $\gamma = \gamma'\gamma^*$), we have:

$$\begin{cases} x(t) = \dfrac{v'_\perp}{\gamma^* \omega'_c} \sin\left(\dfrac{qB'}{\gamma mc} t\right) + v^* t, \\ y(t) = \dfrac{v'_\perp}{\omega'_c} \left[\cos\left(\dfrac{qB'}{\gamma mc} t\right) - 1\right], \\ z(t) = \dfrac{v'_z(0)}{\gamma^*} t, \end{cases} \tag{3.144}$$

and we conclude in the same way as after Eq. 3.141: translation at the $\boldsymbol{E} \wedge \boldsymbol{B}/B^2$ velocity, plus elliptical motion in the x-y plane, plus translation along $\boldsymbol{B} \propto \hat{\boldsymbol{z}}$ due to the initial velocity. But in general there is the sinusoidal term appearing in the expression for τ. We thus expect the particle to describe the ellipses in the x-y plane with a non-uniform velocity, and the motion along z to be not constant, despite the absence of force in this direction, because of the coupling with γ.

When E_y increases toward cB_z, the velocity $v^* = E_y/B_z$ reaches c and γ^* reaches infinity. What happens can be visualized by studying the minor and major axes of the ellipse:

- Along x, it is $v'_\perp/(\gamma^*\omega'_c) = v'_\perp/\omega_c$ (because $B'_z = B_z/\gamma^*$). As E_y increases toward cB_z, nothing happens.
- Along y, it is $v'_\perp/\omega'_c = \gamma^* v'_\perp/\omega_c$. As E_y increases toward cB_z, $\gamma^* \to +\infty$, and the axis length also reaches infinity. Physically, the magnetic field has more and more difficulties to contain the electric acceleration along y, so that the ellipse is wider and wider in the direction of $\boldsymbol{E}$.

When E_y reaches cB_z, the magnetic field $B'_z = B_z/\gamma^*$ vanishes, and as we said the ellipse extends to infinity along the direction of $\boldsymbol{E}$ (which is y): the motion is not confined any more in the y direction. We showed in

Sect. 3.B.5 that when $E = B$, the motion is indeed open, and the particle is freely accelerated by the electric field and endlessly gains energy. The case $E_y > cB_z$ is discussed just after. Trajectories for $E < cB$ and $E > cB$ are shown in Fig. 3.2.

Electric field larger than the magnetic field, $E > cB$

We now assume that $E_y > cB_z$. The situation is different because there is no frame in which E_y vanishes. However, in a frame $\mathcal{R}'$ moving at velocity $\boldsymbol{v}^* = c^2 B_z/E_y\,\hat{\boldsymbol{x}} = c^2 \boldsymbol{E}\wedge\boldsymbol{B}/E^2$, we have (from Eq. 3.135):

$$\boldsymbol{E}' = \hat{\boldsymbol{y}}\,\frac{E_y}{\gamma^*}, \qquad \boldsymbol{B}' = 0. \tag{3.145}$$

In the new frame, the motion is that of a particle in a constant electric field, treated in Sect. 3.B.1. We have:

$$\begin{cases} p'_x = p'_{0x}, \\ p'_y = p'_{0y} + qE'_y t', \\ p'_z = p'_{0z}. \end{cases} \tag{3.146}$$

The Lorentz factor follows as

$$\gamma'(t')mc^2 = \sqrt{\epsilon_0^2 + c^2(p'_{0y} + qE'_y t')^2}, \tag{3.147}$$

with $\epsilon_0^2 = m^2c^4 + c^2{p'_{0x}}^2 + c^2{p'_{0z}}^2$, and the velocity as $\boldsymbol{v}' = \boldsymbol{p}'/(\gamma' m)$. The position can then be deduced, and the trajectory is found to be of the kind $y' \propto \cosh x'_\perp$, as in Eq. 3.120, with $x_\perp = \sqrt{x^2+z^2}$.

We now transform the four momentum back to the initial frame, with a boost at $-\boldsymbol{v}^*$:

$$\begin{cases} \gamma mc = \gamma^*[\gamma' mc + (v^*/c)p'_x], \\ p_x = \gamma^*[p'_x + (v^*/c)\gamma' mc], \\ p_y = p'_y, \\ p_z = p'_z. \end{cases} \tag{3.148}$$

Replacing by the values for primed quantities, this gives:

$$\begin{cases} \gamma = \gamma^*\gamma' + \gamma^*(v^*/c)p'_{0x}/(mc), \\ p_x = \gamma^*[p'_{0x} + (v^*/c)\gamma' mc], \\ p_y = p'_{0y} + qE'_y t', \\ p_z = p'_{0z}. \end{cases} \tag{3.149}$$

The velocity is then deduced as:

$$\begin{cases} \dfrac{v_x}{c} = \dfrac{p'_{0x} + (v^*/c)\gamma' mc}{(v^*/c)p'_{0x} + \gamma' mc}, \\ \dfrac{v_y}{c} = \dfrac{p'_{0y} + qE'_y t'}{\gamma^*[(v^*/c)p'_{0x} + \gamma' mc]}, \\ \dfrac{v_z}{c} = \dfrac{p'_{0z}}{\gamma^*[(v^*/c)p'_{0x} + \gamma' mc]}. \end{cases} \tag{3.150}$$

For the time we have $\mathrm{d}t/\mathrm{d}\tau = \gamma$, $\mathrm{d}t'/\mathrm{d}\tau = \gamma'$, so that

$$\frac{\mathrm{d}t}{\mathrm{d}t'} = \frac{\gamma}{\gamma'} = \gamma^* + \gamma^*\frac{v^*}{c}\frac{p'_{0x}}{mc}\frac{1}{\gamma'}. \tag{3.151}$$

This integrates to

$$t = \gamma^* t' + \frac{\gamma^* v^* p'_{0x}}{cqE'_y} \operatorname{argsh}\left(\frac{c[p'_{0y} + qE'_y t']}{\epsilon_0}\right). \tag{3.152}$$

The fact that γ' is not constant complicates the arithmetic. In particular, we cannot express simply $\mathrm{d}\boldsymbol{x}/\mathrm{d}\tau$ and perform an integration, because γ' depends on τ. Some remarks are of interest:

- t is a monotonic increasing function of t', so that t' also is a monotonic increasing function of t.
- Consequently, γ' is increasing toward infinity (as a function of t or of t').
- So does γ.
- There is no gyration around $\boldsymbol{B}$, both v_x and v_y never change sign (no turn around as in the $E < cB$ case).
- As t' or $t \to +\infty$,

$$\begin{cases} \dfrac{v_x}{c} \xrightarrow{t\to+\infty} \dfrac{v^*}{c}, \\ \dfrac{v_y}{c} \xrightarrow{t\to+\infty} \dfrac{1}{\gamma^*}, \\ \dfrac{v_z}{c} \xrightarrow{t\to+\infty} 0. \end{cases} \tag{3.153}$$

  In the limit of $B_z = 0$, we have $v^* = 0$ and $\gamma^* = 1$, so that at long times $\boldsymbol{v} = c\hat{\boldsymbol{y}}$, which is what we found for a particle in a constant electric field (Sect. 3.B.1). When $B_z \neq 0$, the norm of the asymptotic velocity is still $v^{*2} + c/\gamma^{*2} = c$, but its direction is not that of the electric field. The particle velocity reaches a steady state where the magnetic force $\boldsymbol{v} \wedge \boldsymbol{B}$ compensates the electric force, and travel with an angle with respect to the electric field given by $\arctan v_y/v_x$.

All in all, the magnetic field is not strong enough to transform the trajectory into loops, and the long term motion is a straight line (see Fig. 3.2) at the speed of light, with an angle θ with respect to the electric field direction given by

$$\tan\theta = \gamma^* v^*/c. \tag{3.154}$$

Chapter 4

Presentation and tests of the particle-in-cell code `Apar-T`

Mais cette petite lacune, cette petite brèche, suffit pour que toute cette infinie unité de lois de l'univers soit détruite et remise en question.

Hermann Hesse, *Siddhartha*

Contents

4.1 Outline

This chapter *documents* and *tests* the particle-in-cell code, `Apar-T`, that is used in Chapters 6 and 7 to study magnetic reconnection. It contains part of the article Melzani et al. (2013) (the other part being in the next chapter).

The first version of `Apar-T`, Tristan, was written by O. Buneman in 1990 (Matsumoto and Omura 1993). It was then made parallel by Messmer (2001), and used in Messmer (2002) or Paesold et al. (2005). We largely modified its structure, that now uses Fortran modules and allows for more flexibility, including the possibility of switching between different initial conditions or boundaries by changing entries in a configuration textfile. We adapted outputs and diagnostics to be efficient on large scale runs, the main novelties being parallel outputs in `HDF5` format readable by the visualization software `VisIt`, and the possibility to track a sample of particle trajectories. The code has been run on several machines, using up to 2000 cores.

In this chapter, we first provide a detailed description of `Apar-T` in Sect. 4.3 and Appendix 4.A. This description is motivated by the need for a deep understanding of simulation methods to interpret their results, as is the case for the test problems shown here, and also by the large number of different PIC implementations available.

Then in Sect. 4.4, we present a set of test problems and the results obtained with `Apar-T`. The first test is the study of the fluctuation spectra of a thermal plasma. The second and third tests explore the linear and nonlinear stages of the filamentation instability. A last test is the computation of the linear growth rates of the relativistic tearing instability. Further discussion of the results are presented in Chapter 5, where differences between real, Vlasov, and PIC plasmas are stressed and investigated.

The introduction first puts PIC codes in a historical perspective, and evoke alternatives to the PIC method for kinetic simulations.

4.2 Introduction

4.2.1 A historical perspective on particle-in-cell codes

Full particle codes are now used by a large number of groups worldwide to study plasmas out-of-equilibrium in a large variety of environments, including electronic devices, inertial fusion (Dieckmann et al. 2006; Bret et al. 2010), tokamaks, Earth and solar magnetospheres (Hesse et al. 2001; Daughton et al. 2006; Drake et al. 2006; Klimas et al. 2008; Markidis et al. 2012; Baumann and Nordlund 2012), or high-energy astrophysics (Silva et al. 2003; Pétri and Lyubarsky 2007; Zenitani and Hoshino 2008; Cerutti et al. 2012a; Jaroschek et al. 2005; Nishikawa et al. 2008; Sironi and Spitkovsky 2011b).

Particle simulations actually appeared along with the first computers at universities and in industry around 1950. They first concerned electron beams in vacuum tubes, a device extensively used in the computers themselves. The simulated beams were cold (Hartree 1950) or later hot (Tien and Moshman 1956), and consisted of roughly 300 electron slabs moving in one dimension.

The step to plasma simulations was taken by Buneman (1959). He simulated an electrostatic plasma of 512 ions and electrons in one dimension, and showed that particle codes could be used to study the linear, nonlinear, and saturation phases of instabilities. At the time, the relevance of simulations with so few particles per Debye sphere was not clear and in 1962 Dawson (1962) and Eldridge and Feix (1962) made an important contribution by showing that correct thermal behavior was produced.

All these algorithms used particle-particle interactions, and the first particle-mesh codes to introduce a grid appeared only later (Burger 1965; Hockney 1966; Yu et al. 1965). A great deal of literature on the drawbacks and benefits of the grid then appeared, and is now mostly concentrated in the two reference books of Birsdall and Langdon (1985) and Hockney and Eastwood (1988). Refinements of the algorithms quickly appeared (higher order grid interpolation, quiet codes, etc.), as well as code optimizations, at a time when programs were written in assembly language and depended heavily on machine architecture. Fully electromagnetic, relativistic, and 3D codes appeared with the studies of laser induced fusion (Buneman 1976), and closely resemble today's codes.

In 1967, it was possible for Birdsall (1967) to list the papers concerning simulations, and he noticed that they had grown exponentially since 1956. In 1956, "many particles" meant 300; in 1985, 10^6; in 2008, 10^9; and in 2012, 10^{12}. For more historical details on PIC simulations, one may consult Birdsall (1967, 1999), Hockney and Eastwood (Sect. 9.1, 1988), or the introduction of Birsdall and Langdon (1985).

Today, the latest generation of PIC algorithms consists of large versatile codes, featuring high order integration schemes and efficient parallelization. We can quote codes such as TRISTAN-MP (Spitkovsky 2005), OSIRIS (Fonseca et al. 2002, 2008), VORPAL (Nieter and Cary 2004), WARP (Grote et al. 2005), ALaDyn (Benedetti et al. 2008), iPIC3D (Markidis et al. 2010), Photon-Plasma (Haugboelle et al. 2012), or Zeltron (Cerutti et al. 2013). They employ various simulation methods. The equations solved can differ: electrostatic codes, electromagnetic codes, Darwin approximation (Huang and Ma 2008). The integration scheme can also vary: integration directly on the fields staggered on a grid, either with a charge conserving scheme or via solution of Poisson equation (Cerutti et al. 2012a); or integration of the potential and correction of the discrepancies to charge conservation (Daughton et al. 2006). The time integration can be explicit or implicit (Markidis et al. 2012). Special parts of the numerical scheme can also differ; for example, the order of the field integration or the use of Fourier transforms. The interpolation of particle quantities to grid points and reciprocally can be done by a nearest grid point method (NGP), by a linear weighting (cloud in cell (CIC), or the PIC algorithm in the old terminology), or by a smoother shape (spline interpolation, Esirkepov 2001).

4.2.2 Numerical methods to simulate a kinetic plasma

The particle-in-cell method is not the only method to simulate a plasma at the kinetic level. We now briefly outline others.

Vlasov codes

Vlasov codes directly integrate numerically Vlasov's equation, along with the required Maxwell's equations. Space and velocities are both discretized on a grid, where the distribution function of each species s, denoted by $f_s(\boldsymbol{x}_{ijk}, \boldsymbol{p}_{lmn}, t_q)$, is stored and evolved. The electromagnetic fields are stored on the space grid only. There is also the possibility to add a collision operator to the right-hand side of Vlasov's equation.

Various numerical scheme exist, and can employ usual finite volume or finite element methods. Another possibility is to write Vlasov's equation in

a conservation form[a]:

$$\frac{\partial f_s}{\partial t} + \frac{\partial}{\partial \boldsymbol{x}} \cdot (\boldsymbol{v} f_s) + \frac{\partial}{\partial \boldsymbol{p}} \cdot (\boldsymbol{F} f_s) = 0, \tag{4.1}$$

which implies that along trajectories satisfying $\dot{\boldsymbol{x}}(t) = \boldsymbol{v}(t)$ and $\dot{\boldsymbol{p}}(t) = (q_s/m_s)(\boldsymbol{E}(\boldsymbol{x}, t) + \boldsymbol{v}(t) \wedge \boldsymbol{B}(\boldsymbol{x}, t))$, one has $f_s(\boldsymbol{x}(t), \boldsymbol{v}(t), t) = \text{const}$. The method is then, at each timestep and for each grid point, to compute where the position $\boldsymbol{x}_{ijk}$ and momentum $\boldsymbol{p}_{lmn}$ will be after δt according to the equation of motion. This generally gives new values $\boldsymbol{x}$ and $\boldsymbol{p}$, that are interpolated on the grid. The former value $f_s(\boldsymbol{x}_{ijk}, \boldsymbol{p}_{lmn})$ is then attributed with a weight function to these new grid points.

Unlike PIC simulations, Vlasov solvers present a very low level of noise, and are thus efficient for the study of linear phases of instabilities or of low-amplitude effects. They are also suited for cases where a small number of particles in the tail of the distribution plays an important role, where a PIC code would require huge amounts of particles to correctly sample such a distribution function.

Their main drawback is the ressources they demand. Three-dimensional simulations require the description of a six-dimensional phase space: assuming for example 100 points for each direction, this makes 10^{12} grid points! Even two-dimensional simulations are very demanding.

There are a number of Vlasov simulations of magnetic reconnection. For example Schmitz and Grauer (2006) study the same configuration as Pritchett (2001, GEM configuration with a PIC code) with a Darwin Vlasov code, and Umeda et al. (2009) present a fully electromagnetic Vlasov code with a comparison with the two preceding papers.

Gyrokinetic codes

Gyrokinetic codes are a variant of Vlasov codes, applicable when the magnetic field is strong everywhere, when the dynamics is slow compared to cyclotron motion (ionic and electronic), and when fluctuation amplitudes are small. When it is so, Vlasov's equation is averaged over the cyclotron orbits of the particles. It then describes the evolution of a distribution function with one variable less than for f_s. The variables can be for example the position, the kinetic energy, and the pitch angle (the angle between the velocity vector and the magnetic field).

The advantage over Vlasov codes is that the averaging reduces the phase space from one dimension. The advantage over PIC codes is that the latters need to resolve the Larmor orbits, a constraint that can be very demanding at high magnetizations. For example, kinetic simulations of magnetic reconnection in environments such as pulsar wind nebulae, where the electron magnetization reaches 10^5, are not possible with PIC codes. Note that at such magnetizations, relativistic effects are present and a relativistic gyrokinetic code should be used.

There exists several studies of collisionless magnetic reconnection with gyrokinetic codes. An instructive comparison with PIC simulations can be found in TenBarge et al. (2014).

[a] We note $\boldsymbol{p} = \gamma \boldsymbol{v}$, and define $\boldsymbol{F} \equiv (q_s/m_s)(\boldsymbol{E} + \boldsymbol{v} \wedge \boldsymbol{B})$. Equation 4.1 is equivalent to Vlasov's equation because $\boldsymbol{\nabla}_{\boldsymbol{p}} \cdot (\boldsymbol{E} + \boldsymbol{v} \wedge \boldsymbol{B}) = 0$, even in the relativistic case.

Particle-particle codes

In a particle-particle code, the plasma is described by an ensemble of particles, of positions $\boldsymbol{x}_i$ and velocities $\boldsymbol{v}_i$. At each timestep, the electrostatic force acting on a particle is obtained by summation over all the other particles. For example, for the electric potential at the position of particle i:

$$V_i = \sum_{j \neq i} \frac{q_i q_j}{4\pi\epsilon_0 |\boldsymbol{x}_i - \boldsymbol{x}_j|}, \tag{4.2}$$

and the equation of motion of each particle is thus integrated. The fields are not directly present in the simulation, the Lorentz force being directly computed from the other particles.

The main drawback of this method is that the above sum involves N terms, if N is the total number of particles, and thus N^2 terms must be considered when repeating this procedure for each particle. This is way too much when considering numbers as large as $N = 10^9$ or more. Better scalings than N^2 are now obtained by lumping together neighboring particles when computing the force on a particle far away, and such algorithms are still in use to compute gravitational systems. They are, however, not any more in use today in the plasma community, and have been replaced by the particle-in-cell method. Moreover, the absence of cut-off at low interparticle distances do not allow to artificially reduce the collisionality as is the case for the PIC method. This is an advantage to accurately describe particle-particle collisions, but a disadvantage when considering that the number of particles in the simulation is by far smaller than the particle number in real plasmas, thus implying a biased description of collisional phenomena (see Chapter 5).

PIC codes (particle-mesh codes)

Particle-in-cell codes are the focus of this study. Here, the plasma is represented by a collection of particles with continuous positions and velocities, but the electromagnetic fields are discretized on a grid. The charge and current densities are computed from the particles' positions and velocities, by an interpolation onto the grid points. Reciprocally, the Lorentz force acting on the particles is computed by an interpolation from the fields at grid points to the particle exact position. As stated in Sect. 4.2.1, there are several simulation methods (implicit, explicit, staggered grid, and even adaptive grid with dynamical particle splitting).

These codes are the kinetic codes the most used in the astrophysical community. They are efficient because unlike particle-particle codes they involve only local interactions (with the grid), and unlike Vlasov codes they use a 3D grid (and not 6D). Moreover, an explicit PIC code is simple to program, easy to parallelize, and can offer deep physical insights. The main drawbacks are a large noise level because of the small number of particles per cell, and for the same reason, a physics of collisions and correlations enhanced when compared to the real plasma (this is the subject of Chapter 5).

PIC codes can also include radiative braking or collisions. For example Daughton et al. (2009a,b) perform simulations of a Harris current sheet with a PIC code that treats collisions with a Monte-Carlo treatment of the Fokker-Planck collision term. They can probe the collisional Sweet-Parker

regime, and the transition to collisionless reconnection for sheet thickness of the order of kinetic scales.

δf-PIC codes

δf-PIC codes are a variant of PIC codes where the distribution function is split into an equilibrium and a perturbation part: $f = f_0 + \delta f$. The equilibrium part is associated with fields $\boldsymbol{E}_0$ and $\boldsymbol{B}_0$. The evolution of these fields and of f_0 are not computed. The particles are advanced via the Lorentz force with $\boldsymbol{E}_0$ and $\boldsymbol{B}_0$, and they are then advanced into the perturbations $\boldsymbol{E}_1$ and $\boldsymbol{B}_1$, which are themselves computed from the particle motions deviating from equilibrium.

These codes present low noise levels and allow studies of the linear and weakly non-linear phase of instabilities, of Landau damping, echoes, or plasma waves and modes. They can be used in the non-linear stage, but loose their advantages when $\delta f / f_0$ becomes large.

Hybrid PIC codes

A hybrid code uses a kinetic description for one species, and a fluid description for the other. The electrons are most often the fluid species, which is justified when their kinetic effects are negligible. It implies the choice of a fluid closure for the fluid species, and of a numerical integration scheme.

The advantage is most stringent when electrons and ions behave on very different time and space scales. The disadvantage is that a possible high-energy electron population cannot be taken into account, and cannot provide a back-reaction. This is an issue in relativistic reconnection where the study of the high-energy electron tails is of high interest.

Aunai et al. (2013) provide a comparison between PIC and hybrid simulations of non-relativistic magnetic reconnection in asymmetric Harris current sheets.

4.3 Physical model and numerical implementation

This section presents the numerical scheme used in `Apar-T`. Broadly speaking, `Apar-T` is a parallel electromagnetic relativistic 3D PIC code with a staggered grid, where the fields are integrated via Faraday and Maxwell-Ampère equations, currents are computed by charge conserving volume weighting (CIC), and fields are interpolated with the same CIC volume weighting method.

4.3.1 The PIC plasma

The code simulates the time-evolution of charged particles under the action of the electromagnetic fields that they generate, and the evolution of these fields.

Plasmas in nature contain millions to tens of billions of particles per Debye sphere, and relevant microphysical phenomena spread over numerous Debye lengths. It is impossible to track these particles one by one. Rather, the numerical particles represent numerous real particles, and are consequently called *superparticles*.

A superparticle represents either p real ions (having then a restmass $m_{\rm sp} = p \times m_{\rm i}$ and a charge $q_{\rm sp} = p \times q_{\rm i}$), or p real electrons (having then a restmass $m_{\rm sp} = p \times m_{\rm e}$ and a charge $q_{\rm sp} = p \times q_{\rm e}$). The ratio of ion to electron charge is always $q_{\rm i}/q_{\rm e} = -1$, while that of their restmasses $m_{\rm i}/m_{\rm e}$ can be freely specified. Pair plasmas can thus be simulated. In `Apar-T` the number of real particles per superparticles p is the same for all superparticles at all times, but other codes can introduce superparticle splitting (Fujimoto and Machida 2006; Haugboelle et al. 2012; Cerutti et al. 2013).

We denote the physical size of a grid cell by X_0, a reference number of superparticles per cell by $\rho^0_{\rm sp}$ (including both ion superparticles and electron superparticles), and its associated number density of electrons by $n^0_{\rm e}$. Initially, the plasma is assumed to be quasi-neutral, in the sense that we load the same number of ion superparticles and electron superparticles in each cell. We have the relation

$$2n^0_{\rm e} \times X_0^3 = \text{number of real particles in one cell} = p \times \rho^0_{\rm sp}. \tag{4.3}$$

The equations governing the superparticle plasma are the equation of motion with the Lorentz force for each superparticle, and Maxwell equations coupled to the superparticle motions by the current:

$$\frac{\mathrm{d}}{\mathrm{d}t}(\gamma_{\rm sp}\boldsymbol{v}_{\rm sp}) = \frac{q_{\rm sp}}{m_{\rm sp}}\left(\boldsymbol{e} + \frac{\boldsymbol{v}_{\rm sp}}{c} \wedge \boldsymbol{b}\right), \tag{4.4a}$$

$$\frac{\mathrm{d}}{\mathrm{d}t}\boldsymbol{x}_{\rm sp} = \boldsymbol{v}_{\rm sp}, \tag{4.4b}$$

$$\frac{\partial \boldsymbol{b}}{\partial t} = -c\,\boldsymbol{\nabla} \wedge \boldsymbol{e}, \tag{4.4c}$$

$$\frac{\partial \boldsymbol{e}}{\partial t} = c\,\boldsymbol{\nabla} \wedge \boldsymbol{b} - \frac{1}{\epsilon_0}\boldsymbol{j}, \tag{4.4d}$$

$$\boldsymbol{j} = \sum_{\rm sp} q_{\rm sp}\boldsymbol{v}_{\rm sp} S(\boldsymbol{x} - \boldsymbol{x}_{\rm sp}). \tag{4.4e}$$

Here, c is the speed of light, $\boldsymbol{e}$ the electric field, $\boldsymbol{b} = c\boldsymbol{B}$ is c times the magnetic field; $q_{\rm sp}$, $m_{\rm sp}$, $\gamma_{\rm sp}$, $\boldsymbol{v}_{\rm sp}$, and $\boldsymbol{x}_{\rm sp}$ are the charge, mass, Lorentz factor, velocity, and position of the superparticle number sp. The fields are stored on a grid, and a consequence is that the superparticles are seen by the grid as having a finite shape S, linked to the interpolation scheme used in the code.

In `Apar-T` we do not integrate the two other Maxwell equations because if they hold initially, then fulfilling the equation of conservation of charge and Eqs. 4.4c and 4.4d at all times insures that they remain correct to round-off errors[b]. That the current is indeed computed in a charge conserving way is detailed in Appendix 4.A.1. Initially, the fields and the charge density are correctly built by setting a magnetic field satisfying $\boldsymbol{\nabla} \wedge \boldsymbol{b} = \mu_0 \boldsymbol{j}$, a null electric field, and by placing the superparticles by pairs with one ion superparticle and one electron superparticle on top of each other so that the charge density is zero.

[b]The proof is as follows. Using Eq. 4.4c, we have $\partial_t \boldsymbol{\nabla}\cdot\boldsymbol{B} = \boldsymbol{\nabla}\cdot\partial_t\boldsymbol{B} = -\boldsymbol{\nabla}\cdot(\boldsymbol{\nabla}\wedge\boldsymbol{E}) = 0$. Using Eq. 4.4d, we have $\partial_t \boldsymbol{\nabla}\cdot\boldsymbol{E} = \boldsymbol{\nabla}\cdot\partial_t\boldsymbol{E} = \boldsymbol{\nabla}\cdot(c^2\boldsymbol{\nabla}\wedge\boldsymbol{B} - \epsilon_0^{-1}\boldsymbol{J}) = -\epsilon_0^{-1}\boldsymbol{\nabla}\cdot\boldsymbol{J}$, so that if the conservation of charge $\partial_t\rho + \boldsymbol{\nabla}\cdot\boldsymbol{J} = 0$ holds, then $\partial_t(\boldsymbol{\nabla}\cdot\boldsymbol{E} - \rho/\epsilon_0) = 0$.

4.3.2 Numerical implementation of `Apar-T`

The need for a deep understanding of simulation methods to interpret their results, as is the case for the test problems of Sect. 4.4, motivated a detailed description of `Apar-T`. This section presents important points. More details (numerical scheme and parallelization efficiency) can be found in Appendix 4.A.

Briefly, the global integration scheme of Eqs. 4.4a-4.4e is a time-centered and time-reversible leap-frog scheme, and is second-order accurate in time and space. The electric and magnetic fields are stored on a staggered Yee lattice, which allows for a simple integration explicit in time of Eqs. 4.4c and 4.4d (without the current). The current is computed with the volume change of the superparticles in the grid cells, and added in a time explicit way to the integration of the electric field (Eq. 4.4d).

Temporal and spatial discretization, normalization

The spatial discretization of the code is $X_0 = d_\mathrm{e}^0/n_x$, a fraction n_x of the electron skin depth $d_\mathrm{e}^0 = c/\omega_\mathrm{pe}^0$, where the electron plasma pulsation is $\omega_\mathrm{pe}^0 = \sqrt{n_\mathrm{e}^0 e^2/(\epsilon_0 m_\mathrm{e})}$, with $-e$ and m_e the electron charge and restmass. The timestep Δt is a fraction n_t of the electron plasma period: $\Delta t = T_\mathrm{pe}^0/n_t$, with $T_\mathrm{pe}^0 = 2\pi/\omega_\mathrm{pe}^0$. We stress that the superscript ^{0} is used for quantities based on the reference density n_e^0.

Spatial quantities are normalized by the cell length X_0, and normalized quantities are then denoted with a tilde. For example, the electron Debye length $\lambda_\mathrm{De}^0 = \sqrt{\epsilon_0 T_\mathrm{e}/(n_\mathrm{e}^0 e^2)} = v_\mathrm{th,e}/\omega_\mathrm{pe}^0$ (with $v_\mathrm{th,e} = \sqrt{T_\mathrm{e}/m_\mathrm{e}}$) has for normalized counterpart $\tilde{\lambda}_\mathrm{De}^0 = \lambda_\mathrm{De}^0/X_0 = n_x v_\mathrm{th,e}/c$.

Superparticle volume

The use of a grid for PIC algorithms implies that the fields are known at grid nodes, and that information relative to the superparticles (charge and current) need to be interpolated on the grid. This interpolation is equivalent to considering the superparticles as clouds of charge of finite extension (Langdon 1970). The shape of the cloud then determines the interpolation formula.

In our case, a superparticle is assumed to be a cube of volume $V_\mathrm{sp} = X_0^3$, and the current it produces is calculated by the change of the volume of the superparticle in the cell containing its center. This interpolation scheme is equivalent to linear weighting (CIC) and is exactly charge conserving. Details of the numerical implementation of the current computation can be found in Appendix 4.A. We discuss the implications of the superparticle finite sizes in Chapter 5.

Particle initialization in momentum space

Several momentum distributions can be loaded: Maxwell-Boltzmann distribution with anisotropic temperature, boosted Maxwell-Boltzmann distribution, waterbag distribution, or Maxwell-Jüttner distribution. We have not found in the literature a method for initializing the Maxwell-Jüttner distribution when both the bulk velocity and the temperature are relativistic, so that we present one in Sect. 3.8.

Input, output, and data analysis

Data output and data analysis can be very time consuming for large scale simulations. To reduce data storage and writing time, we implemented parallel output in `HDF5` format[c]. Files are written according to the .h5part format, and can be read by the advanced visualization and data-analysis software `VisIt` (Childs et al. 2012), which is fully parallel, but also by a reader in Python. The .h5part files can either contain the whole simulation data, and then be used to restart the simulation, or be lighter with only a fraction of the particles. These lighter files then include cell-averaged quantities related to the particles, such as the mean particle velocity or number, temperature, highest energy, etc.

We implemented the `VisIt` Libsim in situ library (Whitlock et al. 2011) into `Apar-T`. In this way, `VisIt` is able to connect to the simulation while it is running and to access the solver's data at the current timestep. It can then perform data visualization and data analysis without the need to write data on the hard drive. This feature is fully parallelized, by exploiting the data-distribution model of the code, and as such is not restricted to the current parallelization model. It allows the data-IO from memory to hard drive – which is a major reason for slow-down of simulations using big data-sets – to be significantly reduced. For example, a volume-rendering of 3D data performed in situ takes less time than dumping 10 GB of data to the disk. `VisIt` in situ is also well suited to monitor ongoing simulations and to single-step through the execution and is, in this way, of great help for debugging.

Finally, a set of test problems has been implemented. Based on a Python script, these problems can be automatically run to check code sanity after modifications.

4.4 Examples and code validation

4.4.1 Cold plasma modes

A first test is to simulate a thermal plasma at rest and to observe its modes of oscillation. It is an easy test if we focus on the pulsations for modes of zero wavevector, $\boldsymbol{k} = 0$. To do so, we compute at each timestep t_j the sum of the momentum of the particles along a given direction, for example the x-direction, $\sum_{\rm sp} \gamma_{\rm sp}(t_j)\, v_{{\rm sp},x}(t_j)$, where the summation runs over all the electron superparticles in the simulation (of Lorentz factor $\gamma_{\rm sp}$ and velocity $v_{\rm sp}$). This sum is equivalent to the volume integral of the momentum, and is thus equal to the $\boldsymbol{k} = 0$ Fourier mode of the electron momentum, with a spectral resolution of $2\pi/[\text{box size in units of electron skin depth}]$. We then perform a Fourier transform in time to extract the pulsations of oscillation,

$$F_x(\omega) = \sum_j \exp(i\omega t_j) \times \sum_{\rm sp} \gamma_{\rm sp}(t_j)\, v_{{\rm sp},x}(t_j), \tag{4.5}$$

and similarly along y and z.

For all the simulations of this section, the initial state consists of a homogeneous plasma at rest, with superparticles loaded according to a classical Maxwell-Boltzmann distribution. A uniform background magnetic field

[c] http://www.hdfgroup.org/hdf5/

ω_{ce}	n_t	n_x	ρ_{sp}	$v_{th,e}/c$	$\tilde{\lambda}_{De}$	$\tilde{r}_{ce}$	$\omega_{ce}\Delta t$	$\omega_{//}^{simu}$	$\omega_{\perp}^{simu}$	ω_P^{theory}	ω_L^{theory}	ω_R^{theory}	
0.5	4000	32	4	0.04	1.28	2.56	7.9×10^{-4}	1.01	0.79, 1.28	1.010	0.78	1.28	
″	″	″	16	″	″	″	″	1.01	0.79, 1.28	″	″	″	
1	1000	25	16	″	1	1	6.3×10^{-3}	1.01	0.64, 1.62	1.010	0.62	1.62	Fig. 4.2
″	4000	32	4	″	1.28	1.28	1.6×10^{-3}	1.01	0.64, 1.62	″	″	″	
2	1000	16	4	″	0.64	0.32	1.3×10^{-2}	1.01	0.43, 2.64	1.010	0.41	2.41	
″	1000	25	16	″	1	0.5	″	1.01	0.46, 2.40	″	″	″	
″	4000	43	4	″	1.72	0.86	3.1×10^{-3}	1.01	0.46, 2.40	″	″	″	
″	4000	64	4	″	2.56	1.28	″	1.01	0.46, 2.40	″	″	″	
4	1000	25	4	″	1	0.25	2.5×10^{-2}	1.01	0.32, 4.22	1.010	0.24	4.24	
″	2000	128	4	″	5.12	1.28	1.3×10^{-2}	1.01	0.32, 4.21	″	″	″	

Table 4.1: Theoretical versus experimental pulsations for a magnetized cold plasma. $\omega_{\perp}^{simu}$ and $\omega_{//}^{simu}$ are the peak in the spectra of the parallel and perpendicular total particle momentum from the simulations. The right columns give the theoretical pulsations for a cold plasma. See the main text for the formula. Here $m_i/m_e = 49$, for the expression of the plasma pulsation ω_P, and $m_i/m_e = \infty$ for the expressions of the right and left cut-off pulsations (ω_R and ω_L). The duration of each simulation is $100\,T_{pe}$, implying a spectral precision of $\Delta\omega = 0.01\omega_{pe}$. Ion and electron temperatures are equal. $\tilde{\lambda}_{De}$ and $\tilde{r}_{ce}$ are the electron Debye length and Larmor radius in units of cell number. All pulsations are in units of ω_{pe}.

along $\boldsymbol{z}$ is set up for the magnetized plasma case. Periodic boundaries are used.

When the background magnetic field $\boldsymbol{B}_0$ is strong (electron cyclotron pulsation larger than electron plasma pulsation, $\omega_{ce} \gg \omega_{pe}$), the particle trajectories are Larmor gyrations in $\boldsymbol{B}_0$, unperturbed by collective effects such as Langmuir oscillations. This example then probes the accuracy of the particle motion integrator. When the background magnetic field is weaker ($\omega_{ce} \lesssim \omega_{pe}$), the dynamics is set by Langmuir oscillations possibly modified by $\boldsymbol{B}_0$. These oscillations involve the creation of electric fields by local charge imbalance. The fields set the particles into motion, and the particles then oscillate because of their finite inertia. Several parts of the algorithm are thus involved: electric field production and propagation, as well as particle motion.

No background magnetic field

With no background magnetic field, the only cold modes are the electromagnetic transverse wave of dispersion relation $\omega_{Tr}^2 = \omega_P^2[1 + (kc/\omega_P)^2]$ and the electrostatic Langmuir oscillation at the plasma frequency $\omega_P = \omega_{pe}(1 + m_e/m_i)^{1/2}$. The latter is modified by thermal effects to a wave of dispersion relation $\omega_{La}^2 = \omega_P^2(1 + 3k^2\lambda_D^2)$. Consequently, we expect $F_a(\omega)$ to peak at $\omega_{La}(\boldsymbol{k} = 0) = \omega_{Tr}(\boldsymbol{k} = 0) = \omega_P$.

Our simulations span a large range of parameters: n_x and n_t (spatial and temporal resolution, see Sect. 4.3.2) vary between 5 and 50 and between 300 and 2000, respectively; ρ_{sp} (the number of superparticles per cell) varies between 4 and 32; and the thermal velocity $v_{th,e} = \sqrt{T_e/m_e}$ of the electrons between $0.04c$ and $0.1c$ (the ions have the same temperature as the electrons). This results in Debye lengths between 0.2 and 2 cells. We checked that the simulation box size, comprised between 10 and 30 Debye lengths, does not influence the results.

We use a mass ratio $m_i/m_e = 49$, which results in $\omega_P = 1.010\,\omega_{pe}$. Our simulations last $100\,T_{pe}$, so that the frequency resolution is $\Delta\omega =$

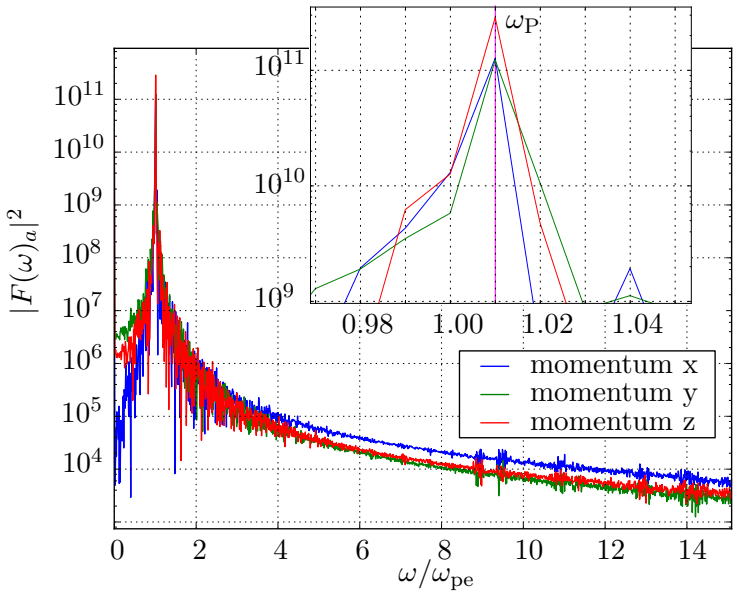

Figure 4.1: Power spectra of the total momentum of the electrons $|F_a|^2$ (Eq. 4.5) with $a = x$, y, or z in the unmagnetized case. The inset is a zoom around the peak. Here $n_x = 25$, $n_t = 500$, $\rho_{sp} = 16$, $v_{th,e} = 0.04c$, $T_i = T_e$, box size of $25 \times 25 \times 25$ cells, duration of $100\,T_{pe}$.

$2\pi/(100T_{pe}) = 0.01\omega_{pe}$.

For all these parameters, we find that the position and width of the frequency peak are always the same as in Fig. 4.1. It coincides with the theoretical plasma pulsation, which is expected because our temporal spectra are for the wavenumber $\boldsymbol{k} = 0$, and because $\omega(\boldsymbol{k} = 0) = \omega_P$ for the two modes present in this situation.

This is the case even for simulations where the Debye length is not resolved. However, an under-resolved Debye length leads to more numerical heating and can trigger instabilities in situations less trivial than a thermal plasma at rest (see Appendix 5.A), so that we have not pushed our investigations too far in this direction.

The main difference between the simulations is that less resolved ones present noisier spectra, and thus more fluctuations. The increase of fluctuation level with decreasing resolution is a universal feature of PIC simulations and is explored in more detail in Sect. 5.2.

With a background magnetic field

In a uniform and cold magnetized plasma, the plasma modes depend solely on the ratio of the electron cyclotron pulsation $\omega_{ce} = eB/m_e$ to the electron plasma pulsation ω_{pe} (for a fixed m_i/m_e). This ratio sets the relative importance of individual particle motion (ω_{ce}) against collective effects (ω_{pe}). In addition, the background magnetic field favors a direction, thus making the mode spectrum anisotropic (however, the mode pulsations for $\boldsymbol{k} = 0$ remain independent of the direction of the wavevector).

For wavevectors parallel to the magnetic field, the Langmuir oscillation remains unchanged because the oscillations of the particles are longitudinal, and thus along $\boldsymbol{B}_0$ and unaffected by the magnetic field. On the other hand, the electromagnetic wave with $\boldsymbol{k}$ along $\boldsymbol{B}_0$ separates into two branches, one starting at $\omega_{\boldsymbol{k}=0} = \omega_L = 0.5[(\omega_{ce}^2 + 4\omega_{pe}^2)^{1/2} - \omega_{ce}]$ and the other at $\omega_{\boldsymbol{k}=0} =$

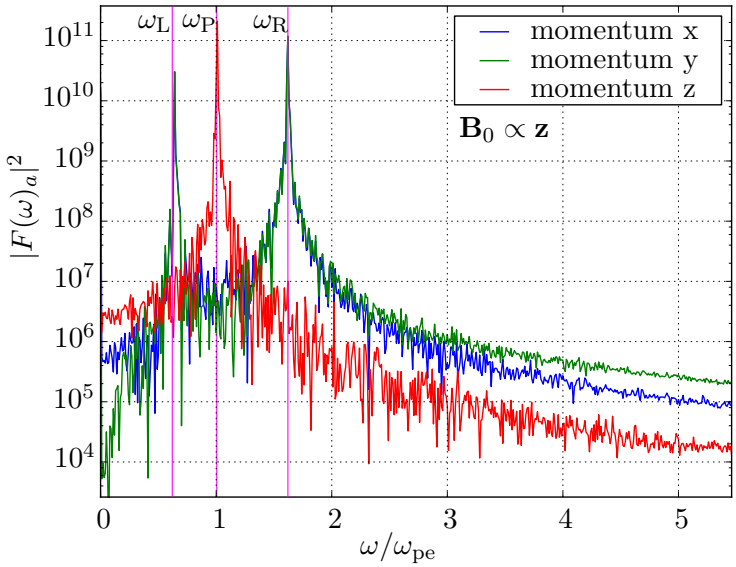

Figure 4.2: Power spectra of the total momentum of the electrons $|F_a|^2$ (Eq. 4.5) with $a = x$, y, or z in the magnetized case. Parameters are given in Table 4.1 (case labeled Fig. 4.2). The purple lines are the pulsations ω_L^{theory}, ω_P^{theory}, and ω_R^{theory}.

$\omega_R = 0.5[(\omega_{ce}^2 + 4\omega_{pe}^2)^{1/2} + \omega_{ce}]$ (see, e.g., Fitzpatrick 2011, Chap. 4), in both cases with particles oscillating in the transverse plane, i.e., perpendicular to $\boldsymbol{B}_0$. Two other branches appear, but they start at $\omega_{\boldsymbol{k}=0} = 0$ and will thus not appear in $F_a(\omega)$.

For wavevectors perpendicular to the magnetic field, the presence of the background magnetic field deforms the Langmuir oscillation $\omega(k) = \omega_P$ into a branch starting from $\omega_{\boldsymbol{k}=0} = \omega_L$, with particle oscillations in the plane perpendicular to $\boldsymbol{B}_0$. The transverse electromagnetic wave still exists with particle oscillations along $\boldsymbol{B}_0$, unaffected by the magnetic field. Another branch appears, which is a deformation of the transverse electromagnetic wave for particle oscillations not along $\boldsymbol{B}_0$, and starts at $\omega_{\boldsymbol{k}=0} = \omega_R$ with oscillations in the plane perpendicular to $\boldsymbol{B}_0$. Another branch appears, starting at $\omega_{\boldsymbol{k}=0} = 0$.

All in all, we expect to find a peak at $\omega = \omega_P$ for the component of the momentum parallel to $\boldsymbol{B}_0$, and two peaks at $\omega = \omega_L$ and ω_R for the component of the momentum perpendicular to $\boldsymbol{B}_0$. We ran the set of simulations described in Table 4.1, with a ratio ω_{ce}/ω_{pe} ranging from 0.5 to 4, n_x from 16 to 128, n_t from 1000 to 4000, and ρ_{sp} from 4 to 16, and we did find the required pulsation peaks for $F_a(\omega)$ (see Fig. 4.2 for a sample spectrum). The positions and widths of these three peaks are almost constant within our parameter range.

We note that the peak positions and widths are not changed even for cases where the thermal Larmor radius $\tilde{r}_{ce} = r_{ce}/X_0 = v_{th,e}/(X_0\omega_{ce}) = \tilde{\lambda}_{De}/(\omega_{ce}/\omega_{pe})$ is not resolved. It is expected that the resolution of the Larmor radius by the grid is of no importance to describe particle trajectories in constant fields, because the interpolation of these fields from grid points to superparticle position gives the same result regardless of the grid size if the fields are constant. The relevant constraint is instead that r_{ce} should be resolved along the trajectory, $v_{sp}\Delta t < r_{ce}$, with v_{sp} the superparticle velocity. This relation is equivalent to $\Delta t < \omega_{ce}^{-1}$.

However, for simulations with under-resolved Larmor radii the electric

n_t	n_x	$\rho_{\rm sp}$	$v_{\rm th,e}/c$	$\tilde{\lambda}_{\rm De}$	$T_{\rm pe}\frac{\rm d}{{\rm d}t}\frac{E_{\rm tot}(t)}{E_{\rm tot}(0)}$
500 to 2000	10	16	0.04	0.4	1.6×10^{-4}
″	10	16	0.10	1	5.8×10^{-5}
″	14	16	0.07	1	3.5×10^{-5}
″	18	16	0.04	0.7	5.3×10^{-5}
300 to 2000	25	4	0.04	1	1.0×10^{-4}
″	25	16	0.04	1	2.5×10^{-5}
″	25	32	0.04	1	1.3×10^{-5}

Table 4.2: Energy conservation for simulations of a thermal plasma with no background magnetic field. The energy increase rate is measured on the total energy normalized by the total initial energy, while time is again normalized with the electron plasma pulsation $T_{\rm pe}$. Here, $m_{\rm i}/m_{\rm e} = 49$ and $T_{\rm i} = T_{\rm e}$.

field energy starts to behave abnormally after some tens of plasma pulsations, and energy conservation curves present an exponential heating (see Sect. 4.4.1) that can lead to dramatic consequences. This parameter range must be avoided.

Energy conservation

Independent of the strength of the background magnetic field, we observe a linear increase of the total energy with time that is due to interactions of particles with the grid (see Appendix 5.A.2). The growth rate is independent of the size of the timestep (from $n_t = 2000$ down to Courant condition $\Delta t \sim X_0/c$, equivalent to $n_t = 2\pi n_x$). Its dependence on the number of superparticles per cell is quite precisely given by $1/\rho_{\rm sp}$. However, its dependence on the spatial resolution n_x and thermal spread $v_{\rm th,e}$ is less clear. In particular, it does not depend only on the product $n_x v_{\rm th,e}/c = \tilde{\lambda}_{\rm De}$. The rate increases with increasing $v_{\rm th,e}$, and decreases with increasing n_x. Some examples are given for reference in Table 4.2.

Simulations with under-resolved Larmor radii $\tilde{r}_{\rm ce} < 1$ show an exponential (instead of linear) increase of the total energy starting after roughly $40\,T_{\rm pe}$. This numerical instability is believed to arise because field perturbation at wavelength $\lambda = 2r_{\rm ce}$ and their aliases ($\pm\lambda + n \times 2\pi/X_0$, with n an integer and X_0 the grid size) are allowed to couple when $2X_0 > \lambda$ (see Appendix 5.A.2). An inspection of the energy curves shows that the energy gain is for the kinetic energy. We note that it did not disturbed the spectra of Sect. 4.4.1 because they were computed before the heating reached a significant level. It is interesting to note that this numerical instability is develops slowly, so that particles with under-resolved Larmor radii in constant fields can be included in simulations if they spend a small amount of time before being heated or before reaching areas with smaller magnetic fields.

4.4.2 Linear growth rates of the counter-streaming instability

Another standard test is to study the linear phase of the counter-streaming instability. We use relativistic streaming velocities to validate the behavior of the algorithm for relativistic particle motions. Moreover, since magnetic fields are generated for this range of parameters, this test also probes the

β_0	n_t	n_x	$\rho_{\rm sp}$	$v_{\rm th}/c$	Box size in $d_{\rm e}$	Λ_p	$\tau^{\rm simu}_{\rm tot\,en}/T_{\rm pe}$	$\tau^{\rm simu}_{\rm fast\,mode}/T_{\rm pe}$	$\tau^{\rm theory}_{\rm max}/T_{\rm pe}$
0.95	1000	20	16	0.1	$3\times3\times30$		0.29 (38%)		0.21
″	″	″	100	″	″		0.27 (29%)		″
″	250	20	16	0.1	$9\times9\times30$		0.27 (29%)	0.24 (14%)	″
0.995	1000	20	4	0.1	$3\times3\times30$	32	0.52 (44%)		0.36
″	″	″	16	″	″	128	0.45 (25%)		″
″	″	″	80	″	″	640	0.43 (19%)		″
″	″	″	160	″	″	1280	0.43 (19%)		″
″	″	″	400	″	″	3200	0.41 (14%)		″
″	″	″	560	″	″	4480	0.42 (17%)		″
″	500	20	4	0.1	″	32	0.51 (42%)		″
″	″	″	80	″	″	640	0.41 (14%)		″
″	″	″	128	″	″	1024	0.43 (19%)		″
″	″	″	200	″	″	1600	0.42 (17%)		″
″	″	″	280	″	″	2240	0.42 (17%)		″
″	250	20	4	0.1	″	32	0.51 (42%)		″
″	″	″	80	″	″	640	0.41 (14%)		″
″	″	″	128	″	″	1024	0.43 (19%)		″
″	″	″	200	″	″	1600	0.42 (17%)		″
″	″	″	280	″	″	2240	0.42 (17%)		″
″	1000	40	80	0.1	″	5120	0.46 (27%)		″
″	2000	40	4	0.1	″	256	0.60 (67%)		″
″	″	″	16	″	″	1024	0.50 (39%)		″
″	″	″	48	″	″	3072	0.46 (27%)		″
″	″	″	74	″	″	4736	0.47 (31%)		″
″	″	″	160	″	″	10024	0.43 (19%)		″
″	2000	40	16	0.075	″	432	0.52 (44%)		″
″	2000	40	16	0.05	″	128	0.58 (61%)		″
″	250	20	80	0.1	$4.5\times4.5\times15$	128	0.41 (14%)	0.38 (6%)	″
″	250	20	4	0.1	$9\times9\times30$	32	0.50 (39%)	0.38 (6%)	″
″	″	″	16	″	″	128	0.48 (33%)	0.38 (6%)	″ [a]
″	″	″	80	″	″	640	0.43 (19%)	0.39 (8%)	″
″	125	10	128	0.1	″	128	0.42 (17%)	0.39 (8%)	″
″	1000	20	16	0.1	″	128	0.46 (27%)	0.38 (6%)	″
″	500	20	16	0.1	″	128	0.46 (27%)	0.38 (6%)	″
0.999	1000	20	100	0.1	$3\times3\times30$		0.61 (15%)		0.53
″	250	20	16	0.1	$9\times9\times30$		0.70 (32%)	0.56 (6%)	″

[a] Simulation reported in Figs. 4.4, 4.5, 4.7.

Table 4.3: Theoretical versus experimental values of the filamentation growth rate τ. Numbers in parenthesis are the discrepancy with respect to $\tau^{\rm theory}_{\rm max}$, i.e., $[\tau^{\rm simu}_{\rm tot\,en}-\tau^{\rm theory}_{\rm max}]/\tau^{\rm theory}_{\rm max}$ and $[\tau^{\rm simu}_{\rm fast\,mode}-\tau^{\rm theory}_{\rm max}]/\tau^{\rm theory}_{\rm max}$. $T_{\rm pe}$ is the plasma period comprising all electrons, and $d_{\rm e}$ the plasma skin depth based on this period. We recall that $d_{\rm e}$ corresponds to n_x cells. We also give the PIC plasma parameter $\Lambda_p = n_{\rm e,sp}\lambda^3_{\rm De} = \rho_{\rm sp}(n_x v_{\rm th}/c)^3$ (see Sect. 5.2.1).

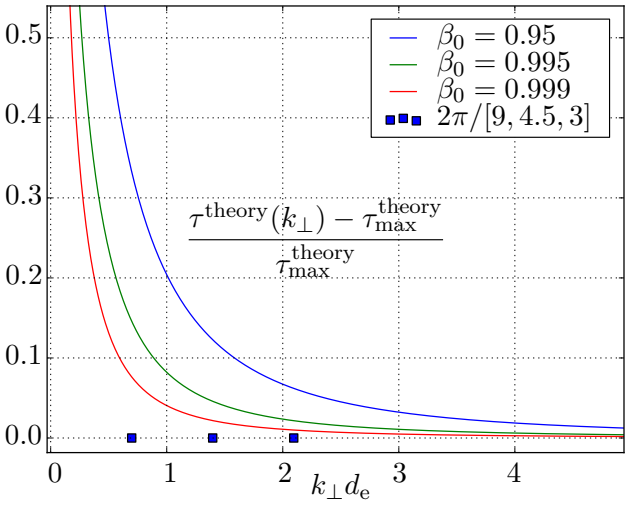

Figure 4.3: Wavenumber dependence of the growth rate $\tau^{\rm theory}(k_\perp)$, represented here as the deviation $[\tau^{\rm theory}(k_\perp) - \tau^{\rm theory}_{\rm max}]/\tau^{\rm theory}_{\rm max}$. We recall that $\tau^{\rm theory}_{\rm max} = \tau^{\rm theory}(k_\perp = +\infty)$. From Eq. 69 of Michno and Schlickeiser (2010). The squares are the resolution in $k_\perp$ for a box of transverse size 9, 4.5, and 3 $d_{\rm e}$.

integration of $\boldsymbol{b}$.

The initial setup consists of two unmagnetized and cold counter-streaming electron-positron beams, with velocity $\pm\beta_0\hat{\boldsymbol{z}}$ and associated Lorentz factor Γ_0. There is no background magnetic field, and the particles are loaded according to a drifting Maxwell-Boltzmann distribution. This situation is unstable, and the kinetic energy of the beam is converted into particle thermal kinetic energy and electromagnetic field energy, the initial perturbation coming from fluctuations due to the finite superparticle number. The linear instability spectrum is described by a branch comprising an electrostatic longitudinal two-stream mode and a transverse electromagnetic filamentation mode, the general case being an oblique mixed mode (Bret et al. 2010).

Theoretical model

We take the growth rates derived analytically by Michno and Schlickeiser (2010) on the basis of a cold two-fluid model and denote this result as theoretical. Our thermal velocity $v_{\rm th}$, identical for both species, is low enough to insure that thermal effects are negligible (Bret et al. 2010, Eq. 28), but high enough to have a resolved Debye length and to avoid numerical instabilities (Appendix 5.A). Our parameters are chosen such that the transverse filamentation mode always dominates. The fastest growing modes are those at large wavenumbers perpendicular to the beams, i.e., $k_\perp d_{\rm e} \gg \sqrt{2}/\Gamma_0^{3/2}$ (with $d_{\rm e} = c/\omega_{\rm pe}$), and that grow according to b_x, $b_y \propto \exp\{t/\tau^{\rm theory}_{\rm max}\}$ with

$$\tau^{\rm theory}_{\rm max} = \frac{1}{2\pi}\sqrt{\frac{\Gamma_0}{2}}\beta_0^{-1}\,T_{\rm pe}. \tag{4.6}$$

The $k_\perp$-dependence of the growth rate is plotted in Fig. 4.3. We see that all modes above a few $d_{\rm e}^{-1}$ quickly reach the maximum growth rate $\tau^{\rm theory}_{\rm max} = \tau^{\rm theory}(k_\perp = +\infty)$.

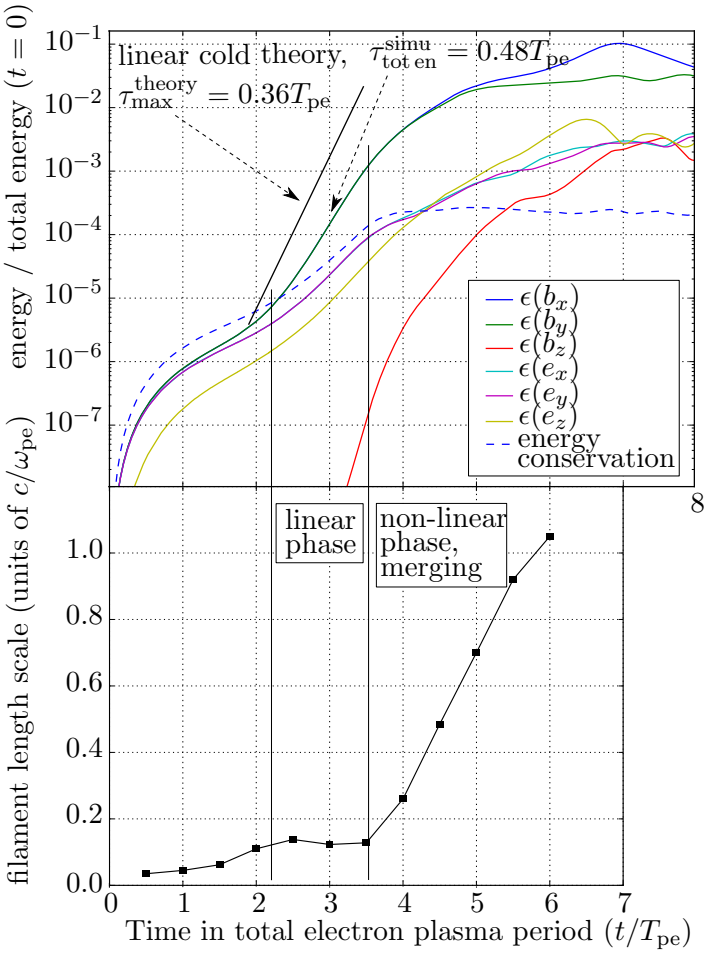

Figure 4.4: **Top**: Energy curves for the filamentation instability (case labeled Fig. 4.4 in Table 4.3). They are normalized by the total initial energy $E^0_{\rm tot}$, which is mostly the kinetic energy of the particles. For example $\epsilon(b_x) = \int {\rm d}V B_x(t)^2/(2\mu_0)/E^0_{\rm tot}$. The curve "energy conservation" is $(E^0_{\rm tot} - {\rm total\,energy}(t))/E^0_{\rm tot}$. After $8T_{\rm pe}$, the situation is more or less steady.
Bottom: Autocorrelation scale of the current amplitude, which traces the scale of the current filaments.

Method of measurement

We measure the growth rates of the magnetic fields b_x and b_y with two methods. The first is a direct measure on the total energy curve, e.g., $\int {\rm d}V\, b_x^2 \propto \exp(2t/\tau)$ (see Fig. 4.4, top, for an illustration). It gives an effective growth rate that we denote by $\tau^{\rm simu}_{\rm tot\,en}$, equal to $0.48T_{\rm pe}$ in this case.

The second consists in following the time evolution of the Fourier modes of the fields. At a fixed time t_0, we compute the 2D Fourier transform of the fields in a plane (x, z) with a fixed y, that we denote by ${\rm FT}_{y=y_0}(t_0, k_x, k_z)$. We then average the power spectrum over all the planes $y = {\rm const}$ to obtain the power spectrum ${\rm PS}(t_0, k_x, k_z) = \sum_{y_0} |{\rm FT}_{y=y_0}(t_0, k_x, k_z)|^2$. We then repeat this procedure for several t_0. The discrete mode spectrum is sampled with $(k_z d_{\rm e}, k_x d_{\rm e}) = 2\pi n_x (i/N_z, j/N_x)$, where N_z and N_x are the total number of cells in the z and x directions, and $i = 0..N_z/2$, $j = 0..N_x/2$. The spectral resolution in the direction perpendicular to the beam is thus $\Delta k_\perp d_{\rm e} = 2\pi n_x/N_x = 2\pi/({\rm box\ width\ in\ } d_{\rm e})$. The squares in Fig. 4.3 represent this spectral resolution for the different box sizes that we use.

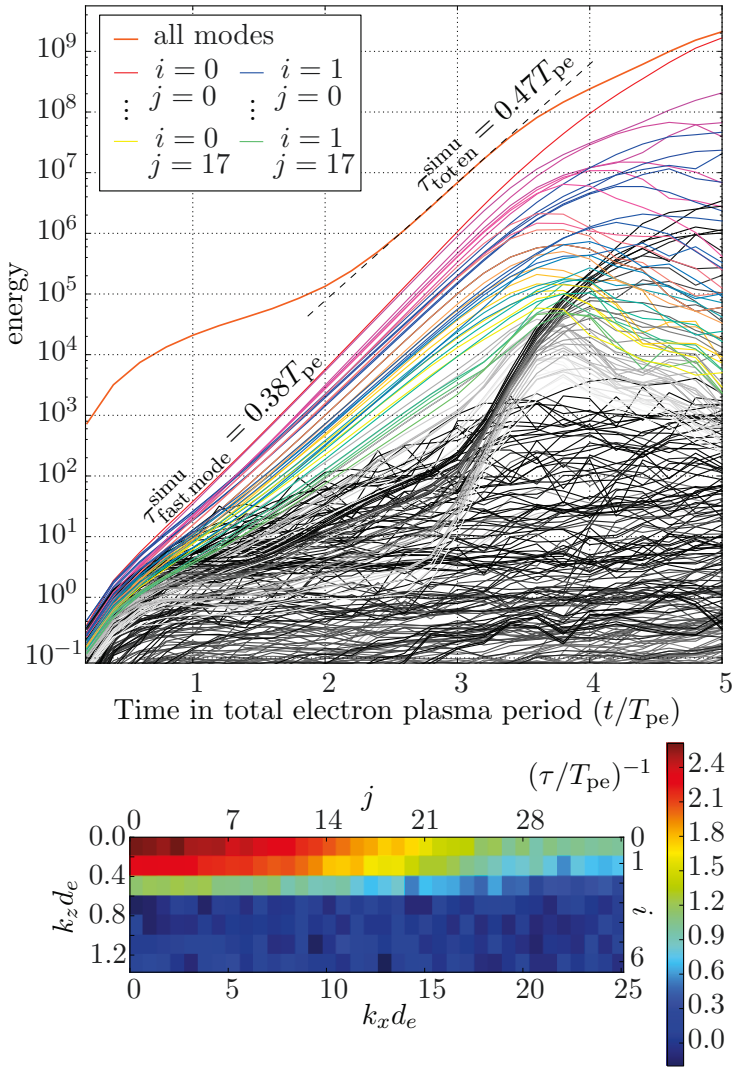

Figure 4.5: **Top**: Growth of individual Fourier modes for b_x (for the run labeled Fig. 4.4 in Table 4.3). The modes shown are those for $i = 0, 1, 2$, and $j = 0, 1, ..., 25$, and one mode every 100 modes for the remaining. We note that the graphic has been cut and that the weak modes actually fill a continuum down to an energy of 10^{-7}. The sum of all 320×90 modes is shown in orange. We recall that mode (i, j) corresponds to $(k_z d_e, k_x d_e) = 2\pi \times 20(i/640, j/180)$.
Bottom: Growth map of the Fourier modes, in units of T_{pe}.

Results

Figure 4.5 is an example of the temporal evolution of the modes of b_x for the same simulation as in Fig. 4.4. The sum of all modes grows at the same effective growth rate as the total energy in b_x (to within $\pm 1\%$), $\tau^{\text{simu}}_{\text{tot en}} = 0.48T_{\text{pe}}$. However, the fastest growing modes are those for $k_z = 0$ and $0 \leq k_x d_e \leq 5$, with $\tau^{\text{simu}}_{\text{fast mode}} = 0.38T_{\text{pe}}$, which is close to the cold-fluid result $\tau^{\text{theory}}_{\text{max}} = 0.36T_{\text{pe}}$. It is seen from Fig. 4.5 that the large difference between the effective growth rate $\tau^{\text{simu}}_{\text{tot en}}$ and the growth rate of the fastest modes $\tau^{\text{simu}}_{\text{fast mode}}$ is due to a significant contribution of all the modes during the whole linear phase. The fastest mode thus never dominates the total energy in the linear phase. We suspect that this is due to the large noise level present in PIC simulations.

These results hold for all the test simulations that we conducted, which

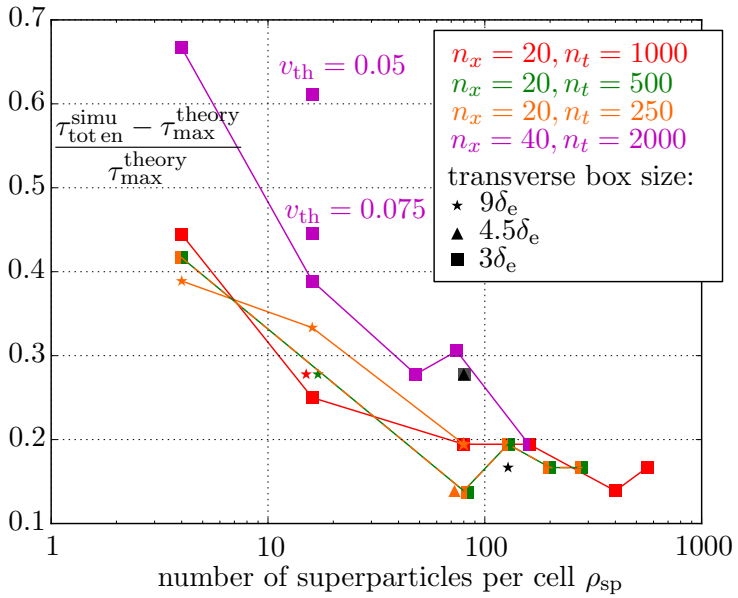

Figure 4.6: Difference between the growth rate measured on the total energy curve $\tau^{\rm simu}_{\rm tot\,en}$ and the theoretical growth rate of the fastest modes $\tau^{\rm theory}_{\rm max}$. Except when labeled otherwise, $v_{\rm th} = 0.1c$. Each symbol corresponds to a transverse box size, and each color to fixed (n_x, n_t).

are summarized in Table 4.3. The effective growth rates $\tau^{\rm simu}_{\rm tot\,en}$ measured on the total energy present various levels of discrepancies with $\tau^{\rm theory}_{\rm max}$, between 14% and 67%. Figure 4.6 shows the dependence of these discrepancies. There is a small sensitivity with respect to the timestep (n_t) and the box size, and an important influence of the spatial resolution (n_x). There is a systematic decrease in the difference when the superparticle number per cell $\rho_{\rm sp}$ is increased (all other parameters are kept constant). Since the fluctuation level in the PIC plasma decreases with increasing $\rho_{\rm sp}$, this indicates that the high fluctuation level excites all the modes and prevents the fastest ones from dominating the energy.

On the other hand, the growth rates $\tau^{\rm simu}_{\rm fast\,mode}$ measured on the fastest modes differ from $\tau^{\rm theory}_{\rm max}$ by a more systematic factor, 14% for $\beta_0 = 0.95$, 7 ± 1% for $\beta_0 = 0.995$, and 6% for $\beta_0 = 0.999$. These systematic differences can be explained by looking at the mode spectrum. In all the simulations, the fastest modes are for $k_z = 0$ and $0 \leq k_x d_{\rm e} \leq 5 - 15$ (see, e.g., Fig. 4.5, bottom). Given the spectral resolution $\Delta k_\perp d_{\rm e} = 2\pi/(\text{box length in } d_{\rm e})$, these modes actually cover a portion of $k_\perp d_{\rm e}$ where the curves $\tau^{\rm theory}(k_\perp)$ of Fig. 4.3 vary significantly and do not yet reach $\tau^{\rm theory}_{\rm max}$. It explains the sign and order of magnitude of the difference $\tau^{\rm simu}_{\rm fast\,mode} - \tau^{\rm theory}_{\rm max}$. It also explains the increasingly better agreement when β_0 increases.

We note that $\boldsymbol{e}$ and b_z are zero in the linear two-fluid theory, and the fact that they are not zero in our simulation (see Fig. 4.4) reflects an early non-linear evolution or the effects of fluctuations and correlations absent from the linear model but present in PIC simulations. These differences are discussed further in Chapter 5.

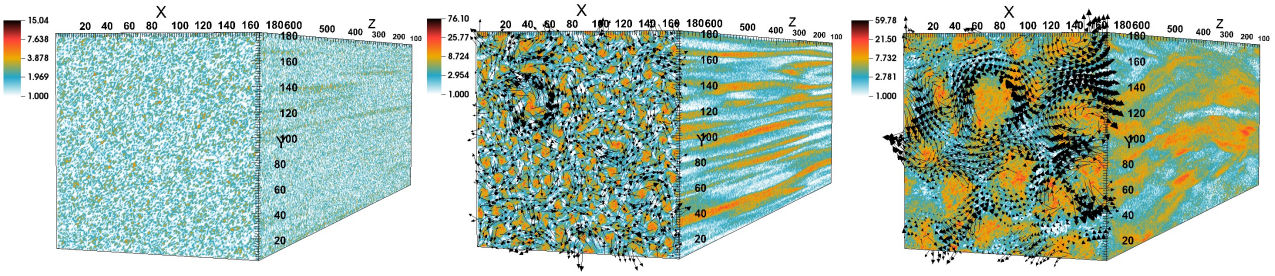

Figure 4.7: Three snapshots of the filamentation instability, at times 2.5, 4, and $5.5T_{\rm pe}$ (from left to right) for the simulation of Fig. 4.4. Colors represent the current magnitude per cell (units are number of superparticles per cell times their mean velocity), while arrows are the magnetic field. Lengths are in cell number.

4.4.3 Non-linear evolution of the filamentation instability: filament merging

We now consider the non-linear phase of the filamentation instability. We study the same counter-streaming configuration as in Sect. 4.4.2, with the setup labeled by Fig. 4.4 in Table 4.3. The energy curves are shown in Fig. 4.4.

As a diagnostic, we focus on the filament growing and merging processes. The linear phase of the filamentation instability produces current filaments. Since they are threaded by parallel currents, they attract each other and, starting from the end of the linear phase, start to merge to produce larger and larger filaments (Medvedev et al. 2005). This is clearly visible in Fig. 4.7.

We measure the size of the filaments by computing the two-dimensional autocorrelation function, in the $x-y$ plane, of the z-averaged current amplitude (z is the direction of the beams). This autocorrelation function is azimuthally averaged to obtain a radial function corr(r). We normalize corr(0) to 1. The scale of the filaments is then taken to be five times the radius where corr(r) = 0.8[d].

The results are shown in Fig. 4.4 (bottom). We clearly see two regimes: one during the linear growth of the filamentation instability (from $t = 2.2$ to $3.6T_{\rm pe}$) where the filament correlation length is set by the wavelength of the fastest growing mode and remains constant, and one in the non-linear regime (after $t = 3.6T_{\rm pe}$) where the filaments merge and thus quickly increase their size. In the second case, the growth is roughly linear with time, which agrees with the PIC simulation results of Dieckmann (2009) for a similar setup. After $t = 6.5T_{\rm pe}$, the filament growth stops. However, we suspect that the periodic boundaries start influencing the dynamics at this point.

4.4.4 Linear growth rates of the relativistic tearing instability

We also study the linear phase of the tearing mode for a relativistic Harris sheet in a pair plasma. Contrary to the preceding case, this example provides a test of the algorithm in a situation where thermal effects are essential.

[d]Taking this scale as the radius at which corr(r) first vanishes yields the same results.

Θ	ω_{ce}/ω_{pe}	$\Gamma_e U_e/c$	L/d_e	n_t	n_x	ρ_{sp}	Box size in d_e	$\frac{\tau^{simu}}{T_{pe}}$	$\frac{\tau^{theory}}{T_{pe}}$	$\frac{\tau^{simu}-\tau^{theory}}{\tau^{simu}}$	
0.01	0.2	0.14	0.72	250	15	1000	$53 \times 0.3 \times 42$	5.4	5	8%	
″	″	″	″	″	″	″	$80 \times 0.3 \times 42$	5.4	″	8%	
0.1	0.61	0.40	0.83	250	15	1000	$53 \times 0.3 \times 42$	2.1	2	5%	Fig. 4.8
1	1.82	0.68	1.62	250	15	1000	$53 \times 0.3 \times 42$	2.5	2.7	7%	

Table 4.4: Theoretical versus experimental values of the tearing growth rate τ. T_{pe} is the plasma period comprising all electrons, and d_e the plasma skin depth based on this period. We recall that d_e corresponds to n_x cells. Other simulations were performed in the case $\Theta = 0.01$, but with an initial setup slightly out-of-equilibrium, and they presented variations in the growth rates of less than 3% when n_x, n_t, and ρ_{sp} were doubled, or when ρ_{sp} was divided by two.

The equilibrium consists of a magnetic field

$$\boldsymbol{B} = \hat{\boldsymbol{z}}\, B_0 \tanh\left(\frac{x}{L}\right), \tag{4.7}$$

sustained by a population of electrons and positrons of equal number density $\propto 1/\cosh^2(x/L)$ flowing with opposite bulk velocities $U_e = -U_i$ in the $\pm y$ directions. We denote the associated Lorentz factor by Γ_e, and the temperature of the two species by $\Theta = T/(m_e c^2)$. The exact relations between the different parameters to satisfy the equilibrium are given in Sect. 3.7. In particular, one should be careful to distinguish between quantities in the frame moving with one species (denoted with a prime) and quantities in the simulation frame. For example, contraction of the electron density leads to $\omega_{pe} = \sqrt{\Gamma_e}\omega'_{pe}$.

The superparticles are loaded according to a drifting Maxwell-Jüttner. There is no initial perturbation, and the instability grows out of the fluctuations produced by the finite number of superparticles.

As can be seen in Table 4.4, the bulk velocities and the temperatures of electrons and positrons are both relativistic. Loading these distributions in a PIC code is a non-trivial task, and we have developed a special method for this, that is presented in Sect. 3.8.

The simulation domain is periodic along z and y. Reflecting boundaries for particles and fields are present along the x direction. There are no background particles, only that of the current sheet.

An example of the energy evolution is presented in Fig. 4.8. After some time, the system becomes unstable and the magnetic field starts reconnecting. As expected, b_z dwindles while b_x rises, which corresponds to the formation of magnetic islands. We measure the linear growth rate on b_x as $\int \mathrm{d}V\, b_x^2 \propto \exp(2t/\tau)$. For comparison, we use the linear growth rates derived by Pétri and Kirk (2007) by linearizing the Vlasov-Maxwell system around the drifting Maxwell-Jüttner distribution 3.8 and the magnetic field of Eq. 4.7.

The results are summarized in Table 4.4. Discrepancies with Pétri and Kirk (2007) range between 5% and 8%. These growth rates vary by less than 3% when the numerical resolution is doubled (i.e., when ρ_{sp}, n_x, and n_t are doubled all together). We restrict our analysis to total energy curves because contrary to the case of the filamentation instability, the linear growth of the field energy spans several orders of magnitude and the fastest modes have enough time to dominate the total energy.

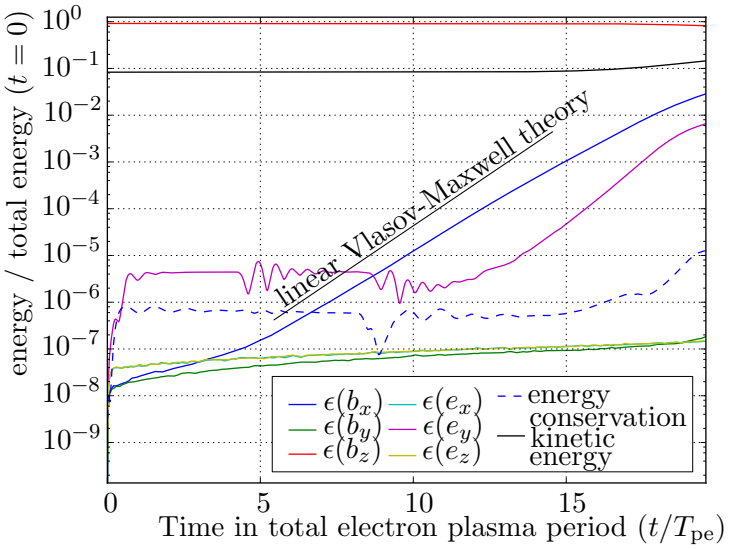

Figure 4.8: Energy curves for the tearing instability (labeled Fig. 4.8 in Table 4.4). Shown are the energy curves, for example $\int \mathrm{d}V B_x(t)^2/(2\mu_0)$. They are normalized by the total initial energy E^0_{tot} (which is mostly the energy in b_z). The curve labeled "energy conservation" is $(E^0_{\mathrm{tot}} - \text{total energy}(t))/E^0_{\mathrm{tot}}$.

We note that when the simulation is launched, an electromagnetic wave is seen to propagate from the sheet in the $\pm x$ directions. This wave is a necessary consequence of the fact that at $t = 0$ we load the superparticles by pairs of electron-positron at the same location, and we set a zero electric field everywhere (see Sect. 4.3.1). The system then has to relax from this very peculiar state: in less than one plasma period, charge screening is established and an electric field appears. It is this field that partly propagates outside of the sheet. It is then reflected on the $\pm x$ boundaries and propagates back to the sheet, causing the oscillations in e_y seen in Fig. 4.8. We have checked that their incidence does not influence the linear growth by using different domain sizes.

It is more puzzling that the sheet contracts slightly just after the beginning of the simulation and the current magnitude at its center rises by $\lesssim 10\%$. This may be related to the fact that our algorithm does not solve the Vlasov-Maxwell system in a strict sense (see also Sects. 5.2 and 5.5.2).

4.5 Conclusion and discussion

We have presented our particle-in-cell code `Apar-T`, and studied several validation tests.

Computation of the spectra from a magnetized or unmagnetized thermal plasma at rest (Sect. 4.4.1) has proven very accurate, with the plasma pulsation and the right and left cutoff pulsations precisely recovered (Figs. 4.1 and 4.2), even in cases where the Debye length and the Larmor radius are not resolved. This proves that the description of individual particle motions in a constant magnetic field and of collective particle dynamics is accurate, and robust with respect to numerical resolution. In particular, we showed that Larmor orbits in a constant magnetic field are well described provided that the cyclotron pulsation is well resolved, independently of the grid size. We found, however, a numerical instability with abnormal behavior in the energy curves and high noise levels for under-resolved Debye

length or under-resolved Larmor radius, so that this parameter range should be avoided.

Simulations of the filamentation instability (Sect. 4.4.2) showed a good agreement with linear cold theories, provided that the growth rates are computed from the temporal evolution of the Fourier modes. Discrepancies with theory then range from 5% to 13%, and can be explained by the wavenumber dependence of the growth rates. On the other hand, the linear growth rates derived from the total energy curves, or equivalently from the sum of all Fourier modes, present larger discrepancies with linear theory, ranging between 12% to 61%. This is explained by the high level of fluctuations in PIC codes that prevent the fastest growing modes to dominate the total energy before the end of the linear phase of the instability.

Simulations of the tearing instability in a relativistic pair plasma gave linear growth rates within 8% of those found by Pétri and Kirk (2007) with an analytical linear Vlasov-Maxwell solution, a result not varying significantly when changing the numerical resolution (Sect. 4.4.4, Fig. 4.8, and Table 4.4). This example, where the shape of the velocity distribution is a key feature, is thus in agreement with the Vlasov-Maxwell description. It also validates the new method used to load the relativistic (in both temperature and bulk velocity) Maxwell-Jüttner distribution that we present in Sect. 3.8, as well as the general relations used for the relativistic Harris equilibrium derived in Sect. 3.7. We note that in this case the total energy curves can be used for evaluation of the linear growth rates because the linear phase spans several orders of magnitude in field intensity, so that the fastest growing modes have enough time to dominate the energy.

All in all, these tests show that our code `Apar-T` is a sound basis for future explorations. They also serve as a base to explore important questions regarding the nature of a PIC plasma, that we discuss in the next chapter.

Appendix 4.A Numerical implementation

This Appendix is the direct continuation of Sect. 4.3. It gives details on the numerical scheme used in `Apar-T`.

4.A.1 Computation of the current

Before going through the normalization of Eqs. 4.4a-4.4e, we have to understand how the current is computed. As said in Sect. 4.3.2, interpolation of particle quantities to grid nodes is done by attributing to the superparticles a finite volume $V_{\rm sp} = X_0^3$. We consider a superparticle, and the cell that contains its center. At time t, the superparticle occupies a volume V_t of the cell. The charge in the cell is given by $Q_{\rm cell}(t) = q_{\rm sp} \times (V_t/V_{\rm sp})$. The charge continuity equation then gives

$$\oiint_{\rm cell} \boldsymbol{j} \cdot \mathrm{d}\boldsymbol{S} = -\frac{dQ_{\rm cell}}{dt} = \frac{V_{t+dt} - V_t}{V_{\rm sp}} \frac{q_{\rm sp}}{dt}. \tag{4.8}$$

The superparticle volume necessarily intersects three faces of the cell that contains its center: one of perpendicular along $\boldsymbol{x}$, one along $\boldsymbol{y}$, and one along $\boldsymbol{z}$. Consequently, the motion of this superparticle will create a current

through these three faces, and we can write

$$\oiint_{\text{cell}} \boldsymbol{j} \cdot \mathrm{d}\boldsymbol{S} = j_x X_0^2 + j_y X_0^2 + j_z X_0^2. \tag{4.9}$$

We have to know which part of the volume variation $V_{t+dt} - V_t$ is attributed to each part of the current. The displacement of the superparticle between t and $t+dt$ is denoted $(\Delta x, \Delta y, \Delta z)$. The volume variation depends on this displacement, and the part of it proportional to Δx is attributed to j_x, and similarly for the y and z components. More specifically, we can write $V_{t+dt} - V_t = A_x \Delta x + A_y \Delta y + A_z \Delta z$. The areas A_i can be evaluated with some geometry (see Sect. 4.A.3). Then (and similarly for y and z):

$$j_x = -\frac{1}{X_0^2} \frac{q_{\text{sp}}}{dt} \frac{A_x \Delta x}{V_{\text{sp}}}. \tag{4.10}$$

This way of computing the current ensures that the discrete charge conservation equation is fulfilled, and justifies the advection of the divergence of the fields.

4.A.2 Normalization

The problem is formulated with as many equations as variables (Eqs. 4.4a-4.4e, variables $\boldsymbol{e}$, $\boldsymbol{b}$, $\boldsymbol{j}$, $\boldsymbol{x}_{\text{sp}}$, and $\boldsymbol{v}_{\text{sp}}$ for each superparticle), and it is possible to normalize the equations in a way independent of any physical quantity. We denote normalized quantities with a tilde.

We choose to normalize lengths by X_0. Consequently, the normalized step-size is unity. Times are normalized by $T_0 = X_0/c$, and velocities are then naturally normalized to $X_0/T_0 = c$. For the fields $\boldsymbol{E}$ and $\boldsymbol{B}$, we use $\boldsymbol{e} = \boldsymbol{E}$ and $\boldsymbol{b} = c\boldsymbol{B}$. These last two quantities are normalized by $e_0 = b_0 = m_{\text{e}} c^2/(eX_0)$. With this, Eqs. 4.4a, 4.4b, and 4.4c transform into

$$\frac{\mathrm{d}\tilde{\boldsymbol{x}}}{\mathrm{d}\tilde{t}} = \tilde{\boldsymbol{v}}, \tag{4.11a}$$

$$\frac{\mathrm{d}\gamma\tilde{\boldsymbol{v}}}{\mathrm{d}\tilde{t}} = \left[\frac{m_{\text{e}}}{m_s}\frac{q_s}{e}\right](\tilde{\boldsymbol{e}} + \tilde{\boldsymbol{v}} \wedge \tilde{\boldsymbol{b}}), \tag{4.11b}$$

$$\frac{\partial\tilde{\boldsymbol{b}}}{\partial\tilde{t}} = -\tilde{\boldsymbol{\nabla}} \wedge \tilde{\boldsymbol{e}}, \tag{4.11c}$$

with $m_s = m_{\text{e}}$ or m_{i} and $q_s = -e$ or e (e is positive).

For the current $\boldsymbol{j}$, the algorithm computes the quantity $A_x \Delta x / V_{\text{sp}}$. Writing for example the x component of Eq. 4.4d gives

$$\frac{\partial\tilde{e_x}}{\partial\tilde{t}} = (\tilde{\boldsymbol{\nabla}} \wedge \tilde{\boldsymbol{b}})_x + \underbrace{\left[\frac{1}{\epsilon_0}\frac{e^2}{m_{\text{e}} c^2 X_0} p \frac{q_s}{e}\right]}_{\alpha} \left[\frac{\tilde{A}_x \Delta\tilde{x}}{\tilde{V}_{sp}}\right] \frac{1}{\widetilde{dt}}. \tag{4.12}$$

Using Eq. 4.3, we can write

$$\alpha = \frac{2\,\mathrm{sgn}(q_s)}{n_x^2 \rho_{\text{sp}}^0}, \tag{4.13}$$

where sgn is the sign of the charge.

With this, all the equations are completely independent of any physical quantity related to the simulated problem, and depend only on space discretization (n_x) and particle coarse-graining (ρ_{sp}^0). Time discretization (n_t) will play a role in time integration.

As a final comment, we note that ρ_{sp}^0 is a priori unrelated to the actual number of superparticles per cell during the simulation. One should, however, make these two values not too far apart, because the size and timesteps are a fraction n_x and n_t of the skin depth and plasma period of a n_{e}^0-density plasma. If, for example, the superparticle density in the simulation is twice ρ_{sp}^0, then n_x cells will now represent two skin depths of the $2n_{\text{e}}^0$-density plasma, and the resolution will decrease. This must be kept in mind in simulations where high density contrasts appear.

4.A.3 Discrete version of the equations

In this section we drop the tilde over normalized quantities. We denote the time at which they are considered by a superscript and their spatial location on the grid by a subscript.

The main loop

The strategy is to use a leap-frog scheme. It has the advantages of being time-centered and reversible, and second-order in time and space.

Before the loop, $\boldsymbol{b}$ and $\boldsymbol{v}$ are known at time $t - dt/2$, and $\boldsymbol{e}$ and $\boldsymbol{x}$ are known at time t. This should also be true for the initial conditions, so that initially we integrate backward the velocities and the $\boldsymbol{b}$-field by $-dt/2$. Injected particles (if any) should also be correctly staggered.

The structure of the main loop is the following:

1. Half advance of $\boldsymbol{b}^{t-dt/2}$ with $\boldsymbol{\nabla} \wedge \boldsymbol{e}^t$; $\boldsymbol{b}$ is now at time t.
2. Update of $\boldsymbol{v}^{t-dt/2}$ with $\boldsymbol{b}^t$ and $\boldsymbol{e}^t$; $\boldsymbol{v}$ is now at time $t + dt/2$.
3. Update of $\boldsymbol{x}^t$ with $\boldsymbol{v}^{t+dt/2}$; $\boldsymbol{x}$ is now at time $t + dt$.
4. Half advance of $\boldsymbol{b}^t$ with $\boldsymbol{\nabla} \wedge \boldsymbol{e}^t$; $\boldsymbol{b}$ is now at time $t + dt/2$.
5. Boundary for $\boldsymbol{b}$.
6. Full advance of $\boldsymbol{e}^t$ with $\boldsymbol{\nabla} \wedge \boldsymbol{b}^{t+dt/2}$; $\boldsymbol{e}$ is now at time $t + dt$.
7. Boundary for $\boldsymbol{e}$.
8. Boundary for particles.
9. Computation of the currents from $\boldsymbol{v}^{t+dt}$ and $\boldsymbol{x}^{t+dt/2}$.
10. Filtering of the currents.
11. Boundary for the currents.
12. Add currents to $\boldsymbol{e}^{t+dt}$.

Integration of the fields

The fields are stored on the grid in a staggered way, with $\boldsymbol{e}$ at the center of the grid edges and $\boldsymbol{b}$ at the center of the grid faces (Fig. 4.9). This is the so-called Yee lattice. It allows an easy integration of the fields, and

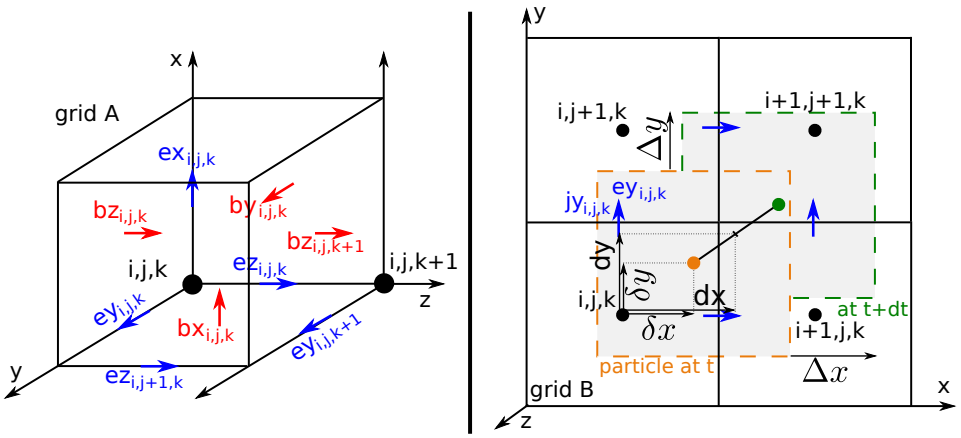

Figure 4.9: Grid and fields locations.

is second-order accurate in time and space (Birsdall and Langdon 1985, Sect. 15),

$$b_{x\,|\,i,j,k}^{t+dt/2} = b_{x\,|\,i,j,k}^{t-dt/2} + dt\,\left(e_{y\,|\,i,j,k+1}^{t} - e_{y\,|\,i,j,k}^{t} - e_{z\,|\,i,j+1,k}^{t} + e_{z\,|\,i,j,k}^{t}\right), \quad (4.14)$$

and similarly for the other components of $\boldsymbol{b}$ and for $\boldsymbol{e}$.

To reduce the effects of Čerenkov emission (see Appendix 5.A.1), we have also implemented a fourth order solver (Greenwood et al. 2004).

Moving the particles

Integration of the equation of motion for the superparticles is done with the algorithm described by Birsdall and Langdon (1985, Sect. 15.4). It is a relativistic generalization of the leap-frog scheme, time centered, time reversible, and second-order accurate. We note however that, as pointed out by Vay (2008), it can have shortcomings for ultrarelativistic particles. In short, Eqs. 4.11a and 4.11b are discretized as

$$\left(\boldsymbol{u}^{t+dt/2} - \boldsymbol{u}^{t-dt/2}\right)/dt = \frac{m_\mathrm{e}}{m}\frac{q}{e}\left\{\boldsymbol{e}^t + \frac{\boldsymbol{u}^{t+dt/2} + \boldsymbol{u}^{t-dt/2}}{2\gamma^t} \wedge \boldsymbol{b}^t\right\}, \quad (4.15a)$$

$$\frac{\boldsymbol{x}^{t+dt} - \boldsymbol{u}^t}{dt} = \frac{\boldsymbol{u}^{t+dt/2}}{\sqrt{1 + (\boldsymbol{u}^{t+dt/2})^2}}, \quad (4.15b)$$

with $\boldsymbol{u} = \gamma\boldsymbol{v}$ and γ the Lorentz factor. Defining

$$\boldsymbol{u}^- = \boldsymbol{u}^{t-dt/2} + qm_\mathrm{e}/(em)\,\boldsymbol{e}^t dt/2, \quad (4.16a)$$

$$\boldsymbol{u}^+ = \boldsymbol{u}^{t+dt/2} - qm_\mathrm{e}/(em)\,\boldsymbol{e}^t dt/2, \quad (4.16b)$$

and substituting into 4.15a leads to

$$\frac{\boldsymbol{u}^+ - \boldsymbol{u}^-}{dt} = \frac{qm_\mathrm{e}/(em)}{2\gamma^t}(\boldsymbol{u}^+ + \boldsymbol{u}^-) \wedge \boldsymbol{b}^t. \quad (4.17)$$

This equation is the classical rotation around a $\boldsymbol{b}$ field (Birsdall and Langdon (1985, Sect. 4.4), Hockney and Eastwood (1988, Sect. 4.7.1)), and is solved via

$$\boldsymbol{u}^+ = \boldsymbol{u}^- + \frac{2}{1 + \left(\frac{\Omega dt}{2}\right)^2}\left(\boldsymbol{u}^- + \boldsymbol{u}^- \frac{\Omega dt}{2}\right) \wedge \Omega, \quad (4.18)$$

with the rotation vector $\Omega = qm_e/(2em\gamma^t)\boldsymbol{b}^t$. Finally, we use

$$\gamma^t = \sqrt{1+(u^-)^2} = \sqrt{1+(u^+)^2}. \tag{4.19}$$

In Eq. 4.15a, the fields have to be known at time t. It explains the need for the half advances of $\boldsymbol{b}$ in the general scheme.

The interpolation of the fields at particle positions is done via a trilinear interpolation. We denote by (i,j,k) the nodes of the main grid A (Fig. 4.9), and we introduce a second grid B whose cell centers are on (i,j,k). Consider a superparticle at position $x = i+\delta x$, $y = j+\delta y$, $z = k+\delta z$. The superparticle is actually a charge cloud of volume equal to a cell, and this volume intersects the cell of the second grid with center (i,j,k) in a volume $V_{i,j,k} = (1-\delta x)(1-\delta y)(1-\delta z)$, the cell of the second grid with center $(i+1,j,k)$ in a volume $V_{i+1,j,k} = \delta x(1-\delta y)(1-\delta z)$, and so on. For a quantity f defined at grid points (i,j,k), the weight associated to $f_{i,j,k}$ is $V_{i,j,k}$, the one associated to $f_{i+1,j,k}$ is $V_{i+1,j,k}$, and so on for a total of 8 points.

However, neither $\boldsymbol{e}$ nor $\boldsymbol{b}$ are defined at grid points (i,j,k) (Fig. 4.9), and they must be first interpolated at grid points before applying the above procedure. This is done for example with $f_{i,j,k} = 0.5(e_{x,i-1,j,k} + e_{x,i,j,k})$ or $f_{i,j,k} = 0.25(b_{z,i,j,k} + b_{z,i-1,j,k} + b_{z,i-1,j-1,k} + b_{z,i,j-1,k})$. Details can be found in Matsumoto and Omura (1993) and Messmer (2001).

We note that the superparticle shape used for interpolation of fields to particle position and for interpolation of the current to grid nodes is the same. This is required to avoid the existence of a self-force on the superparticles and to conserve the total momentum (Birsdall and Langdon 1985, Sect. 8.6).

Computation of the current

The current $\boldsymbol{j}_{i,j,k}$ is defined at the same locations as $\boldsymbol{e}_{i,j,k}$. For current deposition, we again consider the volumes occupied by the superparticle in the grid B cells. As the superparticle moves, these volumes vary. We denote by $(i+\delta x, j+\delta y, k+\delta z)$ the position of the superparticle at $t-dt$, and we assume that it moves from $(\Delta x, \Delta y, \Delta z)$ between $t-dt$ and t.

Consider, for example, the volume of the superparticle in the cell of center (i,j,k). Its variation is given by $dV = (1-\delta x-\Delta x)(1-\delta y-\Delta y)(1-\delta z-\Delta z) - (1-\delta x)(1-\delta y)(1-\delta z)$. Defining $d_x = \delta x + \Delta x/2$, $c_x = 1-d_x$, and similarly for y and z, one finds

$$\begin{aligned} dV = \Delta x\,[-c_y c_z - \Delta y\Delta z/12] \quad &\rightarrow j_{x|i,j,k} \\ + \Delta y\,[-c_z c_x - \Delta z\Delta x/12] \quad &\rightarrow j_{y|i,j,k} \\ + \Delta z\,[-c_x c_y - \Delta x\Delta y/12] \quad &\rightarrow j_{z|i,j,k}. \end{aligned} \tag{4.20}$$

As explained in Appendix 4.A.1, the part of 4.20 proportional to the displacement along x is attributed to $j_{x|i,j,k}$, and so on.

A similar treatment is done with the cells that intersect the superparticle volume. These are cells centered in $(i+\epsilon, j+\eta, k+\xi)$, with ϵ, η and ξ equal either to 0 or 1 (8 cells). For each of these cells, only the faces intersecting the superparticle volume are concerned, so that in total there are only 12 currents to update.

Currents can be smoothed before being added to $\boldsymbol{e}$. This has the effect of reducing electromagnetic noise (see Appendix 5.A.2). This is done in the

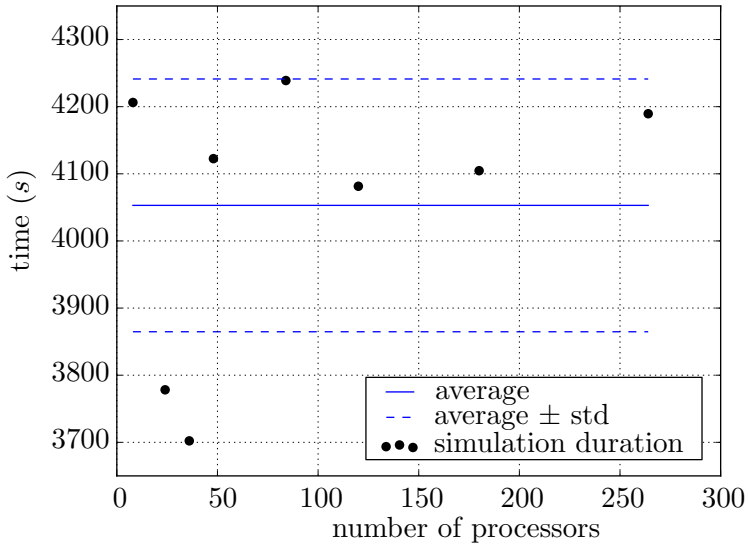

Figure 4.10: Simulation time duration versus number of cores, the spatial domain extending in proportion to the number of cores. The standard deviation corresponds to 4% of the mean value.

following way for the current of cell (i, j, k): attribute a weight of 1 to cell (i, j, k); of 0.5 to cells $(i \pm 1, j, k)$, $(i, j \pm 1, k)$, and $(i, j, k \pm 1)$; of 0.25 to cells $(i \pm 1, j \pm 1, k)$, $(i \pm 1, j, k \pm 1)$, and $(i, j \pm 1, k \pm 1)$; of 0.125 to cells $(i \pm 1, j \pm 1, k \pm 1)$; and normalize the sum of the weights to 1.

4.A.4 Boundaries

Periodic and reflective boundaries are available. The latter simulate a perfect conductor at the domain boundary by imposing the correct values for the electric and magnetic fields ($\boldsymbol{b} = \boldsymbol{e} = 0$ inside the conductor, $\boldsymbol{b}_{\text{normal}} = \boldsymbol{e}_{\text{tangential}} = 0$ at the conductor surface), and by reflecting the particles.

4.A.5 Parallel efficiency

The code parallelization was performed and tested previously by Messmer (2001, Chap. 4). It uses Fortran 90 and MPI. The simulation domain is decomposed in sub-domains of equal length along the z direction, and all the cells and particles of each sub-domain are assigned to a processor. To minimize communications between processors, ghost cells for the fields are added to each sub-domain. Communication between neighboring processors occurs at each step involving the boundaries: for particles leaving or entering the domain, for the fields, and for the currents.

The domain is currently decomposed along one direction only. This is relevant for simulations of collisionless shocks where the domain is elongated along the flow direction, or for 2D magnetic reconnection simulations where the presence of the over-dense current sheet at the domain center would lead to load balancing issues if a 2D domain decomposition were used.

We have tested the efficiency of this implementation with simulations using 16 superparticles per cell and a domain size of $60 \times 60 \times (16 n_{\text{proc}})$, where the number of cores varied from $n_{\text{proc}} = 16$ to 256. The corresponding (weak) scaling results, shown in Fig. 4.10, are satisfactory. Simulation times

scatter with a standard deviation of 4% around a constant value. The scatter is probably due to the uncontrolled node geometry.

Chapter 5

Particle-in-cell algorithms: how do they model plasmas?

> *Indeed, we [numericians] are accused of tomfoolery more than we deserve. We then simply admit to being in good company with the rest of plasma physics, with theorists and experimentalists who also have their kit bags of approximate (and occasionally inaccurate) tools.*
>
> C. Birsdall and A. Langdon,
> *Plasma Physics via Computer Simulations*, 1985

Contents

5.1 Outline

The aim of this chapter is to highlight the approximations involved by the particle-in-cell modeling. It is of interest not only for us and our simulations, but also for any group using PIC algorithms. Birsdall and Langdon (1985) and Hockney and Eastwood (1988) considered such questions. Here we

extend their work, in particular by considering 3D electromagnetic PIC codes. This chapter essentially contains half of the paper Melzani et al. (2013) (and its shorter version Melzani et al. 2014a).

The discretization of the physical equations inevitably leads to numerical precision and instability issues which are, however, not the focus of this chapter. They have been extensively studied, for example by Birsdall and Langdon (1985) and Hockney and Eastwood (1988) (see Appendix 5.A for a short review).

Instead, we explore the consequences of the two building blocks at the base of the PIC model. The first stems from the capability of computers to handle only up to $\sim 10^{10}$ particles, while real plasmas contain from 10^4 to 10^{20} particles per Debye sphere: a coarse-graining step must be used, whereby of the order of $p \sim 10^{10}$ real particles are represented by a single computer superparticle. The second is field storage on a grid with its subsequent finite superparticle size. We introduce the notion of coarse-graining dependent quantities, i.e., physical quantities depending on the number p. They all derive from the plasma parameter Λ, which we show to be proportional to $1/p$.

We explore the consequences of these approximations through two examples in Sect. 5.2: the rapid collision- and fluctuation-induced thermalization of plasmas with different temperatures, that scale with the number of superparticles per grid cell and are a factor $p \sim 10^{10}$ faster than in real plasmas; and the high level of electrostatic fluctuations in a thermal plasma, with corrections due to the finite superparticle sizes. A third important example was already presented in Sect. 4.4.2: the blurring of the linear spectrum of the filamentation instability, where the fastest growing modes do not dominate the total energy because of a high level of fluctuations. The main conclusion arising from these tests is that the collisions and correlations are artificially enhanced in a PIC plasma, but they must be kept negligible toward kinetic physics in order to obtain meaningful results.

In Sect. 5.3, we point out more generally that a PIC code simulates a microstate constituted by a restricted number of finite-sized particles, each representing up to 10^{10} real plasma particles, while the Vlasov-Maxwell system models a plasma macrostate described by a continuous fluid in six-dimensional phase-space. These two descriptions are not equivalent and in particular PIC systems, with their small numbers of particles per Debye sphere, suffer from abnormally high noise levels and include to an unknown degree particle correlations absent from Vlasov-Maxwell equations.

We come back to coarse-graining in Sect. 5.4, where we stress higher-order effects than the simple variation of the coarse-graining dependent quantities.

5.2 Coarse-graining dependent quantities

Particle-in-cell simulations have brought tremendous new insights into astrophysical plasmas, for example through studies of kinetic instabilities in their non-linear phase, kinetic turbulence, particle acceleration via the Fermi-process, or 3D magnetic reconnection and the associated particle acceleration. However, as we will detail in this section, there remain a number of questions with respect to the degree to which PIC models are able to completely mirror real plasmas.

The modeling of a real plasma by a PIC plasma implies two steps (see the right branch of Fig. 5.3): the grouping of many real particles into a single superparticle, known as coarse-graining, and the discretization of the equations with the presence of a grid. Each of these steps raises questions:

1. Coarse-graining: Is plasma behavior still expected with so few superparticles per Debye sphere? Is the noise level too large? With this, do non-linearities appear sooner than in real plasmas? Does the PIC plasma remain collisionless? And what are we losing when we gather the particles into the superparticles?

2. Discretization and grid: At least for explicit schemes, they bring with them numerical stability problems, reviewed in Appendix 5.A. Moreover, the interpolation of superparticle quantities to grid points implies a finite volume for the superparticles, which in turn implies a vanishing two-point force at short distances and thus reduces drastically the influence of collisions; it helps the PIC plasma to be collisionless, but is it enough? And what are the consequences of having superparticles whose sizes reach a significant fraction of the Debye length?

We discuss some of these questions in Sects 5.2.1 to 5.2.4.

The distinguishing feature of the Vlasov-Maxwell description of a plasma is the absence of collisions and of correlations between particles. Given the two preceding points, we can wonder if a PIC plasma can be described by the Vlasov-Maxwell system, or if it has too few superparticles per cell and thus correlation levels that are too high for this description to be accurate. The differences between PIC and Vlasov-Maxwell descriptions are examined in Sect. 5.3.

5.2.1 The plasma parameter Λ

As said earlier and expressed in Eq. 4.3, a real plasma is represented in the computer by grouping many particles into superparticles. This is what is called coarse-graining. Unlike fluid equations[a], Eqs 4.4a-4.4e are not invariant under coarse-graining (because of the definition of the current, Eq. 4.4e). The prototype of p-dependent quantities is the plasma parameter[b] $\Lambda = n\lambda_D^3$, which is close to the number of particles per Debye sphere (we recall that p is the number of particles per superparticles, λ_D the Debye length and n the real particle number density).

The plasma parameter Λ also expresses the ratio of the particles' kinetic energy to their electrostatic potential energy of interaction and, as such, varies as $1/p$ because kinetic energy is proportional to the superparticles' mass $m_{sp} \propto p$ while charge interaction energy involves their charge $q_{sp}^2 \propto p^2$. This can be seen directly by writing $\Lambda_p = n_{sp}\lambda_D^3$ for the superparticle plasma, with n_{sp} the number density of superparticles. The Debye length, being derived from fluid theory, is invariant under coarse-graining, and since

[a] By a fluid model we mean any set of equations where the individual nature of the particles has been smoothed. This is the case of the MHD family, two-fluid models, or the Vlasov-Maxwell system.

[b] In a fully ionized plasma, all coarse-graining dependent quantities can be expressed as the product of a fluid quantity (which is coarse-graining independent) and a parameter expressing a number of particles per fluid volume. Examples of these parameters include $\Lambda = n\lambda_D^3$, $n(c/\omega_{pe})^3$, $n(c/\omega_{pi})^3$, ...

$n = p \times n_{\rm sp}$, one has that

$$\Lambda_p = \frac{\Lambda}{p}, \tag{5.1}$$

with $\Lambda = \Lambda_{p=1}$ the real plasma parameter.

In a real plasma Λ ranges from 10^4 to 10^{20} (for example $\Lambda \sim 10^6$ in solar coronal loops; 10^{12} in the magnetotail, magnetopause, or in typical Crab flares; 10^{17} in AGN jets), while in computer experiments where we have to simulate thousands to millions of Debye spheres, Λ reaches hardly a few tens (for a discussion see, e.g., Bykov and Treumann 2011, Sect. 4). The corresponding number of particles per superparticles then reaches $p \sim 10^3$ to 10^{19}. The question of the relevance of PIC simulations for describing *collisionless plasmas* has thus been asked from the beginning, and concerns both terms, collisionless and plasma, that we now discuss.

Plasma behavior

A weakly coupled plasma is characterized by the predominance of collective effects over individual effects. The ratio of these effects is contained in the plasma parameter Λ_p, which can be seen as the ratio of collective behavior (the interaction of one particle with the electromagnetic fields collectively generated by all others, which is coarse-graining independent) to binary effects (which are proportional to $q_{\rm sp}^2/m_{\rm sp} \propto p$).

Since plasma behavior, with Debye screening and local charge neutrality, requires a high plasma parameter, it is wise to ask how large it should be in a PIC plasma. Birsdall and Langdon (Chap. 1, 1985) and Hockney and Eastwood (1988) have shown that it is not necessary for this ratio to be as high as in real plasmas, and that a Λ_p of about a few suffices for correct plasma behavior.

Collisionless behavior

A plasma behaves collisionlessly if the time and length scales of interest are negligible toward the collision time and the mean-free path, respectively. Since the collision time scales as Λ_p times the plasma period, it is not clear whether a PIC computer plasma with a plasma parameter on the order of unity will be collisionless.

Particle-in-cell plasmas are helped by the superparticle finite sizes, which imply that the two-point force decreases to zero for separations smaller than this size. This fact, albeit degrading the accuracy of single particle dynamics, greatly reduces the relative importance of binary collisions so that in order to correctly simulate a collisionless plasma for scales accessible in simulations, one has to insure that (Chap. 1 Birsdall and Langdon 1985; Hockney and Eastwood 1988)

$$\Lambda_p = n_{\rm sp}\lambda_{\rm D}^3 = \rho_{\rm sp}\tilde{\lambda}_{\rm D}^3 > \text{a few}. \tag{5.2}$$

(Here, $\tilde{\lambda}_{\rm D} = \lambda_{\rm D}/X_0$ is the normalized Debye length. It can be expressed as $\tilde{\lambda}_{\rm D} = n_x v_{\rm th}/c$ with $v_{\rm th} = \sqrt{T/m}$.)

This is all the more true if $r_{\rm c} < X_0$, where X_0 is the grid size and $r_{\rm c}$ is the effective collision radius for Coulomb encounters, expressed by equating the kinetic energy of the meeting particles to their potential energy of interaction: $r_{\rm c} = q_{\rm sp}^2/(4\pi\epsilon_0 T) = \lambda_{\rm D}/\Lambda_p$ ($r_{\rm c}$ is also p-dependent). The Debye length must be resolved for reasons of numerical stability (Sect. 4.4.1

and Appendix 5.A), so that we arrive at an optimal ordering $r_c < X_0 < \lambda_D$, which is allowed only if, again, $\lambda_D/r_c = \Lambda_p > 1$.

However, because the PIC model is a description of a plasma of cloud charges, grazing collisions will still be present and will lead to thermalization (Birsdall and Langdon (Chap. 1, 1985), Hockney and Eastwood (chaps. 1 and 9, 1988)), a point discussed in the next section.

5.2.2 The thermalization time

In a PIC plasma, the behavior of plasma quantities depending on Λ can be guessed by replacing Λ by Λ_p. This is the case for the thermalization time of a plasma by grazing Coulomb collisions (Spitzer 1965) or by electric field fluctuations (p. 282 Birsdall and Langdon 1985), which is on the order of $t_{th} \sim T_P \times \Lambda$ (with T_P the plasma period). This has two important consequences:

- We expect t_{th} to depend on resolution and coarse-graining, roughly as

$$\frac{t_{th}}{T_P} \propto \Lambda_p = \rho_{sp}\tilde{\lambda}_D^3. \tag{5.3}$$

- Since $\Lambda_p = \Lambda/p$ is several orders of magnitude smaller than the real plasma parameter Λ, we expect the thermalization by grazing collisions and fluctuations to be vastly more efficient in PIC codes than in reality.

This can have important consequences in simulations where thermalization plays a key role. For example in real collisionless shocks, the mean free path for collisions $l_{\text{mean free path}}$ is far larger than the shock thickness Δ_{shock} and the thermalization processes are collisionless kinetic instabilities. Since the mean free path $l^{PIC}_{\text{mean free path}} \propto \Lambda_p$ in a PIC plasma is smaller by a factor of $p \sim 10^{10}$ than in a real plasma, it is not obvious that the ordering $l^{PIC}_{\text{mean free path}} \gg \Delta_{shock}$ still holds. To truly describe a collisionless shock with a PIC algorithm, one has to be careful that the unphysically fast thermalization by collisions or fluctuations remains slower than thermalization by kinetic instabilities.

To illustrate the dependence of the collision and fluctuation induced thermalization time, we present simulations that initially have two thermal ion-electron plasmas. The first is cold, with a temperature $T_{1,e}(0) = T_{1,i}(0) = 1.6 \times 10^{-3} m_e c^2$ for its electrons and ions, while the second is hot, with $T_{2,e}(0) = T_{2,i}(0) = 1.8 \times 10^{-2} m_e c^2$. The mass ratio is $m_i/m_e = 25$. The four species interact via collisions and correlations (no sign of plasma kinetic instabilities were found) and tend to reach the same final temperature

$$T_\infty = \frac{T_{1,e}(0) + T_{2,e}(0)}{2}. \tag{5.4}$$

Particle-in-cell results are shown in Fig. 5.1 (top) for the electrons, for four simulations with a number of superparticles per cell (including all species) $\rho_{sp} = 4$, 16, 64, or 128. The other parameters are kept fixed, with $n_x = 25$, $n_t = 500$, and a box size of 25^3 cells. It results in $\Lambda_\infty = 0.25\rho_{sp}(n_x\sqrt{T_\infty/m_e c^2})^3 = 15$, 61, 243, or 485. The temperatures are measured with $T = m\sum_{sp} \boldsymbol{v}_{sp}^2/3$, where the sum runs over all the superparticles

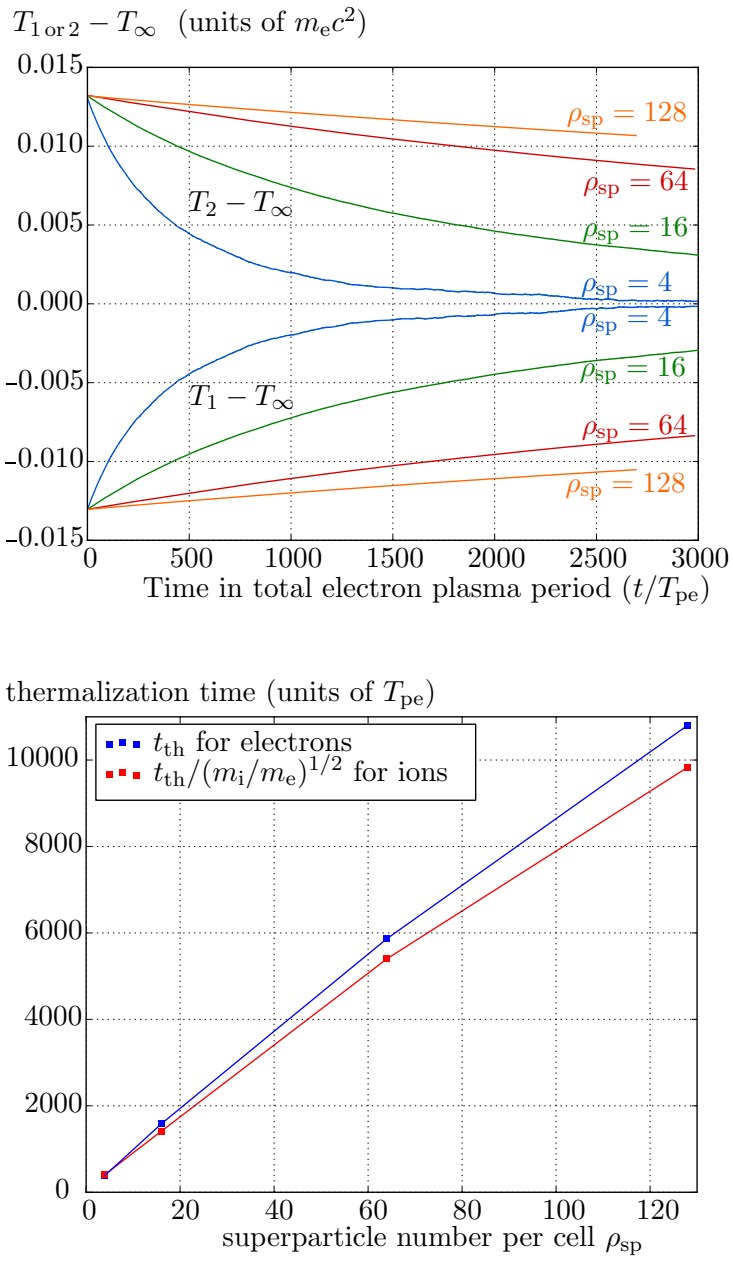

Figure 5.1: **Top**: Electron temperatures for the hot (2) and cold (1) plasmas, from four simulations with different ρ_{sp}. The curves for ion temperatures are similar, except for an overall time dilatation by a factor $\sim (m_i/m_e)^{1/2} = 5$. In this figure we use $T_\infty(t) = (T_1(t) + T_2(t))/2$. Except for $\rho_{sp} = 4$ where there is significant numerical heating, $T_\infty(t)$ is constant in time.
Bottom: Half-thermalization time for ions and electrons, versus number of superparticles per cell. For ions, we have plotted $t_{th}/(m_i/m_e)^{1/2}$. The times reported are measured as the initial slope of the temperature curves in a log-lin plot, and thus correspond to $t_{th}/2$. We see the scaling $t_{th} \propto \rho_{sp}$.

of a given species. In Fig. 5.1 (top) we clearly see a slower thermalization as $\rho_{\rm sp}$ increases.

To evaluate the thermalization times, we use the result of Spitzer (1965): for two species at temperature T_1 and T_2, thermalization occurs according to

$$\begin{aligned} \frac{dT_1}{dt} &= -\frac{dT_2}{dt} = \frac{T_2 - T_1}{t_{\rm th}}, \\ t_{\rm th} &= \frac{3\pi}{2\sqrt{2\pi}} \frac{n\omega_{\rm p1}^{-2}\omega_{\rm p2}^{-2}}{\ln\Lambda^{\rm c}} \left(\frac{T_1}{m_1} + \frac{T_2}{m_2}\right)^{3/2}, \end{aligned} \tag{5.5}$$

with $n = n_1 = n_2$ the particle number density, $\omega_{{\rm p}i} = \sqrt{ne^2/(\epsilon_0 m_i)}$, and $\ln\Lambda^{\rm c}$ the Coulomb logarithm, or the logarithm of the ratio of the largest to closest distances used in the collision integral. In a PIC code, $\ln\Lambda^{\rm c} = \ln\lambda_{\rm D}/X_0$. Clearly, $(T_1(t) + T_2(t))/2$ is constant and equal to T_∞. It follows that if mass m_1 and m_2 are equal, the thermalization time is also constant and can be written

$$t_{\rm th} = \frac{3}{2\sqrt{\pi}} \frac{2\pi}{\omega_{\rm p1}} \frac{\Lambda_\infty}{\ln\Lambda^{\rm c}}, \tag{5.6}$$

with $\Lambda_\infty = n\,[\epsilon_0 T_\infty/(ne^2)]^{3/2}$ the plasma parameter based on the temperature T_∞. It also follows that the temperatures vary exponentially as $T_1 = T_\infty - 0.5[T_2(0) - T_1(0)]\exp\{-2t/t_{\rm th}\}$, and similarly for T_2.

Here we do not find the temperature curves to be strictly exponential, mainly because there are four species. The cold electrons interact with the hot electrons on a timescale t_0, but also with the hot ions on a timescale $m_{\rm i}/m_{\rm e}t_0 = 25t_0$. The cold ions are heated by interactions with the hot ions on a timescale $(m_{\rm i}/m_{\rm e})^{1/2}t_0 = 5t_0$, and by interactions with the hot electrons on a timescale $m_{\rm i}/m_{\rm e}t_0 = 25t_0$. Since the cold ions are heated more slowly than the cold electrons, a temperature difference between these two components appears and they also start heating or cooling each other. Nevertheless, given the separation of scales we expect a measure of the slope around $t = 0$ to reflect the electron-electron or ion-electron thermalization times when measured on the electron or ion temperature curves, respectively.

Results are shown in Fig. 5.1 (bottom). We see that the relation $t_{\rm th} \propto \rho_{\rm sp}$ is roughly correct for both electrons and ions. We also underline the difference with a real plasma, where $t_{\rm th}/T_{\rm pe} \sim \Lambda$ reaches 10^{10} or more, while it is on the order of $\Lambda_p \leq 10^4$ in PIC simulations.

5.2.3 The slowing-down time of high-energy particles

The previous section shows that plasmas thermalize faster if the number of superparticles per cell is small. Not surprisingly, the same effect arise for fast particles: they are slowed down faster if the number of superparticles per cell is small. Two papers study this particular issue: Kato (2013) and May et al. (2014). We briefly review their findings.

Kato (2013) shows that for suprathermal fast particles (i.e., $v \gg v_{\rm th,e}$), the energy loss rate of the particle does not depend on the plasma thermal velocity $v_{\rm th,e}$, and consequently not on the number of particles per Debye sphere. Instead, it depends on the number of superparticles per electron inertial length sphere, $N_{d_{\rm e}} = n_{\rm e}d_{\rm e}^3$. He proves and verifies with simulations

that the energy loss rate is

$$\frac{\mathrm{d}E}{\mathrm{d}t} \propto \frac{1}{N_{d_\mathrm{e}}}. \tag{5.7}$$

He also verifies that it does not depend on the temperature, and that it is independent on the shape factor of the superparticles.

May et al. (2014) propose a similar study. They show that the collision- and fluctuation-induced energy loss rate of suprathermal particles is $\propto q^2/m \propto \Delta^2/\rho_{sp}$ in 2D, with q, m, the charge and mass of the particle, and Δ the cell width. This expression indicates that minimizing these losses can be done either by increasing the number of superparticle per cell, as previously explained, or by increasing the cell size. In particular, when $\Delta > d_\mathrm{e}$, the particle wake field is not well resolved and thus has less effects[c]. However, in this case other electron inertial length physics may be missed.

May et al. (2014) illustrate the importance of the artificially enhanced energy loss for fast ignition simulations. This is also of special interest for simulations of magnetic reconnection under relativistic magnetizations, where one focus point is the creation of high-energy particle distributions. Again, the key point is that the number of superparticles per cell should be large enough so that the artificially enhanced collisional effects, here the energy loss rate of fast particles, remain unimportant for the simulation duration, or when compared to collisionless physics. The best way to check this is to run the same simulation with different numbers of superparticles per cell, and to compare the results.

5.2.4 The field fluctuation level

The previous section showed that the behavior of PIC plasma quantities can be guessed by the substitution $\Lambda \to \Lambda_p$. While it is true for orders of magnitude estimates, this recipe is, however, not exact, and coarse-graining dependent quantities generally follow other relations than their real counterparts with respect to physical parameters (temperature, Debye length, plasma parameter, etc.). The main reason for this is that the finite volume of the superparticles implies a cutoff of the physical processes at smaller scales, an effect that becomes even more important when the superparticle size is close to the Debye length: $\lambda_\mathrm{D}/X_0 = \tilde{\lambda}_\mathrm{D}$ typically ranges between one (or less) and ten in simulations.

This section illustrates this double dependence ($\Lambda \to \Lambda_p$ and superparticle size) with a detailed study of the level of electric field fluctuations ε in a PIC thermal plasma.

In a real plasma in thermal equilibrium, it is given by (Sect. 1.1 Callen 2006)

$$\varepsilon = \frac{\langle \epsilon_0 \boldsymbol{E}^2/2 \rangle}{3nT/2} \sim \frac{1}{\Lambda}, \tag{5.8}$$

where the symbol $\langle \cdot \rangle$ denotes an average over space.

Dieckmann et al. (2004) studied the spectrum of thermal fluctuations in a PIC plasma, but without investigating their levels. Hockney (1971) (see also Hockney and Eastwood (1988)) measured ratios like ε in a series of 2D simulations of thermal plasmas, and found a good agreement with

[c] The slowing down of a suprathermal particle in a real plasma is due to the creation of a wake field produced by the particle that excites the medium, and this wake field acts back on the particle to slow it down.

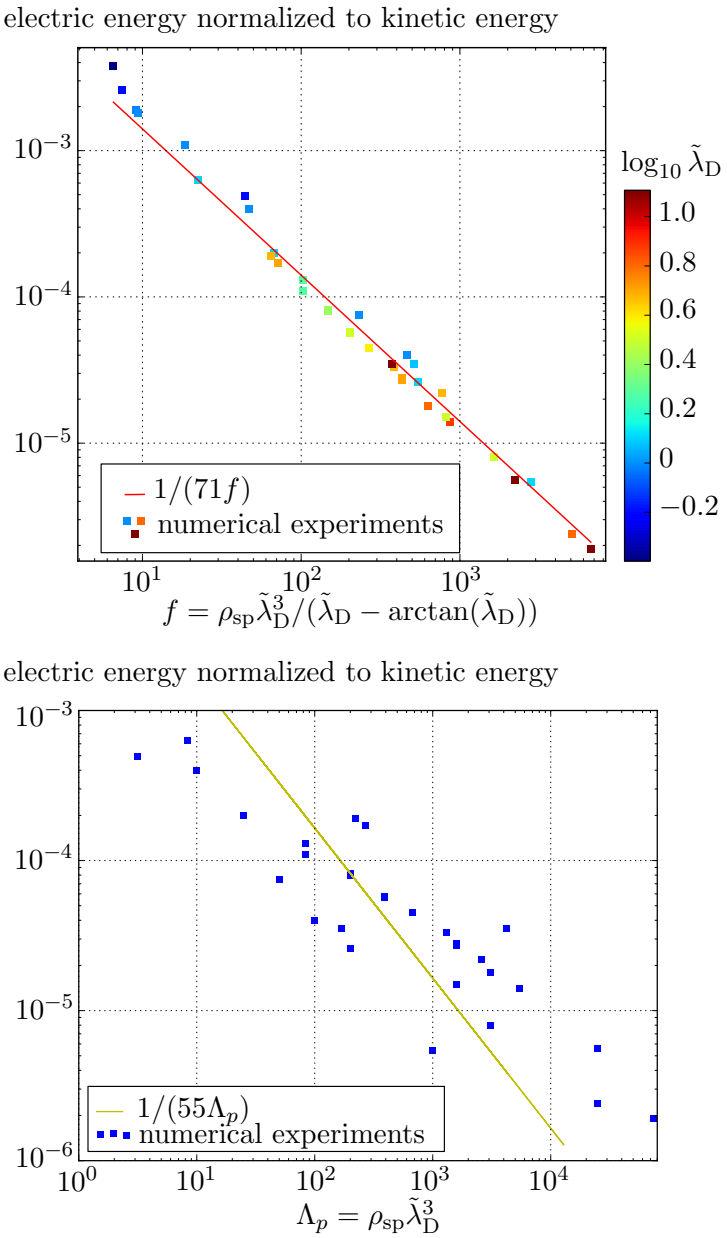

Figure 5.2: Top: Field energy levels as a function of $f = \rho_{sp}\tilde{\lambda}_D^3/(\tilde{\lambda}_D - \arctan\tilde{\lambda}_D)$. The colorbar is $\log_{10}(\tilde{\lambda}_D)$. Blue points at low f have an under-resolved Debye length that could explain the mismatch with $1/f$.
Bottom: Field energy levels versus $\Lambda_p = \rho_{sp}\tilde{\lambda}_D^3$. We clearly see the mismatch between $1/\Lambda_p$ and the results, even if the trend is correct. The large scatter is a hint that Λ is not a relevant parameter to describe field fluctuations.
Top and bottom: Each point is the result from a simulation. The field energy levels are measured as the energy in the x electric field, $\alpha^{-1}\int dV e_x^2/2$ (with α from Eq. 4.13), divided by the kinetic energy of the superparticles, $\sum_{sp}(\gamma_{sp} - 1)$.

the empirical formula $\varepsilon \propto (\tilde{W}^2 + \rho_{\rm sp}\tilde{\lambda}_{\rm D}^2)^{-1}$, where $\tilde{W}$ is the superparticle geometrical size in number of cells. Its algorithm was two dimensional, electrostatic, and based on the integration of the Poisson equation.

We perform these simulations with our 3D electromagnetic code and measure the level of energy in the electric field. We use thermal velocities from $0.04c$ to $0.10c$, $\rho_{\rm sp}$ from 2 to 500, and n_x from 10 to 128. It results in $\tilde{\lambda}_{\rm D} = \lambda_{\rm D}/X_0$ from 0.4 to 12.8, and in $\Lambda_p = n_{\rm sp}\lambda_{\rm D}^3 = \rho_{\rm sp}\tilde{\lambda}_{\rm D}^3$ from 0.1 to 75000. The fluctuation levels do not depend on the timestep (which varies from $n_t = 2000$ down to close to the Courant limit $\Delta t \sim X_0/c$) nor on box size (which is always bigger than n_x). We use a pair plasma, but increasing the mass of the ions would only multiply the fluctuation levels by a constant factor.

The results are summarized in Fig. 5.2: ε is found to be proportional to $(\tilde{\lambda}_{\rm D} - \arctan\tilde{\lambda}_{\rm D})/\rho_{\rm sp}\tilde{\lambda}_{\rm D}^3$, and not exactly to $1/\Lambda_p$. To explain this, we generalize the computation of Hockney to three dimensions.

For a plasma in thermal equilibrium, the energy in the electric field at location $(\boldsymbol{x}, t)$ can be evaluated by adding the electric field produced at $\boldsymbol{x}$ by charges at location $\boldsymbol{x}_0$ and having a velocity $\boldsymbol{v}_0$, $\boldsymbol{E}_{\boldsymbol{x}_0,\boldsymbol{v}_0}(\boldsymbol{x}, t)$,

$$\frac{\epsilon_0\langle \boldsymbol{E}^2(\boldsymbol{x}, t)\rangle}{2} = \int {\rm d}^3\boldsymbol{v}_0 {\rm d}^3\boldsymbol{x}_0 \, \frac{\epsilon_0 \boldsymbol{E}^2_{\boldsymbol{x}_0,\boldsymbol{v}_0}(\boldsymbol{x}, t)}{2} f_0(\boldsymbol{x}_0, \boldsymbol{v}_0), \tag{5.9}$$

where $\langle\cdot\rangle$ means an ensemble average (which coincides with a spatial average); $\boldsymbol{E}_{\boldsymbol{x}_0,\boldsymbol{v}_0}(\boldsymbol{x}, t)$ is a generalization of the Debye electric field for moving particles (Chap. 9 Nicholson 1983); and Eq. 5.9 can be evaluated for a plasma of finite-sized particles as (Hockney 1971; Birsdall and Langdon 1985)

$$\frac{\langle \epsilon_0 \boldsymbol{E}^2/2\rangle}{3nT/2} = \frac{1}{3n} \int \frac{4\pi k^2 {\rm d}k}{(2\pi)^3} \frac{1}{1 + k^2\lambda_{\rm D}^2/S^2(ka)}, \tag{5.10}$$

where $S(ka)$ is the Fourier transform of the shape of the superparticles and a the characteristic size of the superparticles (in our case $a \sim X_0$); $S(ka)$ tends to 1 as $k^{-1} \gg a$.

Equation 5.10 cannot be used as such for a real plasma of point particles ($S(ka) = 1$) because it includes the electric field at arbitrarily small distances from the charge, which has an infinite energy. It leads to Eq. 5.8 only if a truncation at small distances is performed, for example $k < (\alpha\lambda_{\rm D})^{-1}$ with α any constant: $\langle \epsilon_0 \boldsymbol{E}^2/2\rangle$ in Eq. 5.8 is then the energy in the electric field for wavelengths larger than $\alpha\lambda_{\rm D}$. Alternatively and to avoid a cutting procedure, we note that the electric field in Eq. 5.8 can be taken as the total field produced by the particles to maintain the screening Debye clouds (the polarization electric field; see Callen (Sect. 1.1, 2006) [d]).

In the case of a PIC plasma all processes at scales below the grid size $a = X_0$ are ignored, so that the upper bound of the integral is $k_{\rm max} = a^{-1}$ and there is no small scale divergence. Since $S(ka) \sim 1$ for $k \ll a^{-1}$, and given that the integration stops at $k = a^{-1}$, we will assume that $S(ka) = 1$.

[d] As a side note, we remark that simply taking the ratio of the particles' energy of interaction to their kinetic energies, respectively evaluated for each charge as $e^2/(2\epsilon_0 n^{-1/3})$ and $3T/2$, gives $1/(3\Lambda)^{2/3}$, and not $1/\Lambda$. This is because the electric energy of interaction was taken as the unscreened potential at a distance $n^{-1/3}$. If we take it as $e^2/(2\epsilon_0\lambda_{\rm D})$, we indeed find $1/\Lambda$.

Changing to spherical coordinates, using $u = \lambda_D k$ and $\langle E_x^2 \rangle = \langle \boldsymbol{E}^2 \rangle / 3$, we arrive at

$$\frac{\langle \epsilon_0 E_x^2/2 \rangle}{3nT/2} = \frac{1}{18\pi^2} \frac{1}{n\lambda_D^3} \int_{u_{\min}}^{u_{\max}} \mathrm{d}u \, \frac{u^2}{1+u^2}. \tag{5.11}$$

A primitive of the integral is $u - \arctan(u)$. We use $k_{\max} = 1/X_0$ or $u_{\max} = \lambda_D/X_0 = \tilde{\lambda}_D$, while the largest wavelength is given by the simulation domain size and verifies $u_{\min} \ll u_{\max}$. Consequently, we obtain

$$\frac{\langle \epsilon_0 E_x^2/2 \rangle}{3nT/2} = \frac{1}{18\pi^2} \frac{\tilde{\lambda}_D - \arctan \tilde{\lambda}_D}{\rho_{sp} \tilde{\lambda}_D^3}, \tag{5.12}$$

in good agreement with the simulations (Fig. 5.2, top panel), except for the constant factors $18\pi^2 \sim 178$ (which can be attributed to an approximate choice of $u_{\max}$).

The two limits are interesting. For a very high resolution, $\tilde{\lambda}_D \gg 1$, the field energy decreases as $1/(\rho_{sp} \tilde{\lambda}_D^2)$, which is non-trivial and different from what is expected in a real plasma where it decreases as $1/\Lambda = 1/(n\lambda_D^3)$. The empirical formula of Hockney (1971), generalized to 3D, would also predict $\varepsilon \propto 1/(\rho_{sp} \tilde{\lambda}_D^3)$ in the high resolution limit. However, our experiments clearly preclude this dependence, and are compatible with Eq. 5.12 (see Fig. 5.2). The presence of a finite superparticle volume and of the grid is retained in our calculation only in the upper bound of the integral: physically speaking, physical processes with $k^{-1} < X_0$ are smoothed out. This explains the difference between Eq. 5.12 and that of a real plasma.

For low resolutions, $\tilde{\lambda}_D \lesssim 1$, an expansion of the arctangent shows that the field energy behaves as $1/(54\pi\, \rho_{sp})$, which is finite and independent of $\tilde{\lambda}_D$. In a real plasma, ε would go to zero as the screening distance vanishes. That this is not the case here indicates that the screening distance does not vanish, because the finite size of the superparticles also plays the role of the screening mechanism.

5.3 Comparing the PIC and Vlasov-Maxwell models

We now highlight some differences between PIC models and kinetic models based on Liouville or Klimontovich equations. To do so, we recall how the Vlasov-Maxwell system is derived from these formalisms. The footnotes of this section are technical points, and do not require to be read at the first lecture.

A plasma is constituted of many charged particles in mutual electromagnetic interaction. Under relativistic conditions, a plasma microstate is fully characterized by the positions and velocities of the N particles and by the value of the fields at all space points (the fields must be treated as independent from the particles because of retarded interactions), plus the necessary boundary conditions. Within the frame of classical electrodynamics, the time evolution of a microstate is described by Maxwell equations and by the equations of motion for the particles under the action of the Lorentz

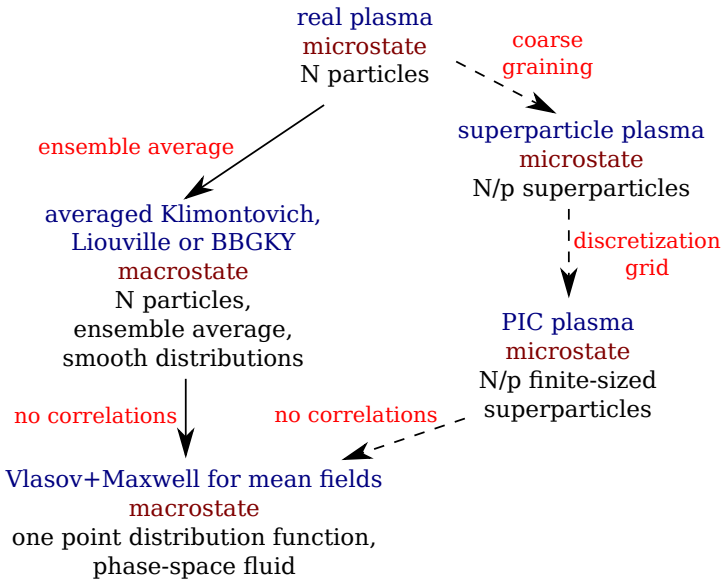

Figure 5.3: Different plasma models. Dashed arrows are transitions showing non-trivial effects. Coarse-graining and discretization are discussed in Sects 5.2.1 to 5.2.4.

force:

$$
\begin{aligned}
&\frac{\mathrm{d}}{\mathrm{d}t}(\gamma_j \boldsymbol{v}_j) = \frac{q_j}{m_j}\left(\boldsymbol{e}_m + \frac{\boldsymbol{v}_j}{c} \wedge \boldsymbol{b}_m\right), \\
&\frac{\mathrm{d}}{\mathrm{d}t}\boldsymbol{x}_j = \boldsymbol{v}_j, \\
&\frac{\partial \boldsymbol{b}_m}{\partial t} = -c\,\boldsymbol{\nabla} \wedge \boldsymbol{e}_m, \\
&\frac{\partial \boldsymbol{e}_m}{\partial t} = c\,\boldsymbol{\nabla} \wedge \boldsymbol{b}_m - \frac{1}{\epsilon_0}\sum_{j=1}^{N} q_j \boldsymbol{v}_j \delta(\boldsymbol{x} - \boldsymbol{x}_j), \\
&\boldsymbol{\nabla} \cdot \boldsymbol{e}_m = \frac{1}{\epsilon_0}\sum_{j=1}^{N} q_j \delta(\boldsymbol{x} - \boldsymbol{x}_j), \\
&\boldsymbol{\nabla} \cdot \boldsymbol{b}_m = 0.
\end{aligned}
\tag{5.13}
$$

Here, c is the speed of light, $\boldsymbol{e}_m$ the microscopic electric field, $\boldsymbol{b}_m = c\boldsymbol{B}_m$ is c times the microscopic magnetic field, q_j, m_j, γ_j, $\boldsymbol{v}_j$, and $\boldsymbol{x}_j$ the charge, mass, Lorentz factor, velocity, and position of the particle number j. We also define its momentum $\boldsymbol{p}_j = m_j \gamma_j \boldsymbol{v}_j$.

At a given time t, a microstate is represented by a point $\{\boldsymbol{x}_j, \boldsymbol{p}_j\}_{j=1..N}$ in the $6N$-dimensional phase-space, and by the fields. One can then consider the collection of microstates having the same macroscopic properties (which can depend on what one is looking for), place them as points in the $6N$-dimensional phase-space, and define the N-particle distribution function $f_N(t, \{\boldsymbol{x}_j, \boldsymbol{p}_j\}_{j=1..N})$ as the number density, at a given time, of these microstates in the $6N$-dimensional phase-space. Given that the number of microstates in phase-space is chosen as a continuum, f_N is a smooth function (Klimontovich 1982; Nicholson 1983). It defines a macrostate, i.e., an ensemble average of a collection of compatible microstates[e]. The dynamic evolution is then obtained by the Liouville equation, which states that the

[e]Liouville equation for f_N (Eq. 5.15) is true whatever the distribution of microstates, be they compatible with a single macrostate, completely random, or arbitrarily chosen.

number of microstates is conserved[f]

$$\frac{\partial f_N}{\partial t} + \sum_{i=1}^{N} \boldsymbol{v}_i \cdot \frac{\partial f_N}{\partial \boldsymbol{x}_i} + \sum_{i=1}^{N} \dot{\boldsymbol{p}}_i \cdot \frac{\partial f_N}{\partial \boldsymbol{p}_i} = 0, \tag{5.15}$$

supplemented by Maxwell equations for the microscopic fields $\boldsymbol{e}_m$ and $\boldsymbol{b}_m$[g] with for sources the particles of the corresponding microstate.

When there is no background magnetic field, and when the particles are non-relativistic, the magnetic field remains negligible toward the electric field. The latter can be computed directly from the particle positions at time t with the use of the electrostatic potential $V(r) = q^2/(4\pi\epsilon_0 r)$ (the Coulomb model). The Liouville equation can then be transformed to the infinite BBGKY hierarchy. The first BBGKY level involves the one-particle distribution function $f_1(t, \boldsymbol{w})$ (with $\boldsymbol{w} = (\boldsymbol{x}, \boldsymbol{p})$), and the two-point distribution function f_2 via the correlation function $g_2(t, \boldsymbol{w}_1, \boldsymbol{w}_2) = f_2(t, \boldsymbol{w}_1, \boldsymbol{w}_2) - f_1(t, \boldsymbol{w}_1) f_1(t, \boldsymbol{w}_2)$:

$$\frac{\partial f_1}{\partial t} + \boldsymbol{v}_1 \cdot \frac{\partial f_1}{\partial \boldsymbol{x}} - \frac{\partial}{\partial \boldsymbol{x}_1} \overline{V}_{t,\boldsymbol{x}_1}[f_1] \cdot \frac{\partial f_1}{\partial \boldsymbol{p}} = C[g_2], \tag{5.16a}$$

$$\overline{V}_{t,\boldsymbol{x}_1}[f_1] = \int \mathrm{d}^6 \boldsymbol{w}_2 V(|\boldsymbol{x}_1 - \boldsymbol{x}_2|) f_1(t, \boldsymbol{w}_2). \tag{5.16b}$$

Here C is an integral operator, vanishing with g_2. The quantity $\overline{V}_{t,\boldsymbol{x}_1}[f_1]$ is the mean potential due to the particle distribution f_1. Since $f_1(\boldsymbol{w})$ is the probability of finding a particle near $\boldsymbol{w}$ independently of the positions of all others, this potential does not include short-range correlations, but only long-range collective effects. It is a macroscopic quantity, just as the fields entering into the Vlasov-Maxwell system (Eq. 5.17)[h].

Approximations can then be made to truncate the BBGKY hierarchy. Evaluations of the right-hand side of Eq. 5.16a can lead, depending on the hypothesis made, to Boltzmann, Landau, Lenard-Balescu, or more refined kinetic equations. For a fully ionized plasma, the relevant approximation parameter is the number of particles per Debye sphere, or plasma parameter Λ. For large Λ, collisions and correlations between small numbers of

But the microstates must be compatible with a single macrostate if one wants to consider f_N as the probability distribution of the microstates for this macrostate. Also in the following, when one writes f_1 as the integral of f_N over all other particles, it has a sense only if f_N is the density of microstates not randomly chosen. See also the footnote with $\langle f^{\mathrm{K}} \rangle = f_1$.

[f] That it conserves the number of microstates can be seen by writing Liouville equation in a conservation form:

$$\frac{\partial f_N}{\partial t} + \sum_{i=1}^{N} \frac{\partial}{\partial \boldsymbol{x}_i}(\boldsymbol{v}_i f_N) + \sum_{i=1}^{N} \frac{\partial}{\partial \boldsymbol{p}_i}(\dot{\boldsymbol{p}}_i f_N) = 0. \tag{5.14}$$

It is equivalent to Eq. 5.15 because $\boldsymbol{\nabla}_{\boldsymbol{p}} \cdot \dot{\boldsymbol{p}} = (q/m) \boldsymbol{\nabla}_{\boldsymbol{p}} \cdot (\boldsymbol{E} + \boldsymbol{v} \wedge \boldsymbol{B}) = 0$.

[g] They are still the microscopic fields (compare with the non-relativistic case where $\boldsymbol{b}_m = 0$ and $\boldsymbol{e}_m$ is computed from the exact potential $V \propto \sum q_i q_j / |\boldsymbol{r}_i - \boldsymbol{r}_j|$). They are also microscopic in the BBGKY hierarchy. They become macroscopic only when we truncate BBGKY, neglecting correlations in their computation.

[h] A note on the scales involved in these macroscopic quantities : according to Nicholson (1983), the small element $\mathrm{d}^6 \boldsymbol{w}$ in $f_1(\boldsymbol{w}) \mathrm{d}^6 \boldsymbol{w} = \langle f^{\mathrm{K}} \rangle (\boldsymbol{w}) \mathrm{d}^6 \boldsymbol{w}$ is to be taken as large toward inter-particle spacing, so that a large number of particles contribute and the quantity do not fluctuate a lot, and small toward the Debye length because at larger scales there are spatial variations (while $f(\boldsymbol{w})$ is a local density). $n^{-1/3} \leq r \leq \lambda_D$ is of course possible in a plasma.

particles are negligible toward interactions of particles with the fields collectively generated by all others. Keeping only these collective interactions is equivalent to a truncation of BBGKY hierarchy at its lowest level, i.e., $g_2 = 0$, and leads to the Vlasov-Maxwell system. Generalized to relativistic plasmas[i] and to two species, it reads

$$\begin{aligned}
&\frac{\partial f_{1,s}}{\partial t} + \boldsymbol{v}\cdot\frac{\partial f_{1,s}}{\partial \boldsymbol{x}} + q_s\left(\boldsymbol{e}+\boldsymbol{v}\wedge\boldsymbol{b}\right)\cdot\frac{\partial f_{1,s}}{\partial \boldsymbol{p}} = 0, \quad s = \mathrm{i},\,\mathrm{e},\\
&\frac{\partial \boldsymbol{b}}{\partial t} = -c\,\boldsymbol{\nabla}\wedge\boldsymbol{e},\\
&\frac{\partial \boldsymbol{e}}{\partial t} = c\,\boldsymbol{\nabla}\wedge\boldsymbol{b} - \frac{1}{\epsilon_0}\sum_{s=\mathrm{i,e}}\iiint \mathrm{d}^3\boldsymbol{p}\, q_s \boldsymbol{v} f_{1,s}(t,\boldsymbol{x},\boldsymbol{p})\\
&\boldsymbol{\nabla}\cdot\boldsymbol{e} = \frac{1}{\epsilon_0}\sum_{s=\mathrm{i,e}}\iiint \mathrm{d}^3\boldsymbol{p}\, q_s f_{1,s}(t,\boldsymbol{x},\boldsymbol{p}),\\
&\boldsymbol{\nabla}\cdot\boldsymbol{b} = 0,
\end{aligned} \tag{5.17}$$

with $f_{1,s}(t,\boldsymbol{x},\boldsymbol{p})$ the one-particle distribution function, for electrons ($s = \mathrm{e}$) or ions ($s = \mathrm{i}$), defined from f_N. It is also a smooth function, and the Vlasov-Maxwell system describes the evolution of a continuous fluid in the six-dimensional phase-space, where information on the individual nature of the particles has been smoothed out. In particular within this description, the plasma parameter Λ is infinite, the fluctuation- and collision-induced thermalization time is infinite, and the level of electric field fluctuations ε is zero. We note that these are analytical properties. Numerical solutions of the Vlasov-Maxwell-system will also not strictly recover the collisionless behavior of the plasma. For instance, numerical diffusion arising necessarily from the discretization of Eqs. 5.17 will also lead to a finite thermalization time. We are, however, not aware of a comprehensive study of such effects for algorithms solving the discretized Vlasov-Maxwell system.

In contrast, the models underlying PIC simulations follow a different path, illustrated in Fig. 5.3. It consists in following the time evolution of the microstate constituted by N/p superparticles and the fields, Eqs. 4.4a-4.4e, with p reaching 10^{10} or more. One of the consequences is that the PIC plasma has a plasma parameter $\Lambda_p = \Lambda/p$ (from Eq. 5.1) far smaller than that of the real plasma, so that it includes relatively large correlation and noise levels.

[i] The relativistic Vlasov-Maxwell system is usually derived by using the Klimontovich formalism, not the Liouville formalism (see, e.g., Nicholson 1983; Klimontovich 1982). The reason is that writing BBGKY hierarchy from Liouville equation makes use of the fact that the force acting on the particles is the instantaneous Coulomb force, which is not the case in the relativistic case. It seems very hard to derive BBGKY with a retarded force, and we are not aware of such a work.

It is, however, possible to derive Vlasov-Maxwell system or a BBGKY hierarchy in the relativistic case with Klimontovich formalism (see, e.g., Nicholson (1983) p. 59, and also Callen (1990) where it is shown that Klimontovich formalism and BBGKY-from-Liouville both lead to the very same Lenard-Balescu equation). Klimontovich distribution function f^{K} is not a density of microstates, but contains the positions and velocities of all the individual particles. It is then ensemble averaged, $\langle f^{\mathrm{K}}\rangle$, as well as the fields, to obtain the desired equations. In the non-relativistic case, the identification $\langle f^{\mathrm{K}}\rangle = f_1$ is valid (see Nicholson (Chap. 3, p. 50-54, 1983) for a simple explanation, or Klimontovich (1982)).

Because of the ensemble-averaging procedure, the formalism again describes a smooth distribution function, and the points of the present discussion remain the same.

5.4 Higher-order effects of coarse-graining

We have highlighted that the coarse-graining step, the description of a real plasma of N particles by a PIC plasma of N/p superparticles, each containing p real particles, involves a reduction of the plasma parameter Λ by a factor p. This is the main effect of coarse-graining. Higher-order effects arise because after coarse-graining, the model ignores the internal dynamics and correlations of the particles contained within a superparticle.

This can be seen by writing explicitly the grouping: we label the particles either by w_n, $n = 1..N$ (with $w = (\boldsymbol{x}, \boldsymbol{p})$), or by w_{ij} with $i = 1..N/p$ representing the group number, and $j = 1..p$ the particle number within this group. We denote by $\overline{w}_{\mathrm{sp},i}$ the position and velocity of the center-of-mass of the group number i. The N-particle distribution function f_N of the real plasma can then be written formally as

$$\begin{aligned} f_N(t, w_1, ..., w_N) &= g_{\mathrm{corr}}(t, w_1, ..., w_N) \\ &+ f_{N/p}(t, \overline{w}_{\mathrm{sp},1}, ..., \overline{w}_{\mathrm{sp},N/p}) \times \prod_{i=1}^{N/p} f_{\mathrm{sp},i}(t, w_{i1}, ..., w_{ip}). \end{aligned} \tag{5.18}$$

This equation introduces $f_{N/p}(t, \overline{w}_{\mathrm{sp},1}, ..., \overline{w}_{\mathrm{sp},N/p})$, the analog of f_N but for the center-of-mass of the particle groups (i.e., of the superparticles); $f_{\mathrm{sp},i}(t, w_{i1}, ..., w_{ip})$, the distribution function of the particles contained within a group, which represents the dynamics and correlations between particles of the same group; and $g_{\mathrm{corr}}(t, w_1, ..., w_N)$, the correlations ignored by writing $f_N = f_{N/p} \times f_{\mathrm{sp},1}..f_{\mathrm{sp},N/p}$, i.e., the correlations between particles of different groups. The PIC approximation then consists in setting $g_{\mathrm{corr}} = 0$ and $f_{\mathrm{sp},i}(t, w_{i1}, ..., w_{ip}) =$ constant.

A complete understanding of these approximations would require developing a BBGKY hierarchy from Eq. 5.18 and making explicit the electric and magnetic field contributions from the particle groups. This is a complex task. We can, however, stress important consequences of the assumption $f_{\mathrm{sp},i}(t, w_{i1}, ..., w_{ip}) =$ constant:

- The superparticles are assumed incompressible. The compressibility due to particle motion within a particle group is thus absent from the coarse-grained plasma.
- The velocity dispersion of the particles within a group is ignored in the coarse-grained plasma. The kinetic pressure resulting from this dispersion is thus also absent.
- The electric fields present in the PIC plasma are computed from the superparticles. This is equivalent to saying that they are computed by taking into account only the monopole distribution of charge created by the internal arrangement of the particles within a group, with higher-order multipole terms neglected. The same holds for the magnetic field.

5.5 Discussion and conclusion

5.5.1 PIC and real plasmas

The widespread use of PIC codes for studying plasmas out-of-equilibrium calls for a deep understanding of the PIC model, and of its relation with a

real plasma and with the Vlasov-Maxwell description. Section 5.2 attempted to provide some explanations.

We have seen that the PIC model lies on two building blocks. The first stems from the capability of computers to handle only up to $\sim 10^{10}$ particles, while real plasmas contain from 10^4 to 10^{20} particles per Debye sphere. This means that a *coarse-graining* step must be used, whereby of the order of $p \sim 10^{10}$ real particles are represented by a single computer superparticle. The second step is field storage on a grid with its subsequent finite superparticle size.

We have introduced the notion of coarse-graining dependent quantities, i.e., physical quantities depending on p. The prototype of such quantities is the plasma parameter Λ, that behaves as $\Lambda_p \propto 1/p$. This vast reduction of Λ induces higher noise levels and correlations, but we have again seen that it does not threaten plasma and collisionless behavior as long as Λ_p remains above unity. All coarse-graining dependent quantities can be expressed as the product of a fluid quantity (which is coarse-graining independent) and a parameter expressing a number of particles per fluid volume. Examples of such parameters include $\Lambda = n\lambda_D^3$, $n(c/\omega_{pe})^3$, $n(c/\omega_{pi})^3$, ... Their behavior in the PIC plasma can be guessed by taking into account the reduction by a factor p of the number of particles, leading for example to the substitution $\Lambda \rightarrow \Lambda_p = \Lambda/p$ in the relevant analytical expressions. We checked this for the collision and fluctuation induced thermalization time (Sect. 5.2.2), which is indeed proportional to the number of computer superparticles per cell; the lower the number the shorter the thermalization time. Bret et al. (2013) similarly reduce the parameter $n(c/\omega_{pe})^3$ by a factor p when applying their theory for the magnetic fluctuation level in a drifting plasma to their PIC simulations. However, the substitution $\Lambda \rightarrow \Lambda_p$ is strictly valid only for point-size particles, and the large finite size of the superparticles, which reaches a fraction of a Debye length, suppresses interactions and fluctuations at shorter wavelengths and modifies these scalings. We have detailed how this works for the electric field fluctuation level in a thermal plasma in Sect. 5.2.4.

We stress that the reduction of the collision and fluctuation induced thermalization time and of other related timescales (e.g., the slowing-down time of fast particles), by 10 or more orders of magnitude, can have important consequences for the relevance of simulations: one has to insure that collisionless kinetic processes remain more efficient than the artificially enhanced collisional and fluctuation induced PIC effects. Similarly, we have seen in Sect 4.4.2 that the high level of fluctuations alter the linear spectrum of instabilities by preventing the fastest growing modes to dominate the total energy.

A more subtle effect of coarse-graining is due to the loss of the dynamics of the p particles represented by each superparticle. We intuitively expect that it will lead to the overall loss of compressibility due to superparticle incompressibility, of the contribution to kinetic pressure of the particle velocity spreading within a superparticle, and of the multipole contribution to the electric and magnetic fields created by the distribution of particles within a superparticle (see Sect. 5.4). The relevance of these missing effects remains unclear.

5.5.2 PIC and Vlasov-Maxwell plasmas

We have highlighted in Sect. 5.3 that a PIC algorithm simulates a plasma of finite-sized charges in their self-fields, and does not strictly solve the Vlasov-Maxwell system. Using the Vlasov's equation assumes that the plasma is represented in phase space by a continuous fluid. In this limit of an infinite number of particles, the plasma parameter Λ and the thermalization time are infinite, and the collision frequency and the thermal field fluctuation levels are zero. Using a PIC algorithm amounts to dividing the continuous phase space fluid into discrete elements, and to following their orbits. In this sense, one can say that we integrate the characteristics of the Vlasov's equation. However, the newly introduced graininess (which is far higher than that of the original plasma) implies the presence of binary collisions and of correlations between superparticles that is not easy to evaluate, in part because they are reduced by the finite size of the superparticles and the subsequent vanishing of the two-point force at short distances (see Sect. 5.2.1). The intricate dependence of Eq. 5.12 is a hint to this complexity. We note that Birsdall and Langdon (Chap. 12, 1985) have derived a generalization of the Balescu-Guernsey-Lenard kinetic equation that includes the use of a grid (and thus of finite sized superparticles), and of the discretization in space and time of the equations. The correlations just mentioned are partly present in this equation, but difficult to extract.

These differences between PIC and Vlasov-Maxwell plasmas are especially enhanced in the linear phase of instabilities. We see two main points. The first is that nonlinear effects absent from the linear theory, and possibly enhanced by the high noise level of the simulation (Sect. 5.2.4), may have visible consequences (Birsdall and Langdon (Sect. 13.6, 1985), Dieckmann et al. (2006)). This example is reported by Daughton (2002) in the context of the drift kink instability of a current sheet: the instability is found to grow faster than predicted by the linear Vlasov theory because the early development of another instability quickly produces non-linear effects. Bret et al. (Fig. 23, 2010) also report significant early non-linear behavior in counter-streaming situations. We have also reported the presence of field components due to non-linear effects in Fig. 4.4.

The second point is that the high level of fluctuations delays the dominance of the fastest growing Fourier modes over the sum of other modes. The consequence is that effective linear growth rates measured from total energy curves appear slower than the growth rates of the fastest modes. This is even more important in instabilities where the linear phase is short, and explains the differences between the effective growth rates and the linear cold theory of the counter-streaming instability measured in Sect. 4.4.2, with discrepancies reaching 60% or more. It may also explain the differences between theory and measured growth rates of Cottrill et al. (2008), Dieckmann et al. (2006), and Haugboelle et al. (2012) for the counter-streaming instability. On the other hand, the differences can be small if the linear phase lasts long enough for the fastest mode to dominate the energy, as is the case for the relativistic tearing instability in Sect. 4.4.4 or for the Weibel instability of Markidis et al. (2010).

5.5.3 Modeling astrophysical plasmas

In the light of what has been said so far one may wonder what this all implies for the modeling of astrophysical plasmas. We attempt to give some answers in the following. We have shown that the PIC description of an astrophysical plasma bears some risk because the plasma parameter Λ is always underestimated, leading to systematic errors in the evaluation of important parameters of the plasma such as the collision and fluctuation induced thermalization time. We stress that this does not lessen the important role of PIC algorithms for deepening our understanding of plasma physics. In particular they also have their virtues, for instance the consideration of certain correlations and of direct particle encounters (with the restrictions discussed in Sect. 5.2). They provide an accurate description of collisionless kinetic processes such as instabilities, and of the induced turbulence and eventual associated thermalization relevant to collisionless environments.

The Vlasov-Maxwell equations perfectly describe a plasma free of collisions and fluctuations. However, their discretization will again introduce different plasma characteristics. A thorough discussion of these effects is still missing. On the other hand, a collisionless description of astrophysical plasmas is not always correct. On larger spatial and temporal scales, the description of flows and the propagation of non-thermal particles must include collisions to a certain degree. In this regime other models, and in particular Fokker-Planck models, have been shown to give a good description of the plasma and have provided significant results. However, Fokker-Planck models have their own drawbacks, notably that they are local and use dragging and diffusion coefficients not self-consistently derived.

These discrepancies between real, PIC, and Vlasov-Maxwell plasmas are complex, and it needs to be discussed in further details under what circumstances which model and which numerical realization comes closest to a real plasma. In the long term, it may be justified to use models including correlations in a more systematic way, for example the Landau or the Lenard-Balescu equation on the theoretical side, and P^3M algorithms on the numerical side (that include short-range particle-particle interactions (Hockney and Eastwood 1988)). Both approaches should then be faced with results from well-controlled collisionless plasma experiments, which are presently in their infancy (see, e.g., Grosskopf et al. 2013).

Appendix 5.A Numerical effects

We have said in Sect. 5.2 that passing from a real plasma to a PIC model implies a discretization of the equations. This step comes with numerical issues that have been largely studied by Birsdall and Langdon (1985) and Hockney and Eastwood (1988). We highlight part of their work here.

5.A.1 Local numerical effects

- Stability of the electric part of the superparticle motion integrator used here requires that $\Omega\Delta t < 2$, with Ω the pulsation of oscillation of the superparticles (usually the plasma pulsation). The magnetic part is unconditionally stable.

- Courant condition for the stability of the field integrator in vacuum is $c\,\Delta t < X_0/\sqrt{2}$.

- The dispersion relation of electromagnetic waves in vacuum is modified by the grid. This modification depends on the angle of propagation with respect to the grid, and waves can have a phase velocity smaller than c (Greenwood et al. 2004). If superparticles with velocity close to c are present, they can overtake light waves and emit Čerenkov radiation. This results in the production of non-physical fields. The situation can be improved with a higher order interpolation scheme for the fields.

5.A.2 Global numerical effects

By considering the algorithm as a whole, Birsdall and Langdon were able to identify numerical effects not predicted by the consideration of subparts alone.

For example, the discrete space representation of the continuous quantities introduces a periodicity in Fourier space of period $k_0 = 2\pi/X_0$ (with X_0 the grid spacing). A physical mode of wavenumber $k = 2\pi/\lambda$ will then have, in the numerical plasma, aliases of wavenumbers $k+nk_0$, and $-k+nk_0$, with n an integer. Instabilities can arise if the physical mode couples resonantly with one of the aliases. This coupling cannot occur if $k < -k + k_0$, i.e., if $\lambda > 2X_0$ (we note that it is Nyquist-Shannon criterion to avoid spectral aliasing). Just as in signal processing, the strength of the aliases can be reduced by low-pass filtering the time-series, and this is what is done by attributing a cloud shape to the superparticles. Aliases are even more reduced when the superparticle shapes have a fast decaying Fourier transform, that is, when they are smoother.

We mention in particular the following effects due to grid aliasing:

- A cold beam of velocity v_{beam} becomes unstable if the Doppler shifted frequency of Langmuir oscillations is near the grid-crossing frequency $k_{\mathrm{grid}}\, v_{\mathrm{beam}}$. The beam is then heated. It is not the case if $\lambda_{\mathrm{D}}/X_0 > 0.046$.

- $\lambda_{\mathrm{D}}/X_0 > 1/\pi$ is needed to avoid an artificial numerical heating of a Maxwellian plasma. Otherwise, the plasma is heated up to the point where λ_{D} reaches X_0/π.

- The rate of passage of the superparticles through the cell faces produces a high-frequency noise; the rougher the superparticle shapes, the more important is the noise.

Similarly to grid effects, a finite timestep implies that harmonics differing from a multiple of $2\pi/\Delta t$ are not differentiated by the algorithm, and there are time aliases as well.

- This implies no other instabilities in the case of a non-magnetized Maxwellian plasma.

- In a magnetized plasma, artificial coupling of cyclotron harmonics can lead to instabilities.

A last point is that the effects of the grid, as well as other errors, act as a random force $F(t)$ on the superparticles. Consequently, the velocity of a superparticle undergoes a random walk, $\mathrm{d}v/\mathrm{d}t \propto F(t)$, and the kinetic energy $\langle v^2 \rangle$ increases linearly with time. Hockney and Eastwood (1988, Sect. 9.2) shows that this is indeed the cause of plasma self-heating in superparticle simulations. This is also what we find in our thermal simulations (see Sect. 4.4.1).

5.A.3 Qualitative constraints on timestep and sizestep

- The step-size X_0 of the grid (which is also roughly the superparticle size), and the time-step Δt, must be smaller than the scales of the phenomena studied. This scale can be an instability wavelength or growth rate, the cyclotron radius or pulsation, gradient scales, etc.

- The same is true for the mean distance between superparticles: $n_{\mathrm{sp}}^{-1/3} < \lambda_{\mathrm{relevant}}$. This is equivalent to having a high enough number of superparticles per volume $\lambda_{\mathrm{relevant}}^3$. The case $\lambda_{\mathrm{relevant}} = \lambda_{\mathrm{D}}$ applies to the description of plasma behavior.

- If thermal effects are important, then one should insure that the distribution function $g(\boldsymbol{p})$ is well represented on scales where these effects are important. It requires a high enough number of superparticles per relevant volume. Birsdall and Langdon (1985, Sect. 15.19) mention that it is sufficient to have a good representation of the relevant projections of g.

- The plasma should remain collisionless: the collision time should be greater than relevant timescales (instability growth rates, etc.).

5.A.4 Limitations for the computation of photon spectra

- The highest frequency represented is $2\pi c/X_0 = 2\pi n_x \omega_{\mathrm{pe}}$, so that high energy radiation is absent from the code and must be computed separately to extract photon spectra. This is done for example by Hededal (2005), Trier Frederiksen et al. (2010), and Nishikawa et al. (2011); and Cerutti et al. (2012a) from superparticle motions, with the inclusion of radiative energy losses. However, even in these cases, effects such as plasma frequency cutoff, Raizin effect, or transition radiation are not described because they are due to the back-reaction of the plasma particles on the electromagnetic waves, waves that are absent from the PIC code and are only computed afterward.

Chapter 6

Relativistic ion-electron magnetic reconnection explored with PIC simulations

It has to be noted that the main reconnection mechanism in Astrophysics is NOT Petschek reconnection, nor is it Hall reconnection, nor anomalous-resistivity reconnection. No, the most important reconnection mechanism in Astrophysics invokes waves, a certain type of waves, in fact. Called handwaves.

Dmitri Uzdensky (Uzdensky 2006)

Contents

6.1 Outline

This chapter explores magnetic reconnection in relativistic ion-electron plasmas with PIC simulations. It contains the article Melzani et al. (2014b). With the next chapter, it constitutes the main achievement of this thesis.

It is organized as follows. Section 6.2 provides the motivations and the context of the study. Section 6.3 describes the simulation setup and parameters.

Section 6.4 presents the results of simulations with antiparallel asymptotic magnetic fields. We investigate the structure of the two-scale diffusion region in Sect. 6.4.2, and explain why we see sharp transitions at the entrance of this region. Next, we turn to the relativistic Ohm's law. In non-relativistic reconnection, non-ideal terms are dominated by thermal inertia, i.e., by the divergence of off-diagonal elements of the pressure tensor. However, in Sect. 6.4.3 we show that at large inflow magnetization, thermal inertia is dominated by bulk inertia. We demonstrate in Sect. 6.4.8 that this is to be expected on the basis of an analytical model. Concerning the reconnection outflows, mass and energy conservation imply that relativistic inflow magnetization results in relativistic temperatures and/or relativistic bulk velocities in the outflows, but say nothing about the balance between the two. In Sect. 6.4.4 we show that in our simulations, thermal energy largely dominates over bulk kinetic energy. We demonstrate analytically in Sect. 6.4.8 that this is to be expected for large inflow magnetization, under the assumption that thermal inertia significantly contributes in Ohm's law. This is an important question that has observational consequences. In Sect. 6.4.5, we detail the structure of the magnetic islands and of their central density dips and isolated centers. Section 6.4.6 studies the reconnection electric field. The relevant normalization is non-trivial for relativistic setups, and we propose to use the relativistic Alfvén speed in the inflow, which leads to rates in a close range, slightly faster than for non-relativistic reconnection.

Section 6.5 highlights differences resulting from the presence of a guide magnetic field.

We summarize and conclude our work in Sect. 6.6, where we also discuss applications to astrophysical objects.

6.2 Introduction

Magnetic reconnection has been the focus of extended studies since its first introduction by Giovanelli (1947, 1948) to explain the sudden release of energy in solar flares. The term itself was coined by Dungey (1958). It is now the key ingredient for theories of coronal heating, solar flares and jets, and coronal mass ejections in the Sun (Priest 1987, and Sect. 2.10.6), of magnetic storms and substorms in the Earth's magnetosphere (Paschmann et al. 2013), and for the behavior of fusion plasmas with, for instance, the sawtooth oscillation in tokamaks (Biskamp 2000). Space physics proves that magnetic reconnection can quickly convert magnetic energy into kinetic energies (bulk flow, heat, non-thermal particles) with fast variability and

high efficiency. Such attributes made it most attractive for high-energy astrophysics to explain, for example,

- transient outflow production in microquasars and quasars (de Gouveia dal Pino and Lazarian 2005; de Gouveia Dal Pino et al. 2010; Kowal et al. 2011; McKinney et al. 2012; Dexter et al. 2014),
- gamma-ray burst outflows and non-thermal emissions (Drenkhahn and Spruit 2002; Giannios and Spruit 2007; McKinney and Uzdensky 2012),
- GeV flares from the Crab nebula (Bednarek and Idec 2011; Uzdensky et al. 2011; Cerutti et al. 2012b,a, 2013),
- flares in AGN jets (Giannios et al. 2009),
- flares in gamma-ray bursts (Lyutikov 2006a; Lazar et al. 2009),
- X-ray flashes (Drenkhahn and Spruit 2002),
- soft gamma-ray repeaters (Lyutikov 2006b; Uzdensky 2011),
- flares in double pulsar systems (Lyutikov and Lazarian 2013),
- the flat radio spectra from galactic nuclei and AGNs (Birk et al. 2001),
- the flat radio spectra from extragalactic jets (Romanova and Lovelace 1992),
- the σ-paradox and particle acceleration at pulsar wind termination shocks (Kirk and Skjæraasen 2003; Pétri and Lyubarsky 2007; Sironi and Spitkovsky 2011a),
- the heating of the lobes of giant radio galaxies (Kronberg et al. 2004),
- the heating of AGN and microquasar coronae and associated flares (Di Matteo 1998; Merloni and Fabian 2001; Goodman and Uzdensky 2008; Reis and Miller 2013; Romero et al. 2014; Zdziarski et al. 2014),
- or energy extraction in the ergosphere of black holes (Koide and Arai 2008).

As pointed out by Uzdensky (2006), magnetic reconnection is of dynamical importance in any environment where magnetic fields dominate the energy budget, so that the energy transfer can have dynamical and observable consequences, and where the rates of reconnection are fast. The latter is known to hold both in collisionless plasmas (Birn et al. 2001) and in collisional plasmas, either via turbulence (Lazarian and Vishniac 1999; Lapenta and Lazarian 2012; Lazarian et al. 2012), or via plasmoid induced reconnection (Loureiro et al. 2007; Uzdensky et al. 2010; Zanotti and Dumbser 2011; Loureiro et al. 2012) (see the discussion of Sects. 2.11.3 and 2.11.4).

Many of these environments are collisionless (Ji and Daughton 2011, and Fig. 2.42), so that fast reconnection must be triggered and sustained by non-ideal terms other than collisional ones, which implies kinetic processes on scales close to the electron inertial length or Larmor radius, with particles largely out-of-equilibrium and possibly comprising high-energy tails. As reviewed in Sect. 2.11.2, these non-ideal terms can be linked to particle inertia and wave-particle resonant interactions or to finite Larmor radius effects in magnetic field gradients. Simulation studies thus require full kinetic codes, such as Vlasov solvers or particle-in-cell algorithms.

Most of the above environments are also relativistic, either because of relativistic velocities (bulk flows or currents) or because the thermal kinetic

energy and/or the magnetic energy density exceeds the restmass energy of the particles. The latter translates into an inflow magnetization greater than unity, $\sigma_{\mathrm{in},s} = B_{\mathrm{in}}^2/(\mu_0 n_{\mathrm{in}} m_s c^2) > 1$, with s denoting ions or electrons. This magnetic energy can be transferred to the particles, and because it is greater than the particles' restmass, relativistic particles are expected. The relation $h_{0,\mathrm{out},s}\Gamma_{\mathrm{out},s} = 1 + \sigma_{\mathrm{in},s}$, with $h_{0,\mathrm{out},s}$ the enthalpy and $\Gamma_{\mathrm{out},s}$ the bulk Lorentz factor of the reconnection outflow (see Sect. 6.4.4, Eq. 6.12), indeed shows that either relativistic temperatures ($h_{0,\mathrm{out},s} > 1$) or relativistic bulk velocities ($\Gamma_{\mathrm{out},s} > 1$) are obtained for the outflows. The relevant magnetization is thus not that of the plasma, which is low because of the ion mass, but that of each species taken individually.

Studies of relativistic reconnection are scarcer than their non-relativistic counterparts (for the latter, see for example the reviews by Birn and Priest 2007; Treumann and Baumjohann 2013), and they mainly deal with pair plasmas. For relativistic pair plasmas, they include:

- analytical works (Kirk 2004; Tenbarge et al. 2010; Kojima et al. 2011) and Sweet-Parker-like analysis (Blackman and Field 1994; Lyutikov and Uzdensky 2003; Lyubarsky 2005),
- 2D MHD simulations (Watanabe and Yokoyama 2006; Zenitani et al. 2011a; Takahashi et al. 2011; Zanotti and Dumbser 2011; Takamoto 2013; Baty et al. 2013),
- two-fluid simulations (Zenitani et al. 2009a,b),
- test particle simulations (Bulanov and Sasorov 1976; Romanova and Lovelace 1992; Larrabee et al. 2003; Cerutti et al. 2012b) (Larrabee et al. include a retroaction of the particles on the fields, in an iterative way),
- 1D PIC simulations (Pétri and Lyubarsky 2007),
- 2D PIC simulations (Jaroschek et al. 2004, 2008; Lyubarsky and Liverts 2008; Sironi and Spitkovsky 2011a; Bessho and Bhattacharjee 2012; Cerutti et al. 2012a, 2013; Zenitani and Hoshino 2001, 2005a, 2007, 2008; Zenitani and Hesse 2008),
- and 3D PIC simulations (Jaroschek et al. 2004; Zenitani and Hoshino 2005b, 2008; Liu et al. 2011; Sironi and Spitkovsky 2011a; Kagan et al. 2013; Cerutti et al. 2014b; Sironi and Spitkovsky 2014).

Relativistic reconnection in ion-electron plasmas has been studied less. We find a test particle simulation (Romanova and Lovelace 1992), a resolution of the diffusion equation (Birk et al. 2001), and a discussion by Sakai et al. (2002) in a 2D PIC simulation of laser fusion beams where reconnection occurs when the filaments of the filamentation instability merge.

The focus of the present work is on relativistic reconnection – as compared to non-relativistic studies – and on ion-electron plasmas – as compared to pair plasmas. Our goals are to carve out aspects that are particular to this regime, to shed light on the underlying physical causes, and to ultimately put our findings in the, admittedly speculative, larger astrophysical context of microquasar and AGN disk coronae and magnetospheres, and of other possible environments with ion-electron relativistic plasmas. Part of our results are also of interest for pair plasmas and for non-relativistic cases.

ω_{ce}/ω_{pe}	L/d_i	$\Gamma_e U_e$	Θ_e	Θ_i	r_{ce}/d_e	L/r_{ce}
1	0.5	0.20	0.25	0.01	0.7	3.8
3	0.5	0.53	2.40	0.096	1.6	1.6
6	1	0.70	10	0.4	3.3	1.5

Table 6.1: Parameters of the current sheet. They hold for a mass ratio of 25, and are independent of the background plasma parameters. The free variables are ω_{ce}/ω_{pe} and L/d_i. The electron and ion temperatures are the same, normalized as $\Theta_s = T_s/(m_s c^2)$. The ions and electrons counterstream with opposite velocities $\pm U_e \hat{\boldsymbol{y}}$ (given here in units of c) and associated Lorentz factors Γ_e. The sheet halfwidth in units of ion inertial lengths is L/d_i, while in units of the thermal Larmor radii (at current sheet center) it is L/r_{ce}.

6.3 Problem setup

6.3.1 Description of the relativistic Harris equilibrium

We use the explicit particle-in-cell code `Apar-T`, presented and tested in Chapter 4. Broadly speaking, it is a parallel electromagnetic relativistic three-dimensional PIC code with a staggered grid, where the fields are integrated via Faraday and Maxwell-Ampère equations, currents computed by a charge conserving volume weighting (CIC), and fields interpolated accordingly.

The simulations start from a Harris equilibrium, which is a solution of the Vlasov-Maxwell system. The magnetic field is

$$\boldsymbol{B}_{rec} = \hat{\boldsymbol{z}}\, B_0 \tanh(x/L)\,, \tag{6.1}$$

(see Figs. 6.1 or 6.2 for axis orientation), and is sustained by a population of electrons and ions of equal number density $n_{cs}(x) = n_{cs}(0)/\cosh^2(x/L)$ (cs stands for current sheet), flowing with bulk velocities U_e and $U_i = -U_e$ in the $\pm y$ directions. We denote the associated Lorentz factors by Γ_e and Γ_i. Each species follows a Maxwell-Jüttner distribution (Eq. 3.83) of normalized temperature $\Theta_s = 1/\mu_s = T_s/m_s c^2$.

We derived the equilibrium relations for relativistic temperatures and current drift speeds, as well as for arbitrary ion to electron mass ratios and temperature ratios, in Sect. 3.7. The equilibrium depends on the ratio ω_{ce}/ω_{pe}, with $\omega_{pe} = (n_{cs}(0)e^2/(\epsilon_0 m_e))^{1/2}$ the electron plasma pulsation defined with the lab-frame number density $n_{cs}(0)$ (not including background particles), and $\omega_{ce} = eB_0/m_e$ the electron cyclotron pulsation in the asymptotic magnetic field (not including the guide field, $e > 0$). Our simulations are, however, not loaded exactly with the equilibrium values, but with a temperature and current speed uniformly in excess of $\sim 10\%$ in order to shorten the otherwise rather long stable phase.

We also set a background plasma of number density (for electrons or for ions) n_{bg} and of temperature $T_{bg,e}$ for electrons and $T_{bg,i}$ for ions. Finally, a guide magnetic field is sometimes considered, i.e., a uniform component $\boldsymbol{B}_G = B_G \hat{\boldsymbol{y}}$. Adding the background plasma or the guide field does not change the Harris equilibrium.

6.3.2 Magnetization and energy fluxes

There are several ways to characterize the magnetization of the configuration. The ratio ω_{ce}/ω_{pe} has no direct physical meaning and is mostly used

$\frac{\omega_{ce}}{\omega_{pe}}$	$\frac{n_{bg}}{n_{cs}(0)}$	$\frac{B_G}{B_0}$		$T_{bg,s}$ (K)	β_s	$h_{0,bg,s}$	$\sigma_s^{cold}(B_{rec})$	$\sigma_s^{hot}(B_{rec})$	$\sigma_{i+e}(B_{rec})$	$V_{A,in}^{NR}$, $V_{A,in}^{R}$
1	0.1	0	ion	1.5×10^7	5×10^{-4}	1	0.4	0.4	0.38	0.63, 0.53
			lec	″	″	1.006	10	9.94		
3	0.31	0	ion	2×10^8	2.5×10^{-3}	1	1.16	1.16	1.11	1.08, 0.73
			lec	″	″	1.086	29	27		
3	0.1	0	ion	2×10^8	7.5×10^{-4}	1	3.6	3.6	3.26	1.90, 0.88
			lec	3×10^9	1.1×10^{-2}	2.57	90	35		
3	0.1	0	ion	1.5×10^7	5.6×10^{-5}	1	3.6	3.6	3.46	1.90, 0.88
			lec	″	″	1.006	90	89		
3	0.1	0	ion	2×10^8	7.5×10^{-4}	1	3.6	3.6	3.45	1.90, 0.88
			lec	″	″	1.086	90	83		
3	0.1	0.5	ion	1.5×10^7	4.5×10^{-5}	1	3.6	3.6	3.46	1.90, 0.81
			lec	″	″	1.006	90	89		
3	0.1	1	ion	1.5×10^7	2.8×10^{-5}	1	3.6	3.6	3.46	1.90, 0.66
			lec	″	″	1.006	90	89		
6	0.1	0	ion	8×10^8	7.5×10^{-4}	1.014	14.4	14.2	13.5	3.80, 0.97
			lec	″	″	1.37	360	260		

Table 6.2: Physical input parameters of the simulations and resulting magnetizations of the *background* plasma. The enthalpy of the background plasma is $h_{0,bg,s}$. Its cold magnetization $\sigma_s^{cold}(B)$ is defined by Eq. 6.5, σ_s^{hot} by Eq. 6.4, and $\sigma_{i+e}(B)$ by Eq. 6.6. In all cases, we assume $\Gamma_{in} \sim 1$. The background plasma $\beta_s = n_s T_s/(B^2/2\mu_0) = 2\Theta_s/\sigma_s^{cold}(B)$ includes the guide field ($\sigma_s^{cold}(B_{tot}) = \sigma_s^{cold}(B_0) + \sigma_s^{cold}(B_G)$). The Alfvén speeds, defined in Sect. 6.3.3, do not take the temperature into account, and are given in units of c. For the relativistic Alfvén speed, when there is a guide field we display the $\hat{\boldsymbol{z}}$-projection: $V_{A,in}^{R} \cos\theta$, with $\theta = \arctan B_G/B_0$.

as a simulation label.

The magnetization σ_s^{hot} of the background plasma species s is the ratio of the energy flux in the reconnecting magnetic field to that in the particles (restmass, thermal, bulk). The electromagnetic energy flux is the Poynting flux. Far from the current sheet, it reads as

$$\frac{\boldsymbol{E} \wedge \boldsymbol{B}}{\mu_0} = \frac{\boldsymbol{E} \wedge \boldsymbol{B}_{rec}}{\mu_0} + \frac{\boldsymbol{E} \wedge \boldsymbol{B}_G}{\mu_0} = \frac{B_{rec}^2}{\mu_0} v_{E_y \times B_{rec}} \hat{\boldsymbol{x}} + \frac{B_G^2}{\mu_0} v_{E_y \times B_{rec}} \hat{\boldsymbol{x}}, \quad (6.2)$$

where $\boldsymbol{B} = B_{rec}\hat{\boldsymbol{z}} + B_G\hat{\boldsymbol{y}}$ and $v_{E_y \times B_{rec}} = E_y/B_{rec}$. This splitting of the energy flux into two contributions, one from the magnetic field that will reconnect, the other from the guide field that will mostly be compressed, is possible only if the electric field is normal to $\boldsymbol{B}$, which is indeed the case in the ideal outer area because of the tendency of the plasma to screen parallel electric fields. For the particles, the energy flux of species s is (Eq. 3.79)

$$n_{lab,s} \langle v \gamma m_s c^2 \rangle_s = n_{lab,s} \Gamma_s h_{0,s} \bar{v}_s m_s c^2, \quad (6.3)$$

with $n_{lab,s}$ the particle number density in the lab frame (= Γ_s times that in the comoving frame), $\langle \cdot \rangle_s$ denoting an average over momentum of the distribution function, m_s the particle mass, $\bar{v}_s$ their bulk velocity, Γ_s the associated Lorentz factor, and $h_{0,s}$ their comoving enthalpy (drawn in Fig. 3.1

for a thermal distribution). All in all, the magnetization of species s is

$$\begin{aligned}\sigma_s^{\rm hot}(B_{\rm rec}) &= \frac{E\times B_{\rm rec}/\mu_0}{n_{{\rm lab},s}\langle v\gamma m_s c^2\rangle_s} = \frac{B_{\rm rec}^2/\mu_0}{n_{{\rm lab},s}m_s c^2\Gamma_s h_{0,s}}\\ &= \frac{\sigma_s^{\rm cold}(B_{\rm rec})}{\Gamma_s h_{0,s}},\end{aligned} \tag{6.4}$$

with $\sigma_s^{\rm cold}$ the magnetization of the plasma without taking temperature effects and relativistic bulk motion into account:

$$\sigma_s^{\rm cold}(B) = \frac{B^2}{\mu_0 n_{{\rm lab},s}m_s c^2}. \tag{6.5}$$

If $\sigma_s^{\rm cold}(B_{\rm rec})$ exceeds unity, then it is possible to transfer to the particles an amount of energy from the reconnecting field that exceeds their restmass, i.e., it is possible to obtain relativistic particles. We do not include the guide field $B_{\rm G}\hat{\boldsymbol{y}}$ in the definition of the magnetization because it is mostly compressed and does not transfer energy to the particles.

Finally, the total magnetization of the plasma is

$$\sigma_{\rm i+e}(B_{\rm rec}) = \frac{B_{\rm rec}^2/\mu_0}{\sum_s n_{{\rm lab},s}m_s c^2\Gamma_s h_{0,s}} = \frac{\sigma_{\rm i}^{\rm cold}(B_{\rm rec})}{\sum_s \Gamma_s h_{0,s}(m_s/m_{\rm i})}. \tag{6.6}$$

In the inflow part of our simulations, we have $h_{0,{\rm i}}\sim 1$, $h_{0,{\rm e}}<2.6$, and $m_{\rm i}=25m_{\rm e}$ for the range of background temperatures considered here, so that the particle energy flux is largely dominated by the restmass energy flux of the ions, which is $n_{{\rm lab},{\rm i}}\bar{v}_{\rm i}m_{\rm i}c^2$, and has no temperature dependence. We thus have $\sigma_{\rm i+e}\sim\sigma_{\rm i}^{\rm cold}$, and $\sigma_{\rm i+e}$ is not a good representative of the electron physics and of the possibility that they are relativistically magnetized. The inflow magnetizations in our simulations are presented in Table 6.2.

6.3.3 Alfvén velocities

We give the definitions of the Alfvén speeds that will be used to discuss the normalization of the reconnection electric field in Sect. 6.4.6. They are reported in Table 6.2.

The Alfvén velocity in the inflow plasma, far from the current sheet, is expressed in the comoving plasma frame and is, respectively in the non-relativistic and relativistic cases,

$$V_{\rm A,in}^{\rm NR} = \frac{B_{\rm tot}}{\sqrt{\mu_0 n_{0,{\rm bg}}(m_{\rm e}+m_{\rm i})}}, \tag{6.7a}$$

$$V_{\rm A,in}^{\rm R} = c\left(\frac{\sigma_{\rm i+e}(B_{\rm tot})}{1+\sigma_{\rm i+e}(B_{\rm tot})}\right)^{1/2} \simeq \frac{V_{\rm A,in}^{\rm NR}}{\sqrt{\left(V_{\rm A,in}^{\rm NR}\right)^2/c^2+1}}, \tag{6.7b}$$

where $\sigma_{\rm i+e}(B_{\rm tot})$ is to be expressed in the comoving frame (Eq. 6.6 with $n_{{\rm lab},s}=n_{0,{\rm bg}}$ the comoving density and $\Gamma_s=1$), and where $B_{\rm tot}=(B_0^2+B_{\rm G}^2)^{1/2}$. For the relativistic expression 6.7b, the first equality is general and derived from the relativistic ideal MHD description (Gedalin 1993), while the second holds only because $m_{\rm i}\gg m_{\rm e}$ and the total enthalpy is dominated by the ion contribution. When there is a guide magnetic field, we show in Sect. 6.5.3 that it is relevant to project the Alfvén speed into the

direction of the reconnecting magnetic field ($\hat{\boldsymbol{z}}$), i.e., to consider $V_{\mathrm{A,in}}^{\mathrm{R}} \cos\theta$ with $\tan\theta = B_{\mathrm{G}}/B_0$.

A hybrid Alfvén speed is often defined in the literature as depending on the asymptotic magnetic field (without the guide field) and on the comoving density at the center of the current sheet:

$$V_{\mathrm{A},0}^{\mathrm{NR}} = \frac{B_0}{\sqrt{\mu_0 n_{0,\mathrm{cs}}(0)(m_{\mathrm{e}} + m_{\mathrm{i}})}} = \left(\frac{m_{\mathrm{e}}}{m_{\mathrm{e}} + m_{\mathrm{i}}}\right)^{1/2} \frac{\omega_{\mathrm{ce}}}{\omega_{0,\mathrm{pe}}}\, c, \tag{6.8}$$

where a subscript 0 indicates a comoving quantity. Its relativistic generalization is denoted by $V_{\mathrm{A},0}^{\mathrm{R}}$, and is obtained with Eq. 6.7b but with parameters of the plasma at the center of the current sheet in the magnetization.

6.3.4 Simulation parameters and resolution tests

The physical parameters of the main simulations are given in Tables 6.1 and 6.2. We consider a mass ratio $m_{\mathrm{i}}/m_{\mathrm{e}} = 25$, except for one simulation with pairs. The background plasma number density is $n_{\mathrm{bg}} = 0.1 n_{\mathrm{cs}}(0)$ or $0.3 n_{\mathrm{cs}}(0)$. Its temperature is varied between $T_{\mathrm{bg}} = 1.5 \times 10^7\,\mathrm{K}$ ($2.5 \times 10^{-3} m_{\mathrm{e}}c^2$) and $3 \times 10^9\,\mathrm{K}$ ($0.5 m_{\mathrm{e}}c^2$). The magnetization depends on the ratio $\omega_{\mathrm{ce}}/\omega_{\mathrm{pe}} = 1$, 3, or 6, leading to inflow magnetizations σ_s^{hot} between 10 and 260 for electrons, or 0.4 and 14 for ions. The current sheet is either of initial halfwidth $L = 0.5 d_{\mathrm{i}} = 2.5 d_{\mathrm{e}}$, or $L = 1 d_{\mathrm{i}}$ in the $\omega_{\mathrm{ce}}/\omega_{\mathrm{pe}} = 6$ case, with d_{e}, d_{i} the inertial lengths defined at current sheet center. We stress that for relativistic temperatures the sheet width in terms of Larmor radii will not be the same for simulations with different $\omega_{\mathrm{ce}}/\omega_{\mathrm{pe}}$ (Eq. 3.92); see L/r_{ce} in Table 6.1.

The numerical resolution is set by the number of cells n_x per electron inertial length d_{e}, by the number of timesteps n_t per electron plasma period $2\pi/\omega_{\mathrm{pe}}$, and by the number of computer particles (the so-called superparticles) per cell ρ_{sp}. The quantities d_{e}, ω_{pe}, and ρ_{sp} are defined at $t = 0$ at the center of the current sheet, where the particle density is highest. For the simulations of Table 6.2, we take $n_x = 9$ and $n_t = 150$ (250 for $\omega_{\mathrm{ce}}/\omega_{\mathrm{pe}} = 6$). We checked with a simulation with twice this resolution ($\omega_{\mathrm{ce}}/\omega_{\mathrm{pe}} = 3$, $n_x = 18$, $n_t = 250$) that all of the presented results are not affected[a].

Concerning the number of superparticles per cell, the simulations of Table 6.2 use $\rho_{\mathrm{sp}} = 1820$ (1090 for $n_{\mathrm{bg}}/n_{\mathrm{cs}}(0) = 0.3$). For the case $n_{\mathrm{bg}}/n_{\mathrm{cs}}(0) = 0.1$, this corresponds to 1650 electron and ion superparticles per cell for the plasma of the current sheet and to 170 for the background plasma. The density profile of the current sheet plasma is set by changing the number of superparticles per cell when going away from the center. We stressed in Chapter 5 that because of their low numbers of superparticles per cell when compared to real plasmas, PIC simulations present high levels of collisionality. One should thus ensure that collisionless kinetic processes remain faster than collisional effects (e.g., for thermalization), essentially by taking a large enough number Λ^{PIC} of superparticles per Debye sphere. For example, with $\Theta_{\mathrm{e}} = 2.4$ the electron Debye length is 20 cells large, and we have initially at

[a] Throughout this section, "all the results" means the time evolution of the reconnection rate and of the width of the diffusion zone for electrons and ions, the distribution functions of high-energy particles, the temperature curves in the diffusion zone, the energy content in the outflows, as well as the relative weight of the terms in Ohm's law.

the center of the current sheet: $\Lambda^{\rm PIC} \sim 364 \times 20 \times 20 = 7.3 \times 10^5$ superparticles. For a background plasma with $T_{\rm bg} = 2 \times 10^8$ K: $\Lambda^{\rm PIC} = 133$. We performed a simulation identical to the one with $\omega_{\rm ce}/\omega_{\rm pe} = 3$, $n_{\rm bg}/n_{\rm cs}(0) = 0.1$, $T_{\rm bg} = 2 \times 10^8$ K, but with half the superparticles, and found no change in the results. It shows that the main simulations use a large enough $\rho_{\rm sp}$.

Boundaries are periodic along z and y. At the top and bottom x boundaries we use reflective boundaries, i.e., we place a perfectly conducting wall that reflects waves and particles. The number of cells for the standard simulations is 4100×6144. The length along y is of no dynamical importance, and the dimensions correspond to a 2D simulation with 455 initial electron inertial lengths along x and 683 along z, typically with 4×10^9 superparticles. It takes $70\,T_{\rm pe}$ for light waves to start from the current sheet, reflect at the $\pm x$ boundaries, and come back to the sheet. This corresponds to $(18, 52, 106)\omega_{\rm ci}^{-1}$, or $(450, 1300, 2650)\omega_{\rm ce}^{-1}$ for, respectively, simulations with $\omega_{\rm ce}/\omega_{\rm pe} = 1, 3, 6$. The light travel time in the z direction is longer. Except for run $\omega_{\rm ce}/\omega_{\rm pe} = 1$, all the analyses presented here are for shorter times and are thus not affected by boundaries. To check this, we performed a larger simulation with 8000×10240 cells (i.e., 888×1138 initial electron inertial length) for the case $\omega_{\rm ce}/\omega_{\rm pe} = 3$, $n_{\rm bg}/n_{\rm cs}(0) = 0.1$, $T_{\rm bg} = 2 \times 10^8$ K, with the same n_t, n_x, $\rho_{\rm sp}$. The corresponding light-crossing time is now $136\,T_{\rm pe} = 101\omega_{\rm ci}^{-1} = 2535\omega_{\rm ce}^{-1}$. All the results are the same, which shows that we do not suffer from boundary effects.

6.4 Results with no guide field

This section explores results for simulations with no guide field, where the magnetic field above and below the current sheet is antiparallel.

6.4.1 Overall structure and evolution

We first summarize the general picture, raising important points that are detailed in the next subsections. The initial kinetic equilibrium is unstable to the collisionless tearing mode, which in all presented simulations is triggered by the noise level and by the slightly out-of-equilibrium initial state. We have studied in detail the linear phase of this instability with PIC simulations for pair plasmas (Sect. 4.4.4) and found growth rates within 5% of the analytical derivations of Pétri and Kirk (2007) made on the basis of a linearization of the Vlasov-Maxwell system. Physically, the instability is driven by the particles freely bouncing in the layer of magnetic field reversal (Coppi et al. 1966), with a mechanism similar to a filamentation instability: perturbations in B_x and B_z lead to a bunching of the particles, which in turn increase the magnetic field perturbation. It leads to the formation of alternating X- and O-points, here with no privileged location because we impose no localized initial perturbation (Fig. 6.1).

With the appearance of X- and O-points, the magnetic flux variations across fixed contours induce an out-of-plane electric field $E_y\hat{\boldsymbol{y}} \propto -\hat{\boldsymbol{y}}$, which amplifies the initial current along $-y$, which in turn increases the magnetic field in order to cancel out the former magnetic flux variations and prevent reconnection. However, non-ideal processes forbid an ideal plasma response, and allow the triggering of reconnection and the existence of a finite electric field at the current sheet center, where ideal Ohm's law would otherwise read

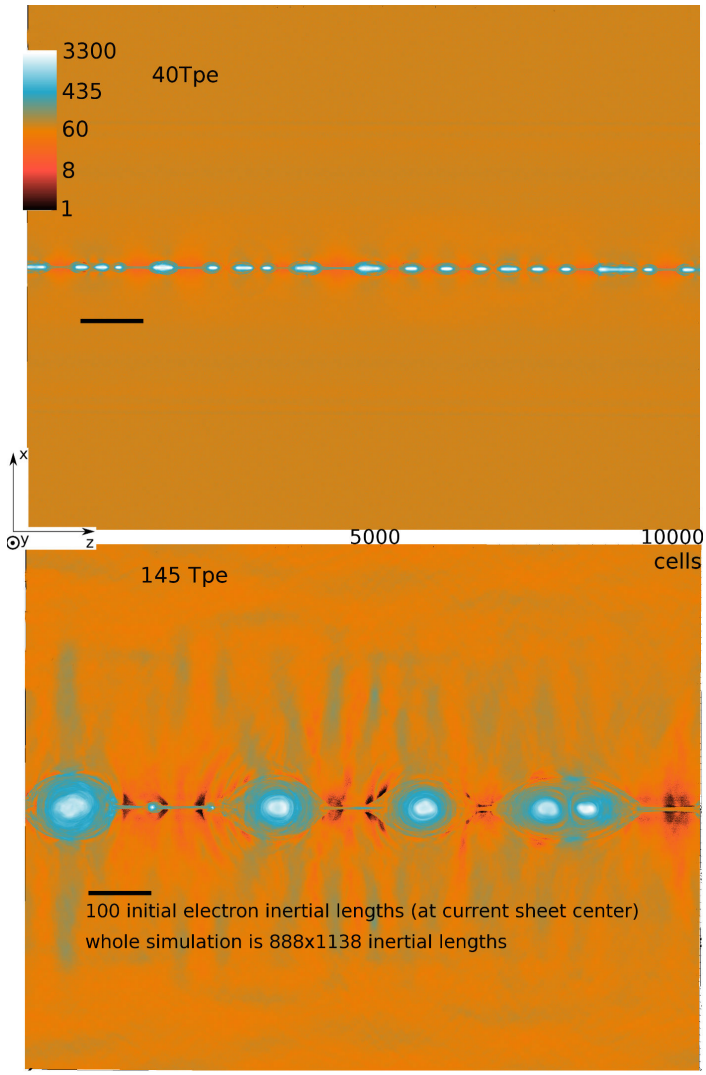

Figure 6.1: Electron number density in the whole simulation domain, at two different times. From run $\omega_{ce}/\omega_{pe} = 3$, $\sigma_e^{hot} = 89$, $T_{bg} = 1.5 \times 10^7$ K. Units are the number of electron superparticles per cell, lengths are in cell numbers. Here $40T_{pe} = 30\omega_{ci}^{-1} = 750\omega_{ce}^{-1}$.

$E_y = 0$. This electric field E_y is at the heart of the reconnection process, because it is responsible for transfering energy from the magnetic field to particles in the diffusion region. We detail Ohm's law and the contribution of each non-ideal term in Sect. 6.4.3.

Plasma and magnetic fields decouple in the non-ideal region, and flux tubes can "reconnect", producing new flux tubes strongly bent that accelerate the plasma outward in the $\pm\hat{\boldsymbol{z}}$ directions, thus producing the exhaust outflows. This depletion of particles and/or the spreading of the electric field E_y outside the current sheet create an inflow from the ideal zone toward the current sheet: particles $E \times B$ drift at a speed $\boldsymbol{v}_{in} = \boldsymbol{E} \times \boldsymbol{B}/B^2 = E_y/B_z\hat{\boldsymbol{x}}$. The incoming particles are then accelerated along $\hat{\boldsymbol{y}}$ by E_y once they enter the non-ideal region where they are unmagnetized (because there $E > cB$). The structure of this central region is investigated in Sect. 6.4.2.

The exhaust outflows, which in the MHD view are driven by the magnetic field tension force, are produced by particles accelerated by E_y along $\hat{\boldsymbol{y}}$ and then slowly rotating owing to the increasingly strong magnetic field B_x

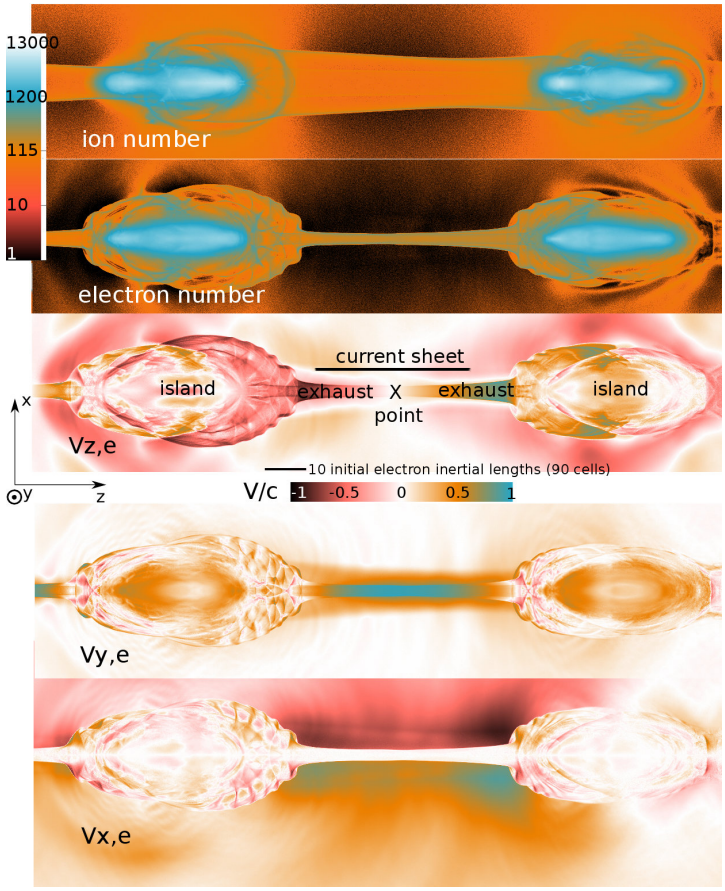

Figure 6.2: Zoom around a X-point showing various fluid quantities. From run $\omega_{ce}/\omega_{pe} = 3$, $\sigma_e^{hot} = 89$, $T_{bg} = 1.5 \times 10^7$ K, at $t = 40T_{pe} = 30\omega_{ci}^{-1} = 750\omega_{ce}^{-1}$and $z \sim 3024$ cells. Units for particle densities are particle numbers per cell. The temperatures at the same time are shown in Fig. 6.10, and cuts along x and z in Figs. 6.4 (upper-right), 6.7, 6.8, and 6.9 (right).

as one goes away from the X-point (Fig. 6.3). As they do so, particles still gain energy as long as $q_s E_y \hat{\boldsymbol{y}} \cdot \boldsymbol{v} > 0$. The energy content of these outflows comprises a Poynting flux, bulk kinetic energy, and thermal energy, with respective weights that depend on the background plasma parameters, as studied in Sect. 6.4.4. The balance between inflow and outflow can lead, depending on the conditions, to a steady state Sweet-Parker-like configuration.

In the configuration of the simulations the initial perturbation is not localized in space, so that several X-points appear, with islands inbetween that collect the flux of particles and of the reconnected magnetic field. The islands are trapped between two exhausts, and the bulk energy of the outflows is converted into heat by random scatterings in the complex electric and magnetic structures at the island entrance and inside the islands (Fig. 6.10), however with particle distributions that are not necessarily thermal (see Sect. 6.4.5). The islands grow and, since they are threaded by parallel currents (along $-\hat{\boldsymbol{y}}$), attract each other via the Lorentz force and merge, thus growing even more. As time goes on, the island number dwindles and the space inbetween them increases, forming elongated current sheets composed of a X-point surrounded by two elongated exhausts (see Fig. 6.2). We stop the simulations when only two or three islands remain.

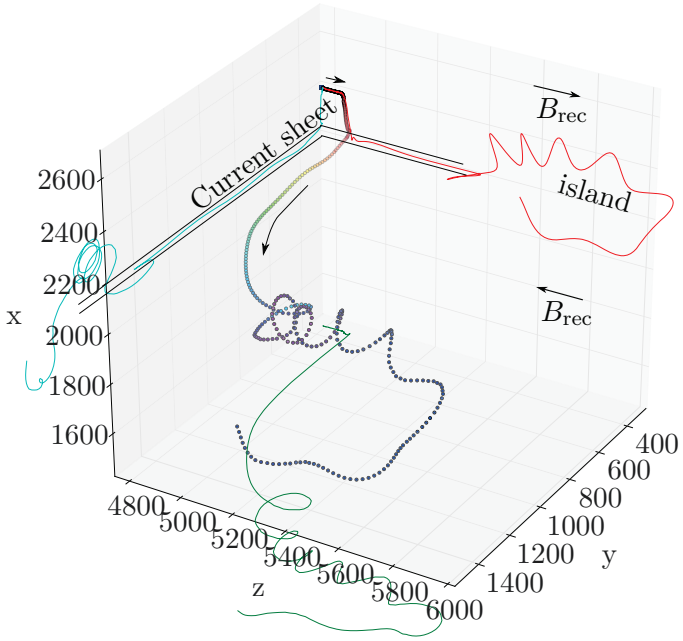

Figure 6.3: Typical trajectory for a particle, here an electron. Note the Speiser-like oscillatory motion inside the current sheet. Axis scales are given in cell numbers, with 9 cells representing one initial electron inertial length d_{e}. Dot colors are the particle Lorentz factor. Solid lines are projections onto the x-y, y-z, and z-x planes. The y direction is not described in the simulations, and is here reconstructed on the basis of an invariance of the electromagnetic fields along y.

6.4.2 Inflow: two-scale diffusion region and sharp transitions

We now examine the inflow of plasma into the diffusion region. In the literature, for antiparallel reconnection (i.e., no guide field), its width is found to scale with the particles inertial length, a result that we show to also hold for relativistic reconnection in Sect. 6.4.2. The originality of the following results is the formation of a very sharp transition at the entrance of the diffusion regions, which we explore in Sect. 6.4.2.

Width of the diffusion region

The diffusion region is, by definition, the area where impeding mechanisms (which can be collisions, inertia and collective interactions, or finite Larmor effects) prevent the particles from responding in an ideal way to the electric fields induced by magnetic flux variations. The magnetic field and the plasma are then not coupled any more, the former can freely diffuse, and reconnection can start or be sustained. Defining the diffusion region is thus a matter of finding the area where the non-ideal processes dominate over ideal behavior.

Defining unambiguous criteria to identify this region is a complex subject (Ishizawa and Horiuchi 2005; Klimas et al. 2010), especially in the presence of a guide field (Hesse et al. 2002, 2004; Liu et al. 2014), in 3D simulations (Pritchett 2013), or in asymmetric configurations (Zenitani et al. 2011b). In our case, as we show in Sect. 6.4.2, there is a sharp increase in particle density when the inflow plasma reaches the central part, where particles are retained by bouncing motions around the reversing magnetic field. It is associated with a sharp drop in inflow velocity, a rise in temperature, and a

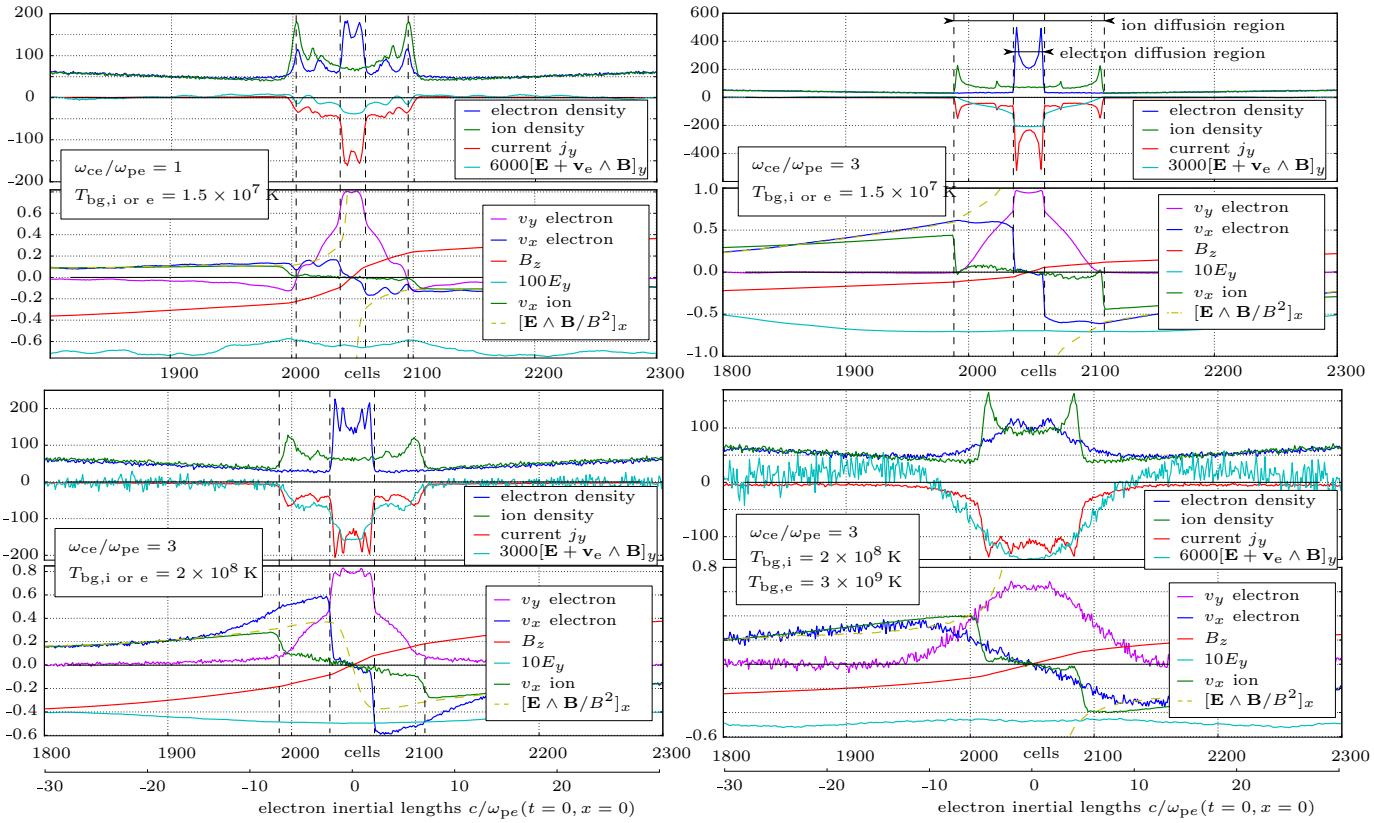

Figure 6.4: Cut along x through the X-point for four simulations, as indicated in the insets. The times are $t = 40T_{pe} = 30\omega_{ci}^{-1} = 750\omega_{ce}^{-1}$ for the cases $\omega_{ce}/\omega_{pe} = 3$, and $t = 142T_{pe} = 35\omega_{ci}^{-1} = 875\omega_{ce}^{-1}$ for the case $\omega_{ce}/\omega_{pe} = 1$.

violation of the frozen-in relation $\boldsymbol{E}+\bar{\boldsymbol{v}}_s\wedge\boldsymbol{B}=0$. We identify the diffusion region with this area of increased density.

Because of their lighter mass and fastest response, electrons remain frozen to the magnetic field longer than ions. The ion diffusion region is thus larger than the electron one. In all the antiparallel simulations, we find the expected two-scale (ion and electron) diffusion region. It can be seen in Fig. 6.4, where we present a cut along x through a X-point at a given time for different simulations. The width δ_s of the diffusion region is roughly given by the inertial length d_s of the corresponding species, defined with the particle density at the center of the diffusion region, i.e., $\delta_s \sim d_s = c/\sqrt{n_s(x=0,t)q_s^2/\epsilon_0 m_s}$, with throughout all simulations $0.5 \leq \delta_i/d_i \leq 1$ and $1 \leq \delta_e/d_e \leq 1.5$ (Fig. 6.5). This scaling is expected from the basic arguments exposed in Sect. 2.12.1, and is also found in PIC simulations of non-relativistic ion-electron magnetic reconnection (e.g., Pritchett 2001; Klimas et al. 2010).

In the case of hot background electrons ($T_{bg,e} = 3\times10^9$ K, with a corresponding background plasma $\beta_e = 1.1\times10^{-2}$), the transition is less sharp, and the width is larger than the inertial length. The sharpness is discussed in Sect. 6.4.2, and the larger extent is expected because inflowing particles have faster speeds, and thus larger Larmor radii and larger bouncing motions. The width δ_s should thus also depend on the β_s parameter of the inflow.

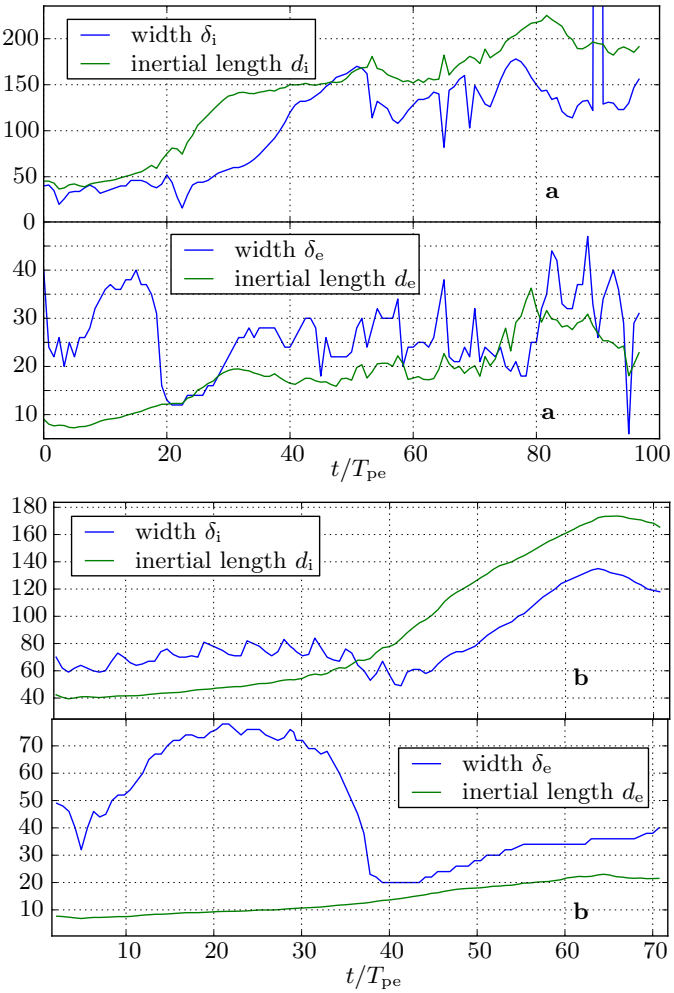

Figure 6.5: Width of the diffusion region δ_s, and inertial length d_s measured at the center of the diffusion region, for ions and electrons. Panels *a* are for the simulation with $\omega_{ce}/\omega_{pe} = 3$, $\sigma_e^{hot} = 89$, $T_{bg} = 1.5 \times 10^7$ K and $B_G = 0$; panels *b* for $\omega_{ce}/\omega_{pe} = 6$, $\sigma_e^{hot} = 260$. The phase between 0 and $18T_{pe}$ for panels *a* (0 and $33T_{pe}$ for panels *b*) corresponds to times where the tearing instability has not yet started. The decrease in δ_e between 18 and $20T_{pe}$ for *a* (33 and $37T_{pe}$ for *b*) is the linear and non-linear growth phase of the instability.

Sharpness of the inflow boundaries

We see from Fig. 6.4 that the boundary of the diffusion region, defined by the increase in particle number density, is very sharp in some cases (especially for the case $\omega_{ce}/\omega_{pe} = 3$ with a cold background plasma). These sharp transitions are *not* the trace of a shock between the incoming plasma and the over-dense diffusion region. First, because the inflow bulk velocity is not supersonic, in the sense that we have $\bar{v}_{in,s} < C_{fms}$, with C_{fms} the phase speed of waves propagating perpendicular to the magnetic field $\boldsymbol{B}_0$, i.e., the fast magnetosonic velocity in relativistic MHD (Alfvén and slow waves do not propagate perpendicularly to $\boldsymbol{B}_0$, also, see Sect. 3.5 for references concerning relativistic MHD). Second, because the width of the transition between inflow plasma and diffusion region plasma is, in the sharpest case, less than an electron inertial length, while we know that the thermalization of a cold inflow by collisionless kinetic processes occurs on a width of some inertial length, also with the formation of a precursor upstream (e.g., Plotnikov et

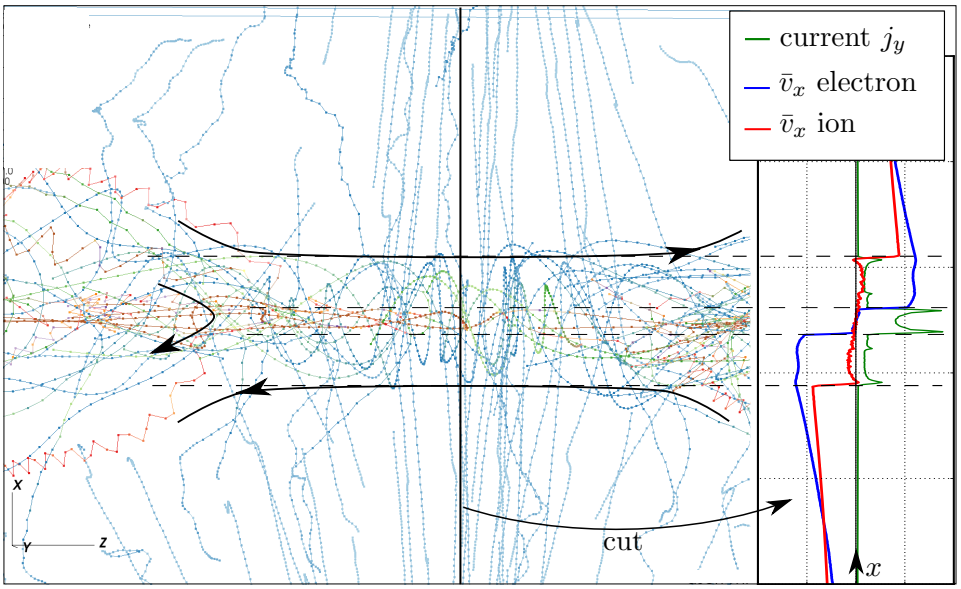

Figure 6.6: Trajectories of a sample of particles, and on the right fluid velocities and current for a cut through the X-point.

al. 2013) that is not seen here. Third, because there is no variations in the magnetic field across the sharp particle density variation.

Instead, we explain these sharp transitions by quasi-ballistic motions of the particles entering the diffusion region. Figure 6.6 shows some particle trajectories: they travel toward the diffusion region because of the electric field E with a guiding center velocity given by $\boldsymbol{v}_{E\times B} = \boldsymbol{E} \times \boldsymbol{B}/B^2$, they reach the magnetic field reversal, overshoot to the other side because of their inertia, turn around the increasingly strong magnetic field, and then oscillate around the $B = 0$ line before being ejected toward the islands (because they have a large v_y in the B_x field, see Sect. 6.4.1 and Fig. 6.3 for a trajectory in 3D). This well explains the fluid point of view of Fig. 6.4: averaging over particles to obtain the fluid particle number density or fluid velocity, the sharpness of the transitions comes from all particles of the same species turning around at roughly the same location.

It also explains the M shape of the particle densities of Fig. 6.4: particles spend more time at the edge of the diffusion region, when turning back, than at the center, hence the peaks at the edges and the depletion at the center. The fluid velocity profiles are also well explained by the particle view. We note that an M shape is also reported in the context of the inversion electric field layer (Chen et al. 2011, and references therein). Here we do not find any trace of the inversion layer in the electric field. A possible explanation may be that our electrons are relativistic.

Concerning the sharp transitions, the question is thus to know why and under which conditions all the particles of a species turn back at the same location. They will do so if they all enter the diffusion region with the same velocity, i.e., if their thermal velocity is lower than their bulk velocity: $v^{\rm th}_{{\rm in},s} \ll \bar{v}_{{\rm in},s} \sim v_{E\times B}$. Table 6.3 presents the ratio $v^{\rm th}_{{\rm in},s}/\bar{v}_{{\rm in},s}$ for the different simulations of Fig. 6.4. For a given magnetization, here $\omega_{\rm ce}/\omega_{\rm pe} = 3$, we clearly see a correlation between a small $v^{\rm th}_{{\rm in},s}/\bar{v}_{{\rm in},s}$ and a sharp transition. In particular, in the case with very hot electrons ($v^{\rm th}_{\rm in,e}/\bar{v}_{\rm th,e} = 1.8$) and relatively cold ions ($v^{\rm th}_{\rm in,i}/\bar{v}_{\rm in,i} = 0.1$), the electron particle number and velocities

$\frac{\omega_{ce}}{\omega_{pe}}$	$T_{bg,e}$ (K)	$T_{bg,i}$ (K)	$\Theta_{bg,e}$	$\Theta_{bg,i}$	$\frac{v_{in,e}^{th}}{\bar{v}_{in,e}}$	$\frac{v_{in,i}^{th}}{\bar{v}_{in,i}}$	Sharpness: elecs.	and ions	$\tilde{r}_{ci,in}$	$\tilde{r}_{ce,in}$
1	1.5×10^7	1.5×10^7	2.5×10^{-3}	10^{-4}	0.1	0.02	sharp	sharp	0.6	3.18
3	1.5×10^7	1.5×10^7	2.5×10^{-3}	10^{-4}	0.1	0.02	very sharp	very sharp	0.2	1.1
3	2×10^8	2×10^8	3×10^{-2}	10^{-3}	0.3	0.1	sharp	sharp	0.7	3.7
3	3×10^9	2×10^8	5×10^{-1}	10^{-3}	1.8	0.1	smooth	sharp	3	3.7

Table 6.3: Values related to the sharpness of the edge of the diffusion region. Here $\Theta_s = T_s/(m_s c^2)$, $v_{in,s}^{th} = \sqrt{T_s/m_s}$, and $\bar{v}_{in,s}$ the fluid velocity at the entrance of the diffusion region of species s, measured in Fig. 6.4. Also, $\tilde{r}_{cs}$ is the thermal Larmor radius in number of cells with $r_{cs} = \langle(\gamma v_\perp)^2\rangle^{1/2}/\omega_{cs}$, estimated with the formula for a Maxwell-Jüttner plasma at rest as $r_{cs} = (c/\omega_{ce})\sqrt{2\Theta_s \kappa_{32}(1/\Theta_s)}$ (Eq. 3.18 or Table 3.1). The indication of sharpness is qualitative, see Fig. 6.4 for details.

present smooth variations, while the same curves for ions do exhibit sharp transitions. This is in accordance with the explanation of sharp transitions by the cold nature, in terms of the ratio $v_{in}^{th}/v_{E\times B}$, of the inflowing plasma.

The influence of the magnetization on the sharpness of the transitions is seen by comparing the two first simulations of Table 6.3, with $\omega_{ce}/\omega_{pe} = 1$ and 3 and same ratio $v_{in,s}^{th}/\bar{v}_{in,s}$ (plotted in the top part of Fig. 6.4). A smaller magnetization implies a smoother shape. We understand this as a consequence of particles turning back on a scale given by their Larmor radii in the magnetic field at the sheet entrance, which is smaller when ω_{ce}/ω_{pe} is higher.

As a final remark concerning resolution, we note that in the coldest cases, the thermal Larmor radius of the electrons is smaller than a cell length. The resolution of the Larmor radius on the grid is, however, not important for integrating particle trajectories in constant fields, because interpolation of field quantities to particle position then provides the same (constant) values, regardless of the cell size. What matters is the temporal resolution, $\omega_{cs}\Delta t < 1$ (see Sect. 4.4.1). Here, we have $\omega_{cs}\Delta t = 0.04$ and 0.12 for $\omega_{ce}/\omega_{pe} = 1$ or 3. Also, a test run with a spatial and temporal resolution increased by a factor two leads to the same structures.

In summary, the sharp transitions are explained by collective bouncing motions allowed by the cold nature of the inflow: $v_{in,s}^{th} \ll \bar{v}_{in,s}$. Such transitions may also occur in non-relativistic reconnection, but then the inflow speed $\bar{v}_{in,s} \sim E/B$ is low and the background plasma should be very cold. They are likely to be more common in relativistic reconnection, where $\bar{v}_{in,s} \sim E/B$ is larger. This may be why, to our knowledge, they have never been reported in other simulations.

6.4.3 The relativistic Ohm's law

We explore the balance of terms in Ohm's law. The literature concerning 2D non-relativistic reconnection largely shows that for antiparallel reconnection, the dominant term is thermal inertia either in ion-electron (Klimas et al. 2010; Shay et al. 2007; Fujimoto 2009) or pair (Bessho and Bhattacharjee 2005) plasmas, and this is the key element of various analytical models (e.g., Hesse et al. 2011). On the other hand, reconnection with a guide field is sustained by electron bulk inertia on skin-depth scales, and thermal inertia on Larmor radius scales (Hesse et al. 2002, 2004; Liu et al. 2014). Existing studies with relativistic pair plasmas confirm the non-relativistic

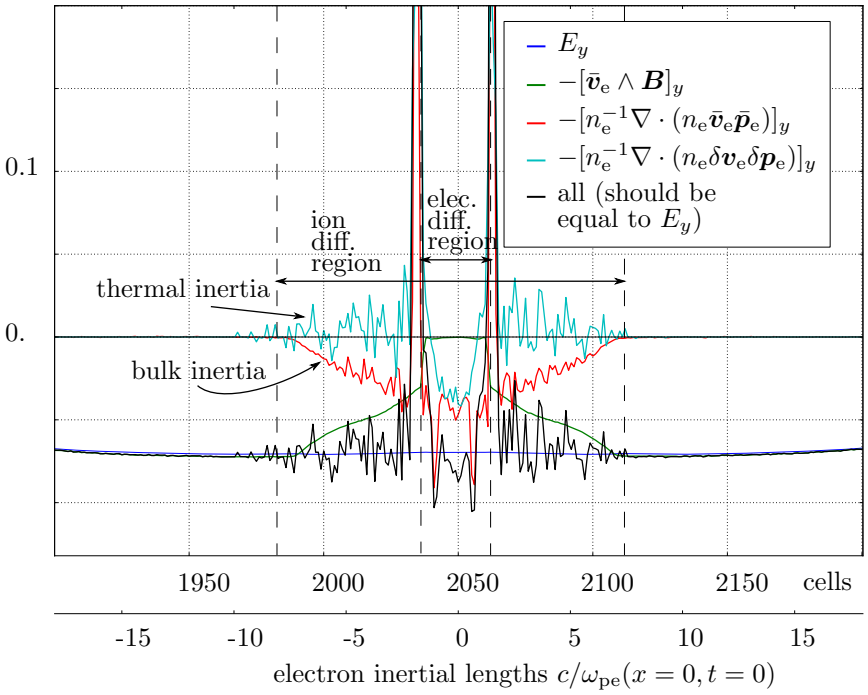

Figure 6.7: Different components of Ohm's law (Eq. 6.9) for a cut along x through a X-point (the same as in Figs. 6.2, 6.4 upper-right, 6.8, 6.9 right, and 6.10). Run $\omega_{ce}/\omega_{pe} = 3$, $\sigma_e^{hot} = 89$, $T_{bg} = 1.5 \times 10^7$ K, $B_G = 0$, $t = 40T_{pe} = 30\omega_{ci}^{-1} = 750\omega_{ce}^{-1}$.

trend: with no guide field, Hesse and Zenitani (2007), Bessho and Bhattacharjee (2012), and Zenitani et al. (2009a) find a dominating contribution of thermal inertia, while with a guide field Hesse and Zenitani (2007) find a significant contribution of the time derivative of bulk momentum $\partial_t(n_e\bar{p}_y)$. Here we explore the situation in ion-electron relativistic plasmas for antiparallel reconnection. We show for the first time in the antiparallel case that bulk inertia contributes at least as much as thermal inertia for high inflow magnetizations. We explain that this is due to a relativistic inflow magnetization in Sect. 6.4.8.

Ohm's law is presented in the non-relativistic case in Sect. 2.7. It is the fluid equation of motion for the lighter particles (the electrons), and is a means to evaluating the relative weight of the different non-ideal terms, allowing reconnection with a simple *fluid* picture. Understanding the weight and localization of each term is a first step toward building an effective resistivity for fluid models (resistive MHD, two-fluid codes, hybrid codes), where concrete resistive parametrizations can lead to very different behaviors, for instance changing from steady to unsteady states in Zenitani et al. (2009b), or triggering (or not) a Petsheck-like configuration depending on the localization and gradients of the resistivity (Baty et al. 2006).

The relativistic Ohm's law for electrons is directly derived from the equation of conservation of momentum for the electron fluid, Eq. 3.72, which

is itself obtained from Vlasov's equation in Sect. 3.4. It reads as

$$\begin{aligned}\frac{q_\mathrm{e}}{m_\mathrm{e}}(\boldsymbol{E}+\bar{\boldsymbol{v}}_\mathrm{e}\wedge\boldsymbol{B}) &= \frac{1}{n_\mathrm{e}}\frac{\partial}{\partial t}(n_\mathrm{e}\bar{\boldsymbol{p}}_\mathrm{e})+\frac{1}{n_\mathrm{e}}\frac{\partial}{\partial \boldsymbol{x}}\cdot(n_\mathrm{e}\langle\boldsymbol{p}_\mathrm{e}\boldsymbol{v}_\mathrm{e}\rangle)\\ &= \underbrace{\frac{1}{n_\mathrm{e}}\frac{\partial}{\partial t}(n_\mathrm{e}\bar{\boldsymbol{p}}_\mathrm{e})+\frac{1}{n_\mathrm{e}}\frac{\partial}{\partial \boldsymbol{x}}\cdot(n_\mathrm{e}\bar{\boldsymbol{p}}_\mathrm{e}\bar{\boldsymbol{v}}_\mathrm{e})}_{\text{bulk inertia}}\\ &\qquad + \underbrace{\frac{1}{n_\mathrm{e}}\frac{\partial}{\partial \boldsymbol{x}}\cdot(n_\mathrm{e}\langle\delta\boldsymbol{p}_\mathrm{e}\delta\boldsymbol{v}_\mathrm{e}\rangle)}_{\text{thermal inertia}}.\end{aligned} \tag{6.9}$$

Here we use for simplicity quantities computed in the simulation (or lab) frame; e.g., n_e is the electron number density in the lab-frame (denoted by $n_\mathrm{lab,e}$ in Sect. 3.4). Brackets $\langle\cdot\rangle_s$ or an overbar denote an average in momentum space over the particles distribution function. We also used the definition $\delta\boldsymbol{p}=\boldsymbol{p}-\bar{\boldsymbol{p}}$ where $\boldsymbol{p}=\gamma\boldsymbol{v}$ is the momentum. The left-hand side of Eq. 6.9 is the ideal part, and is set equal to 0 in ideal MHD. On the right-hand side are terms linked to finite inertia (i.e., particles do not respond perfectly to the electric field variations because of their inertia):

- The first term is a part of bulk inertia. However, it vanishes in steady state so we neglect it (this is validated a posteriori).
- The second term is inertia linked to the bulk flow and is denoted as *bulk inertia*. It comes from the overall structure of the flow around the sheet (the profiles of the mean quantities: increase in $\bar{v}$, $\bar{p}$).
- The third term is inertia linked to microscopic thermal motion and is denoted as *thermal inertia*. It comes from the divergence of the off-diagonal terms of the pressure tensor, and can be anticipated by a study of the temperature curves.

We analyze Ohm's law in the direction of the reconnection electric field ($\hat{\boldsymbol{y}}$ here). Given the invariance along y, the divergence terms have two contributions: $\sum_k \partial_k(p_k v_y) = \partial_x(p_x v_y)+\partial_z(p_z v_y)$. A computation of the divergence requires a smoothing of the quantities, especially for the thermal inertia term, which is very noisy.

We show in Fig. 6.7 the results for a cut through the X-point for the simulation with $\omega_\mathrm{ce}/\omega_\mathrm{pe}=3$ and $T_\mathrm{bg}=1.5\times10^7$ K ($\sigma_\mathrm{e}^\mathrm{hot}=89$). Ohm's law is satisfied everywhere, except at the sharp transitions at the entrance of the electron diffusion region, where the derivatives diverge. Different areas emerge:

- The electrons are ideal outside of the ion diffusion region.
- In the ion diffusion region, $|\bar{\boldsymbol{v}}_\mathrm{e}\wedge\boldsymbol{B}|$ decreases linearly.

  The bulk inertia term $\sum_k \partial_k(n_\mathrm{e}\bar{p}_k\bar{v}_y)$ rises linearly to compensate. The term $\partial_x(n_\mathrm{e}\bar{p}_x\bar{v}_y)$ wins out over $\partial_z(n_\mathrm{e}\bar{p}_z\bar{v}_y)$. The contribution of the former is understandable when looking at $\bar{p}_x$ and $\bar{v}_y$, which increase when we get closer to the sheet in this region (see Fig. 6.4 for $\bar{v}_y$).

  The thermal inertia term $\sum_k \partial_k(n_\mathrm{e}\delta p_k\delta v_y)$ is slightly positive, and partly cancels the contribution of bulk inertia. This cancellation is also reported in Fujimoto (2009) and Klimas et al. (2010) for non-relativistic ion-electron plasmas, and in Bessho and Bhattacharjee

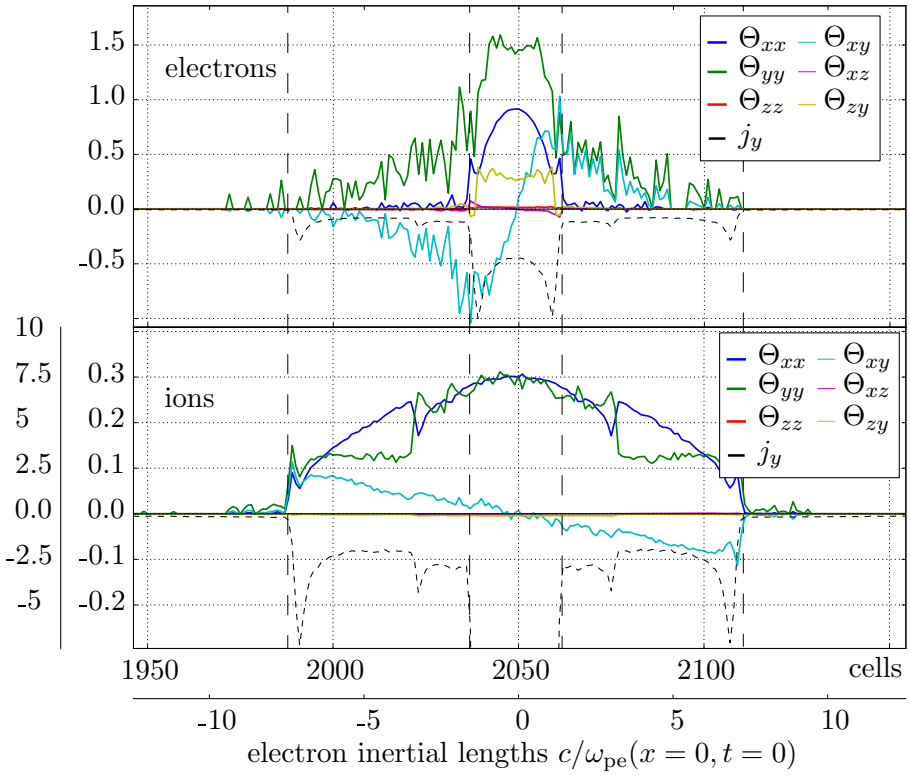

Figure 6.8: Temperatures for a cut along x through the same X-point as in Figs. 6.2, 6.4 upper-right, 6.9 right, and 6.10. Run with $\omega_{\rm ce}/\omega_{\rm pe} = 3$, $\sigma_{\rm e}^{\rm hot} = 89$, $T_{\rm bg} = 1.5 \times 10^7$ K. We define $\Theta_{mn,s} = T_{mn,s}/m_s c^2$ with $s =$ i or e. For the ion temperatures, the inner vertical axis is $\Theta_{\rm i}$, the outer one is $\Theta_{\rm i} \times m_{\rm i}/m_{\rm e}$, and it shows that $T_{\rm i} > T_{\rm e}$.

(2012) for relativistic pairs. Only $\partial_x(n_{\rm e}\delta p_x \delta v_y)$ contributes and is negative, which is easily seen when looking at the temperature curves $T_{xy,{\rm e}}$ and $T_{zy,{\rm e}}$ (Fig. 6.8).

- In the electron diffusion region, the $\bar{\boldsymbol{v}}_{\rm e} \wedge \boldsymbol{B}$ term vanishes (because B is very weak and $\bar{v}_x = 0$).

  The bulk inertia term is constant and due only to the term $\partial_z(n_{\rm e}\bar{p}_z\bar{v}_y)$, which is expected to contribute given that $\bar{v}_y \sim$ const and $\bar{p}_z \propto z - z_{\rm X-point}$ in this region (Fig. 6.9). The other term, $\partial_x(n_{\rm e}\bar{p}_x\bar{v}_y)$, vanishes because $\bar{p}_x =$ const $= 0$ in this area.

  The thermal inertia term $\sum_k \partial_k(n_{\rm e}\delta p_k \delta v_y)$ contributes as much as the bulk inertia term. Only $\partial_x(n_{\rm e}\delta p_x \delta v_y)$ contributes, and it is negative, which is easily seen when looking at the temperature curves $T_{xy,{\rm e}}$ and $T_{zy,{\rm e}}$ in Fig. 6.8.

A cut along x through other X-points in the simulation leads to the same results. Also, a cut along z through the X-point reveals that the results of the electron region hold throughout the center of the current sheet, with a slow increase in the $\bar{\boldsymbol{v}}_{\rm e} \wedge \boldsymbol{B}$ term as we get near the islands.

In summary, non-ideal terms in the ion regions are due to bulk inertia and, in the electron diffusion region, to an interestingly equal contribution of bulk and thermal inertia. For other runs with $\omega_{\rm ce}/\omega_{\rm pe} = 3$ ($\sigma_{\rm e}^{\rm hot} = 27$ to 89), we also find an equal contribution from thermal and bulk inertia. For the most magnetized run, $\omega_{\rm ce}/\omega_{\rm pe} = 6$ ($\sigma_{\rm e}^{\rm hot} = 260$), the contribution of

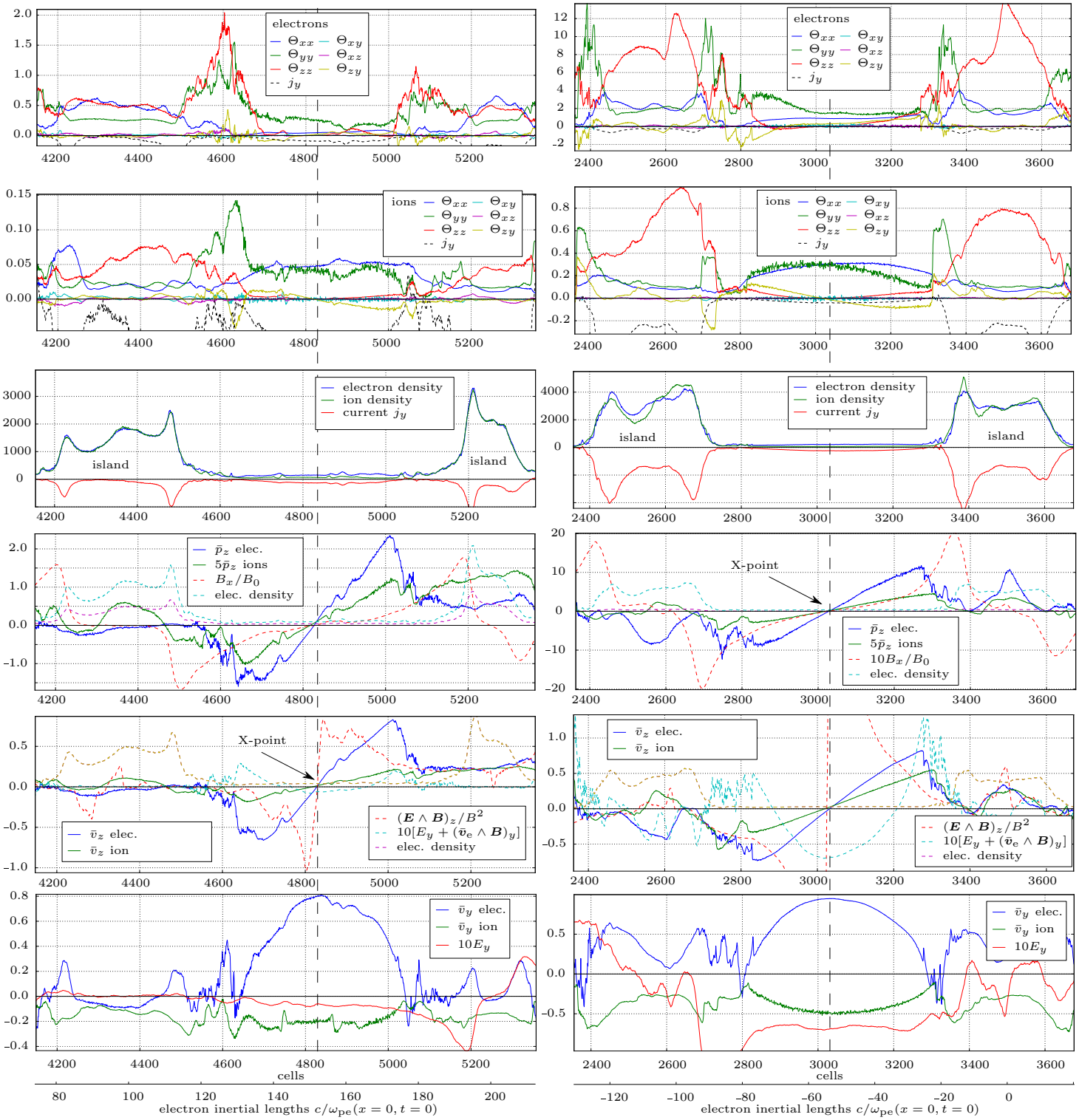

Figure 6.9: Cut along z through the X-point.
Left: Run $\omega_{ce}/\omega_{pe} = 1$, $\sigma_e^{hot} = 9.9$, same X-point as in Fig. 6.4, $t = 142T_{pe} = 35\omega_{ci}^{-1} = 875\omega_{ce}^{-1}$.
Right: Run $\omega_{ce}/\omega_{pe} = 3$, $\sigma_e^{hot} = 89$, $T_{bg} = 1.5\times10^7\,\mathrm{K}$, $B_G = 0$, same X-point and time as in Figs. 6.2, 6.4 upper-right, 6.7, 6.8, and 6.10 ($t = 40T_{pe} = 30\omega_{ci}^{-1} = 750\omega_{ce}^{-1}$).

$\frac{\omega_{ce}}{\omega_{pe}}$	$\frac{n_{bg}}{n_0}$	$T_{bg,e}$, $T_{bg,i}$ (K)	$\sigma_{in,e}^{cold}$	$\sigma_{in,i}^{cold}$		electrons		ions	
1	0.1	1.5×10^7, idem	10	0.4	$\Gamma_{out,s} - 1$	0.49	31%	0.02	20%
					$\Gamma_{out,s}(h_{0,out,s} - 1)$	1.07	69%	0.08	80%
3	0.31	2.0×10^8, idem	29	1.2	$\Gamma_{out,s} - 1$	0.71	14%	0.065	22%
					$\Gamma_{out,s}(h_{0,out,s} - 1)$	4.34	86%	0.24	78%
3	0.1	3×10^9, 2×10^8	90	3.6	$\Gamma_{out,s} - 1$	0.089	1%	0.056	9%
					$\Gamma_{out,s}(h_{0,out,s} - 1)$	15	99%	0.54	91%
3	0.1	1.5×10^7, idem	90	3.6	$\Gamma_{out,s} - 1$	0.63	5%	0.13	20%
					$\Gamma_{out,s}(h_{0,out,s} - 1)$	11	95%	0.5	80%
3	0.1	2.0×10^8, idem	90	3.6	$\Gamma_{out,s} - 1$	0.38	4%	0.091	14%
					$\Gamma_{out,s}(h_{0,out,s} - 1)$	9.7	96%	0.56	86%
6	0.1	8.0×10^8, idem	360	14	$\Gamma_{out,s} - 1$	0.42	1%	0.19	8%
					$\Gamma_{out,s}(h_{0,out,s} - 1)$	51	99%	2.2	92%

Table 6.4: Energy content of the outflows. The energy flux due to the bulk flow mean velocity is proportional to $\Gamma_{out,s}-1$, and the energy flux due to kinetic particle motions and pressure work is proportional to $\Gamma_{out,s}(h_{0,out,s}-1)$ (see Eq. 6.13). Here $B_G/B_0 = 0$. Quantities are measured at their maximum value, which is reached at the end of the exhausts along z.

bulk inertia exceeds that of thermal inertia by a factor 1.5 to 3. We show in Sect. 6.4.8 with analytical estimations that the high magnetization for electrons indeed allows bulk inertia to overreach thermal inertia, with the former scaling as $\sigma_{in,e}^{cold}$ and the latter as $\left(\sigma_{in,e}^{cold}\right)^{1/2}$. This effect is present in our simulations and not in the references previously mentioned with antiparallel fields, because our background electron magnetization is greater. It is thus a new regime that challenges the thermal inertia paradigm at high electron magnetizations. We discuss the possible consequences in Sect. 6.6.2.

6.4.4 Outflow: energy content of the exhaust jets

It can easily be shown (Sect. 6.4.4) from analytical considerations that the outflows from the diffusion region should have relativistic bulk velocities and/or relativistic temperatures. In our simulation data, the thermal part always clearly dominates the bulk kinetic energy part, more strongly for more relativistic cases (Sect. 6.4.4). A refined analytical estimate explains why in Sect. 6.4.8.

A simple analytical estimation

As explained in Sect. 6.4.1, bipolar outflow jets are naturally produced from each side of the X-points. They are clearly visible in Fig. 6.2. An estimation of the energy content of these outflows can be easily obtained in steady state by using the conservation of particle number and of energy. To do so, we consider that the diffusion region for species s has a length D_s (along z) and a width δ_s (along x). We generalize the situation to cases where there is a guide field B_G. We denote quantities entering (leaving) this region by a subscript "in" ("out", respectively).

Conservation of particle number (Eq. 3.71) between inflow and outflow gives the relation $n_{in,s}v_{in,s}D_s = n_{out,s}v_{out,s}\delta_s$. The inflow velocity

is estimated by the $E \times B$ velocity as $v_{\mathrm{in},s} = E_y/B_0$. Regarding energy conservation (Eq. 3.79), the inflow energy flux includes the particle energies, and the reconnecting and guide field Poynting fluxes (Eqs. 6.2 and 6.3): $D_s n_{\mathrm{in},s} m_s c^2 \bar{p}_{\mathrm{in},s} + D_s v_{\mathrm{in},s} \cdot B_0^2/\mu_0 + D_s v_{\mathrm{in},s} \cdot B_{\mathrm{G,in}}^2/\mu_0$. We assume that in the outflow the energy in the reconnected magnetic field B_0 is negligible compared to particle energy, so that the energy flux is $\delta_s n_{\mathrm{out},s} m_s c^2 \bar{p}_{\mathrm{out},s} + \delta_s v_{\mathrm{out},s} \cdot B_{\mathrm{G,out}}^2/\mu_0$. Equating the two fluxes and combining this with the conservation of particle number, we obtain

$$\frac{\bar{p}_{\mathrm{out},s}}{\bar{v}_{\mathrm{out},s}} = \frac{\bar{p}_{\mathrm{in},s}}{\bar{v}_{\mathrm{in},s}} + \sigma_{\mathrm{in},s}^{\mathrm{cold}}(B_0) + \sigma_{\mathrm{in},s}^{\mathrm{cold}}(B_{\mathrm{G,in}})(1-\alpha), \tag{6.10}$$

with $(1-\alpha) = \left(1 - \frac{n_{\mathrm{in},s} B_{\mathrm{G,out}}^2}{n_{\mathrm{out},s} B_{\mathrm{G,in}}^2}\right)$. The guide field is usually merely compressed, so that $1-\alpha \simeq 0$.

Equation 6.10 is independent of the $\boldsymbol{p}$ dependence of the distribution function f_s. However, some insight can be gained by considering a distribution that is isotropic in the comoving frame, for which we have the result $\bar{\boldsymbol{p}} = h_0(T)\Gamma\bar{\boldsymbol{v}}$, with h_0 the comoving enthalpy (as defined and pictured for a Maxwell-Jüttner distribution in Fig. 3.1), and $\Gamma = (1 - \bar{\boldsymbol{v}}^2/c^2)^{-1/2}$. If, in addition, we neglect the contribution of the guide field and assume an inflow plasma with non-relativistic temperatures and non-relativistic velocities, Eq. 6.10 becomes[b]

$$h_{0,\mathrm{out},s}\Gamma_{\mathrm{out},s} = 1 + \sigma_{\mathrm{in},s}^{\mathrm{cold}}(B_0). \tag{6.12}$$

We underline that the magnetization $\sigma_{\mathrm{in},s}^{\mathrm{cold}}(B_0)$ is to be taken at the entrance of the diffusion region of species s, where it can differ from its asymptotic value because of a decrease in magnetic field and particle number density (as in Fig. 6.4).

We clearly see that for a relativistic inflow plasma where $B^2/\mu_0 > nmc^2$ and hence $\sigma_{\mathrm{in},s}^{\mathrm{cold}}(B_0) > 1$, magnetic reconnection is expected to produce outflows with either relativistic bulk velocities ($\Gamma_{\mathrm{out},s} > 1$) or relativistic temperatures ($h_{0,\mathrm{out},s} > 1$), or both. We also see that since $\sigma_s^{\mathrm{cold}} \propto 1/m_s$, electrons will be more accelerated/heated than ions and that relativistic electrons ($\sigma_{\mathrm{e}}^{\mathrm{cold}} > 1$) can be expected even at low ion magnetizations ($\sigma_{\mathrm{i}}^{\mathrm{cold}} = \sigma_{\mathrm{e}}^{\mathrm{cold}} \times m_{\mathrm{e}}/m_{\mathrm{i}} \ll 1$).

Results from simulations

We first check whether the energy estimate of Eqs. 6.10 and 6.12 holds in all simulations. This is the case up to a factor $\lesssim 2$. An only approximate correspondence is to be expected because this relation assumes a simple geometry with, in particular, a constant inflow velocity along the diffusion region and no energy exchange between the species. For example, in Fig. 6.4, for $\omega_{\mathrm{ce}}/\omega_{\mathrm{pe}} = 3$ and $T_{\mathrm{bg}} = 1.5 \times 10^7$ K, we measure $1 + \sigma_{\mathrm{in},s}^{\mathrm{cold}}(B_0) = 1.8$ in the inflow for ions and 6.2 for electrons, while at the outflow maximal velocity

[b] We note that the non-relativistic limit of Eq. 6.12, with $h_{0,\mathrm{out},s} \sim 1$ and $\bar{v}_{\mathrm{out},s} \ll c$, is

$$\bar{v}_{\mathrm{out},s} = \sqrt{2\sigma_{\mathrm{in},s}^{\mathrm{cold}}(B_0)} = \sqrt{2} V_{\mathrm{s,A}}^{\mathrm{in}}(B_0), \tag{6.11}$$

where $V_{\mathrm{s,A}}^{\mathrm{in}}(B_0)$ is the non-relativistic inflow Alfvén speed with only the mass of species s. It only comprises the component B_0, so that if there is a guide field, this is the projection of the total Alfvén speed onto the outflow direction $\hat{\boldsymbol{z}}$.

(Fig. 6.9) we have $\bar{p}_{\mathrm{out},s}/\bar{v}_{\mathrm{out},s} = 1.7$ for ions and 13 for electrons. These orders of magnitude hold for all cases.

A more refined analysis of the energy content of the outflow, split into its thermal and bulk contributions, can be performed. To do so, we decompose the particle energy flux as (see Sect. 3.4)

$$\begin{aligned} n_s\langle\gamma m_s c^2 \boldsymbol{v}\rangle_s &= n_s m_s c^2 h_{0,\mathrm{out},s}\Gamma_{\mathrm{out},s}\bar{\boldsymbol{v}}_{\mathrm{out},s} \\ &= n_s m_s c^2 \bar{\boldsymbol{v}}_{\mathrm{out},s}\left[1 + (\Gamma_{\mathrm{out},s} - 1) + \Gamma_{\mathrm{out},s}(h_{0,\mathrm{out},s} - 1)\right]. \end{aligned} \tag{6.13}$$

On the right-hand side, the first term is the restmass energy flux, and is the same as that from the inflow. The second is the kinetic energy of a cold bulk flow of velocity $\bar{\boldsymbol{v}}_{\mathrm{out},s}$. The third is the energy transported by thermal motions in the plasma rest frame and by pressure work, and we denote it as the enthalpy flux. We note that these definitions match those of Zenitani et al. (2009a), who performed a similar analysis with two-fluid simulations of relativistic reconnection in pair plasmas.

We measure the maximum outflow velocity $\bar{v}_{\mathrm{out},s}$, deduce the Lorentz factor $\Gamma_{\mathrm{out},s}$, measure the maximum in momentum $\bar{p}_{\mathrm{out},s}$, and compute the enthalpy $h_{0,\mathrm{out},s} = \bar{p}_{\mathrm{out},s}/(\Gamma_{\mathrm{out},s}\bar{v}_{\mathrm{out},s})$. From these values, we estimate in Table 6.4 the balance of particle energy between each of the terms of Eq. 6.13.

In all cases, a large fraction of the particle energy flux is in thermal kinetic energy, not in bulk flow kinetic energy. For electrons, we see that the thermal part clearly dominates more as one increases the relativistic nature of the inflow (e.g., 69% in the thermal part for the less relativistic case, 99% for the most relativistic). This is also the case for ions: from 80% to 92% in the thermal part as the ion magnetization increases. The $T_{\mathrm{bg,i}} = 2 \times 10^8$ K case is exceptional with 91% in the thermal energy, but this large percentage is likely explained by interactions with the hot electrons $T_{\mathrm{bg,e}} = 3 \times 10^9$ K. We explain why thermally dominated outflows are expected at high inflow magnetization with a refined analytical model in Sect. 6.4.8.

6.4.5 Islands structure

Turning to the magnetic islands, we emphasize that they are magnetically isolated, have an M-shaped density distribution, and are hot with anisotropic temperatures.

After being expelled along $\pm z$ in the outflow, the particles meet the magnetic islands that separate each pair of X-points. The islands are initially formed by the tearing of the current sheet. They then consist only of particles of the current sheet, plus those of the background plasma that were inside the current sheet location. Small at the beginning, they grow by collecting particles from the outflows at their periphery and by merging with other islands. A remarkable property is that particles from the background plasma cannot enter inside the islands, but are scattered by the strong magnetic field structure surrounding the island and circle around it. Consequently, the particles at the island centers remain the same throughout the whole simulation, even after many island-merging events. This matter is explored in more detail in Chapter 7 (consult Fig. 7.6 for an illustration). We stress here two main points.

First, the trapped particles are heated by the island contraction (which occurs when two islands merge), so that the central temperatures are very

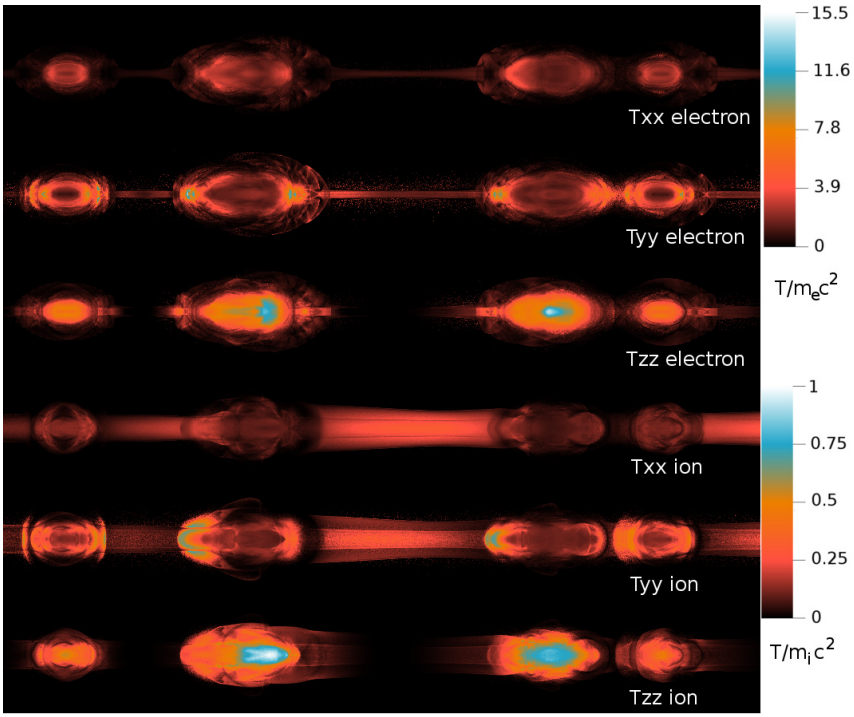

Figure 6.10: Temperatures for same simulation and time as in Figs. 6.2, 6.4 upper-right, 6.8, and 6.9 right. Note the different units for ions and electrons. Since $m_\mathrm{i}c^2 = 25m_\mathrm{e}c^2$, the ions are actually hotter than the electrons.

high for both species, highly anisotropic (Figs. 6.9 and 6.10), with a dominance of T_{zz}. The island centers are also where the currents are the strongest.

Second, as said above, most of the inflowing background particles populate a region around the center, while the central part of the island mainly consists of particles originally from the current sheet. As a result, after some time the surrounding part becomes denser than the isolated central part. A cut along z through an island center indeed (Fig. 6.9) reveals, for the particle density, an M shape with a central dip and two shoulders. This may explain observed density dips at the center of magnetic islands during magnetotail reconnection events (Khotyaintsev et al. 2010), without invoking island merging or particle escape along the flux tube.

6.4.6 Reconnection electric field and reconnection rate

As shown in Sect. 2.11.1, the rate of variation of magnetic field flux across a X-point, $\mathrm{d}\Phi_{B_z}/\mathrm{d}t = (\mathrm{d}/\mathrm{d}t)\int_{x=0}^{\text{X-point}} B_z \mathrm{d}x$, is equal in two-dimensional configurations to the y component E_y of the electric field at the X-point location. In addition, $\mathrm{d}\Phi_{B_z}/\mathrm{d}t$ is in part determined by the outflow velocity, because the latter sets the rate at which magnetic field is extracted from around the X-point (see e.g., in a resistive MHD context, Borovsky and Hesse 2007; Cassak and Shay 2007). Since one expects $\bar{v}_\mathrm{out} \propto V_\mathrm{A}$ in non-relativistic setups, the reconnection rate E_y is usually normalized either to $B_0 V_{\mathrm{A},0}^\mathrm{NR}$, with $V_{\mathrm{A},0}^\mathrm{NR}$ the hybrid Alfvén speed of Eq. 6.8, or to $B_0 V_{\mathrm{A,in}}^\mathrm{NR}$, with $V_{\mathrm{A,in}}^\mathrm{NR}$ the Alfvén speed in the inflow of Eq. 6.7a. These normalizations are chosen so that the normalized rate, $E^* = E_y/B_0 V_\mathrm{A}$, stays close to the same set of values. For example, it has been shown that it gives identical results

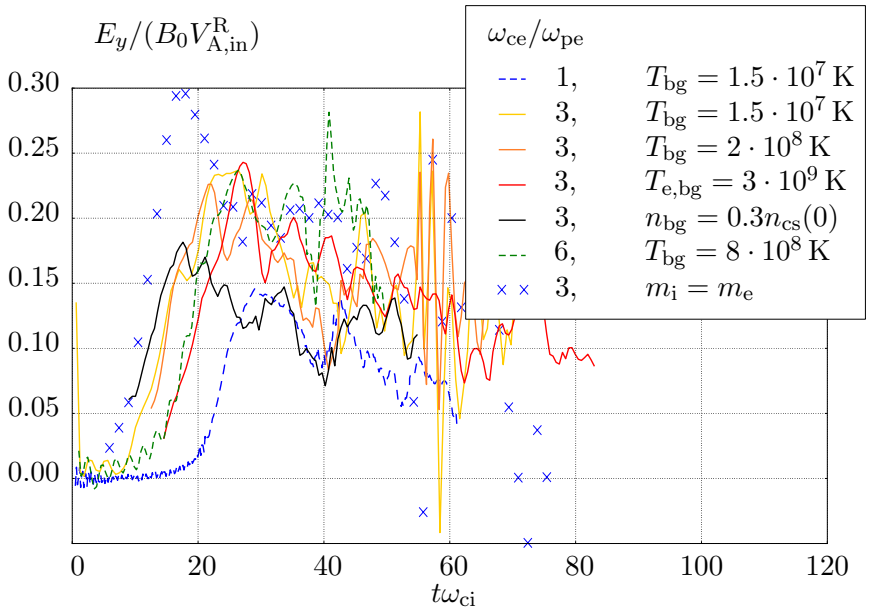

Figure 6.11: Time evolution of the normalized reconnection electric field $E_y/(B_0 V^{\mathrm{R}}_{\mathrm{A,in}})$, measured at the X-point of various simulations. The velocity $V^{\mathrm{R}}_{\mathrm{A,in}}$ is given in Table 6.2, and $B_0 = 0.11$, 0.33, or 0.66 for $\omega_{\mathrm{ce}}/\omega_{\mathrm{pe}} = 1$, 3, or 6, respectively. Time is normalized by the ion cyclotron pulsation, but the growth rate of the collisionless relativistic tearing mode is not proportional to ω_{ci} (Pétri and Kirk 2007), hence the different time lags and shapes. In particular, for $\omega_{\mathrm{ce}}/\omega_{\mathrm{pe}} = 6$, the timescale of the plot is divided by 3. For pairs, the timescale is $t\omega_{\mathrm{ce}}/25$.

when varying the mass ratio (e.g., Hesse et al. (1999), or Ricci et al. (2002, 2003) for $m_{\mathrm{i}}/m_{\mathrm{e}} = 25, 180, 1836$ with an implicit PIC code)[c].

In the following we turn to our relativistic case and ask whether a normalization can be found that confines the range of values for E^* in a narrow range and relaxes to the above normalization in the non-relativistic case. We argue here that the normalization by the hybrid Alfvén speed is not relevant, because it does not depend on the particle number density of the inflow, while the ratio E_y/B_0 clearly does. This is seen for the simulation with $n_{\mathrm{bg}} = 0.3 n_{\mathrm{cs}}(0)$, for which E_y/B_0 peaks at $0.13c$, compared to the otherwise identical simulation with $n_{\mathrm{bg}} = 0.1 n_{\mathrm{cs}}(0)$, where E_y/B_0 peaks at $0.20c$. On the other hand, the inflow Alfvén speed $V^{\mathrm{NR}}_{\mathrm{A,in}} \propto 1/\sqrt{n_{\mathrm{bg}}}$, and thus leads to closer normalized rates. We consequently exclude hybrid quantities for normalization.

In a relativistic configuration, the non-relativistic Alfvén speed can increase to infinity. However, the ratio E_y/B_0 is also the $E \times B$ velocity of the incoming plasma and cannot exceed the speed of light. The normalizing Alfvén velocity should thus also saturate to some value, which is why we choose to normalize the electric field by

$$E^* = \frac{E_y}{B_0 V^{\mathrm{R}}_{\mathrm{A,in}}}, \tag{6.14}$$

with $V^{\mathrm{R}}_{\mathrm{A,in}}$ the relativistic Alfvén speed in the inflow (Eq. 6.7b), which cannot

[c]However, going down to $m_{\mathrm{i}}/m_{\mathrm{e}} = 1$ leads to less systematic results. For example, Fujimoto (2009) reports $E^* = 0.15$ for $m_{\mathrm{i}}/m_{\mathrm{e}} = 100$ and 0.08 for pairs. Liu et al. (2014) report close rates for $m_{\mathrm{i}}/m_{\mathrm{e}} = 1$ and 25. Here we performed a simulation with $m_{\mathrm{i}}/m_{\mathrm{e}} = 1$ and find a peak reconnection rate $E^* = 0.30$, which is greater than for $m_{\mathrm{i}}/m_{\mathrm{e}} = 25$ (Fig. 6.11).

exceed c. The time evolution of E^* is shown in Fig. 6.11. Several comments can be made.

First, the rate E^* is not sensitive to the background plasma temperatures, as can be seen for the simulations $\omega_{ce}/\omega_{pe} = 3$, $n_{bg} = 0.1n_{cs}(0)$, no guide field, and $T_{bg} = 1.5\times10^7$, 2×10^8 and 3×10^9 K. This contrasts with the interpretation of Hesse and Zenitani (2007), who attribute a lower rate to a higher inflow temperature. In addition to the temperatures, the magnetization of their simulation also changes and may also affect the rates. Coming back to our simulations, we note that we use very low background plasma β ($< 10^{-2}$, Table 6.2), and that a weak plasma β dependence is expected for higher values (e.g., TenBarge et al. 2014, have rates E^* multiplied by ~ 2 when β passes from 0.01 to 1).

Second, the reconnection rate for the simulation with a higher background particle density ($n_{bg} = 0.3n_{cs}(0)$, $E^* = 0.18$) remains lower than its counterpart with $n_{bg} = 0.1n_{cs}(0)$ ($E^* = 0.23$). This is in line with the pair plasma simulations of Bessho and Bhattacharjee (2012) who found a similar rate for $n_{bg} = 0.1n_{cs}(0)$ ($E^* = 0.19$) and a higher rate for $n_{bg} = 0.01n_{cs}(0)$ ($E^* = 0.36$). The reconnection rate thus increases with decreasing background plasma density, which is also coherent with the β dependence mentioned above.

Finally, the normalization leads to very similar values of E^* for the relativistic cases ($\omega_{ce}/\omega_{pe} = 3$ or 6), with $E^* = 0.17$-0.24, but to a significantly lower rate for the less relativistic case ($\omega_{ce}/\omega_{pe} = 1$), with $E^* = 0.14$. More generally, the values for the relativistic cases are higher than those reported in the literature for undriven, symmetric reconnection with zero guide field in *non-relativistic* ion-electron plasmas. For the peak values of E^* (once normalized in the same way as here) we can cite: Birn et al. (2001) and Pritchett (2001): 0.09, Fujimoto (2006, 2009): 0.15, Daughton et al. (2006): 0.08, Klimas et al. (2010): 0.07–0.09, and the theoretical work of Hesse et al. (2009a,b) predicting a maximum rate of 0.28. Our results thus suggest higher rates for relativistic reconnection, a fact already seen in relativistic simulations of pair plasmas with, e.g., Zenitani and Hoshino (2007) ($E^* = 0.2$), Cerutti et al. (2012a) ($E^* = 0.17$), or Bessho and Bhattacharjee (2012) ($E^* = 0.19$ and 0.36).

In conclusion, the relativistic Alfvén speed of the inflow provides the best normalization for the reconnection electric field, in that it is robust from non-relativistic to relativistic flows. Corresponding rates are in a close range (0.14–0.25), which is higher than the rates found in non-relativistic simulations with the same normalization (0.07–0.15). The rate does not depend on the inflow temperature at low β, but is nevertheless not universal: it decreases with increasing background particle number density. Generalization to the presence of a guide field is discussed in Sect. 6.5.3.

6.4.7 Hall field and dispersive waves

We can see in Fig. 6.4 that inside the ion diffusion region, but outside of the electron diffusion region, ions have a low fluid velocity, while electrons still $E \times B$ drift toward their diffusion region. This results in a net current roughly given by $q_e n_e \bar{\boldsymbol{v}}_e = q_e n_e \boldsymbol{E} \wedge \boldsymbol{B}/B^2$, which is the Hall current. As explained in Sects. 2.12.1 and 2.12.4, this current continues along the magnetic separatrices in the outflow direction, and is at the origin of a quadripolar magnetic field directed along $\pm\hat{\boldsymbol{y}}$. This Hall magnetic field,

with the quadripolar structure, is present in our simulations. It has a weak intensity (between 1% and 10% of B_0). The charge separation between electrons and ions (Fig. 6.4) also leads to the creation of a Hall electric field directed along $+\hat{\boldsymbol{x}}$ in the $x < 0$ region and $-\hat{\boldsymbol{x}}$ in the $x < 0$ region. Both the magnetic and electric Hall fields are absent in a simulation with pairs.

The difference in the dynamical response of ions and electrons also allows the existence of waves with a quadratic dispersion relation, $\omega \propto k^2$, below ion scales (either whistler waves or kinetic Alfvén waves, see Rogers et al. 2001). Observations of the same reconnection rate for any simulation model allowing these waves (PIC, electron-MHD, Hall-MHD, two-fluid with and without electron inertia, hybrid simulations, see Birn et al. 2001; Shay et al. 2007; Rogers et al. 2001), as well as theoretical considerations (see Sect. 2.12.1), have led to the thesis that these waves are essential to allow for fast reconnection rates. However, this view is questioned by a number of simulations that do not support quadratic dispersive waves, but still support fast rates (hybrid simulations with no Hall term, pair plasmas, or strong guide field regime, see Karimabadi et al. 2004; Bessho and Bhattacharjee 2005; Daughton et al. 2006; Daughton and Karimabadi 2007; Liu et al. 2014). It is thus interesting to see whether our simulation data can provide any further insight into the matter.

A prediction of the dispersive wave physics is that the reconnection rate is controlled solely by the ion physics and not by the electrons. According to Daughton et al. (2006), it should be independent of the electron diffusion region length. We could, however, not reproduce their analysis because the electron diffusion zone length is, in our case, limited by the standing islands. It cannot stretch to high values, so we are unable to conclude for or against of the dispersive wave paradigm.

However, we underline that the simulation with $m_\mathrm{i}/m_\mathrm{e} = 1$ that we performed features an identical (and even slightly greater, Fig. 6.11) reconnection rate than simulations with $m_\mathrm{i}/m_\mathrm{e} = 25$. It thus points toward a negligible influence of the dispersive waves on the rates, or to another mechanism that allows fast rates in pair plasmas.

6.4.8 Simulation-based scaling analysis

The energy content of the outflows and the balance between thermal and bulk inertia in Ohm's law were explored with the simulations in Sects. 6.4.3 and 6.4.4. The aim of the present section is to investigate these points with a simple analytical model in order to gain physical insight into these phenomena and to extrapolate our simulation results to a larger parameter space.

We extend the analytical results of Sect. 6.4.4, where particle number and energy conservation allowed an estimation of the quantity $h_{0,\mathrm{out},s}\Gamma_{\mathrm{out},s}$ (Eqs. 6.10 or 6.12) by now also using the equation of conservation of momentum (Eq. 3.72).

Thermal versus bulk electron inertia

We first investigate the relative weight of thermal and bulk electron inertia. At the center of the electron diffusion region, we learn from Sect. 6.4.3 that the reconnection electric field is sustained by electron thermal and bulk

inertia, with only the terms $\partial_x(n_\mathrm{e}\langle\delta p_x\delta v_y\rangle)$ and $\partial_z(n_\mathrm{e}\bar{p}_z\bar{v}_y)$ contributing to either one of them, respectively.

- Concerning thermal inertia, the temperature tensor is defined via Eq. 3.64, so that $\langle\delta p_x\delta v_y\rangle = c^2\Theta_{xy,\mathrm{e}}/\Gamma_\mathrm{e}$. We see in Fig. 6.8 that $\Theta_{xy,\mathrm{e}}$ is linear in the electron diffusion region. It vanishes at the center because there the distribution function f_e is symmetric with respect to v_x. It is maximal at the diffusion region edge with a value $\Theta^\mathrm{edge}_{xy,\mathrm{e}}$. Consequently, we approximate the thermal inertia contribution by $(c^2\Theta^\mathrm{edge}_{xy,\mathrm{e}}/\Gamma^\mathrm{in}_\mathrm{e})/\delta_\mathrm{e}$, where δ_e is the width of the electron diffusion region.
- For the bulk inertia term, we use the fact that $\bar{p}_z$ rises linearly from the center to its maximum value denoted by $\bar{p}^\mathrm{out}_z$ over a distance $D_\mathrm{e}/2$ and that $\bar{v}_y$ has a vanishing derivative at the center (Fig. 6.9). Consequently, it can be estimated as $\bar{v}^\mathrm{center}_y\bar{p}^\mathrm{out}_z/D_\mathrm{e}$.

All in all, from Ohm's law (Eq. 6.9), the electric field at the center of the diffusion region is

$$\begin{aligned} E^\mathrm{center}_y &= \frac{m_\mathrm{e}}{q_\mathrm{e}n_\mathrm{e}}\left(\frac{\partial}{\partial\boldsymbol{x}}\cdot(n_\mathrm{e}\langle\delta\boldsymbol{p}_\mathrm{e}\delta\boldsymbol{v}_\mathrm{e}\rangle)+\frac{\partial}{\partial\boldsymbol{x}}\cdot(n_\mathrm{e}\bar{\boldsymbol{p}}_\mathrm{e}\bar{\boldsymbol{v}}_\mathrm{e})\right)_y \\ &\sim \frac{m_\mathrm{e}}{q_\mathrm{e}}\left(\frac{c^2\Theta^\mathrm{edge}_{xy,\mathrm{e}}}{\delta_\mathrm{e}\Gamma^\mathrm{in}_\mathrm{e}}+\frac{\bar{v}^\mathrm{center}_y\bar{p}^\mathrm{out}_z}{D_\mathrm{e}}\right). \end{aligned} \tag{6.15}$$

The next step is to use the constancy of E_y, which is respected well in the simulations: $E^\mathrm{center}_y = E^\mathrm{in}_y = \bar{v}_\mathrm{in}B_0$. We note, however, that at the entrance of the diffusion regions B is different than the asymptotic value B_0, and that the $E\times B$ drift does not strictly hold (see Fig. 6.4). If we introduce the inertial length in the inflow, $d^\mathrm{in}_\mathrm{e} = c\sqrt{\epsilon_0 m_\mathrm{e}/(n^\mathrm{in}_\mathrm{e}e^2)}$, and the inflow magnetization $\sigma^\mathrm{cold}_\mathrm{in,e} = B_0^2/(\mu_0 m_\mathrm{e}n^\mathrm{in}_\mathrm{e}c^2)$, we ultimately obtain

$$\frac{\delta_\mathrm{e}}{d^\mathrm{in}_\mathrm{e}}\left(\sigma^\mathrm{cold}_\mathrm{in,e}\right)^{1/2}\frac{\bar{v}_\mathrm{in}}{c} = \frac{\Theta^\mathrm{edge}_{xy,\mathrm{e}}}{\Gamma^\mathrm{in}_\mathrm{e}}+\frac{\delta_\mathrm{e}}{D_\mathrm{e}}\frac{\bar{v}^\mathrm{center}_y\bar{p}^\mathrm{out}_z}{c^2}. \tag{6.16}$$

We now proceed to derive approximate scaling relations for cases where either thermal or bulk inertia dominate the reconnection electric field.

- First, if thermal inertia dominates over bulk inertia, then Eq. 6.16 gives

$$\frac{\Theta^\mathrm{edge}_{xy,\mathrm{e}}}{\Gamma^\mathrm{in}_\mathrm{e}} = \frac{\delta_\mathrm{e}}{d^\mathrm{in}_\mathrm{e}}\left(\sigma^\mathrm{cold}_\mathrm{in,e}\right)^{1/2}\frac{\bar{v}_\mathrm{in,e}}{c}\propto\left(\sigma^\mathrm{cold}_\mathrm{in,e}\right)^{1/2}. \tag{6.17}$$

  There are thus several factors contributing to $\Theta^\mathrm{edge}_{xy,\mathrm{e}}$. The diffusion zone width δ_e is dynamically set during the reconnection process. It can be close to the particles' gyroradius at the center of the current sheet, or to the plasma inertial length at the center of the current sheet. In all our simulations, we find that the latter assumption holds throughout time to within a factor 2 (Sect. 6.4.2), and in any case, $\delta_\mathrm{e}/d^\mathrm{in}_\mathrm{e}$ is expected to be of order unity.

  The inflow speed is set by the reconnection electric field, $\bar{v}_\mathrm{in} = E_y/B_0 = E^*V^\mathrm{R}_\mathrm{A,in}$ with E^* the normalized reconnection rate (which lies in the range 0.1-0.25, Sect. 6.4.6) and $V^\mathrm{R}_\mathrm{A,in}$ the relativistic Alfvén speed in the inflow. For relativistic setups we thus have $\bar{v}_\mathrm{in}\sim E^*c$.

The inflow magnetization can be arbitrarily large. It is thus the main actor in producing relativistic temperatures, and thermal inertia scales as $\Theta_{xy,\mathrm{e}}^{\mathrm{edge}} \propto \left(\sigma_{\mathrm{in,e}}^{\mathrm{cold}}\right)^{1/2}$.

- Second, the term corresponding to bulk inertia in Eq. 6.16 can be estimated with the help of Eq. 6.10 (with $\bar{p}_{\mathrm{out},s} = \bar{p}_z^{\mathrm{out}}$, $\bar{v}_{\mathrm{out},s} = \bar{v}_z^{\mathrm{out}}$, and neglecting the guide field):

$$\frac{\delta_{\mathrm{e}}}{D_{\mathrm{e}}} \frac{\bar{v}_y^{\mathrm{center}} \bar{p}_z^{\mathrm{out}}}{c^2} = \frac{\delta_{\mathrm{e}}}{D_{\mathrm{e}}} \frac{\bar{v}_y^{\mathrm{center}} \bar{v}_z^{\mathrm{out}}}{c^2} \left(\frac{\bar{p}_{\mathrm{in}}}{\bar{v}_{\mathrm{in}}} + \sigma_{\mathrm{in,e}}^{\mathrm{cold}} \right). \tag{6.18}$$

The ratio $\delta_{\mathrm{e}}/D_{\mathrm{e}}$ is of order 1/10 in our simulations. If we neglect the term $\bar{p}_{\mathrm{in}}/\bar{v}_{\mathrm{in}}$, which is of order unity for non-relativistic inflow temperatures, we see that bulk inertia scales with $\sigma_{\mathrm{in,e}}^{\mathrm{cold}}$.

In conclusion, thermal inertia scales at most as $\left(\sigma_{\mathrm{in,e}}^{\mathrm{cold}}\right)^{1/2}$, and bulk inertia as $\sigma_{\mathrm{in,e}}^{\mathrm{cold}}$. Consequently, regarding the non-ideal terms in Ohm's law in the electron diffusion region, we expect bulk inertia to outweigh thermal inertia at high inflow electron magnetization.

Energy content of the outflows

We now turn to the energy content of the outflows to see whether we can explain their thermally dominated character for relativistic runs. The temperature in the outflows is dominated by $\Theta_{xx,\mathrm{e}}$ or $\Theta_{yy,\mathrm{e}}$, which we denote by $\Theta_{\mathrm{e}}^{\mathrm{out}}$. We first have to link $\Theta_{\mathrm{e}}^{\mathrm{out}}$ to $\Theta_{xy,\mathrm{e}}^{\mathrm{edge}}$. The outflow temperature at the center of the diffusion region is roughly constant along z throughout the area of linear increase of $\bar{v}_z$ (Fig. 6.9), because particles on their way from the X-point to the exhaust mainly turn into the reconnected magnetic field and thus do not really gain thermal agitation, but convert it from one component of Θ to another. We can thus assume $\Theta_{\mathrm{e}}^{\mathrm{out}} = \Theta_{\mathrm{e}}^{\mathrm{center}}$. We now would like to assume $\Theta_{xy,\mathrm{e}}^{\mathrm{edge}} \sim \Theta_{xx,\mathrm{e}}^{\mathrm{center}}$. This indeed holds for electrons in the case of Fig. 6.8. However, this does not hold in all simulations, and $\Theta_{xy,\mathrm{e}}^{\mathrm{edge}}$ is between 1/10 to 10 times $\Theta_{xx,\mathrm{e}}^{\mathrm{center}}$. This is due to the different origin of these components: $\Theta_{xx,\mathrm{e}}^{\mathrm{center}}$ reflects particles in Speiser orbits going up and down along x with a zero bulk x-velocity, while $\Theta_{xy,\mathrm{e}}^{\mathrm{edge}}$ reflects the asymmetry of the distribution function with respect to v_x due to the newly entering particles at the edge of the diffusion zone.

With the previous remark in mind, we still make the hypothesis $\Theta_{xy,\mathrm{e}}^{\mathrm{edge}} \sim \Theta_{xx,\mathrm{e}}^{\mathrm{center}}$. Next, if we assume that thermal inertia contributes significantly in Ohm's law, we obtain, with the scaling of Eq. 6.17,

$$\Theta_{\mathrm{e}}^{\mathrm{out}} \propto \left(\sigma_{\mathrm{in,e}}^{\mathrm{cold}}\right)^{1/2}. \tag{6.19}$$

For relativistic temperatures we have $h_{0,\mathrm{out,e}} \simeq 4\Theta_{\mathrm{e}}^{\mathrm{out}}$ (Fig. 3.1), so that with Eq. 6.19 we see that a relativistic inflow magnetization implies $h_{0,\mathrm{out,e}} \propto \left(\sigma_{\mathrm{in,e}}^{\mathrm{cold}}\right)^{1/2}$. On the other hand, energy conservation gives, in its simplest form (Eq. 6.12 with $\sigma_{\mathrm{e}}^{\mathrm{cold}}(B_0) \gg 1$):

$$h_{0,\mathrm{out,e}} \Gamma_{\mathrm{out,e}} \sim \sigma_{\mathrm{in,e}}^{\mathrm{cold}}. \tag{6.20}$$

Thus,

$$\Gamma_{\rm out,e} \propto \left(\sigma_{\rm in,e}^{\rm cold}\right)^{1/2}. \tag{6.21}$$

We finally turn to the ratio of energy fluxes in the outflow. We see with Eq. 6.13 that the flux associated with kinetic bulk energy is $\Gamma_{\rm out,e}-1$. With Eq. 6.21 (and for $\Gamma_{\rm out,e} \gg 1$), this flux is $\Gamma_{\rm out,e} \propto \left(\sigma_{\rm in,e}^{\rm cold}\right)^{1/2}$. The flux associated with thermal kinetic energy and pressure work is $h_{0,\rm out,e}\Gamma_{\rm out,e}-1$, and with Eq. 6.20 we have $h_{0,\rm out,e}\Gamma_{\rm out,e}-1 \sim \sigma_{\rm in,e}^{\rm cold}$. The ratio of thermal-to-bulk energy fluxes is thus $\propto \left(\sigma_{\rm in,e}^{\rm cold}\right)^{1/2}$, meaning that relativistic inflow magnetization inevitably implies reconnection exhausts dominated by thermal energy, which is what we see in our simulations (Table 6.4), even if the scalings derived here do not hold exactly because of the many assumptions involved.

In conclusion, we have shown that *under the hypothesis of non-ideal effects sustained by thermal inertia*, relativistic inflow magnetizations produce thermally dominated outflows. The physical reason is that the reconnection electric field E_y is large in the inflow region, so that thermal inertia must be high in order to sustain E_y in the central region, which implies high temperatures.

However, we also demonstrated that thermal inertia is not expected to dominate for very relativistic inflows. When this is the case, there is no constraints from Ohm's law on the temperature, and we cannot decide on the ratio of thermal to bulk energy fluxes. Since this ratio is $(h_{0,\rm out,e}\Gamma_{\rm out,e}-1)/(\Gamma_{\rm out,e}-1) \sim h_{0,\rm out,e}$, a relativistic outflow temperature on the order of $m_{\rm e}c^2$ suffices to give thermally dominated outflows.

For our simulations, thermal inertia contributes equally or less than bulk inertia (Sect. 6.4.3), but still significantly, so that the outflows are thermally dominated.

6.5 Effects of a guide field

Except in special configurations, the generic reconnection geometry involves asymptotic fields that are not antiparallel. An angle different from 180° can be described by the addition of a uniform guide magnetic field $\boldsymbol{B}_{\rm G} = B_{\rm G}\hat{\boldsymbol{y}}$ to the antiparallel configuration. Such configurations have been largely studied in the non-relativistic case (e.g., Pritchett and Coroniti 2004; Drake et al. 2005; Goldman et al. 2011; Le et al. 2013; Graf von der Pahlen and Tsiklauri 2014), and feature significant differences with the antiparallel case. Here we only focus on the reconnection rates and on the island structure, and postpone a study of other points to a future publication. We present results from two simulations, with $B_{\rm G} = 0.5B_0$ and $B_{\rm G} = B_0$.

6.5.1 Overall structure

We first stress that because of the presence of the guide field, in both cases $B_{\rm G} = 0.5B_0$ and B_0, the relation $cB > E$ holds everywhere through time and space, hence also the relation $cB > E_\perp$ (with $E_\perp$ the component perpendicular to $\boldsymbol{B}$). Consequently, particle acceleration is not possible in directions perpendicular to $\boldsymbol{B}$, and is only allowed along the field lines at places where $\boldsymbol{E}\cdot\boldsymbol{B} \neq 0$. Such parallel electric fields are allowed by the

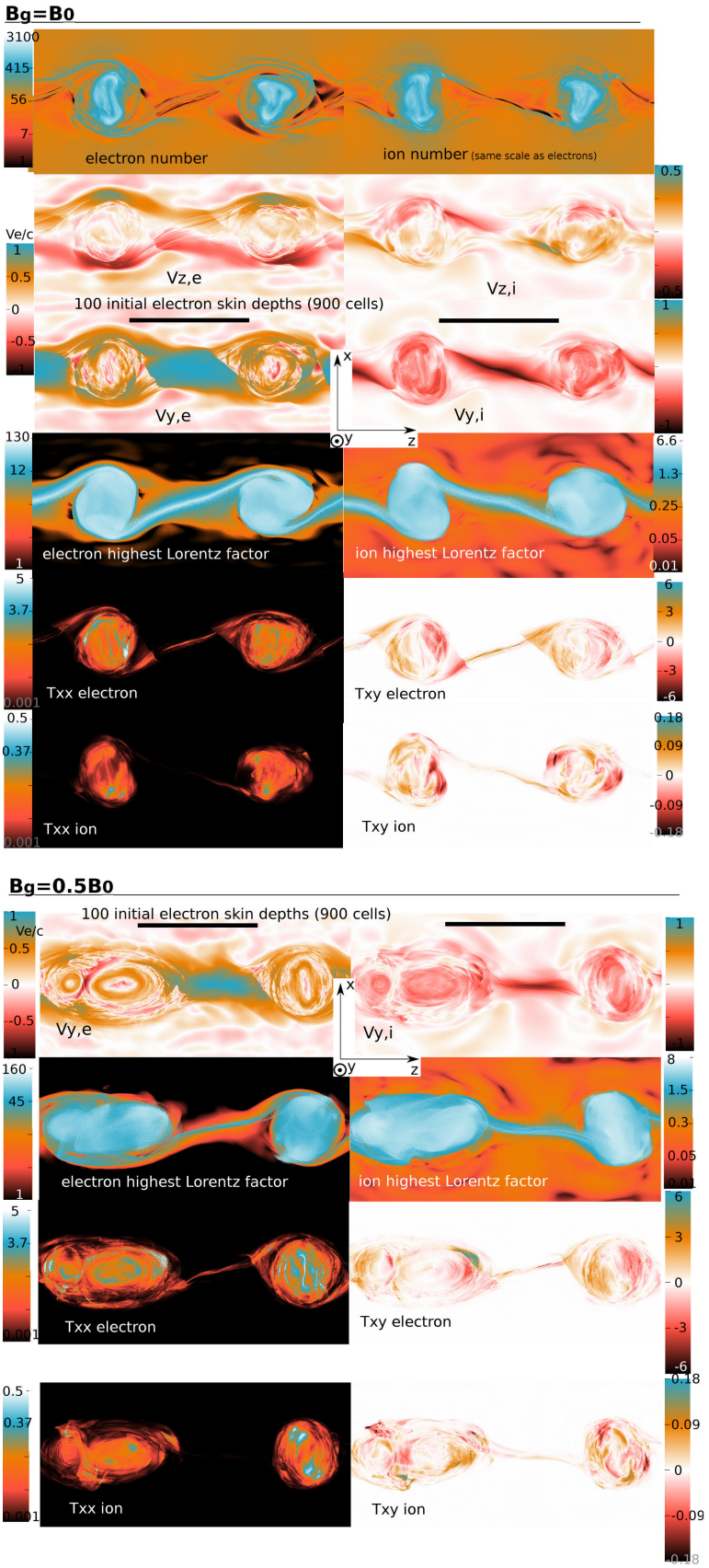

Figure 6.12: **Top:** Simulation with $\boldsymbol{B}_{\rm G} = B_0\hat{\boldsymbol{y}}$, time $t = 37\omega_{\rm ci}^{-1} = 935\omega_{\rm ce}^{-1}$. **Bottom:** Simulation with $\boldsymbol{B}_{\rm G} = 0.5B_0\hat{\boldsymbol{y}}$, time $t = 37\omega_{\rm ci}^{-1} = 935\omega_{\rm ce}^{-1}$, same scale as for $\boldsymbol{B}_{\rm G} = B_0\hat{\boldsymbol{y}}$.

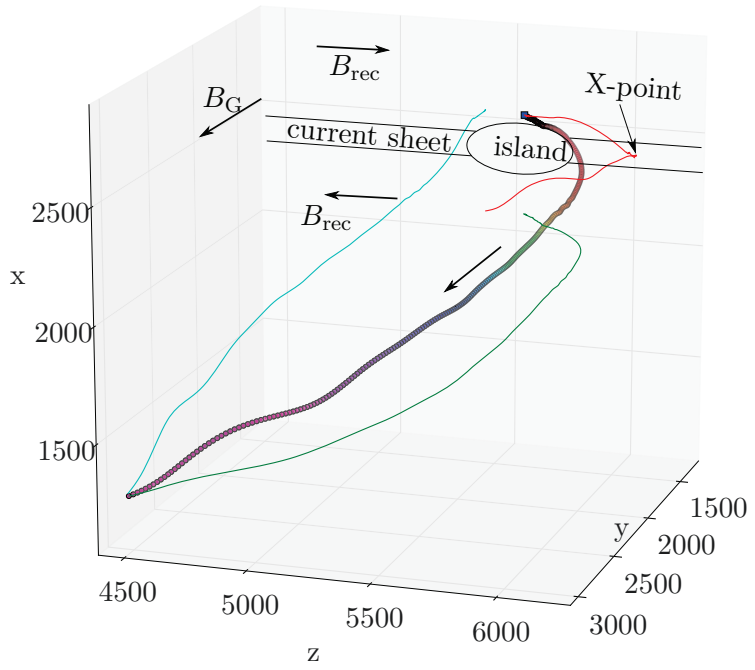

Figure 6.13: Typical trajectory for a particle, here an electron, for simulation with $\boldsymbol{B}_{\rm G} = B_0\hat{\boldsymbol{y}}$. Axis scales are given in cell numbers, with 9 cells representing one initial electron inertial length. Dot colors are the particle Lorentz factor, from 1 to 60 here. Solid lines are projections onto the x-y, y-z, and z-x planes.

non-idealness of the plasma response, $\boldsymbol{E} + \bar{\boldsymbol{v}}_s \wedge \boldsymbol{B} \neq 0$, and are indeed found at and around the X-points.

Just as in the zero guide field case, the plasma accelerated by E_y is slowly deviated by the reconnected B_x component, which produces outflows directed along $\pm z$. However, particles from these outflows feel the Lorentz force from the guide field, and their trajectories are tilted against the z axis, as is evident in Fig. 6.12. Reversing the guide field from $+\hat{\boldsymbol{y}}$ to $-\hat{\boldsymbol{y}}$ tilts them in the opposite direction. We underline that while the tilt angle is indeed smaller for a smaller guide field, it also depends on the background plasma pressure, as shown by TenBarge et al. (2014).

In the present case, $\boldsymbol{E}_y \propto -\hat{\boldsymbol{y}}$. Electrons are thus accelerated along the field lines in the $+\hat{\boldsymbol{y}}$ direction. Their motion along the field lines results in a projected (x-z plane) motion directed toward positive z where $\boldsymbol{B} \cdot \hat{\boldsymbol{z}} > 0$ (i.e., in the $x > 0$ area), or toward negative z where $\boldsymbol{B} \cdot \hat{\boldsymbol{z}} < 0$ (i.e., in the $x < 0$ area). It results in large and fast electron flows above and below the current sheet, and to a rotation around the islands in a direction opposed to cyclotron gyration. Ions are accelerated toward $-\hat{\boldsymbol{y}}$ and counterstream with respect to the electrons.

Particles reaching the central part are accelerated along y by E_y and, because they always feel a magnetic field $cB > E$, they are guided by the magnetic field and spend more time in the acceleration region for strong $B_{\rm G}$ (Fig. 6.13). Consequently, $\bar{v}_y$ is greater than with no guide field under similar conditions, and reaches high values on a larger area (compare $\bar{v}_y$ in Figs. 6.2 and 6.12).

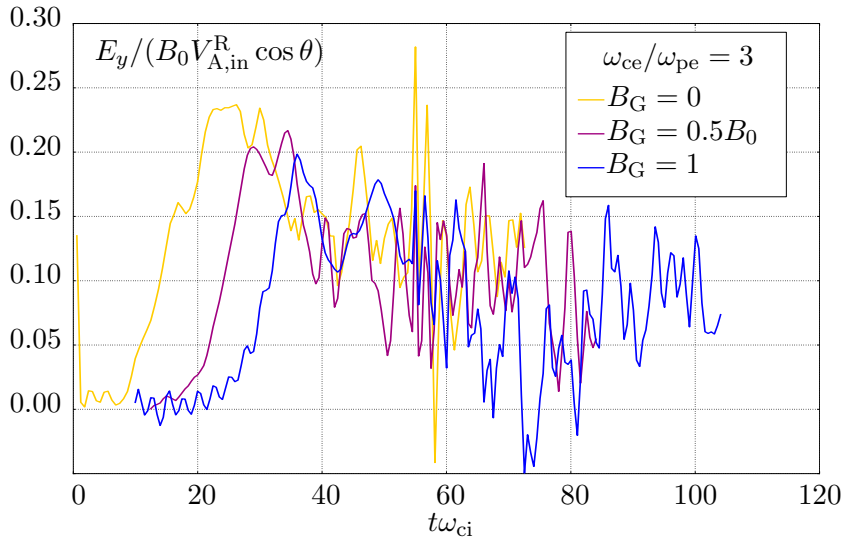

Figure 6.14: Time evolution of the normalized reconnection electric field $E_y/(B_0 V^{\rm R}_{\rm A,in}\cos\theta)$, measured at the X-point of various simulations. The velocity $V^{\rm R}_{\rm A,in}\cos\theta$ is given in Table 6.2. Time is normalized by the ion cyclotron pulsation. Here $B_0 = 0.33$, $V^{\rm R}_{\rm A,in} = 0.88c$, $\cos\theta = (1 + B^2_{\rm G}/B^2_0)^{-1/2} = 1$, 0.89, 0.71.

6.5.2 Islands' structure

The structure of the islands resembles the no-guide field case: their centers are composed of particles initially in the current sheet, with background particles only circling at the periphery. They are the hottest and strongest current-carrying part of the simulations. There are, however, important differences.

First, the inclination of the outflows makes the island asymmetric, with electrons rotating around in a direction opposite to that of ions (when looking at the motion projection in the x-z plane). Second, as islands form and contract, the guide magnetic field is compressed and increases in strength. In the simulation with $B_{\rm G} = 0.5B_0$, it passes from $0.5B_0$ initially to 1.8-$2.1B_0$ in the islands, while in the simulation with $B_{\rm G} = B_0$, it passes from B_0 initially to 2.1-$2.4B_0$ in the islands. Third, because of the strong magnetic field along y, temperatures are isotropized along x and z (in the no-guide field case we had $\Theta_{zz} \sim 2\Theta_{xx}$). Here $\Theta_{zz} \simeq \Theta_{yy} \simeq \Theta_{xx}$ equal to up to 4 for electrons and 0.2 for ions. This is a value close to the average $(\Theta_{zz} + \Theta_{yy} + \Theta_{xx})/3$ of the zero guide field case. Off-diagonal terms are an order of magnitude smaller.

6.5.3 Reconnection electric field and reconnection rate

In the normalization of Sect. 6.4.6, $E^* = E_y/(B_0 V^{\rm R}_{\rm A,in})$, the Alfvén velocity includes the total magnetic field $\boldsymbol{B} = B_0(\hat{\boldsymbol{z}} + \alpha\hat{\boldsymbol{y}})$. In the presence of a guide field ($\alpha \neq 0$), Alfvén waves propagating along the magnetic field do so in a direction that makes an angle $\theta = \arctan\alpha$ with the outflow direction $\hat{\boldsymbol{z}}$. As we explained in Sect. 6.4.6, the reconnection electric field is in part set by the velocity at which the field lines are extracted from the X-point, i.e., by the outflow velocity. This outflow velocity is mostly set by the projection of the Alfvén speed onto the outflow direction (Eq. 6.11 in the non-relativistic limit, Eq. 6.10 in the general case). Consequently, it seems justified to normalize the electric field with the projection of the Alfvén speed onto the

$\hat{\boldsymbol{z}}$ direction, i.e., to use

$$E^* = \frac{E_y}{B_0 V_{\mathrm{A,in}}^{\mathrm{R}} \cos\theta}. \tag{6.22}$$

Figure 6.14 shows the time evolution of E^* for three simulations with $B_{\mathrm{G}}/B_0 = 0$, 0.5, 1, with otherwise identical parameters. The peak reconnection rate decreases when the guide field increases: 0.24, 0.22, and 0.20. This is also the kind of dependence found in PIC simulations of ion-electron non-relativistic reconnection (Ricci et al. 2003; Huba 2005; TenBarge et al. 2014; Liu et al. 2014), relativistic pair reconnection (Hesse and Zenitani 2007), or two-fluid simulations of relativistic reconnection (Zenitani et al. 2009a)[d]. Consequently, relativistic reconnection in ion-electron plasmas does not bring new effects in this respect. However, we underline that the normalization used here allows minimizing the scatter in E^* for the various simulations.

6.6 Summary and discussion

6.6.1 Summary

We investigate magnetic reconnection in low β ion-electron plasmas (mass ratio of 25) with 2D PIC simulations, under relativistic conditions, i.e., the magnetic energy of the inflowing plasma exceeds its restmass energy. The simulations start from a Harris kinetic equilibrium with no localized perturbation. For diagnostics and analytical models, we use momentum and energy fluid equations based on lab-frame quantities (Sect. 3.4). They have the advantage of being valid regardless of the particle distribution function, while the usual relativistic fluid equations using comoving quantities are restricted to isotropic comoving distribution functions.

For antiparallel reconnection, the structure of the diffusion region has a width (in the inflow direction) δ_s given by the respective inertial length d_s of the species s, measured at the center of the diffusion region. A high inflow temperature increases this width. At the entrance of the diffusion regions for simulations at low background $\beta \leq 2.5 \times 10^{-3}$, we find sharp transitions in the fluid quantities that were not reported elsewhere. We argue that they are not shocks. Instead, they occur when the inflowing particles have a thermal velocity that is far lower than their bulk $E \times B$ velocity, so that they enter the diffusion region with the same velocity and bounce back at the same location. We stress that these sharp transitions are not a feature of relativistic reconnection, because they depend only on the cold nature of the inflow. However, the phenomenon should be more common in relativistic reconnection because then the inflow bulk velocity $v_{E\times B} \sim E/B$ is large.

We detail the balance of terms in the relativistic Ohm's law for antiparallel reconnection. The ion diffusion region is dominated by bulk inertia (as defined in Eq. 6.9). In the electron diffusion region, bulk inertia contributes equally or more than thermal inertia. The latter result challenges the thermal-inertia-dominated paradigm that holds for non-relativistic or mildly relativistic antiparallel reconnection. We show analytically that a significant contribution of bulk inertia is to be expected

[d] We note, however, that in asymmetric reconnection the rate increases with the guide field strength, see Aunai et al. (2013), Hesse et al. (2013).

whenever the inflow magnetization $\sigma_{\rm e}^{\rm cold}$ (cold, meaning that the temperature is not taken into account, see Eq. 6.5) of the *electrons* is high, because then bulk inertia $\partial_z(\bar{p}_z\bar{v}_y) \sim \bar{p}_z c/D \propto \sigma_{\rm e}^{\rm cold}/D$ can exceed thermal inertia $\partial_x(\delta p_x \delta v_y) \propto (\sigma_{\rm e}^{\rm cold})^{1/2}/\delta$. This is a new result that should hold for any large electron magnetization.

For the reconnection outflows we analytically show from mass and energy conservation that reconnection is expected to produce relativistic outflow temperatures and/or relativistic outflow bulk velocities. From simulations we find that outflow thermal energy dominates over bulk kinetic energy (from 70% to 99%, for simulations with increasing background magnetization). A more refined analytical analysis shows that this is expected if the reconnection electric field is sustained by thermal inertia. If bulk inertia dominates the thermal inertia, as expected at very high inflow magnetization, then our simple analytical model does not allow a conclusion about the cold or hot nature of the outflows. Also, our simulations do not probe high enough electron magnetizations to reach this regime: at $\sigma_{\rm e}^{\rm cold} = 90$, thermal inertia contributes 50% of the reconnection electric field, and this fraction goes down to 25-40% at $\sigma_{\rm e}^{\rm cold} = 360$, which is significant enough for the hypothesis of $E_{\rm rec}$ sustained by thermal inertia to hold.

For the islands we show that, with or without a guide field, their centers consist mainly of particles initially in the current sheet that were gathered inside the island during the tearing instability, that do not mix with the background plasma even after many island merging events. Particles of the background plasma cannot reach the inner parts because of the strong magnetic field surrounding the islands, and thus circle around the central part. As a result, the central part is less dense than its immediate surrounding. This may explain observed density dips at the center of magnetic islands during magnetotail reconnection events (Khotyaintsev et al. 2010), without invoking island merging or particle escape along the flux tube. Islands are also the hottest parts of the flow, with fully anisotropic temperatures in the antiparallel case, and distributions close to gyrotropic with a guide field.

We argue that the reconnection rates are to be normalized by the asymptotic magnetic field and relativistic Alfvén speed in the inflow, projected onto the outflow direction if there is a guide field: $E^* = E_y/(B_0 V_{\rm A,in}^{\rm R} \cos\theta)$. This leads to rates in a narrow range: E^* peaks between 0.14–0.25. However, we stress that there is no universal value for E^* as defined here or elsewhere. First, because other studies show that it depends on the inflow plasma β (increasing with decreasing β). Here we find no dependence on the background plasma temperature, but smaller rates for larger particle number densities. Second, we find larger rates for the relativistic setups (0.18–0.25) than for the mildly relativistic case (0.15). These rates are also larger than those reported in the literature for ion-electron non-relativistic reconnection (0.07–0.15 for Birn et al. 2001; Pritchett 2001; Fujimoto 2006, 2009; Daughton et al. 2006; Klimas et al. 2010). This points toward relativistic reconnection being slightly faster than non-relativistic reconnection. This trend is reinforced by simulations in relativistic pair plasmas ($E^* = 0.3$ in our case or, e.g., 0.17–0.36 for Zenitani and Hoshino 2007; Bessho and Bhattacharjee 2012; Cerutti et al. 2012a). We note that this is against the interpretation of Hesse and Zenitani (2007) of a smaller rate for more relativistic setups. Third, we confirm that a guide field leads to a smaller normalized rate.

We explore the consequences of adding a guide magnetic field. The flow structure is strongly disturbed for two reasons: the Lorentz force associated with the guide field, and the relation $E < cB$ everywhere. The acceleration region is now defined by the condition $\boldsymbol{E}\cdot\boldsymbol{B} \neq 0$. Inflowing ion and electron Larmor radii are smaller than the island scales or magnetic gradient scales, and remain so even after the acceleration phase by $E_{\rm rec}$, because this phase conserves the perpendicular-to-$\boldsymbol{B}$ momentum. Particles thus remain tied to the field lines everywhere, including in the acceleration region where they spend more time before being deviated in the outflows.

6.6.2 Astrophysical outlook, objects and orders of magnitude

This study may serve as micro-physics input for analyses on larger scales concerning magnetic energy conversion in relativistic ion-electron plasmas, as should be encountered in the coronae of AGN and microquasar accretion flows, in the lobe of radio galaxies, or inside relativistic jets from AGNs or GRBs. We now discuss such applications and give estimates for key parameters in these objects: magnetic field B, electron number density $n_{\rm e}$, magnetizations $\sigma_s^{\rm cold}$ (where cold means that only the restmass energy is taken into account, not the temperature, Eq. 6.5), with $s = $ i, e for ions or electrons, and Alfvén speeds $V_{\rm A}^{\rm R}$. The properties of magnetic reconnection as studied here only depend on the inflow magnetization and temperatures, regardless of the real values of B and $n_{\rm e}$. This is true at least as long as effects such as pair creation and annihilation, radiative braking, or Compton drag on the electrons, can be neglected. These effects are discussed in Sects. 7.5.4 and 7.A.

The next chapter will also lead to astrophysical implications, that will be discussed in its own conclusive section 7.5.3. For clarity, we use the same subsection titles here in Sect. 6.6.2 and in Sect. 7.5.3. The organization of these two sections follows from the realization that magnetic reconnection can play a major role for four particular purposes: large scale outflow launching, high-energy flare production, steady emission of radiation, and plasma heating or non-thermal particle production. We discuss in which objects these phenomena are observed, give orders of magnitude for the main parameters, and point out where our work is applicable. Also, Table 7.5 summarizes the physical conditions encountered in the objects mentioned here.

Toward a new regime: non-dissipative reconnection?

Our finding of a reconnection electric field sustained equally or more by bulk inertia than by thermal inertia for large inflow electron magnetization ($\sigma_{\rm e}^{\rm cold} \geq 90$), and the extrapolation of Sect. 6.4.8, indicate that bulk inertia might end up dominating at even higher inflow electron magnetizations. This was also envisioned by Hesse and Zenitani (2007), and reconnection in such a regime would bear significant differences with the standard picture. However, we nuance the assertion of Hesse and Zenitani (2007) that reconnection would then be a reversible process: as underlined in Sect. 6.4.8, the reconnection outflows may be thermally dominated even when bulk inertia dominates Ohm's law. A definite answer to these questions requires very high magnetizations, which we can hardly reach with a PIC code and which

may require relativistic gyrokinetic codes.

Highly magnetized environments, such as pulsar winds near the termination shock ($\sigma_e^{cold} = 10^{13}$, Bucciantini et al. 2011; Sironi and Spitkovsky 2011a), or other objects with $\sigma_e^{cold} \ggg 1$ discussed in what follows, are likely to support this reconnection regime[e]

Large scale transient outflow production, the example of microquasars

Large scale magnetic reconnection events may be at the origin of large scale transient jets in microquasar systems (de Gouveia dal Pino and Lazarian 2005; de Gouveia Dal Pino et al. 2010; Kowal et al. 2011; McKinney et al. 2012; Dexter et al. 2014). For example, a magnetically arrested disk can form around the black hole, and a reconnection event can be triggered by an incoming accreted magnetic field reversal. Reconnection then occurs in the accretion disk corona, near the black hole, where particle densities and magnetic fields are high.

Here, we have shown that the reconnection outflows are thermally dominated, with a bulk Lorentz factor not necessarily increasing with the inflow magnetization and featuring low values ($\Gamma \sim 1.6$ at most, Table 6.4). However, applications to large scale outflows triggered by reconnection events require some care. The outflows studied in the present manuscript originate in the electron diffusion region, and feature ion/electron decoupling. At larger distances, if not bounded by the islands and by our periodic setup, electrons and ions are expected to couple and to follow the ideal MHD dynamic. The scale on which they can propagate is fixed by larger scales than simulated here.

On the other hand, it is expected and observed (Khotyaintsev et al. 2006) that magnetic energy conversion also takes place along the magnetic separatrices far away from the dissipation region, on length scales of hundreds of ion inertial lengths (see Sect. 2.12.4 for an overview of the physics of the separatrices). This conversion occurs through instabilities that produce thermal and non-thermal electrons (Drake et al. 2005; Egedal et al. 2009, 2012; Lapenta et al. 2014), and through the complex structure of collisionless non-linear waves (slow shock, compound wave, rotational wave) by which the magnetized inflowing plasma transits to the hot and unmagnetized outflow on MHD scales (Liu et al. 2012; Higashimori and Hoshino 2012). It is this large scale outflow that should be identified as the transient reconnection-driven jets in microquasar models. In the magnetosphere close to the black hole, de Gouveia dal Pino and Lazarian (2005) estimate on the basis of an analytical model, $n_e \sim 5 \times 10^{15}\,\mathrm{cm}^{-3}$, $B \sim 7 \times 10^7$ G, which gives electron and ion magnetizations $\sigma_e^{cold} \sim 10^5$ and $\sigma_i^{cold} \sim 60$, and an Alfvén speed $V_A^R \sim c$ (see Table 7.5, line a, for wider estimates). This is clearly in the relativistic regime. The energy content of the *large scale* outflows in this case has not been studied, but we can expect from the collisionless slow shocks, or rotational discontinuities at the separatrices, to produce a thermally dominated outflow. It may not be so for other jet production mechanisms, and could help distinguishing in favor or against reconnection scenarios.

[e] We note that magnetar magnetospheres, even if they feature magnetizations exceeding $\sigma_e^{cold} = 10^{13}$ (Lyutikov and Lazarian 2013), support a very different reconnection regime due to pair and photon creations (Uzdensky 2011).

Another unknown is what becomes of the ambient plasma that is expelled by the first reconnected field lines ahead of the dipolarization front. In our study, it would correspond to half of a magnetic island, ejected out of the simulation box. The ambient plasma would be the plasma from the current sheet trapped in the island. As we demonstrate, this plasma does not mix with the reconnected plasma and is simply compressed and heated (see Vapirev et al. 2013, for a 3D case where instabilities imply magnetic to kinetic energy conversion). In an open configuration, it would be at the head of the large scale outflow.

Flares in extragalactic jets

Flare-like activity in the GeV-TeV range is observed from extragalactic jets, and may possibly be explained by local reconnection events inside the jet, which produce smaller jets (the reconnection exhausts) which in turn radiate the expected photons (Giannios et al. 2009). This γ-ray emission region may be located close to the black hole ($< 0.05\,\mathrm{pc}$, Giroletti et al. 2004), where $B \sim 0.02\text{-}0.2\,\mathrm{G}$ and the plasma magnetization is high. For example, Giannios et al. (2009) take $\sigma_\mathrm{i}^\mathrm{cold} = 100$, which leads to $\sigma_\mathrm{e}^\mathrm{cold} = 2 \times 10^5$ and $V_\mathrm{A} \sim c$. This is in the regime where bulk inertia should dominate in Ohm's law. Also, Giannios et al. (2009) use energy considerations to estimate that the blobs emitted from the reconnection exhausts should be $\sim 10^{14}\,\mathrm{cm}$, i.e., based on its estimated particle density, 10^{10} ion inertial lengths. Here again, the physics far from the dissipation region should play an important role in producing such large scale structures.

Steady radio emission from extragalactic jets

Another case for relativistic magnetic reconnection is inside jets from AGNs on scales of 10-100 kpc. Radio spectra may be explained by radiation linked to reconnection events (Romanova and Lovelace 1992). Observations of AGN jets indicate $B \sim 10\text{-}30\mu\mathrm{G}$, $n \sim 0.8\text{-}5\times10^{-8}\mathrm{cm}^{-3}$, and electron magnetizations in the range $\sigma_\mathrm{e}^\mathrm{cold} \sim 500\text{-}2500$ (Schwartz et al. 2006), which implies ion magnetizations $\sigma_\mathrm{i}^\mathrm{cold} \sim 0.3\text{-}1.3$ and Alfvén speeds $\sim 0.5\text{-}0.8c$. Again, our results apply in these cases, and in particular the electron magnetizations are in the very relativistic range where bulk inertia should dominate in Ohm's law.

Plasma heating in AGN and microquasar coronae and in radio galaxy lobes

Observations and models suggest that AGN and microquasar coronae, and the lobes of radio galaxies, contain hot plasmas. A possible heating mechanism is by magnetic reconnection events. We address the issue of magnetic energy conversion and distribution in these relativistic environments in Sect. 7.5.3.

6.6.3 Astrophysical outlook, further discussion

High-energy particle production

The proposed normalization of the reconnection rate with the relativistic inflow Alfvén speed $V_\mathrm{A,in}^\mathrm{R}$, $E^* = E_\mathrm{rec}/(B_0 V_\mathrm{A,in}^\mathrm{R} \cos\theta)$, leads to E^* in a close

range (0.14-0.25), and because it only relies on inflow quantities, it allows for an easy prediction of the reconnection electric field. In particular, the ratio $E_{\rm rec}/B_0$ is a key quantity for estimating the timescale of energy dissipation or the maximum energy gain for particles. It is interesting to notice that for very relativistic plasmas, $V^{\rm R}_{\rm A,in}$ saturates at c, so that $E_{\rm rec}/B_0$ saturates at $\sim 0.2c$. It may imply that the hardness of the high-energy tails saturates. We explore these matters in Chapter 7. Briefly, we find for a given species a power law tail whenever its background magnetization is relativistic (above a few), with an index depending both on the inflow magnetization and inflow Alfvén speed. The reason for the latter is precisely because of the link between $V^{\rm R}_{\rm A,in}$ and E_y/B_0.

Other complications

We finally point out that the present study is oversimplified in many respects. Magnetic reconnection in magnetized coronae and jets probably often implies asymmetric plasmas from each side of the current sheet, guide fields (Aunai et al. 2013; Hesse et al. 2013; Eastwood et al. 2013), and also normal fields (along $\hat{\boldsymbol{x}}$ here) reminiscent of the ambient magnetic field. The last point has been studied in the context of the Earth's magnetotail (Pritchett 2005a, 2010; Sitnov and Swisdak 2011). Also, the initial conditions chosen in the simulations are arbitrary and do not necessarily reflect the real environments. Explored alternatives to the Harris sheet include X-point collapse (e.g., Graf von der Pahlen and Tsiklauri 2014) or force-free equilibrium (e.g., Liu et al. 2014) and show little differences with the Harris case. However, three-dimensional initial configurations should also be considered, because in a real environment most of the energy dissipation may occur at 3D nulls, involving for example spine-fan reconnection, or at quasi-separatrix layers (Birn and Priest 2007; Pontin 2011). Few kinetic simulations exist for such setups (Baumann and Nordlund 2012; Olshevsky et al. 2013). A related point is the external forcing, i.e., the large scale plasma flow that can increase the magnetic field gradients and trigger reconnection. Studies (Pei et al. 2001; Pritchett 2005b; Ohtani and Horiuchi 2009; Klimas et al. 2010) show that the reconnection rate E^* is then fixed by the boundary conditions, and is thus larger than the spontaneous rate. The timescale of the forcing also proves to be important (Pei et al. 2001). These considerations, as well as some of the points made earlier on, highlight the multi-scale nature of reconnection in the context of concrete astrophysical objects – and demonstrate the need for corresponding multi-scale simulation studies, a field still in its infancy (e.g., Horiuchi et al. 2010; Innocenti et al. 2013; Daldorff et al. 2014)

Another central question is the validity of the 2D findings in three dimensions. Magnetic islands then become extended filaments, modulated or broken by instabilities in the third dimension or by a lack of coherence of the tearing instability (Jaroschek et al. 2004; Zenitani and Hoshino 2008; Daughton et al. 2011; Liu et al. 2011; Kagan et al. 2013; Markidis et al. 2013). It may imply more mixing of the current sheet particles with those of the background plasma. Concerning the validity of our claims on Ohm's law, 3D PIC simulations in non-relativistic plasmas have shown that anomalous resistivity due to microinstabilities remains a negligible dissipation mechanism in the diffusion region (Liu et al. 2013b; Karimabadi et al. 2013), where the reconnection electric field is still sustained by thermal electron inertia.

The scaling analysis of Sect. 6.4.8 should thus remain valid, as should the conclusion that bulk inertia dominates at high inflow magnetization.

Chapter 7

The energetics of relativistic reconnection: ion-electron repartition and particle distribution hardness

> "John? Do you remember that paper on extra-solar activity I published?"
> "Yeah, sure."
> "I found evidence of a series of super-flares from a star in the outer-Pleiades region."
> "Right."
> "The numbers are a warning, but not just to me or any random group. They're a warning to everyone." (He takes his computer) "The super-flare, *in our own solar system.*" (He shows a simulation) "A hundred microtesla wave of radiation that would destroy our ozone layer, *killing every living organism on the planet.*"
> (Both ponder for a moment)
> "We have to let everyone know."
>
> *Knowing*, a 2009 Hollywood movie

Contents

7.1 Outline

This chapter mostly contains the article Melzani et al. (2014c). It is the continuation of the previous Chapter 6. We use the same simulations (plus some news), and now look at the fate of the magnetic energy: how much is transferred to the particles? with which ion-electron repartition? what is the hardness of the particle distributions? and what are the acceleration mechanisms? We try to provide answers to these questions, and we discuss astrophysical implications.

Section 7.2 introduces the context of the study, and Sect. 7.3 describes the simulation setups and the diagnostics used. In particular, we study separately the particles that are initially inside the current sheet, and those that are initially outside. This separation between current sheet and background particles is essential because, as we show, these two populations remain separated and undergo very different acceleration mechanisms, resulting in very different distributions.

Section 7.4 describes the results, first for a reference case (Sect. 7.4.1), then for several cases with no guide field (Sect. 7.4.2) and with a guide field (Sect. 7.4.3). We find that 45 to 75% of the total initial magnetic energy ends up in kinetic energy, this fraction increasing with the inflow magnetization. Depending on the guide field strength, ions get from 30 to 60% of the total kinetic energy. The background population forms power law distributions, both for electrons and ions, with indexes that depend both on the inflow magnetization of the considered species and on the inflow Alfvén speed, and that can be harder than for the case of collisionless shocks. A criteria for a hard tail is a magnetization far larger than unity, and an Alfvén speed close to c. For electrons, the latter condition implies an electron magnetization larger than the mass ratio. The presence of a guide field deforms the power law shape.

We draw astrophysical consequences in Sect. 7.5. Our demonstration that magnetic reconnection can furnish power law distributed high-energy particles, either ions or electrons, if the above criteria is fulfilled, has important applications for various models that assume the existence of such particle populations.

7.2 Introduction

Magnetic reconnection is a prime mechanism invoked to launch large scale outflows, to produce high-energy particles, radiation and high-energy flares, or to efficiently heat plasmas, in a variety of astrophysical objects. It is a candidate to explain, for example (we give the same list as in Sect. 6.2): transient outflow production in microquasars and quasars (de Gouveia dal Pino and Lazarian 2005; de Gouveia Dal Pino et al. 2010; Kowal et al. 2011; McKinney et al. 2012; Dexter et al. 2014), gamma-ray burst outflows and non-thermal emissions (Drenkhahn and Spruit 2002; Giannios and Spruit 2007; McKinney and Uzdensky 2012), GeV flares from the Crab nebula (Bednarek and Idec 2011; Uzdensky et al. 2011; Cerutti et al. 2012b,a,

2013), flares in AGN jets (Giannios et al. 2009), flares in gamma-ray bursts (Lyutikov 2006a; Lazar et al. 2009), X-ray flashes (Drenkhahn and Spruit 2002), soft gamma-ray repeaters (Lyutikov 2006b; Uzdensky 2011), flares in double pulsar systems (Lyutikov and Lazarian 2013), the flat radio spectra from galactic nuclei and AGNs (Birk et al. 2001), the flat radio spectra from extragalactic jets (Romanova and Lovelace 1992), the σ-paradox and particle acceleration at pulsar wind termination shocks (Kirk and Skjæraasen 2003; Pétri and Lyubarsky 2007; Sironi and Spitkovsky 2011a), the heating of the lobes of giant radio galaxies (Kronberg et al. 2004), the heating of AGN and microquasar coronae and associated flares (Di Matteo 1998; Merloni and Fabian 2001; Goodman and Uzdensky 2008; Reis and Miller 2013; Romero et al. 2014; Zdziarski et al. 2014), or energy extraction in the ergosphere of black holes (Koide and Arai 2008).

In all these cases, it is crucial to know the amount of magnetic energy transferred to the particles during a reconnection event, the relative fraction distributed to ions and electrons, as well as the distribution in momentum space of the accelerated particles. The aim of this manuscript is to shed light on these questions. In the literature, several acceleration mechanisms by magnetic reconnection have been identified, that we reviewed in Sect. 2.15. We describe again those that are of interest for the present study in the remaining of this introduction. Their relative importance depends on the plasma parameters and on the magnetic field geometry.

One acceleration mechanism occurs when particles are trapped in contracting magnetic islands, and thus accelerated by the induced electric field when they are reflected on the two approaching sides. It can be efficient in collisionless plasmas (Drake et al. 2006, 2010; Bessho and Bhattacharjee 2012) or in collisional plasmas (Kowal et al. 2011) where reconnection is fast because of turbulence. In non-relativistic plasmas, because of the small particle velocities, the Larmor radii can be smaller than the island gradient scales. If it is the case, then particle motions are adiabatic inside and around the islands, and particle-in-cell simulations and analytical estimations agree that this mechanism produces power law spectra, with indexes $p = -\mathrm{d}\log n_\mathrm{e}(\gamma)/\mathrm{d}\log\gamma = 1.3$ or softer depending on the plasma β and island aspect ratio (Drake et al. 2006). In plasmas with relativistic magnetizations, the Larmor radii of the accelerated particles likely exceed the island scales, at least at early times, so that another analytical approach has to be employed (Bessho and Bhattacharjee 2012), and there is no analytical expression for the resulting spectra. PIC simulations in relativistic pair plasmas show that this mechanism contributes significantly to the building of the high-energy population (Bessho and Bhattacharjee 2012; Sironi and Spitkovsky 2014), a result that we confirm to also hold for relativistic ion-electron reconnection. In addition, since the island edges are the place of strong motional electric fields, particles can gain energy there without necessarily turning around the whole island. Liu et al. (2011) report that in their relativistic pair plasma simulations, most particles are energized in this way. Jaroschek et al. (2004) also find that this scenario is important.

Another acceleration mechanism, also relying on the first-order Fermi process and on stochasticity, is the bouncing motion of particles between the two inflows converging from both sides of the current sheet. Energy is gained when the particle turns around, and is transferred by the motional electric field $\boldsymbol{E} = -\boldsymbol{v}\wedge\boldsymbol{B}$ present in the inflow. Drury (2012) derives the

power law spectrum for non-relativistic particles: $\mathrm{d}n(v)/\mathrm{d}v \propto v^{-p}$ with v the velocity, $p = (r+2)/(r+1)$, where $r = n_{\mathrm{out}}/n_{\mathrm{in}}$ is the compression ratio that is not restricted to low values as in the case of shocks. Giannios (2010) derives the maximal Lorentz factor produced in the relativistic case, and Bosch-Ramon (2012) discusses conditions for entering in this acceleration regime. This mechanism does not rely on a direct acceleration by the reconnection electric field E_{rec} when particles are demagnetized at the center of the diffusion region, but makes use of the motional electric field in the inflow. It is thus efficient in non-relativistic and/or collisional plasmas (Kowal et al. 2011) where direct acceleration by E_{rec} is known to be negligible. It requires particles crossing the current sheet and bouncing on the other side, i.e., having a Larmor radius in the asymptotic field that is larger than the sheet width, which is generally true only for pre-accelerated particles or hot inflows. We show here that for cold inflows and relativistic setups, electrons and ions do not cross the current sheet, and so do not undergo this acceleration mechanism.

A third acceleration mechanism is by the reconnection electric field E_{rec}, which is initially induced by magnetic field flux variations, and sustained in steady or quasi-steady state by the non-ideal response of the plasma. In the diffusion region, the condition $E > cB$ for antiparallel reconnection, or $\boldsymbol{E} \cdot \boldsymbol{B} \neq 0$ if there is a guide field, defines an acceleration region where particles can be freely accelerated and directly gain energy. In any case, the reconnection electric field is alone responsible for transferring energy between the magnetic field and the particles, and thus obviously for accelerating particles. But to what extent this kinetic energy is distributed between the bulk flow velocity of the outflows, their thermal energy, and a possible high-energy tail, as well as the properties of the high-energy tail, are open questions. This mechanism is inefficient for non-relativistic reconnection because the acceleration zone has a too small length (along z here) (Drake et al. 2010; Kowal et al. 2011; Drury 2012) and affects too few particles, but is efficient under relativistic conditions where the larger reconnection electric field creates a wider acceleration zone (Zenitani and Hoshino 2001, 2007). It has indeed been found, with PIC simulations of relativistic reconnection, that power law tails are produced through particle acceleration by E_{rec}. Several indexes are found, for example, measuring the index p as $\mathrm{d}n_{\mathrm{e}}/\mathrm{d}\gamma \propto \gamma^{-p}$ and retaining only relativistic particle-in-cell simulations that all concern pair plasmas: Zenitani and Hoshino (2001) (2D): $p = 1$ for particles around the X-point and for the total spectra; Zenitani and Hoshino (2007) (2D): $p = 3.2$ and 2.4 at late times; Jaroschek et al. (2004) (2D): $p = 1$ for particles around the X-point, modified to $p = 3$ by island acceleration in the whole domain; Jaroschek et al. (2008) (2D, two colliding current sheets): power law; Sironi and Spitkovsky (2011a) (2D, stripped pulsar wind): $p = 1.4$ after the shock; Cerutti et al. (2013) (2D): $p = 3.8$; Sironi and Spitkovsky (2014) (2D without guide field): $p = 4$, 3, 2, 1.5 for inflow magnetizations $\sigma = 1$, 3, 10, 30, 50 and a saturation above 50, and $p = 2.3$ in 3D with $\sigma = 10$. On the other hand, Kagan et al. (2013) (3D) find a high-energy tail but interpret it as not having a power law shape. On the analytical side, Zenitani and Hoshino (2001) present a toy model predicting power laws, and Bessho and Bhattacharjee (2012) derive the spectrum of particles escaping from an antiparallel X-point (see Sect. 7.5.4). Also, it is noticeable that the ultrarelativistic test particle simulations of Cerutti et al.

(2012b) produce very hard power laws ($p \sim -0.5$), with electrons accelerated along Speiser orbits without any stochasticity. This diversity of results calls for a unified analysis of simulations with various initial configurations, which we aim to provide here.

Other acceleration mechanisms exist, especially far from the diffusion region. A first example is stochastic acceleration in the turbulence associated with reconnection (Kowal et al. 2011; Hoshino 2012). A second, important example, is at the magnetic separatrices that separate the non-reconnected/reconnected regions (Sect. 2.12.4), where plasma flows through a non-linear wave structure (see also Sect. 7.5.4). Particle acceleration should also occur at the dipolarization front (Sect. 2.12.5). Our simulation setup, with no localized initial perturbation, precludes the existence of these other mechanisms, and instead we focus on acceleration close to the diffusion region and inside islands, which is likely to be important in relativistic setups.

This chapter is dedicated to relativistic ion-electron plasmas, for which no such study exists yet. These plasmas are likely present in AGN and microquasar coronae, in microquasar jets (Kotani et al. 1994; Díaz et al. 2013), or possibly in GRB and AGN jets. Physical parameters and applications are discussed in Sect. 7.5.3.

7.3 Simulation setups

7.3.1 The simulations

We perform 2D PIC simulations of magnetic reconnection, mainly in an ion-electron plasma of mass ratio $m_\mathrm{i}/m_\mathrm{e} = 25$. We also present one simulation for each value $m_\mathrm{i}/m_\mathrm{e} = 1$, 12, and 50. The simulations are the same as those of Chapter 6, with some new runs. We refer to Sect. 6.3 for the description of the initial state. We briefly recall that it consists in a Harris equilibrium with no localized perturbation, so that islands and X-points form everywhere. The asymptotic field along x is denoted by B_0, the guide field along y by B_G, the particle number density at the center of the current sheet by $n_\mathrm{cs}(0)$, that in the background plasma by n_bg, and the background plasma temperatures by $T_\mathrm{bg,i}$ and $T_\mathrm{bg,e}$.

The free parameters are the characteristics of the background plasma ($n_\mathrm{bg}/n_\mathrm{cs}(0)$, $T_\mathrm{bg,i}$ and $T_\mathrm{bg,e}$); the strength of the guide field B_G/B_0; the width of the magnetic field reversal in electron inertial lengths L/d_e; and the magnetization of the current sheet plasma with respect to the asymptotic magnetic field, here expressed via $\omega_\mathrm{ce}/\omega_\mathrm{pe}$ (ω_ce is the electron cyclotron pulsation in the asymptotic magnetic field B_0, ω_pe is the electron plasma pulsation at the current sheet center at $t = 0$). The background plasma magnetization results from the above variables. The simulations, and the background plasma parameters and magnetizations, are listed in Table 7.1. The parameters of the current sheet are given in Table 7.2.

We recall that the magnetizations and the Alfvén speeds are defined in Sects. 6.3.2 and 6.3.3.

7.3.2 Resolution and domain size

The numerical resolution is set by the number of cells n_x per electron inertial length d_e, by the number of timesteps n_t per electron plasma period

$\frac{\omega_{ce}}{\omega_{pe}}$	$\frac{n_{bg}}{n_{cs}(0)}$	$\frac{B_G}{B_0}$	σ_{i+e}	$\frac{V_{A,in}^R}{c}$		$T_{bg,s}$ (K)	β_s	$\sigma_s^{hot}(B_{rec})$	$p = -\frac{d\log n(\gamma)}{d\log\gamma}$
1	0.1	0	0.38	0.53	ion	1.5×10^7	5×10^{-4}	0.4	no power law
($m_i = 25m_e$)					elec.	″	″	9.9	4-5
3	0.31	0	1.11	0.73	ion	2×10^8	2.5×10^{-3}	1.2	8
($m_i = 25m_e$)					elec.	″	″	27	2.2-2.6
3	0.1	0	3.26	0.88	ion	2×10^8	7.5×10^{-4}	3.6	6.5
($m_i = 25m_e$)					elec.	3×10^9	1.1×10^{-2}	35	2.8
3	0.1	0	3.46	0.88	ion	1.5×10^7	5.6×10^{-5}	3.6	not investigated
($m_i = 25m_e$)					elec.	″	″	89	″
3	0.1	0	3.45	0.88	ion	2×10^8	7.5×10^{-4}	3.6	5.8
($m_i = 25m_e$)					elec.	″	″	83	1.5-2
	Identical as above, but larger box ($888\times1138\,d_e$ instead of $455\times683\,d_e$)								4.8
	and longer duration								1.8
3	0.1	0.5	3.46	0.81	ion	1.5×10^7	4.5×10^{-5}	3.6	8
($m_i = 25m_e$)					elec.	″	″	89	no power law
3	0.1	1	3.46	0.66	ion	1.5×10^7	2.8×10^{-5}	3.6	8
($m_i = 25m_e$)					elec.	″	″	89	1.5
6	0.1	0	13.5	0.97	ion	8×10^8	7.5×10^{-4}	14	3.6
($m_i = 25m_e$)					elec.	″	″	260	1.2
3	0.1	0	41.4	0.988	ion	2×10^8	7.5×10^{-4}	83	1.5
(pairs)					elec.	″	″	″	″
3	0.1	0	6.9	0.93	ion	2×10^8	7.5×10^{-4}	7.5	3.6
($m_i = 12m_e$)					elec.	″	″	83	1.5
6	0.1	0	6.9	0.93	ion	8×10^8	7.5×10^{-4}	7.1	5
($m_i = 50m_e$)					elec.	″	″	260	1.5

Table 7.1: Parameters of the inflow (or background) plasma, and resulting power law index p, sorted in order of increasing magnetization (except for the last line). The parameters of the current sheet, for each value (ω_{ce}/ω_{pe}, m_i/m_e), are listed in Table 7.2. The background plasma $\beta_s = n_s T_s/(B^2/2\mu_0) = 2\Theta_s/\sigma_s^{cold}(B)$ includes the guide field. The magnetization σ_s^{hot} is defined by Eq. 6.4, and σ_{i+e} is the total magnetization (Eq. 6.7b). The Alfvén speed $V_{A,in}^R$ is defined by Eq. 6.6. When there is a guide field, the value displayed is $V_{A,in}^R\cos\theta$ (Sect. 7.3.1). The index of the power law component of the background population (when there is one) is p.

m_i/m_e	ω_{ce}/ω_{pe}	L/d_i	$\Gamma_e\beta_e$	Θ_e	Θ_i	L/r_{ce}
1	3	2.5	0.53	2.40	2.40	1.6
12	3	0.5	0.53	2.40	0.2	1.1
25	1	0.5	0.20	0.25	1.0×10^{-2}	3.8
25	3	0.5	0.53	2.40	9.6×10^{-2}	1.6
25	6	1	0.70	10	0.4	1.5
50	6	0.7	0.60	10	0.2	1.5

Table 7.2: Parameters of the current sheet. To each row in the table can correspond different background plasma parameters, and hence different simulations. The full simulation list is presented in Table 7.1. Here, the electron and ion temperatures are the same, denoted by $\Theta_e = T_e/(m_e c^2)$ and $\Theta_i = T_i/(m_i c^2)$. The electrons and ions counterstream with opposite velocities $\pm\beta_e c$ and associated Lorentz factors Γ_e. The sheet halfwidth in units of ion inertial lengths is L/d_i, while in units of electron thermal Larmor radii it is L/r_{ce}.

$2\pi/\omega_{\rm pe}$, and by the number of computer particles (the so-called superparticles) per cell $\rho_{\rm sp}$. The quantities $d_{\rm e}$, $\omega_{\rm pe}$, and $\rho_{\rm sp}$ are defined at $t = 0$ at the center of the current sheet. Here we take $n_x = 9$ and $n_t = 150$ (except for $\omega_{\rm pe}/\omega_{\rm ce} = 6$ where $n_t = 250$). We checked by doubling n_x and n_t that the particle distributions, the energy repartition, particle mixing, or the maximal Lorentz factors, are not affected by the resolution.

Concerning the number of superparticles per cell at the center of the current sheet, we use $\rho_{\rm sp} = 1090$ for $n_{\rm bg}/n_{\rm cs}(0) = 0.3$, and $\rho_{\rm sp} = 1820$ for $n_{\rm bg}/n_{\rm cs}(0) = 0.1$, except for $m_{\rm i}/m_{\rm e} = 50$ where $\rho_{\rm sp} = 910$. This corresponds, for the case $n_{\rm bg}/n_{\rm cs}(0) = 0.1$, to 1650 electron and ion superparticles per cell for the plasma of the current sheet, and to 170 for the background plasma. We stress in Chapter 5 that because of their low numbers of superparticles per cell when compared to real plasmas, PIC simulations present high levels of correlations and collisionality, and thus thermalize faster. In the same line of thought, Kato (2013) and May et al. (2014) show that because of these enhanced correlations, high-energy particles are slowed down quickly in PIC plasmas. One should thus ensure that collisionless kinetic processes remain faster than collisional effects, essentially by taking a large enough number $\Lambda^{\rm PIC}$ of superparticles per Debye sphere and per inertial length sphere, the former constraint being more restrictive. For example, with $\Theta_{\rm e} = 2.4 = 1.4 \times 10^{10}\,{\rm K}/(m_{\rm e}c^2)$ the electron Debye length is 20 cells large, and initially at the center of the current sheet we have $\Lambda^{\rm PIC} \sim 1820 \times 20 \times 20 = 7.3 \times 10^5$ superparticles. For a background plasma with $T_{\rm bg} = 2 \times 10^8\,{\rm K}$, we have $\Lambda^{\rm PIC} = 133$. We performed a simulation with half as many superparticles per cell, and saw no difference, especially concerning particle distributions, energy repartition, particle mixing, or maximal Lorentz factor. It indicates that we are not affected by $\rho_{\rm sp}$.

Boundaries are periodic along z and y, reflective along x. The simulation with $m_{\rm i}/m_{\rm e} = 50$ uses a domain size of 8000×10240 cells. The number of cells of the simulations with other mass ratios is 4100×6144, corresponding to 455×683 initial electron inertial lengths $d_{\rm e}$, typically with 4×10^9 superparticles. We performed a simulation with twice as small a domain along z: particle distributions are identical as long as there is a significant number of islands and X-points in the domain (≥ 4), but differ afterward: in the smaller simulation, the distribution cutoff is at lower energies, and the power laws are steeper (softer). Consequently, we do not consider the data when the island number shrinks below 4. We also performed a simulation with a larger domain (8000×10240 cells, i.e., 888×1138 inertial lengths $d_{\rm e}$, this is the main simulation of Sect. 7.4.1) and otherwise identical parameters: the electron distribution saturates identically to the 4100×6144 case, but the ion distribution reaches a harder final state. It indicates that our domain size and simulation duration are large enough for electrons, but possibly not for ions. The latter may build harder spectra and reach higher energies in real systems.

7.3.3 Diagnostics

We initially select roughly 200 000 particles (out of the 4 to 14 billions in total) uniformly in space and write their positions, velocities, as well as the magnetic and electric fields they undergo, once every few timesteps. The visualization of these data is performed with the visualization software

`VisIt` (Childs et al. 2012). We divide the followed particles into two populations: those that are initially located inside the current sheet (colored in red and denoted by "current sheet" or by a subscript cs), and those initially outside (marked in green and denoted by "background particles" or by a subscript bg). In other words, red particles are those[a] satisfying

$$\text{distance from middle plane at } t = 0 < 2L, \tag{7.1}$$

while green particles satisfy

$$\text{distance from middle plane at } t = 0 > 2L. \tag{7.2}$$

Changing the limiting length from $2L$ to between $1.5L$ and $3L$ has been confirmed has not influencing the presented results. An example is shown in Fig. 7.1. As we will show, these two populations almost do not mix spatially, and undergo very different acceleration mechanisms, resulting in completely different particle energy distributions. Particles from the background plasma, accelerated by the reconnection, are expected to dominate in number and energy for very large systems. This is why we focus more on the green population.

7.4 Results

We first present results from a reference simulation in Sect. 7.4.1, and then study modifications due to varying the background particle number density, magnetic field, or temperature without considering a guide field in Sect. 7.4.2. The consequences of a guide field are explored in Sect. 7.4.3.

7.4.1 Main case

We start by presenting the results of the simulation with $\omega_{ce}/\omega_{pe} = 3$, $n_{bg} = 0.1n_{cs}(0)$, $T_{bg,i} = T_{bg,e} = 2 \times 10^8\,\mathrm{K}$, resulting in a magnetization in the background plasma $\sigma_{i,e}^{hot} = 3.6, 83$ for ions and electrons, respectively (defined by Eq. 6.4, see also Tables 7.1 and 7.2), and in an inflow Alfvén speed $V_{A,in}^{R} = 0.88c$.

The background electron distribution (the green curves in Fig. 7.1) starts rising and taking a power law shape around $t = 500\omega_{ce}^{-1}$, which corresponds to the starting of the reconnection instability. What happens is that the reconnection electric field E_{rec} spreads in the background plasma and sets the particles into motion in an $E \times B$ drift directed toward the current sheet. More and more background particles thus pass in the current sheet, where they are demagnetized and able to gain energy via E_{rec}. The power law component thus comprises more and more particles. After gaining energy in the acceleration zone, particles accumulate around the magnetic islands and swirl around them. They are subsequently accelerated when islands merge and contract. The power law index passes from a soft initial value of $p = -\mathrm{d}\log n(\gamma)/\mathrm{d}\log\gamma = 3$ to a harder final value that converges to $p \sim 1.8$. We stopped the simulation at $t = 3750\omega_{ce}^{-1}$, when there were still enough islands and X-points so that we are not affected by boundaries (Sect. 7.3.2).

[a] Note that the current sheet population defined here comprises most of the particles that initially carry the current, plus the particles from the plasma at rest that are initially satisfying Eq. 7.1.

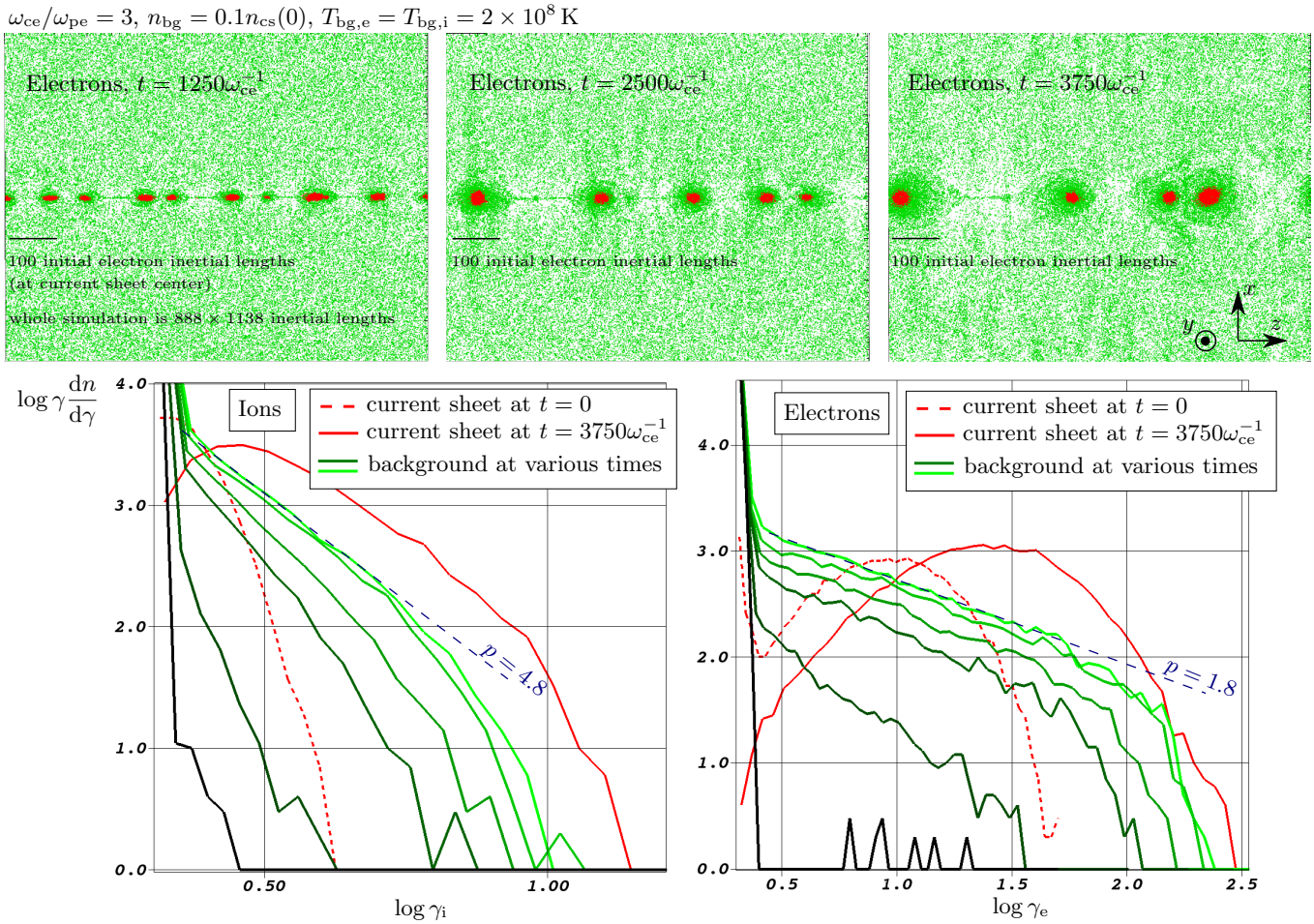

Figure 7.1: Data from the main simulation (Sect. 7.4.1), with a background magnetization respectively for ions and electrons $\sigma_{i,e}^{hot} = 3.6, 83$.
Top: snapshots of a random selection of electrons in the whole simulation domain. Red particles are inside the current sheet at $t = 0$, green ones are outside.
Bottom: Lorentz factor distributions. Red (green) curves concern the red (green) population. For the green curves, times are ordered as dark to light green, with values 0, 750, 1500, 2250, 3000, $3750\omega_{ce}^{-1}$, i.e., one curve every $750\omega_{ce}^{-1} = 250\omega_{pe}^{-1} = 50\omega_{pi}^{-1} = 30\omega_{ci}^{-1}$. The blue dashed line indicates the final power law slope of the background-accelerated particles.

Concerning the current sheet electrons, their distribution is shown at $t = 0$ by a red dashed line in Fig. 7.1, and consists then in a thermal hot plasma. When the reconnection instability starts, this population is heated by the formation and contraction of islands. This heating slowly progresses at later times as islands merge, to result in the solid red curve of Fig. 7.1.

Concerning ions, their background magnetization is only slightly relativistic ($\sigma_i^{hot} = 3.6$). The current sheet population is heated, while the background population distribution is power law like, with a final index $p \sim 4.8$. This is similar to non-relativistic simulations where all species form steep spectra.

It is evident from the top panels of Fig. 7.1 that the green electrons from the background plasma do not penetrate deep inside the islands and, on the other hand, that the red electrons initially from the current sheet do not escape from the islands, even when they merge. The two populations thus

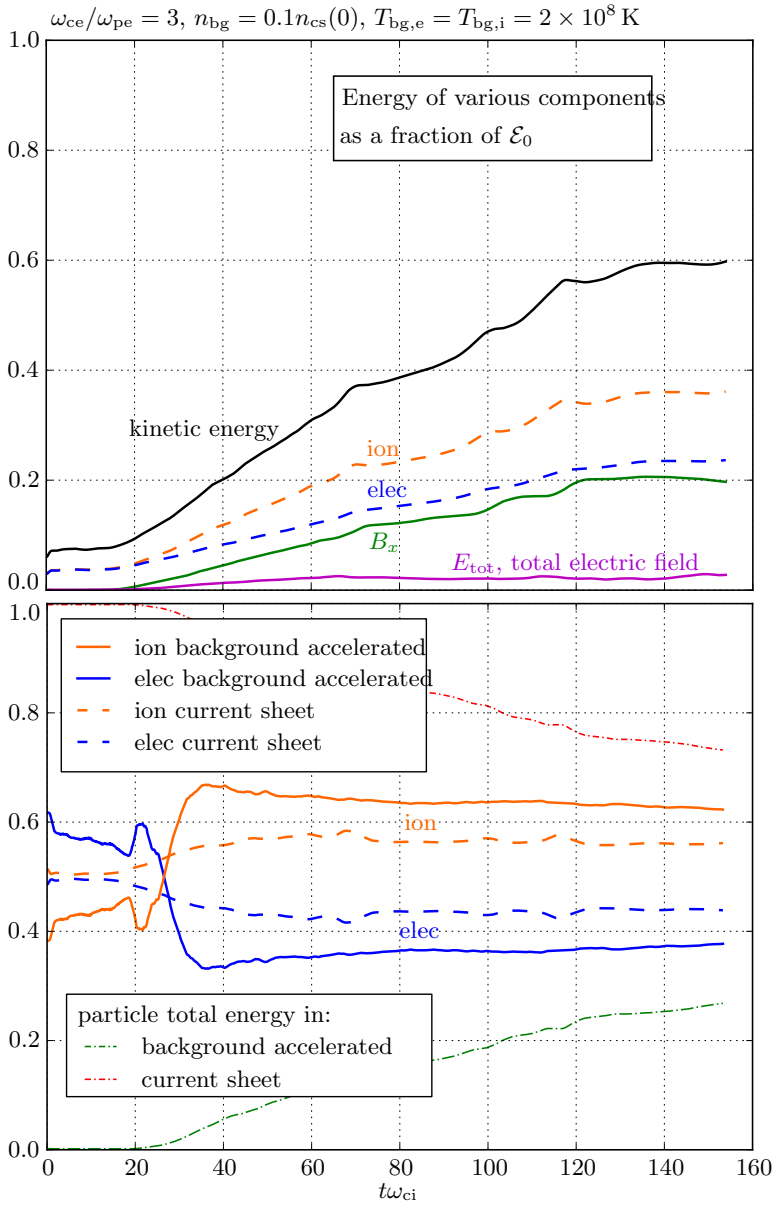

Figure 7.2: Energy distribution for the main simulation (Sect. 7.4.1), with a background magnetization for ions and electrons $\sigma_{i,e}^{hot} = 3.6, 83$, respectively.
Top: Energy in the total electric field E_{tot}, in the x component of the magnetic field, and in the particles (also decomposed into the ion and electron contributions). These energies are computed on a fixed area, that corresponds to the location of the background particles, or field lines, that reach the current sheet before the end of the simulation. The total initial energy in this area is $\mathcal{E}_0$. We note that the energy in E_{tot} is mostly the energy in the y component E_y. Also, the energy of B_y is 0.5% of that of B_x.
Bottom: Orange and blue curves are the energy repartition between ions and electrons for the current sheet particles (dashed), and for the background particles that have been accelerated (solid). They are normalized so that their sum is 1. The red and green curve show the energy repartition between current sheet particles and background-accelerated particles.

remain almost separated. This is because particles from the background plasma are scattered by the strong magnetic field structure surrounding the islands, and thus swirl around these field lines, performing circles around the islands but not reaching the inside. On their side, red particles from the islands cannot escape because of the very same magnetic field structure. This remains true for ions, but less so because of their larger Larmor radius. Figure 7.6 illustrates this population separation for several simulations.

The energy repartition between fields and particles is shown in Fig. 7.2 (top). This energy is computed over a fixed rectangle in space, defined to include all particles that will reach the center of the current sheet before the end of the simulation. It thus excludes regions that, because of the finite simulation length, are never in contact with the current sheet. Energies are normalized by $\mathcal{E}_0$, the total initial energy in this area, which is to $\sim 90\%$ the energy in the magnetic field. The energy in the magnetic field is transferred to the kinetic energy of the particles ($0.6\mathcal{E}_0$ in the final state), to the reconnected magnetic field B_x ($0.2\mathcal{E}_0$), and to the reconnection electric field E_y ($0.03\mathcal{E}_0$). The components B_y, E_x, and E_z get a far smaller amount of energy ($\sim 0.005\mathcal{E}_0$). A first conclusion is that the portion of dissipated magnetic energy is large. Table 7.3 presents this analysis for several simulations. It shows that the amount of dissipated magnetic energy is even larger at larger inflow magnetization. A second important aspect is the energy repartition between ions and electrons. In Fig. 7.2 (bottom), we show this repartition for the background particles that have been accelerated, i.e., for the particles of the tails in Fig. 7.1 (green curves). The ions weight as 60% of this kinetic energy, the electrons 40%, and this ratio remains constant with time. The same repartition roughly holds for particles in the current sheet (red population). Table 7.3 shows that this repartition holds for various simulations with different magnetizations and mass ratios, provided that there is no guide magnetic field. We note that the percentages given in Table 7.3 are not sensitive to the specific time when they are determined. We obtain essentially the same percentages if we repeat the analysis but consider only those particles (and their associated rectangular region and energy $\mathcal{E}_0$) that reach the current sheet before half of the total simulation time.

7.4.2 Case studies, no guide field

Influence of the background plasma density

We now compare the main case with a simulation with identical parameters except for the background plasma number density: $n_{\rm bg} = 0.3n_{\rm cs}(0)$ instead of 0.1, resulting in a smaller magnetization $\sigma_{\rm i,e}^{\rm hot} = 1.2$, 27 in the background. The corresponding inflow Alfvén speed is $V_{\rm A,in}^{\rm R} = 0.73c$. The evolution is similar: weak mixing of the two populations, heating of the particles from the current sheet, and acceleration of the particles from the background to form a power law. The power law for electrons has a final index p between 2.2 and 2.6 (Fig. 7.3), and for ions around $p \sim 8$. This is softer than in the $n_{\rm bg} = 0.1n_{\rm cs}(0)$ case, which is expected because a higher background plasma density implies a lower background plasma magnetization, and as we show here (see also Sironi and Spitkovsky 2014), softer power laws. It is, however, noticeable that more magnetic energy is transferred to the particles: the kinetic energy is 74% of the total energy, while it is only 62% for the case

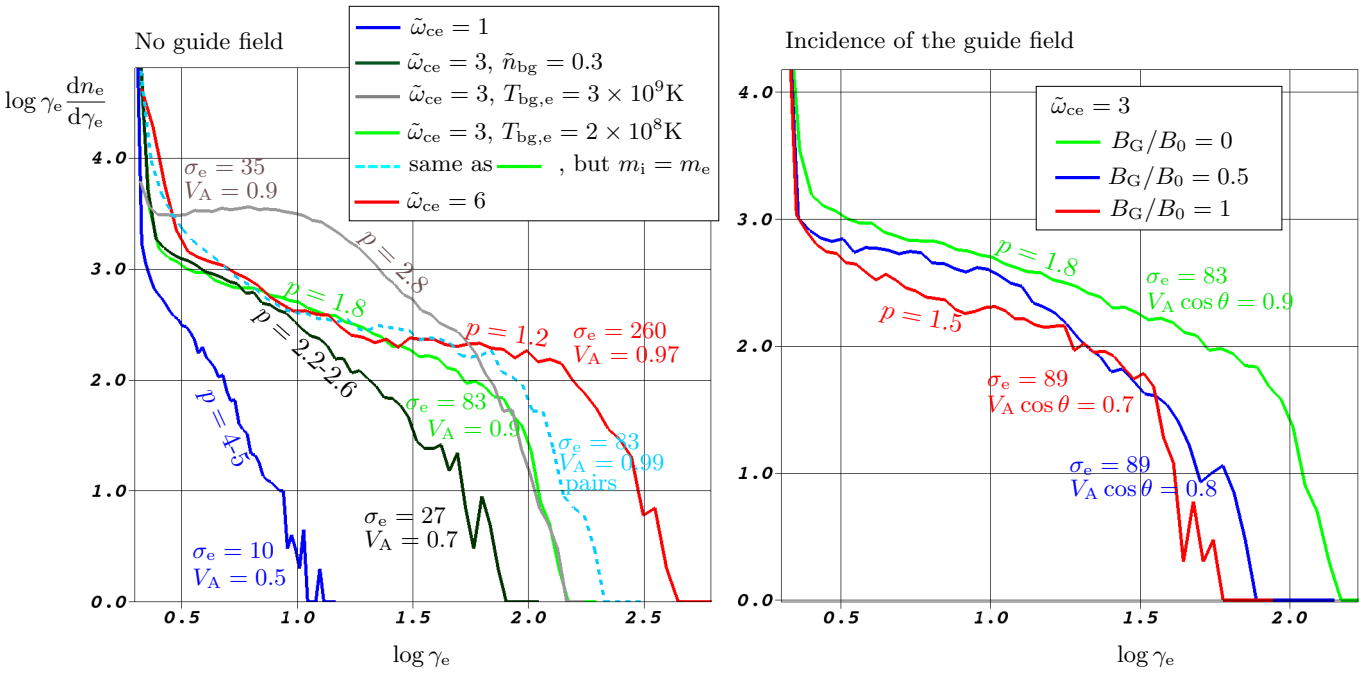

Figure 7.3: Lorentz factor distributions for background electrons (green population), for various simulations with $m_i/m_e = 25$ or 1, in the final state. Times are $t = 600\omega_{pe}^{-1} = 1800\omega_{ce}^{-1}$ for all simulations, except for $\omega_{ce}/\omega_{pe} = 1$ ($t = 1350\omega_{pe}^{-1} = 1350\omega_{ce}^{-1}$), and for $\omega_{ce}/\omega_{pe} = 6$ ($t = 600\omega_{pe}^{-1} = 3600\omega_{ce}^{-1}$). Notations are abbreviated: $\tilde{\omega}_{ce} = \omega_{ce}/\omega_{pe}$, $\tilde{n}_{bg} = n_{bg}/n_{cs}(0)$, σ_e stands for $\sigma_e^{hot}(B_{rec})$, and V_A for $V_{A,in}^R \cos\theta/c$ (with $\theta = \arctan B_G/B_0$). Unless specified, $\tilde{n}_{bg} = 0.1$. The power law indexes are p. The precise setups are reported in Table 7.1 for each σ_e. The light-green curve ($\sigma_e = 83$, $V_A = 0.9$) is the same on the left and right panel, and is the final state of the simulation of Fig. 7.1.

with $n_{bg} = 0.1 n_{cs}(0)$.

Influence of the inflow magnetization

We vary the asymptotic magnetic field strength by varying the parameter ω_{ce}/ω_{pe} of the Harris equilibrium. Increasing this parameter results in a higher magnetic field, and in a hotter current sheet plasma in order to maintain the pressure balance. It allows probing different background plasma magnetizations. Our results indicate harder power laws at higher magnetizations (Fig. 7.3 for the simulations with $\omega_{ce}/\omega_{pe} = 1$, 6, to also be compared with the simulation $\omega_{ce}/\omega_{pe} = 3$, $T_{bg,e} = 2 \times 10^8$ K). The comparison is as follows:

- The case at low inflow magnetization ($\omega_{ce}/\omega_{pe} = 1$, $\sigma_{i,e}^{hot} = 0.4$, 9.9, $V_{A,in}^R = 0.53c$) presents a power law-like spectrum for background-accelerated electrons (green population) with a large index, between 3 and 4, thus decreasing fast and reaching $\gamma_{max} \sim 10$. The ion distribution is not power law like and is very steep. The final kinetic energy is 48% of the total initial energy.
- The intermediate case ($\omega_{ce}/\omega_{pe} = 3$, $\sigma_{i,e}^{hot} = 3.6$, 90, $V_{A,in}^R = 0.88c$) presents a power law-like spectrum for the background particles with, for electrons $p \sim 1.5$-2 and $\gamma_{max} \sim 100$, for ions $p \sim 5.8$. The final kinetic energy is 62% of the total initial energy.

- The most magnetized and relativistic case ($\omega_{ce}/\omega_{pe} = 6$, $\sigma_{i,e}^{hot} = 14, 260$, $V_{A,in}^{R} = 0.97c$) exhibits a very flat spectrum for background-accelerated electrons, with an index around 1.2, and reaches $\gamma_{max} \sim 300$. Background accelerated ions have a power law distribution with index $p \sim 3.6$, which is interestingly close to the index for electrons at the same magnetization (the simulation with $\omega_{ce}/\omega_{pe} = 1$, where $\sigma_{e}^{hot} = 9.9$ and $p \sim 4.5$), and highlights the relevance of σ_s of each species to characterize the power law. The final kinetic energy is 73% of the total initial energy.

For both electrons and ions, this emphasizes that only relativistic reconnection setups (i.e., $\sigma_s^{hot} > 1$ for each species s) can produce power laws, with harder indexes for higher magnetizations.

Influence of the inflow temperature

Coming back to the main simulation with $\omega_{ce}/\omega_{pe} = 3$, $n_{bg} = 0.1n_{cs}(0)$, $T_{bg,e} = T_{bg,i} = 2 \times 10^8$ K, we now increase the background temperature of the electrons to reach $T_{bg,e} = 3\times10^9$ K (giving $\sigma_{i,e}^{hot} = 3.6, 35$, $V_{A,in}^{R} = 0.88c$), which is almost the temperature of the current sheet electrons ($\Theta_e = 2.4 = 1.4\times10^{10}\,\mathrm{K}/(m_e c^2)$). Electrons from the background plasma already have a high energy when reaching the acceleration region, and their initial energy is then a significant fraction of the energy gain furnished by E_{rec}. As a consequence, the power law is less visible (Fig 7.3, gray curve). However, as time goes by and as more and more particles from the hot background are accelerated, we expect it to dominate the particle distribution more and more. Its index is $p = 2.8$, softer than the colder case. This is expected because a relativistic temperature decreases the plasma magnetization from 89 to 35 here, and we do have an index close to the one for $n_{bg} = 0.3n_{cs}(0)$, which had a similar magnetization ($\sigma_e^{hot} = 27$, $p \sim 2.5$).

Background accelerated ions have a power law distribution with index $p \sim 6.5$. This is close to their index in the simulation with $\omega_{ce}/\omega_{pe} = 3$, $T_{bg,e} = T_{bg,i} = 2 \times 10^8$ K, which is identical except for the initial electron temperature ($p \sim 5.8$). It shows that electrons have a weak influence on ions.

7.4.3 Case study, guide field

We now analyze simulations with a guide magnetic field $\boldsymbol{B}_G = B_G\hat{\boldsymbol{y}}$.

Figure 7.3 (right) presents the final electron distributions from simulations with $B_G = 0$, $0.5B_0$, and B_0. In the intermediate case ($B_G = 0.5B_0$), the spectrum of the background-accelerated electrons shows no clear power law, but extends over a range similar to the no-guide field case. In the strong guide field case ($B_G = B_0$), the spectrum of the same electron population seems flatter, with a power law index of ~ 1.5 (over a narrow range). The background plasma magnetization in the three simulations is similar (the guide field is not included in this magnetization parameter, and should not be, because it is not converted into particle energy). The harder particle distribution should thus be explained by other means. We recall that quite generally, the particles accelerated at the X-point are slowly deflected toward the reconnection exhausts by the x component of B. But B_x vanishes at the X-point and increases when going away from it, so that the farther from the X-point a particle enters the diffusion region, the faster it will be

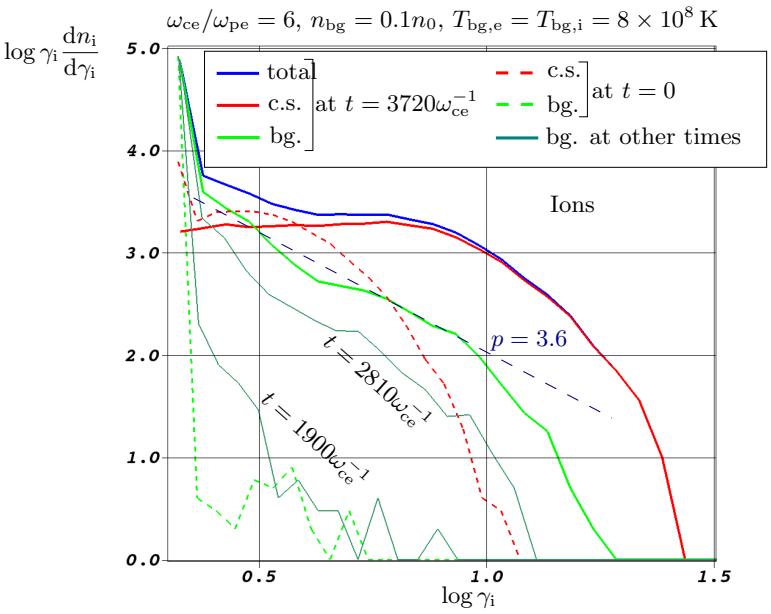

Figure 7.4: Lorentz factor distributions for ions. Simulation with $\omega_{ce}/\omega_{pe} = 6$, $\sigma_{i,e}^{hot} = 14,260$ in the background.

deflected and the less it will be accelerated. The area where an efficient acceleration occurs is thus limited along z by the increase in B_x. But with a guide field, this efficient acceleration region is extended along z (as shown in Sect. 6.5), because accelerated particles are guided by the guide field and prevented from being deviated by B_x. Background particles are more accelerated, and a flatter spectrum is indeed expected.

Because of their larger Larmor radii, background-accelerated ions are less affected by the guide field. They present a power law distribution with index $p = 8$ for both guide field strengths.

Table 7.4 shows the energy repartition for the guide field simulations. In both cases, the final kinetic energy is $\sim 44\%$ of the total initial energy (we do not include the guide field B_y in this initial energy because it cannot be transferred to the particles, and indeed varies by less than a few percent during the simulation). This is less than in the $B_G = 0$ case, where this percentage is 62%. The kinetic energy repartition between accelerated ions and electrons is 46%/54% (ions/electrons) for $B_G = 0.5B_0$, and 33%/67% for $B_G = B_0$. This contrasts with the 60%/40% ratio at $B_G = 0$, since here electrons get more energy than do ions.

7.5 Summary and discussion

7.5.1 Summary

We study the production of high-energy particles by magnetic reconnection in relativistic ion-electron plasmas based on the same 2D PIC simulation data presented in Chapter 6. The variety of parameters employed (particle density, temperature, or magnetic field in the background plasma, guide field, mass ratio) allows important aspects of this problem to be grasped. In all cases particles can be divided into two populations that only weakly mix: (i) Particles initially inside the current sheet are trapped inside the magnetic islands as soon as they form during the tearing instability, and

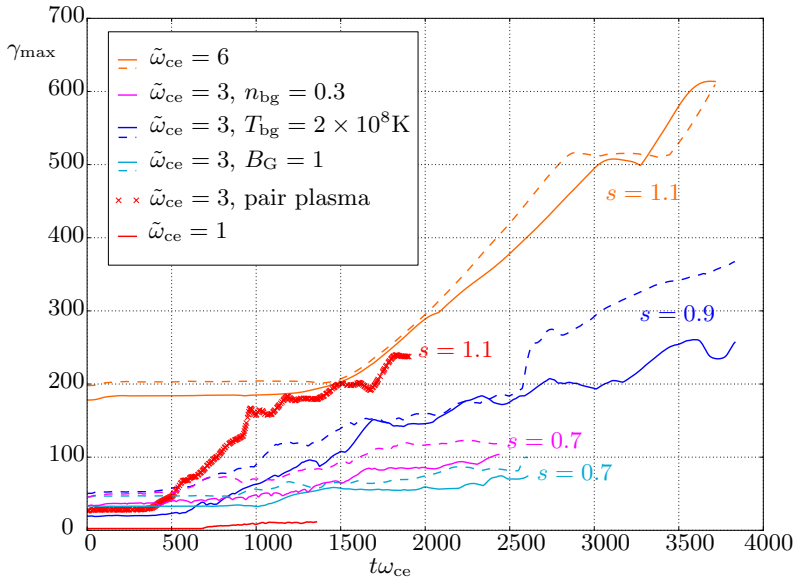

Figure 7.5: Maximum Lorentz factor of the background particles for various simulations with $m_{\rm i}/m_{\rm e} = 25$ or 1. Solid lines are for electrons, dashed lines for ions and represent $m_{\rm i}/m_{\rm e} \times \gamma_{\rm i,max}$. Also, $\tilde{\omega}_{\rm ce} = \omega_{\rm ce}/\omega_{\rm pe}$. A log-log plot shows that the Lorentz factors grow as t^s, with the index s shown in the figure.

remain trapped by the strong circling magnetic structure, even after many island merging events. They are heated by the contraction of the islands. (ii) Particles from the background plasma $E \times B$ drift toward the diffusion region, where either $E < cB$ in the no-guide field case, or $\boldsymbol{E} \cdot \boldsymbol{B} \neq 0$ in the guide field case, allows them to be accelerated directly. As they escape along the reconnection exhaust, they cannot penetrate inside the island because of the strong magnetic structure surrounding them, so they circle at the periphery, where they can gain more energy.

Particles of population (ii) tend to form a power law whenever their magnetization is greater than unity and the inflow Alfvén speed is not too small (Figs. 7.1 and 7.3), though sometimes not with a clear and unique slope. The indexes depend on the temperature, particle density, and magnetic field in the background plasma, as well as on the guide field strength. With no guide field, results suggest that the power law index for species s depends mainly on the background plasma Alfvén speed $V_{\rm A,in}^{\rm R}$, and on the background plasma magnetization for species s, independent of whether it is due to the magnetic field strength, a lower particle density, or a relativistic temperature. A higher magnetization leads to a harder power law: for the electrons, $p = -{\rm d}\log n(\gamma)/{\rm d}\log\gamma = 4.5$, 2.4, 2.8, 1.7, 1.2 respectively for magnetizations $\sigma_{\rm e}^{\rm hot} = 10$, 27, 35, 89, 260 (see Table 7.1). This is expected for reasons exposed in Sect. 7.5.2. These indexes are harder than for collisionless shock acceleration, where $p > 2$ (Bell 1978; Sironi and Spitkovsky 2011b). Ions have a magnetization that is $m_{\rm i}/m_{\rm e}$ times less than electrons (for identical or non-relativistic temperatures). As expected, they behave non-relativistically for low magnetizations $\sigma_{\rm i}^{\rm hot}$: no power law at $\sigma_{\rm i}^{\rm hot} = 0.4$; steep ones for $\sigma_{\rm i}^{\rm hot} = 1.2$, 3.6 ($p = 8$, 5.5); and beginning of formation of significant power laws at higher magnetization: $p = 3.6$ for $\sigma_{\rm i}^{\rm hot} = 14$, mimicking the values reached for electrons at the same $\sigma_{\rm e}$.

The presence of a weak guide field deforms the power law, and the presence of a strong guide field allows for a slightly harder spectrum (Fig. 7.3,

right) because it allows particles to stay longer in the acceleration region by guiding them in the direction of the reconnection electric field.

The degree of mixing between the two populations (i) and (ii) essentially depends on the ratio of the Larmor radii of the particles in the magnetic field surrounding the islands, to the island radius. A hotter background temperature implies more mixing, and so does a weaker guide field. Also, ions have larger Larmor radii and penetrate the islands more easily. This is illustrated in Fig. 7.6. We stress that even for high background electron temperatures (bottom right panel), the two electron populations remain clearly separated.

The total particle distribution is the sum of populations (i) and (ii), and it depends on their relative importance. We underline that our simulations are limited in time by the box size. In reality, longer times can be reached and more background particles can be accelerated, so that the background-accelerated population, and its power law nature, will dominate in the end. It calls for care when interpreting PIC particle distributions: either very long simulations (also demanding large domains) or the proposed decomposition should be used.

The percentage of magnetic energy converted into kinetic energy is larger at larger inflow magnetization: the final kinetic energy rises to 48%, 62%, 73% of the total initial energy, for respective inflow magnetizations $\sigma_{\rm e}^{\rm hot} = 9.9$, 83, 260 (see Table 7.3) at $m_{\rm i}/m_{\rm e} = 25$. This fraction is lower with a guide magnetic field ($\sim 44\%$, Table 7.4).

The energy repartition between accelerated ions and electrons from the background plasma depends mainly on the strength of the guide magnetic field. With no guide field, it is roughly 60% for ions and 40% for electrons, with variations within 3% when varying the background temperature, magnetization and Alfvén speed. With a guide field of $0.5B_0$ and B_0, the ion/electron repartition becomes 46%/54% and 33%/67%, respectively, with electrons getting more energy than ions. Our conclusion is thus that overall, ions and electrons are almost equally energized. It is, however, essential to know whether this remains true at realistic mass ratios. With no guide field, our simulations with $m_{\rm i}/m_{\rm e} = 12$ and $m_{\rm i}/m_{\rm e} = 50$ show a variation of $\sim 3\%$, which cannot be distinguished from the variation due to the different background magnetizations of these simulations. Consequently, and even if higher mass ratios should be tested, it seems that the $\sim 60\%/40\%$ repartition will hold at higher $m_{\rm i}/m_{\rm e}$. The case with a guide magnetic field will be explored in more depth in a future work.

The maximum Lorentz factor of the background particles (ii) is shown in Fig. 7.5. A larger guide field leads to lower the highest Lorentz factors, and this is expected because the reconnection electric field becomes weaker with increasing guide field (Sect. 6.5.3). A log-log plot shows that the rate of increase is roughly $\gamma_{\rm max} \propto t^s$, with s ranging from 0.7 to 1.1 as the magnetization rises, with identical values for ions and electrons. Particles inside the islands follow the same trend. We stress that this is faster than in collisionless shock acceleration where $\gamma_{\rm max} \propto t^{0.5}$ (Bell 1978). We also note that the maximal Lorentz factor does not saturate. It should saturate in very large systems when the inter-island distance becomes greater than the particle Larmor radii in the reconnected field B_x, and when island merging ceases.

simulation parameters					final energy in % of $\mathcal{E}_0$			ion/electron energy repartition			
$\frac{\omega_{ce}}{\omega_{pe}}$	$\frac{n_{bg}}{n_{cs}(0)}$	σ_i^{hot}	σ_e^{hot}	$\frac{V_{A,in}^R}{c}$	B_x	E_{tot}	kinetic energy	cs ions	cs elec	bg ions	bg elec
$m_i/m_e = 50$											
6	0.1	7.1	260	0.93	21%	5%	74%	54%	46%	63%	37%
$m_i/m_e = 25$											
1	0.1	0.4	9.9	0.53	11%	1%	48%	67%	33%	60%	40%
3	0.1	3.6	83	0.88	20%	3%	62%	56%	44%	63%	37%
3	0.3	1.2	27	0.73	17%	4%	74%	61%	39%	62%	38%
6	0.1	14	260	0.97	18%	4%	73%	53%	47%	60%	40%
$m_i/m_e = 12$											
3	0.1	7.5	83	0.93	21%	2%	72%	55%	45%	60%	40%
$m_i/m_e = 1$											
3	0.1	83	83	0.99	34%	8%	87%	50%	50%	50%	50%

Table 7.3: Energy distribution between fields and particles at the end of different simulations. cs stands for the current sheet population, bg for the background population. The final energy in the electric field is E_{tot}, and is dominated by the energy in E_y. The energy in B_x is denoted by B_x. As explained in Fig. 7.2, $\mathcal{E}_0$ is the total (mostly magnetic) initial energy in the "reconnection area", which is the area from where the particles reach the current sheet before the end of the simulation. Because of the difficulty of precisely measuring this area, the percentage has to be taken with a ±5% relative uncertainty. The energy repartition between ions and electrons is not affected by this.

simulation parameters					final energy in % of $\mathcal{E}_0$			ion/electron energy repartition			
$\frac{\omega_{ce}}{\omega_{pe}}$	$\frac{n_{bg}}{n_{cs}(0)}$	σ_i^{hot}	σ_e^{hot}	$\frac{V_{A,in}^R}{c}$	B_x	E_{tot}	kinetic energy	cs ions	cs elec	bg ions	bg elec
$B_G/B_0 = 0.5$											
3	0.1	3.6	89	0.81	16%	4%	43%	60%	40%	46%	54%
$B_G/B_0 = 1$											
3	0.1	3.6	89	0.66	18%	5%	45%	57%	43%	33%	67%

Table 7.4: Same as Table 7.3, but for cases where there is a guide field. Here $m_i/m_e = 25$. In this case $\mathcal{E}_0$ does not include the guide magnetic field B_y, because this component is not transferred to the particles (the energy in B_y remains constant to within 5% throughout the simulation).

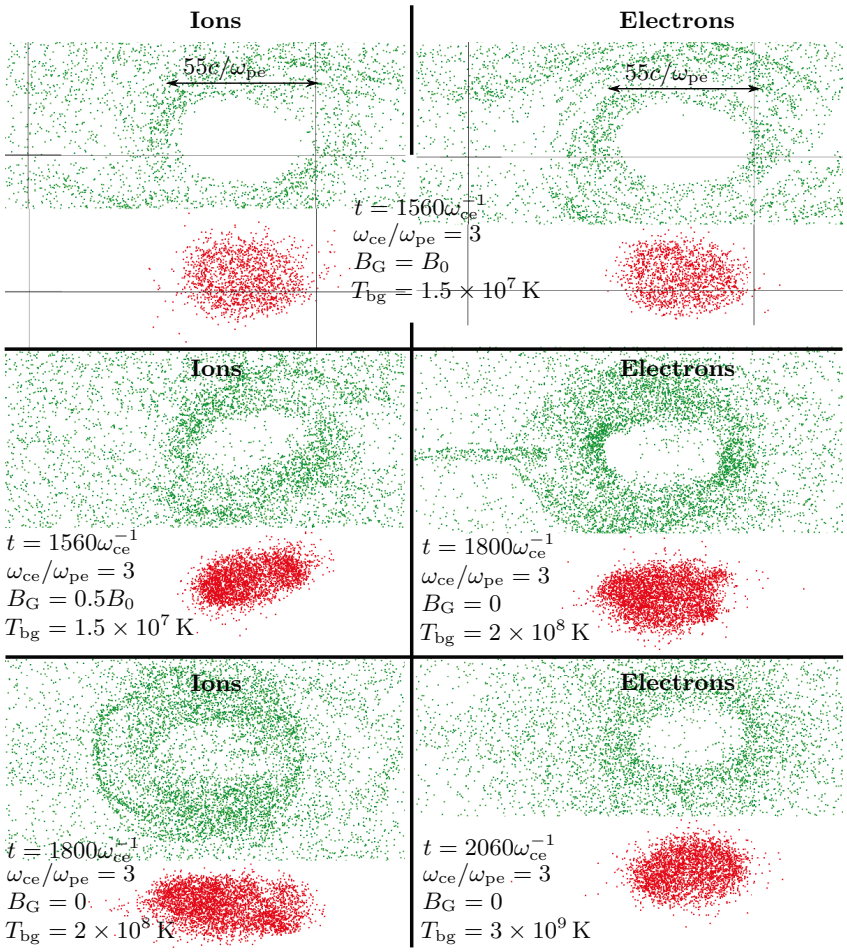

Figure 7.6: Particle mixing in the islands. Each panel is a zoom around a magnetic island and shows particles initially outside of the current sheet in green, and particles initially located inside the current sheet in red and shifted below for clarity. Each snapshot is taken at the end of the simulations, and these islands result from the merging of many small and then larger islands (from around 20 islands at the end of the linear phase of the tearing instability, to 3 big islands at the end), and yet the two particle populations remain separated. The mass ratio is 25 in all cases.

7.5.2 Discussion

Acceleration mechanisms

The main acceleration mechanism for the background population (ii) is direct acceleration by the reconnection electric field. However, other acceleration mechanisms are present. It can be seen by dividing the background population into several subgroups, each comprising particles in a slab $x_{min} < x < x_{max}$ at $t = 0$. We can then follow the spatial evolution of these slabs, along with the evolution of their momentum distribution function. After gaining energy in the acceleration region by E_{rec}, background particles escape along the reconnection exhausts, and circle at the island periphery following the strong magnetic field structure. Contraction of the islands (when they merge) creates strong motional electric fields $\boldsymbol{E} = -\boldsymbol{v} \wedge \boldsymbol{B}$ that accelerate these particles. Also, two merging islands create a reconnection event with a reconnection electric field along $+\hat{\boldsymbol{y}}$, that can transfer energy to particles. The combination of these three mechanisms is

also reported for pairs by Bessho and Bhattacharjee (2012) and Sironi and Spitkovsky (2014).

We find no trace of Fermi acceleration between the converging inflows, as studied analytically or with test particles by Giannios (2010), Kowal et al. (2011), Drury (2012), or Bosch-Ramon (2012), because particles cannot cross the current sheet (see Fig. 6.6), but bounce back and forth only inside the diffusion region where they are constantly accelerated by the reconnection electric field. Fermi acceleration is possible only if inflowing particles of species s are energetic enough to cross the diffusion region, i.e., have a Larmor radius $\gamma m_s v/eB_0$ that is larger than the diffusion zone width δ_s. The latter is roughly one inertial length measured at its center (Sect. 6.4.2), so that the crossing condition can be written $\gamma v/c > (\sigma_s^{\rm cold} n_{\rm bg}/n_{\rm cs})^{1/2}$ (with $\sigma_s^{\rm cold}$ the background magnetization defined by Eq. 6.5, and $n_{\rm bg}$ and $n_{\rm cs}$ the background and current sheet density). The right-hand side is greater than unity for a relativistic inflow magnetization. This mechanism thus requires already accelerated particles in the inflow, which is possible for very high temperatures, or for an out-of-equilibrium component pre-accelerated by other mechanisms outside of the diffusion region such as neighboring reconnection sites, or large scale flow turbulence (see Sect. 7.5.4). We have neither of these in our simulations, and their presence in real situations should be addressed.

We now turn to the building of the power law spectrum in our simulations. The basic idea is that particles enter the acceleration region at all distances from the central X-point, with those entering near the center being deviated toward the exhausts by B_x more slowly than those entering at the edges. They thus gain more energy, and a monoenergetic inflow is transformed into a broader distribution. The ingredient to build a power law, underlined by Zenitani and Hoshino (2001), is that relativistic particles have a Larmor radius that increases with their Lorentz factor: high-energy particles rotate slowly in B_x and are held in the acceleration region even longer as they are accelerated, thus facilitating the creation of hard tails. With this argument alone, Zenitani and Hoshino (2001) predict a power law with index $p \propto cB_x/E_{\rm rec}$, but their model is very simple. Bessho and Bhattacharjee (2012) analytically derive the spectra of particles accelerated by $E_{\rm rec}$ and escaping from the X-point, and find $\mathrm{d}n/\mathrm{d}\gamma \propto \gamma^{-1/4}\exp\{-a\gamma^{1/2}\}$. It is a power law with an exponential cutoff, occurring at higher energies for relativistic X-points because $a \propto cB_x/E_{\rm rec}$. In the end, the X-point accelerated particles gain more energy around the contracting islands and during reconnection events between merging islands, to result in the distribution that we show in this paper.

Condition for hard high-energy tails

It appears from our data that the hardness of the energy distribution for species s is controlled by its background magnetization $\sigma_s^{\rm hot}$ and by the Alfvén speed $V_{\rm A,in}^{\rm R}$. The power law is harder for higher magnetizations (Table 7.2). For a fixed magnetization $\sigma_{\rm e}^{\rm hot} = 83$, the simulations with $m_{\rm i}/m_{\rm e} = 1$, 12, and 25 feature different inflow Alfvén speeds $V_{\rm A,in}^{\rm R} = 0.988$, 0.93, and 0.88, and also different power law indexes for electrons: $p = 1.5$, 1.6, 1.8, respectively. Similarly, when compared to our work at a given electron magnetization, the PIC simulations of Sironi and Spitkovsky (2014) for pair plasmas present harder distributions, simply because with pairs and

a given σ_e, the Alfvén speed is higher. A higher inflow Alfvén speed thus leads to harder distributions.

This can be interpreted as follows. The building of a high-energy tail for species s requires two ingredients: an inflow magnetization $\sigma_s > 1$ so that the transfer of magnetic energy can exceed the particles' restmass, and thus accelerate them to relativistic energies; and a large enough ratio $E_{\rm rec}/(cB_0)$ in order to have a hard distribution. The latter condition roughly states that the residence time $\gamma m_s/(q_s B_x)$ of a particle in the acceleration region must be longer than its acceleration time $\gamma m_s c/(q_s E_{\rm rec})$ by $E_{\rm rec}$. This is supported by the analytical models of Zenitani and Hoshino (2001) and Bessho and Bhattacharjee (2012) cited above. Given that the reconnection rate[b] $E^* = E_{\rm rec}/(B_0 V^{\rm R}_{\rm A,in}\cos\theta)$ lies in a narrow range for various simulations ($E^* \sim 0.14$-0.30, Sects. 6.4.6 and 6.5.3), the condition of a large ratio $E_{\rm rec}/(cB_0) = E^* V^{\rm R}_{\rm A,in}\cos\theta/c$ consequently translates into a relativistic inflow Alfvén speed $V^{\rm R}_{\rm A,in}$ and into a not too strong guide field ($\cos\theta = (1 + B_{\rm G}^2/B_0^2)^{-1/2}$).

For the ions, a hard distribution requires $\sigma_{\rm i}^{\rm hot} \gg 1$ and $V^{\rm R}_{\rm A,in} \sim c$. But the condition $V^{\rm R}_{\rm A,in} \sim c$ is equivalent to a total magnetization $\sigma_{\rm i+e}(B_{\rm tot}) > 1$ (Eq. 6.7b), which is already fulfilled if $\sigma_{\rm i}^{\rm hot} \gg 1$. For the electrons, a hard distribution requires $\sigma_{\rm e}^{\rm hot} \gg 1$ and $V^{\rm R}_{\rm A,in} \sim c$. The latter translates to $\sigma_{\rm i+e}(B_{\rm tot}) > 1$, so that we have (if we neglect temperature effects): $\sigma_{\rm e}^{\rm cold} \sim (1 + m_{\rm i}/m_{\rm e})\sigma_{\rm i+e} > 1 + m_{\rm i}/m_{\rm e} \sim 2000$. Here the condition on the Alfvén speed is consequently more stringent than the condition on the magnetization. We conclude that hard ion distributions are obtained when $\sigma_{\rm i}^{\rm hot} \gg 1$, and hard electron distributions when $V^{\rm R}_{\rm A,in} \sim c$.

We finally point out that the Alfvén speed, and thus also the ratio $E_{\rm rec}/B_0$, saturates at c for strong magnetizations. We consequently expect the particle distribution hardness to also saturate to some value with, as indicated by our simulations, a power law index p slightly below 1.2. Reconnection in environments with $\sigma_{\rm i}^{\rm hot} \gg 1$ should thus produce ion and electron distributions with power law index $p \lesssim 1$.

7.5.3 Astrophysical outlook, objects and orders of magnitude

We now turn to astrophysical applications of the work presented in this chapter. Just as in Sect. 6.6.2, we are interested in four major domains where magnetic reconnection can play a key role: large scale outflow launching, high-energy flare production, steady emission of radiation, and plasma heating or non-thermal particle production. We discuss which objects these phenomena are observed in, give orders of magnitude for the main parameters, and point out where our work is applicable. Table 7.5 summarizes the physical conditions encountered in the objects mentioned here.

Large scale transient outflow production, the example of microquasars

Large scale magnetic reconnection events may be at the origin of large scale transient jets in microquasar systems, for example via a magnetic field re-

[b] The residence time $\gamma m_s/(q_s B_x)$ implies the reconnected field B_x, and not the inflowing component B_0 as in the reconnection rate. However, the ratio B_0/B_x is roughly the same for all magnetizations and all simulations.

Objects with ion-electron plasmas (with also pairs)	B (G)	n_e (cm^{-3})	T_e (K)	σ_e^{cold}	$V_{A,in}^R/c$
Microquasar coronae, X-ray emitting region[a]	10^5-10^7	10^{13}-10^{16}	10^9	10^{-1}-10^5	0.003-1
AGN coronae, X-ray emitting region[b]			10^9	1.7-180	0.03-0.3
Giant radio galaxy lobes[c]	10^{-6}-10^{-5}	3×10^{-6}	10^6	0.8-80	0.02-0.2
Extragalactic jet, γ-ray emitting region (< 0.05 pc)[d]	12	80		2×10^5	~ 1
Extragalactic jet, radio emitting region (kpc scales)[e]	1-3 $\times 10^{-5}$	0.8-5 $\times 10^{-8}$		500-2500	~ 1
GRB jet, at radius of fast reconnection[f]	7×10^8	10^{10}	10^8	5×10^{12}	0.9
Objects with pair plasmas	B (G)	n_e (cm^{-3})	T_e (K)	σ_e^{cold}	$V_{A,in}^R/c$
At the termination shock of pulsar winds[g]	10^4	0.1-10		10^{13}	~ 1
In pulsar wind nebula[h]	5×10^{-3}	5 to 10^3	$\gamma \sim$ 10-10^9	< 0.5	0.6

[a] Analytical disk and corona models, de Gouveia dal Pino and Lazarian (2005), Di Matteo (1998), Merloni and Fabian (2001), and Reis and Miller (2013); matching observed spectra with radiation models, Del Santo et al. (2013) and Romero et al. (2014).
[b] Analytical disk and corona models, Di Matteo (1998), Merloni and Fabian (2001), and Reis and Miller (2013).
[c] Observations, Kronberg et al. (2004).
[d] Analytical model assuming $\sigma_i^{cold} = 100$, Giannios et al. (2009). See also Giroletti et al. (2004) for magnetic field measurements (0.2 G, but on larger scales).
[e] Observations, Schwartz et al. (2006). See also Romanova and Lovelace (1992).
[f] Analytical model, McKinney and Uzdensky (2012). Pairs are also present, with $n_{pair} \sim 10 n_e$.
[g] Analytical model and observations, Bucciantini et al. (2011) and Sironi and Spitkovsky (2011a).
[h] Analytical model and observations, Atoyan and Aharonian (1996), Meyer et al. (2010), Uzdensky et al. (2011), and Cerutti et al. (2013). The plasma distribution function is a broken power law with Lorentz factors γ in the indicated range. We note that Cerutti et al. (2013) considers only the high-energy electron population, and hence has larger magnetizations.

Table 7.5: Order of magnitude for physical parameters in astrophysical environments. Other orders of magnitude can be found in Figs. 1.1 and 2.42.

versal accreted onto a magnetically arrested disk. We refer to Sect. 6.6.2 for a discussion concerning such events.

Flares in AGN and microquasar coronae and in extragalactic jets

Flare-like emission of high-energy photons is observed, for example, in the γ-ray region of AGN jets (Giannios 2010), or in microquasar and AGN coronae (Di Matteo 1998; Merloni and Fabian 2001; Reis and Miller 2013). Concerning AGN jets, flares in the GeV-TeV range are observed, and may come from close to the AGN ($< 0.05\,\mathrm{pc}$, Giroletti et al. 2004). There, Giannios et al. (2009) assume an ion magnetization $\sigma_\mathrm{i}^\mathrm{cold} \sim 100$, which gives an Alfvén speed $\sim c$ (Table 7.5, line d). Concerning the coronae of AGNs and microquasars, various models constrained by observations predict ion magnetizations in the range $\sigma_\mathrm{i}^\mathrm{cold} \sim 10^{-5}$-$10^{2}$ (Table 7.5, lines a and b). In the most magnetized case, the Alfvén speed is $\sim c$. According to our results, reconnection in such environments should produce electron distributions with hard tails ($p \sim 1$), and if we apply our results for electrons to the ions, the latter should also form hard tails ($p \sim 2$).

Quite generally, high-energy flares can be explained by reconnecting events under three conditions: the large scale magnetic field must possess enough energy and the large scale flow or the flow turbulence must lead to enough reconnection events; the reconnection process must produce high-energy particles with hard distributions; these high-energy particles must be able to radiate. The first point is linked to the large scale properties of the object and can be investigated with simulations on large scales, while the last two points concern microphysics and must be addressed with first principle simulations. We believe to have answered the second point: magnetic reconnection does produce hard high-energy distributions whenever the ion magnetization is above unity, which can indeed be the case in the environments mentioned above. Concerning photon emission, we expect particles trapped inside the islands (population i) to produce mostly thermal synchrotron-Bremsstrahlung. On the other hand, particles accelerated at the X-point (population ii) are likely to radiate collimated beams when suddenly encountering the strong magnetic field structure at the end of the exhausts, at the island entrance. This was demonstrated in the no-guide field case by Cerutti et al. (2012a) in pair plasmas, and should also hold for ion-electron plasmas because the overall magnetic structure is not too different. The radiation spectrum is then anisotropic and reaches energies on the order of $\gamma^2\omega_\mathrm{ce}$ with γ the particles Lorentz factor and $\omega_\mathrm{ce} = eB/m_\mathrm{e}$. With a guide field, radiation should occur together with particle acceleration in the $\boldsymbol{E}\cdot\boldsymbol{B} \neq 0$ area, because particles then swirl around the guide field. It should consequently be more regular and less flare-like (Cerutti et al. 2013). Since reconnection with a guide field is more generic in the complex magnetic field structures of coronae or jets than antiparallel reconnection, the question of photon emission in such a case is very relevant.

Steady radio emission from extragalactic jets

Magnetic reconnection can produce radiation in a wide range of frequencies, which for the synchrotron component depends on the strength of the reconnecting magnetic field. An example is the radio emission, on kilo-parsec scales, of extragalactic jets. Explanation of these spectra can invoke mag-

netic reconnection events, in particular to explain the hard photon indexes (Romanova and Lovelace 1992). Observations indicate electron magnetizations in the range $\sigma_{\rm e}^{\rm cold} \sim$ 500-2500 (Table 7.5, line e), which corresponds to ion magnetizations $\sigma_{\rm i}^{\rm cold} \sim$ 0.3-1.3 and to Alfvén speeds $\sim$ 0.5-0.8c. This is between the two cases $\omega_{\rm ce}/\omega_{\rm pe} = 1$ and $\omega_{\rm ce}/\omega_{\rm pe} = 3$ of our study, for which the kinetic energy takes a large amount of the magnetic energy (between 45% and 60%, Tables 7.3 and 7.4), and is distributed as 60/40% to 30/70% between ions and electrons, respectively, depending on the guide field strength. Most importantly, for these parameters the background-accelerated electrons form power laws with indexes between 4.5 and 1.5 (Table 7.2 and Fig. 7.3), which can then indeed emit hard spectra.

Plasma heating in AGN and microquasar coronae and in radio galaxy lobes

Magnetic reconnection can also efficiently heat the plasma by converting the magnetic field energy.

Photon emission in the hard state of microquasars and AGNs is believed to come from inverse-Compton scattering of seed photons by the electrons of a corona. To achieve this, these electrons must reach temperatures of the order of 10^9 K, i.e., $\Theta_{\rm e} = T_{\rm e}/m_{\rm e}c^2 \sim 0.2$. In microquasars, a coronal population of non-thermal high-energy electrons is also required by the observation of MeV photons (Poutanen and Veledina 2014). A proposed mechanism for plasma heating and non-thermal particle production is by magnetic reconnection (Di Matteo 1998; Merloni and Fabian 2001; Reis and Miller 2013). Alfvén speeds in these coronae are estimated to be of the order of 0.003c-c (Table 7.5, line a). In our corresponding simulations, the final kinetic energy is a large fraction of the initial magnetic energy (48% at $V_{\rm A} = 0.5c$, up to 75% at $V_{\rm A} = 0.88c$, Table 7.3), thus allowing an efficient energy transfer to the plasma. For this range of Alfvén speeds, accelerated electron distributions can be steep ($p > 4$ for $V_{\rm A} = 0.5c$) or hard ($p \sim 1.2$ for $V_{\rm A} = 0.97c$), and in the latter case reconnection can indeed produce a non-thermal population.

An important point is the question of the energy repartition between ions and electrons: if most of the magnetic energy goes to ions, and because of the low collisionality of these dilute environments, a large temperature difference can be sustained (Di Matteo et al. 1997). Our results show that energy is almost equally distributed between ions (60% to 30%) and electrons (40% to 70%), so that we do not expect large temperature differences (as studied in some models, Di Matteo et al. 1997) from this heating mechanism.

Other models of the MeV component from microquasars invoke the emission of electrons in the jet, and require hard electron distributions with indexes $p \sim 1.5$ (Zdziarski et al. 2014). The ion magnetization in these models needs to be larger than unity. Our work demonstrates that magnetic reconnection in these conditions can provide such hard electron spectra.

Similar questions arise concerning the heating of the lobes of radio galaxies (Kronberg et al. 2004). There, $n \sim 3 \times 10^{-6}\,{\rm cm}^{-3}$ for the number densities, and $B \sim 5\,\mu$G for the equipartition magnetic field with values that can be locally ten times higher, which gives magnetizations $\sigma_{\rm e}^{\rm cold} \sim$ 0.8-80 and Alfvén speeds $\sim$ 0.02c-0.2c. Our conclusions also apply there, especially for the ion/electron energy repartition.

Finally, we underline that the energy distribution by acceleration processes far downstream of the diffusion region requires another study.

Very high energy particle production

A final application concerns the extraterrestrial PeV neutrinos detected by IceCube (IceCube Collaboration 2013). They can come from the photopion ($p\gamma$) interaction of high-energy protons or ions produced by high-energy machines (such as, e.g., GRBs, Petropoulou et al. 2014). The ability of magnetic reconnection to accelerate ions in highly magnetized environments is then very relevant. We find that the highest Lorentz factor for ions follows the same trend as for electrons ($\gamma \propto t^s$, $s \sim 0.7$-1.1), and for ion magnetization $\sigma_\mathrm{i} \gg 1$ we expect ions to feature the same power law spectra as electrons, with a slope $p \lesssim 1.2$.

7.5.4 Astrophysical outlook, further discussion

Scaling of the results, importance of radiative braking, Compton drag and pairs

The reconnection physics with the Harris geometry described in this paper only depends on the inflow plasma magnetization and temperature, and not on the absolute values of magnetic field and particle number density. For example, reconnection in a microquasar corona close to the hole, and in the γ-ray emitting region of an extragalactic jet, takes place with the same magnetizations (Table 7.5) and thus features the same reconnection rate, particle spectra or energy repartition, even if magnetic field strengths differ by six orders of magnitude (provided, however, that the geometry is the same). This is true as long as reconnection occurs in the collisionless regime, an issue discussed, for example, by Goodman and Uzdensky (2008) and Ji and Daughton (2011) (see Sect. 2.11.3 for an overview). Also, it requires that effects such as radiative braking by emission or Compton drag, or pair annihilations, do not perturb the reconnection physics. Such effects imply the actual values of magnetic field and particle number densities and can lead to a very different physics for the same magnetization. To evaluate this, we estimate in Appendix 7.A when an electron loses a significant fraction of its energy during any given time or over a length scale that is dynamically important for the magnetic reconnection physics. These time and length scales are taken as a cyclotron or plasma period, or as an inertial scale. Particles will eventually radiate and cool farther away, but with no influence on the reconnection physics. We summarize the main points of this appendix here.

Radiative braking due to synchrotron radiation remains negligible on cyclotron scales as long as (from Eq. 7.6):

$$\left(\frac{\gamma}{100}\right)^2 \frac{B}{10^{11}\,\mathrm{G}} < 1, \tag{7.3}$$

where γ is the Lorentz factor of an electron. This is negligible for all objects of Table 7.5, except in the pulsar wind nebulae where γ can reach 10^9 (Meyer et al. 2010). Radiative braking due to Coulomb collisions can be estimated by assuming a thermal Bremsstrahlung, and remains negligible on inertial

length scales as long as (from Eq. 7.7):

$$\left(\frac{T_\mathrm{e}}{m_\mathrm{e}c^2}\right)^{1/2}\left(\frac{n_\mathrm{e}}{5\times10^{12}\mathrm{cm}^{-3}}\right)^{3/2}<1. \tag{7.4}$$

This is the case for objects of Table 7.5, except in microquasar coronae close to the black hole where n_e is high.

Compton drag does not affect the electron dynamics on inertial length scales as long as

$$\frac{\gamma}{100}\left(\frac{1\mathrm{cm}^{-3}}{n_\mathrm{e}}\right)^{1/2}\frac{U_\mathrm{ph}}{10^{10}\mathrm{erg/cm}^3}<1, \tag{7.5}$$

with U_ph the radiation field energy density (Eq. 7.8). For a blackbody spectrum, this remains true for photon temperatures $T_\mathrm{ph}<10^6\,\mathrm{K}$. Consequently, objects with electron temperatures $T_\mathrm{e}>10^6\,\mathrm{K}$ on scales large enough so that the optical depth is important and photons are thermalized, are in the range where Compton drag is efficient. It should be noted that the electrons locally heated by the magnetic reconnection cannot thermalize the radiation, because the reconnection region is optically thin (Eq. 7.9). Alternatively, the photon energy density U_ph produced by the magnetic reconnection can be computed from the synchrotron or Bremsstrahlung emissivity, assuming that the emission takes place over a volume $(ad_\mathrm{e})^3$ with d_e the electron inertial length and a a geometrical factor. Compton drag against the synchrotron photons is negligible as long as $a(B/1\mathrm{G})^2(\gamma/100)^3<10^{36}$ (from Eq. 7.11), and that due to Bremsstrahlung photons as long as $a(T_\mathrm{e}/10^8\mathrm{K})^{1/2}\,(n_\mathrm{e}/1\mathrm{cm}^{-3})\,(\gamma/100)<10^{38}$ (from Eq. 7.13). Compton drag by these photon fields is thus negligible for all objects of Table 7.5. The radiation field can also originate from outside of the reconnection region. For example, at a distance R from an object emitting at a fraction α of the Eddington luminosity, the photon energy density can be estimated as $U_\mathrm{ph}=\alpha(R_\mathrm{S}/R)^2(10\,\mathrm{km}/R_\mathrm{S})\times10^{15}\,\mathrm{erg/cm}^3$, with R_S the Schwarzschild radius of the object. The threshold where Compton drag against these photons is significant can be reached in the inner parts of microquasar coronae if n_e is not too high (as given by Eq. 7.15) (see also Goodman and Uzdensky 2008).

Finally, photons of energy above $m_\mathrm{e}^2c^4/\epsilon_0$ can annihilate with ambient photons (of typical energy ϵ_0) to produce pairs. This can be the case if $B(\gamma/100)^2>2\times10^9\,\mathrm{G}$ for high-energy synchrotron photons, or if $T_\mathrm{e}>10^9\,\mathrm{K}$ for Bremsstrahlung (Eqs. 7.16 and 7.17). Inverse Compton events can also produce such photons if the electron Lorentz factors are $\gamma>m_\mathrm{e}c^2/\epsilon_0$ (see Appendix 7.A).

In any case, pair creation will disturb the reconnection dynamic only if the creation occurs inside or close to the reconnection region. The mean-free-path $l_{\gamma\gamma}$ of high-energy photons should thus be compared to an inertial length d_e. For a blackbody gas of photons at temperature T_ph, we have $l_{\gamma\gamma,\mathrm{BB}}/d_\mathrm{e}=(n_\mathrm{e}/1\mathrm{cm}^{-3})^{1/2}(10^6\mathrm{K}/T_\mathrm{ph})^3$ (Eq. 7.19). However, as underlined previously, a blackbody spectrum of photons is not easy to achieve. If photons cannot be thermalized, then the $\gamma\gamma$ opacity must be computed from the rate of production of photons by synchrotron and Bremsstrahlung radiation in the reconnection region. Concerning Bremsstrahlung emission, we find with Eq. 7.24 that pairs form far away from the reconnection region for all objects of Table 7.5. Concerning synchrotron emission, we find with

Eq. 7.22 that for radio lobes, radio emitting regions of extragalactic jets, or pulsar wind nebulae, $l_{\gamma\gamma,\mathrm{sync}} \gg d_\mathrm{e}$ holds, so that pairs form far away from the reconnection site. For microquasar coronae close to the hole, for extragalactic jet γ-ray regions, for GRB jets, or for pulsar wind termination shocks, however, we have $l_{\gamma\gamma,\mathrm{sync}} \ll d_\mathrm{e}$, and pairs form inside the reconnection region. For microquasars, the photon field can also be deduced from the energy density at a distance R from an object emitting at a fraction of the Eddington luminosity. We find with Eq. 7.26 that pair production can be significant for high luminosities, small radii, and not too high particle densities. Such a regime is studied by Uzdensky (2011).

Other acceleration sites during reconnection

In this manuscript, we investigate particle acceleration in or close to the diffusion region. Other energy conversion locations exist around reconnection sites. One is along the magnetic separatrices far downstream of the diffusion region (observed, e.g., at the magnetopause: Khotyaintsev et al. 2006), on length scales of hundreds of ion inertial lengths. There, magnetic energy conversion occurs as the plasma flows through the complex structure of collisionless non-linear waves (slow shock(s), compound wave, rotational wave). Instabilities and parallel electric fields in these regions can produce thermal and non-thermal electrons (Drake et al. 2005; Egedal et al. 2009, 2012). This shock structure has been investigated in the non-relativistic case (Liu et al. 2012; Higashimori and Hoshino 2012). In a relativistic situation, the different phase speeds of the waves may lead to different results. Of particular interest is the energy distribution between bulk, thermal, ion, and electron components, and its importance relative to the locations discussed here.

Another site for particle acceleration is at the dipolarization front (Vapirev et al. 2013), where the first reconnected field lines are swept away and drag the ambient plasma. Such a situation is prone to instabilities and particle acceleration.

Also, turbulence associated with magnetic reconnection can lead to particle acceleration via a second-order Fermi process.

We emphasize, however, that high-energy particle production in and near the diffusion zone, directly by the reconnection electric field as discussed in the present manuscript, should be of great importance for relativistic inflow magnetizations because the electric field is very large ($E_\mathrm{rec}/B_0 \sim 0.2V_\mathrm{A,in}^\mathrm{R} \sim 0.2c$, Sects. 6.4.6 and 6.5.3).

Open questions

The present study offers useful insights into the properties of magnetic reconnection, but remains simplified in many respects. Reconnection configurations in real environments are likely to often involve guide fields, but also asymmetric plasmas and fields from each side of the current sheet (Aunai et al. 2013; Eastwood et al. 2013), or normal magnetic fields (i.e., along $\hat{\boldsymbol{x}}$ here) owing to the ambient field (e.g., for the magnetotail, Pritchett 2005a). Magnetic reconnection is also likely to be forced by external plasma and field line motions (Lyubarsky and Liverts 2008). The reconnection electric field is then imposed by the forcing (Pei et al. 2001; Pritchett 2005b; Ohtani and Horiuchi 2009; Klimas et al. 2010), and can be larger than in

the spontaneous case. Particle acceleration can consequently be enhanced. The initial equilibrium can also have an impact on the late evolution and particle distributions. Study of 2D situations such as X-point collapse or force-free equilibrium (e.g., Graf von der Pahlen and Tsiklauri 2014; Liu et al. 2014) shows few differences with the Harris case, and we expect them to produce the same kind of distributions. However, full 3D initial configurations can lead to very different outcomes, as suggested by the few existing kinetic studies (Baumann and Nordlund 2012; Olshevsky et al. 2013). Reconnection and particle acceleration at 3D nulls or at quasi separatrix layers (Pontin 2011) deserves further research.

A crucial question concerns the validity of our results in a real 3D reconnection event. Magnetic islands then become extended filaments, modulated or broken by instabilities in the third dimension or by a lack of coherence of the tearing instability (Jaroschek et al. 2004; Zenitani and Hoshino 2008; Daughton et al. 2011; Liu et al. 2011; Kagan et al. 2013; Markidis et al. 2013). For this reason we may expect more particle mixing, but current sheet particles may also still be trapped in the strong magnetic structure surrounding the filaments. Particle acceleration at X-points may also be disturbed. However, 3D results in pair plasmas by Sironi and Spitkovsky (2014) are encouraging since they show that energization is still efficient, and leads to power law tails with similar indexes, essentially because the small scale physics around the X-point and during filament mergings is the same as in 2D.

There is also a strong need to understand the interplay between large and small scales better. Coronal heating by reconnection, or large scale outflow launching, are cases where the large scale flow sets the conditions for the occurrence of reconnection, which in turn largely modifies the large scale flow conditions. For example, Jiang et al. (2014) show that global simulations of the formation of an accretion disk corona requires understanding the role of reconnection in the MRI turbulence. Shocks, possibly collisionless, are also fundamental microphysical processes that shape the flow on all scales of accreting black holes (Walder et al. 2014). Daldorff et al. (2014) illustrate the power of a coupled MHD/PIC approach with a simulation of the Earth's magnetosphere.

Finally, we emphasize that the ability of magnetic reconnection to accelerate protons or heavier ions is a key question, first because they can produce mesons and then pairs, which can lead to a different photon spectrum and second because this channel can produce neutrinos, and characterizing the neutrino spectrum from high-energy objects is compulsory for distinguishing it from those predicted by dark matter models. With high-energy extraterrestrial neutrinos now being detected (IceCube Collaboration 2013), this is a very exciting perspective.

Appendix 7.A The importance of radiative braking, Compton drag, and pair creations

Two relevant issues are the importance of radiative braking and of pair creation. We first investigate radiative braking of electrons, and then study the opacity of high energy photons to $\gamma\gamma$ annihilations.

Electron braking by emission of radiation or by Compton drag

Electrons lose energy by emitting photons when being scattered by magnetic fields (synchrotron-like radiation) or by Coulomb collisions (Bremsstrahlung-like radiation), or when colliding with photons (inverse-Compton events). For the synchrotron component, the energy $\delta E_{\rm sync}$ lost by an electron of Lorentz factor γ and velocity βc, gyrating in a magnetic field B, averaged over pitch angles, and during one cyclotron orbit, is (Rybicki and Lightman 1979):

$$\frac{\delta E_{\rm sync}}{\gamma m_{\rm e} c^2} = \frac{8\pi}{9}\beta^2\gamma^2\frac{r_0\omega_{\rm ce}}{c} = \frac{B}{1.4\times10^{11}{\rm G}}\left(\frac{\gamma}{100}\right)^2, \tag{7.6}$$

with r_0 the classical electron radius and $\omega_{\rm ce} = eB/m_{\rm e}$. On the other hand, electron cooling by Coulomb collisions can be evaluated via the thermal Bremsstrahlung emission formula, giving an energy $\delta E_{\rm Brem}$ lost during one plasma period $\omega_{\rm pe}^{-1}$:

$$\frac{\delta E_{\rm Brem}}{m_{\rm e}c^2} = \left(\frac{T_{\rm e}}{m_{\rm e}c^2}\right)^{1/2}\left(\frac{n_{\rm e}}{5\times10^{12}\,{\rm cm}^{-3}}\right)^{3/2}. \tag{7.7}$$

It shows that synchrotron braking is not relevant for the objects of Table 7.5, except for pulsar wind nebulae and very high Lorentz factor electrons, while braking by Bremsstrahlung emission is significant for reconnection in microquasar magnetospheres close to the black hole.

The last braking mechanism is inverse-Compton scattering of ambient photons by electrons. The energy δE lost by an electron during one plasma period $\omega_{\rm pe}^{-1}$ is at most[c]

$$\begin{aligned}\frac{\delta E_{\rm IC}}{\gamma m_{\rm e}c^2} &= \frac{4}{3}\frac{\sigma_{\rm T}c\beta^2\gamma}{\omega_{\rm pe}}\frac{U_{\rm ph}}{m_{\rm e}c^2}\\ &= \frac{\gamma\beta^2}{100}\left(\frac{1\,{\rm cm}^{-3}}{n_{\rm e}}\right)^{1/2}\frac{U_{\rm ph}}{1.7\times10^{10}{\rm erg/cm}^3},\end{aligned} \tag{7.8}$$

where $U_{\rm ph}$ is the photon energy density and $\sigma_{\rm T}$ is Thomson cross section. For a blackbody radiation, the energy density is given by $U_{\rm ph} = (\pi^2/15)\,T_{\rm ph}^4/(\hbar c)^3$. It reaches the density $1.7\times10^{10}{\rm erg/cm}^3$ for $T_{\rm ph} = 1.2\times10^6{\rm K}$. Below this temperature, electrons do not significantly lose energy by Compton drag, while above they do.

However, it should be noted that a blackbody radiation at $T_{\rm ph}$ requires the thermalization of the photons produced by the hot electrons, a fact impossible to achieve on an inertial length scale $d_{\rm e}$ given that the mean-free-path to Compton scattering is

$$\frac{l_{\rm Compt}}{d_{\rm e}} = \frac{1}{d_{\rm e}\sigma_{\rm T}n_{\rm e}} = \left(\frac{9\times10^{36}\,{\rm cm}^{-3}}{n_{\rm e}}\right)^{1/2}, \tag{7.9}$$

and would thus imply densities $n_{\rm e}\sim10^{36}\,{\rm cm}^{-3}$. The radiation produced by the hot electrons in the reconnection region consequently escapes from this region before being thermalized. If we assume that the photons are produced over an optically thin volume $(ad_{\rm e})^3$, with a a geometrical factor, and that the emissivity is ${\rm d}W_{\rm ph}/{\rm d}t{\rm d}V$, then the energy density of the gas

[c] At most, because Klein-Nishina effects can only reduce the energy loss.

of photons is $U_{\rm ph} \sim a d_{\rm e}/c \times {\rm d}W_{\rm ph}/{\rm d}t{\rm d}V$. Expressions for $U_{\rm ph}$ should thus be obtained for synchrotron and Bremsstrahlung radiations.

Concerning synchrotron radiation, the total power emitted by an electron is $P_{\rm emit,sync} = (4/9) r_0^2 c \beta^2 \gamma^2 B^2$, and the emissivity is $\sim n_{\rm e} P_{\rm emit,sync}$, so that

$$\begin{aligned} U_{\rm ph,sync} =& 9 \times 10^{-26}\,{\rm erg/cm^3} \\ & \times a \left(\frac{B}{1\,{\rm G}}\right)^2 \left(\frac{n_{\rm e}}{1\,{\rm cm^{-3}}}\right)^{1/2} \left(\frac{\gamma\beta}{100}\right)^2 . \end{aligned} \tag{7.10}$$

This expression can be inserted into Eq. 7.8, to yield:

$$\frac{\delta E_{\rm IC,sync}}{\gamma m_{\rm e} c^2} = 5.3 \times 10^{-36} \times a \left(\frac{B}{1\,{\rm G}}\right)^2 \beta \left(\frac{\gamma\beta}{100}\right)^3 , \tag{7.11}$$

which is always well below unity for the objects of Table 7.5.

As for Bremsstrahlung radiation, we use the emissivity for a thermalized plasma at temperature $T_{\rm e}$, to find

$$\begin{aligned} U_{\rm ph,Brem} =& 2.5 \times 10^{-28}\,{\rm erg/cm^3} \\ & \times a \left(\frac{T_{\rm e}}{10^8\,{\rm K}}\right)^{1/2} \left(\frac{n_{\rm e}}{1\,{\rm cm^{-3}}}\right)^{3/2} . \end{aligned} \tag{7.12}$$

Once inserted into Eq. 7.8, it yields:

$$\frac{\delta E_{\rm IC,Brem}}{\gamma m_{\rm e} c^2} = 1.5 \times 10^{-38} \times a \left(\frac{T_{\rm e}}{10^8\,{\rm K}}\right)^{1/2} \left(\frac{n_{\rm e}}{1\,{\rm cm^{-3}}}\right) \frac{\gamma\beta^2}{100}, \tag{7.13}$$

which is again always well below unity for objects of Table 7.5.

The photon field can also originate from outside of the reconnection region. For example, $U_{\rm ph}$ can be evaluated at a distance R from an object of mass M emitting at a fraction α of the Eddington luminosity $L_{\rm Edd} = 4\pi G M m_{\rm i} c/\sigma_{\rm T}$:

$$\begin{aligned} U_{\rm ph} = \frac{\alpha L_{\rm Edd}}{4\pi R^2 c} &= \alpha \left(\frac{R_{\rm S}}{R}\right)^2 \frac{m_{\rm i} c^2}{2\sigma_{\rm T} R_{\rm S}} \\ &= \alpha \left(\frac{R_{\rm S}}{R}\right)^2 \frac{10\,{\rm km}}{R_{\rm S}} \times 10^{15}\,{\rm erg/cm^3}, \end{aligned} \tag{7.14}$$

with $R_{\rm S}$ the Schwarzschild radius of the object. With Eq. 7.8, it gives a loss per $\omega_{\rm pe}^{-1}$ given by

$$\frac{\delta E_{\rm IC,Edd}}{\gamma m_{\rm e} c^2} = 6 \times 10^4 \times \left(\frac{1\,{\rm cm^{-3}}}{n_{\rm e}}\right)^{1/2} \frac{\gamma\beta^2}{100} \alpha \left(\frac{R_{\rm S}}{R}\right)^2 \frac{10\,{\rm km}}{R_{\rm S}}. \tag{7.15}$$

High-energy photons and opacity to $\gamma\gamma$-annihilation

The photons emitted by the accelerated electrons (of Lorentz factor γ, velocity βc) can be due either to synchrotron or to Bremsstrahlung radiation. In the synchrotron case, photon energies can reach

$$\begin{aligned} h\nu_{\rm sync} &= \frac{3\gamma^2 \omega_{\rm ce}}{2\pi\beta} \\ &= 3.5 \times 10^{-4}\,{\rm eV} \frac{B}{1\,{\rm G}} \left(\frac{\gamma}{100}\right)^2 \\ &= 6.8 \times 10^{-10} m_{\rm e} c^2 \frac{B}{1\,{\rm G}} \left(\frac{\gamma}{100}\right)^2 . \end{aligned} \tag{7.16}$$

Also, a thermal Bremsstrahlung spectra from electrons at temperature T_e cuts-off above $h\nu_\mathrm{therm} \simeq T_\mathrm{e}$, i.e., above

$$h\nu_\mathrm{therm} = m_\mathrm{e}c^2 \, \frac{T_\mathrm{e}}{6\times10^9\,\mathrm{K}}. \tag{7.17}$$

High-energy photons can annihilate with lower energy photons of energy ϵ_0 only if they have an energy above $m_\mathrm{e}^2c^4/\epsilon_0$ (Gould and Schréder 1967), which requires at least a high-energy photon above 0.5MeV. Synchrotron radiation can produce such photons in pulsar wind nebulae, and thermal Bremsstrahlung can do so in microquasars and GRBs.

Also, high-energy photons can be produced by inverse-Compton collisions between ambient photons of energy ϵ_0 and high-energy electrons of Lorentz factor γ. The outcome of such a collision is a high-energy photon of energy up to $\gamma^2\epsilon_0$, so that $\gamma > m_\mathrm{e}c^2/\epsilon_0$ is needed to produce pairs.

It is then interesting to compute the mean-free-path $l_{\gamma\gamma}$ of such high-energy photons. Their annihilation creates pairs, which will affect the reconnection dynamics only if they are created near the reconnection site. The relevant quantity is thus $l_{\gamma\gamma}/d_\mathrm{e}$, with d_e the electron inertial length. We only seek an order-of-magnitude estimate. From Gould and Schréder (1967), we can approximate the optical depth $\tau_{\gamma\gamma}$ for a high-energy photon (energy E) traveling a length l through a gas of lower energy photons (with a typical energy ϵ_0, of number density n_ph) as

$$\tau_{\gamma\gamma} \sim l\,\pi r_0^2\,n_\mathrm{ph}\,f(m_\mathrm{e}^2c^4/\{E\epsilon_0\}), \tag{7.18}$$

where r_0 is the classical electron radius, and f is a function depending on the exact gas photon distribution. Generally, f is maximal and equal to ~ 1 for $E = \epsilon_0$. For example, if the gas of photons is a blackbody at temperature T_ph, then $\epsilon_0 = T_\mathrm{ph}$, $n_\mathrm{ph} = 2\zeta(3)/\pi^2\,(T_\mathrm{ph}/(\hbar c))^3$, with $\zeta(3) \sim 1.202$, and f is at its maximum for $E = T_\mathrm{ph}$ with a value $1/2\zeta(3)$. The mean-free-path is defined such that $\tau_{\gamma\gamma} = 1$. In the blackbody case, we have

$$\frac{l_{\gamma\gamma,\mathrm{BB}}}{d_\mathrm{e}} \sim \frac{1}{\pi r_0^2 d_\mathrm{e} n_\mathrm{ph}} = \left(\frac{n_\mathrm{e}}{1\,\mathrm{cm}^{-3}}\right)^{1/2} \left(\frac{10^6\,\mathrm{K}}{T_\mathrm{ph}}\right)^3. \tag{7.19}$$

Consequently, if $T_\mathrm{ph} < 10^6\,\mathrm{K}$, then the $\gamma\gamma$ annihilations occur well outside the reconnection region and do not affect the process; while for higher photon temperatures the annihilation occurs after a free flight of less than an inertial length, i.e., inside the reconnection region. For an unspecified photon number density, Eq. 7.19 can be written

$$\frac{l_{\gamma\gamma}}{d_\mathrm{e}} \sim \frac{1}{\pi r_0^2 d_\mathrm{e} n_\mathrm{ph}} = \left(\frac{n_\mathrm{e}}{1\,\mathrm{cm}^{-3}}\right)^{1/2} \frac{2\times10^{19}\,\mathrm{cm}^{-3}}{n_\mathrm{ph}}. \tag{7.20}$$

However, as previously noted, a blackbody radiation at T_ph requires the thermalization of the photons by the hot electrons, which is impossible to achieve if these electrons are confined to the reconnection region on inertial length scales (Eq. 7.9). Again, in the optically thin case the radiation number density should be estimated as $n_\mathrm{ph} \sim ad_\mathrm{e}/c \times \mathrm{d}n_\mathrm{ph}/\mathrm{d}t$, with $\mathrm{d}n_\mathrm{ph}/\mathrm{d}t$ the production rate of photons and $(ad_\mathrm{e})^3$ the volume of the emission region. We then evaluate n_ph for synchrotron and Bremsstrahlung radiation, and for the vicinity of an object emitting at a given luminosity.

For synchrotron radiation, this can be roughly estimated by dividing the total power emitted by an electron by the characteristic energy $h\nu_\mathrm{sync}$

(Eq. 7.16), and then multiplying by the electron number density. After some manipulations, one arrives at $\mathrm{d}n_{\mathrm{ph}}/\mathrm{d}t = P_{\mathrm{emit}}/(h\nu_{\mathrm{sync}}) = 0.1\omega_{\mathrm{ce}}$, so that

$$n_{\mathrm{ph,sync}} = 0.1a\frac{\omega_{\mathrm{ce}}}{\omega_{\mathrm{pe}}}\, n_{\mathrm{e}}, \tag{7.21}$$

with ω_{pe} the non-relativistic plasma pulsation associated to d_{e}. We can rewrite $\omega_{\mathrm{ce}}/\omega_{\mathrm{pe}} = (\sigma_{\mathrm{e}}^{\mathrm{cold}})^{1/2}$ with $\sigma_{\mathrm{e}}^{\mathrm{cold}} = B^2/(\mu_0 n_{\mathrm{e}} m_{\mathrm{e}} c^2)$. Inserting $n_{\mathrm{ph,sync}}$ into Eq. 7.20, we have

$$\frac{l_{\gamma\gamma,\mathrm{sync}}}{d_{\mathrm{e}}} \sim a^{-1} \left(\frac{1\,\mathrm{cm}^{-3}}{n_{\mathrm{e}}}\right)^{1/2} \left(\frac{10^{10}}{\sigma_{\mathrm{e}}^{\mathrm{cold}}}\right)^{1/2}. \tag{7.22}$$

For radio lobes, radio-emitting regions of extragalactic jets or pulsar wind nebulae, $l_{\gamma\gamma,\mathrm{sync}} \gg d_{\mathrm{e}}$ holds, so that pairs form far away from the reconnection site. For microquasar coronae close to the hole, for extragalactic jet γ-ray region, for GRB jets, or for pulsar wind termination shocks, we have $l_{\gamma\gamma,\mathrm{sync}} \ll d_{\mathrm{e}}$ and pairs form inside the reconnection region.

For Bremsstrahlung radiation, one can estimate the photon number density by dividing the Bremsstrahlung emissivity P_{emit} by the typical energy T_{e}, and multiplying by a photon escape length ad_{e}. We find

$$n_{\mathrm{ph,Brem}} = 1.8\times 10^{-20}\,\mathrm{cm}^{-3}\, a \left(\frac{10^8\,\mathrm{K}}{T_{\mathrm{e}}}\right)^{1/2} \left(\frac{n_{\mathrm{e}}}{1\,\mathrm{cm}^{-3}}\right)^{3/2}. \tag{7.23}$$

Inserting into Eq. 7.20, we have

$$\frac{l_{\gamma\gamma,\mathrm{Brem}}}{d_{\mathrm{e}}} \sim 10^{39}\times a^{-1} \left(\frac{1\,\mathrm{cm}^{-3}}{n_{\mathrm{e}}}\right) \left(\frac{T_{\mathrm{e}}}{10^8\,\mathrm{K}}\right)^{1/2}. \tag{7.24}$$

We have $l_{\gamma\gamma,\mathrm{Brem}} \gg d_{\mathrm{e}}$ for all objects of Table 7.5.

For microquasars, the photon field number density can also be evaluated at a distance R from a source emitting at αL_{Edd}. To do so, we divide the energy density of Eq. 7.14 by a typical frequency $h\nu_{\mathrm{typ}}$, to obtain:

$$n_{\mathrm{ph}} = \alpha \left(\frac{R_{\mathrm{S}}}{R}\right)^2 \frac{10\,\mathrm{km}}{R_{\mathrm{S}}} \frac{1\,\mathrm{keV}}{h\nu_{\mathrm{typ}}} \times 10^{24}\,\mathrm{cm}^{-3}. \tag{7.25}$$

Inserting into Eq. 7.20, we obtain

$$\frac{l_{\gamma\gamma,\mathrm{Edd}}}{d_{\mathrm{e}}} \sim 2\times 10^{-5} \times \left(\frac{n_{\mathrm{e}}}{1\,\mathrm{cm}^{-3}}\right)^{1/2} \alpha^{-1} \left(\frac{R}{R_{\mathrm{S}}}\right)^2 \frac{R_{\mathrm{S}}}{10\,\mathrm{km}} \frac{h\nu_{\mathrm{typ}}}{1\,\mathrm{keV}}. \tag{7.26}$$

Consequently, close to the central object, for high luminosities and electron number densities that are not too high, pair creation will be very significant.

Chapter 8

Summary and perspectives

Est-il rien de plus surprenant
Qu'un rêveur qui demande au mystère tonnant,
À ces bleus firmaments où se croisent les sphères,
De lui conter à lui curieux leurs affaires,
Et qui veut avec l'ombre et le gouffre profond
Entrer en pourparlers pour savoir ce qu'ils font ?

Victor Hugo, *La Légende des siècles*, XLVI

The starting point of this thesis was the study of wind-accreting microquasar systems, such as Cygnus X-1, from large to small scales. The large scale dynamics is studied by our group with hydrodynamic or MHD simulations (Walder et al. 2014) that use an adaptive mesh to encompass scales from the circum-binary environment down to a few gravitational radii of the black hole. These simulations have shown a rich dynamics, with the wind accreted onto the black hole via a network of shocks, and with the intermittent formation of disk-like structures at smaller scales. However, a large fraction of the flow is collisionless with respect to reconnection or to shocks, and fluid simulations do not describe these phenomena at a fundamental level. For example, they do not include a non-thermal particle population produced at shocks or by reconnection, that can carry a significant fraction of the total energy, neither do they describe correctly the efficiency of reconnection to convert magnetic energy, or the way this energy is distributed between ions and electrons. Such effects are of paramount importance for the overall dynamics, for example to determine the heating of the disk corona, or to produce observable signatures via high-energy particle production and the subsequent radiation.

It was thus necessary to explore also the microphysics side. Magnetic reconnection in microquasar accretion flows is collisionless, relativistic, and occurs in ion-electron plasmas, but such a regime has never been studied so far. It naturally became the focus point of this thesis. Of course, it also has applications for the fundamental understanding of reconnection, and to several other astrophysical objects, like AGN coronae, extragalactic jets, radio galaxy lobes, and so on.

Now in this last short chapter, we summarize our main achievements, that concern both PIC algorithms and magnetic reconnection. We also mention outstanding perspectives.

8.1 Summary

The physics of reconnection and of relativistic plasmas

Before fully studying relativistic reconnection, we had to understand standard reconnection. It is a rich and passionating field, and our learnings led to the review Chapter 2.

We also had to understand specific aspects of relativistic plasmas, which are now gathered in Chapter 3. They include new material: properties of the relativistic thermal momentum distribution (the Maxwell-Jüttner distribution), how to correctly load this distribution in a PIC code, and the full relativistic Harris equilibrium. They also include known subjects, such as relativistic MHD waves, a derivation of the relativistic two-fluid equations from Vlasov's equation, or relativistic particle motion in constant fields.

Particle-in-cell algorithms: how do they model real plasmas?

The study of collisionless reconnection at a fundamental level requires the use of a kinetic code, and we chose the particle-in-cell method. Using a PIC code raises questions regarding the way by which it approximates the real plasma, and the first part of this thesis was dedicated to analyzing these discrepancies. This is the work exposed in Chapters 4 and 5.

The main approximations of the PIC model are the discretization of the fields on a grid, which implies that particles have a finite size, and the fact that the PIC plasma generally contains several billions less particles than the real plasma. We mainly focus on this last point, that we see as a coarse-graining step. Each PIC particle is a superparticle that represents $p \gg 1$ real particles. Any physics described by fluid equations does not depend on p: this is the case of MHD, two-fluid models, or of the Vlasov-Maxwell system. This last example indicates that physics described by Vlasov's equation, i.e, with no collisions and no correlations, can be well approached by a PIC code. There are, however, coarse-graining dependent quantities. This is the case of the plasma parameter – the number of particles per Debye sphere – and of any number of particles per fluid volume, which will be p times smaller in the PIC code. A major consequence is that collisions and fluctuations are artificially enhanced, by a factor $p \gg 1$, as compared to real plasmas.

We study this effect on specific examples. The thermalization time of two Maxwellian plasmas initially at two different temperatures scales linearly with the number of superparticles per cell, and is a factor $p \gg 1$ faster than for a real plasma. The level of electrostatic fluctuations in a thermal plasma decreases with the number of superparticles per Debye sphere, in a non-trivial way because of finite superparticle size, that we specify. This larger level of fluctuations, or noise, by a factor of the order of p as compared to a real plasma, has an impact on the linear phase of instabilities. In particular, for the filamentation instability, the fastest growing mode does not dominate the total energy, and the overall growth rate thus depends on the number of superparticles and on the resolution, with discrepancies reaching 50%. We underline that contrary to thermalization times, which are abnormally small or not compared to a given timescale, the level of fluctuation is an instantaneous property, that holds at any time.

All in all, a correct physical description by a PIC algorithm requires

enhanced collisional effects to be kept negligible compared to collisionless physics, and fluctuation levels to be kept at a low enough level. For example, thermalization should occur via collisionless instabilities, not via the enhanced level of collisions and fluctuations; or fast particles should not be significantly slowed down by the enhanced collisions throughout the duration of the simulation; or the competition between instabilities should not be biased by a large level of fluctuations. The best way to insure that collisionless physics dominates and that fluctuations are negligible remains to run the same simulation with different values for p, for example by varying the number of superparticles per cell.

Relativistic ion-electron magnetic reconnection

After a good understanding of the PIC algorithms as our method of study, came the study of magnetic reconnection. It is the work exposed in Chapters 6 and 7. We perform 2D PIC simulations of reconnection in ion-electron plasmas, that start from a Harris current sheet with no localized initial perturbation. We use relativistic inflow magnetizations, $\sigma_{\rm i}^{\rm hot} = 0.4$ to 14 and $\sigma_{\rm e}^{\rm hot} = 10$ to 260 for ions and electrons, respectively, with mass ratios $m_{\rm i}/m_{\rm e} = 1$ to 50.

In Chapter 6, we investigate the specificities of reconnection in the relativistic regime. We identify outstanding properties: (i) For relativistic inflow magnetizations (here $10 \leq \sigma_{\rm e} \leq 360$), the reconnection outflows are dominated by thermal agitation instead of bulk kinetic energy. (ii) At large inflow electron magnetization ($\sigma_{\rm e} \geq 80$), the reconnection electric field is sustained more by bulk inertia than by thermal inertia. It challenges the thermal-inertia paradigm and its implications. (iii) The inflows feature sharp transitions at the entrance of the diffusion zones. These are not shocks but result from particle ballistic motions, all bouncing at the same location, provided that the thermal velocity in the inflow is far lower than the inflow $E \times B$ bulk velocity. (iv) Island centers are magnetically isolated from the rest of the flow, and can present a density depletion at their center. (v) The reconnection rates are slightly larger than in non-relativistic studies. They are best normalized by the inflow relativistic Alfvén speed, projected in the outflow direction if there is a guide field, which then leads to rates in a close range (0.14–0.25), thus allowing for an easy estimation of the reconnection electric field.

In Chapter 7, we turn to the energetics of reconnection. We find that 45 to 75% of the total initial magnetic energy ends up in kinetic energy, this fraction increasing with the inflow magnetization. Depending on the guide field strength, ions get from 30 to 60% of the total kinetic energy (at $B_{\rm G}/B_0 = 0$ and 1, respectively). We show that it is essential to study separately the particles that are initially inside the current sheet, and those that are initially outside, because these two populations only weakly mix, undergo different acceleration mechanisms, and present very different particle distributions. The background population, formed by particles initially outside of the sheet that are continuously brought toward the current sheet, is expected to dominate the spectrum for long times. We find that this population forms power law distributions, both for electrons and ions, with indexes that depend both on the inflow magnetization of the considered species and on the inflow Alfvén speed. These indexes can be harder than for the case of collisionless shocks: for the electrons, $p = -{\rm d}\log n_{\rm e}(\gamma)/{\rm d}\log\gamma = 1.2$ at

$\sigma_{\rm e}^{\rm hot} = 260$. A criteria for a hard tail is a magnetization above 10, and an Alfvén speed close to c. For electrons, the latter condition implies an ion magnetization $\gtrsim 1$, and thus an electron magnetization larger than the mass ratio. The presence of a guide field deforms the power law shape.

We draw astrophysical consequences in Sects. 6.6.2 and 7.5.4. Our demonstration that magnetic reconnection can furnish power law distributed high-energy particles, either ions or electrons, has important applications for various models that assume with no prior justification the existence of such particle populations. In particular, the above criteria concerning magnetization and Alfvén speed must be fulfilled. Also, if plasma heating occurs via reconnection, then the almost equal energy repartition between ions and electrons that we found precludes the existence of large temperature differences.

8.2 Perspectives

The understanding of magnetic reconnection, of high-energy processes, and of large scale machines such as microquasars, remains partial. We will not review the many fundamental questions still to be addressed in the field of reconnection – why is it fast, what is the link with turbulence, how is it triggered... – but rather we list interrogations closely linked to our specific work which, as every contribution, answered and raised questions.

One of these questions regards the energy repartition between ions and electrons during reconnection events. Observations in the Earth's magnetosphere, in experimental devices, or non-relativistic kinetic simulations, suggest that ions are more heated than electrons. But for relativistic magnetizations, we find that this fact holds only in the absence of guide field, while with a guide field ions get less energy than electrons. Our results, if confirmed at realistic mass ratios, may help understanding why.

Another question concerns magnetic reconnection at extremely large magnetizations. We have probed regimes with electron magnetizations of several hundreds, and shown that the reconnection electric field is sustained more by bulk inertia than by thermal inertia. At even larger magnetizations, as can be encountered in pulsar nebulae, we predicted that bulk inertia should totally dominate. Reconnection in these regimes may bring surprises, and must be explored with relativistic gyrokinetic simulations. An even less clear regime is reached when pair production is important enough to alter the reconnection dynamics. This is a largely unexplored physical domain.

Another issue regards the formation of hard particle distributions. Our work agrees with that of Sironi and Spitkovsky (2014), which concerns pair plasmas: we equally find that the final power law index depends on the inflow magnetization (and Alfvén speed if we have ions instead of positrons), ranging in steady state from ~ 1 to very steep, with steady state meaning that a larger simulation gives the same result. However, the recent work of Guo et al. (2014) claims that a slope of 1 is reached whatever the initial magnetization, provided that the system is large enough and that particles cannot escape. The only difference between our simulations is that we and Sironi and Spitkovsky use a Harris initial state, while Guo et al. use a force-free initial state. The small guide field present in a force-free state may change the particle trajectories, and allow different acceleration mechanisms. In any case, these three works have clearly demonstrated that

relativistic reconnection efficiently produces hard particle distributions with slopes saturating at $p \sim 1$, in our own work also for ions, but the dependence of the hardness p on the external parameters and initial state (including also for asymmetric or 3D initializations) remains to be further explored.

It is also unclear whether the first-order Fermi mechanism can operate for particles bouncing between the convergent reconnection inflows. As we underlined, it requires pre-accelerated particles, that may or may not be present in a given environment. Dedicated kinetic simulations, with a background plasma containing such populations, should help to clarify the efficiency and the outcome of this process. In particular, the distance traveled by particles before being scattered back may be far larger than kinetic scales, so that collisions and drag could slow them down.

The fact that the three first large scale kinetic simulations addressing particle acceleration in relativistic reconnection – Sironi and Spitkovsky (2014), Melzani et al. (2014c), Guo et al. (2014) – were published within a few months by three independent groups, underlines the growing interest for these questions. The last decade has brought the realization that collisionless shocks are very common and are efficient particle accelerators. The same realization for collisionless magnetic reconnection is now becoming clear: collisionless reconnection is ubiquitous, and is very efficient in converting magnetic energy into non-thermal high-energy particles with hard distributions. Discovering how precisely, especially in 3D configurations, and at locations away from the central non-ideal region, are the next challenges to overtake. We may be helped in this task by the recent advent of laser experiments, which could allow an experimental study of relativistic reconnection (e.g., Ping et al. 2014).

This recent interest in collisionless reconnection is certainly motivated by the need of various models to find an efficient plasma heating mechanism and a non-thermal particle injector in relativistic magnetized environments, and by the recent discovery of high-energy flares: GeV from the Crab nebula, GeV-TeV from the base of extragalactic jets, and flares again in microquasar coronae. Understanding these systems where microphysics and large scale fluid dynamics are intimately coupled is another grand challenge. In particular, we must know which reconnection geometries are actually realized in a given system, and what is the reconnection feedback on the large scales. It may require the development of multi-scale multi-physics simulation tools, a path that several groups are starting to explore (e.g., Horiuchi et al. 2010; Innocenti et al. 2013; Daldorff et al. 2014). These high-energy systems may also be the progenitors of the very high-energy cosmic rays received on Earth, and also of the very high-energy extraterrestrial neutrinos recently detected by IceCube, whose origin is presently unknown. Solving the dark matter problem will require to know whether these high-energy particles originate from high-energy machines or not. What is the high-energy cut-off for ions, electrons, neutrinos or photons, and the corresponding flux, produced by microquasars, gamma-ray bursts, active galactic nuclei, extragalactic jets, magnetars, pulsar nebulae..., constitutes a cornerstone for answering one of this century's great enigma, in which reconnection will undoubtedly play a key role.

List of symbols

$\boldsymbol{B}$, $\boldsymbol{b}$	Magnetic field $\boldsymbol{B}$ and unit vector $\boldsymbol{b} = \boldsymbol{B}/B$
β	Ratio v/c; or plasma β, i.e., ratio of kinetic to magnetic pressures: $n_s T_s/(B^2/2\mu_0)$
c	Speed of light
d_s	Inertial length, or skin depth, of species s, $c/\omega_{\mathrm{p}s}$
D, D_s	Length of the diffusion region (of species s)
δ_s	Width of the diffusion region of species s
$\delta\boldsymbol{p}$	$\boldsymbol{p} - \bar{\boldsymbol{p}}$
$\delta\boldsymbol{v}$	$\boldsymbol{v} - \bar{\boldsymbol{v}}$
e	Absolute value of the electron charge
$\hat{e}_0$	Comoving gas internal energy per unit volume, $n_0\langle(\gamma - 1)mc^2\rangle_0$
E^*, R	Normalized reconnection rate, $E/(B_0 V_{\mathrm{A,in}}^{\mathrm{R}} \cos\theta)$, see Eqs. 6.14 and 6.22
ϵ_0	Vacuum permittivity
$\mathcal{E}_0$	Total initial energy in the area where particles reach the current sheet before the end of the simulation
f, f_s	Distribution function (for species s), in momentum and space
g, g_s	Distribution function (for species s), in momentum only, normalized to unity
G	Gravitational constant
Γ_s	Lorentz factor associated with the bulk velocity, $(1 - \bar{\boldsymbol{v}}_s^2/c^2)^{-1/2}$
γ	Lorentz factor of an individual particle
$\hat{\gamma}$	Adiabatic exponent
h, $\hbar$	Planck constant, reduced Planck constant
h_0, h_{0s}, h_s	Comoving enthalpy of the plasma (of species s)
K_n	Modified Bessel function of the nth kind
$\kappa_{ij}(x)$	Ratio $K_i(x)/K_j(x)$
l_{mfp}	Mean free path for collisions
$l_{\boldsymbol{\nabla}B}$	Gradient scale of the magnetic field
L	Length of the current sheet in Harris equilibrium
L_{Edd}	Eddington luminosity, $4\pi GMm_{\mathrm{i}}c/\sigma_{\mathrm{T}}$
λ_{De}	Electron Debye length, $\sqrt{\epsilon_0 T_{\mathrm{e}}/(n_{\mathrm{e}}e^2)} = v_{\mathrm{th,e}}/\omega_{\mathrm{pe}}$
Λ	Plasma parameter, $n_{\mathrm{e}}\lambda_{\mathrm{De}}^3$
Λ_p, Λ^{PIC}	Plasma parameter of the PIC plasma with p real particles per superparticles, $\rho_{\mathrm{sp}}(n_x v_{\mathrm{th}}/c)^3 = \Lambda/p$
$M_\odot$	Solar mass, $1.989 \times 10^{30}\,\mathrm{kg}$
m_s, m_{e}, m_{i}	Mass of species s, with $s = \mathrm{i}$ for ions, $s = \mathrm{e}$ for electrons
μ_0	Vacuum permeability
μ_s	Inverse of the normalized temperature, $1/\Theta_s = m_s c^2/T_s$

n_t	Number of timesteps per plasma period $T_{\rm pe}$, defined with the initial electron density
n_x	Number of cells per initial electron inertial length
$n_{\rm cs}(0)$	Plasma number density at the center of the current sheet, at $t = 0$, for electrons or ions
$n_{\rm bg}$	Plasma number density in the background plasma, of electrons or of ions
$\omega_{\rm P}$	Total plasma pulsation, $(\omega_{\rm pe}^2 + \omega_{\rm pi}^2)^{1/2}$
$\omega_{{\rm p}s}$	Plasma pulsation of species s, $\sqrt{n_s q_s^2/(\epsilon_0 m_s)}$
$\omega_{{\rm c}s}$	Cyclotron pulsation (non-relativistic) of a particle of species s, $\lvert q_s\rvert B/m_s$
$\omega_c^{\rm R}$	Cyclotron pulsation (relativistic expression), $\lvert q\rvert B/(\gamma m)$
p	Number of particles of the real plasma represented by a single superparticle; or power law index of the particle distribution, $p = -{\rm d}\log n(\gamma)/{\rm d}\log\gamma$
$\boldsymbol{p}$	Momentum of a particle without the mass, $\gamma\boldsymbol{v}$, except in Sects. 3.6 and 3.B where it denotes $\gamma m\boldsymbol{v}$, and except in Sect. 3.8 where it denotes $\gamma\boldsymbol{v}/c$
$\tilde{\boldsymbol{p}}$	Normalized momentum of a particle, $\gamma\boldsymbol{v}/c$
$\hat{\boldsymbol{p}}$	Momentum of a particle, $\gamma m\boldsymbol{v}$
$\bar{\boldsymbol{p}}_s$, $\langle\boldsymbol{p}\rangle_s$	Fluid momentum for species s, average of $\boldsymbol{p} = \gamma\boldsymbol{v}$ over the distribution function f_s
P, P_s	Comoving pressure (for species s)
q_s	Charge of particle of species s
r_0	Classical electron radius, $e^2/(4\pi\epsilon_0 m_{\rm e}c^2) = 2.8\times10^{-15}\,{\rm m}$
$r_{{\rm c}s}$	Larmor radius of particle of species s, $\gamma v_\perp/(\lvert q_s\rvert B/m_s)$ for one particle, while a thermal velocity has to be chosen if it is the thermal Larmor radius
$R_{\rm S}$	Schwarzschild radius, $2GM/c^2$
$\rho_{\rm sp}$, $\rho_{\rm sp}^0$	Number of superparticles per cell, including electron superparticles and ion superparticles
$S_{\rm L}$	Lundquist number, $\mu_0 L V_{\rm A}/\eta$
$\sigma_s^{\rm cold}(B)$	Magnetization of species s, without taking into account the temperature or bulk motion, see Eq. 6.5
$\sigma_s^{\rm hot}(B)$	Magnetization of species s, taking into account the temperature and the bulk motion, see Eq. 6.4
$\sigma_{\rm i+e}(B)$	Magnetization of the plasma (including ions and electrons), taking into account temperature and bulk motion, see Eq. 6.6
$\sigma_{\rm T}$	Thomson cross section, $(8\pi/3)r_0^2 = 0.67\times10^{-24}\,{\rm cm}^2$
T_s	Temperature of species s, in energy unit, $k_{\rm B}\times$ temperature in Kelvin
$T_{\rm bg}$, $T_{{\rm bg},s}$	Temperature of species s in the background plasma, in energy units
Θ, Θ_s	Normalized temperature, $T_s/(m_s c^2)$
U_s	Fluid velocity for species s, average of $\boldsymbol{v}$ over the distribution function g_s
$v_{{\rm th},s}$	Thermal velocity of species s, $\sqrt{T_s/m_s}$
$v_{E\times B}$	E cross B velocity, $\boldsymbol{E}\wedge\boldsymbol{B}/B^2$
$\bar{\boldsymbol{v}}_s$, $\langle\boldsymbol{v}\rangle_s$	Fluid velocity for species s, average of $\boldsymbol{v}$ over the distribution function g_s
$V_{\rm A,in}^{\rm NR}$	Alfvén velocity, non-relativistic expression, defined in the asymptotic inflow, see Eq. 6.7a

$V_{\mathrm{A,in}}^{\mathrm{R}}$	Alfvén velocity, relativistic expression, defined in the asymptotic inflow, see Eq. 6.7b
$V_{\mathrm{A},0}^{\mathrm{NR}}$	Alfvén velocity, non-relativistic expression, defined with the asymptotic magnetic field and the density at the center of the current sheet, see Eq. 6.8
$V_{\mathrm{A},0}^{\mathrm{R}}$	Alfvén velocity, relativistic expression, counterpart of $V_{\mathrm{A},0}^{\mathrm{NR}}$
w_0	Comoving gas enthalpy, $h_0 n_0 mc^2$

List of Figures

List of Tables

Index

Bibliography

Alfvén, H. (1942), "Existence of Electromagnetic-Hydrodynamic Waves", *Nature* 150, pp. 405–406, DOI: 10.1038/150405d0, URL: http://adsabs.harvard.edu/abs/1942Natur.150..405A.

Alfvén, H. (1976), "On frozen-in field lines and field-line reconnection", *Journal of Geophysical Research* 81.22, pp. 4019–4021, ISSN: 2156-2202, DOI: 10.1029/JA081i022p04019, URL: http://dx.doi.org/10.1029/JA081i022p04019.

Appleton, E. V. (1947), "The Ionosphere", *Nobel Lectures*, URL: http://www.nobelprize.org/nobel_prizes/physics/laureates/1947/appleton-lecture.html.

Atoyan, A. M. and F. A. Aharonian (1996), "On the fluxes of inverse Compton gamma-rays expected from the Crab Nebula.", *A&A Sup. Series* 120, p. C453, URL: http://adsabs.harvard.edu/abs/1996A\%26AS..120C.453A.

Aunai, N., M. Hesse, S. Zenitani, M. Kuznetsova, C. Black, R. Evans, and R. Smets (2013), "Comparison between hybrid and fully kinetic models of asymmetric magnetic reconnection: Coplanar and guide field configurations", *Physics of Plasmas* 20.2, p. 022902, DOI: 10.1063/1.4792250, arXiv: 1302.0506, URL: http://adsabs.harvard.edu/abs/2013PhPl...20b2902A.

Barkov, M., S. S. Komissarov, V. Korolev, and A. Zankovich (2014), "A multidimensional numerical scheme for two-fluid relativistic magnetohydrodynamics", *MNRAS* 438, pp. 704–716, DOI: 10.1093/mnras/stt2247, arXiv: 1309.5221, URL: http://adsabs.harvard.edu/abs/2014MNRAS.438..704B.

Baty, H., E. R. Priest, and T. G. Forbes (2006), "Effect of nonuniform resistivity in Petschek reconnection", *Physics of Plasmas* 13.2, p. 022312, DOI: 10.1063/1.2172543, URL: http://adsabs.harvard.edu/abs/2006PhPl...13b2312B.

Baty, H., J. Petri, and S. Zenitani (2013), "Explosive reconnection of double tearing modes in relativistic plasmas: application to the Crab flares", *MNRAS* 436, pp. L20–L24, DOI: 10.1093/mnrasl/slt104, arXiv: 1308.0906, URL: http://adsabs.harvard.edu/abs/2013MNRAS.436L..20B.

Baumann, G. and Å. Nordlund (2012), "Particle-in-cell Simulation of Electron Acceleration in Solar Coronal Jets", *Astrophysical Journal* 759, L9, p. L9, DOI: 10.1088/2041-8205/759/1/L9, arXiv: 1205.3486, URL: http://adsabs.harvard.edu/abs/2012ApJ...759L...9B.

Bednarek, W. and W. Idec (2011), "On the variability of the GeV and multi-TeV gamma-ray emission from the Crab nebula", *MNRAS* 414, pp. 2229–2234, DOI: 10.1111/j.1365-2966.2011.18539.x, arXiv: 1011.4176, URL: http://cdsads.u-strasbg.fr/abs/2011MNRAS.414.2229B.

Begelman, M. and M. Rees (2009), *Gravity's Fatal Attraction*, ed. by Begelman, M. & Rees, M., URL: http://adsabs.harvard.edu/abs/2009gfa..book.....B.

Bell, A. R. (1978), "The acceleration of cosmic rays in shock fronts. I", *MNRAS* 182, pp. 147–156, URL: http://adsabs.harvard.edu/abs/1978MNRAS.182..147B.

Bellan, P. M. (2006), *Fundamentals of Plasma Physics*, ed. by Bellan, P. M., URL: http://adsabs.harvard.edu/abs/2006fpp..book.....B.

Belmont, G., N. Aunai, and R. Smets (2012), "Kinetic equilibrium for an asymmetric tangential layer", *Physics of Plasmas* 19.2, 022108, p. 022108, DOI: 10.1063/1.3685707, URL: http://adsabs.harvard.edu/abs/2012PhPl...19b2108B.

Belmont, G., R. Grappin, F. Mottez, F. Pantellini, and G. Pelletier (2014), *Collisionless Plasmas in Astrophysics*, ed. by Wiley-VCH.

Benedetti, C., A. Sgattoni, G. Turchetti, and P. Londrillo (2008), "ALaDyn: A High-Accuracy PIC Code for the Maxwell Vlasov Equations", *IEEE Transactions on Plasma Science* 36, pp. 1790–1798, DOI: 10.1109/TPS.2008.927143, URL: http://adsabs.harvard.edu/abs/2008ITPS...36.1790B.

Bessho, N. and A. Bhattacharjee (2005), "Collisionless Reconnection in an Electron-Positron Plasma", *Physical Review Letters* 95.24, 245001, p. 245001, DOI: 10.1103/PhysRevLett.95.245001, URL: http://adsabs.harvard.edu/abs/2005PhRvL..95x5001B.

Bessho, N. and A. Bhattacharjee (2012), "Fast Magnetic Reconnection and Particle Acceleration in Relativistic Low-density Electron-Positron Plasmas without Guide Field", *The Astrophysical Journal* 750.2, p. 129, URL: http://stacks.iop.org/0004-637X/750/i=2/a=129.

Birdsall, C. K. (1967), "Computer Experiments with Charged Particles, Charged Fluids and Plasmas: a Classification and Bibliography", *NASA Special Publication* 153, p. 375, URL: http://adsabs.harvard.edu/abs/1967NASSP.153..375B.

— (1999), "Pioneering in Plasma Simulation", in: *Dynamical Systems, Plasmas and Gravitation*, ed. by P. G. L. Leach, S. E. Bouquet, J.-L. Rouet, and E. Fijalkow, vol. 518, Lecture Notes in Physics, Berlin Springer Verlag, p. 383, DOI: 10.1007/BFb0105944, URL: http://adsabs.harvard.edu/abs/1999LNP...518..383B.

Birk, G. T., A. R. Crusius-Wätzel, and H. Lesch (2001), "Hard Radio Spectra from Reconnection Regions in Galactic Nuclei", *APJ* 559, pp. 96–100, DOI: 10.1086/322394, eprint: arXiv:astro-ph/0106565, URL: http://adsabs.harvard.edu/abs/2001ApJ...559...96B.

Birn, J. and E. R. Priest (2007), *Reconnection of magnetic fields : magnetohydrodynamics and collisionless theory and observations*, URL: http://adsabs.harvard.edu/abs/2007rmfm.book.....B.

Birn, J., J. F. Drake, M. A. Shay, B. N. Rogers, R. E. Denton, M. Hesse, M. Kuznetsova, Z. W. Ma, A. Bhattacharjee, A. Otto, and P. L. Pritchett (2001), "Geospace Environmental Modeling (GEM) magnetic reconnection challenge", *J. Geoph. Research* 106, pp. 3715–3720, DOI: 10.1029/1999JA900449, URL: http://adsabs.harvard.edu/abs/2001JGR...106.3715B.

Birsdall, C. and A. Langdon (1985), *Plasma Physics via Computer Simulation*, ed. by McGraw-Hill, New-York.

Biskamp, D. (2000), *Magnetic Reconnection in Plasmas*, ed. by Biskamp, D., URL: http://adsabs.harvard.edu/abs/2000mrp..book.....B.

Blackman, E. G. and G. B. Field (1994), "Kinematics of relativistic magnetic reconnection", *Physical Review Letters* 72, pp. 494–497, DOI: 10.1103/PhysRevLett.72.494, URL: http://adsabs.harvard.edu/abs/1994PhRvL..72..494B.

Boozer, A. H. (2013), "Model of magnetic reconnection in space and astrophysical plasmas", *Physics of Plasmas (1994-present)* 20.3, 032903, pp. –, DOI: http://dx.doi.org/10.1063/1.4796051, URL: http://scitation.aip.org/content/aip/journal/pop/20/3/10.1063/1.4796051.

Borovsky, J. E. and M. Hesse (2007), "The reconnection of magnetic fields between plasmas with different densities: Scaling relations", *Physics of Plasmas* 14.10, p. 102309, DOI: 10.1063/1.2772619, URL: http://adsabs.harvard.edu/abs/2007PhPl...14j2309B.

Bosch-Ramon, V. (2012), "Fermi I particle acceleration in converging flows mediated by magnetic reconnection", *A&A* 542, A125, A125, DOI: 10.1051/0004-6361/201219231, arXiv: 1205.3450, URL: http://cdsads.u-strasbg.fr/abs/2012A%26A...542A.125B.

Bret, A., L. Gremillet, and M. E. Dieckmann (2010), "Multidimensional electron beam-plasma instabilities in the relativistic regime", *Physics of Plasmas* 17.12, p. 120501, DOI: 10.1063/1.3514586, URL: http://adsabs.harvard.edu/abs/2010PhPl...17l0501B.

Bret, A., A. Stockem, F. Fiuza, C. Ruyer, L. Gremillet, R. Narayan, and L. O. Silva (2013), "Collisionless shock formation, spontaneous electromagnetic fluc-

tuations, and streaming instabilities", *Physics of Plasmas* 20.4, p. 042102, DOI: 10.1063/1.4798541, arXiv: 1303.4095, URL: http://adsabs.harvard.edu/abs/2013PhPl...20d2102B.

Bucciantini, N., J. Arons, and E. Amato (2011), "Modelling spectral evolution of pulsar wind nebulae inside supernova remnants", *MNRAS* 410, pp. 381–398, DOI: 10.1111/j.1365-2966.2010.17449.x, URL: http://adsabs.harvard.edu/abs/2011MNRAS.410..381B.

Bulanov, S. V. and P. V. Sasorov (1976), "Energy spectrum of particles accelerated in the neighborhood of a line of zero magnetic field", *Soviet. Astron.* 19, pp. 464–468, URL: http://adsabs.harvard.edu/abs/1976SvA....19..464B.

Buneman, O. (1959), "Dissipation of Currents in Ionized Media", *Physical Review* 115, pp. 503–517, DOI: 10.1103/PhysRev.115.503, URL: http://adsabs.harvard.edu/abs/1959PhRv..115..503B.

— (1976), "The advance from 2D electrostatic to 3D electromagnetic particle simulation", *Computer Physics Communications* 12, p. 21, DOI: 10.1016/0010-4655(76)90007-2, URL: http://adsabs.harvard.edu/abs/1976CoPhC..12...21B.

Burger, P. (1965), "Theory of Large-Amplitude Oscillations in the One-Dimensional Low-Pressure Cesium Thermionic Converter", *Journal of Applied Physics* 36, pp. 1938–1943, DOI: 10.1063/1.1714378, URL: http://adsabs.harvard.edu/abs/1965JAP....36.1938B.

Bykov, A. M. and R. A. Treumann (2011), "Fundamentals of collisionless shocks for astrophysical application, 2. Relativistic shocks", *Astronomy and Astrophysics Review* 19, p. 42, DOI: 10.1007/s00159-011-0042-8, arXiv: 1105.3221, URL: http://adsabs.harvard.edu/abs/2011A%26ARv..19...42B.

Callen, J. (1990), *Plasma kinetic theory and radiation processes*, URL: http://homepages.cae.wisc.edu/~callen/NEEP725_89.pdf.

— (2006), *Fundamentals of Plasma Physics*, URL: http://homepages.cae.wisc.edu/~callen/book.html.

Carrington, R. C. (1859), "Description of a Singular Appearance seen in the Sun on September 1, 1859", *MNRAS* 20, pp. 13–15, URL: http://adsabs.harvard.edu/abs/1859MNRAS..20...13C.

Cassak, P. A. and M. A. Shay (2007), "Scaling of asymmetric magnetic reconnection: General theory and collisional simulations", *Physics of Plasmas* 14.10, p. 102114, DOI: 10.1063/1.2795630, URL: http://adsabs.harvard.edu/abs/2007PhPl...14j2114C.

Cerutti, B., G. R. Werner, D. A. Uzdensky, and M. C. Begelman (2012a), "Beaming and Rapid Variability of High-energy Radiation from Relativistic Pair Plasma Reconnection", *Astrophysical Journal* 754, L33, p. L33, DOI: 10.1088/2041-8205/754/2/L33, arXiv: 1205.3210, URL: http://adsabs.harvard.edu/abs/2012ApJ...754L..33C.

Cerutti, B., D. A. Uzdensky, and M. C. Begelman (2012b), "Extreme Particle Acceleration in Magnetic Reconnection Layers: Application to the Gamma-Ray Flares in the Crab Nebula", *APJ* 746, 148, p. 148, DOI: 10.1088/0004-637X/746/2/148, arXiv: 1110.0557, URL: http://adsabs.harvard.edu/abs/2012ApJ...746..148C.

Cerutti, B., G. R. Werner, D. A. Uzdensky, and M. C. Begelman (2013), "Simulations of Particle Acceleration beyond the Classical Synchrotron Burnoff Limit in Magnetic Reconnection: An Explanation of the Crab Flares", *APJ* 770, 147, p. 147, DOI: 10.1088/0004-637X/770/2/147, arXiv: 1302.6247, URL: http://adsabs.harvard.edu/abs/2013ApJ...770..147C.

— (2014a), "Gamma-ray flares in the Crab Nebula: A case of relativistic reconnection?", *ArXiv e-prints*, arXiv: 1401.3016, URL: http://adsabs.harvard.edu/abs/2014arXiv1401.3016C.

— (2014b), "Three-dimensional Relativistic Pair Plasma Reconnection with Radiative Feedback in the Crab Nebula", *APJ* 782, 104, p. 104, DOI: 10.1088/0004-637X/782/2/104, arXiv: 1311.2605, URL: http://adsabs.harvard.edu/abs/2014ApJ...782..104C.

Chacón-Acosta, G., L. Dagdug, and H. A. Morales-Técotl (2010), "Manifestly covariant Jüttner distribution and equipartition theorem", *Phys. Rev. E* 81.2, 021126, p. 021126, DOI: 10.1103/PhysRevE.81.021126, arXiv: 0910.1625, URL: http://adsabs.harvard.edu/abs/2010PhRvE..81b1126C.

Chapman, S. and V. C. A. Ferraro (1930), "A New Theory of Magnetic Storms.", *Nature* 126, pp. 129–130, DOI: 10.1038/126129a0, URL: http://adsabs.harvard.edu/abs/1930Natur.126..129C.

Chen, L.-J., W. S. Daughton, B. Lefebvre, and R. B. Torbert (2011), "The inversion layer of electric fields and electron phase-space-hole structure during two-dimensional collisionless magnetic reconnection", *Physics of Plasmas* 18.1, p. 012904, DOI: 10.1063/1.3529365, URL: http://adsabs.harvard.edu/abs/2011PhPl...18a2904C.

Childs, H., E. Brugger, B. Whitlock, J. Meredith, S. Ahern, K. Bonnell, M. Miller, G. H. Weber, C. Harrison, D. Pugmire, T. Fogal, C. Garth, A. Sanderson, E. W. Bethel, M. Durant, D. Camp, J. M. Favre, O. Rübel, and P. Navrátil (2012), "VisIt: An End-User Tool For Visualizing and Analyzing Very Large Data", in: *High Performance Visualization—Enabling Extreme-Scale Scientific Insight*, pp. 357–372.

Coppi, B., G. Laval, and R. Pellat (1966), "Dynamics of the Geomagnetic Tail", *Physical Review Letters* 16, pp. 1207–1210, DOI: 10.1103/PhysRevLett.16.1207, URL: http://adsabs.harvard.edu/abs/1966PhRvL..16.1207C.

Cottrill, L. A., A. B. Langdon, B. F. Lasinski, S. M. Lund, K. Molvig, M. Tabak, R. P. J. Town, and E. A. Williams (2008), "Kinetic and collisional effects on the linear evolution of fast ignition relevant beam instabilities", *Physics of Plasmas* 15.8, p. 082108, DOI: 10.1063/1.2953816, URL: http://adsabs.harvard.edu/abs/2008PhPl...15h2108C.

Cubero, D., J. Casado-Pascual, J. Dunkel, P. Talkner, and P. Hänggi (2007), "Thermal Equilibrium and Statistical Thermometers in Special Relativity", *Physical Review Letters* 99.17, 170601, p. 170601, DOI: 10.1103/PhysRevLett.99.170601, arXiv: 0705.3328, URL: http://adsabs.harvard.edu/abs/2007PhRvL..99q0601C.

Daldorff, L. K. S., G. Tóth, T. I. Gombosi, G. Lapenta, J. Amaya, S. Markidis, and J. U. Brackbill (2014), "Two-way coupling of a global Hall magnetohydrodynamics model with a local implicit particle-in-cell model", *Journal of Computational Physics* 268, pp. 236–254, DOI: 10.1016/j.jcp.2014.03.009, URL: http://cdsads.u-strasbg.fr/abs/2014JCoPh.268..236D.

Daughton, W. (2002), "Nonlinear dynamics of thin current sheets", *Physics of Plasmas* 9, pp. 3668–3678, DOI: 10.1063/1.1499118, URL: http://adsabs.harvard.edu/abs/2002PhPl....9.3668D.

Daughton, W. and H. Karimabadi (2007), "Collisionless magnetic reconnection in large-scale electron-positron plasmas", *Physics of Plasmas* 14.7, p. 072303, DOI: 10.1063/1.2749494, URL: http://adsabs.harvard.edu/abs/2007PhPl...14g2303D.

Daughton, W. and V. Roytershteyn (2012), "Emerging Parameter Space Map of Magnetic Reconnection in Collisional and Kinetic Regimes", *Space Science Review* 172, pp. 271–282, DOI: 10.1007/s11214-011-9766-z, URL: http://cdsads.u-strasbg.fr/abs/2012SSRv..172..271D.

Daughton, W., J. Scudder, and H. Karimabadi (2006), "Fully kinetic simulations of undriven magnetic reconnection with open boundary conditions", *Physics of Plasmas* 13.7, p. 072101, DOI: 10.1063/1.2218817, URL: http://adsabs.harvard.edu/abs/2006PhPl...13g2101D.

Daughton, W., V. Roytershteyn, B. J. Albright, H. Karimabadi, L. Yin, and K. J. Bowers (2009a), "Influence of Coulomb collisions on the structure of reconnection layers", *Physics of Plasmas* 16.7, p. 072117, DOI: 10.1063/1.3191718, URL: http://cdsads.u-strasbg.fr/abs/2009PhPl...16g2117D.

— (2009b), "Transition from collisional to kinetic regimes in large-scale reconnection layers", *Physical Review Letters* 103.6, 065004, p. 065004, DOI: 10.

1103/PhysRevLett.103.065004, URL: http://cdsads.u-strasbg.fr/abs/2009PhRvL.103f5004D.

Daughton, W., V. Roytershteyn, H. Karimabadi, L. Yin, B. J. Albright, B. Bergen, and K. J. Bowers (2011), "Role of electron physics in the development of turbulent magnetic reconnection in collisionless plasmas", *Nature Physics* 7, pp. 539–542, DOI: 10.1038/nphys1965, URL: http://adsabs.harvard.edu/abs/2011NatPh...7..539D.

Dawson, J. (1962), "One-Dimensional Plasma Model", *Physics of Fluids* 5, pp. 445–459, DOI: 10.1063/1.1706638, URL: http://adsabs.harvard.edu/abs/1962PhFl....5..445D.

de Gouveia dal Pino, E. M. and A. Lazarian (2005), "Production of the large scale superluminal ejections of the microquasar GRS 1915+105 by violent magnetic reconnection", *A&A* 441, pp. 845–853, DOI: 10.1051/0004-6361:20042590, URL: http://adsabs.harvard.edu/abs/2005A%26A...441..845D.

de Gouveia Dal Pino, E. M., P. P. Piovezan, and L. H. S. Kadowaki (2010), "The role of magnetic reconnection on jet/accretion disk systems", *A&A* 518, A5, A5, DOI: 10.1051/0004-6361/200913462, arXiv: 1005.3067, URL: http://adsabs.harvard.edu/abs/2010A%26A...518A...5D.

Del Santo, M., J. Malzac, R. Belmont, L. Bouchet, and G. De Cesare (2013), "The magnetic field in the X-ray corona of Cygnus X-1", *MNRAS* 430, pp. 209–220, DOI: 10.1093/mnras/sts574, arXiv: 1212.2040, URL: http://adsabs.harvard.edu/abs/2013MNRAS.430..209D.

Dexter, J., J. C. McKinney, S. Markoff, and A. Tchekhovskoy (2014), "Transient jet formation and state transitions from large-scale magnetic reconnection in black hole accretion discs", *MNRAS* 440, pp. 2185–2190, DOI: 10.1093/mnras/stu581, arXiv: 1312.1691, URL: http://cdsads.u-strasbg.fr/abs/2014MNRAS.440.2185D.

Di Matteo, T. (1998), "Magnetic reconnection: flares and coronal heating in active galactic nuclei", *MNRAS* 299, p. L15, DOI: 10.1046/j.1365-8711.1998.01950.x, eprint: arXiv:astro-ph/9805347, URL: http://adsabs.harvard.edu/abs/1998MNRAS.299L..15D.

Di Matteo, T., E. G. Blackman, and A. C. Fabian (1997), "Two-temperature coronae in active galactic nuclei", *MNRAS* 291, pp. L23–L27, eprint: astro-ph/9705079, URL: http://adsabs.harvard.edu/abs/1997MNRAS.291L..23D.

Díaz María, T., J. C. A. Miller-Jones, S. Migliari, J. W. Broderick, and T. Tzioumis (2013), "Baryons in the relativistic jets of the stellar-mass black-hole candidate 4U1630-47", *Nature* 504, pp. 260–262, DOI: 10.1038/nature12672, URL: http://cdsads.u-strasbg.fr/abs/2013Natur.504..260D.

Dieckmann, M. E. (2009), "The filamentation instability driven by warm electron beams: statistics and electric field generation", *Plasma Physics and Controlled Fusion* 51.12, p. 124042, DOI: 10.1088/0741-3335/51/12/124042, arXiv: 0910.0228, URL: http://adsabs.harvard.edu/abs/2009PPCF...5114042D.

Dieckmann, M. E., A. Ynnerman, S. C. Chapman, G. Rowlands, and N. Andersson (2004), "Simulating Thermal Noise", *Phys. Scripta* 69, p. 456, DOI: 10.1238/Physica.Regular.069a00456, URL: http://adsabs.harvard.edu/abs/2004PhyS...69..456D.

Dieckmann, M. E., J. T. Frederiksen, A. Bret, and P. K. Shukla (2006), "Evolution of the fastest-growing relativistic mixed mode instability driven by a tenuous plasma beam in one and two dimensions", *Physics of Plasmas* 13.11, p. 112110, DOI: 10.1063/1.2390687, URL: http://adsabs.harvard.edu/abs/2006PhPl...13k2110D.

Drake, J. F., M. A. Shay, W. Thongthai, and M. Swisdak (2005), "Production of Energetic Electrons during Magnetic Reconnection", *Phys. Rev. Lett.* 94 (9), p. 095001, DOI: 10.1103/PhysRevLett.94.095001, URL: http://link.aps.org/doi/10.1103/PhysRevLett.94.095001.

Drake, J. F., M. Swisdak, H. Che, and M. A. Shay (2006), "Electron acceleration from contracting magnetic islands during reconnection", *Nature* 443, pp. 553–

556, DOI: 10.1038/nature05116, URL: http://adsabs.harvard.edu/abs/2006Natur.443..553D.

Drake, J. F., P. A. Cassak, M. A. Shay, M. Swisdak, and E. Quataert (2009a), "A Magnetic Reconnection Mechanism for Ion Acceleration and Abundance Enhancements in Impulsive Flares", *Astrophysical Journal* 700, pp. L16–L20, DOI: 10.1088/0004-637X/700/1/L16, URL: http://adsabs.harvard.edu/abs/2009ApJ...700L..16D.

Drake, J. F., M. Swisdak, T. D. Phan, P. A. Cassak, M. A. Shay, S. T. Lepri, R. P. Lin, E. Quataert, and T. H. Zurbuchen (2009b), "Ion heating resulting from pickup in magnetic reconnection exhausts", *Journal of Geophysical Research (Space Physics)* 114, A05111, p. 5111, DOI: 10.1029/2008JA013701, URL: http://cdsads.u-strasbg.fr/abs/2009JGRA..114.5111D.

Drake, J. F., M. Opher, M. Swisdak, and J. N. Chamoun (2010), "A Magnetic Reconnection Mechanism for the Generation of Anomalous Cosmic Rays", *APJ* 709, pp. 963–974, DOI: 10.1088/0004-637X/709/2/963, arXiv: 0911.3098, URL: http://adsabs.harvard.edu/abs/2010ApJ...709..963D.

Drenkhahn, G. and H. C. Spruit (2002), "Efficient acceleration and radiation in Poynting flux powered GRB outflows", *A&A* 391, pp. 1141–1153, DOI: 10.1051/0004-6361:20020839, eprint: arXiv:astro-ph/0202387, URL: http://adsabs.harvard.edu/abs/2002A%26A...391.1141D.

Drury, L. O. (2012), "First-order Fermi acceleration driven by magnetic reconnection", *MNRAS*, p. 2661, DOI: 10.1111/j.1365-2966.2012.20804.x, arXiv: 1201.6612, URL: http://arxiv.org/abs/1201.6612.

Dungey, J. W. (1958), "The Neutral Point Discharge Theory of Solar Flares. a Reply to Cowling's Criticism", in: *Electromagnetic Phenomena in Cosmical Physics*, ed. by B. Lehnert, vol. 6, IAU Symposium, p. 135, URL: http://adsabs.harvard.edu/abs/1958IAUS....6..135D.

— (1961), "Interplanetary Magnetic Field and the Auroral Zones", *Physical Review Letters* 6, pp. 47–48, DOI: 10.1103/PhysRevLett.6.47, URL: http://adsabs.harvard.edu/abs/1961PhRvL...6...47D.

Dunkel, J. and P. Hänggi (2009), "Relativistic Brownian motion", *physrep* 471, pp. 1–73, DOI: 10.1016/j.physrep.2008.12.001, arXiv: 0812.1996, URL: http://adsabs.harvard.edu/abs/2009PhR...471....1D.

Eastwood, J. P., T. D. Phan, M. Øieroset, M. A. Shay, K. Malakit, M. Swisdak, J. F. Drake, and A. Masters (2013), "Influence of asymmetries and guide fields on the magnetic reconnection diffusion region in collisionless space plasmas", *Plasma Physics and Controlled Fusion* 55.12, 124001, p. 124001, DOI: 10.1088/0741-3335/55/12/124001, URL: http://adsabs.harvard.edu/abs/2013PPCF...55l4001E.

Egedal, J., W. Fox, N. Katz, M. Porkolab, M. ØIeroset, R. P. Lin, W. Daughton, and J. F. Drake (2008), "Evidence and theory for trapped electrons in guide field magnetotail reconnection", *Journal of Geophysical Research (Space Physics)* 113, A12207, p. 12207, DOI: 10.1029/2008JA013520, URL: http://cdsads.u-strasbg.fr/abs/2008JGRA..11312207E.

Egedal, J., W. Daughton, J. F. Drake, N. Katz, and A. Lê (2009), "Formation of a localized acceleration potential during magnetic reconnection with a guide field", *Physics of Plasmas* 16.5, p. 050701, DOI: 10.1063/1.3130732, URL: http://adsabs.harvard.edu/abs/2009PhPl...16e0701E.

Egedal, J., W. Daughton, and A. Le (2012), "Large-scale electron acceleration by parallel electric fields during magnetic reconnection", *Nature Physics* 8, pp. 321–324, DOI: 10.1038/nphys2249, URL: http://adsabs.harvard.edu/abs/2012NatPh...8..321E.

Eldridge, O. C. and M. Feix (1962), "One-Dimensional Plasma Model at Thermodynamic Equilibrium", *Physics of Fluids* 5, pp. 1076–1080, DOI: 10.1063/1.1724476, URL: http://adsabs.harvard.edu/abs/1962PhFl....5.1076E.

Eriksson, S., M. ØIeroset, D. N. Baker, C. Mouikis, A. Vaivads, M. W. Dunlop, H. RèMe, R. E. Ergun, and A. Balogh (2004), "Walén and slow-mode shock analyses in the near-Earth magnetotail in connection with a substorm onset on 27

August 2001", *Journal of Geophysical Research (Space Physics)* 109, A10212, p. 10212, DOI: 10.1029/2004JA010534, URL: http://adsabs.harvard.edu/abs/2004JGRA..10910212E.

Esirkepov, T. Z. (2001), "Exact charge conservation scheme for Particle-in-Cell simulation with an arbitrary form-factor", *Computer Physics Communications* 135, pp. 144–153, DOI: 10.1016/S0010-4655(00)00228-9, URL: http://adsabs.harvard.edu/abs/2001CoPhC.135..144E.

Fitzpatrick, R. (2011), *The Physics of Plasmas*, URL: http://farside.ph.utexas.edu/teaching/plasma/plasma.html.

Fonseca, R. A., L. O. Silva, F. S. Tsung, V. K. Decyk, W. Lu, R. C., W. B. Mori, S. Deng, S. Lee, and T. e. a. Katsouleas (2002), "OSIRIS: A Three-Dimensional, Fully Relativistic Particle in Cell Code for Modeling Plasma Based Accelerators", *Lecture Notes in Computer Science* 2331, pp. 342–351, DOI: 10.1007/3-540-47789-6_36, URL: http://www.springerlink.com/content/0p7ulb2dm944lglq/.

Fonseca, R. A., S. F. Martins, L. O. Silva, J. W. Tonge, F. S. Tsung, and W. B. Mori (2008), "One-to-one direct modeling of experiments and astrophysical scenarios: pushing the envelope on kinetic plasma simulations", *Plasma Physics and Controlled Fusion* 50.12, p. 124034, DOI: 10.1088/0741-3335/50/12/124034, arXiv: 0810.2460, URL: http://adsabs.harvard.edu/abs/2008PPCF...50l4034F.

Freidberg, J. P. (2007), *Plasma Physics and Fusion Energy*,

Fujimoto, K. (2006), "Time evolution of the electron diffusion region and the reconnection rate in fully kinetic and large system", *Physics of Plasmas* 13.7, p. 072904, DOI: 10.1063/1.2220534, URL: http://adsabs.harvard.edu/abs/2006PhPl...13g2904F.

— (2009), "Fast magnetic reconnection in a kinked current sheet", *Physics of Plasmas* 16.4, p. 042103, DOI: 10.1063/1.3106685, URL: http://adsabs.harvard.edu/abs/2009PhPl...16d2103F.

Fujimoto, K. and S. Machida (2006), "Electromagnetic full particle code with adaptive mesh refinement technique: Application to the current sheet evolution", *Journal of Computational Physics* 214, pp. 550–566, DOI: 10.1016/j.jcp.2005.10.003, URL: http://adsabs.harvard.edu/abs/2006JCoPh.214..550F.

Gedalin, M. (1993), "Linear waves in relativistic anisotropic magnetohydrodynamics", *Phys. Rev. E* 47, pp. 4354–4357, DOI: 10.1103/PhysRevE.47.4354, URL: http://adsabs.harvard.edu/abs/1993PhRvE..47.4354G.

Giannios, D. (2010), "UHECRs from magnetic reconnection in relativistic jets", *MNRAS* 408, pp. L46–L50, DOI: 10.1111/j.1745-3933.2010.00925.x, arXiv: 1007.1522, URL: http://adsabs.harvard.edu/abs/2010MNRAS.408L..46G.

Giannios, D. and H. C. Spruit (2007), "Spectral and timing properties of a dissipative γ-ray burst photosphere", *A&A* 469, pp. 1–9, DOI: 10.1051/0004-6361:20066739, eprint: astro-ph/0611385, URL: http://cdsads.u-strasbg.fr/abs/2007A%26A...469....1G.

Giannios, D., D. A. Uzdensky, and M. C. Begelman (2009), "Fast TeV variability in blazars: jets in a jet", *MNRAS* 395, pp. L29–L33, DOI: 10.1111/j.1745-3933.2009.00635.x, arXiv: 0901.1877, URL: http://adsabs.harvard.edu/abs/2009MNRAS.395L..29G.

Giovanelli, R. G. (1947), "Magnetic and Electric Phenomena in the Sun's Atmosphere associated with Sunspots", *MNRAS* 107, p. 338, URL: http://adsabs.harvard.edu/abs/1947MNRAS.107..338G.

— (1948), "Chromospheric Flares", *MNRAS* 108, p. 163, URL: http://adsabs.harvard.edu/abs/1948MNRAS.108..163G.

Giroletti, M., G. Giovannini, L. Feretti, W. D. Cotton, P. G. Edwards, L. Lara, A. P. Marscher, J. R. Mattox, B. G. Piner, and T. Venturi (2004), "Parsec-Scale Properties of Markarian 501", *APJ* 600, pp. 127–140, DOI: 10.1086/379663, eprint: astro-ph/0309285, URL: http://adsabs.harvard.edu/abs/2004ApJ...600..127G.

Goldman, M. V., G. Lapenta, D. L. Newman, S. Markidis, and H. Che (2011), "Jet Deflection by Very Weak Guide Fields during Magnetic Reconnection", *Physical Review Letters* 107.13, 135001, p. 135001, DOI: 10.1103/PhysRevLett.107.135001, arXiv: 1011.0103, URL: http://adsabs.harvard.edu/abs/2011PhRvL.107m5001G.

Goodman, J. and D. Uzdensky (2008), "Reconnection in Marginally Collisionless Accretion Disk Coronae", *APJ* 688, pp. 555–558, DOI: 10.1086/592345, arXiv: 0804.4481, URL: http://adsabs.harvard.edu/abs/2008ApJ...688..555G.

Gould, R. J. and G. P. Schréder (1967), "Pair Production in Photon-Photon Collisions", *Physical Review* 155, pp. 1404–1407, DOI: 10.1103/PhysRev.155.1404, URL: http://adsabs.harvard.edu/abs/1967PhRv..155.1404G.

Graf von der Pahlen, J. and D. Tsiklauri (2014), "The effect of guide-field and boundary conditions on collisionless magnetic reconnection in a stressed X-point collapse", *Physics of Plasmas* 21.1, 012901, p. 012901, DOI: 10.1063/1.4861258, arXiv: 1312.5366, URL: http://adsabs.harvard.edu/abs/2014PhPl...21a2901G.

Greenwood, A. D., K. L. Cartwright, J. W. Luginsland, and E. A. Baca (2004), "On the elimination of numerical Cerenkov radiation in PIC simulations", *Journal of Computational Physics* 201, Provided by the SAO/NASA Astrophysics Data System, pp. 665–684, DOI: 10.1016/j.jcp.2004.06.021, URL: http://adsabs.harvard.edu/abs/2004JCoPh.201..665G.

Grosskopf, M., R. Drake, C. Kuranz, E. Rutter, J. Ross, N. Kugland, C. Plechaty, B. Remington, A. Spitkovsky, L. Gargate, G. Gregori, A. Bell, C. Murphy, J. Meinecke, B. Reville, Y. Sakawa, Y. Kuramitsu, H. Takabe, D. Froula, G. Fiksel, F. Miniati, M. Koenig, A. Ravasio, E. Liang, W. Fu, N. Woolsey, and H.-S. Park (2013), "Simulation of laser-driven, ablated plasma flows in collisionless shock experiments on OMEGA and the NIF", *High Energy Density Physics* 9.1, pp. 192 –197, DOI: 10.1016/j.hedp.2012.11.004, URL: http://www.sciencedirect.com/science/article/pii/S1574181812001309.

Grote, D. P., A. Friedman, J.-L. Vay, and I. Haber (2005), "The WARP Code: Modeling High Intensity Ion Beams", in: *Electron Cyclotron Resonance Ion Sources*, ed. by M. Leitner, vol. 749, American Institute of Physics Conference Series, pp. 55–58, DOI: 10.1063/1.1893366, URL: http://adsabs.harvard.edu/abs/2005AIPC..749...55G.

Guo, F., H. Li, W. Daughton, and Y.-H. Liu (2014), "Formation of Hard Power-laws in the Energetic Particle Spectra Resulting from Relativistic Magnetic Reconnection", *ArXiv e-prints*, arXiv: 1405.4040, URL: http://adsabs.harvard.edu/abs/2014arXiv1405.4040G.

Hale, G. E. (1908), "On the Probable Existence of a Magnetic Field in Sun-Spots", *APJ* 28, p. 315, DOI: 10.1086/141602, URL: http://adsabs.harvard.edu/abs/1908ApJ....28..315H.

Hartree, D. R. (1950), "Some calculations of transients in an electronic valve", *Appl.Sci.Res.* 1, pp. 379–390, DOI: 10.1007/BF02919956.

Harvey, J. W. (2006), "Chromospheric Magnetism", in: *Astronomical Society of the Pacific Conference Series*, ed. by R. Casini and B. W. Lites, vol. 358, Astronomical Society of the Pacific Conference Series, p. 419, URL: http://adsabs.harvard.edu/abs/2006ASPC..358..419H.

Hau, L.-N. and B.-J. Wang (2007), "On MHD waves, fire-hose and mirror instabilities in anisotropic plasmas", *Nonlinear Processes in Geophysics* 14, pp. 557–568, URL: http://adsabs.harvard.edu/abs/2007NPGeo..14..557H.

Haugboelle, T., J. Trier Fredriksen, and A. Nordlund (2012), "Photon-Plasma: a modern high-order particle-in-cell code", *ArXiv e-prints*, arXiv: 1211.4575, URL: http://adsabs.harvard.edu/abs/2012arXiv1211.4575H.

Hededal, C. (2005), "Gamma-Ray Bursts, Collisionless Shocks and Synthetic Spectra", PhD thesis, , Niels Bohr Institute, URL: http://adsabs.harvard.edu/abs/2005PhDT.....2H.

Hesse, M. and S. Zenitani (2007), "Dissipation in relativistic pair-plasma reconnection", *Physics of Plasmas* 14.11, p. 112102, DOI: 10.1063/1.2801482, URL: http://cdsads.u-strasbg.fr/abs/2007PhPl...14k2102H.

Hesse, M., K. Schindler, J. Birn, and M. Kuznetsova (1999), "The diffusion region in collisionless magnetic reconnection", *Physics of Plasmas* 6, pp. 1781–1795, DOI: 10.1063/1.873436, URL: http://cdsads.u-strasbg.fr/abs/1999PhPl...6.1781H.

Hesse, M., M. Kuznetsova, and J. Birn (2001), "Particle-in-cell simulations of three-dimensional collisionless magnetic reconnection", *J. Geoph. Research* 106, pp. 29831–29842, DOI: 10.1029/2001JA000075, URL: http://adsabs.harvard.edu/abs/2001JGR...10629831H.

Hesse, M., M. Kuznetsova, and M. Hoshino (2002), "The structure of the dissipation region for component reconnection: Particle simulations", *Geophysical Review Letters* 29, 1563, p. 1563, DOI: 10.1029/2001GL014714, URL: http://cdsads.u-strasbg.fr/abs/2002GeoRL..29.1563H.

Hesse, M., M. Kuznetsova, and J. Birn (2004), "The role of electron heat flux in guide-field magnetic reconnection", *Physics of Plasmas* 11, pp. 5387–5397, DOI: 10.1063/1.1795991, URL: http://cdsads.u-strasbg.fr/abs/2004PhPl...11.5387H.

Hesse, M., S. Zenitani, M. Kuznetsova, and A. Klimas (2009a), "A simple, analytical model of collisionless magnetic reconnection in a pair plasma", *Physics of Plasmas* 16.10, p. 102106, DOI: 10.1063/1.3246005, URL: http://adsabs.harvard.edu/abs/2009PhPl...16j2106H.

— (2009b), "Erratum: "A simple, analytical model of collisionless magnetic reconnection in a pair plasma" [Phys. Plasmas 16, 102106 (2009)]", *Physics of Plasmas* 16.12, p. 129906, DOI: 10.1063/1.3275791, URL: http://adsabs.harvard.edu/abs/2009PhPl...16l9906H.

Hesse, M., N. Aunai, S. Zenitani, M. Kuznetsova, and J. Birn (2013), "Aspects of collisionless magnetic reconnection in asymmetric systems", *Physics of Plasmas* 20.6, p. 061210, DOI: 10.1063/1.4811467, URL: http://adsabs.harvard.edu/abs/2013PhPl...20f1210H.

Hesse, M., T. Neukirch, K. Schindler, M. Kuznetsova, and S. Zenitani (2011), "The Diffusion Region in Collisionless Magnetic Reconnection", *Space Science Reviews* 160.1-4, pp. 3–23, ISSN: 0038-6308, DOI: 10.1007/s11214-010-9740-1, URL: http://dx.doi.org/10.1007/s11214-010-9740-1.

Higashimori, K. and M. Hoshino (2012), "The relation between ion temperature anisotropy and formation of slow shocks in collisionless magnetic reconnection", *Journal of Geophysical Research (Space Physics)* 117, A01220, p. 1220, DOI: 10.1029/2011JA016817, arXiv: 1201.4213, URL: http://adsabs.harvard.edu/abs/2012JGRA..117.1220H.

Hockney, R. W. (1966), "Computer Experiment of Anomalous Diffusion", *Physics of Fluids* 9, pp. 1826–1835, DOI: 10.1063/1.1761939, URL: http://adsabs.harvard.edu/abs/1966PhFl....9.1826H.

— (1971), "Measurements of Collision and Heating Times in a Two-Dimensional Thermal Computer Plasma", *Journal of Computational Physics* 8, p. 19, DOI: 10.1016/0021-9991(71)90032-5, URL: http://adsabs.harvard.edu/abs/1971JCoPh...8...19H.

Hockney, R. W. and J. W. Eastwood (1988), *Computer simulation using particles*, URL: http://adsabs.harvard.edu/abs/1988csup.book.....H.

Hodgson, R. (1859), "On a curious Appearance seen in the Sun", *MNRAS* 20, pp. 15–16, URL: http://adsabs.harvard.edu/abs/1859MNRAS..20...15H.

Hoh, F. C. (1966), "Stability of Sheet Pinch", *Physics of Fluids* 9, pp. 277–284, DOI: 10.1063/1.1761670, URL: http://adsabs.harvard.edu/abs/1966PhFl...9..277H.

Horiuchi, R., S. Usami, H. Ohtani, and T. Moritaka (2010), "Magnetic Reconnection Controlled by Multi-Hierarchy Physics in an Open System", *Plasma and Fusion Research* 5, p. 2006, DOI: 10.1585/pfr.5.S2006, URL: http://adsabs.harvard.edu/abs/2010PFR.....5S2006H.

Hoshino, M. (2012), "Stochastic Particle Acceleration in Multiple Magnetic Islands during Reconnection", *Physical Review Letters* 108.13, 135003, p. 135003, DOI: 10.1103/PhysRevLett.108.135003, arXiv: 1201.0837, URL: http://cdsads.u-strasbg.fr/abs/2012PhRvL.108m5003H.

Huang, J. and Z.-W. Ma (2008), "Reconnection Rate in Collisionless Magnetic Reconnection under Open Boundary Conditions", *Chinese Physics Letters* 25, pp. 1764–1767, DOI: 10.1088/0256-307X/25/5/066, URL: http://adsabs.harvard.edu/abs/2008ChPhL..25.1764H.

Huba, J. D. (2005), "Hall magnetic reconnection: Guide field dependence", *Physics of Plasmas* 12.1, p. 012322, DOI: 10.1063/1.1834592, URL: http://adsabs.harvard.edu/abs/2005PhPl...12a2322H.

IceCube Collaboration (2013), "Evidence for High-Energy Extraterrestrial Neutrinos at the IceCube Detector", *Science* 342.6161, DOI: 10.1126/science.1242856, eprint: http://www.sciencemag.org/content/342/6161/1242856.full.pdf, URL: http://adsabs.harvard.edu/abs/2013Sci...342E...1I.

Innocenti, M. E., G. Lapenta, S. Markidis, A. Beck, and A. Vapirev (2013), "A Multi Level Multi Domain Method for Particle In Cell plasma simulations", *Journal of Computational Physics* 238, pp. 115–140, DOI: 10.1016/j.jcp.2012.12.028, arXiv: 1201.6208, URL: http://adsabs.harvard.edu/abs/2013JCoPh.238..115I.

Ishizawa, A. and R. Horiuchi (2005), "Suppression of Hall-Term Effects by Gyroviscous Cancellation in Steady Collisionless Magnetic Reconnection", *Phys. Rev. Lett.* 95 (4), p. 045003, DOI: 10.1103/PhysRevLett.95.045003, URL: http://link.aps.org/doi/10.1103/PhysRevLett.95.045003.

Jackson, J. D. (1998), *Classical Electrodynamics, 3rd Edition*, ed. by Jackson, J. D., URL: http://adsabs.harvard.edu/abs/1998clel.book.....J.

Jaroschek, C. H. and M. Hoshino (2009), "Radiation-Dominated Relativistic Current Sheets", *Physical Review Letters* 103.7, 075002, p. 075002, DOI: 10.1103/PhysRevLett.103.075002, URL: http://adsabs.harvard.edu/abs/2009PhRvL.103g5002J.

Jaroschek, C. H., R. A. Treumann, H. Lesch, and M. Scholer (2004), "Fast reconnection in relativistic pair plasmas: Analysis of particle acceleration in self-consistent full particle simulations", *Physics of Plasmas* 11, pp. 1151–1163, DOI: 10.1063/1.1644814, URL: http://adsabs.harvard.edu/abs/2004PhPl...11.1151J.

Jaroschek, C. H., H. Lesch, and R. A. Treumann (2005), "Ultrarelativistic Plasma Shell Collisions in γ-Ray Burst Sources: Dimensional Effects on the Final Steady State Magnetic Field", *APJ* 618, pp. 822–831, DOI: 10.1086/426066, URL: http://adsabs.harvard.edu/abs/2005ApJ...618..822J.

Jaroschek, C. H., M. Hoshino, H. Lesch, and R. A. Treumann (2008), "Stochastic particle acceleration by the forced interaction of relativistic current sheets", *Advances in Space Research* 41, pp. 481–490, DOI: 10.1016/j.asr.2007.07.001, URL: http://adsabs.harvard.edu/abs/2008AdSpR..41..481J.

Ji, H. and W. Daughton (2011), "Phase diagram for magnetic reconnection in heliophysical, astrophysical, and laboratory plasmas", *Physics of Plasmas* 18.11, p. 111207, DOI: 10.1063/1.3647505, arXiv: 1109.0756, URL: http://adsabs.harvard.edu/abs/2011PhPl...18k1207J.

Jiang, Y.-F., J. M. Stone, and S. W. Davis (2014), "Radiation Magnetohydrodynamic Simulations of the Formation of Hot Accretion Disk Coronae", *APJ* 784, 169, p. 169, DOI: 10.1088/0004-637X/784/2/169, arXiv: 1402.2979, URL: http://cdsads.u-strasbg.fr/abs/2014ApJ...784..169J.

Jüttner, F. (1911), "Das Maxwellsche Gesetz der Geschwindigkeitsverteilung in der Relativtheorie", *Annalen der Physik* 339, pp. 856–882, DOI: 10.1002/andp.19113390503, URL: http://adsabs.harvard.edu/abs/1911AnP...339..856J.

Kagan, D., M. Milosavljević, and A. Spitkovsky (2013), "A Flux Rope Network and Particle Acceleration in Three-dimensional Relativistic Magnetic Recon-

nection", *APJ* 774, 41, p. 41, DOI: 10.1088/0004-637X/774/1/41, arXiv: 1208.0849, URL: http://adsabs.harvard.edu/abs/2013ApJ...774...41K.

Karimabadi, H., D. Krauss-Varban, J. D. Huba, and H. X. Vu (2004), "On magnetic reconnection regimes and associated three-dimensional asymmetries: Hybrid, Hall-less hybrid, and Hall-MHD simulations", *Journal of Geophysical Research (Space Physics)* 109, A09205, p. 9205, DOI: 10.1029/2004JA010478, URL: http://adsabs.harvard.edu/abs/2004JGRA..109.9205K.

Karimabadi, H., W. Daughton, and J. Scudder (2007), "Multi-scale structure of the electron diffusion region", *Geophysical Review Letters* 34, L13104, p. 13104, DOI: 10.1029/2007GL030306, URL: http://adsabs.harvard.edu/abs/2007GeoRL..3413104K.

Karimabadi, H., V. Roytershteyn, W. Daughton, and Y.-H. Liu (2013), "Recent Evolution in the Theory of Magnetic Reconnection and Its Connection with Turbulence", *Space Science Review* 178, pp. 307–323, DOI: 10.1007/s11214-013-0021-7, URL: http://cdsads.u-strasbg.fr/abs/2013SSRv..178..307K.

Kato, T. N. (2013), "Energy Loss of High-Energy Particles in Particle-in-Cell Simulation", *ArXiv e-prints*, arXiv: 1312.5507, URL: http://adsabs.harvard.edu/abs/2013arXiv1312.5507K.

Khotyaintsev, Y. V., A. Vaivads, A. Retinò, M. André, C. J. Owen, and H. Nilsson (2006), "Formation of Inner Structure of a Reconnection Separatrix Region", *Phys. Rev. Lett.* 97 (20), p. 205003, DOI: 10.1103/PhysRevLett.97.205003, URL: http://link.aps.org/doi/10.1103/PhysRevLett.97.205003.

Khotyaintsev, Y. V., A. Vaivads, M. André, M. Fujimoto, A. Retinò, and C. J. Owen (2010), "Observations of Slow Electron Holes at a Magnetic Reconnection Site", *Phys. Rev. Lett.* 105 (16), p. 165002, DOI: 10.1103/PhysRevLett.105.165002, URL: http://link.aps.org/doi/10.1103/PhysRevLett.105.165002.

Kirk, J. G. (2004), "Particle Acceleration in Relativistic Current Sheets", *Physical Review Letters* 92.18, 181101, p. 181101, DOI: 10.1103/PhysRevLett.92.181101, eprint: astro-ph/0403516, URL: http://adsabs.harvard.edu/abs/2004PhRvL..92r1101K.

Kirk, J. G. and O. Skjæraasen (2003), "Dissipation in Poynting-Flux-dominated Flows: The σ-Problem of the Crab Pulsar Wind", *APJ* 591, pp. 366–379, DOI: 10.1086/375215, eprint: arXiv:astro-ph/0303194, URL: http://adsabs.harvard.edu/abs/2003ApJ...591..366K.

Klimas, A., M. Hesse, and S. Zenitani (2008), "Particle-in-cell simulation of collisionless reconnection with open outflow boundaries", *Physics of Plasmas* 15.8, p. 082102, DOI: 10.1063/1.2965826, URL: http://adsabs.harvard.edu/abs/2008PhPl...15h2102K.

Klimas, A., M. Hesse, S. Zenitani, and M. Kuznetsova (2010), "Particle-in-cell simulation of collisionless driven reconnection with open boundaries", *Physics of Plasmas* 17.11, p. 112904, DOI: 10.1063/1.3510480, URL: http://adsabs.harvard.edu/abs/2010PhPl...17k2904K.

Klimontovich, I. L. (1982), "Kinetic theory of nonideal gases and nonideal plasmas", *Oxford Pergamon Press International Series on Natural Philosophy* 105, URL: http://adsabs.harvard.edu/abs/1982OISNP.105.....K.

Knizhnik, K., M. Swisdak, and J. F. Drake (2011), "The Acceleration of Ions in Solar Flares during Magnetic Reconnection", *Astrophysical Journal* 743, L35, p. L35, DOI: 10.1088/2041-8205/743/2/L35, arXiv: 1108.5750, URL: http://adsabs.harvard.edu/abs/2011ApJ...743L..35K.

Koide, S. and K. Arai (2008), "Energy Extraction from a Rotating Black Hole by Magnetic Reconnection in the Ergosphere", *APJ* 682, pp. 1124–1133, DOI: 10.1086/589497, arXiv: 0805.0044, URL: http://adsabs.harvard.edu/abs/2008ApJ...682.1124K.

Kojima, Y., J. Oogi, and Y. E. Kato (2011), "Relativistic magnetic reconnection at X-type neutral points", *A&A* 531, A47, A47, DOI: 10.1051/0004-6361/201116562, arXiv: 1104.1003, URL: http://adsabs.harvard.edu/abs/2011A%26A...531A..47K.

Kotani, T., N. Kawai, T. Aoki, J. Doty, M. Matsuoka, K. Mitsuda, F. Nagase, G. Ricker, and N. E. White (1994), "Discovery of the double Doppler-shifted emission-line systems in the X-ray spectrum of SS 433", *Publications of the Astronomical Society of Japan* 46, pp. L147–L150, URL: http://cdsads.u-strasbg.fr/abs/1994PASJ...46L.147K.

Kowal, G., A. Lazarian, E. T. Vishniac, and K. Otmianowska-Mazur (2009), "Numerical Tests of Fast Reconnection in Weakly Stochastic Magnetic Fields", *APJ* 700, pp. 63–85, DOI: 10.1088/0004-637X/700/1/63, arXiv: 0903.2052, URL: http://adsabs.harvard.edu/abs/2009ApJ...700...63K.

Kowal, G., E. M. de Gouveia Dal Pino, and A. Lazarian (2011), "Magnetohydrodynamic Simulations of Reconnection and Particle Acceleration: Three-dimensional Effects", *APJ* 735, 102, p. 102, DOI: 10.1088/0004-637X/735/2/102, arXiv: 1103.2984, URL: http://adsabs.harvard.edu/abs/2011ApJ...735..102K.

Kowal, G., A. Lazarian, E. T. Vishniac, and K. Otmianowska-Mazur (2012), "Reconnection studies under different types of turbulence driving", *Nonlinear Processes in Geophysics* 19, pp. 297–314, DOI: 10.5194/npg-19-297-2012, arXiv: 1203.2971, URL: http://cdsads.u-strasbg.fr/abs/2012NPGeo..19..297K.

Kronberg, P. P., S. A. Colgate, H. Li, and Q. W. Dufton (2004), "Giant Radio Galaxies and Cosmic-Ray Acceleration", *Astrophysical Journal* 604, pp. L77–L80, DOI: 10.1086/383614, URL: http://adsabs.harvard.edu/abs/2004ApJ...604L..77K.

Laing, E. W. and D. A. Diver (2013), "Ultra-relativistic electrostatic Bernstein waves", *Plasma Physics and Controlled Fusion* 55.6, 065006, p. 065006, DOI: 10.1088/0741-3335/55/6/065006, URL: http://adsabs.harvard.edu/abs/2013PPCF...55f5006L.

Lamers, H. J. G. L. M. and J. P. Cassinelli (1999), *Introduction to Stellar Winds*, URL: http://adsabs.harvard.edu/abs/1999isw..book.....L.

Landau, L. D. and E. M. Lifshitz (1975), *The classical theory of fields*, URL: http://adsabs.harvard.edu/abs/1975ctf..book.....L.

Langdon, A. B. (1970), "Effects of the Spatial Grid in Simulation Plasmas", *Journal of Computational Physics* 6, p. 247, DOI: 10.1016/0021-9991(70)90024-0, URL: http://adsabs.harvard.edu/abs/1970JCoPh...6..247L.

Lapenta, G. and A. Lazarian (2012), "Achieving fast reconnection in resistive MHD models via turbulent means", *Nonlinear Processes in Geophysics* 19, pp. 251–263, DOI: 10.5194/npg-19-251-2012, arXiv: 1110.0089, URL: http://adsabs.harvard.edu/abs/2012NPGeo..19..251L.

Lapenta, G., S. Markidis, A. Divin, D. Newman, and M. Goldman (2014), "Separatrices: the crux of reconnection", *ArXiv e-prints*, arXiv: 1406.6141, URL: http://adsabs.harvard.edu/abs/2014arXiv1406.6141L.

Larrabee, D. A., R. V. E. Lovelace, and M. M. Romanova (2003), "Lepton Acceleration by Relativistic Collisionless Magnetic Reconnection", *APJ* 586, pp. 72–78, DOI: 10.1086/367640, eprint: arXiv:astro-ph/0210045, URL: http://adsabs.harvard.edu/abs/2003ApJ...586...72L.

Lazar, A., E. Nakar, and T. Piran (2009), "Gamma-Ray Burst Light Curves in the Relativistic Turbulence and Relativistic Subjet Models", *Astrophysical Journal* 695, pp. L10–L14, DOI: 10.1088/0004-637X/695/1/L10, arXiv: 0901.1133, URL: http://cdsads.u-strasbg.fr/abs/2009ApJ...695L..10L.

Lazarian, A. and E. T. Vishniac (1999), "Reconnection in a Weakly Stochastic Field", *APJ* 517, pp. 700–718, DOI: 10.1086/307233, eprint: arXiv:astro-ph/9811037, URL: http://adsabs.harvard.edu/abs/1999ApJ...517..700L.

Lazarian, A., G. L. Eyink, and E. T. Vishniac (2012), "Relation of astrophysical turbulence and magnetic reconnection", *Physics of Plasmas* 19.1, p. 012105, DOI: 10.1063/1.3672516, arXiv: 1112.0022, URL: http://adsabs.harvard.edu/abs/2012PhPl...19a2105L.

Le, A., J. Egedal, O. Ohia, W. Daughton, H. Karimabadi, and V. S. Lukin (2013), "Regimes of the Electron Diffusion Region in Magnetic Reconnection", *Physical*

Review Letters 110.13, 135004, p. 135004, DOI: 10.1103/PhysRevLett.110.135004, URL: http://cdsads.u-strasbg.fr/abs/2013PhRvL.110m5004L.

Le, A., J. Egedal, J. Ng, H. Karimabadi, J. Scudder, V. Roytershteyn, W. Daughton, and Y.-H. Liu (2014), "Current sheets and pressure anisotropy in the reconnection exhaust", *Physics of Plasmas* 21.1, 012103, p. 012103, DOI: 10.1063/1.4861871, URL: http://cdsads.u-strasbg.fr/abs/2014PhPl...21a2103L.

Liang, E., M. Boettcher, and I. Smith (2011), "Magnetic Field Generation and Particle Energization at Relativistic Shear Boundaries in Collisionless Electron-Positron Plasmas", *ArXiv e-prints*, arXiv: 1111.3326, URL: http://adsabs.harvard.edu/abs/2011arXiv1111.3326L.

Liu, C., N. Deng, J. Lee, T. Wiegelmann, R. L. Moore, and H. Wang (2013a), "Evidence for Solar Tether-cutting Magnetic Reconnection from Coronal Field Extrapolations", *Astrophysical Journal* 778, L36, p. L36, DOI: 10.1088/2041-8205/778/2/L36, arXiv: 1310.5098, URL: http://adsabs.harvard.edu/abs/2013ApJ...778L..36L.

Liu, W., H. Li, L. Yin, B. J. Albright, K. J. Bowers, and E. P. Liang (2011), "Particle energization in 3D magnetic reconnection of relativistic pair plasmas", *Physics of Plasmas* 18.5, p. 052105, DOI: 10.1063/1.3589304, arXiv: 1005.2435, URL: http://adsabs.harvard.edu/abs/2011PhPl...18e2105L.

Liu, Y.-H., J. F. Drake, and M. Swisdak (2012), "The structure of the magnetic reconnection exhaust boundary", *Physics of Plasmas* 19.2, p. 022110, DOI: 10.1063/1.3685755, arXiv: 1111.7039, URL: http://adsabs.harvard.edu/abs/2012PhPl...19b2110L.

Liu, Y.-H., W. Daughton, H. Karimabadi, H. Li, and V. Roytershteyn (2013b), "Bifurcated Structure of the Electron Diffusion Region in Three-Dimensional Magnetic Reconnection", *Physical Review Letters* 110.26, 265004, p. 265004, DOI: 10.1103/PhysRevLett.110.265004, URL: http://cdsads.u-strasbg.fr/abs/2013PhRvL.110z5004L.

Liu, Y.-H., W. Daughton, H. Karimabadi, H. Li, and S. Peter Gary (2014), "Do dispersive waves play a role in collisionless magnetic reconnection?", *Physics of Plasmas* 21.2, 022113, p. 022113, DOI: 10.1063/1.4865579, URL: http://adsabs.harvard.edu/abs/2014PhPl...21b2113L.

Loureiro, N. F., A. A. Schekochihin, and S. C. Cowley (2007), "Instability of current sheets and formation of plasmoid chains", *Physics of Plasmas* 14.10, p. 100703, DOI: 10.1063/1.2783986, eprint: astro-ph/0703631, URL: http://adsabs.harvard.edu/abs/2007PhPl...14j0703L.

Loureiro, N. F., R. Samtaney, A. A. Schekochihin, and D. A. Uzdensky (2012), "Magnetic reconnection and stochastic plasmoid chains in high-Lundquist-number plasmas", *Physics of Plasmas* 19.4, p. 042303, DOI: 10.1063/1.3703318, arXiv: 1108.4040, URL: http://adsabs.harvard.edu/abs/2012PhPl...19d2303L.

Lyubarsky, Y. and M. Liverts (2008), "Particle Acceleration in the Driven Relativistic Reconnection", *APJ* 682, pp. 1436–1442, DOI: 10.1086/589640, arXiv: 0805.0085, URL: http://adsabs.harvard.edu/abs/2008ApJ...682.1436L.

Lyubarsky, Y. E. (2005), "On the relativistic magnetic reconnection", *MNRAS* 358, pp. 113–119, DOI: 10.1111/j.1365-2966.2005.08767.x, eprint: arXiv:astro-ph/0501392, URL: http://adsabs.harvard.edu/abs/2005MNRAS.358..113L.

Lyutikov, M. (2006a), "Did Swift measure gamma-ray burst prompt emission radii?", *MNRAS* 369, pp. L5–L8, DOI: 10.1111/j.1745-3933.2006.00161.x, eprint: astro-ph/0601557, URL: http://cdsads.u-strasbg.fr/abs/2006MNRAS.369L...5L.

— (2006b), "Magnetar giant flares and afterglows as relativistic magnetized explosions", *MNRAS* 367, pp. 1594–1602, DOI: 10.1111/j.1365-2966.2006.10069.x, eprint: astro-ph/0511711, URL: http://cdsads.u-strasbg.fr/abs/2006MNRAS.367.1594L.

Lyutikov, M. and A. Lazarian (2013), "Topics in Microphysics of Relativistic Plasmas", *Space Science Review* 178, pp. 459–481, DOI: 10.1007/s11214-013-

9989-2, arXiv: 1305.3838, URL: http://cdsads.u-strasbg.fr/abs/2013SSRv..178..459L.

Lyutikov, M. and D. Uzdensky (2003), "Dynamics of Relativistic Reconnection", *APJ* 589, pp. 893–901, DOI: 10.1086/374808, eprint: arXiv:astro-ph/0210206, URL: http://adsabs.harvard.edu/abs/2003ApJ...589..893L.

Markidis, S., P. Henri, G. Lapenta, A. Divin, M. V. Goldman, D. Newman, and S. Eriksson (2012), "Collisionless magnetic reconnection in a plasmoid chain", *Nonlinear Processes in Geophysics* 19, pp. 145–153, DOI: 10.5194/npg-19-145-2012, arXiv: 1202.2663, URL: http://adsabs.harvard.edu/abs/2012NPGeo..19..145M.

Markidis, S., P. Henri, G. Lapenta, A. Divin, M. Goldman, D. Newman, and E. Laure (2013), "Kinetic simulations of plasmoid chain dynamics", *Physics of Plasmas* 20.8, p. 082105, DOI: 10.1063/1.4817286, arXiv: 1306.1050, URL: http://adsabs.harvard.edu/abs/2013PhPl...20h2105M.

Markidis, S., G. Lapenta, and Rizwan-uddin (2010), "Multi-scale simulations of plasma with iPIC3D", *Mathematics and Computers in Simulation* 80.7, pp. 1509–1519, ISSN: 0378-4754, DOI: 10.1016/j.matcom.2009.08.038, URL: http://www.sciencedirect.com/science/article/pii/S0378475409002444.

Matsumoto, H. and Y. Omura (1993), *Computer Space Plasma Physics: Simulation Techniques and Software*, URL: http://www.terrapub.co.jp/e-library/cspp/index.html.

May, J., J. Tonge, I. Ellis, W. B. Mori, F. Fiuza, R. A. Fonseca, L. O. Silva, and C. Ren (2014), "Enhanced stopping of macro-particles in particle-in-cell simulations", *Physics of Plasmas* 21.5, 052703, p. 052703, DOI: 10.1063/1.4875708, arXiv: 1401.1198, URL: http://adsabs.harvard.edu/abs/2014PhPl...21e2703M.

McClintock, J. E. and R. A. Remillard (2006), "Black hole binaries", in: *Compact stellar X-ray sources*, ed. by W. H. G. Lewin and M. van der Klis, pp. 157–213, URL: http://adsabs.harvard.edu/abs/2006csxs.book..157M.

McKinney, J. C. and D. A. Uzdensky (2012), "A reconnection switch to trigger gamma-ray burst jet dissipation", *MNRAS* 419, pp. 573–607, DOI: 10.1111/j.1365-2966.2011.19721.x, arXiv: 1011.1904, URL: http://adsabs.harvard.edu/abs/2012MNRAS.419..573M.

McKinney, J. C., A. Tchekhovskoy, and R. D. Blandford (2012), "General relativistic magnetohydrodynamic simulations of magnetically choked accretion flows around black holes", *MNRAS* 423, pp. 3083–3117, DOI: 10.1111/j.1365-2966.2012.21074.x, arXiv: 1201.4163, URL: http://cdsads.u-strasbg.fr/abs/2012MNRAS.423.3083M.

Medvedev, M. V., M. Fiore, R. A. Fonseca, L. O. Silva, and W. B. Mori (2005), "Long-Time Evolution of Magnetic Fields in Relativistic Gamma-Ray Burst Shocks", *Astrophysical Journal* 618, pp. L75–L78, DOI: 10.1086/427921, eprint: arXiv:astro-ph/0409382, URL: http://adsabs.harvard.edu/abs/2005ApJ...618L..75M.

Melzani, M., C. Winisdoerffer, R. Walder, D. Folini, J. M. Favre, S. Krastanov, and P. Messmer (2013), "Apar-T: code, validation, and physical interpretation of particle-in-cell results", *A&A* 558, A133, A133, DOI: 10.1051/0004-6361/201321557, arXiv: 1308.5892, URL: http://adsabs.harvard.edu/abs/2013A\%26A...558A.133M.

Melzani, M., R. Walder, D. Folini, and C. Winisdoerffer (2014a), "Differences Between Real and Particle-In Plasmas: Effects of Coarse-Graining", *International Journal of Modern Physics Conference Series* 28, 1460194, p. 60194, DOI: 10.1142/S201019451460194X, arXiv: 1311.4709, URL: http://adsabs.harvard.edu/abs/2014IJMPS..2860194M.

Melzani, M., R. Walder, D. Folini, C. Winisdoerffer, and J. M. Favre (2014b), "Relativistic magnetic reconnection in collisionless ion-electron plasmas explored with particle-in-cell simulations", *A&A accepted*, DOI: 10.1051/0004-6361/201424083, arXiv: 1404.7366, URL: http://adsabs.harvard.edu/abs/2014arXiv1404.7366M.

— (2014c), "The energetics of relativistic magnetic reconnection: ion-electron repartition and particle distribution hardness", *A&A accepted*, DOI: 10.1051/0004-6361/201424193, arXiv: 1405.2938, URL: http://adsabs.harvard.edu/abs/2014arXiv1405.2938M.

Merloni, A. and A. C. Fabian (2001), "Accretion disc coronae as magnetic reservoirs", *MNRAS* 321, pp. 549–552, DOI: 10.1046/j.1365-8711.2001.04060.x, eprint: astro-ph/0009498, URL: http://cdsads.u-strasbg.fr/abs/2001MNRAS.321..549M.

Messmer, P. (2001), "Observations and simulations of particle acceleration in solar flares", PhD thesis, Institute of Astronomy, ETH Zürich, Switzerland, No 14412, URL: http://e-collection.library.ethz.ch/view/eth:24259.

— (2002), "Temperature isotropization in solar flare plasmas due to the electron firehose instability", *A&A* 382, pp. 301–311, DOI: 10.1051/0004-6361:20011583, eprint: arXiv:astro-ph/0111303, URL: http://cdsads.u-strasbg.fr/abs/2002A%26A...382..301M.

Meyer, M., D. Horns, and H.-S. Zechlin (2010), "The Crab Nebula as a standard candle in very high-energy astrophysics", *A&A* 523, A2, A2, DOI: 10.1051/0004-6361/201014108, arXiv: 1008.4524, URL: http://adsabs.harvard.edu/abs/2010A%26A...523A...2M.

Michno, M. J. and R. Schlickeiser (2010), "On the Magnetization of Cosmic Outflows: Plasma Modes and Instabilities of Unmagnetized Plasma Beams", *APJ* 714, pp. 868–880, DOI: 10.1088/0004-637X/714/1/868, URL: http://adsabs.harvard.edu/abs/2010ApJ...714..868M.

Mihalas, D. and B. W. Mihalas (1984), *Foundations of radiation hydrodynamics*, ed. by Mihalas, D. & Mihalas, B. W., URL: http://adsabs.harvard.edu/abs/1984oup..book.....M.

Moore, R. L. and A. C. Sterling (2006), "Initiation of Coronal Mass Ejections", *Washington DC American Geophysical Union Geophysical Monograph Series* 165, p. 43, URL: http://adsabs.harvard.edu/abs/2006GMS...165...43M.

Moreno-Insertis, F., K. Galsgaard, and I. Ugarte-Urra (2008), "Jets in Coronal Holes: Hinode Observations and Three-dimensional Computer Modeling", *The Astrophysical Journal Letters* 673.2, p. L211, URL: http://stacks.iop.org/1538-4357/673/i=2/a=L211.

Mott-Smith, H. M. (1971), "History of "Plasmas"", *Nature* 233, p. 219, DOI: 10.1038/233219a0, URL: http://adsabs.harvard.edu/abs/1971Natur.233..219M.

Narayan, R. and J. E. McClintock (2008), "Advection-dominated accretion and the black hole event horizon", *New Astronomy Review* 51, pp. 733–751, DOI: 10.1016/j.newar.2008.03.002, arXiv: 0803.0322, URL: http://adsabs.harvard.edu/abs/2008NewAR..51..733N.

Narayan, R. and I. Yi (1994), "Advection-dominated accretion: A self-similar solution", *Astrophysical Journal* 428, pp. L13–L16, DOI: 10.1086/187381, eprint: arXiv:astro-ph/9403052, URL: http://adsabs.harvard.edu/abs/1994ApJ...428L..13N.

Narayan, R., R. Mahadevan, and E. Quataert (1998), "Advection-dominated accretion around black holess", in: *Theory of Black Hole Accretion Disks*, ed. by M. A. Abramowicz, G. Bjornsson, & J. E. Pringle, p. 148, eprint: arXiv:astro-ph/9803141, URL: http://adsabs.harvard.edu/abs/1998tbha.conf..148N.

Nicholson, D. R. (1983), *Introduction to Plasma Theory*, ed. by John Wiley & Sons.

Nieter, C. and J. R. Cary (2004), "VORPAL: a versatile plasma simulation code", *Journal of Computational Physics* 196, pp. 448–473, DOI: 10.1016/j.jcp.2003.11.004, URL: http://adsabs.harvard.edu/abs/2004JCoPh.196..448N.

Nishikawa, K.-I., Y. Mizuno, G. J. Fishman, and P. Hardee (2008), "Particle Acceleration, Magnetic Field Generation, and Associated Emission in Collisionless Relativistic Jets", *International Journal of Modern Physics D* 17, pp. 1761–1767, DOI: 10.1142/S0218271808013388, arXiv: 0801.4390, URL: http://adsabs.harvard.edu/abs/2008IJMPD..17.1761N.

Nishikawa, K.-I., J. Niemiec, M. Medvedev, B. Zhang, P. Hardee, A. Nordlund, J. Frederiksen, Y. Mizuno, H. Sol, M. Pohl, D. H. Hartmann, and G. J. Fishman (2011), "Simulation of Relativistic Shocks and Associated Self-consistent Radiation", in: *American Institute of Physics Conference Series*, ed. by V. Florinski, J. Heerikhuisen, G. P. Zank, & D. L. Gallagher, vol. 1366, American Institute of Physics Conference Series, pp. 163–171, DOI: 10.1063/1.3625602, arXiv: 1111.3622, URL: http://adsabs.harvard.edu/abs/2011AIPC.1366..163N.

NIST Digital Library of Mathematical Functions (2013), http://dlmf.nist.gov/, Release 1.0.6 of 2013-05-06, Online companion to Olver, Lozier, Boisvert, and Clark (2010), URL: http://dlmf.nist.gov/.

Ohtani, H. and R. Horiuchi (2009), "Open Boundary Condition for Particle Simulation in Magnetic Reconnection Research", *Plasma and Fusion Research* 4, p. 24, DOI: 10.1585/pfr.4.024, URL: http://adsabs.harvard.edu/abs/2009PFR.....4...24O.

Olshevsky, V., G. Lapenta, and S. Markidis (2013), "Energetics of Kinetic Reconnection in a Three-Dimensional Null-Point Cluster", *Phys. Rev. Lett.* 111 (4), p. 045002, DOI: 10.1103/PhysRevLett.111.045002, URL: http://link.aps.org/doi/10.1103/PhysRevLett.111.045002.

Olver, F. W. J., D. W. Lozier, R. F. Boisvert, and C. W. Clark, eds. (2010), *NIST Handbook of Mathematical Functions*, Print companion to *NIST Digital Library of Mathematical Functions* (2013), New York, NY: Cambridge University Press.

Ono, Y., H. Tanabe, Y. Hayashi, T. Ii, Y. Narushima, T. Yamada, M. Inomoto, and C. Z. Cheng (2011), "Ion and Electron Heating Characteristics of Magnetic Reconnection in a Two Flux Loop Merging Experiment", *Phys. Rev. Lett.* 107 (18), p. 185001, DOI: 10.1103/PhysRevLett.107.185001, URL: http://link.aps.org/doi/10.1103/PhysRevLett.107.185001.

Padmanabhan, T. (2000), *Theoretical Astrophysics - Volume 1, Astrophysical Processes*, ed. by Padmanabhan, T., DOI: 10.2277/0521562406, URL: http://adsabs.harvard.edu/abs/2000thas.book.....P.

— (2001), *Theoretical Astrophysics - Volume 2, Stars and Stellar Systems*, ed. by Padmanabhan, T., DOI: 10.2277/0521562414, URL: http://adsabs.harvard.edu/abs/2001thas.book.....P.

Paesold, G., E. G. Blackman, and P. Messmer (2005), "On particle acceleration and trapping by Poynting flux dominated flows", *Plasma Physics and Controlled Fusion* 47, pp. 1925–1947, DOI: 10.1088/0741-3335/47/11/005, eprint: arXiv:astro-ph/0508530, URL: http://cdsads.u-strasbg.fr/abs/2005PPCF...47.1925P.

Parker, E. N. (1957), "Sweet's Mechanism for Merging Magnetic Fields in Conducting Fluids", *J. Geoph. Research* 62, pp. 509–520, DOI: 10.1029/JZ062i004p00509, URL: http://adsabs.harvard.edu/abs/1957JGR....62..509P.

— (1963), "The Solar-Flare Phenomenon and the Theory of Reconnection and Annihiliation of Magnetic Fields.", *apjs* 8, p. 177, DOI: 10.1086/190087, URL: http://adsabs.harvard.edu/abs/1963ApJS....8..177P.

Parnell, C. E. (2012), "Conference on magnetic reconnection, UPMC, Jussieu", in: URL: http://www.physique.upmc.fr/fr/recherche/plasma_a_upmc/seminaires_manifestations_communes/journee_plasmas_26_27_09_2012.html.

Parnell, C. E. and K. Galsgaard (2004), "Elementary heating events - magnetic interactions between two flux sources. II. Rates of flux reconnection", *A&A* 428, pp. 595–612, DOI: 10.1051/0004-6361:20034350.

Paschmann, G., M. Øieroset, and T. Phan (2013), "In-Situ Observations of Reconnection in Space", *Space Science Review* 178, pp. 385–417, DOI: 10.1007/s11214-012-9957-2, URL: http://adsabs.harvard.edu/abs/2013SSRv..178..385P.

Pei, W., R. Horiuchi, and T. Sato (2001), "Long time scale evolution of collisionless driven reconnection in a two-dimensional open system", *Physics of Plasmas* 8, pp. 3251–3257, DOI: 10.1063/1.1375150, URL: http://adsabs.harvard.edu/abs/2001PhPl....8.3251P.

Pétri, J. and J. G. Kirk (2007), "Growth rates of the Weibel and tearing mode instabilities in a relativistic pair plasma", *Plasma Physics and Controlled Fusion* 49, pp. 1885–1896, DOI: 10.1088/0741-3335/49/11/009, arXiv: 0710.1246, URL: http://adsabs.harvard.edu/abs/2007PPCF...49.1885P.

Pétri, J. and Y. Lyubarsky (2007), "Magnetic reconnection at the termination shock in a striped pulsar wind", *A&A* 473, pp. 683–700, DOI: 10.1051/0004-6361:20066981, URL: http://adsabs.harvard.edu/abs/2007A%26A...473..683P.

Petropoulou, M., D. Giannios, and S. Dimitrakoudis (2014), "What IceCube neutrinos teach us about the GRB location", *ArXiv e-prints*, arXiv: 1405.2091, URL: http://adsabs.harvard.edu/abs/2014arXiv1405.2091P.

Petschek, H. E. (1964), "Magnetic Field Annihilation", *NASA Special Publication* 50, p. 425, URL: http://adsabs.harvard.edu/abs/1964NASSP..50..425P.

Ping, Y. L., J. Y. Zhong, Z. M. Sheng, X. G. Wang, B. Liu, Y. T. Li, X. Q. Yan, X. T. He, J. Zhang, and G. Zhao (2014), "Three-dimensional fast magnetic reconnection driven by relativistic ultraintense femtosecond lasers", *Phys. Rev. E* 89.3, 031101, p. 031101, DOI: 10.1103/PhysRevE.89.031101, URL: http://adsabs.harvard.edu/abs/2014PhRvE..89c1101P.

Plotnikov, I., G. Pelletier, and M. Lemoine (2013), "Particle transport and heating in the microturbulent precursor of relativistic shocks", *MNRAS* 430, pp. 1280–1293, DOI: 10.1093/mnras/sts696, arXiv: 1206.6634, URL: http://cdsads.u-strasbg.fr/abs/2013MNRAS.430.1280P.

Pomraning, G. C. (1973), *The equations of radiation hydrodynamics*, URL: http://adsabs.harvard.edu/abs/1973erh..book.....P.

Pontin, D. I. (2011), "Three-dimensional magnetic reconnection regimes: A review", *Advances in Space Research* 47, pp. 1508–1522, DOI: 10.1016/j.asr.2010.12.022, arXiv: 1101.0924, URL: http://cdsads.u-strasbg.fr/abs/2011AdSpR..47.1508P.

Poutanen, J. and A. Veledina (2014), "Modelling Spectral and Timing Properties of Accreting Black Holes: The Hybrid Hot Flow Paradigm", *Space Science Review*, pp. 1–25, ISSN: 0038-6308, DOI: 10.1007/s11214-013-0033-3, URL: http://adsabs.harvard.edu/abs/2014SSRv..tmp....1P.

Priest, E. R. (1987), *Solar magneto-hydrodynamics*. URL: http://adsabs.harvard.edu/abs/1987smh..book.....P.

— (2011), "MHD reconnection", *Scholarpedia*, DOI: doi:10.4249/scholarpedia.2371, URL: http://www.scholarpedia.org/article/MHD_reconnection.

Priest, E. R. and T. G. Forbes (1986), "New models for fast steady state magnetic reconnection", *J. Geoph. Research* 91, pp. 5579–5588, DOI: 10.1029/JA091iA05p05579, URL: http://adsabs.harvard.edu/abs/1986JGR....91.5579P.

Pritchett, P. L. (2001), "Geospace Environment Modeling magnetic reconnection challenge: Simulations with a full particle electromagnetic code", *J. Geoph. Research* 106, pp. 3783–3798, DOI: 10.1029/1999JA001006, URL: http://adsabs.harvard.edu/abs/2001JGR...106.3783P.

— (2005a), "Externally driven magnetic reconnection in the presence of a normal magnetic field", *Journal of Geophysical Research (Space Physics)* 110, A05209, p. 5209, DOI: 10.1029/2004JA010948, URL: http://cdsads.u-strasbg.fr/abs/2005JGRA..110.5209P.

— (2005b), "The "Newton Challenge": Kinetic aspects of forced magnetic reconnection", *Journal of Geophysical Research (Space Physics)* 110, A10213, p. 10213, DOI: 10.1029/2005JA011228, URL: http://cdsads.u-strasbg.fr/abs/2005JGRA..11010213P.

— (2010), "Onset of magnetic reconnection in the presence of a normal magnetic field: Realistic ion to electron mass ratio", *Journal of Geophysical Research (Space Physics)* 115, A10208, p. 10208, DOI: 10.1029/2010JA015371, URL: http://cdsads.u-strasbg.fr/abs/2010JGRA..11510208P.

— (2013), "The influence of intense electric fields on three-dimensional asymmetric magnetic reconnection", *Physics of Plasmas* 20.6, p. 061204, DOI: 10.1063/1.4811123, URL: http://adsabs.harvard.edu/abs/2013PhPl...20f1204P.

Pritchett, P. L. and F. V. Coroniti (2004), "Three-dimensional collisionless magnetic reconnection in the presence of a guide field", *Journal of Geophysical Research (Space Physics)* 109, A01220, p. 1220, DOI: 10.1029/2003JA009999, URL: http://adsabs.harvard.edu/abs/2004JGRA..109.1220P.

Régnier, S., C. E. Parnell, and A. L. Haynes (2008), "A new view of quiet-Sun topology from Hinode/SOT", *A&A* 484, pp. L47–L50, DOI: 10.1051/0004-6361:200809826, arXiv: 0805.1602, URL: http://cdsads.u-strasbg.fr/abs/2008A%26A...484L..47R.

Reis, R. C. and J. M. Miller (2013), "On the Size and Location of the X-Ray Emitting Coronae around Black Holes", *Astrophysical Journal* 769, L7, p. L7, DOI: 10.1088/2041-8205/769/1/L7, arXiv: 1304.4947, URL: http://adsabs.harvard.edu/abs/2013ApJ...769L...7R.

Ricci, P., G. Lapenta, and J. U. Brackbill (2002), "GEM reconnection challenge: Implicit kinetic simulations with the physical mass ratio", *Geophysical Research Letters* 29.23, pp. 3–1–3–4, ISSN: 1944-8007, DOI: 10.1029/2002GL015314, URL: http://dx.doi.org/10.1029/2002GL015314.

— (2003), "Electron acceleration and heating in collisionless magnetic reconnection", *Physics of Plasmas (1994-present)* 10.9, pp. 3554–3560, DOI: http://dx.doi.org/10.1063/1.1598207, URL: http://scitation.aip.org/content/aip/journal/pop/10/9/10.1063/1.1598207.

Rogers, B. N., R. E. Denton, J. F. Drake, and M. A. Shay (2001), "Role of Dispersive Waves in Collisionless Magnetic Reconnection", *Physical Review Letters* 87.19, 195004, p. 195004, DOI: 10.1103/PhysRevLett.87.195004, URL: http://adsabs.harvard.edu/abs/2001PhRvL..87s5004R.

Romanova, M. M. and R. V. E. Lovelace (1992), "Magnetic field, reconnection, and particle acceleration in extragalactic jets", *A&A* 262, pp. 26–36, URL: http://adsabs.harvard.edu/abs/1992A%26A...262...26R.

Romero, G. E., F. L. Vieyro, and S. Chaty (2014), "Coronal origin of the polarization of the high-energy emission of Cygnus X-1", *A&A* 562, L7, p. L7, DOI: 10.1051/0004-6361/201323316, arXiv: 1402.0524, URL: http://cdsads.u-strasbg.fr/abs/2014A%26A...562L...7R.

Rybicki, G. B. and A. P. Lightman (1979), *Radiative processes in astrophysics*, ed. by Rybicki, G. B. & Lightman, A. P., URL: http://adsabs.harvard.edu/abs/1979rpa..book.....R.

Sakai, J.-I., S. Saito, H. Mae, D. Farina, M. Lontano, F. Califano, F. Pegoraro, and S. V. Bulanov (2002), "Ion acceleration, magnetic field line reconnection, and multiple current filament coalescence of a relativistic electron beam in a plasma", *Physics of Plasmas* 9, pp. 2959–2970, DOI: 10.1063/1.1484156, URL: http://adsabs.harvard.edu/abs/2002PhPl....9.2959S.

Schmitz, H. and R. Grauer (2006), "Kinetic Vlasov simulations of collisionless magnetic reconnection", *Physics of Plasmas* 13.9, p. 092309, DOI: 10.1063/1.2347101, eprint: physics/0608175, URL: http://cdsads.u-strasbg.fr/abs/2006PhPl...13i2309S.

Schrijver, C. J., R. Dobbins, W. Murtagh, and S. M. Petrinec (2014), "Assessing the impact of space weather on the electric power grid based on insurance claims for industrial electrical equipment", *ArXiv e-prints*, arXiv: 1406.7024, URL: http://adsabs.harvard.edu/abs/2014arXiv1406.7024S.

Schwartz, D. A., H. L. Marshall, J. E. J. Lovell, D. W. Murphy, G. V. Bicknell, M. Birkinshaw, J. Gelbord, M. Georganopoulos, L. Godfrey, D. L. Jauncey, E. S. Perlman, and D. M. Worrall (2006), "Chandra Observations of Magnetic Fields and Relativistic Beaming in Four Quasar Jets", *APJ* 640, pp. 592–602, DOI: 10.1086/500102, eprint: astro-ph/0601632, URL: http://cdsads.u-strasbg.fr/abs/2006ApJ...640..592S.

Shay, M. A., J. F. Drake, and M. Swisdak (2007), "Two-Scale Structure of the Electron Dissipation Region during Collisionless Magnetic Reconnection", *Physical Review Letters* 99.15, 155002, p. 155002, DOI: 10.1103/PhysRevLett.99.155002, arXiv: 0704.0818, URL: http://adsabs.harvard.edu/abs/2007PhRvL..99o5002S.

Shibata, K. and S. Tanuma (2001), "Plasmoid-induced-reconnection and fractal reconnection", *Earth, Planets, and Space* 53, pp. 473–482, eprint: astro-ph/0101008, URL: http://cdsads.u-strasbg.fr/abs/2001EP%26S...53..473S.

Silva, L. O., R. A. Fonseca, J. W. Tonge, J. M. Dawson, W. B. Mori, and M. V. Medvedev (2003), "Interpenetrating Plasma Shells: Near-equipartition Magnetic Field Generation and Nonthermal Particle Acceleration", *Astrophysical Journal* 596, pp. L121–L124, DOI: 10.1086/379156, eprint: arXiv:astro-ph/0307500, URL: http://adsabs.harvard.edu/abs/2003ApJ...596L.121S.

Sironi, L. and A. Spitkovsky (2011a), "Acceleration of Particles at the Termination Shock of a Relativistic Striped Wind", *APJ* 741, 39, p. 39, DOI: 10.1088/0004-637X/741/1/39, arXiv: 1107.0977, URL: http://adsabs.harvard.edu/abs/2011ApJ...741...39S.

— (2011b), "Particle Acceleration in Relativistic Magnetized Collisionless Electron-Ion Shocks", *APJ* 726, pp. 75–+, DOI: 10.1088/0004-637X/726/2/75, arXiv: 1009.0024, URL: http://adsabs.harvard.edu/abs/2011ApJ...726...75S.

— (2014), "Relativistic Reconnection: An Efficient Source of Non-thermal Particles", *Astrophysical Journal* 783, L21, p. L21, DOI: 10.1088/2041-8205/783/1/L21, arXiv: 1401.5471, URL: http://adsabs.harvard.edu/abs/2014ApJ...783L..21S.

Sitnov, M. I. and M. Swisdak (2011), "Onset of collisionless magnetic reconnection in two-dimensional current sheets and formation of dipolarization fronts", *Journal of Geophysical Research (Space Physics)* 116, A12216, p. 12216, DOI: 10.1029/2011JA016920, URL: http://cdsads.u-strasbg.fr/abs/2011JGRA..11612216S.

Smets, R., N. Aunai, G. Belmont, C. Boniface, and J. Fuchs (2014), "On the relationship between quadrupolar magnetic field and collisionless reconnection", *Physics of Plasmas (1994-present)* 21.6, 062111, pp. –, DOI: http://dx.doi.org/10.1063/1.4885097, URL: http://scitation.aip.org/content/aip/journal/pop/21/6/10.1063/1.4885097.

Speiser, T. W. (1965), "Acceleration of particles in the neutral sheet of the geomagnetic tail.", in: *International Cosmic Ray Conference*, vol. 1, International Cosmic Ray Conference, p. 147, URL: http://adsabs.harvard.edu/abs/1965ICRC....1..147S.

Spitkovsky, A. (2005), "Simulations of relativistic collisionless shocks: shock structure and particle acceleration", in: *Astrophysical Sources of High Energy Particles and Radiation*, ed. by T. Bulik, B. Rudak, & G. Madejski, vol. 801, American Institute of Physics Conference Series, pp. 345–350, DOI: 10.1063/1.2141897, eprint: arXiv:astro-ph/0603211, URL: http://adsabs.harvard.edu/abs/2005AIPC..801..345S.

Spitzer, L. (1965), *Physics of fully ionized gases*, URL: http://adsabs.harvard.edu/abs/1965pfig.book.....S.

Sweet, P. A. (1958), "The Neutral Point Theory of Solar Flares", in: *Electromagnetic Phenomena in Cosmical Physics*, ed. by B. Lehnert, vol. 6, IAU Symposium, p. 123, URL: http://adsabs.harvard.edu/abs/1958IAUS....6..123S.

Swisdak, M. (2013), "The Generation of Random Variates From a Relativistic Maxwellian Distribution", *ArXiv e-prints*, arXiv: 1305.5226, URL: http://adsabs.harvard.edu/abs/2013arXiv1305.5226S.

Takahashi, H. R., T. Kudoh, Y. Masada, and J. Matsumoto (2011), "Scaling Law of Relativistic Sweet-Parker-type Magnetic Reconnection", *Astrophysical Journal* 739, L53, Provided by the SAO/NASA Astrophysics Data System, p. L53, DOI: 10.1088/2041-8205/739/2/L53, arXiv: 1108.3891, URL: http://adsabs.harvard.edu/abs/2011ApJ...739L..53T.

Takamoto, M. (2013), "Evolution of Relativistic Plasmoid Chains in a Poynting-dominated Plasma", *APJ* 775, 50, p. 50, DOI: 10.1088/0004-637X/775/1/50, arXiv: 1307.5677, URL: http://adsabs.harvard.edu/abs/2013ApJ...775..50T.

Tenbarge, J. M., R. D. Hazeltine, and S. M. Mahajan (2010), "Relativistic Petschek reconnection with pressure anisotropy in a pair-plasma", *MNRAS* 403, pp. 335–

341, DOI: 10.1111/j.1365-2966.2009.16116.x, URL: http://adsabs.harvard.edu/abs/2010MNRAS.403..335T.

TenBarge, J. M., W. Daughton, H. Karimabadi, G. G. Howes, and W. Dorland (2014), "Collisionless reconnection in the large guide field regime: Gyrokinetic versus particle-in-cell simulations", *Physics of Plasmas* 21.2, 020708, p. 020708, DOI: 10.1063/1.4867068, arXiv: 1312.5166, URL: http://adsabs.harvard.edu/abs/2014PhPl...21b0708T.

Tien, P. K. and J. Moshman (1956), "Monte Carlo Calculation of Noise Near the Potential Minimum of a High-Frequency Diode", *Journal of Applied Physics* 27, pp. 1067–1078, DOI: 10.1063/1.1722543, URL: http://adsabs.harvard.edu/abs/1956JAP....27.1067T.

Treumann, R. A., C. H. Jaroschek, R. Nakamura, A. Runov, and M. Scholer (2006), "The role of the Hall effect in collisionless magnetic reconnection", *Advances in Space Research* 38, pp. 101–111, DOI: 10.1016/j.asr.2004.11.045, URL: http://adsabs.harvard.edu/abs/2006AdSpR..38..101T.

Treumann, R. A., R. Nakamura, and W. Baumjohann (2011), "Relativistic transformation of phase-space distributions", *Annales Geophysicae* 29, pp. 1259–1265, DOI: 10.5194/angeo-29-1259-2011, arXiv: 1105.2120, URL: http://adsabs.harvard.edu/abs/2011AnGeo..29.1259T.

Treumann, R. A., W. Baumjohann, and W. D. Gonzalez (2012), "Collisionless reconnection: The sub-microscale mechanism of magnetic field line interaction", *ArXiv e-prints*, arXiv: 1202.6209, URL: http://adsabs.harvard.edu/abs/2012arXiv1202.6209T.

Treumann, R. A. and W. Baumjohann (2013), "Collisionless Magnetic Reconnection in Space Plasmas", *Frontiers in Physics* 1.31, ISSN: 2296-424X, DOI: 10.3389/fphy.2013.00031, URL: http://www.frontiersin.org/space_physics/10.3389/fphy.2013.00031/abstract.

Trier Frederiksen, J., T. Haugbølle, M. V. Medvedev, and Å. Nordlund (2010), "Radiation Spectral Synthesis of Relativistic Filamentation", *Astrophysical Journal* 722, pp. L114–L119, DOI: 10.1088/2041-8205/722/1/L114, arXiv: 1003.1140, URL: http://adsabs.harvard.edu/abs/2010ApJ...722L.114F.

Umeda, T., K. Togano, and T. Ogino (2009), "Two-dimensional full-electromagnetic Vlasov code with conservative scheme and its application to magnetic reconnection", *Computer Physics Communications* 180, pp. 365–374, DOI: 10.1016/j.cpc.2008.11.001, URL: http://cdsads.u-strasbg.fr/abs/2009CoPhC.180..365U.

Uzdensky, D. A. (2006), "Magnetic Reconnection in Astrophysical Systems", *ArXiv Astrophysics e-prints*, eprint: arXiv:astro-ph/0607656, URL: http://adsabs.harvard.edu/abs/2006astro.ph..7656U.

— (2011), "Magnetic Reconnection in Extreme Astrophysical Environments", *Space Science Review* 160, pp. 45–71, DOI: 10.1007/s11214-011-9744-5, arXiv: 1101.2472, URL: http://adsabs.harvard.edu/abs/2011SSRv..160...45U.

Uzdensky, D. A., N. F. Loureiro, and A. A. Schekochihin (2010), "Fast Magnetic Reconnection in the Plasmoid-Dominated Regime", *Physical Review Letters* 105.23, 235002, p. 235002, DOI: 10.1103/PhysRevLett.105.235002, arXiv: 1008.3330, URL: http://cdsads.u-strasbg.fr/abs/2010PhRvL.105w5002U.

Uzdensky, D. A., B. Cerutti, and M. C. Begelman (2011), "Reconnection-powered Linear Accelerator and Gamma-Ray Flares in the Crab Nebula", *Astrophysical Journal* 737, L40, p. L40, DOI: 10.1088/2041-8205/737/2/L40, arXiv: 1105.0942, URL: http://adsabs.harvard.edu/abs/2011ApJ...737L..40U.

Vapirev, A. E., G. Lapenta, A. Divin, S. Markidis, P. Henri, M. Goldman, and D. Newman (2013), "Formation of a transient front structure near reconnection point in 3-D PIC simulations", *Journal of Geophysical Research (Space Physics)* 118, pp. 1435–1449, DOI: 10.1002/jgra.50136, URL: http://adsabs.harvard.edu/abs/2013JGRA..118.1435V.

Vay, J.-L. (2008), "Simulation of beams or plasmas crossing at relativistic velocity", *Physics of Plasmas* 15.5, p. 056701, DOI: 10.1063/1.2837054, URL: http://adsabs.harvard.edu/abs/2008PhPl...15e6701V.

Walder, R., M. Melzani, D. Folini, C. Winisdoerffer, and J. M. Favre (2014), "Simulation of microquasars – the challenge of scales", *ASTRONUM 2013, Conf. Proceedings, in press, astro-ph:1405.0600*, arXiv: 1405.0600, URL: http://adsabs.harvard.edu/abs/2014arXiv1405.0600W.

Watanabe, N. and T. Yokoyama (2006), "Two-dimensional Magnetohydrodynamic Simulations of Relativistic Magnetic Reconnection", *Astrophysical Journal* 647, pp. L123–L126, DOI: 10.1086/507520, eprint: arXiv:astro-ph/0607285, URL: http://adsabs.harvard.edu/abs/2006ApJ...647L.123W.

Whitlock, B., J. M. Favre, and J. Meredith (2011), "Parallel In Situ Coupling of Simulation with a Fully Featured Visualization System", in: In Proceedings of the 11th Eurographics Symposium on Parallel Graphics and Visualization (EGPGV'11), pp. 101–109.

Winter, W. (2012), "Neutrinos from Cosmic Accelerators Including Magnetic Field and Flavor Effects", *ArXiv e-prints*, arXiv: 1201.5462, URL: http://adsabs.harvard.edu/abs/2012arXiv1201.5462W.

Yamada, M. (2011), "Understanding the Dynamics of Magnetic Reconnection Layer", *Space Science Review* 160, pp. 25–43, DOI: 10.1007/s11214-011-9789-5, URL: http://adsabs.harvard.edu/abs/2011SSRv..160...25Y.

Yamada, M., R. Kulsrud, and H. Ji (2010), "Magnetic reconnection", *Reviews of Modern Physics* 82, pp. 603–664, DOI: 10.1103/RevModPhys.82.603, URL: http://adsabs.harvard.edu/abs/2010RvMP...82..603Y.

Yu, S. P., G. P. Kooyers, and O. Buneman (1965), "Time-Dependent Computer Analysis of Electron-Wave Interaction in Crossed Fields", *Journal of Applied Physics* 36, pp. 2550–2559, DOI: 10.1063/1.1714528, URL: http://adsabs.harvard.edu/abs/1965JAP....36.2550Y.

Zanotti, O. and M. Dumbser (2011), "Numerical simulations of high Lundquist number relativistic magnetic reconnection", *MNRAS* 418, pp. 1004–1011, DOI: 10.1111/j.1365-2966.2011.19551.x, arXiv: 1103.5924, URL: http://adsabs.harvard.edu/abs/2011MNRAS.418.1004Z.

Zdziarski, A. A., P. Pjanka, M. Sikora, and Ł. Stawarz (2014), "Jet contributions to the broad-band spectrum of Cyg X-1 in the hard state", *MNRAS* 442, pp. 3243–3255, DOI: 10.1093/mnras/stu1009, arXiv: 1403.4768, URL: http://adsabs.harvard.edu/abs/2014MNRAS.442.3243Z.

Zenitani, S. and M. Hesse (2008), "Self-Regulation of the Reconnecting Current Layer in Relativistic Pair Plasma Reconnection", *APJ* 684, pp. 1477–1485, DOI: 10.1086/590425, arXiv: 0805.4286, URL: http://adsabs.harvard.edu/abs/2008ApJ...684.1477Z.

Zenitani, S. and M. Hoshino (2001), "The Generation of Nonthermal Particles in the Relativistic Magnetic Reconnection of Pair Plasmas", *Astrophysical Journal* 562, pp. L63–L66, DOI: 10.1086/337972, URL: http://adsabs.harvard.edu/abs/2001ApJ...562L..63Z.

— (2005a), "Relativistic Particle Acceleration in a Folded Current Sheet", *Astrophysical Journal* 618, pp. L111–L114, DOI: 10.1086/427873, eprint: arXiv:astro-ph/0411373, URL: http://adsabs.harvard.edu/abs/2005ApJ...618L.111Z.

— (2005b), "Three-Dimensional Evolution of a Relativistic Current Sheet: Triggering of Magnetic Reconnection by the Guide Field", *Physical Review Letters* 95.9, 095001, p. 095001, DOI: 10.1103/PhysRevLett.95.095001, eprint: astro-ph/0505493, URL: http://adsabs.harvard.edu/abs/2005PhRvL..95i5001Z.

— (2007), "Particle Acceleration and Magnetic Dissipation in Relativistic Current Sheet of Pair Plasmas", *APJ* 670, pp. 702–726, DOI: 10.1086/522226, arXiv: 0708.1000, URL: http://adsabs.harvard.edu/abs/2007ApJ...670..702Z.

— (2008), "The Role of the Guide Field in Relativistic Pair Plasma Reconnection", *APJ* 677, pp. 530–544, DOI: 10.1086/528708, arXiv: 0712.2016, URL: http://adsabs.harvard.edu/abs/2008ApJ...677..530Z.

Zenitani, S., M. Hesse, and A. Klimas (2009a), "Relativistic Two-fluid Simulations of Guide Field Magnetic Reconnection", *APJ* 705, pp. 907–913, DOI: 10.1088/

0004-637X/705/1/907, arXiv: 0909.1955, URL: http://adsabs.harvard.edu/abs/2009ApJ...705..907Z.

Zenitani, S., M. Hesse, and A. Klimas (2009b), "Two-Fluid Magnetohydrodynamic Simulations of Relativistic Magnetic Reconnection", *APJ* 696, pp. 1385–1401, DOI: 10.1088/0004-637X/696/2/1385, arXiv: 0902.2074, URL: http://adsabs.harvard.edu/abs/2009ApJ...696.1385Z.

— (2011a), "Fluid and Magnetofluid Modeling of Relativistic Magnetic Reconnection", in: *American Institute of Physics Conference Series*, ed. by V. Florinski, J. Heerikhuisen, G. P. Zank, & D. L. Gallagher, vol. 1366, American Institute of Physics Conference Series, pp. 138–144, DOI: 10.1063/1.3625599, arXiv: 1101.0370, URL: http://adsabs.harvard.edu/abs/2011AIPC.1366..138Z.

Zenitani, S., M. Hesse, A. Klimas, and M. Kuznetsova (2011b), "New Measure of the Dissipation Region in Collisionless Magnetic Reconnection", *Physical Review Letters* 106.19, 195003, p. 195003, DOI: 10.1103/PhysRevLett.106.195003, arXiv: 1104.3846, URL: http://adsabs.harvard.edu/abs/2011PhRvL.106s5003Z.

Zenitani, S., I. Shinohara, T. Nagai, and T. Wada (2013), "Kinetic aspects of the ion current layer in a reconnection outflow exhaust", *Physics of Plasmas* 20.9, p. 092120, DOI: 10.1063/1.4821963, arXiv: 1306.2705, URL: http://adsabs.harvard.edu/abs/2013PhPl...20i2120Z.

Zhang, S.-N. (2013), "Black hole binaries and microquasars", *Frontiers of Physics* 8, pp. 630–660, DOI: 10.1007/s11467-013-0306-z, arXiv: 1302.5485, URL: http://adsabs.harvard.edu/abs/2013FrPhy...8..630Z.